FLUORIDE ION DONOR-ACCEPTOR PROPERTIES OF *cis*-OsO_2F_4 AND LEWIS ACID PROPERTIES OF OsO_3F_2 AND $XeOF_4$

FLUORIDE ION DONOR-ACCEPTOR PROPERTIES OF *cis*-OsO_2F_4 AND LEWIS ACID PROPERTIES OF OsO_3F_2 AND $XeOF_4$

By

MICHAEL J. HUGHES

A Thesis

Submitted to the School of Graduate Studies

in Partial Fulfillment of the Requirements

for the Degree

Doctor of Philosophy

McMaster University

DOCTOR OF PHILOSOPHY — McMaster University

(Chemistry) — Hamilton, Ontario

TITLE: FLUORIDE ION DONOR-ACCEPTOR PROPERTIES OF *cis*-OsO_2F_4 AND LEWIS ACID PROPERTIES OF OsO_3F_2 AND $XeOF_4$

AUTHOR: Michael J. Hughes, B. Sc. (Acadia University)

SUPERVISOR: Professor Gary J. Schrobilgen

NUMBER OF PAGES: 424, xxxii

ABSTRACT

Reaction of *cis*-OsO_2F_4 with the strong Lewis acid, SbF_5, yields [*cis*-OsO_2F_3][Sb_2F_{11}] which has been characterized by single crystal X-ray crystallography and low-temperature Raman spectroscopy. The structure of the salt consists of a closely associated ion-pair in which a fluorine atom from the anion coordinates to the cation rendering the osmium atom pseudo-octahedral. Reaction of *cis*-OsO_2F_4 with the fluoride ion sources [M][F] (M = Cs^+ and $N(CH_3)_4^+$) yielded the corresponding salts of the $OsO_2F_5^-$ anion. The structure of this anion was studied by Raman spectroscopy and ^{19}F NMR spectroscopy which revealed that the geometry of the anion is a *cis*-dioxo monocapped trigonal prism. The anion represents a rare example of a d^0 seven-coordinate species. Attempts to obtain the crystal structure of this anion, however, proved unsuccessful. Dissolution of [M][OsO_2F_5] in CH_3CN and subsequent crystal growth yielded crystals of *cis*-OsO_2F_4·[M][CH_2CN]. The structure represents the first examples of an isolated CH_2CN^- anion, formed by a fluoride ion from *cis*-$OsO_2F_5^-$ abstracting a proton from the CH_3CN solvent to give *cis*-OsO_2F_4, CH_2CN^- and HF. In a separate crystal growth, crystals of *cis*-OsO_2F_4 were grown by sublimation from an XeF_6 melt. Together with the structures of *cis*-OsO_2F_4·[M][CH_2CN], the *cis*-OsO_2F_4 structure represent the first examples of non-disordered crystal structures of *cis*-OsO_2F_4.

Dissolution of the fluorine bridged polymer *fac*-$(OsO_3F_2)_\infty$ in $XeOF_4$ at room temperature resulted in a new phase of OsO_3F_2, namely the fluorine bridged dimer $(OsO_3F_2)_2$. The crystal structure of the dimer grown from $XeOF_4$ solvent contains two adducted $XeOF_4$ molecules which coordinate to the terminal fluorines of the dimer (one

per osmium atom) to give a structural unit formulated as $(OsO_3F_2)_2 \cdot 2XeOF_4$. Both osmium atoms are six-coordinate with a *fac*-trioxo arrangement. Further removal of $XeOF_4$ under dynamic vacuum yields only the dimer which was characterized by Raman spectroscopy and rearranges to the open chain polymeric structure of *fac*-OsO_3F_2 when warmed to room temperature. When CH_3CN is used as a solvent, the nitrogen atom adducts to $(OsO_3F_2)_\infty$ to form $OsO_3F_2(NCCH_3)$. In SO_2ClF solution both the *fac*- and *mer*-isomers are observed by ^{19}F, ^{15}N, and ^{1}H NMR spectroscopy, while only the *fac*-isomer is present in the solid state.

Stoichiometric amounts of XeF_6 and $(OsO_3F_2)_\infty$ react to form the $[XeF_5][\mu\text{-}F(OsO_3F_2)_2]$, $[XeF_5][OsO_3F_3]$, and $[Xe_2F_{11}][OsO_3F_3]$ salts. The series provides the first examples of noble-gas cations that are stabilized by metal oxide fluoride anions, and the first example of a $\mu\text{-}F(OsO_3F_2)_2^-$ salt. The osmium atoms in all three salts are six-coordinate with *fac*-trioxo arrangements. The anions and cations of each ion pair are highly associated through fluorine bridges from the anion to the cation rendering the coordination spheres of the xenon atoms in the $[XeF_5][\mu\text{-}F(OsO_3F_2)_2]$ and $[Xe_2F_{11}][OsO_3F_3]$ salts 9-coordinate, while for the $[XeF_5][OsO_3F_3]$ salt it is 8-coordinate. The $[XeF_5][\mu\text{-}F(OsO_3F_2)_2]$ salt is unique in that it provides the first example of a 9-coordinate Xe atom where all contacts originate within a single ion-pair.

The molecular addition compounds, $XeOF_4 \cdot NgF_2$ (Ng = Kr or Xe), have been synthesized by dissolution of NgF_2 in $XeOF_4$ solution. The crystal structures of these addition compounds are similar, with the NgF_2 molecules coordinating to the open face of the square pyramidal $XeOF_4$ molecule. The coordination spheres of the xenon atoms of

the $XeOF_4$ molecule in both structures are 9-coordinate. For $XeOF_4 \cdot XeF_2$ all of the contacts are to four symmetrically equivalent XeF_2 molecules, whereas for $XeOF_4 \cdot KrF_2$ contacts are to two symmetrically equivalent KrF_2 molecules, one crystallographically independent KrF_2 molecule, and one to an adjacent $XeOF_4$ molecule. The $XeOF_4 \cdot KrF_2$ adduct provides the first example of a mixed noble gas adduct.

ACKNOWLEDGEMENTS

I wish to thank my supervisor Professor Gary J. Schrobilgen for providing me with an exciting, interesting, and challenging avenue of research. In addition, I wish to thank him for his guidance, enthusiasm, insight, drive and support through the entirety of my time at McMaster.

I would also like to thank the members of my supervisory committee, Dr. Ignacio Vargas-Baca and Dr. David J. Emslie, for their insightful discussions and interest in my research projects.

Furthermore, I would like to thank Dr. Hélène P. A. Mercier for her advice and guidance throughout the numerous discussions we have had over the course of this work. As well as numerous hours she has spent helping solve various crystal structures, troubleshooting calculations, and writing publications together.

I am grateful to Schrobilgen group members, David Brock and Greg Smith who have been with me through my entire time here and have provided insightful discussions, constant support and have always been able to put my time here in perspective. In addition I would like to thank Babak Behnam-Azad and Kazuhiko Matsumoto for their assistance and expertise with the $OsO_2F_5^-$ and $XeOF_4$ projects, respectively.

Thanks also to other past and present members of the Schrobilgen research group, namely Bernard E. Pointner, Vural Bilir, Matt D. B. Moran, Maria Ivanova, Jonathan Paxon, and Corey J. Lapierre for all their help, encouragement and stimulating discussions. I also would like to thank all of my friends who I have met at McMaster who

have encouraged me through the years and always been able to inject some fun into my life.

For their help with their respective facilities, I would like to thank Dr. Jim Britten and Dr. Hilary Jenkis (X-ray crystallographic facilities), Dr. Steve Kornic (NMR and Spectroscopy facilities), Dr. Don Hughes (NMR facility), Michael Palme (Chemistry Glassblowing Shop), and Grzegorz Szymanski (ETC facility, University of Guelph).

I would like to acknowledge the Natural Sciences and Engineering Research Council (NSERC) and McMaster University for financial support in the form of scholarships and bursaries over the years.

I would like to thank my family, including my parents Sharon and David Hughes and my grandmother Kaye Wolff for their constant support and belief that I could do anything I put my mind to. Also I would like to thank my mother-in-law and brother-in-law Linda and Matt Cuthbert for their support through this process.

Finally, I would like to thank my wife Heather Cuthbert for her unwavering support and love. She was able to make me see the light when I was at my lowest points and has been a constant in my drive to complete this thesis.

PREFACE

The following Chapters have been published, in part or in whole, by the American Chemical Society (ACS). All experimental and computational work was conducted by the author except the ^{15}N NMR study of the $OsO_3F_2(CH_3CN)$ adduct in Chapter 7 which was conducted by Dr. M. Gerken.

Chapter 3: Hughes, M. J.; Mercier, H. P. A.; Schrobilgen, G. J. *Inorg. Chem.* **2010**, *49*, 271–284

Chapter 6: Hughes, M. J.; Mercier, H. P. A.; Schrobilgen, G. J. *Inorg. Chem.* **2009**, *48*, 4478–4490.

Chapter 7: Hughes, M. J.; Gerken, M.; Mercier, H. P. A.; Schrobilgen, G. J. *Inorg. Chem.* **2010**, *49*, 4768–4780.

Chapter 8: Hughes, M. J.; Mercier, H. P. A.; Schrobilgen, G. J. *Inorg. Chem.* **2010**, *49*, 3501–3515.

The work presented in **Chapter 5** is a continuation of a prior study by Dr. M. Gerken and provides a more detailed structural investigation of the *cis*-$OsO_2F_5^-$ anion. Prior to the current work the [M][*cis*-OsO_2F_5] (M = Cs^+, NO^+, and $N(CH_3)_4^+$) salt had been synthesized and preliminarily characterized by ^{19}F NMR and Raman spectroscopy.

LIST OF ABBREVIATIONS AND SYMBOLS

General

SAE	Society of Automotive Engineers
ax	axial
eq	equatorial
aHF	anhydrous hydrogen fluoride
CCD	charge-coupled device
GUI	Graphical User Interface
FT	Fourier transform
FEP	perfluoroethylene/perfluoropropylene copolymer
IR	infrared
Kel-F	chlorotrifluoroethylene polymer
VSEPR	valence shell electron pair repulsion
av	average
o.d.	outer diameter
equiv	equivalents
ψ	dihedral angle

Raman Spectroscopy

$\Delta\nu$	frequency
amu	atomic mass unit
u	atomic mass unit

cm^{-1}	wavenumber
ν	stretching mode
δ	in-plane bend
δ_{umb}	umbrella mode
ρ_w	wagging mode
ρ_r	rocking mode
ρ_t	twisting mode
o.o.p.	out-of-plane
i.p.	in-plane
s	symmetric
as	assymetric
n.o.	not observed
i.a.	in-active
sh	shoulder
br	broad

Nuclear Magnetic Resonance Spectroscopy

NMR	nuclear magnetic resonance
ppm	parts per million
δ	chemical shift
I	nuclear spin quantum number
J	scalar coupling constant, in Hz

Hz	Hertz, or cycles per second
FID	free induction decay
SF	spectral frequency
SW	sweep width
TD	time domain
PW	pulse width
$\Delta\nu_{1/2}$	line width at half height
WF	width factor
t	triplet

X-ray Crystallography

$a, b, c, \alpha, \beta, \gamma$	unit cell parameters
V	unit cell volume
λ	wavelength
Z	molecules per unit cell
V_m	molecular volume (V/Z)
mol. wt.	molecular weight
ρ	density
μ	absorption coefficient
F	structure factor
R_1	conventional agreement index
w	overall weight parameter
wR_2	weighted agreement index

Computational and Thermochemical

DFT	density functional theory
NPA	natural population analysis
NBO	natural bond orbital/natural bond order
V_m	Volume of a salt
I	ionicity of a salt
ΔH^o	standard enthalpy of reaction
ΔH_f^o	standard enthalpy of formation
$\Delta H_{sub}{}^o$	enthalpy of sublimation
$\Delta H_{vap}{}^o$	enthalpy of vaporization
ΔH_L	lattice enthalpy
S^o	absolute standard entropy
ΔG^o	standard free energy of reaction

TABLE OF CONTENTS

page

LIST OF TABLES

LIST OF FIGURES

CHAPTER 1

INTRODUCTION

1.1. Chemistry of the +8 Oxidation State

The +8 oxidation state is the highest attained formal oxidation state in the Periodic Table of the Elements. Only three elements exhibit this oxidation state, namely, osmium, ruthenium, and xenon. The stabilization of the plus eight oxidation state has only been achieved by using highly electronegative ligating atoms such as F, O, and N. The chemistry of Os(VIII), although limited, is the most developed among these three elements because of the high thermodynamic stability of the tetroxide, OsO_4 ($\Delta H_f^\circ = -390.8 \pm 5.9$ kJ mol^{-1}), the synthetic precursor for all Os(VIII) compounds.[1] The perosmate anion, OsO_6^{4-} has been characterized as its Ag_{13}^{4+} salt and is the first homoleptic osmium(VIII) oxo-anion. This salt was synthesized by a solid state reaction of ground mixtures of silver and osmium at 300 °C under 15 MPa of O_2 pressure. The crystal structure consists of Ag_{13}^{4+} icosahedra and OsO_6^{4-} octahedra.[2, 3]

Ruthenium tetroxide ($\Delta H_f^\circ = -239 \pm 5.9$ kJ mol^{-1})[4] is considerably less stable than OsO_4. If heated above 100 °C, RuO_4 decomposes explosively to RuO_2. As a result, the chemistry of Ru(VIII) is not well developed and RuO_4 is, in fact, the only Ru(VIII) compound known.

Xenon tetroxide is a highly endothermic compound and decomposes explosively into its elements with the release of 642 kJ mol^{-1} of energy at room temperature, however, XeO_4 will detonate at much lower temperatures.[5] As a result, the preparation of Xe(VIII)

compounds requiring XeO_4 as the starting material is even more limited. The perxenate anion, XeO_6^{4-} can be synthesized by hydrolysis of XeF_6 in alkaline solution (eq 1.1 and 1.2)[6] and has been characterized as its Na^+ [6-9] and K^+ [10] salts. Recently, XeO_4 has been

$$XeF_6 + 4[Na][OH] \xrightarrow{NaOH_{(aq)}} [Na][H][XeO_4] + 3[Na][HF_2] \quad (1.1)$$

$$2[Na][H][XeO_4] + 2NaOH \xrightarrow{NaOH_{(aq)}} [Na]_4[XeO_6] + Xe + O_2 + 2\,H_2O \quad (1.2)$$

stabilized in SO_2ClF, BrF_5 and HF solvents and characterized by ^{129}Xe and ^{17}O NMR. The Lewis acid properties of XeO_4 have been demonstrated by the synthesis of $XeO_4{\cdot}NCCH_3$ and $XeO_4F_2^{2-}$ and their subsequent characterization by Raman spectroscopy.

1.2. Osmium(VIII) Chemistry

1.2.1. Neutral Osmium(VIII) Oxide Fluorides

Two neutral oxide fluorides of Os(VIII) are currently known, OsO_3F_2 and *cis*-OsO_2F_4.[11] In addition, there was a preliminary report of a third, yet unknown oxide fluoride, $OsOF_6$,[12] which was later shown to be *cis*-OsO_2F_4 based on the Raman spectrum.[13]

Osmium(VIII) trioxide difluoride, formed by reaction of OsO_4 with ClF_3 (eq 1.3), is an orange solid at room temperature.[11] Vibrational spectroscopy on matrix-isolated samples

$$OsO_4 + ClF_3 \xrightarrow[25\ ^{\circ}C]{ClF_3} OsO_3F_2 + Cl_2 + \text{chlorine oxide fluorides?} \quad (1.3)$$

have established a trigonal bipyramidal geometry (D_{3h}) for matrix isolated OsO_3F_2,[14, 15] while the vibrational spectra of solid OsO_3F_2 have established a *fac*-trioxo fluorine bridged polymer.[16-18] Three distinct phases of $(OsO_3F_2)_\infty$ have been identified by X-ray powder diffraction: a low-temperature (< 90 °C) α-phase (monoclinic), a β-phase (orthorhombic) at

intermediate temperatures (90 – 130 °C), and a γ-phase (orthorhombic) at high temperatures (> 130 °C)[19] and the single-crystal structure of the low-temperature monoclinic phase (Figure 1.1) confirms the *fac*-trioxo arrangement, and the fluorine-bridged infinite chain structure.[11]

Osmium(VIII) dioxide tetrafluoride, formed by reaction of OsO_4 with KrF_2 in anhydrous HF at room temperature (eq 1.4), is a deep magenta-colored solid having a vapor

$$OsO_4 + 2KrF_2 \xrightarrow[25\ ^\circ C]{HF} cis\text{-}OsO_2F_4 + 2Kr + O_2 \qquad (1.4)$$

pressure of ca. 1 Torr at room temperature.[11, 13, 20] The ^{19}F NMR spectrum of *cis*-OsO_2F_4 in anhydrous HF shows an A_2X_2 coupling pattern and, along with the vibrational spectrum, are consistent with the *cis*-OsO_2F_4 isomer.[11, 20] The ^{19}F NMR spectrum provides a rare example of coupling to ^{187}Os ($^1J(^{19}F–^{187}Os)$ = 35.1 Hz and 59.4 Hz). The ^{187}Os chemical shift (1431±10 ppm) was reported and the ^{187}Os spectrum was acquired by inverse correlation using ^{19}F as the observed nuclide.[20] The crystal structure of *cis*-OsO_2F_4 (Figure 1.2) has been reported but is severely disordered and/or twinned and does not provide accurate structural parameters or a definitive assignment of a *cis*- or *trans*-isomer because the positions of the oxygen atoms could not be unequivocally determined.[11] A prior gas-phase electron-diffraction structure (Figure 1.3) had confirmed the *cis*-dioxo configuration in the gas phase, providing detailed structural parameters that were not available from the disordered crystal structure.[20]

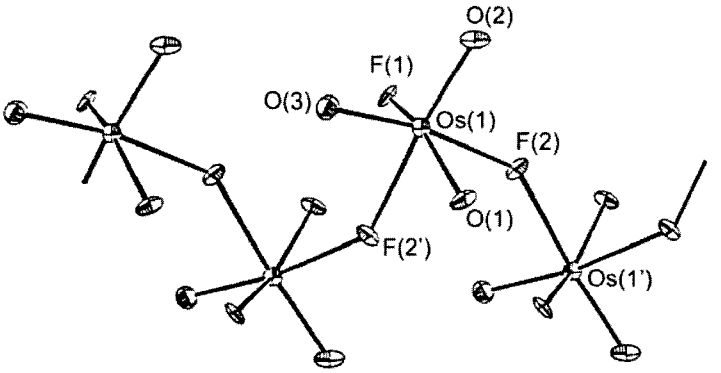

Figure 1.1. The $(OsO_3F_2)_\infty$ chain in the X-ray crystal structure of OsO_3F_2.[11]

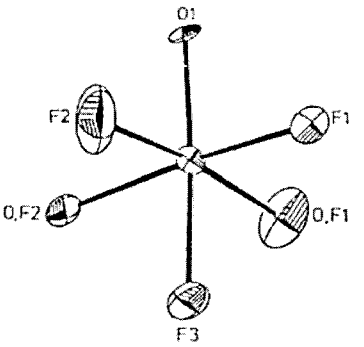

Figure 1.2. The *cis*-OsO_2F_4 molecular unit in the disordered X-ray crystal structure of *cis*-OsO_2F_4. The O,F label refers to the disordered oxygen/fluorine atom pair.[11]

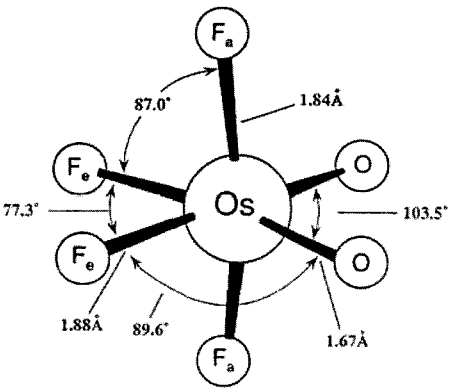

Figure 1.3. The gas-phase electron diffraction structure of *cis*-OsO_2F_4.[20]

1.2.2. Fluoride Ion Donor Properties of Osmium(VIII) Oxide Fluorides

Cations of Os(VIII) oxide fluorides can be formed by reaction of the parent neutral oxide fluoride with a strong fluoride ion acceptor PnF_5 (Pn = As, Sb). The only structurally characterized Os(VIII) oxide fluoride cations are OsO_3F^+ [21] and μ-$F(OsO_2F_3)_2^+$.[22]

The OsO_3F^+ salt has also been structurally characterized as its PnF_6^- salts or as HF adducts of these salts and is formed by reaction of OsO_3F_2 with PnF_5 in HF solution (eq 1.5).[21] The cation is highly associated with the anion and/or solvent HF molecules in all

$$OsO_3F_2 + PnF_5 + n\text{HF} \xrightarrow[25\ ^\circ\text{C}]{\text{HF}} [OsO_3F][PnF_6]\cdot n\text{HF} \quad (n = 0,1,2) \qquad (1.5)$$

these structures and retains its octahedral coordination and the *fac*–trioxo geometry (Figure 1.4). The $[OsO_3F][Sb_3F_{16}]$ structure has also been determined and the OsO_3F^+ cation is tetrahedral and does not interact with the large $Sb_3F_{16}^-$ anion (Figure 1.5). Although not structurally characterized, there is Raman spectroscopic evidence for the μ-$F(OsO_3F)_2^+$ cation.[21]

Reaction of *cis*-OsO_2F_4 with PnF_5 in HF solution yields the fluorine bridged dinuclear osmium cation μ-$F(cis\text{-}OsO_2F_3)_2^+$ (eq 1.6).[22] The μ-$F(cis\text{-}OsO_2F_3)_2^+$ cation

$$2\ cis\text{-}OsO_2F_4 + n\text{PnF}_5 \xrightarrow[25\ ^\circ\text{C}]{\text{HF}} [\mu\text{-}F(cis\text{-}OsO_2F_3)_2][\text{Pn}_n\text{F}_{5n+1}] \quad (n = 1, 2) \qquad (1.6)$$

has been characterized by single crystal X-ray diffraction and is fluorine bridged, with pseudo-octahedral *cis*-dioxo OsO_2F_4-units (Figure 1.6). The $OsO_2F_3^+$ cation was formed by reaction of *cis*-OsO_2F_4 with SbF_5 in liquid SbF_5 but a salt was not isolated. The ^{19}F NMR spectrum consists of a doublet and triplet pattern consistent with a trigonal bipyramidal cation (C_{2v} symmetry) having two *cis*-oxygen atoms in the equatorial plane.[22]

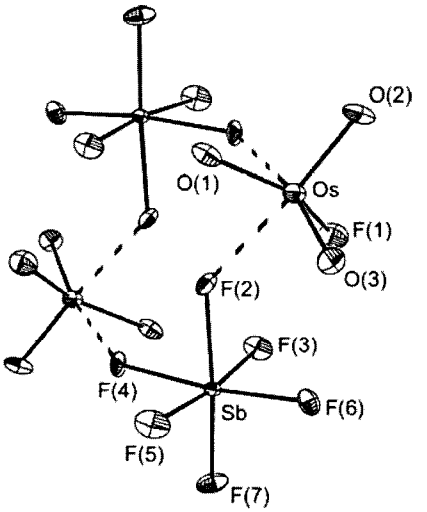

Figure 1.4. The $(FO_3Os{-}{-}FSbF_5)_2$ dimer in the X-ray crystal structure of $[OsO_3F][SbF_6]$.[21]

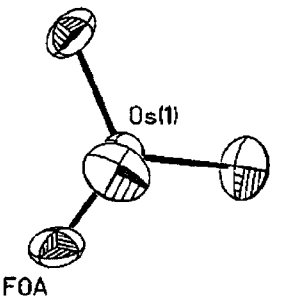

Figure 1.5. The OsO_3F^+ cation in the X-ray crystal structure of $[OsO_3F][Sb_3F_{16}]$.[21]

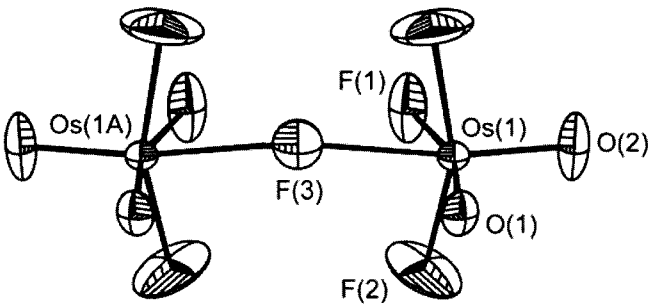

Figure 1.6. The μ-$F(OsO_2F_3)_2^+$ cation in the X-ray crystal structure of $[\mu\text{-}F(OsO_2F_3)_2][Sb_2F_{11}]$.[22]

1.2.3. Osmium(VIII) Oxide Fluoride Anions

The oxide fluoride anions of Os(VIII) compounds are limited to the OsO_4F^-, $OsO_4F_2^{2-}$, and $OsO_3F_3^-$ anions which are formed by reaction of OsO_4 or $(OsO_3F_2)_\infty$ with a fluoride ion source.

The OsO_4F^- anion is formed by reaction of $[N(CH_3)_4][F]$ with OsO_4 in CH_3CN solution (eq 1.7)[23] and has been characterized by vibrational spectroscopy, and single-

$$[N(CH_3)_4][F] + OsO_4 \xrightarrow[25\ ^\circ C]{CH_3CN} [N(CH_3)_4][OsO_4F] \quad (1.7)$$

crystal X-ray diffraction (Figure 1.7). The structure is a distorted trigonal bipyramid in which the fluorine ligand occupies an apical position.[23] The $OsO_4F_2^{2-}$ anion is formed by the reaction of a 2:1 molar ratio of $[N(CH_3)_4][F]$ with OsO_4 in CH_3CN solution at –20 °C (eq 1.8)[23] and its Raman spectrum is consistent with a *cis*-difluoro geometry.[23] The most

$$2[N(CH_3)_4][F] + OsO_4 \xrightarrow[-20\ ^\circ C]{CH_3CN} [N(CH_3)_4]_2[OsO_4F_2] \quad (1.8)$$

recent characterization of the $N(CH_3)_4^+$ salts of OsO_4F^- and $OsO_4F_2^{2-}$ have shown that the previous studies claiming the formation of $OsO_4F_2^{2-}$ by reaction of aqueous solutions of [Cs][F] or [Rb][F] with OsO_4 (eq 1.9)[24] were erroneous and actually yielded OsO_4F^-.[23]

$$OsO_4 + [M][F] \xrightarrow[25\ ^\circ C]{H_2O,\ [M][F]} [M]_2[OsO_4F_2] \quad (M = Rb^+, Cs^+) \quad (1.9)$$

The $OsO_3F_3^-$ anion has been synthesized by reaction of NOF (eq 1.10) or $[N(CH_3)_4][F]$ (eq 1.11) with OsO_3F_2,[23] or by heating an alkali metal fluoride with OsO_3F_2 (eq 1.12).[24, 25] Characterization by vibrational spectroscopy,[23, 24] EXAFS,[26] and single-

$$NOF + OsO_3F_2 \xrightarrow{120\text{-}150\ ^\circ C} [NO][OsO_3F_3] \quad (1.10)$$

$$[N(CH_3)_4][F] + OsO_3F_2 \xrightarrow[25\ ^\circ C]{HF} [N(CH_3)_4][OsO_3F_3] \quad (1.11)$$

$$[M][F] + OsO_3F_2 \xrightarrow[-78\ to\ -60\ ^\circ C]{NOF} [M][OsO_3F_3] \quad (M = Cs, K, Rb) \quad (1.12)$$

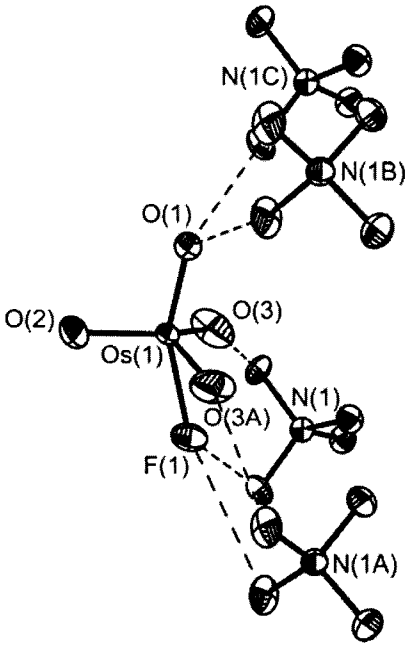

Figure 1.7. The OsO_4F^- anion in the X-ray crystal structure and $[N(CH_3)_4][OsO_4F]$ and its contacts with the $N(CH_3)_4^+$ cations; hydrogen atoms are not shown.[23]

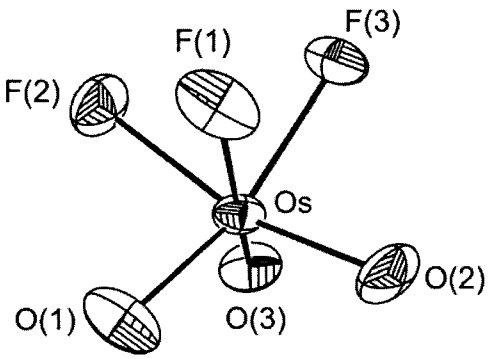

Figure 1.8. The *fac*-$OsO_3F_3^-$ anion in the X-ray crystal structure of $[N(CH_3)_4][$*fac*-$OsO_3F_3]$.[23]

crystal X-ray diffraction (Figure 1.8)[23] confirmed a pseudo-octahedral, *fac*-trioxo geometry (C_{3v} symmetry).

Reaction of *cis*-OsO_2F_4 with [Cs][F] (eq 1.13),[27] FNO (eq 1.14), or $[N(CH_3)_4][F]$ in FNO solvent (eq 1.15)[28] has been proposed to yield the $OsO_2F_5^-$ anion, however, the

$$[Cs][F] + \textit{cis}\text{-}OsO_2F_4 \xrightarrow{95\ ^\circ C} [Cs][OsO_2F_5] \quad (1.13)$$

$$FNO + \textit{cis}\text{-}OsO_2F_4 \overset{FNO}{\rightleftharpoons} [NO][OsO_2F_5] \quad (1.14)$$

$$[N(CH_3)_4][F] + \textit{cis}\text{-}OsO_2F_4 \xrightarrow[-78\ ^\circ C]{FNO} [N(CH_3)_4][OsO_2F_5] \quad (1.15)$$

structure of this anion is not well established. The ^{19}F NMR spectra in FNO, HF, or CH_3CN solvents suggest a *cis*-dioxo monocapped square antiprismatic geometry,[28] however, the Raman spectrum was not fully assigned.[27]

1.3. Osmium(VI) Oxide Fluoride Chemistry

Two Os(VI) oxide fluorides have been reported, $OsOF_4$ and OsO_2F_2, however, the synthesis of OsO_2F_2 has not been confirmed.[29] The precursor to Os(VI) oxide fluoride chemistry, OsF_6, is synthesized by the reaction of osmium with fluorine gas at high temperature (eq 1.16).[30] It has been fully characterized by vibrational spectroscopy,[31, 32]

$$Os + 3F_2 \xrightarrow{95\ ^\circ C} OsF_6 \quad (1.16)$$

UV/visible spectrometry,[33] photoelectron spectroscopy,[34] X-ray powder diffraction,[31] and single-crystal X-ray diffraction (Figure 1.9).[35] The structure of OsF_6 is octahedral (O_h symmetry).

Hydrolysis of OsF_6 in HF solution (eq 1.17),[36] or reaction of OsF_6 with boric oxide (eq 1.18)[37] yields osmium(VI) oxide tetrafluoride, $OsOF_4$. It is also possible to

$$OsF_6 + H_2O \xrightarrow[25\,^{\circ}C]{HF} OsOF_4 + 2HF \qquad (1.17)$$

$$3OsF_6 + B_2O_3 \xrightarrow{25\,^{\circ}C} 3OsOF_4 + 2BF_3 \qquad (1.18)$$

synthesize $OsOF_4$ by reduction of $OsOF_5$ on a hot tungsten filament or by static heating of Os, O and F,[38] or by reaction of OsF_6 with OsO_4,[39] however, all of these syntheses also produced $OsOF_5$ or OsO_4. Osmium oxide tetrafluoride has been characterized by powder X-ray diffraction,[36, 40] electron diffraction,[39, 40] and single-crystal X-ray diffraction.[38, 41] It was originally postulated that $OsOF_4$ is tetrameric in the solid state,[38] but it was later shown to have two crystalline modifications, both of which are fluorine-bridged polymers (Figure 1.10).[41]

1.4. The *trans*-Influence

The mutual influence of ligands in transition metal compounds has been extensively discussed in the literature.[42] A multiply-bonded ligand atom causes an elongation of the bond trans to that ligand based on the orbital interaction energy.[43] This *trans*-influence has been used to explain the exclusive preference for the *cis*- or *fac*-configuration of d^0 transition metal dioxo-complexes (e.g., *cis*-$MoO_2F_2{\cdot}2THF$ (THF = tetrahydrofuran),[44] (*cis*-$ReO_2F_3)_\infty$,[45] *cis*-$ReO_2F_4^-$,[45] μ-F(*cis*-$ReO_2F_3)_2^-$,[45] *cis*-$Re_3O_6F_{10}^-$,[45] *cis*-TcO_2F_3,[46] *cis*-$TcO_2F_4^-$,[47] *cis*-$VO_2F_4^{3-}$ [48]) and trioxo-species (e.g., *fac*-$(OsO_3F_2)_\infty$,[11] *fac*-$OsO_3F_3^-$,[23] *fac*-$OsO_3F{\cdot}HF^+$,[21] *fac*-ReO_3F,[49] *fac*-$ReO_3F(NCCH_3)_2$,[45] *fac*-$WO_3F_3^{3-}$ [50]).

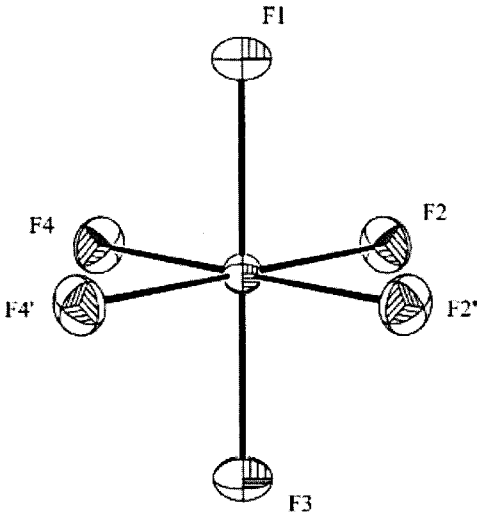

Figure 1.9. The X-ray crystal structure of OsF_6.[35]

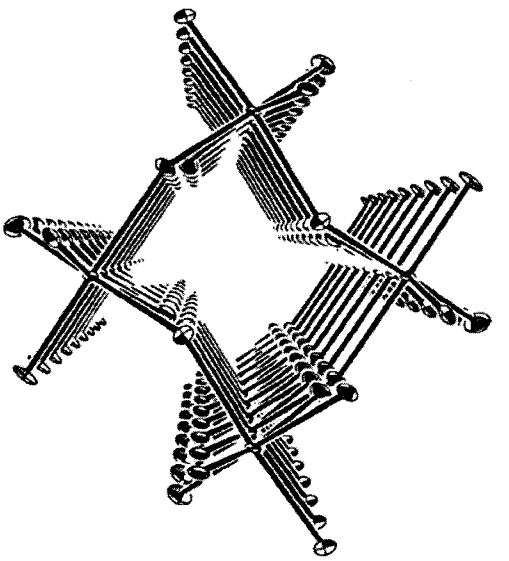

Figure 1.10. The X-ray crystal structure of polymeric $OsOF_4$ showing the packing along the axis of the helical chain.[41]

The preference for the *cis*-dioxo geometry is counter to the predicted VSEPR geometry but can be understood in terms of the spacial relationship of the strong π-donor oxygen atoms and d-orbital involvement where the fluorine ligands are unable to compete as effectively as oxygen for the $d_{t_{2g}}$ orbitals of osmium.[47] The d_{xy}, d_{xz}, and d_{yz} orbitals ($d_{t_{2g}}$) are of the correct symmetry to π-bond with π-donor ligands that are cis to each other (Figure 1.11). For a *trans*-dioxo isomer, only two of these orbitals have the correct symmetry. In the *fac*-trioxo isomer, all three orbitals can interact with two p_π orbitals, while for the *mer*-trioxo isomer only one d orbital is of the correct symmetry to interact with three p_π orbitals of the three oxygen ligands.

A study of the topology of the electron density and its Laplacian for *cis*-$CrO_2F_4^{2-}$ has rationalized that the *cis*-arrangement is a result of a nonspherical core caused by ligand distortion.[51] For a *cis*-isomer, there are four resulting charge concentrations, two of which are opposite the oxygen atoms, and two which are located along a plane bisecting the O–Cr–O bond angle so that the four concentrations have an approximate tetrahedral arrangement. By contrast, for a *trans*-isomer, there are eight charge concentrations with an overall cubic arrangement. The tetrahedral arrangement of charge concentrations is expected to be lower in energy when compared with a cubic arrangement (Figure 1.12) because the charge is dispersed, thus accounting for a preference for the *cis*-dioxo geometry. The preference for the *fac*- over the *mer*-trioxo geometry can likely be accounted for in terms of a similar charge concentration arrangement.

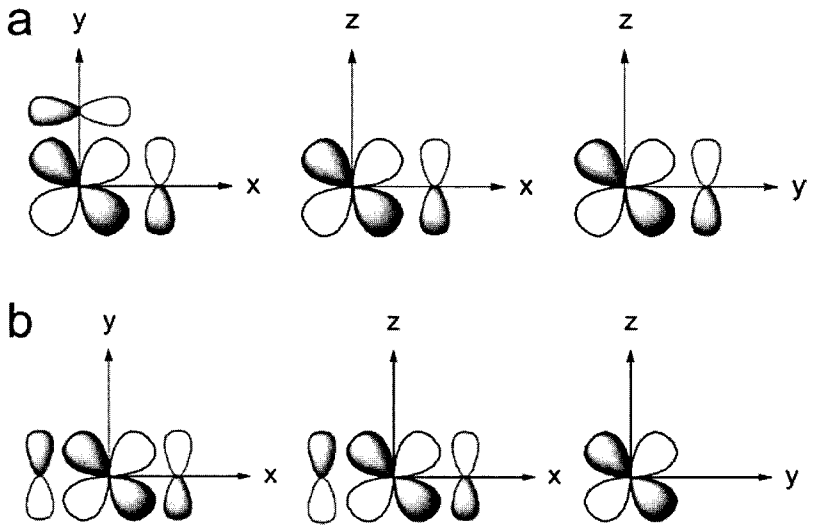

Figure 1.11. Diagram showing the overlap of the filled p orbitals of the oxygen ligands and the empty $d_{t_{2g}}$ orbitals of a transition metal in pseudo-octahedral (a) *cis*-dioxo and (b) *trans*-dioxo complexes.[28]

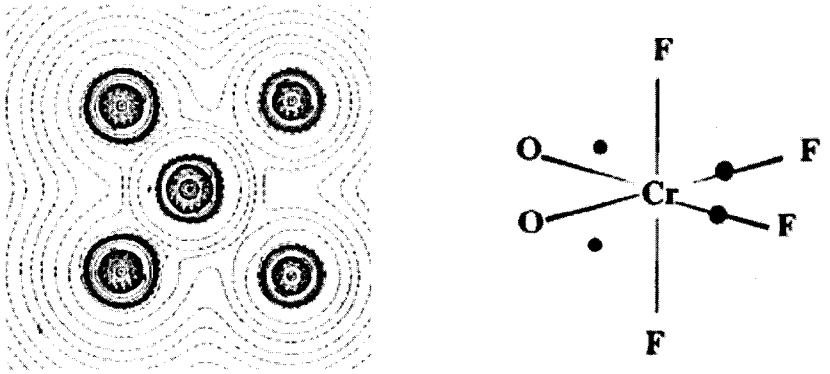

Figure 1.12. Contour maps of the Laplacian, $L = -\nabla^2\rho(r)$, for *cis*-$CrO_2F_4^{2-}$ through the $[O_2CrF_2]$-plane, with a diagram showing the positions and relative sizes of the charge concentrations in the outer shell of the core of Cr.[51]

1.5. The Cyanomethyl Anion, CH_2CN^-

Acetonitrile is often used as a solvent for high oxidation state compounds because of its known resistance to oxidation.[23, 52] However, it has been shown to undergo H^+ abstraction by the strongly basic fluoride ion to form the HF_2^- and CH_2CN^- anions (eq 1.19). The CH_2CN^- anion reacts with CH_3CN to form the intense red-brown condensation product, $H_2NC(CH_3)C(H)CN$ (eq 1.20).[53] The propensity for a fluoride ion to abstract a

$$2F^- + CH_3CN \longrightarrow HF_2^- + CH_2CN^- \quad (1.19)$$

$$CH_2CN^- + H^+ + CH_3CN \longrightarrow H_2NC(CH_3)C(H)CN \quad (1.20)$$

proton from CH_3CN makes it a less suitable solvent for anion formation at higher temperatures.[54] At lower temperatures (ca. –10 °C down to its freezing point), CH_3CN has been widely used as a solvent to form high-valent, high-coordination number oxofluoro-anions by reaction of the neutral oxide fluoride with $[N(CH_3)_4][F]$.[23]

The CH_2CN^- anion is a reactive intermediate in condensation reactions involving nitriles,[55] and is used in organic synthesis as a nucleophile (eq 1.21)[56] or as a ligand in organometallic chemistry to form compounds such as $P(CH_2CN)_3$ (eq 1.22).[57] The CH_2CN^- ligand is able to coordinate to metal centers through C, and adducts of this type

$$PhSeSePh + CH_2CN^- \longrightarrow PhSeCH_2CN + PhSe^- \ (Ph = C_6H_5) \quad (1.21)$$

$$PCl_3 + 3Bu_3SnCH_2CN \xrightarrow[1\ h]{CH_3CN} P(CH_2CN)_3 + 3Bu_3SnCl \quad (1.22)$$

$$(Bu = CH_3CH_2CH_2CH_2)$$

have been characterized by single-crystal X-ray diffraction (e.g. $P(CH_2CN)_3$,[57] $[(Ph_3P)_2N][Ir(CO)_2(CH_2CN)_2]$,[58] and $[Li(THF)][Zn_3(CH_2CN)_3(LiBr)(NP(CH_3)_3)_4]$[59]). Presently, there are no examples of crystal structures that contain well isolated CH_2CN^-

anions. The Na^+ [55] and Li^+ [60] salts of the CH_2CN^- anion have been characterized by both infrared and ^1H NMR spectroscopy.

1.6. Xenon(VI) Chemistry

1.6.1. Xenon Hexafluoride

The structure of XeF_6 has been extensively studied in both the solid and liquid states. In the solid state, there are six known crystallographic modifications of XeF_6[61-63] that are comprised of XeF_5^+ and F^- ions that associate to form fluorine-bridged tetramers or hexamers in the solid state.[61, 62] Xenon hexafluoride has a low melting point (49.5 °C).[64] In the liquid state, XeF_6 is intense yellow-green[65] and the Raman spectrum suggests that it exists as tetramers that are best described as a combination of XeF_5^+ and F^- ions.[66] Xenon hexafluoride is also highly soluble in anhydrous HF solution[65] and has been shown by ^{19}F and ^{129}Xe NMR studies to exist as a $(XeF_6)_4$ tetramer[67] where all 24 fluorine atoms are fluxional and equally distributed over four chemically equivalent xenon atoms.[68]

Xenon hexafluoride is the strongest fluoride ion donor among the binary fluorides of xenon,[69] and forms XeF_5^+ salts and $Xe_2F_{11}^+$ salts (Table 1.1) with a variety of main-group and metal fluorides. In all cases, the XeF_5^+ and $Xe_2F_{11}^+$ cations are extensively associated with their counter anions through fluorine bridge contacts and the xenon atoms are either eight- or nine-coordinate (Figure 1.13).

Table 1.1. Known XeF_5^+ and $Xe_2F_{11}^+$ Salts and Their References

XeF_5^+ Salts		$Xe_2F_{11}^+$ salts	
Anion	Refs.	Anion	Refs.
AgF_4^-	70, 71		
$Al_2F_7^-$	72		
AsF_6^-	73-78	AsF_6^-	65
$AsF_6^- \cdot n(XeF_2)$[b]	79		
AuF_6^-	65	**AuF_6^-**	80, 81
AuF_4^-	71		
BF_4^-	65, 73, 77, 78		
BiF_6^-	82	BiF_6^-	82
CrF_5^-	83	CeF_6^{2-}	82
CoF_4^-	84		
DyF_3^{3-}	85		
FeF_4^-	84		
GaF_4^-	72		
GeF_5^-	86		
GeF_6^{2-}	87		
HfF_6^{2-}	87		
IrF_6^-	82	IrF_6^-	82
$M_2F_9^-$[c]	85	LnF_6^-[d]	85
MoF_6^-	82	MoF_6^-	82
NbF_6^-	82	NbF_6^-	82
NiF_6^{2-}	88	**NiF_6^{2-}**	89
		PF_6^-	65, 74
$Pb_4F_{17}^-$	90	PbF_6^{2-}	90
PdF_6^{2-}	65, 91		
$Pr_4F_{17}^-$	85		
PtF_6^-	65, 92	PtF_6^-	82
RuF_6^-	65, 93		
SbF_6^-	77, 94, 95	SbF_6^-	94
$Sb_2F_{11}^-$	77		
ScF_4^-	82		
$Sn_4F_{17}^-$	90	SnF_6^{2-}	90, 96
SO_3F^-	77, 97		
TaF_6^-	82	TaF_6^-	82
UF_6^-	82	UF_6^-	82
		VF_6^-	98
		YbF_6^{3-}	85
ZrF_5^-	87		

[a] Anions in bold denote salts that have known crystal structures. [b] (n = ½, 1, 2). [c] (M = Ce, Tb). [d] (Ln = Er, Ho, Lu, Tm, Y, Yb).

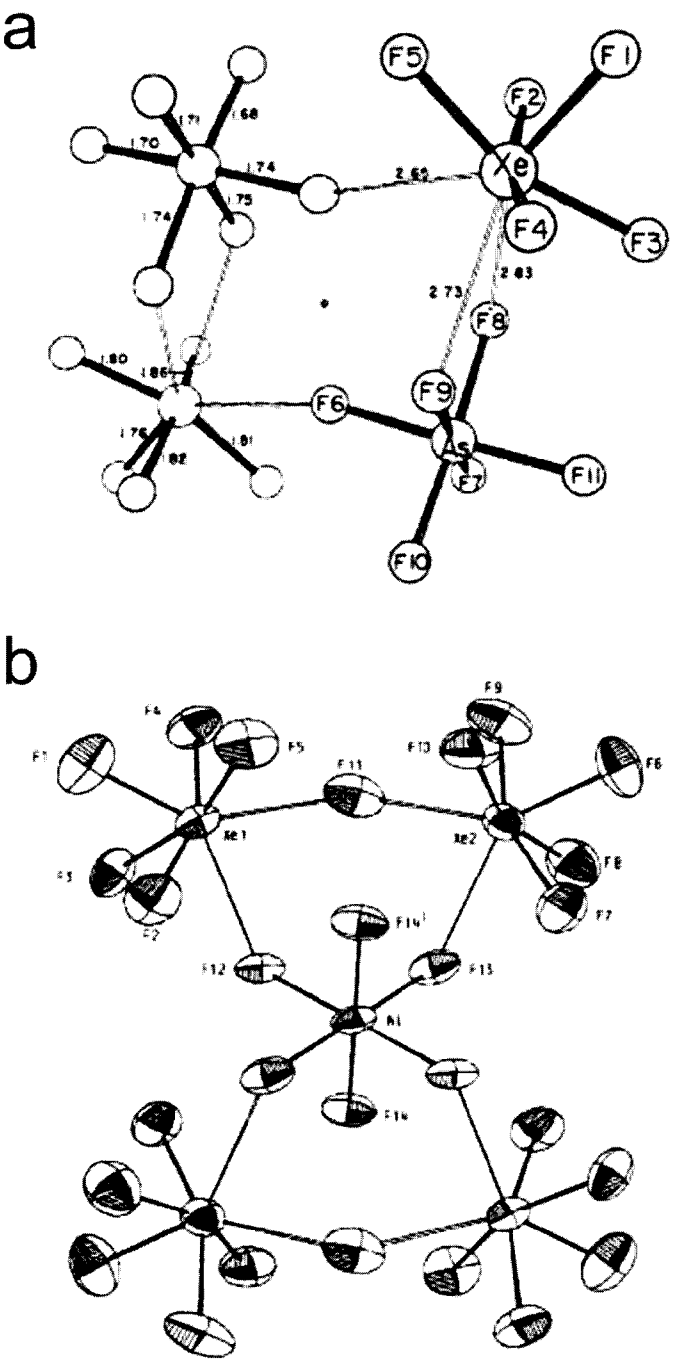

Figure 1.13. The X-ray crystal structure (a) $[XeF_5][AsF_6]$[76] and (b) $[Xe_2F_{11}][NiF_6]$.[89]

1.6.2. Xenon Oxide Tetrafluoride

The $XeOF_4$ molecule has been structurally well characterized by ^{19}F NMR,[99] photoelectron,[100] Raman,[101] and gas-phase microwave spectroscopy,[102-104] and by single-crystal X-ray diffraction.[95] Xenon oxide tetrafluoride has been shown to have a square pyramidal geometry based on a AX_4YE VSEPR arrangement, with an axial oxygen atom, four co-planar fluorine atoms in equatorial positions, and an axial valence electron lone pair. The only crystal structure containing the $XeOF_4$ molecule is $[XeF_5][SbF_6]\cdot XeOF_4$ (Figure 1.14).[95] The xenon atom of the $XeOF_4$ molecule in this structure has a short Xe···F contact with a fluorine atom of the SbF_6^- anion but has no contacts with the XeF_5^+ cation. The fluorine bridge interaction does not significantly distort the square-pyramidal geometry of the $XeOF_4$ molecule nor does it result in significant elongation of the Sb–F bridge bond.

1.7. Molecular Adducts of Xenon and Krypton Difluoride

Xenon difluoride forms molecular adducts of the form $xXeF_2\cdot yMF_z$ (where x = 1–3; y = 1,2; z = 3–6; M = As, Au, B, Bi, Br, Cr, Hf, I, Ir, Mn, Mo, Nb, Os, P, Pd, Pt, Rh, Ru, Sb, Si, Sn, Ta, Ti, U, V, W, Xe, and Zr).[82] Xenon difluoride also acts as a weak ligand towards "naked" metal cations functioning as either a terminal or a bridging group by coordination through its fluorine ligands.

Terminal XeF_2 ligands interact through only one fluorine atom resulting in lengthening of the bridge bond and contraction of the terminal bond (e.g., $[Cd(XeF_2)_5][PF_6]_2$,[105] $2CrF_4\cdot XeF_2$,[83] $[Mg(XeF_2)_4)[AsF_6]_2$ (Figure 1.15),[106]

$[Nd(XeF_2)_{2.5}][AsF_6]_3$,[107] $[XeF_5][AsF_6]\cdot 2XeF_2$,[79] and $[XeF_5][AsF_6]\cdot XeF_2$[79]). In these cases, the fluoride ion is not completely transferred to the acceptor as in the case of strong fluoride ion acceptors such as SbF_5 and AsF_5 to give $[XeF][SbF_6]$,[108] $[XeF][Sb_2F_{11}]$,[109] and $[XeF][AsF_6]$ salts.[110] Bridging XeF_2 ligands coordinate in two ways, symmetrically and asymmetrically. Structures containing symmetrically bridged XeF_2 resemble network structures where both Xe–F bond lengths are equivalent and symmetric (e.g. $[Ag(XeF_2)_2][AsF_6]$,[111] $[Ba(XeF_2)_5][SbF_6]_2$ (Figure 1.16),[112] $[Ba(XeF_2)_5][AsF_6]_2$,[113] $IF_5\cdot XeF_2$ (Figure 1.17),[114] $[M(XeF_2)_3][AsF_6]_2$ (M = Pb, Sr),[115] $XeF_4\cdot XeF_2$,[116] $XeOF_4\cdot XeF_2$,[75] and $2([XeF_5][AsF_6])\cdot XeF_2$[79]). Asymmetrically bridged structures contain one short and one longer contact to XeF_2 and can occur in either network or molecular structures (e.g., $[Ba(XeF_2)_4)][PF_6]_2$,[117] $[BrOF_2][AsF_6]\cdot XeF_2$,[118] $[BrOF_2][AsF_6]\cdot 2KrF_2$ (Figure 1.18a),[118] $[Ca(XeF_2)_4][AsF_6]_2$,[119] $[Ca(XeF_2)_5][PF_6]_2$,[105] $[Mg(XeF_2)_2)[AsF_6]_2$,[106] $[Pb_3(XeF_2)_{11}][PF_6]_6$,[120] and $[Sr_3(XeF_2)_{10}][PF_6]_6$[120]).

Adducts of XeF_2 to transition metal oxide fluorides of the form MOF_4 (M = Mo and W) have been characterized by ^{19}F and ^{129}Xe NMR,[121, 122] and Raman spectroscopy.[122, 123] The metal fluorine bond in the M---F–Xe bridge has been shown to be non-labile at low temperature by ^{19}F and ^{129}Xe NMR studies and it has been found that there is isomerization between oxygen- and fluorine- bridged XeF groups on the NMR time scale for adducts of the form $n WOF_4\cdot XeF_2$ (n = 2,3).[121]

In contrast, there are relatively few examples of adducted KrF_2 molecules. The majority of adducts are represented by those formed with the transition metal center of

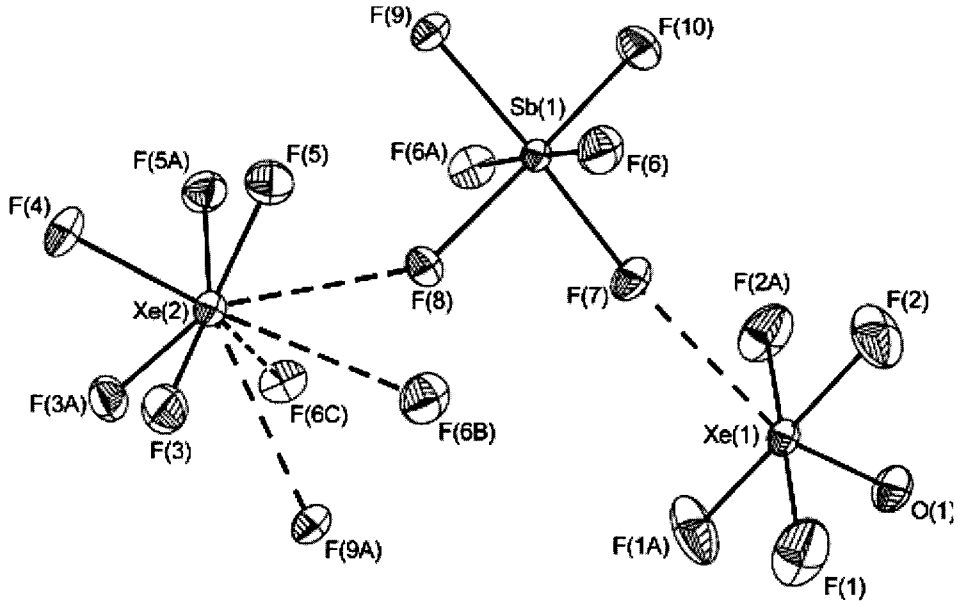

Figure 1.14. The X-ray crystal structure of $[XeF_5][SbF_6]\cdot XeOF_4$.[95]

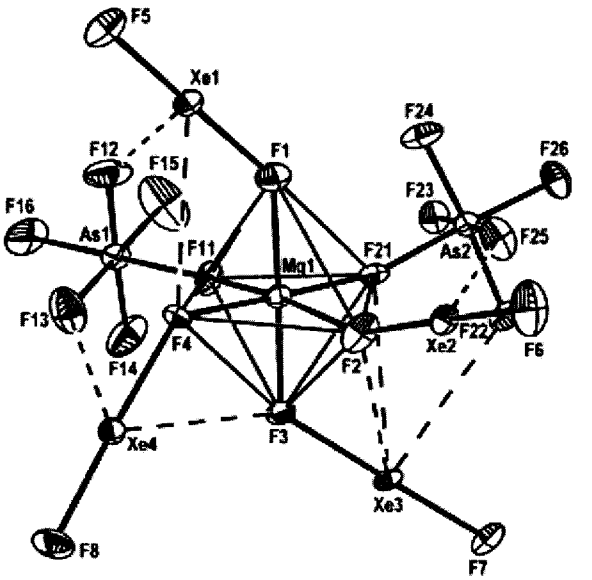

Figure 1.15. The coordination sphere of Mg^{2+} in the X-ray crystal structure of $[Mg(XeF_2)_4][AsF_6]_2$.[106]

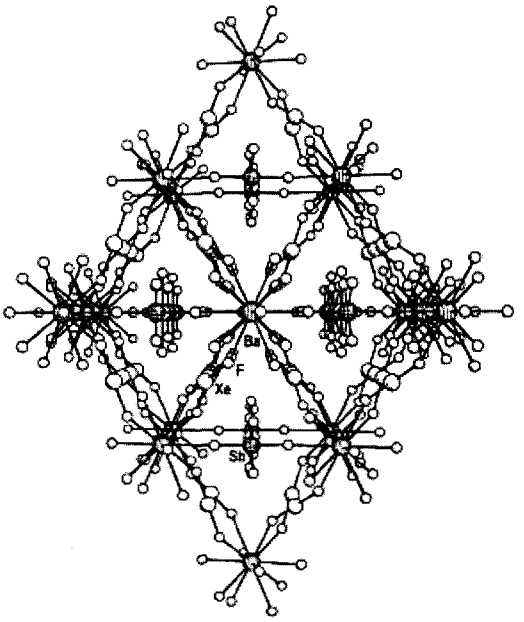

Figure 1.16 The packing in the structure of $[Ba(XeF_2)_5][SbF_6]_2$ displaying the $Ba(SbF_6)_2 \cdot XeF_2$ and XeF_2 layers.[112]

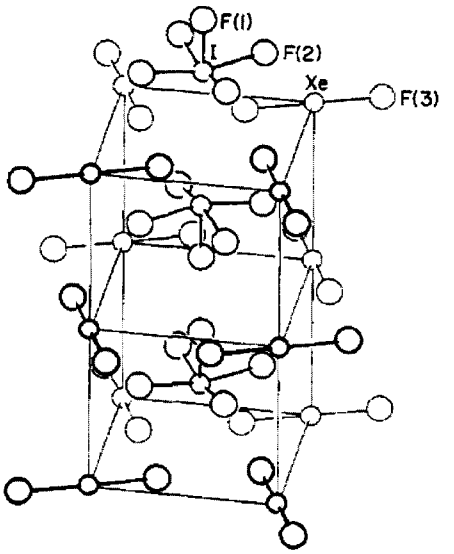

Figure 1.17. The X-ray crystal structure of $IF_5 \cdot XeF_2$ showing the basal to basal and apical to apical environment of IF_5 and XeF_2 molecules.[114]

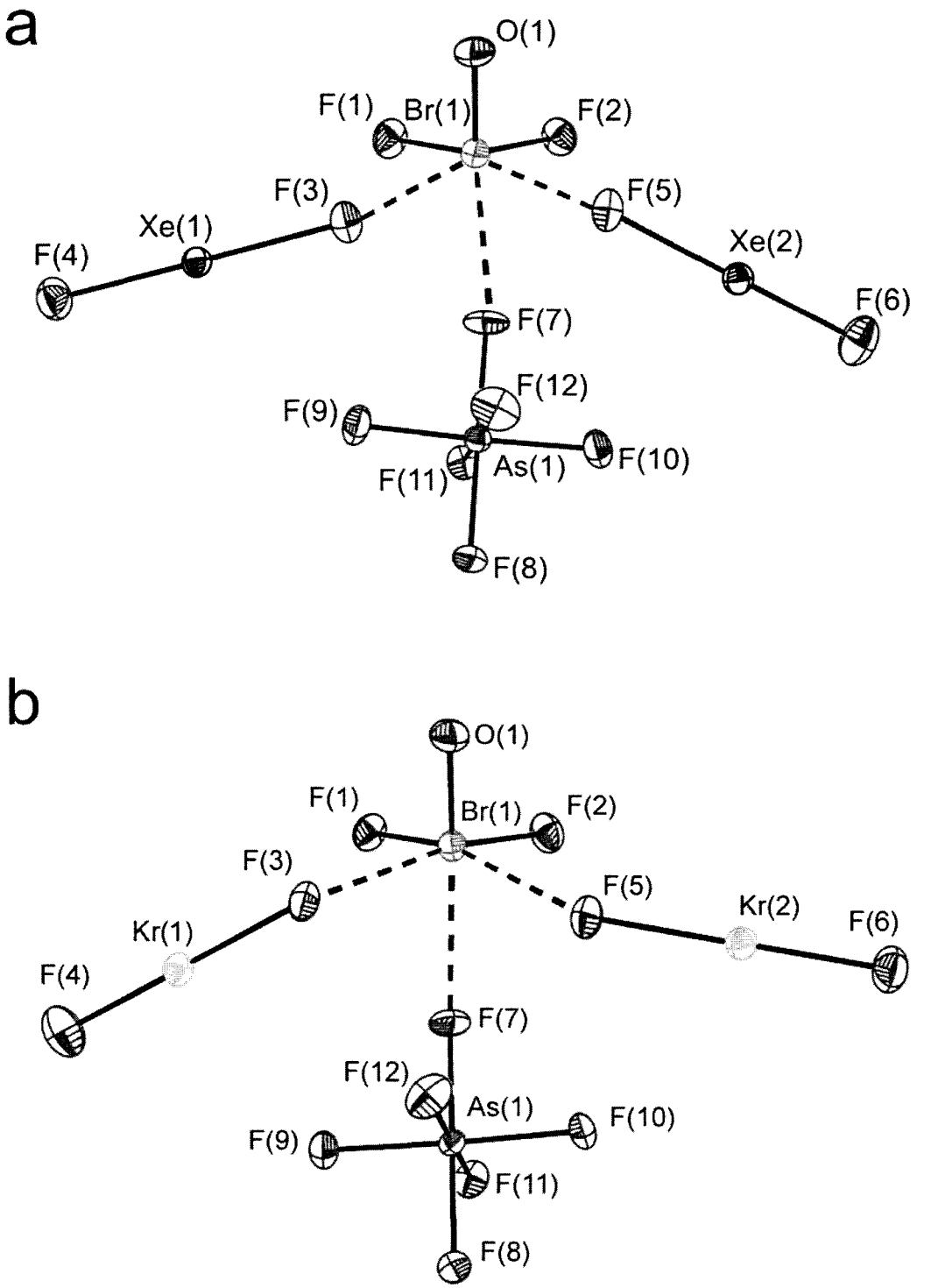

Figure 1.18. The X-ray crystal structures of (a) $[BrOF_2][AsF_6]\cdot 2XeF_2$[118] and (b) $[BrOF_2][AsF_6]\cdot 2KrF_2$.[124]

MOF_4 (M = Cr,[125] Mo,[123] and W[123]), which have been characterized by low-temperature ^{19}F NMR and vibrational spectroscopy. The only crystal structures of KrF_2 adducts are $[Kr_2F_3][SbF_6]_2 \cdot KrF_2$,[126] and the recently synthesized $[BrOF_2][AsF_6] \cdot 2KrF_2$ (Figure 1.18b)[124] which both contain terminally bridged KrF_2 molecules. Presently, there are no examples of KrF_2 molecules that are bridged between two heavy atoms.

1.8. Purpose and Scope of the Present Work

The purpose of this research is to extend the somewhat limited chemistry of osmium(VIII) oxide fluorides. This includes the extension of the fluoride ion donor and acceptor properties of the highest oxide fluoride of osmium(VIII), *cis*-OsO_2F_4, using the strong Lewis acid SbF_5 and fluoride ion donors such as $[N(CH_3)_4][F]$, [Cs][F], and FNO. While there have been a preliminary reports of both the $OsO_2F_3^+$ cation[22] and the $OsO_2F_5^-$ anion,[28] their full characterization have not realized. A goal of the present work is to arrive at definitive proof for the structures of these ions.

Another facet of the present work deals with the interaction of the polymeric osmium(VIII) oxide fluoride, *fac*-OsO_3F_2, with the xenon(VI) compounds, XeF_6 and $XeOF_4$. Xenon hexafluoride is a known fluoride ion donor and will likely form a salt with OsO_3F_2. Such a salt would be the first example of a XeF_5^+ or $Xe_2F_{11}^+$ cation stabilized by a transition metal oxide fluoride. Xenon oxide tetrafluoride is not as strong a fluoride ion donor as XeF_6, but, square pyramidal $XeOF_4$ might coordinate to OsO_3F_2 through a fluorine bridge to the open face of the square pyramid. A compound with a Os–F---Xe linkage would provide the first example of an Os(VIII) oxide fluoride formally

coordinated to a Xe(VI) compound. The interaction of Os(VIII) oxide fluorides with Xe(VI) fluorides and oxide fluorides should allow for new information on the structure and bonding of both Os(VIII) and Xe(VI) compounds including extending the coordination sphere of Xe beyond six, and new salts and phases of OsO_3F_2.

A final direction for this work involves the $XeOF_4 \cdot XeF_2$ molecular addition compound which is known but has not been fully structurally characterized.[75] The complete structural characterization of $XeOF_4 \cdot XeF_2$ should confirm the previously published structural model. A natural extension of the study of $XeOF_4 \cdot XeF_2$ will be to investigate the interaction of the binary krypton fluoride, KrF_2, with $XeOF_4$. Formation of a $XeOF_4 \cdot KrF_2$ molecular addition compound by analogy would provide the first example of a mixed noble gas adduct.

The compounds synthesized in this study will be structurally characterized by use of a combination of ^{1}H, ^{13}C, ^{19}F, and ^{129}Xe NMR spectroscopy, Raman spectroscopy as well as single-crystal X-ray diffraction and will be augmented by the use of quantum-chemical calculations.

CHAPTER 2

EXPERIMENTAL SECTION

2.1. Standard Techniques

2.1.1. Dry Box and Vacuum Line Techniques

The compounds used and prepared during the course of this work were highly moisture- and temperature-sensitive, and were handled under rigorously anhydrous conditions on glass and metal vacuum line systems or in an inert atmosphere (N_2 gas) dry box (Vacuum Atmospheres Model DLX, oxygen and moisture < 0.1 ppm) equipped with a glass cryowell for handling low-temperature samples inside the dry box. Preparative work inside the dry box requiring low temperatures was accomplished using a metal Dewar filled with 4.5 mm copper-plated spheres (air rifle BB's) that had previously been cooled to ca. –140 °C in the glass cryowell (–196 °C) of the dry box.

Preparative work involving volatile fluorides that attack glass (e.g, HF and $XeOF_4$) was carried out on metal vacuum lines constructed primarily from 316 stainless steel and nickel and fitted with 316 stainless steel valves (Autoclave Engineers, Inc., Figure 2.1). Pressures were measured at ambient temperatures using MKS Model PDR-5B pressure transducers having wetted surfaces constructed of Inconel. The pressure transducer possessed a range of 0–1150 Torr, which was accurate to ±0.5 Torr.

Reactions that did not involve transfer of materials that attack glass were carried out on Pyrex glass vacuum lines equipped with grease-free 6-mm J. Young PTFE/glass

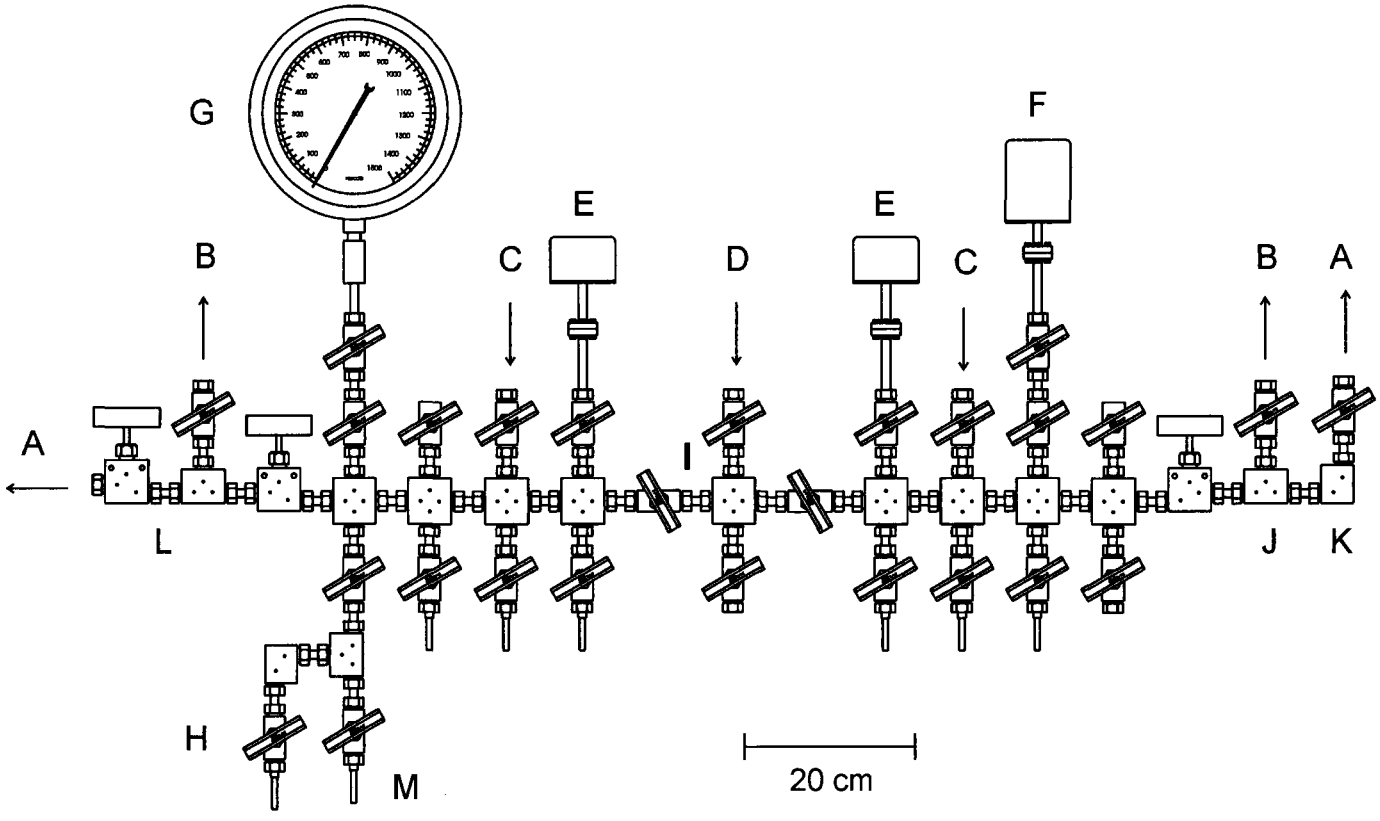

Figure 2.1. Schematic diagram of metal vacuum line system: (A) outlet to liquid nitrogen and charcoal (Norit) traps followed by a two-stage direct-drive rotary vacuum pump (Edwards, E2M8) – hard vacuum, (B) outlet to soda lime and liquid nitrogen traps followed by a two-stage direct-drive rotary vacuum pump (Edwards, E2M8) – rough vacuum, (C) dry nitrogen inlet, (D) fluorine inlet, (E) MKS Model PDR-5B pressure transducer (0 – 1000 Torr), (F) MKS Model PDR-5B pressure transducer (0 – 10 Torr), (G) Bourdon pressure gauge (0 – 1500 Torr), (H) $^{3}/_{8}$-in. 316 stainless steel high pressure valve (Autoclave Engineers, 30BM6071), (I) 316 stainless steel cross, (J) 316 stainless steel T-piece, (K) 316 stainless steel L-piece, (L) nickel connectors, (M) ¼-in. o.d., $^{1}/_{8}$-in. i.d. nickel tube.

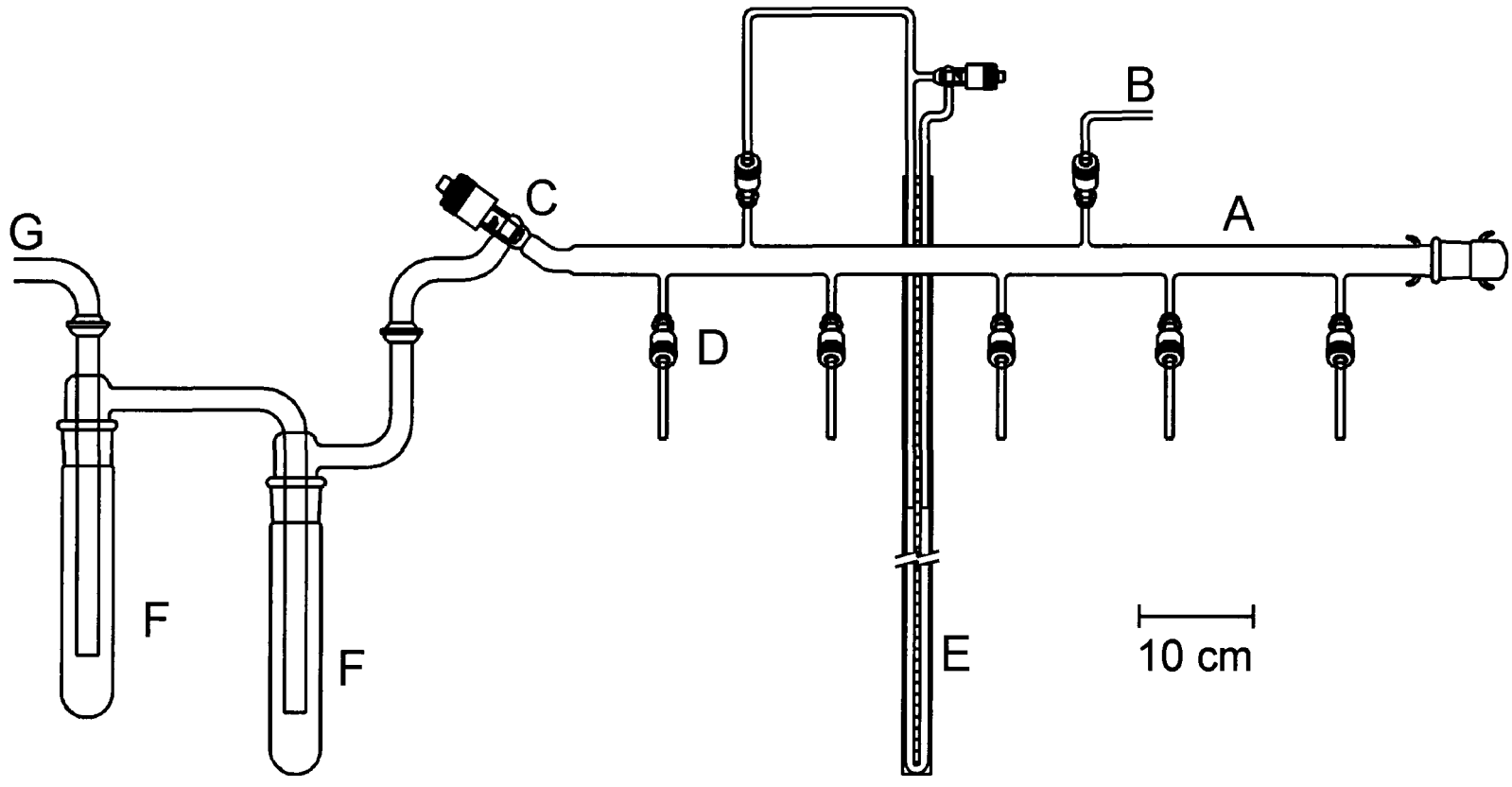

Figure 2.2. Glass vacuum line used for the manipulation of non-corrosive volatile materials; (A) main vacuum manifold, (B) dry N_2 inlet, (C) 15-mm greaseless J-Young valve with PTFE barrel, (D) 6-mm greaseless J-Young valve with PTFE barrel, (E) mercury manometer, (F) liquid N_2 cold trap, and (G) outlet to vacuum pump.

stopcocks outfitted with PTFE barrels (Figure 2.2). Pressures inside the glass manifold were monitored using a mercury manometer.

Vacuum on the glass vacuum lines (ca. 10^{-3}–10^{-4} Torr) was accomplished using Edwards two-stage internal vane E2M8 direct-drive vacuum pumps. Vacuum was maintained on the metal line using two E2M8 vacuum pumps; the first, a roughing pump, was used primarily for the removal of volatile fluoride and oxide fluoride compounds. The rough pump was used to pump reactive, volatile fluorine compounds through a fluoride/fluorine trap consisting of a stainless steel tube (ca. 60 cm, 15 cm dia.) packed with soda lime absorbent (Fisher Scientific, 4–8 mesh), followed by a final trapping procedure, utilizing a glass liquid nitrogen trap to remove CO_2 and water formed by reaction of fluoride materials with soda lime and other volatile materials that were unreactive towards soda lime. The second vacuum pump provided the high vacuum (ca. 10^{-4} Torr) source for the manifold and was fitted with a glass liquid nitrogen trap.

2.1.2. Preparative Apparatus and Sample Vessels

All synthetic work was carried out in reactors constructed from lengths of ¼-in. and 4-mm o.d. FEP tubing which were heat-sealed at one end and heat-flared (45° SAE) at the other. In general, the tubing was fashioned into either straight reactos, "beaded" reactors, or vessels equipped with sidearms. A typical "beaded" vessel was fashioned from a ¼-in. o.d. FEP reaction tube by blowing three consecutive, 8- to 9-mm diameter bubbles, having center-to-center distances of 10 to 20 mm, into heated portions of the tube commencing near the heat-sealed end of the vessel. The tubing was connected to Kel-F valves, encased in aluminum housings, using brass flare fittings. All vessels were

then connected to a glass vacuum line using Cajon fittings and were rigorously dried by pumping (a minimum of 6 h) under dynamic vacuum. Vessels were then connected to the metal vacuum line using a PTFE Swagelok union and passivated with ca. 1000 Torr of F_2 for ca. 12 h. Once passivated, vessels were evacuated under dynamic vacuum to remove all volatile impurities and back-filled with dry N_2 (ca. 1000 Torr) prior to use. Similarly, connections made to a metal vacuum line were dried under dynamic vacuum and passivated with F_2 gas overnight. Connections made to a glass vacuum line were dried under dynamic vacuum overnight.

Nuclear magnetic resonance spectra were acquired using tubes prepared from 4-mm o.d. FEP tubing. One end of each tube was heat-sealed using the end of a heated thin-walled 5-mm o.d. glass NMR tube, while the other end was fused to ca. 5 cm of ¼-in. o.d. thick-walled tubing. The end was subsequently heat-flared (45° SAE) for connection to a Kel-F valve. Prior to acquisition of the NMR data, the sample tubes were heat-sealed under dynamic vacuum using a nichrome wire resistance furnace of appropriate diameter. Otherwise, NMR samples were prepared in 5-mm o.d. thin wall precision glass NMR tubes (Wilmad) fused to ¼-in. o.d. lengths of glass tubing which were in turn attached to 4-mm J. Young PTFE/glass stopcocks by use of ¼-in. stainless steel Cajon Ultratorr unions fitted with Viton O-rings. The NMR tubes were then vacuum-dried for 8–12 h before use.

Low-temperature Raman spectra of solids (ca. –160 °C) were recorded on samples prepared in both thin-walled ¼-in. and 4-mm. FEP tubing, as well as 5-mm o.d. glass tubes fused to ¼-in. o.d. lengths of glass tubing which were, in turn, attached to 4-mm J.

Young PTFE/glass stopcocks by use of ¼-in. stainless steel Cajon Ultratorr unions fitted with Viton O-rings.

All connections to vacuum lines were made using thick-walled ¼-in. FEP tubing in conjunction with either a ¼-in. PTFE Swagelok connector outfitted with PTFE compression fittings (ferrules) or ¼-in. stainless steel Cajon Ultra-Torr connectors outfitted with stainless steel compression fittings and Viton rubber O-rings.

2.2. Preparation and Purification of Starting Materials

2.2.1. Sources and Purification of N_2, Ar, F_2, H_2, Xe, Kr, $^{18}O_2$, Cl_2, and NO

House nitrogen gas was generated by boiling off liquid nitrogen (Air Liquide) and was further dried through a freshly regenerated bed of type 4Å molecular sieves. High purity argon gas (VitalAire), also employed for the back pressuring of reaction vessels, was used without further purification. Technical grade fluorine gas (Air Products), H_2 (Air Liquide), Xe (Air Products, 99.995%), Kr (Air Products, 99.995%) and $^{18}O_2$ (Enritech Enrichment Technologies, 98.14%) were used without further purification. Chlorine gas (Air Liquide) was dried by passing through concentrated sulfuric acid and condensed in a U-trap at –78 °C where it was stored ready for use. Nitrogen oxide, NO (Matheson, >99%) was purified by condensing commercial NO into a 30-mL nickel can at –196 °C, followed by warming to –120 °C using an ethanol slush, and condensing the NO gas into the reaction vessel at –196 °C.

2.2.2. Purification of Anhydrous HF, SO_2ClF, CH_3CN, $(CH_3)_2CHOH$, $(CH_3CH_2)_2O$, and NH_3

Anhydrous hydrogen fluoride, HF (Harshaw Chemical Co.), was purified by addition of ca. 5 atm of fluorine gas to a commercial HF sample contained in a nickel can for a period of ca. one month prior to use, converting residual water to HF and O_2. After removal of O_2 and excess F_2 by pumping at –196 °C, the HF was warmed to room temperature and then distilled into a previously dried and F_2 passivated Kel-F storage vessel equipped with a Kel-F valve and stored at room temperature for future use. Transfer of HF was accomplished by vacuum distillation from the Kel-F storage vessel, on a metal vacuum line, through connections constructed from FEP, as shown in Figure 2.3.

Sulfuryl chloride fluoride (Allied Chemical Co., Baker and Adams Division, >90%, ca. 100 g crude material) was purified by fractional distillation through two FEP U-tube traps cooled to –78 and –90 °C, respectively, effectively removing the inert impurity SO_2F_2. The remaining SO_2ClF was then condensed into an FEP U-tube containing ca. 80 g of SbF_5 at –78 °C and slowly warmed to room temperature with vigorous mixing to remove SO_2, which is known to rapidly reduce xenon(II) and other oxidant species. The purified SO_2ClF was then transferred to an FEP U-tube cooled to –78 °C and containing dry KF. Again, the mixture was slowly warmed to room temperature with vigorous mixing and allowed to stand with periodic mixing at room temperature for ca. 2 h to remove any residual HF. The sample was again cooled to –78 °C and condensed into a 1.25-in. o.d. FEP reaction vessel containing XeF_2 (1.7 g) and

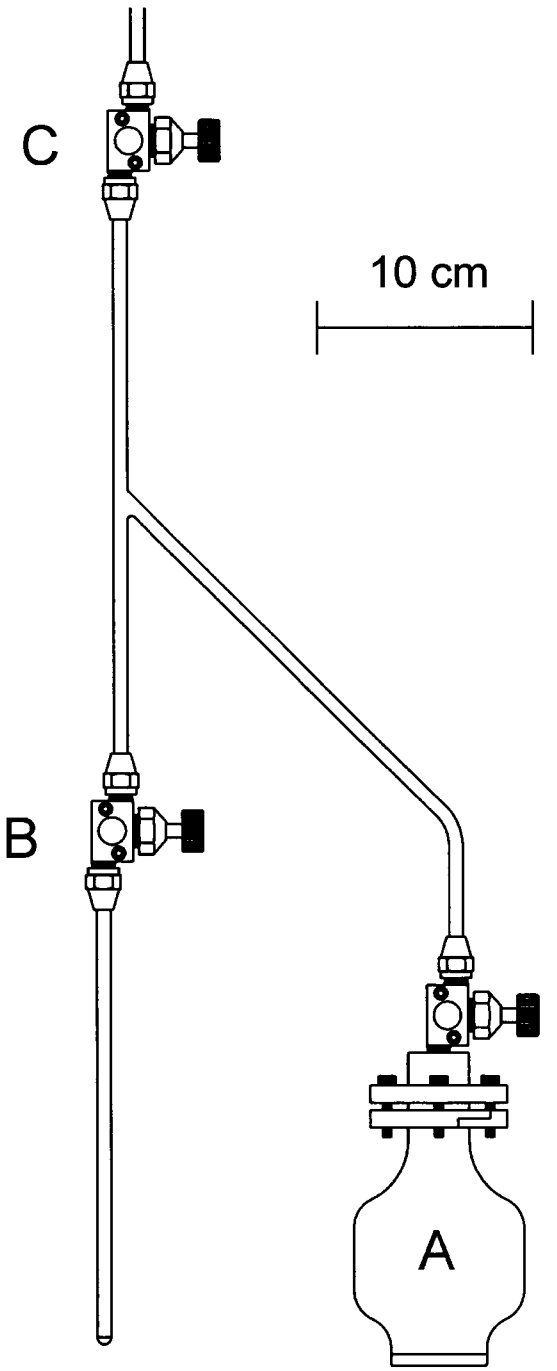

Figure 2.3. Hydrogen fluoride distillation apparatus; (A) Kel-F storage vessel containing HF, (B) FEP reaction vessel fitted with a Kel-F valve, (C) Kel-F valve connected to vacuum manifold.

allowed to stand for 24 h to ensure all impurities with reducing properties had been fluorinated (e.g., residual SO_2 is fluorinated to form inert SO_2F_2). Finally, the liquid was distilled by dynamic pumping at –78 °C into a glass vessel, outfitted with a 6-mm J. Young all-glass stopcock, over a bed of dry KF. The purity of the sample was assessed by ^{1}H, ^{17}O, and ^{19}F NMR spectroscopy of a neat sample recorded at –80 °C, in which only small amounts of SO_2F_2 (2.2%) were found. Transfers were performed using a glass vacuum line by vacuum distillation of SO_2ClF through a submanifold comprised of a Y-shaped glass connector joined to the reaction vessel by means of ¼-in. stainless steel cajon unions equipped with viton O-rings (Figure 2.4). The sample was stored at room temperature until used.

Acetonitrile (Caledon, HPLC Grade) was purified according to the literature method.[127] Transfers were performed using a glass vacuum line by vacuum distillation of CH_3CN through a submanifold comprised of a Y-shaped glass connector joined to the reaction vessel by means of ¼-in. stainless steel cajon unions equipped with viton O-rings (Figure 2.5).

Isopropanol (Fluka Chemika, 99.5%) was dried over molecular sieves (Type 4A, Caledon) in a dry glass bulb equipped with a 4-mm J. Young glass stopcock. The molecular sieves were dried under dynamic vacuum for 24 h at 250 °C prior to use as a drying agent.

Anhydrous diethyl ether (Et_2O, Fischer) was further dried over sodium metal by the literature method.[128] Liquid ammonia, NH_3, (Matheson) was dried over sodium metal and stored at –78 °C. All solvents were transferred by static vacuum distillation using a

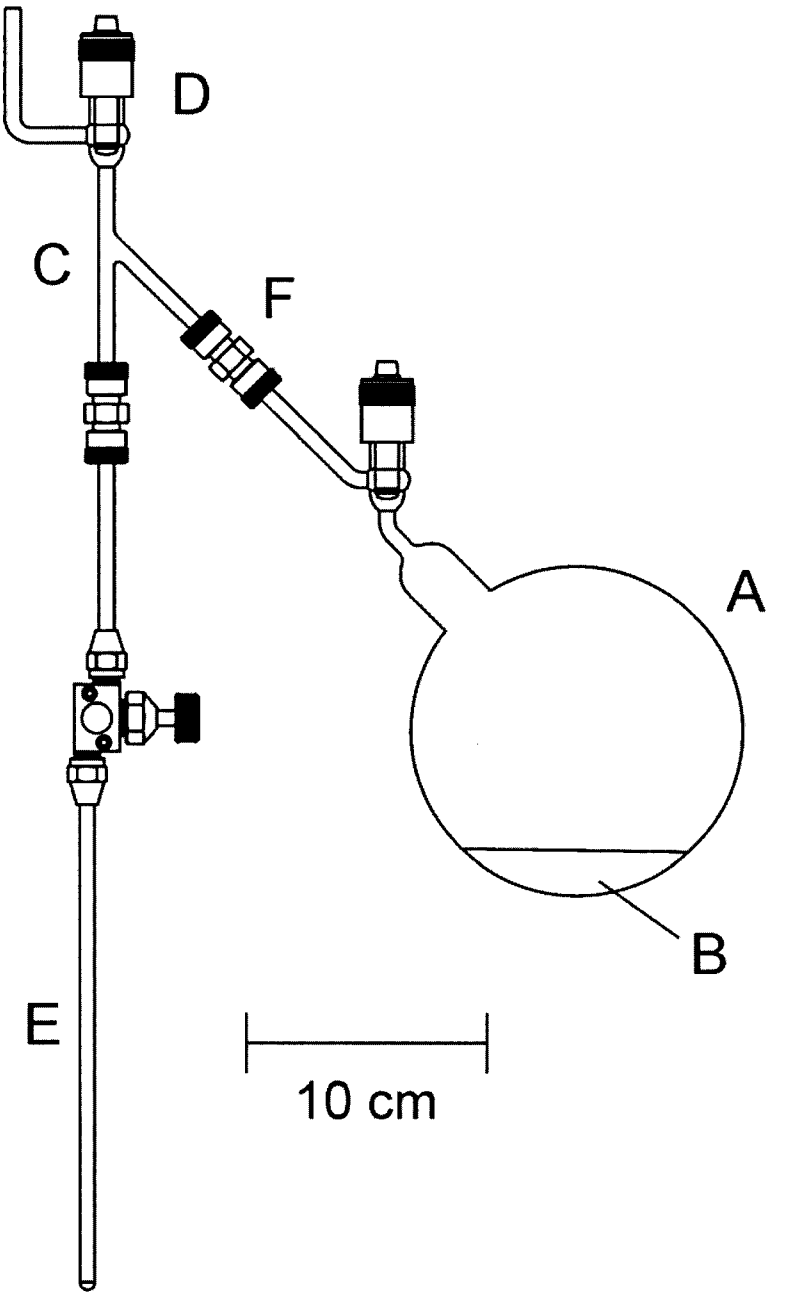

Figure 2.4. Apparatus used for the vacuum transfer of SO_2ClF solvent; (A) 250-mL glass vessel equipped with a 4-mm J. Young all-glass stopcock, (B) bed of dry, powdered KF, (C) glass Y-connector, (D) 6-mm J. Young PTFE/glass valve, (E) FEP reaction vessel fitted with a Kel-F valve, (F) ¼-in. stainless steel Cajon Ultratorr union.

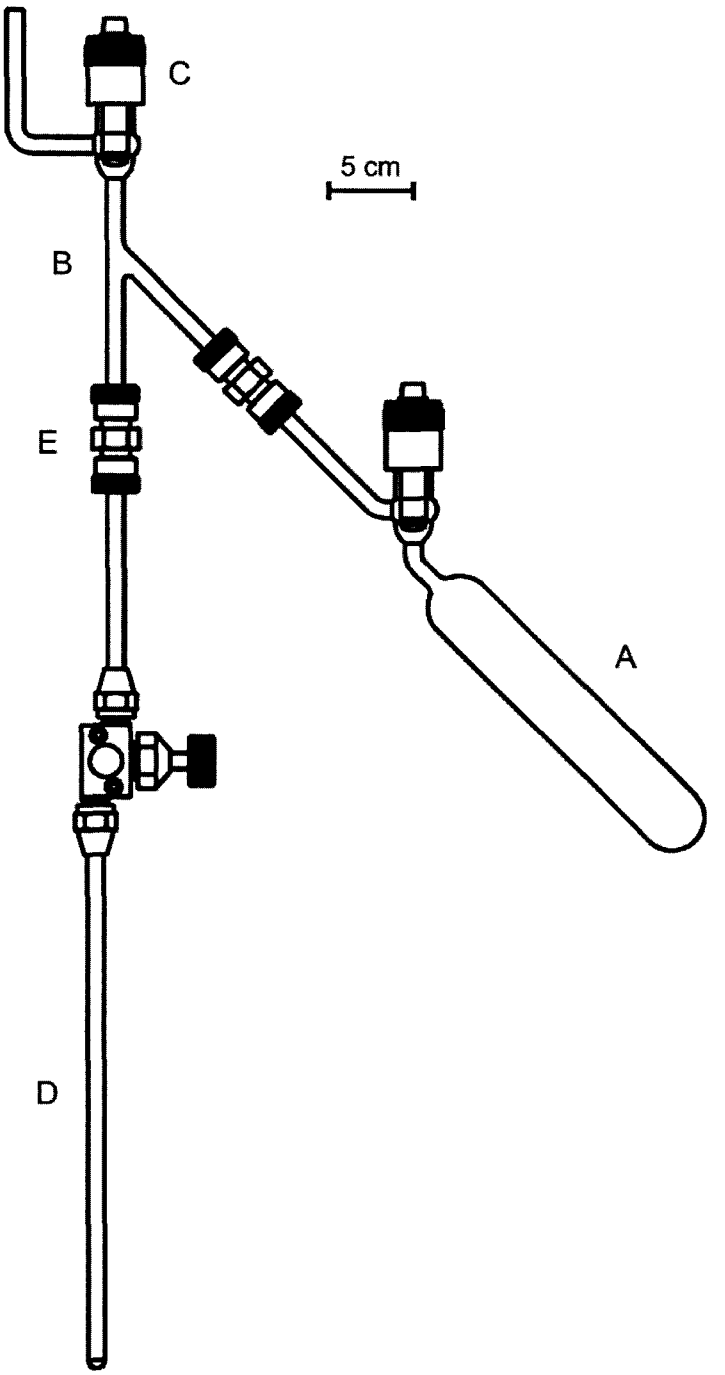

Figure 2.5. Glass submanifold used for the static vacuum distillation of anhydrous organic solvents; (A) Pyrex solvent storage vessel, (B) glass Y-piece, (C) 6-mm J. Young PTFE/glass valve, (D) FEP reaction vessel equipped with a Kel-F valve, (E) ¼-in. stainless steel Cajon connector fitted with Viton O-rings.

glass vacuum line and a glass submanifold in a configuration similar to that depicted in Figure 2.5.

2.2.3. Os Metal, OsO_4, H_2O, and $Os^{18}O_4$

Osmium metal powder, Os, (Aldrich, 99.9%) was dried on a glass vacuum for 24 h and subsequently dried in the evacuated port of the dry box for a minimum of 60 min. Natrual abundance OsO_4 (Aldrich, 99.8%) and H_2O (Caledon, HPLC grade) were used without further purification.

Oxygen-18 enriched osmium tetroxide, $Os^{18}O_4$ was prepared by combustion of the metal powder as a modification of the method described by Brauer.[129] In a typical experiment, osmium metal powder (1.00 g, 5.26 mmol) was added to a 9-mm o.d. quartz reaction tube (Figure 2.6) through a 4-mm J. Young glass valve with a PTFE barrel. The reactor was placed in a horizontal position and the powdered metal was spread along the length of the quartz tube. Reduction of the osmium metal was achieved by heating the metal to redness with a natural gas-oxygen torch in the presence of successive aliquots of H_2 (ca. 850 torr) until water evolution ceased, followed by hot removal of H_2O under vacuum. Additional aliquots of H_2 were added and heated to ensure that all H_2O had been removed. The dry metal was then quantitatively converted to $Os^{18}O_4$ by admitting aliquots of $^{18}O_2$ gas to the reaction vessel and heating the metal to red heat with a natural gas-oxygen torch until combustion ceased. The $Os^{18}O_4$ that formed condensed as a pale yellow solid in the cooler regions of the reactor. The reactor was allowed to cool to room temperature before a second aliquot of oxygen gas was admitted. The procedure was repeated until no osmium metal remained. After combustion was complete, the vessel was

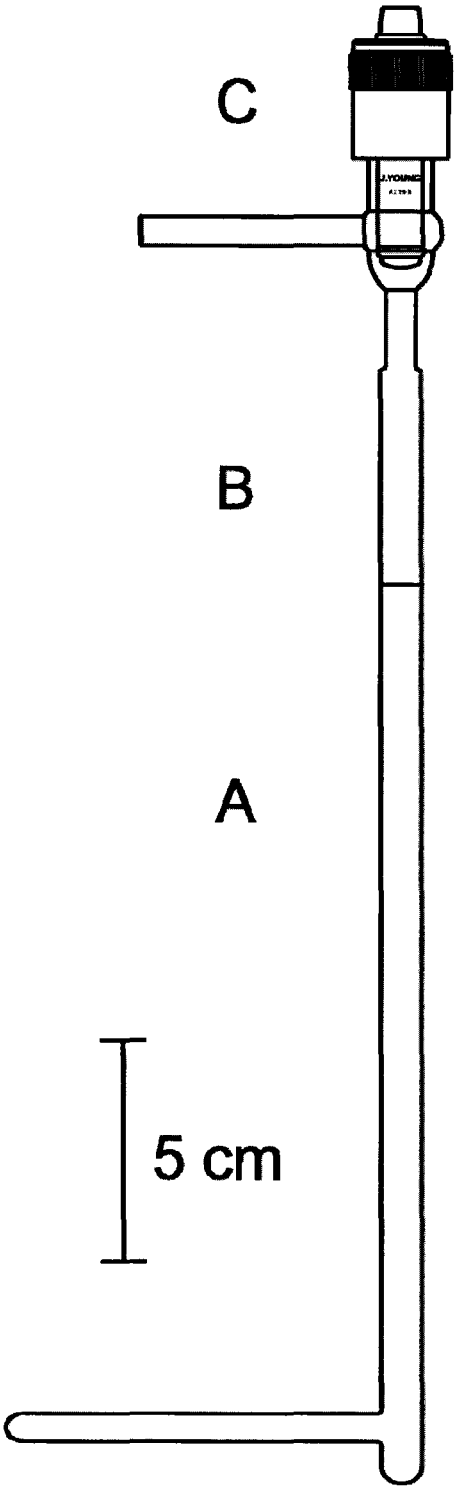

Figure 2.6. Reactor used for the preparation of $Os^{18}O_4$; (A) 9-mm o.d. quartz tube, (B) graded joint, (C) 4-mm J. Young PTFE/glass valve.

evacuated and $Os^{18}O_4$ was melted and poured under static vacuum into the 6-mm o.d. side arm by gently heating the reactor with a heat-gun. The side tube was removed inside a dry box and the metal was stored under N_2.

2.2.4. Drying of [K][F], [Cs][F], and Preparation of $[N(CH_3)_4][F]$, and NOF

Finely ground [K][F] (J. T. Baker Chemical Co., 99%) was dried under dynamic vacuum at ca. 250 °C in a glass vessel for a minimum of 3 days. The solid was stored in the glass drying vessel in a dry box until used.

Cesium fluoride, [Cs][F] (Aldrich, 99.9%) was dried by fusion in a platinum crucible, followed by transfer of the molten liquid to the dry box port where it was immediately evacuated. Upon transferring to the dry nitrogen atmosphere of a dry box, the solidified sample was ground to a fine powder and stored in the dry box until used.

Tetramethylammonium fluoride, $[N(CH_3)_4][F]$, was prepared according to the literature method by titration of $[N(CH_3)_4][OH]$ with 47% aqueous HF to its equivalence point.[53] After drying the product under dynamic vacuum at 150 °C, the remaining traces of water were removed by repeatedly dissolving the salt in isopropanol and removing the water/isopropanol azeotrope under dynamic vacuum at room temperature and then at 150 °C.

Nitrosyl fluoride, NOF, was prepared by reaction of NO and F_2 in a 30-mL nickel vessel. Pure NO gas was initially measured into a 2-L nickel vessel (ca. 833 Torr, 0.0905 mol) followed by condensing into a 30-mL reaction vessel at –196 °C. After transfer, the metal vacuum line was pumped to remove any residual NO. Fluorine gas was then condensed into an intermediate 30-mL measuring can at –196 °C. The can was then

warmed to –183 °C using a liquid oxygen bath and F_2, free of non-volatile contaminants (i.e., HF, CF_4, OF_2, and/or NF_3), was allowed into the vacuum line manifold and attached 2-L nickel vessel. The purified F_2 (384 Torr, 0.0417 mol) was then condensed from the 2-L vessel into the reaction vessel cooled to –196 °C. The reaction vessel was then closed and allowed to warm slowly to room temperature. After ca. 1 h at room temperature, the vessel was again cooled to –196 °C and the residual F_2 was removed under dynamic vacuum. The procedure was repeated a second time to give a combined yield of 8.63 g (0.1762 mol) of NOF. Small amounts of NO_2F (2.2%) and NOF_3 (0.85%) were estimated by recording the ^{19}F NMR spectrum of the liquid product at –80 °C. A fluorine-passivated submanifold, constructed from 316 stainless steel and nickel and dedicated to the transfer of NOF, was passivated with NOF prior to transfer of NOF to a reaction vessel. The success of the passivation was determined by a visual check of the color of the NOF condensed into an auxillary tube. If the solid NOF was colorless to very faint blue, consistent with the absence or a trace amount of N_2O_3, the NOF was deemed to be chemically pure and ready to use.

2.2.5. Preparation of ClF_3

Chlorine trifluoride (ClF_3) was prepared by direct fluorination of chlorine in a nickel vessel. Chlorine (0.114 mol) and fluorine (0.360 mol) gases were transferred into a 834 mL nickel vessel with a chlorine to fluorine ratio of 1:3.2. The mixture was heated to 250 °C for 19 h. The furnace was turned off and the mixture was allowed to cool over a period of 12 h to room temperature. The product was used directly from the reaction vessel after excess fluorine gas had been removed under vacuum at –196 °C.

2.2.6. Preparation of XeF_2, KrF_2, XeF_6, and $XeOF_4$

Xenon difluoride was prepared according to the literature method[130] and stored in a Kel-F tube inside a dry box prior to use.

Krypton difluoride was prepared by use of a 316 stainless steel hot-wire reactor (Figure 2.7) equipped with a nickel filament, similar to that originally described by Bezmel'nitsyn et al.[131] and subsequently modified by Kinkead et al.[132] The filament was fabricated from a $^1/_{16}$-in nickel rod tightly wound about a second length of $^1/_{16}$-in rod that was, in turn, coiled and stretched into a helix. In a typical preparation, the hot-wire reactor was pressurized with 1000 Torr (50 mmol) of krypton and then cooled to –196 °C in a 20-L Dewar. After reaching thermal equilibrium, the reactor was pressurized with 25 Torr of F_2 and the DC power supply for the nickel filament was adjusted to ca. 6 V and 30 A (the filament was dull red in color under these conditions). The F_2 pressure increased to ca. 45 Torr after the power supply was turned on and was regulated between 25 and 45 Torr by the periodic addition of F_2 during the synthesis. The declining F_2 pressure was used to qualitatively monitor the production of KrF_2, and additional Kr (1.0 to 2.0 mmol) was condensed into the reactor when the rate of KrF_2 production slowed or ceased. Upon completion of the reaction (ca. 12 h), excess F_2 was removed under dynamic vacuum at –196 °C. The excess Kr and crude KrF_2 were recovered as a pale pink solid (the coloration arises from chromium oxide fluoride contamination) by allowing the reactor to slowly warm to room temperature while dynamically pumping the volatile contents through a ½-in o.d. FEP U-trap (–196 °C). The Kr/KrF_2 mixture was then warmed to

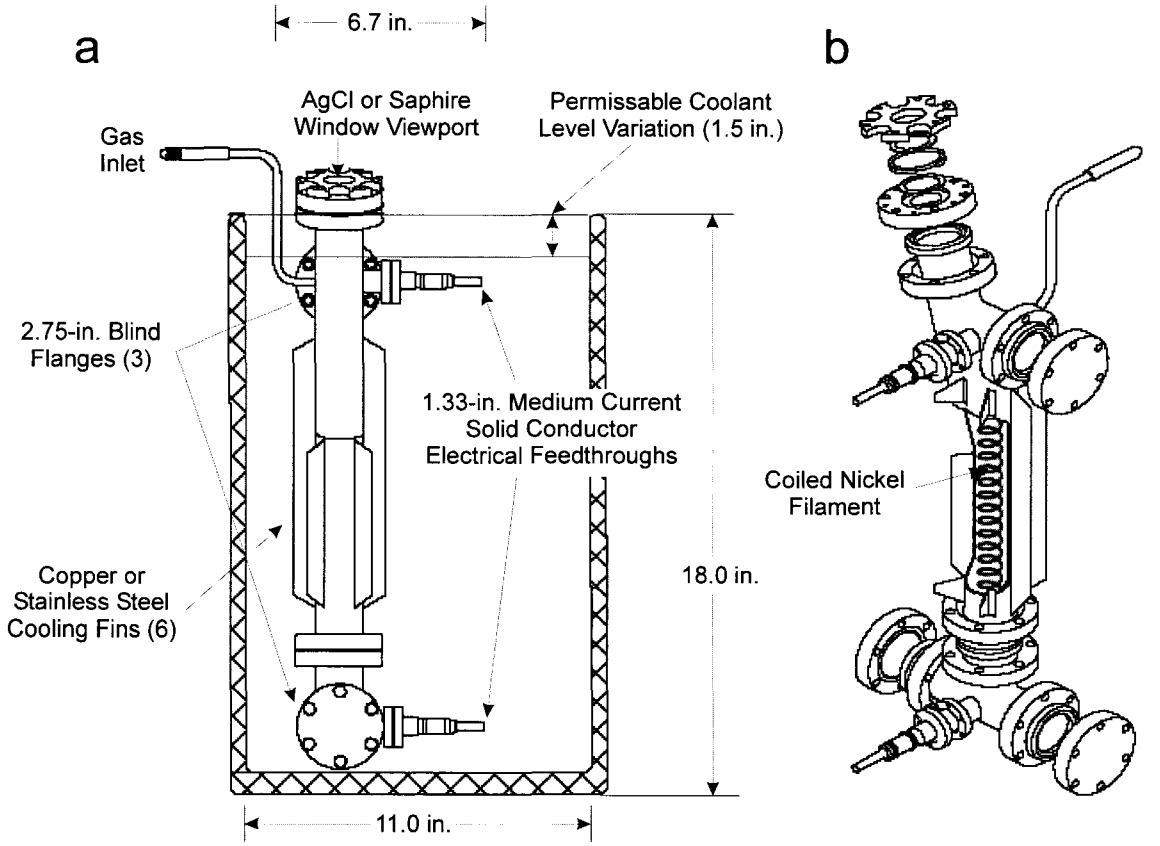

Figure 2.7. The stainless steel hot-wire reactor used for the preparation of KrF_2. (a) External view and dimensions of a hot-wire reactor submerged in a liquid nitrogen coolant bath. (b) A perspective drawing of the hot-wire reactor showing the flange assembly and nickel filament (cut away region). Reproduced with permission from ref 28

–78 °C under dynamic vacuum to remove the unreacted Kr. The crude KrF_2 was purified by briefly warming the sample to 0 °C and flash distilling off the more volatile chromium oxide fluorides. The remaining colorless KrF_2 was finally warmed to room temperature and rapidly sublimed into a $^3/_8$-in o.d. FEP tube equipped with a Kel-F valve, where it was stored under 1000 Torr of N_2 or Ar at -78 °C until used. This synthesis is highly reproducible and typically yields 2.5 to 3.0 g of purified KrF_2 over a 12 h period.

Xenon hexafluoride (XeF_6) was prepared by a method similar to that outlined by Chernick and Malm.[133] Xenon and F_2 were transferred into a nickel vessel with a xenon to fluorine ratio of 1:22 and a total autogeneous pressure of 56 atm at room temperature. The mixture was heated to 250 °C for 24 h and slowly cooled to 47 °C over a period of 16 h before turning off the furnace and allowing the mixture to cool to room temperature. Excess F_2 was removed by releasing the pressure at –78 °C into a 5L Monel storage vessel used to recover and recycle F_2. Unreacted F_2 was removed from the nickel vessel under vacuum at –78 °C. The product was vacuum distilled into a ½-in. o.d. FEP storage vessel equipped with a Kel-F valve. The purity was assessed using Raman spectroscopy. Only trace amounts of XeF_4 were detected.

Xenon oxide tetrafluoride was synthesized by hydrolysis of XeF_6 as previously described.[134]

2.2.7. Purification of SbF_5

Antimony pentafluoride (Ozark Mahoning) was purified by vacuum distillation as previously described,[135] and stored in a glass vessel inside a desiccator until used. Subsequent transfers of SbF_5 were performed by use of a dry all-glass syringe in the inert

atmosphere of a glove bag which had previously been purged with dry nitrogen for at least 12 h.

2.2.8. Potassium Bis(trimethylsilylamide) ([K][$C_6H_{18}Si_2N$])

Potassium bis(trimethylsilylamide), [K][$(CH_3)_3Si)_2N$] (Aldrich, 95%) was dried in the evacuated port of the dry box for a minimum of 60 min. and was exposed to the dry box atmosphere for at least two days prior to use.

2.2.9. OsO_3F_2 and *cis*-$Os^{16/18}O_2F_4$

Osmium trioxide difluoride (OsO_3F_2) was prepared by reaction of OsO_4 with excess ClF_3 at room temperature according to the literature method.[11] Osmium dioxide tetrafluoride was synthesized either by reaction of OsO_4 (Koch-Light, 99.6%) or previously synthesized $Os^{18}O_4$ with KrF_2 in aHF or by reaction of OsO_3F_2 with excess KrF_2 in HF solvent as previously described.[20] The purities of the compounds were checked by Raman spectroscopy to ensure completeness of the reactions.

2.2.10. OsF_6 and $OsOF_4$

Osmium hexafluoride (OsF_6) was prepared by the standard literature method[30] by direct fluorination of osmium with fluorine in a Monel vessel at 300 °C over a period of 4 h. Osmium oxide tetrafluoride ($OsOF_4$) was prepared by two methods; (1) by slow warming of an HF solution of OsF_6, (53.2 mg, 0.175 mmol) and H_2O, (3.10 mg, 0.172 mmol) to room temperature in a ¼-in. o.d. FEP reactor as previously described;[36] and (2) by reaction of OsO_4 (203 mg, 0.799 mmol) with OsF_6 (0.967 g, 3.180 mmol) at 180 °C in an 80 mL nickel vessel as previously described.[41] The products of both reactions were recovered as green powders.

2.2.11. [K][CH_2CN]

The cyanomethyl anion ([K][CH_2CN]) was synthesized using a modification of the published synthesis of [Na][CH_2CN].[55] The synthetic apparatus consisted of two cylindrical vessels, each outfitted with a grease-free 4-mm J. Young Teflon/glass stopcock joined by means of a 12.1 cm length of 7 mm o.d. Pyrex glass tubing outfitted with a grease-free 4-mm J. Young Teflon/glass stopcock so that both sides of the reactor could be isolated from one another (Figure 2.8). In a typical reaction, arm (B) of the H-shaped vessel was loaded with 1.048 g (5.252 mmol) of [K][$((CH_3)_3Si)_2N$] and a Teflon coated magnetic stirring, and arm (A) was loaded with 0.2142 g (5.212 mmol) of CH_3CN. Aproximately 1.3 mL of Et_2O was distilled onto the CH_3CN and approximately 15 mL of Et_2O was distilled onto the [K][$((CH_3)_3Si)_2N$] which dissolved upon warming to –78 °C. The central stopcock was opened and the CH_3CN/Et_2O solution was slowly poured in small amounts onto the [K][$((CH_3)_3Si)_2N$]. White [K][CH_2CN] precipitated from solution upon addition of the CH_3CN solution to the Et_2O solution of [K][$((CH_3)_3Si)_2N$]. The solid was not filtered as previously described,[55] but the supernatant was displaced through a Teflon cannula with dry argon gas and the precipitate was washed with 5 aliquots of 10 mL of dry Et_2O. A Kel-F cap having two $\frac{1}{16}$-in. holes was used to cap arm "D" of the H-shaped vessel and was sealed by means of a Viton O-ring (See Figure 2.9). Prior to assembly, a $\frac{1}{16}$-in. o.d. Teflon tube was passed through one hole of the Kel-F cap which had a slow stream of argon slowly passing through it. The Teflon tube end was positioned in the glass arm of the H-tube. The air in the glass arm was first displaced with argon, then the J. Young valve was opened and the

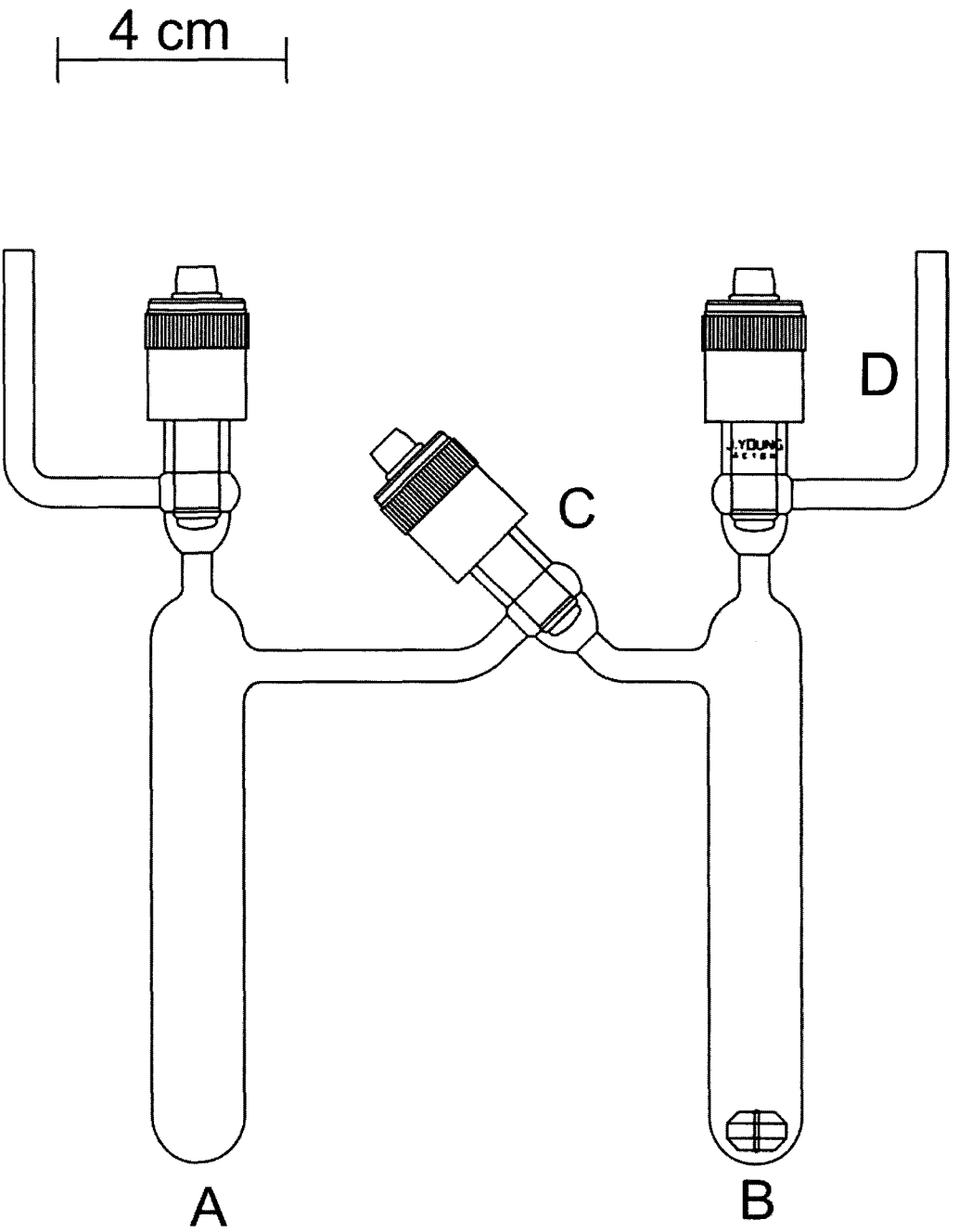

Figure 2.8. Glass H-shaped reaction vessel used for the synthesis of [K][CH_2CN]; (A) Pyrex glass reaction vessel (arm A), (B) Pyrex glass reaction vessel (arm B), (C) 4-mm J. Young Teflon/glass stopcock, (D) ¼-in. glass tube for vacuum connection. Reproduced with permission from Ref 136

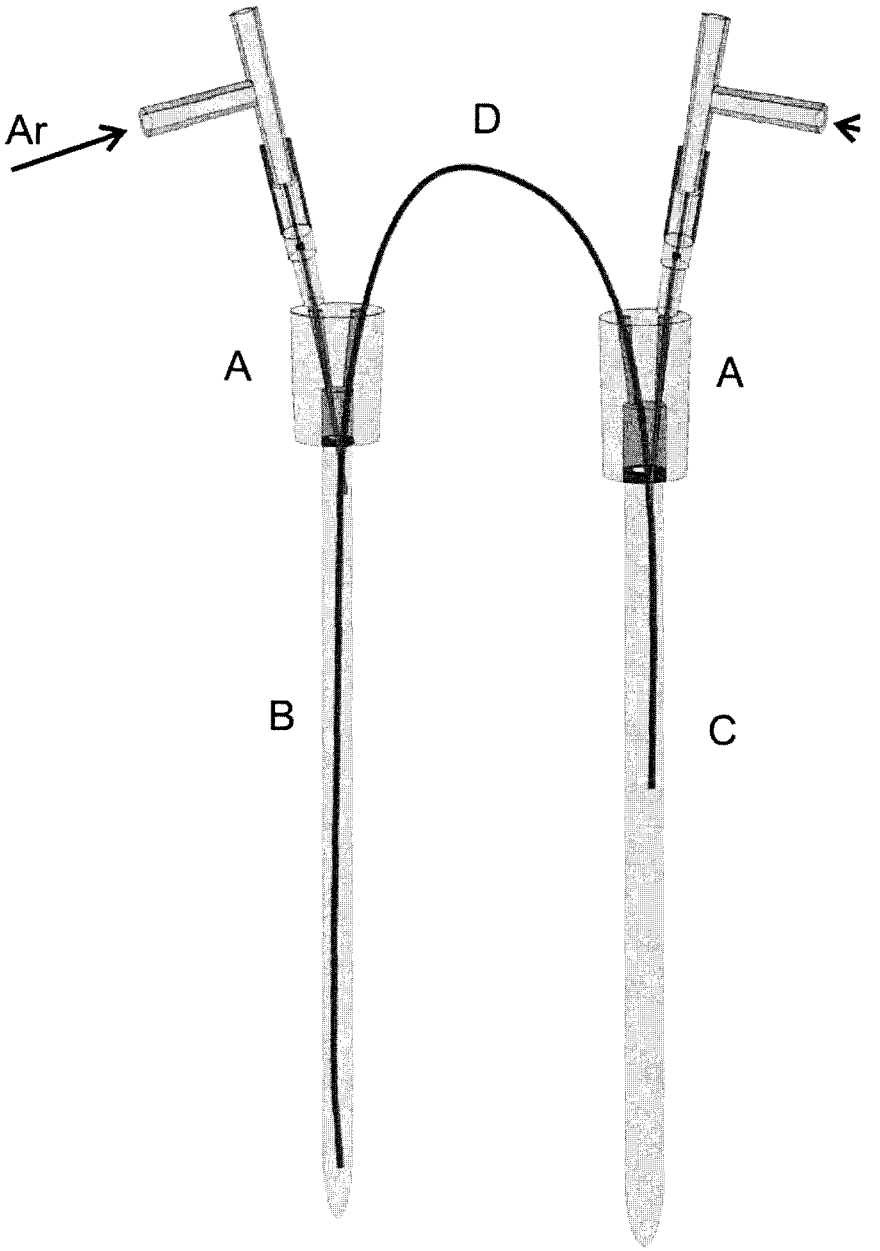

Figure 2.9. Apparatus used to transfer solutions under a flow of argon gas. (A) Kel-F cap equipped with a viton O-ring, (B) Source FEP reaction tube, (C) Target FEP tube, (D) $^{1}/_{16}$-in. o.d. Teflon tube used for transferring solutions. Reproduced with permission from Ref 137

nitrogen in the reaction vessel was displaced with argon. A second Teflon capillary tube was inserted through the outlet hole of the Kel-F cap while maintaining the argon flow. The capillary tube was pushed through the J. Young valve using the stopcock valve to guide the tube down into the reaction vessel. Lowering the outlet tube into the ether solution forced the clear supernatant though the Teflon cannula tube into a 250 mL round bottom flask. The capillary tube was removed from the reaction vessel and the J. Young valve was closed. This procedure was repeated three times after which the reactor and contents were pumped to dryness on a glass vacuum line. Raman samples were obtained by transferring the solid to a 5-mm o.d. glass tube equipped with a J. Young valve.

2.3. Fluoride Ion Donor Properties of *cis*-OsO_2F_4

2.3.1. Synthesis of $[OsO_2F_3][Sb_2F_{11}]$

A fluorine-passivated ¼-in. o.d. FEP reaction tube was loaded with 0.1055 g (0.3541 mmol) of deep burgundy colored *cis*-OsO_2F_4 inside a nitrogen-filled dry box. The reaction tube was then transferred to a glove bag purged with dry N_2 and an excess of SbF_5, 0.500 g (2.31 mmol), was syringed into the tube. Upon warming the reactor and contents to room temperature, *cis*-OsO_2F_4 slowly dissolved giving a deep orange solution having a significantly lower viscosity than that of pure SbF_5, which was indicative of $Sb_nF_{5n+1}^-$ anion formation. The reaction vessel was pumped at 0 °C to remove excess SbF_5. After pumping for 40 h, 0.2559 g (0.3498 mmol) of orange powder remained which was identified as $[OsO_2F_3][Sb_2F_{11}]$ (98.8% yield) by Raman spectroscopy.

2.3.2. Attempted Syntheses of $[OsO_2F_3][SbF_6]$

Following a procedure similar to that outlined above, 0.0602 g (0.202 mmol) of *cis*-OsO_2F_4 was loaded into a reaction tube followed by the addition of 0.5056 g (2.333 mmol) of SbF_5. After warming the reactor and contents to room temperature, *cis*-OsO_2F_4 slowly dissolved in SbF_5, giving a deep orange solution which had a significantly lower viscosity than pure SbF_5. Excess SbF_5 was removed by pumping at 0 °C for 3 days, yielding an orange powder identified by Raman spectroscopy as $[OsO_2F_3][Sb_2F_{11}]$. Further pumping on the sample followed by periodic weighing and characterization by Raman spectroscopy revealed loss of SbF_5 from the sample. After 6 days of pumping, an orange powder (0.1110 g) remained which was identified by Raman spectroscopy as $[\mu\text{-}F(OsO_2F_3)_2][Sb_2F_{11}]$ (0.1078 mmol; 107% yield).

In another attempt to isolate $[OsO_2F_3][SbF_6]$, 0.06635 g (0.2251 mmol) of *cis*-OsO_2F_4 was transferred into a ¼-in. o.d. FEP reaction vessel equipped with a ¼-in. o.d. FEP sidearm fused at a right angle to the main tube and excess SbF_5 (ca. 0.25 g, 1.16 mmol) was added followed by condensation of ca. 1 mL of aHF onto the sample at –196 °C. Upon warming to room temperature, the sample rapidly dissolved to give a light orange solution. The sample was cooled to –78 °C, whereupon a light orange solid precipitated. The Raman spectrum of the solid was recorded under aHF at –150 °C and was shown to be $[\mu\text{-}F(OsO_2F_3)_2][Sb_2F_{11}]$. Excess HF and SbF_5 were removed under dynamic vacuum at 0 °C. Pumping for 5 h yielded a free-flowing orange powder (0.1152 g) identified by Raman spectroscopy as $[\mu\text{-}F(OsO_2F_3)_2][Sb_2F_{11}]$ (0.1119 mmol; 99.4% yield).

In a final attempt to synthesize $[OsO_2F_3][SbF_6]$, $[OsO_2F_3][Sb_2F_{11}]$ was prepared from 0.06404 g (0.2148 mmol) of *cis*-OsO_2F_4 and an excess of SbF_5 (ca. 0.25g, 1.16 mmol) in a ¼-in. o.d. FEP reaction tube as previously described (vide supra). Two equivalents of *cis*-OsO_2F_4 (0.1201 g, 0.4027 mmol) were added to freshly prepared $[OsO_2F_3][Sb_2F_{11}]$ (0.1520 g, 0.2077 mmol) followed by condensation of ca. 1 mL of aHF onto the sample at –196 °C. Upon warming to room temperature, the sample slowly dissolved to give a magenta-colored solution. The sample was cooled to –78 °C, whereupon a magenta solid corresponding to *cis*-OsO_2F_4 precipitated. The Raman spectrum was recorded under aHF at –150 °C and showed that a mixture of $[\mu\text{-}F(OsO_2F_3)_2][Sb_2F_{11}]$ and *cis*-OsO_2F_4 was present. Hydrogen fluoride removal under dynamic vacuum at –78 °C followed by pumping for 3 h at –78 °C yielded a finely divided mixture of orange and magenta crystallites identified by Raman spectroscopy as $[\mu\text{-}F(OsO_2F_3)_2][Sb_2F_{11}]$[22] and *cis*-$OsO_2F_4$.[11] Upon warming to 90 °C for 1 h, the sample turned completely magenta as *cis*-OsO_2F_4 neared its melting point. The Raman spectrum (–150 °C) of the heated mixture showed no signs of further reaction.

2.3.3. $[OsO_2F_3][Sb_2F_{11}]$ Crystal Growth

Crystals of $[OsO_2F_3][Sb_2F_{11}]$ were obtained from a sample comprised of 0.0821g (0.275 mmol) of *cis*-OsO_2F_4 and excess SbF_5 (0.500 g, 2.31 mmol) in a ¼–in. o.d. FEP beaded reactor (vide supra). The sample was placed in a near-horizontal position, distributing the SbF_5 solution equally among the three wells of the beaded reactor. Slow removal of SbF_5 under dynamic vacuum at 0 °C resulted in crystal growth within each well of the reaction vessel. After 30 h, SbF_5 solvent had been completely removed and

pumping was halted. The tube and orange crystalline samples were cooled to −78 °C and backfilled with dry N_2. A crystal of $[OsO_2F_3][Sb_2F_{11}]$ having the dimensions 0.26 x 0.12 x 0.06 mm^3 was selected at −105 ±3 °C for low-temperature X-ray structure determination and was mounted in a cold stream (–173 °C) on a goniometer head as previously described.[23]

2.4. Fluoride Ion Acceptor Properties of *cis*-OsO_2F_4 and $OsOF_4$

2.4.1. Synthesis of $[Cs][OsO_2F_5]$

In a typical synthesis, 113.6 mg (0.381 mmol) of *cis*-OsO_2F_4 and 67.6 mg (0.445 mmol) of CsF (15% excess of CsF) were loaded into a 4-mm FEP tube fitted with a Kel-F valve inside a dry box. The mixture was heated to 95 °C in an oil bath for periods of one min. followed by mixing until a homogeneous orange solid formed and no *cis*-OsO_2F_4 was visible.

2.4.2. Synthesis of $[N(CH_3)_4][OsO_2F_5]$

In a typical synthesis, 56.33 mg (0.177 mmol) of *cis*-OsO_2F_4 and 15.4 mg (0.181 mmol) of $[N(CH_3)_4][F]$ were loaded inside the dry box into a dry and previously fluorine passivated ¼-in. o.d. FEP reactor fitted with a Kel-F valve at ca. –150 °C. Excess FNO solvent was condensed onto the solid and, upon melting the FNO at –78 °C, a vigorous reaction ensued during which the magenta/white heterogeneous solid mixture changed to orange under FNO. The excess FNO was removed under dynamic vacuum at –78 °C.

2.4.3. Synthesis of [NO][OsO_2F_5]

A previously dried and fluorine passivated 4-mm FEP reaction tube was loaded with 16.59 mg (0.0556 mmol) of *cis*-OsO_2F_4. Excess FNO was condensed onto the solid yielding a red/brown solution above the undissolved *cis*-OsO_2F_4 at –78 °C.

Alternately, inside the dry box, 16.59 mg (0.0556 mmol) of *cis*-OsO_2F_4 was transferred into a 4-mm FEP tube. Approximately 2.5 cm of HF was distilled onto the solid. Excess FNO was condensed onto the solution and allowed to react at –78 °C. After 12 h, a red/brown solution had formed over undissolved magenta *cis*-OsO_2F_4.

2.4.4. Synthesis of [NO][$OsOF_5$]

A previously dried and fluorine passivated 4-mm FEP reaction tube containing 12.46 mg (0.0442 mmol) of $OsOF_4$ was connected to a metal vacuum line through a three-way FEP connector which was, in turn, also connected to the FNO storage vessel and an empty FEP tube. The FNO vessel was cooled to –78 °C and the FNO was first distilled into the empty tube at –196 °C to check for purity and quantity. The empty tube was then warmed to –78 °C and an excess of FNO was distilled onto the $OsOF_4$ at –196 °C. The reaction was warmed to –78 °C and allowed to proceed for ca. 12 h. A brown solution formed above a dark solid. The FNO was then removed by dynamic vacuum at –78 °C leaving behind a grey solid.

2.4.5. Synthesis of [Cs][$OsOF_5$]

A 4-mm tube was loaded with 9.0 mg (0.0032 mmol) of $OsOF_4$ and 6.6 mg (0.0043 mmol) of CsF inside the dry box at –150 °C. Approximately 2.5 cm of HF was distilled onto the solid and the reaction mixture was allowed to slowly warm to room

temperature whereupon a brown solution formed. The HF was removed under dynamic vacuum yielding a brown solid.

2.4.6. Crystal Growth

2.4.6.1. $[Cs][OsO_3F_3]\cdot CH_3CN$

Crystals of $[Cs][OsO_3F_3]\cdot CH_3CN$ were obtained from an NMR sample composed of 9.0 mg (0.0032 mmol) of $OsOF_4$ (prepared by the hydrolysis of OsO_4 in HF[36]) and 6.6 mg (0.0043 mmol) of CsF that had been previously reacted in HF and subsequently isolated that was dissolved in CH_3CN solvent (see Synthesis of $[Cs][OsOF_5]$) in a 4-mm o.d. FEP reactor. The sample was warmed to 25 °C to dissolve as much solid as possible and was subsequently cooled to –30 °C. The tube was placed in a near-horizontal position, distributing the CH_3CN solution along the length of the reaction vessel. Slow cooling of the solution from –30 to –40 °C over a period of 5 h resulted in the growth of orange block-shaped crystals. The crystals were isolated by removal of the bulk CH_3CN through a Teflon cannula at –45 °C using an overpressure of argon.[138] A crystal having the dimensions 0.23 x 0.12 x 0.09 mm^3 was selected at –105 ±3 °C for low-temperature X-ray structure determination and was mounted in a cold stream (–173 °C) on a goniometer head as previously described.[23]

2.4.6.2. *cis*-$OsO_2F_4\cdot[Cs][CH_2CN]$

Crystals of *cis*-$OsO_2F_4\cdot[Cs][CH_2CN]$ were obtained from a sample composed of 0.1368 g (0.3039 mmol) of $[Cs][OsO_2F_5]$ and 0.5192 g (0.3147 mmol) of [Cs][F] dissolved in CH_3CN in a ¼-in. FEP T-shaped reactor. A purple solution above an amorphous brown solid was present when the reactor and contents were warmed to

–20 °C. Red crystals of *cis*-OsO_2F_4·[Cs][CH_2CN] grew at 0 °C over a period of 3 h in the vertical arm of the reaction vessel and settled on top of the brown precipitate. Crystals were isolated by decanting the solvent into the horizontal arm and were dried along with the brown material under dynamic vacuum at –78 °C. The red crystals were separated from the brown solid under a microscope in the course of crystal mounting. The crystal used for X-ray structure determination had the dimensions 0.18 x 0.14 x 0.10 mm^3.

2.4.6.3. *cis*-OsO_2F_4·[$N(CH_3)_4$][CH_2CN]

Crystals of *cis*-OsO_2F_4·[$N(CH_3)_4$][CH_2CN] were obtained from a sample composed of 0.0677 g (0.177 mmol) of [$N(CH_3)_4$][OsO_2F_5] dissolved in CH_3CN in a ¼-in. FEP tube. Red crystals were grown between –15 and –28 °C. When sufficient crystals of good quality had grown, the tube was severed under a flow of argon and sealed with a Kel-F cap having two $^1/_{16}$-in. holes which was sealed onto the FEP reaction tube by means of a Viton O-ring (See Figure 2.9). Prior to assembly, a $^1/_{16}$-in. o.d. Teflon tube was passed through one hole of the Kel-F cap which had a slow steam of argon slowly passing through it. The Teflon tube end was positioned well above the supernatant and the nitrogen in the reaction tube was displaced with argon through the second hole in the Kel-F cap. A second Teflon capillary tube was inserted through the outlet hole of the Kel-F cap while maintaining the argon flow. Lowering the outlet tube into the solution forced the pale red supernatant through the tube into a second ¼-in. o.d. FEP container cooled to –78 °C. The Kel-F cap was removed and the tube was sealed with a Swagelok Ultra-Torr union connected to a Kel-F valve. The crystals were dried under dynamic

vacuum at –30 °C. The crystal used for X-ray structure determination had the dimensions 0.18 x 0.18 x 0.14 mm^3.

2.4.6.4. *cis*-OsO_2F_4·[Cs][CH_2CN]·0.3HF

Crystals of *cis*-OsO_2F_4·[Cs][CH_2CN]·0.3HF were obtained from a sample comprised of 0.0100 g (0.0222 mmol) of [Cs][OsO_2F_5] dissolved in CH_3CN in a ¼-in. FEP reaction vessel. Orange plate-like crystals of *cis*-OsO_2F_4·[Cs][CH_2CN]·0.3HF and colorless block-shaped crystals grew between 0 and –35 °C over a period of 11 h. The crystals were isolated by removal of the solvent under dynamic vacuum at –40 °C. The orange crystals were selected and mounted for X-ray diffraction. The crystal used for X-ray structure determination had the dimensions 0.20 x 0.20 x 0.02 mm^3.

2.4.6.5. *cis*-OsO_2F_4

Crystals of *cis*-OsO_2F_4 were obtained from a sample comprised of 0.0377 g (0.126 mmol) of *cis*-OsO_2F_4 and 0.150 g (0.611 mmol) XeF_6 in a 4-mm FEP tube. The mixture was heated to 45 °C whereupon XeF_6 melted and *cis*-OsO_2F_4 was soluble in the molten XeF_6. Purple crystals of *cis*-OsO_2F_4 and colorless crystals of XeF_6 were grown by sublimation from XeF_6 solution at 45 °C over a period of 4 days. Crystals of XeF_6 and *cis*-OsO_2F_4 grew in cooler portions of the tube and in some cases, the XeF_6 crystals encased the *cis*-OsO_2F_4 crystals. The purple plates encased in XeF_6 were of better quality than the crystals which were not encased, and were carefully broken out of the larger XeF_6 crystal and used for X-ray diffraction. The crystal used for X-ray structure determination had the dimensions 0.11 x 0.06 x 0.05 mm^3.

2.5. Xenon (VI) Adducts of *fac*-OsO_3F_2

2.5.1. Syntheses of $(OsO_3F_2)_2 \cdot 2XeOF_4$ and $(OsO_3F_2)_2$

Inside a nitrogen-filled dry box, a fluorine passivated FEP reaction vessel was loaded with 0.02803 g (0.1015 mmol) of orange $(OsO_3F_2)_\infty$. The reaction vessel was then transferred to a metal vacuum line and ca. 1.0 g (4.5 mmol) of $XeOF_4$ was distilled into it. Upon warming to room temperature, an orange suspension formed which slowly dissolved with agitation over a period of several hours to form a deep orange colored solution. The reaction vessel was attached to a metal vacuum line through a FEP U-trap cooled to −196 °C and excess $XeOF_4$ was removed under dynamic vacuum at 0 °C. Pumping for ca. 2½ min yielded an orange solid that was identified as $(OsO_3F_2)_2 \cdot 2XeOF_4$ (0.04931 g, 0.04936 mmol) by Raman spectroscopy. Associated $XeOF_4$ was removed from the adduct by further pumping on the solid at 0 °C for 3 h, producing a yellow powder identified as $(OsO_3F_2)_2$ (0.02720 g, 0.04924 mmol) by Raman spectroscopy. The dimer underwent a phase transition to $(OsO_3F_2)_\infty$ when warmed to and maintained at room temperature for 1½ h, whereas the Raman spectrum of the $XeOF_4$ adduct showed no change when the sample was held at room temperature for up to 5 h. Slow dissociation of $XeOF_4$ and rearrangement of $(OsO_3F_2)_2$ to $(OsO_3F_2)_\infty$ was, however, detected upon further standing at room temperature and was complete after 21 days.

2.5.2. $(OsO_3F_2)_2 \cdot 2XeOF_4$ Crystal Growth

Crystals of $(OsO_3F_2)_2 \cdot 2XeOF_4$ were obtained from a sample comprised of 0.0502 g (0.182 mmol) of OsO_3F_2 dissolved in excess $XeOF_4$ (ca. 0.500 g, 2.24 mmol) and contained in a ¼-in. o.d. FEP T-shaped reactor. The sample vessel was placed in a near-

horizontal position, distributing the $XeOF_4$ solution along the length of the reaction vessel. Slow cooling of the solution to 0 °C over 3 h resulted in the growth of light orange needles while the supernatant remained deep orange in color. Crystals were isolated by decanting the solvent at –5 °C under dry nitrogen into the sidearm of the FEP vessel, which was immersed in liquid nitrogen, followed by drying of the crystalline product under dynamic vacuum at –20 °C before the sidearm containing the supernatant was removed by heat sealing off this arm of the reaction vessel under dynamic vacuum at –196 °C. A crystal of $(OsO_3F_2)_2 \cdot 2XeOF_4$ having the dimensions 0.17 x 0.04 x 0.03 mm^3 was selected at –105 ±3 °C for low-temperature X-ray structure determination and was mounted in a cold stream (–173 °C) on a goniometer head as previously described.[23]

2.6. Lewis Base Adducts of OsO_3F_2

2.6.1. Syntheses of *fac*-$OsO_3F_2(NCCH_3) \cdot 2CH_3CN$ and *fac*-$OsO_3F_2(NCCH_3)$

In a typical synthesis, a fluorine passivated FEP tube was loaded inside a dry box with 0.0545 g (0.1973 mmol) of orange $(OsO_3F_2)_\infty$ using a Teflon scoop fitted to a $\frac{1}{16}$-in. Ni rod. The reaction vessel was then transferred to a glass vacuum line and ca. 0.1 mL of CH_3CN was condensed into the tube at –196 °C. Upon warming to –40 °C with agitation, a yellow-brown precipitate and orange supernatant resulted. Excess CH_3CN was removed under dynamic vacuum at –40 °C, initially yielding *fac*-$OsO_3F_2(NCCH_3) \cdot 2CH_3CN$ which was followed by the formation of *fac*-$OsO_3F_2(NCCH_3)$ upon further pumping at –40 °C. Both compounds were isolated as yellow-brown solids. The sample composition was monitored by Raman spectroscopy.

2.6.2. *fac*-$OsO_3F_2(NCCH_3)\cdot 2CH_3CN$ Crystal Growth

Crystals of *fac*-$OsO_3F_2(NCCH_3)\cdot 2CH_3CN$ were obtained from a sample composed of 0.021 g (0.076 mmol) of $(OsO_3F_2)_\infty$ and excess (ca 0.2 mL) CH_3CN in a ¼-in. o.d. FEP beaded reactor with three wells for crystal growth. The reactor was warmed to –40 °C, whereupon $(OsO_3F_2)_\infty$ dissolved, forming a yellow-brown solution. The reactor was placed in a horizontal position, distributing the CH_3CN solution among the three wells that had been blown into the FEP vessel. The solution was maintained between –41 and –45 °C over 6 h, resulting in the growth of light orange blocks while the supernatant solution retained its yellow-brown color. The orange blocks were isolated by removal of the supernatant through a Teflon cannula using an overpressure of argon, followed by evacuation and drying of the crystalline product under dynamic vacuum at –45 °C for 10 min. A crystal having the dimensions 0.23 x 0.12 x 0.09 mm^3 was selected at –105 ±3 °C for low-temperature X-ray structure determination and was mounted in a cold stream (–173 °C) on a goniometer head as previously described.[23]

2.7. Fluoride Ion Acceptor Properties of OsO_3F_2

Note: prolonged heating (> 2 h) of all three salts mentioned in sections 2.7.1–2.7.3 to 50 °C under 1 atm of nitrogen led to sublimation of XeF_6 out of the heated zone and condensation on the cooler walls of the reaction vessel.

2.7.1. Synthesis of $[XeF_5][\mu\text{-}F(OsO_3F_2)_2]$

On a metal vacuum line, 0.0296 g (0.121 mmol) of XeF_6 was sublimed into a ¼-in. o.d. FEP weighing vessel. Inside the dry box, a 4-mm FEP reaction tube was loaded

with 0.0496 g (0.180 mmol) of orange $(OsO_3F_2)_\infty$. The reaction vessel and weighing vessel were then transferred to a metal vacuum line and XeF_6 (0.0228 g, 0.0930 mmol) was sublimed from the weighing vessel into the reaction vessel containing $(OsO_3F_2)_\infty$ under static vacuum at –196 °C. Warming the reaction mixture to 25 °C initially resulted in a deep orange liquid and unreacted $(OsO_3F_2)_\infty$. The sample solidified, as $(OsO_3F_2)_\infty$ was consumed, to form orange crystalline $[XeF_5][\mu\text{-}F(OsO_3F_2)_2]$. Heating the sample at 50 °C for 1 h under 1 atm of dry N_2 to ensure complete reaction did not result in any physical changes.

2.7.2. Synthesis of $[XeF_5][OsO_3F_3]$

Following a synthetic procedure similar to that outlined for $[XeF_5][\mu\text{-}F(OsO_3F_2)_2]$, 0.0772 g (0.315 mmol) of XeF_6 was initially sublimed into a ¼-in. FEP weighing vessel and 0.0675 g (0.244 mmol) of $(OsO_3F_2)_\infty$ was loaded into a 4-mm FEP reaction vessel. Xenon hexafluoride (0.0614 g, 0.250 mmol) was sublimed from the weighing vessel into the reaction vessel containing $(OsO_3F_2)_\infty$. Upon warming to room temperature (25 °C), a deep orange liquid formed. The sample was heated at 50 °C for 1 h under 1 atm of dry N_2 to ensure complete reaction, and upon cooling to 0 °C, an orange crystalline solid formed.

2.7.3. Synthesis of $[Xe_2F_{11}][OsO_3F_3]$

Following a synthetic procedure similar to that outlined for $[XeF_5][\mu\text{-}F(OsO_3F_2)_2]$, 0.1255 g (0.512 mmol) of XeF_6 was initially sublimed into a ¼-in. FEP weighing vessel and 0.0601 g (0.218 mmol) of orange $(OsO_3F_2)_\infty$ was loaded into a ¼-in. FEP reaction vessel. Xenon hexafluoride, 0.1224 g (0.499 mmol) was sublimed from the weighing vessel into the reaction vessel containing $(OsO_3F_2)_\infty$. Upon warming the reaction mixture

to room temperature (25 °C), a light orange crystalline solid formed. The sample was then warmed to 50 °C under 1 atm of dry N_2, whereupon the sample melted, forming a deep orange liquid which solidified upon cooling to room temperature.

2.7.4. Crystal Growth

2.7.4.1. $[XeF_5][\mu\text{-}F(OsO_3F_2)_2]$

Crystals of $[XeF_5][\mu\text{-}F(OsO_3F_2)_2]$ were obtained from a sample consisting of 0.0496 g (0.180 mmol) of $(OsO_3F_2)_\infty$ and 0.0228 g (0.0930 mmol) of XeF_6 in a ¼-in. FEP reactor. The mixture was fused at 50 °C and allowed to cool to room temperature over a period of 1h, yielding small orange, block-shaped crystals. The crystalline sample was initially cooled to 0 °C and then to –78 °C for storage. The crystal used for X-ray structure determination had the dimensions 0.39 x 0.10 x 0.10 mm^3.

2.7.4.2. $[XeF_5][OsO_3F_3]$

Crystals of $[XeF_5][OsO_3F_3]$ were obtained from a sample consisting of 0.0675 g (0.244 mmol) of $(OsO_3F_2)_\infty$ and 0.0614 g (0.2503 mmol) of XeF_6 in a ¼-in. FEP reactor. The mixture was warmed to 25 °C, whereupon the reactants fused to form a deep orange liquid. The reaction vessel was placed in a near-horizontal position, distributing the liquid along the length of the reactor. The reactor and contents were cooled in a water bath from 25 to 0 °C over a 2 h period, which resulted in the growth of light orange block-shaped crystals as the liquid solidified. The crystalline sample was initially cooled to 0 °C and then to –78 °C for storage. The crystal used for X-ray structure determination had the dimensions 0.21 x 0.21 x 0.20 mm^3.

2.7.4.3. $[Xe_2F_{11}][OsO_3F_3]$

Crystals of $[Xe_2F_{11}][OsO_3F_3]$ were obtained from a sample mixture consisting of 0.0621 g (0.224 mmol) of $(OsO_3F_2)_\infty$ and 0.2559 g (1.043 mmol) of XeF_6 in a ¼-in. o.d. FEP beaded reactor with three wells for crystal growth.[139] The mixture was warmed to 40 °C in a water bath and the orange liquid that formed was distributed among the three wells when the reactor was placed in a horizontal position. The bath was slowly cooled to 15 °C over 12 h which resulted in the growth of orange needles of $[Xe_2F_{11}][OsO_3F_3]$ in the wells and growth of colorless plates of XeF_6 which had deposited by sublimation along the length of the reactor. The crystalline sample was initially cooled to 0 °C and then to –78 °C for storage. The crystal used for X-ray structure determination had the dimensions 0.39 x 0.11 x 0.07 mm^3.

2.8. Binary Noble-Gas Fluoride Adducts of $XeOF_4$

2.8.1. Synthesis of $XeOF_4 \cdot XeF_2$

Inside a nitrogen-filled dry box, a fluorine passivated 4-mm FEP reaction vessel was loaded with 0.04471 g (0.2641 mmol) of XeF_2. The reaction vessel was then transferred to a metal vacuum line and ca. 0.5 g (2.2 mmol) of $XeOF_4$ was distilled into the tube. Upon warming to 25 °C, a colorless solution formed. The reaction vessel was attached to a metal vacuum line through an FEP U-trap cooled to −196 °C and excess $XeOF_4$ was removed under dynamic vacuum at 0 °C. Pumping for 2 h yielded a white solid that was characterized by Raman spectroscopy.

2.8.2. Synthesis of $XeOF_4 \cdot KrF_2$

On a metal vacuum line, 0.0231 g (0.190 mmol) of KrF_2 was sublimed into a pre-weighed 4-mm fluorine passivated FEP reaction vessel. Excess, ca. 0.100 g (0.448 mmol), $XeOF_4$ was then condensed onto KrF_2 that had been sublimed into the reaction vessel at –196 °C. The reaction vessel was warmed to –20 °C and a colorless solution formed. The sample composition was monitored by Raman spectroscopy, using the ν(XeO) and ν(KrF) stretches as calibration points, as the excess $XeOF_4$ was removed under dynamic vacuum at –20 °C. The sample composition stopped changing after 6 h and it was apparent that both $XeOF_4 \cdot KrF_2$ and excess $XeOF_4$ were being removed together.

2.8.3. Synthesis of $XeOF_4 \cdot n KrF_2$

On a metal vacuum line, 0.0564 g (0.251 mmol) of $XeOF_4$ was condensed into a pre-weighed 4-mm fluorine passivated FEP reaction vessel. On a metal vacuum line, 0.0607 g (0.498 mmol) of KrF_2 was sublimed into a pre-weighed 4-mm fluorine passivated FEP weighing vessel. The pre-weighed KrF_2 was then sublimed into the reaction vessel. Upon warming to –20 °C, a wet white solid formed. The reaction at –20 °C was followed by Raman spectroscopy for 12 h until there was no change in the Raman spectrum recorded after 1 h intervals of reaction. After 12 h, the sample was a white solid at –20 °C consisting of unreacted KrF_2 and $XeOF_4 \cdot n KrF_2$.

2.8.4. Crystal Growth

2.8.4.1. $XeOF_4 \cdot XeF_2$

Crystals of $XeOF_4 \cdot XeF_2$ were obtained from a sample composed of 0.1358 g (0.8022 mmol) of XeF_2 and ca. 0.67 g (3.00 mmol) of $XeOF_4$ contained in a ¼-in. o.d. FEP reactor equipped with a sidearm. The reactor was warmed to 25 °C and a clear colorless solution formed. The reactor was placed in the horizontal position, distributing the liquid along the length of the reactor. The reactor was slowly cooled to –36 °C over 1 h resulting in growth of colorless kaleidoscope-like plates. The colorless plates were isolated by decanting the solvent at –37 °C under dry nitrogen into the sidearm of the FEP vessel, which was immersed in liquid nitrogen, followed by evacuation and vacuum drying of the crystalline product under dynamic vacuum at –40 °C before the sidearm containing the supernatant was removed by heat sealing off this portion of the reaction vessel under dynamic vacuum at –196 °C. A crystal of $XeOF_4 \cdot XeF_2$ having the dimensions 0.04 x 0.07 x 0.13 mm^3 was selected for low-temperature X-ray structure determination at –105 ±3 °C and was mounted in a cold stream (–173 °C) on a goniometer head as previously described.[23]

2.8.4.2. $XeOF_4 \cdot KrF_2$

Crystals of $XeOF_4 \cdot KrF_2$ were obtained from a sample composed of KrF_2 and excess $XeOF_4$ contained in a ¼-in. o.d. FEP reactor equipped with a sidearm. The reactor was warmed to –20 °C and a clear colorless solution formed. The reactor was placed in the horizontal position, distributing the liquid along the length of the reactor and cooled to –36 °C. The reactor was slowly cooled to –41 °C over 3 h resulting in growth of

colorless needles while the solution remained colorless. The colorless needles were isolated by decanting as much solvent as possible at –41 °C under dry nitrogen into the sidearm of the FEP vessel, which was immersed in liquid nitrogen. The sidearm containing the supernatant was removed by heat sealing off this portion of the reaction vessel under dynamic vacuum at –196 °C. Excess $XeOF_4$ that could not be decanted froze around the crystals and could not be pumped off at –41 °C. A crystal of $XeOF_4 \cdot KrF_2$ having the dimensions 0.07 x 0.10 x 0.15 mm^3 was isolated from the frozen $XeOF_4$ and was selected for low-temperature X-ray structure determination at –105 ±3 °C and was mounted in a cold stream (–173 °C) on a goniometer head as previously described.[23]

2.9. Raman Spectroscopy

The Raman spectra recorded during the course of this Thesis were collected using two spectrometers, which are each described in detail in the subsequent sections. All samples except $[Cs][OsO_2F_5]$ and $[Cs][Os^{18}O_2F_5]$ were recorded on the Bruker RFS 100 FT Raman Spectrometer.

2.9.1. Bruker RFS 100 FT Raman Spectrometer

Low-temperature Raman spectra were recorded on a Bruker RFS 100 FT Raman Spectrometer equipped with a quartz beam splitter, a liquid nitrogen-cooled germanium diode detector and a R495 low-temperature accessory providing temperatures ranging from –40 to –160 °C with an estimated error of ±1 °C. The backscattered (180°) radiation was sampled. The scanner velocity was 5 kHz and the wavelength range for acquisition lay between 5894 and 10394 cm^{-1} when shifted relative to the laser line at 9394 cm^{-1}

(1064.5 nm), giving a spectral range of 3501 to -999 cm^{-1}. The usable Stokes range was 50 – 3500 cm^{-1} with a spectral resolution of 1 cm^{-1}. Fourier transformation was accomplished using a Blackman Harris 4-term apodization and a zero-filling factor of 2. The 1064-nm line of a Nd YAG Laser (400 mW maximum output) was used for excitation of the sample with a laser spot of < 0.1 mm. Typically 300 scans were performed, and increased to 1200 – 2400 for weak scatterers, at a laser power of 300 mW.

2.9.2. Renishaw Invia Raman Spectrometery

Room temperature Raman spectra were recorded on a Renishaw Invia Laser Raman Spectrometer equipped with a mapping stage and microscope. The spectrometer was equipped with a green laser operating at 514 nm (25 mW maximum output) and a red laser operating at 785 or 782 nm (300 mW maximum output) which were focused using a holographic grating with 1200 lines/mm. The usable Stokes range was 100 – 4000 cm^{-1} with a spectral resolution of 1 cm^{-1}. Typically 2-7 scans were performed.

2.10. Nuclear Magnetic Resonance Spectroscopy

Low-temperature NMR spectra were recorded unlocked (field drift < 0.1 Hz h^{-1}) on a Bruker DRX-500 spectrometer [11.745 T; ^{1}H (500.138 MHz), ^{13}C (125.755 MHz), ^{15}N (50.693 MHz), ^{19}F (470.592 MHz), ^{129}Xe (138.086 MHz)] using XWINNMR or TOPSPIN as the computer software. The spectrometer was equipped with a Bruker 5-mm broad band inverse probe. The NMR probe was cooled using a nitrogen flow and variable temperature controller (BV-T 3000). The ^{19}F spectra were acquired in 32 or 64 K

memories with a spectral width setting of 160-24 kHz, yielding data acquisition times of 0.197-1.39 s and a data point resolutions of 2.54-0.36 Hz/data point; a pulse width of 8.5-2.5 μs was used. The ^{1}H, ^{13}C, ^{15}N, ^{19}F, and ^{129}Xe NMR spectra were referenced at 30 °C to external samples of $Si(CH_3)_4$ (^{1}H and ^{13}C), CH_3NO_2, $CFCl_3$, and $XeOF_4$, respectively. The chemical shift convention used was a positive value signifies a chemical shift to high frequency with respect to the reference compound, and vice versa. A summary of typical spectroscopic parameters used for the spectra acquired for this Thesis is provided in Table 2.1. In some cases, Gaussian rather than exponential multiplication was used to process the FID's, and is indicated within the relevant discussions.

2.11. Single Crystal X-ray Diffraction

2.11.1. Crystal Growth and Isolation

The majority of the crystals used for structure determination by X-ray crystallography were grown in the low-temperature crystal growing apparatus depicted in Figure 2.10. The following procedure summarizes the general approach used to grow crystals from solutions using the temperature gradient method.

Solvent (ca. 1 mL or less) was condensed onto the compound (ca. 0.3 mmol) at –196 °C that had been synthesized in situ in one arm of a ¼-in o.d. FEP T-shaped reactor fitted with a Kel-F valve. The reactor was warmed so as to just effect dissolution, and while maintained at that temperature, the reactor was attached to a vacuum line and pressurized to ca. 1 atm with dry nitrogen. After removal from the vacuum line, the arm containing the

Table 2.1. Summary of Typical Spectroscopic Parameters Used for NMR Spectroscopy

Acquisition Parameter[a]	^{1}H	^{13}C	^{15}N	^{19}F	^{129}Xe
B_0 = 11.744 T					
SF (MHz)	500.130	125.755	50.693	470.592	138.857
TD (K)	16-32	16	32	32 to 160	128
SW (kHz)	20	24	50	24 to 100	1000
Hz/pt	0.15-61	1.52	3.05	0.43 to 1.53	0.76
PW (μs)	2.5	6.0	12.0	8.5	10.0
RD (s)	0.05 to 2.5	2.0 to 5.0	5.0	0.05 to 1.00	0.1
NS	8 to 500	2000 to 16,000	153,000	1000 to 3800	7000

[a] The abbreviations denote: B_0, external magnetic field; SF, spectral frequency; TD, time domain; SW, sweep width; PW, pulse width; RD, relaxation delay; NS, number of scans

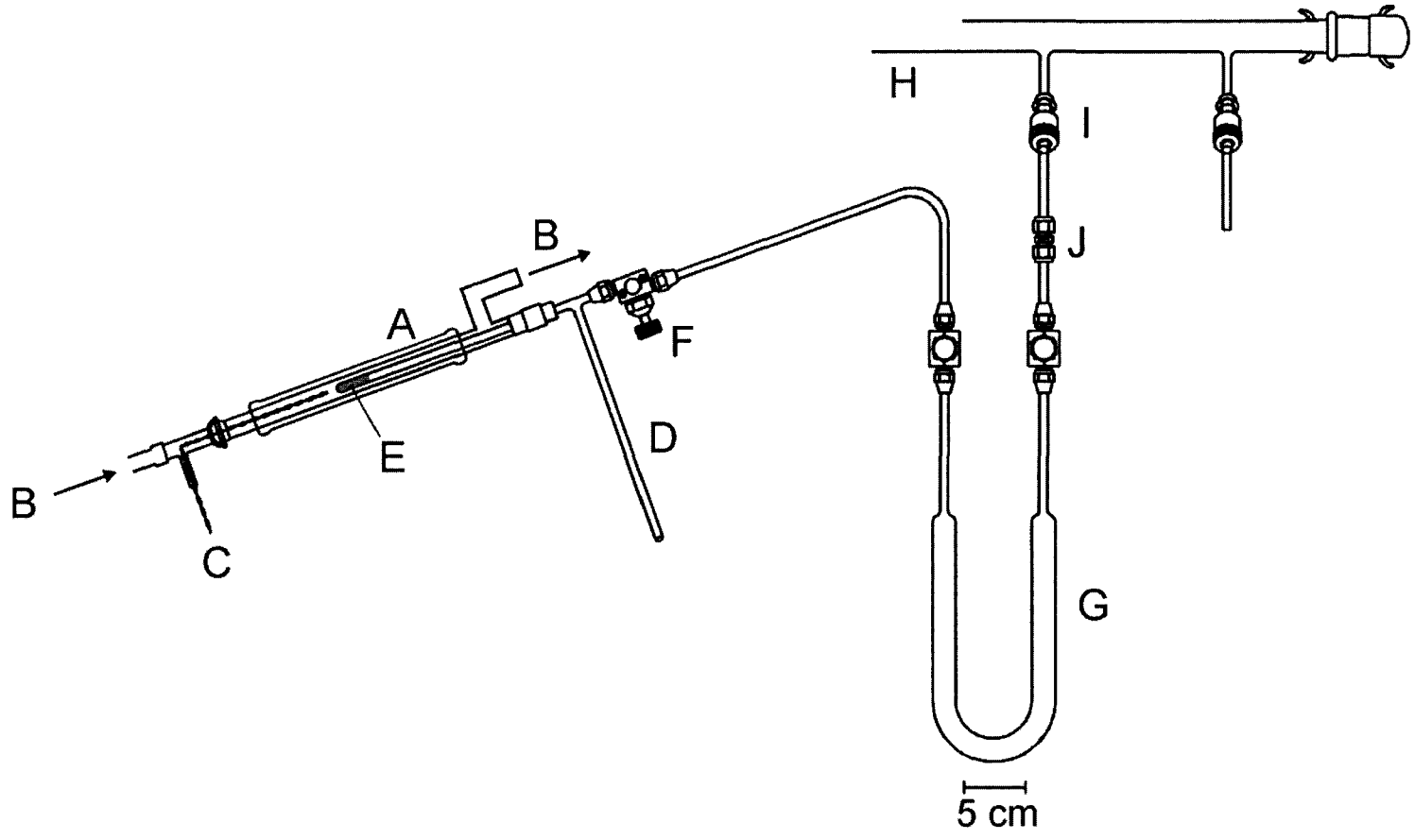

Figure 2.10. Low-temperature crystal growing apparatus; (A) glass-jacketed dewar, (B) nitrogen cold flow, (C) thermocouple lead, (D) T-shaped FEP reaction vessel with side arm, (E) sample region, (F) Kel-F valve, (G) FEP U-trap, (H) glass vacuum manifold, (I) greaseless J. Young valve with PTFE barrel, amd (J) PTFE Swagelok or stainless steel Swagelok Ultra-Torr union. Reproduced with permission from Ref 28

solution was inserted into the glass dewar of a crystal growing apparatus[126] that had been previously adjusted to the same temperature and then inclined at ca. 5° from horizontal. The temperature was then slowly lowered, usually over several hours, whereupon crystals began to grow on the walls of the FEP vessel. The reactor was then maintained at that temperature for a further period of time to allow for more complete crystallization. Crystals were isolated by decanting the solvent under dry nitrogen into the side arm of the FEP vessel which was immersed in liquid nitrogen, followed by evacuation and vacuum drying of the crystalline product under dynamic vacuum at ca. –80 °C before the side-arm containing the supernatant was heat-sealed off. A crystal having dimensions less than 0.40 x 0.40 x 0.40 mm^3 was selected at –105 ±2 °C for low-temperature X-ray structure determination and was mounted in a cold stream (–173 °C) on a goniometer head as described in the next section.[23]

2.11.2. Low-Temperature Crystal Mounting

Because most of the samples investigated in this work were thermally unstable and/or moisture sensitive, all of the samples investigated were mounted at low temperature using the apparatus depicted in Figures 2.11 and 2.12. The reaction vessels containing the samples were first cut open below the Kel-F valve under a flow of dry argon gas, using an inverted glass funnel, while maintaining the sample at –78 °C. The sample was then quickly dumped into the aluminum trough of the crystal mounting apparatus under a stream of dry argon, precooled (–104 ±2 °C) by the regulated passage of dry nitrogen gas flow through a 5-L dewar filled with liquid N_2 (Figure 2.11). The temperature inside the trough was measured using a copper-constantan thermocouple

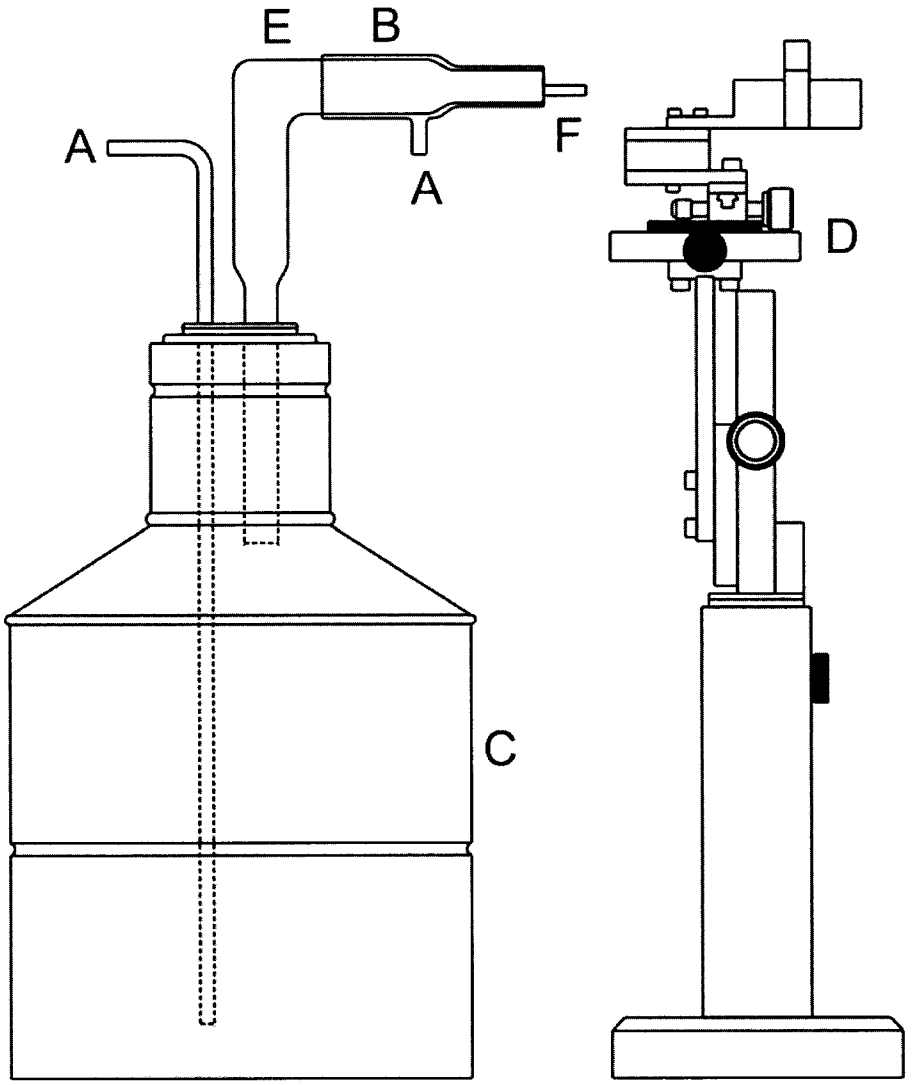

Figure 2.11. Low-temperature crystal mounting apparatus; (A) nitrogen inlet, (B) glass sleeve for ambient nitrogen flow (optional), (C) liquid N_2 dewar, (D) adjustable support stage, (E) silvered dewar (glass), (F) aluminum trough. Reproduced with permission from Ref 28

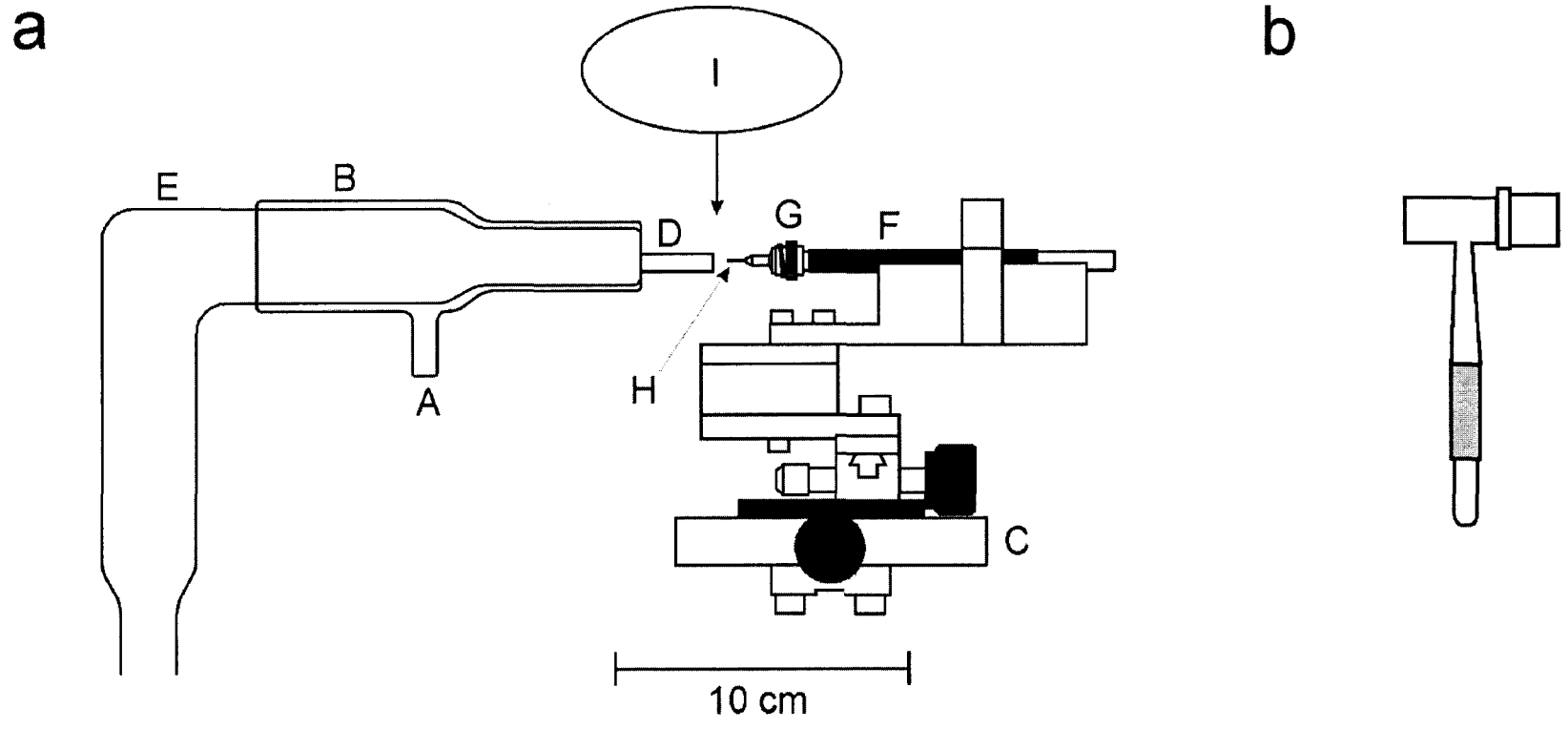

Figure 2.12. (a) Enlarged view of the crystal mounting apparatus; (A) ambient nitrogen gas flow inlet, (B) glass sleeve for ambient nitrogen gas flow, (C) adjustable support stage, (D) aluminum trough, (E) silvered glass jacketed dewar, (F) magnetic-tipped wand affixed to (G) the magnetic-based copper pin-fibre assembly, (H) glass fibre. (I) stereo-zoom microscope, (b) cryotongs employed in the transfer of the copper pin-fibre assembly with affixed crystal from the support stage to the goniometer head. Reproduced with permission from Ref 28

positioned in the sample region of the trough. Using an additional glass sleeve, which was fitted into a concentric position around the silvered cold-flow dewar, an ambient nitrogen gas flow was slowly passed through the sleeve in order to maintain a laminar flow, thereby reducing atmospheric moisture build up in the trough. Crystals were then selected using a stereo-zoom microscope and mounted on a glass fibre (0.05 to 0.1-mm o.d.) using perfluorinated polyether oil (Ausimont Inc., Fomblin Z15 or Z25) which served as an adhesive upon freezing at low temperature. The glass fibre was previously mounted with epoxy cement to a copper pin fitted to a magnetic base and affixed to the end of a magnetic wand (Hampton Research). The magnetic wand could be fastened to an adjustable support stage such that samples could be inspected under the stereo-zoom microscope once affixed to the glass fiber. The mounted crystal and magnetic pin were quickly (ca. 5 s) transferred from the crystal mounting apparatus to the magnetic mount of the goniometer by means of cryotongs (Hampton Research) which were precooled in liquid N_2 prior to use. The crystals were maintained at low temperature on the goniometer head by a cold N_2 gas flow provided by a Molecular Structure Corporation cryostat system.

2.11.3. Data Collections

The crystallographic data acquired during the course of this Thesis were collected using two diffractometers, which are described in the subsequent sections. Both instruments were equipped with Oxford Cryosystems low-temperature cryostream accessories that provided a stream of cold, gaseous N_2 for low-temperature data

collection. Both instruments were controlled by a Cryostream Controller 700 (Oxford Cryosystems).

2.11.3.1. Siemens P4 Diffractometer

The Siemens diffractometer was equipped with a Siemens 1K CCD area detector controlled by SMART[140] and a rotating anode (molybdenum) emitting Kα radiation monochromated (λ = 0.71073 Å) by a graphite crystal. Diffraction data collection (–173 °C) consisted of a full φ-rotation at $\chi = 0^{\circ}$ using 0.3° (1040 + 30) frames, followed by a series of short (80 frames) ω scans at various φ and χ settings to fill the gaps. The crystal-to-detector distance was 5.006–5.016 cm, and the data collection was carried out in a 512 × 512 pixel mode using 2 × 2 pixel binning. Processing of the raw data was completed using SAINT+,[141] which applied Lorentz and polarization corrections to three-dimensionally integrated diffraction spots.

2.11.3.2. Bruker SMART APEX II Diffractometer

The Bruker SMART APEX II diffractometer was equipped with an APEX II 4K CCD area detector and a 3-axis goniometer, controlled by the APEX2 Graphical User Interface (GUI) software,[142] and a sealed tube X-ray source (Mo target) emitting Kα radiation monochromated (λ = 0.71073 Å) by a graphite crystal. Diffraction data collection was typically at –173 °C consisting of a full φ-rotation at a fixed $\chi = 54.74^{\circ}$ with 0.36° (1010) frames, followed by a series of short (250 frames) ω scans at various φ settings to fill the gaps. The crystal-to-detector distance was 4.882–4.976 cm, and the data collection was carried out in a 512 × 512 pixel mode using 2 × 2 pixel binning. Processing of the raw data was completed using the APEX2 GUI software,[142] which

applied Lorentz and polarization corrections to three-dimensionally integrated diffraction spots.

2.11.4. Solution and Refinement of Structures

The program SADABS[141] was used for the scaling of diffraction data, the application of a decay correction, and an empirical absorption correction based on the intensity ratios of redundant reflections. The XPREP program was used to confirm the unit cell dimensions and the crystal lattices. The final refinements were obtained by introducing anisotropic parameters for all the atoms, an extinction parameter, and the recommended weight factor. The maximum electron densities in the final difference Fourier maps were located around the heavy atoms. All calculations were performed using the SHELXTL package for the structure determination, refinement, and molecular graphics.[143] Structure solutions for most stuctures were obtained by direct methods which located the Os, Xe, Sb, and/or Kr atoms. Successive difference Fourier syntheses revealed the positions of the fluorine, oxygen, carbon, and/or nitrogen atoms. The space group assignments were confirmed through the use of the PLATON[144] software using the ADSYM program.

The positions of the hydrogen atoms in the crystal structures of [Cs][*fac*-OsO_3F_3]·CH_3CN, *cis*-OsO_2F_4·[Cs][CH_2CN] and the free CH_3CN molecule of the *fac*-$OsO_3F_2(NCCH_3)$·CH_3CN were located on the difference map. For the *cis*-OsO_2F_4·[$N(CH_3)_4$][CH_2CN] structure, and the adducted CH_3CN ligand of the *fac*-$OsO_3F_2(NCCH_3)$·CH_3CN structure the positions of the hydrogen atoms were calculated and refined using AFIX restraints.

A first solution was obtained for the structure of *cis*-OsO_2F_4 in $P6_5$ by direct methods which located the central osmium atom. The difference Fourier map resulting from the full-matrix least squares refinement revealed six light atoms which relative bond lengths differed enough to allow their unambiguous attribution to oxygen or fluorine atoms. The introduction of these positions gave a residual factor R_1 of 0.33. Several parameters however presented an abnormal behavior, suggesting the possibility of a twin. The program ROTAX was run and suggested the twin law ($100\ \bar{1}\bar{1}0\ 00\bar{1}$). A refinement was carried out using this law, giving rise to a drastic drop of R_1 to 0.15, indicating it was the correct law. At this stage, the possibility of a racemic twin or wrong absolute structure was suggested by the program. Although the absolute structure was checked, it was shown that the contribution of a racemic twin had to be taken into consideration. The final twin law used was ($100\ \bar{1}\bar{1}0\ 00\bar{1}\ \bar{4}$), and gave rise to a R_1 value of 0.0483.

A first solution was obtained for the structure of *cis*-OsO_2F_4·[Cs][CH_2CN]·0.3HF in C_m by direct methods which located one osmium atom and one cesium atom on general position, as well as two osmium atoms and two cesium atoms on special positions. The difference Fourier map resulting from the full-matrix least squares refinement revealed light atoms around the Os atoms. For the Os positioned on the general position, the relative bond lengths to Os differed enough to allow the unambiguous attribution to oxygen or fluorine atoms. For the Os atoms positioned on special positions, some bond lengths looked more like intermediate Os-O and Os-F bond lengths, suggesting a positional disorder between oxygen and fluorine atoms, which ratio (50:50) is imposed by symmetry. The difference map also revealed other light atoms which were attributed to

CH_2CN^- anions. The refinement of all of these atoms with anisotropic parameters gave a reasonable residual R_1 of 0.0686. At this stage, some significant electron density could still be located in three different areas of the difference map. This density was allocated to HF molecules with a partial occupancy of 0.30. The positions of the hydrogen atoms of the CH_2CN^- anions were calculated, but no attempt was made to calculate the positions of the hydrogen atoms associated to the HF molecules in view of their small occupancy. The introduction of these HF molecules improved the residual to an R_1 value of 0.042. The final refinement also involved the use of a racemic twin law.

2.12. X-ray Powder Diffraction

2.12.1. Sample Preparation.

A low-temperature mounting technique similar to that described for mounting thermally unstable and/or moisture sensitive single crystals (See section 2.11.2.) was used to mount a powdered sample of $[OsO_2F_3][Sb_2F_{11}]$. The cold (–78 °C) sample tube was cut open under a dry argon stream and dumped onto an aluminium trough cooled by a dry nitrogen cold stream (−105 ±3 °C). The closed end of a 0.3 mm glass capillary was attached by means of epoxy to a metallic pin having a magnetic interface. The flat edge of a stainless steel stylus was used to crush the microcrystalline sample and the powdered material was forced into the open end of the mounted capillary to a depth of ca. 2 mm under the nitrogen cold stream. The sample was quickly transferred to the goniometer head of the X-ray diffractometer by means of a cryotongs, previously cooled to −196 °C, and attached to the magnetic interface of the goniometer head.

2.12.2. Collection and Processing of X-ray Powder Data

The powdered sample of $[OsO_2F_3][Sb_2F_{11}]$ (vide supra) was centered on a Bruker SMART APEX II diffractometer, equipped with an APEX II 4K CCD area detector and a triple-axis goniometer, controlled by the APEX2 Graphical User Interface (GUI) software,[142] and a sealed source emitting graphite-monochromated Mo-Kα radiation (λ = 0.71073 Å). Diffraction data was collected at −150 °C and consisted of a 360° rotation for φ and fixed χ, 2θ and ω angles of 54.76°, 18°, and 9°, respectively. The sample was also equilibrated at −173 °C for 30 min and the data collection was repeated. The sample-to-detector distance was 16.940 cm and the data collection was carried out in a 512 x 512 pixel mode using 2 x 2 pixel binning. The two-dimensional powder analysis and integration around χ was completed using the GADDS[145] program resulting in a standard one dimensional intensity versus 2θ plot. The powder pattern was calculated for the single crystal data using the Mercury[146] program and was compared with the powder data using the TOPAS[147] program.

2.13. Electronic Structure Calculations

All calculations were performed using the Gaussian 98,[148] Gaussian 03,[149] and/or Gaussian 09[150] software packages. Geometries were fully optimized using density functional theory (B3LYP, SVWN, and/or PBE1PBE). For calculations involving Os, the Stuttgart semi-relativistic large core and effective core pseudopotential basis sets (SDDall) augmented for F, O, N, Xe, and/or Sb with two d-type polarization functions by Huzinaga[151] was used at the SVWN level and the Stuttgart basis set augmented by one

f-type polarization function (α_f Os 0.886)[152] for osmium and aug-cc-pVTZ basis sets for antimony, oxygen, and fluorine were used at the B3LYP level. The 6-21G* basis set was used for the calculation of the CH_2CN^- anion.

Pseudo-potentials were used with the aug-cc-pVTZ basis set for osmium, antimony, krypton, and/or xenon. The combined use of the aug-cc-pVTZ and aug-cc-pVTZ-PP basis sets are indicated as aug-cc-pVTZ(-PP). Basis sets were obtained online from the EMSL Basis Set Exchange (https://bse.pnl.gov/bse/portal).[153, 154] The levels and basis sets were benchmarked by calculating *cis*-OsO_2F_4,[18] $Sb_2F_{11}^-$,[139] CH_3CN,[155] and $XeOF_4$[18] as previously described. Fundamental vibrational frequencies were calculated along with Raman intensities, and Natural Bond Orbital (NBO) analyses were obtained for the optimized local minima. The program GaussView[156] was used to visualize the vibrational displacements that form the basis of the vibrational mode descriptions presented.

CHAPTER 3

FLUORIDE ION DONOR PROPERTIES OF *cis*-OsO_2F_4: SYNTHESIS, RAMAN SPECTROSCOPIC STUDY, AND X-RAY CRYSTAL STRUCTURE OF $[OsO_2F_3][Sb_2F_{11}]$

3.1 Introduction

Relatively few high-valent transition metal oxide fluoride cations are known. For example, the only group 7 oxide fluoride cations that have been structurally characterized are MOF_4^+,[157, 158] μ-$F(MOF_4)_2^+$,[157, 158] and $MO_2F_2^+$ [46, 159] (M = Re, Tc). Examples of oxide fluoride cations of Os(VIII) are also sparse with only OsO_3F^+ [21] and μ-$F(cis\text{-}OsO_2F_3)_2^+$ [22] having been fully structurally characterized.

The OsO_3F^+ cation has been characterized in its $[OsO_3F][PnF_6]$ (Pn = As, Sb), $[OsO_3F][HF]_2[AsF_6]$, $[OsO_3F][HF][SbF_6]$, and $[OsO_3F][Sb_3F_{16}]$ salts by low-temperature Raman spectroscopy and single-crystal X-ray diffraction.[21] The PnF_6^- salts contain OsO_3F^+ cations that strongly interact with the anion by means of fluorine bridges and/or coordinate HF to osmium through fluorine to give six-coordinate osmium. In contrast, the disordered OsO_3F^+ cation of $[OsO_3F][Sb_3F_{16}]$, with an osmium coordination number of four, is well isolated from the weakly fluoro-basic $Sb_3F_{16}^-$ anion.

The μ-$F(cis\text{-}OsO_2F_3)_2^+$ cation has been synthesized by reaction of *cis*-OsO_2F_4 with either SbF_5 or AsF_5 in anhydrous HF (aHF) solvent and by reaction of *cis*-OsO_2F_4 with liquid AsF_5, and isolated as the $Sb_2F_{11}^-$ and AsF_6^- salts.[22] The crystal structure of $[\mu\text{-}F(cis\text{-}OsO_2F_3)_2][Sb_2F_{11}]$ reveals that the cation consists of two symmetry-related $OsO_2F_3^+$ units that are fluorine bridged to one another. The osmium atoms are six-

coordinate, with the oxygen ligands of each osmium atom cis to one another and the fluorine bridge atom trans to two oxygen ligands.

The $OsO_2F_3^+$ cation has been generated in solution by dissolution of *cis*-OsO_2F_4 in liquid SbF_5 and was characterized by ^{19}F NMR and Raman spectroscopy in SbF_5 solution, but was not isolated and structurally characterized in the solid state.[22] The doublet and triplet coupling patterns resulting from $^2J(^{19}F–^{19}F)$ coupling in the ^{19}F NMR spectrum are consistent with a trigonal bipyramidal cation geometry in which the oxygen atoms and a fluorine atom are in equatorial positions and two fluorine atoms are in axial positions. The polymeric $Sb_nF_{5n+1}^-$ anions generated upon ionization of *cis*-OsO_2F_4 in this medium are expected to be very weakly fluoro-basic and to weakly interact with the cation by means of fluorine bridges. The fluorine bridge environments and their attendant couplings to the fluorine resonances of $OsO_2F_3^+$, however, were not observed in the prior NMR study,[22] and are therefore presumed to be labile on the ^{19}F NMR time scale. The Raman spectrum of $OsO_2F_3^+$ in SbF_5 solvent was assigned under C_{2v} symmetry based on the ^{19}F NMR spectrum and the calculated frequencies for the energy-minimized gas-phase trigonal bipyramidal geometry.[22]

In the current study, the first $OsO_2F_3^+$ salt has been isolated and structurally characterized by single-crystal X-ray diffraction and low-temperature Raman spectroscopy. The thermochemistries of the reactions of *cis*-OsO_2F_4 with PnF_5 (Pn = As, Sb) have also been investigated in the gas-phase and in the solid state.

3.2. Results and Discussion

3.2.1. Synthesis of $[OsO_2F_3][Sb_2F_{11}]$ and Attempted Synthesis of $[OsO_2F_3][SbF_6]$

The salt, $[OsO_2F_3][Sb_2F_{11}]$, was synthesized by dissolution of *cis*-OsO_2F_4 in liquid SbF_5 (eq 3.1). Polycrystalline samples of the salt and single crystals suitable for X-ray

$$cis\text{-}OsO_2F_4 + 2SbF_5 \xrightarrow[25\ ^\circ C]{SbF_5} [OsO_2F_3][Sb_2F_{11}] \quad (3.1)$$

structure determination were isolated by slow removal of SbF_5 solvent under dynamic vacuum at 0 °C, yielding deep orange $[OsO_2F_3][Sb_2F_{11}]$ in nearly quantitative yield.

In an attempt to isolate $[OsO_2F_3][SbF_6]$, the $[OsO_2F_3][Sb_2F_{11}]$ salt was pumped under vacuum to remove SbF_5 according to eq 3.2. Monitoring of the sample composition by Raman spectroscopy at intervals during pumping revealed that the only species present were $[OsO_2F_3][Sb_2F_{11}]$ and $[\mu\text{-}F(OsO_2F_3)_2][Sb_2F_{11}]$ at constant sample mass, the only species remaining was $[\mu\text{-}F(OsO_2F_3)_2][Sb_2F_{11}]$ (eq 3.3).[22]

$$[OsO_2F_3][Sb_2F_{11}] \xrightarrow[0\ ^\circ C]{vac} [OsO_2F_3][SbF_6] + SbF_5 \quad (3.2)$$

$$2[OsO_2F_3][Sb_2F_{11}] \xrightarrow[0\ ^\circ C]{vac} [\mu\text{-}F(OsO_2F_3)_2][Sb_2F_{11}] + 2SbF_5 \quad (3.3)$$

In other attempts to isolate $[OsO_2F_3][SbF_6]$, (1) *cis*-OsO_2F_4 was dissolved in aHF containing a 10-fold excess of SbF_5 with respect to the $OsO_2F_3^+$ cation. Anhydrous HF solvent was used to favor the more fluoro-basic SbF_6^- anion and the formation of $[OsO_2F_3][SbF_6]$. Again, Raman spectroscopy confirmed that only $[\mu\text{-}F(OsO_2F_3)_2][Sb_2F_{11}]$ was isolated (eq 3.4). (2) A mixture of *cis*-OsO_2F_4 and $[OsO_2F_3][Sb_2F_{11}]$ in a 2:1 molar-ratio was allowed to react in aHF at 25 °C. Raman spectroscopy revealed that only

$$2cis\text{-}OsO_2F_4 + 2SbF_5 \xrightarrow[25^\circ C]{HF/SbF_5} [\mu\text{-}F(OsO_2F_3)_2][Sb_2F_{11}] \quad (3.4)$$

[μ-F(OsO_2F_3)$_2$][Sb_2F_{11}] had formed in admixture with *cis*-OsO_2F_4 when HF was removed under dynamic vacuum at –78 °C (eq 3.5). Fusion of the resulting mixture at 90 °C for 1 h also did not result in further reaction.

$$2cis\text{-}OsO_2F_4 + [OsO_2F_3][Sb_2F_{11}] \xrightarrow[-78\ ^\circ C]{HF} [\mu\text{-}F(OsO_2F_3)_2][Sb_2F_{11}] + cis\text{-}OsO_2F_4 \qquad (3.5)$$

3.2.2. X-ray Crystal Structure of [OsO_2F_3][Sb_2F_{11}]

Details of data collection parameters and other crystallographic information are provided in Table 3.1 and geometric parameters are listed in Table 3.2. The crystal structure consists of discrete [OsO_2F_3][Sb_2F_{11}] ion pairs (Figure 3.1a) that are well isolated from one another. There is a short contact (2.190(3) Å) between the osmium atom and a terminal fluorine atom, F(4), cis to the Sb(1)---F(9)---Sb(2) bridge of the $Sb_2F_{11}^-$ anion. Such *cis*-fluorine bridge arrangements have been observed for other $Sb_2F_{11}^-$ salts; e.g., [XeF_3][Sb_2F_{11}],[160] [XeF][Sb_2F_{11}],[109] [XeF(HF)][Sb_2F_{11}],[161] [BrF_4][Sb_2F_{11}],[162] [(F_3As)AuXe][Sb_2F_{11}],[163] and [N_5][Sb_2F_{11}].[164] The two bridging fluorine atoms of the [OsO_2F_3][Sb_2F_{11}] ion pair, F(4) and F(9), lay only 0.121 and 0.072 Å, respectively, out of the [Sb(1), Sb(2), Os]-plane.

The [OsO_2F_3][Sb_2F_{11}] ion pairs are stacked, without alternation, along the *c*-axis but alternate along the *a*- and *b*-axes (Figure A1) so that the anions and cations of different ion pairs face one another in columns that run parallel to these axes. The resulting F···F and O···F contacts between nearest-neighbor ion pairs are long and near the sums of the van der Waals radii for oxygen and fluorine.[165, 166]

Table 3.1. Summary of Crystal Data and Refinement Results for $[OsO_2F_3][Sb_2F_{11}]$

chem formula	$OsO_2F_{14}Sb_2$
space group	$P\bar{1}$ (No. 2)
a (Å)	7.4284(3)
b (Å)	8.6649(4)
c (Å)	10.0394(4)
α (deg)	97.597(2)
β (deg)	111.263(2)
γ (deg)	110.697(2)
V (Å^3)	537.39(4)
molecules/unit cell	2
mol wt (g mol^{-1})	1463.40
calcd density (g cm^{-3})	4.522
T (°C)	−173
μ (mm^{-1})	16.98
R_1 [a]	0.0426
wR_2 [b]	0.0694

[a] R_1 is defined as $\Sigma\| F_o | - | F_c \| / \Sigma | F_o |$ for $I > 2\sigma(I)$. [b] wR_2 is defined as $\{\Sigma[w(F_o^2 - F_c^2)^2]/\Sigma w(F_o^2)^2\}^{1/2}$ for $I > 2\sigma(I)$.

Table 3.2. Experimental Geometrical Parameters for $[OsO_2F_3][Sb_2F_{11}]$ and Calculated Geometrical Parameters for $[OsO_2F_3][Sb_2F_{11}]$, $OsO_2F_3^+$, and $Sb_2F_{11}^-$

	Bond Lengths (Å)						
	exptl[a]	calcd					
	$[OsO_2F_3][Sb_2F_{11}]$	$[OsO_2F_3][Sb_2F_{11}]$ (C_1)		$OsO_2F_3^+$ (C_{2v})		$Sb_2F_{11}^-$ (C_1)	
		SVWN[b]	B3LYP[c]	SVWN[b]	B3LYP[c]	SVWN[b]	B3LYP[d]
Os–F(1)	1.812(4)	1.870	1.862	1.836	1.828		
Os–F(2)	1.791(3)	1.835	1.826	1.828	1.824		
Os–F(3)	1.806(3)	1.852	1.843	1.828	1.824		
Os–O(1)	1.654(4)	1.696	1.670	1.689	1.663		
Os–O(2)	1.764(4)	1.708	1.677	1.689	1.663		
Os---F(4)	2.190(3)	2.089	2.086				
Sb(1)–F(4)	1.958(3)	2.085	2.104			1.909	1.895
Sb(1)–F(5)	1.851(3)	1.892	1.876			1.904	1.895
Sb(1)–F(6)	1.836(3)	1.879	1.866			1.902	1.896
Sb(1)–F(7)	1.844(3)	1.881	1.872			1.908	1.896
Sb(1)–F(8)	1.837(3)	1.884	1.878			1.906	1.898
Sb(1)---F(9)	1.995(3)	2.027	1.992			2.080	2.076
Sb(2)---F(9)	2.060(3)	2.139	2.197			2.080	2.076
Sb(2)–F(10)	1.862(3)	1.884	1.874			1.906	1.898
Sb(2)–F(11)	1.848(4)	1.892	1.877			1.909	1.896
Sb(2)–F(12)	1.856(4)	1.890	1.882			1.908	1.894
Sb(2)–F(13)	1.844(3)	1.935	1.907			1.904	1.896
Sb(2)–F(14)	1.855(4)	1.903	1.890			1.902	1.894
	Bond Angles (°)						
O(1)–Os–O(2)	99.9(2)	103.1	102.3	108.6	108.7		
O(1)–Os–F(1)	100.1(2)	97.6	96.6	125.7	125.7		
O(1)–Os–F(2)	100.2(2)	96.6	96.8	95.5	95.4		
O(1)–Os–F(3)	100.1(2)	100.1	97.6	95.5	95.4		
O(1)–Os---F(4)	179.2(2)	173.7	175.0				

O(2)–Os–F(1)	159.9(2)	158.5	160.9	125.7	125.7		
O(2)–Os–F(2)	90.3(2)	96.1	95.8	95.5	95.4		
O(2)–Os–F(3)	88.6(2)	89.9	92.4	95.5	95.4		
O(2)–Os---F(4)	80.9(2)	81.8	82.6				
F(1)–Os–F(2)	87.8(2)	87.0	84.5	80.6	80.7		
F(1)–Os–F(3)	86.2(2)	80.8	82.4	80.6	80.7		
F(1)–Os---F(4)	79.1(1)	78.0	78.5				
F(2)–Os–F(3)	159.6(2)	160.4	161.6	164.6	161.4		
F(2)–Os---F(4)	79.5(1)	78.8	82.2				
F(3)–Os---F(4)	80.2(1)	83.7	82.5				
Os---F(4)–Sb(1)	173.0(2)	135.8	154.4				
F(4)–Sb(1)–F(5)	86.6(2)	83.3	84.1			89.3	89.9
F(4)–Sb(1)–F(6)	171.5(1)	175.3	175.5			170.0	172.4
F(4)–Sb(1)–F(7)	87.1(2)	81.6	82.8			88.9	89.6
F(4)–Sb(1)–F(8)	90.9(1)	85.9	86.4			94.7	93.8
F(4)–Sb(1)---F(9)	83.4(1)	86.1	84.4			83.9	86.3
F(5)–Sb(1)–F(6)	92.0(2)	96.6	96.2			90.6	89.9
F(5)–Sb(1)–F(7)	168.6(2)	161.1	165.3			171.2	172.2
F(5)–Sb(1)–F(8)	94.7(2)	94.3	92.6			94.5	94.0
F(5)–Sb(1)---F(9)	84.5(1)	81.5	86.1			86.3	87.0
F(6)–Sb(1)–F(7)	92.9(2)	97.5	96.3			89.7	89.6
F(6)–Sb(1)–F(8)	97.6(2)	98.8	98.0			95.3	93.8
F(6)–Sb(1)---F(9)	88.0(1)	89.2	91.2			86.1	86.1
F(7)–Sb(1)–F(8)	94.9(1)	95.9	93.1			94.2	93.8
F(7)–Sb(1)---F(9)	85.3(1)	86.1	86.1			85.0	85.3
F(8)–Sb(1)---F(9)	174.3(2)	171.0	170.8			179.2	179.1
Sb(1)---F(9)---Sb(2)	170.0(2)	142.0	158.2			133.7	161.5
F(9)---Sb(2)–F(10)	178.5(2)	176.0	178.5			178.4	179.1
F(9)---Sb(2)–F(11)	85.5(1)	84.2	83.3			83.9	85.6
F(9)---Sb(2)–F(12)	85.3(1)	84.2	83.7			85.0	86.8
F(9)---Sb(2)–F(13)	84.4(1)	81.0	82.7			86.3	85.6

F(9)---Sb(2)–F(14)	85.2(1)	81.6	83.6	86.1	86.7
F(10)–Sb(2)–F(11)	94.1(2)	97.4	96.6	94.7	93.8
F(10)–Sb(2)–F(12)	96.2(2)	99.4	97.8	94.2	93.9
F(10)–Sb(2)–F(13)	94.2(2)	95.3	95.8	94.5	93.8
F(10)–Sb(2)–F(14)	95.1(2)	96.4	96.5	95.3	93.8
F(11)–Sb(2)–F(12)	89.4(2)	91.6	90.7	88.9	89.7
F(11)–Sb(2)–F(13)	90.5(2)	87.3	88.9	89.3	89.5
F(11)–Sb(2)–F(14)	170.7(2)	165.3	166.7	170.0	172.4
F(12)–Sb(2)–F(13)	169.7(2)	165.2	166.3	171.3	172.4
F(12)–Sb(2)–F(14)	88.6(2)	90.8	89.8	89.7	90.0
F(13)–Sb(2)–F(14)	89.9(2)	86.7	87.5	90.6	89.7

[a] For the atom labeling scheme see Figure 3.1. [b] The SDDall basis set was used, augmented for F, O and Sb with two d-type polarization functions. [c] The Stuttgart basis set was used for Os with the f functional. The aug-cc-pVTZ basis sets were used for all other atoms. [d] The aug-cc-pVTZ(-PP) basis set was used.

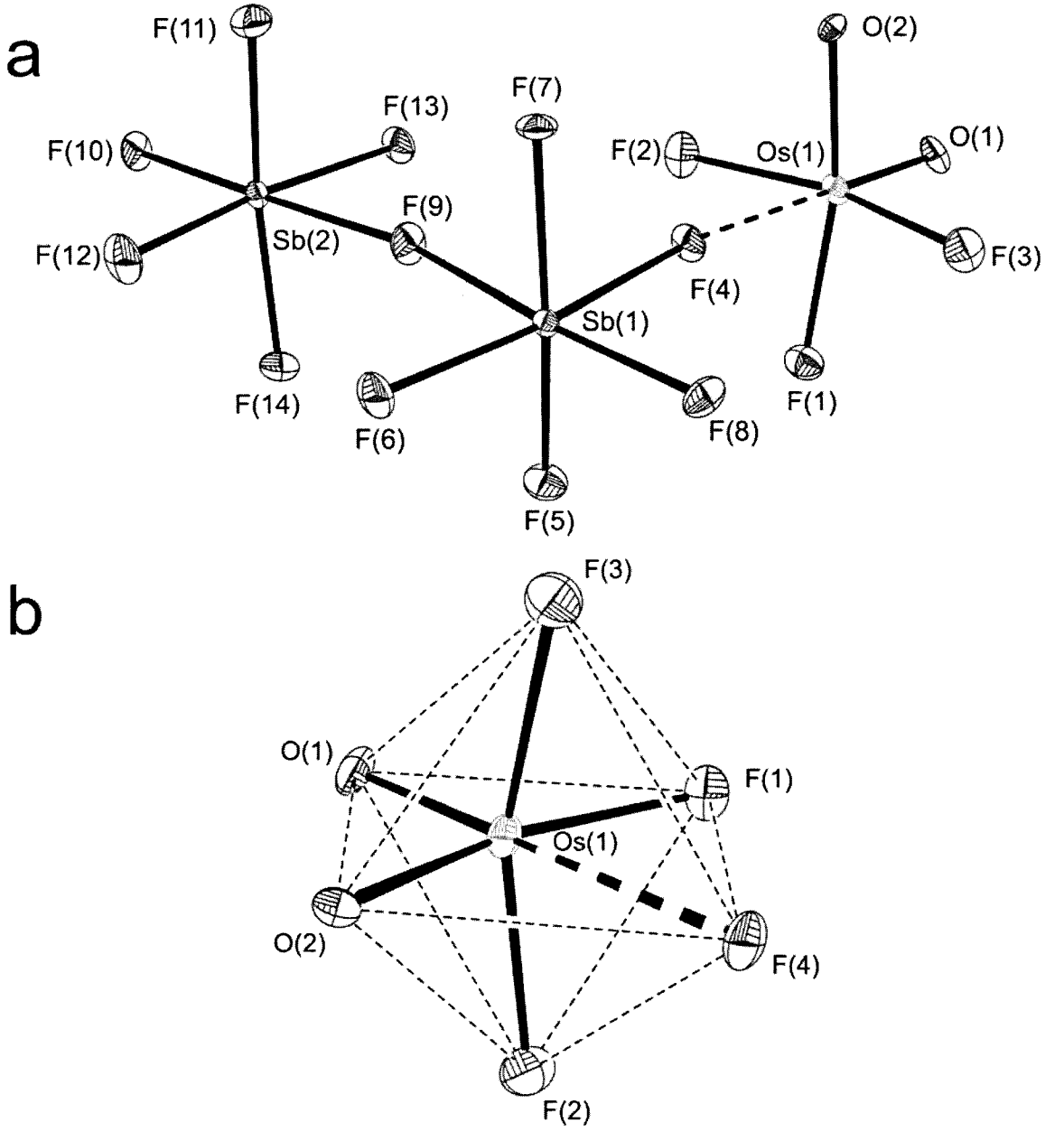

Figure 3.1. (a) Structural unit in the X-ray crystal structure of [*cis*-OsO_2F_3][Sb_2F_{11}] with thermal ellipsoids drawn at the 70% probability level. (b) Visualization of the octahedron formed by the light atoms of the OsO_2F_4-unit.

The oxygen atoms of $OsO_2F_3^+$ are cis to one another as found in $(OsO_3F_2)_\infty$,[11] $(OsO_3F_2)_2 \cdot 2XeOF_4$,[18] *cis*-$OsO_2F_4$,[20] and F(*cis*-$OsO_2F_3)_2^+$ [22] and in other transition metal oxide fluorides such as $MoO_2F_2 \cdot 2THF$ (THF = tetrahydrofuran),[44] *cis*-$TcO_2F_4^-$,[47] TcO_2F_3,[46] ReO_2F_3,[45] *cis*-$ReO_2F_4^-$,[45] μ-F(*cis*-$ReO_2F_3)_2^-$,[45] and $Re_3O_6F_{10}^-$.[45] The *cis*-dioxo geometry may be accounted for in terms of the relative spatial orientations of the approximate $d_{t_{2g}}$ orbitals of the d^0 metal and the availability of filled oxygen p donor orbitals.[167]

The lengths of the Os–O(1) bond trans to the bridging fluorine atom (1.654(4) Å) and the Os–O(2) bond trans to a terminal fluorine atom (1.764(4) Å) are comparable to those found in μ-F$(OsO_2F_3)_2^+$ (1.65(1) and 1.73(1) Å, respectively)[22] and $(OsO_3F_2)_\infty$ (1.69(1)/1.68(1) Å and 1.73(1) Å, respectively).[11] The terminal Os–F(1,2,3) bond lengths (1.812(4), 1.791(3), 1.806(3) Å) are also comparable to those in μ-F(*cis*-$OsO_2F_3)_2^+$ (1.79(1), 1.76(1) Å). The Os---F(4) bridge bond (2.190(3) Å) is somewhat longer than the Os---F bridge bonds of $(OsO_3F_2)_\infty$ (2.126(1), 2.108(1) Å),[11] $(OsO_3F_2)_2 \cdot 2XeOF_4$ (2.117(5) Å),[18] and μ-F(*cis*-$OsO_2F_3)_2^+$ (2.086(3) Å)[22] and is consistent with an ion-pair interaction.

The *trans*-position of the bridging fluorine, F(4), results from the *trans*-influence of the doubly bonded oxygen, O(1), which competes more effectively for the osmium $d_{t_{2g}}$ orbitals than F(4). Consequently, the F(4) atom is more strongly bonded to the Sb atom with a bond length of 1.958(3) Å and a negative charge that is less than those of the terminal fluorine ligands bonded to osmium and antimony (see Section 3.2.4). The bond length trend, Os–O(1) < Os–O(2), is also a consequence of less effective competition of the bridging fluorine atom (F(4)) for the empty metal $d_{t_{2g}}$ orbitals than the terminal

fluorine atom (F(1)). The tendency for bridging fluorine atoms to occupy positions trans to O atoms has also been noted in other transition metal oxide fluorides and their cations, e.g., μ-F(*cis*-$OsO_2F_3)_2^+$,[22] $(OsO_3F_2)_2 \cdot 2XeOF_4$,[18] $(OsO_3F_2)_\infty$,[11] polymeric $TcO_2F_3 \cdot SbF_5$,[46] $ReO_2F_3 \cdot SbF_5$,[158] μ-F$(TcOF_4)_2^+$,[158] μ-F$(ReOF_4)_2^-$,[157] μ-F(*cis*-$ReO_2F_3)_2^+$,[45] $Re_3O_6F_{10}^-$,[47] WOF_4,[168] and $MoOF_4$.[168]

Removal of a fluoride ion from *cis*-OsO_2F_4 to form *cis*-$OsO_2F_3^+$ results in contraction of the terminal Os–F bond lengths relative to those of *cis*-OsO_2F_4 (1.883(3) and 1.843(3) Å).[20] This is expected because cation formation results in a higher Os charge and a higher electronegativity for Os, leading to shorter and more covalent Os–F bonds. The length of the Os–O(1) bond trans to the bridging fluorine atom (1.654(4) Å) is comparable to that of *cis*-OsO_2F_4 (1.674(4) Å)[20] while the Os-O(2) bond length trans to the terminal fluorine ligand (1.764(4) Å) is longer than that of *cis*-OsO_2F_4. The longer Os–O(2) bond length likely results from a secondary bonding interaction between O(2) and F(8) of an adjacent $Sb_2F_{11}^-$ anion (O(2)···F(8), 2.808(4) Å).

The light atoms of the $OsO_2F_3^+$ cation and F(4) of the $Sb_2F_{11}^-$ anion comprise a distorted octahedral coordination sphere about osmium (Figure 3.1b). Although there is significant variation in the bond lengths around the osmium atom, the octahedron formed by the light atoms is relatively undistorted as shown by the ranges of nearest-neighbor ligand atom contacts.[169] The Os–F(1,2,3) and Os–O(2) bonds are bent away from the Os–O(1) bond, towards the longer Os---F(4) bridge bond. The F(1), F(2), O(2), and F(3) atoms are coplanar within ±0.003 Å and the bond angles subtended by the Os–O(1) bond and this plane are all very close to 100°. The osmium atom is displaced from the center of

the light atom octahedron towards O(1), lying 0.314 Å out of the [F(1), F(2), O(2), F(3)]-plane. In contrast, the Os atom is coplanar, to within ±0.02 Å, with the two remaining orthogonal ligand planes, [O(1), F(2), F(3), F(4)] and [O(1), O(2), F(1), F(4)]. This distortion is consistent with that observed for the μ-F(*cis*-$OsO_2F_3)_2^+$ cation,[22] where each Os atom is also displaced towards an O atom trans to the fluorine bridge. The out-of-center displacements of the Os atoms of both cations differ from their counterparts in *cis*-OsO_2F_4,[20] *cis*-$ReO_2F_4^-$,[45] and *cis*-$TcO_2F_4^-$,[47] where the metal atom is symmetrically displaced towards both O atoms of the *cis*-MO_2 group, with the orthogonal [O, M, O]- and [F_{ax}, M, F_{ax}]-planes bisecting each other.

The anion-cation close contact results in significant elongation of the Sb(1)–F(4) bridge bond (1.958(3) Å) when compared with the average of the terminal Sb–F bond lengths (1.847(3) Å). Such elongations have been noted for other ion pairs, e.g., [XeF][Sb_2F_{11}] (1.93(4), 1.84(4) Å)[109] and [XeF_3][Sb_2F_{11}] (1.90(1), 1.85(1) Å),[160] and [$Ir_4(CO)_8(\mu$-$F_2)(Sb_2F_{11})_2$] (1.886(3), 1.856(3) Å).[170] The Os---F(4)–Sb bridge angle (173.0(2)°) is slightly bent and compares well with those of [BrF_4][Sb_2F_{11}] (Br---F–Sb (170(5)°)),[162] [XeF_3][Sb_2F_{11}] (Xe---F–Sb (171.6(1)°),[160] and [(F_3As)AuXe][Sb_2F_{11}] (Au---F–Sb (173.26(2)°)).[163] The Sb(1)---F(9)---Sb(2) bond angle is also slightly bent (170.0(2)°). Both bridge angles are in good agreement with the fluorine bridge angles of other cubic close-packed structures such as WOF_4 (173(1)°),[171] [SeF_3][NbF_6] (173(3), 171(6), 176(8), 176(4)°),[172] [SeF_3][Nb_2F_{11}] (166(2), 177(1), 167(2), 170(2)°),[173] and [NbF_4][SbF_6] (162.9(8), 164.0(8)°).[174]

The $Sb_2F_{11}^-$ anion has a nearly eclipsed conformation, with a dihedral angle, ψ, between the SbF_4 equatorial planes of the SbF_5 units that share the fluorine bridge atom of 6.9° for F(5,7,8,9) and F(9,10,11,14) and 5.3° for F(4,6,8,9) and F(9,10,12,13). The correlation between the M---F---M bridge angle of a $M_2F_{11}^-$ anion and ψ is well-documented,[162] and results from minimization of steric repulsions between the nearest neighbor fluorine atoms of each octahedron as the M---F---M angle decreases and ψ increases. Accordingly, ψ is 0° when the M---F---M is 180°, reaching a maximum of 45° when M---F---M is ca. 145°.

3.2.3 Raman Spectroscopy

The solution Raman spectrum of *cis*-OsO_2F_4 in liquid SbF_5 has been previously assigned based on a trigonal bipyramidal geometry for the $OsO_2F_3^+$ cation and polymeric $Sb_nF_{5n+1}^-$ anions.[22] The low-temperature solid-state Raman spectrum of $[OsO_2F_3][Sb_2F_{11}]$ has been obtained in the present study (Figure 3.2.). The higher spectral resolution, knowledge of the X-ray crystal structure, and a factor-group analysis have enabled the complete vibrational assignment of the $[OsO_2F_3][Sb_2F_{11}]$ ion pair.

The observed and calculated frequencies and their assignments are listed in Table 3.3. The spectral assignments for $[OsO_2F_3][Sb_2F_{11}]$ were made by comparison with calculated frequencies and Raman intensities of the gas-phase $[OsO_2F_3][Sb_2F_{11}]$ ion pair, $Sb_2F_{11}^-$ (Table 3.3), and the $[OsO_2F_3][SbF_6]$ ion pair (Table A1), which are in good agreement at the SVWN/SDDall(-PP) and B3LYP/aug-cc-pVTZ(-PP) levels of theory.

The calculated $Sb_2F_{11}^-$ frequencies show better agreement with the experimental values than those previously calculated at the B3LYP/3-21G* level.[175, 176] The previous

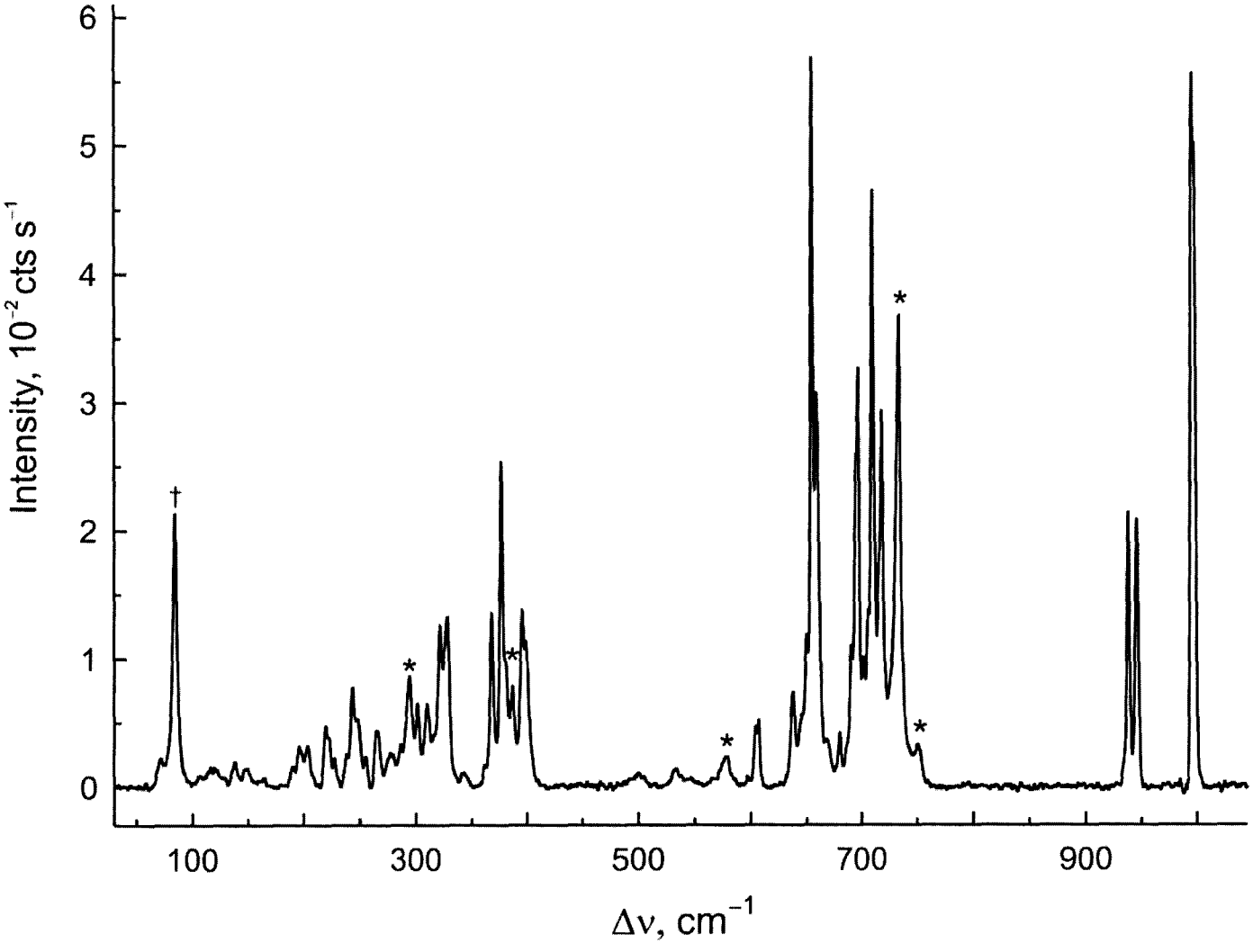

Figure 3.2. Raman spectrum of $[OsO_2F_3][Sb_2F_{11}]$ recorded at –150 °C using 1064-nm excitation; the symbols denote FEP sample tube lines (*) and an instrumental artifact (†).

Table 3.3 Raman Frequencies, Intensities, and Assignments for $[OsO_2F_3][Sb_2F_{11}]$ and Calculated Vibrational Frequencies and Assignments for $[OsO_2F_3][Sb_2F_{11}]$ and $Sb_2F_{11}^-$

$[OsO_2F_3][Sb_2F_{11}]$	$[OsO_2F_3][Sb_2F_{11}]$ (C_1)			Sb_2F_{11} (C_1)		
exptl[a]	calcd[b]		assgnts[c,d]	calcd[b]		assgnts[c,e]
	SVWN[f]	B3LYP[g]		SVWN[f]	B3LYP[h]	
997(89), 995(99)	1006(70)[71]	1055(76)[63]	$\nu(OsO_1) + \nu(OsO_2)$			
946(37), 938(37)	973(79)[25]	1024(25)[64]	$\nu(OsO_1) - \nu(OsO_2)$			
718(52), 716 sh	734(32)[91]	732(7)[158]	$\nu(OsF_2) - \nu(OsF_3)$			
709(82), 706(24) 702(18)	710(108)[64]	710(28)[101]	$\nu(OsF_1) + \nu(OsF_2) + \nu(OsF_3)$			
696(58), 695 sh	695(19)[93]	712(1)[96]	$\nu(SbF_5) - \nu(SbF_7)$	666(<0.1)[195]	675(<0.1)[259]	$[\nu(SbF_5) - \nu(SbF_7)] + [\nu(Sb'F_{14}) - \nu(Sb'F_{11})]$
691(19), 686 sh	677(12)[132]	700(6)[134]	$\nu(SbF_6)$	665(<1)[236]	675(<0.1)[266]	$[\nu(SbF_6) - \nu(SbF_4)] + [\nu(Sb'F_{14}) - \nu(Sb'F_{11})] + [\nu(Sb'F_{13}) - \nu(Sb'F_{12})]$
680(7)	672(21)[39]	695(1)[58]	$\nu(Sb'F_{11}) - \nu(Sb'F_{14})$	655(<1)[25]	667(<0.1)[8]	$[\nu(SbF_5) - \nu(SbF_7)] + [\nu(Sb'F_{11}) - \nu(Sb'F_{14})]$
669(6)	664(14)[59]	685(15)[42]	$\nu(SbF_8) + \nu(Sb'F_{10})$	655(<1)[24]	667(<0.1)[<1]	$[\nu(SbF_4) - \nu(SbF_6)] + [\nu(Sb'F_{13}) - \nu(Sb'F_{12})]$
659(54), 654(100)	668(14)[41]	676(4)[86]	$\nu(Sb'F_{12}) - \nu(Sb'F_{13})$	632(19)[26]	641(29)[3]	$\nu(SbF_8) + \nu(Sb'F_{10})$
649(21), 646(10)	657(3)[172]	673(2)[154]	$\nu(SbF_8) - \nu(Sb'F_{10})$	625(2)[191]	632(<1)[166]	$\nu(SbF_8) - \nu(Sb'F_{10})$
638(13)	660(12)[22]	651(7)[28]	$\nu(OsF_1) - [\nu(OsF_2) + \nu(OsF_3)]$			
608(7), 604(8)	628(23)[16]	640(8)[34]	$\nu(SbF_5) + \nu(SbF_4) + \nu(SbF_9)$	614(<1)[1]	622(<1)[92]	$[\nu(SbF_4) + \nu(SbF_5) + \nu(SbF_6) + \nu(SbF_7) + \nu(SbF_9)] - [\nu(Sb'F_{11} + \nu(Sb'F_{12}) + \nu(Sb'F_{13}) + \nu(Sb'F_{14}) + \nu(Sb'F_9)]$
578(4)	617(54)[37]	632(38)[28]	$\nu(Sb'F_{11}) + \nu(Sb'F_{14})$	611(56)[8]	615(38)[2]	$[\nu(SbF_4) + \nu(SbF_5) + \nu(SbF_6) + \nu(SbF_7)] + [\nu(Sb'F_{11}) + \nu(Sb'F_{12}) + \nu(Sb'F_{13}) + \nu(Sb'F_{14})]$
n.o.	562(12)[74]	578(20)[23]	$[\nu(Sb'F_{12}) + \nu(Sb'F_{13})] - [\nu(Sb'F_{11}) + \nu(Sb'F_{14})]$	584(4)[2]	578(3)[<1]	$[\nu(SbF_4) + \nu(SbF_6)] - [\nu(SbF_5) + \nu(SbF_7)] + [\nu(Sb'F_{12}) + \nu(Sb'F_{13})] - [\nu(Sb'F_{11}) + \nu(Sb'F_{14})]$
533(2)	504(9)[132]	511(10)[154]	$[\nu(OsF_4) - \nu(SbF_4)] + [\nu(Sb'F_9) - \nu(SbF_9)]$	583(3)[1]	578(3)[<1]	$[\nu(SbF_4) + \nu(SbF_6)] - [\nu(SbF_5) + \nu(SbF_7)] + [\nu(Sb'F_{11}) + \nu(Sb'F_{14})] - [\nu(Sb'F_{12}) + \nu(Sb'F_{13})]$
500(1)	475(32)[40]	466(2)[109]	$[\nu(OsF_4) - \nu(SbF_4)] - [\nu(Sb'F_9) - \nu(SbF_9)]$	475(<1)[135]	473(<0.1)[168]	$\nu(SbF_9) - \nu(Sb'F_9)$
n.o.	385(14)[8]	410(8)[15]	$\delta(O_1OsO_2)$			
399(20), 396(24)	358(3)[3]	375(6)[1]	$\delta(O_2OsF_2) + \delta(F_1OsF_3)$			
380 sh, 377(45)	367(5)[17]	339(4)[5]	$\delta(O_1OsF_2) + \delta(F_3OsF_9)$			
368(24), 362(2)	315(4)[3]	332(3)[16]	$\delta(F_1OsF_4) + \rho_w(F_2OsF_3)$			
343(1)	324(3)[20]	304(2)[1]	$\delta_{umb}(OsO_2F_1F_2F_3) + \rho_r(O_1OsF_4) + \delta_{umb}(SbF_4F_5F_8F_9)$			
317 sh, 310(11), 302(11)	302(8)[1]	300(1)[35]	$[OsO_2F_3][Sb_2F_{11}]$ coupled def.	347(3)[31]	298(<1)[27]	$\nu(SbF_9) + \nu(Sb'F_9)$
286(6)	286(2)[12]	290(1)[55]	$\delta(F_{13}Sb'F_{14}) - \delta(F_7SbF_9)$			
276(4) br	265(3)[42]	287(1)[11]	$\delta(F_{12}Sb'F_{14}) + \delta(F_9Sb'F_{11}) - \delta(F_9SbF_7)$	272(<1)[<0.1]	284(<0.1)[40]	$\delta(SbF_9Sb') + \delta_{umb}(SbF_{4,6,7,8}) + \delta_{umb}(Sb'F_{11,12,13,14})$
n.o.	253(8)[13]	280(<1)[5]	$[OsO_2F_3][Sb_2F_{11}]$ coupled def.			

264(7)	243(<1)[42]	276(2)[35]	$\rho_w(F_2OsF_3) + \delta(F_4SbF_5) - \delta(F_{11}Sb'F_{12})$	264(<0.1)[75]	283(<0.1)[77]	$\rho_w(F_5SbF_8) + \rho_w(F_7SbF_9) + \rho_w(F_9Sb'F_{10}) + \rho_w(F_{12}Sb'F_{13})$
255(4)	256(8)[41]	264(1)[26]	$\delta(F_{12}Sb'F_{14}) - \delta(F_{11}Sb'F_{13}) + \rho_t(F_9Sb'F_{10})$	252(2)[8]	271(1)[<0.1]	$\delta(F_6SbF_7) + \delta(F_4SbF_5) + \delta(F_{13}Sb'F_{11}) - \delta(F_{14}Sb'F_{12})$
247 sh, 244(13)	245(12)[26]	264(<1)[31]	$\delta(F_{11}Sb'F_{12}F_{10})$	251(1)[2]	271(1)[<1]	$\delta(F_6SbF_7) + \delta(F_4SbF_5) - \delta(F_{13}Sb'F_{11}) - \delta(F_{14}Sb'F_{12})$
239(4), 238(4)	234(3)[8]	259(1)[13]	$\rho_w(SbF_6F_8F_{13}) + \delta(F_7SbF_7)$	247(1)[10]	266(1)[2]	$\delta_{umb}(SbF_{6,7,8}) + \delta_{umb}(Sb'F_{10,11,12}) - [\delta(F_4SbF_7) + \delta(F_{13}Sb'F_{14})]$
n.o	268(2)[1]	248(1)[132]	$\rho_t(F_5SbF_8) + \delta(F_6SbF_9) + \delta(F_8SbF_9) + \delta_{ring}(Sb'F_{11}F_{12}F_{13}F_{14})$	245(1)[43]	267(1)[<0.1]	$\delta_{umb}(SbF_{4,5,8}) + \delta_{umb}(Sb'F_{10,12,14})$
n.o	226(3)[55]	242(1)[40]		242(<1)[14]	257(<1)[22]	$\delta_{umb}(SbF_{4,5,8}) - \delta_{umb}(Sb'F_{10,12,14})$
n.o.	222(7)[88]	224(1)[76]	$[OsO_2F_3][Sb_2F_{11}]$ coupled def.	233(<1)[12]	254(<0.1)[11]	$[\delta(F_6SbF_9) + \delta(F_4SbF_5)] - [\delta(F_5Sb'F_{14}) + \delta(F_{10}Sb'F_{11})]$
228 (4), 220(8)	199(1)[1]	220(1)[14]		223(<0.1)[192]	243(<0.1)[256]	$\rho_w(F_4SbF_5) + \rho_w(F_6SbF_7) + \rho_w(F_{11}Sb'F_{12}) + \rho_w(F_{13}Sb'F_{14})$
n.o.	190(10)[17]	208(2)[14]	$\delta(F_{10}Sb'F_{11}) - \delta(F_{10}Sb'F_{14})$			
204(5)	178(1)[3]	199(1)[4]		193(1)[<1]	213(1)[<0.1]	
196(5)	187(1)[6]	193(1)[9]	$[OsO_2F_3][Sb_2F_{11}]$ coupled def.	188(1)[1]	212(1)[<0.1]	def. ($Sb_2F_{11}^-$)
190(2)	148(1)[1]	186(<1)[2]		186(1)[2]	183(<1)[<1]	
164(1)	186(9)[11]	167(<1)[8]	$\delta(F_4SbF_7) + \rho_t(F_4SbF_9) + \rho_w(F_5SbF_7)$	157(<1)[<0.1]	174(<0.1)[<0.1]	$[\rho_w(F_6SbF_9) + \rho_w(F_7SbF_{10})] - [\rho_w(F_5SbF_7) + \rho_w(F_{12}SbF_{13})]$
148(2)	156(1)[<1]	143(1)[<1]	$OsO_2F_3^+$ def. mode			
137(3)	141(1)[2]	128(<1)[<1]	$\rho_t(F_{11}Sb'F_{13}) - \rho_t(F_{12}Sb'F_{14})$			
n.o	128(1)[1]	125(<1)[2]	$Sb_2F_{11}^-$ coupled def.			
n.o.	119(<1)[3]	121(<0.1)[1]	$[OsO_2F_3][Sb_2F_{11}]$ coupled def.	123(<0.1)[<1]	141(<0.1)[<0.1]	$[\rho_w(F_5SbF_7) + \rho_w(F_{12}Sb'F_{13})] - [\rho_w(F_4SbF_6) + \rho_w(F_{11}Sb'F_{12})]$
n.o.	110(<1)[1]	104(<1)[5]	$Sb_2F_{11}^-$ coupled def./torsion	120(<0.1)[<1]	141(<0.1)[<0.1]	$[\rho_w(F_5SbF_7) + \rho_w(F_{11}Sb'F_{12})] - [\rho_w(F_4SbF_6) + \rho_w(F_{12}Sb'F_{13})]$
n.o.	80(<1)[<1]	98(<1)[1]	$Sb_2F_{11}^-$ coupled def.	110(<1)[<1]	118(1)[<1]	ρ_{rock}(arcund Sb and Sb')
n.o.	75(<1)[1]	78(<1)[<0.1]	$[OsO_2F_3][Sb_2F_{11}]$ coupled def.			
n.o.	46(1)[1]	60(<1)[1]	$\rho_t(F_1OsF_2) + \rho_t(O_2OsF_3)$	96(<0.1)[<0.1]	104(<0.1)[<0.1]	
n.o.	41(<1)[<0.1]	53(<1)[<0.1]	$[OsO_2F_3][Sb_2F_{11}]$ coupled def.	87(<0.1)[<1]	103(<0.1)[<0.1]	$\rho_{torsion}$(around Sb and Sb')
n.o.	89(<1)[<1]	43(<1)[1]		57(<0.1)[<0.1]	18(<0.1)[<0.1]	
	69(<1)[1]	37(<1)[2]	$[OsO_2F_3][Sb_2F_{11}]$ def.	23(<0.1)[<0.1]	13(<0.1)[<0.1]	
	61(<1)[<1]	32(<1)[<1]				ρ_{rock}(arcund Sb and Sb')
n.o.	101(1)[<0.1]	30(<0.1)[<1]	$Sb_2F_{11}^-$ coupled def.	34(<0.1)[<0.1]	4(<0.1)[<0.1]	

[a] The Raman spectrum was recorded on a microcrystalline sample in a FEP sample tube at −150 °C using 1064-nm excitation. The experimental Raman intensities (in parentheses) are relative intensities with the most intense band given a value of 100. The abbreviations denote shoulder (sh) and not observed (n.o.). [b] Values in parentheses denote calculated Raman intensities (amu $Å^{-4}$) and values in square brackets denote calculated infrared intensities (km mol^{-1}). [c] The symbols denote stretch (ν), bend (δ), umbrella (δ_{umb}), and wag (ρ_w). The abbreviation, def., denotes a deformation mode(s). [d] Assignments are based on the B3LYP structure; see Figure 3.4a for the atom labeling scheme. [e] Assignments are based on the SVWN-optimized structure; see Figure 3.4c for the atom labeling scheme. [f] SVWN/SDDall(-PP). [g] B3LYP/Stuttgart aug-cc-pVTZ(-PP). [h] B3LYP/aug-cc-pVTZ(-PP).

calculations overestimated the Sb–F stretching frequencies by ca. 70 cm^{-1}, whereas the frequencies calculated in the current study are overestimated by ca. 30 cm^{-1}.

The vibrational modes (51 A) of the $[OsO_2F_3][Sb_2F_{11}]$ ion pair corresponding to the gas-phase energy-minimized symmetry, C_1, are all predicted to be Raman and infrared active. It is apparent from Table 3.3 that the majority of the bands are split into two components. Consequently, a factor-group analysis was undertaken based on the crystal structure determination (see Section 3.2.2). The analysis (Table 3.4) correlated the gas-phase symmetry of the ion pair (C_1) to its site symmetry (C_1) which, in turn, was correlated to the unit cell symmetry (C_i). The factor-group analysis, however, revealed that the Raman bands of $[OsO_2F_3][Sb_2F_{11}]$ are not expected to be split. X-ray powder diffraction patterns (Figure 3.3) recorded on the same sample confirmed that a single phase was present between the temperature at which the Raman spectrum was recorded (–150 °C) and the temperature at which the single-crystal X-ray data were collected (–173 °C). Moreover, the powder patterns recorded at –150 and –173 °C were in agreement with the powder pattern calculated from the single-crystal data. It may be concluded that the splitting does not arise from a phase transition in this temperature range. In addition to the centrosymmetric space group, $P\bar{1}$, the structure was solved in the $P1$ space group, which could account for the splittings in the Raman spectrum (Table 3.4), however, the refinement in this space group proved to be unstable, with the thermal parameters of many light atoms becoming non-positive when attempting to refine them anisotropically. Presently, the splittings of the Raman bands cannot be accounted for unless the unit cell is not truly centrosymmetric and the vibrational spectrum better

Table 3.4. Factor-Group Analyses for $[OsO_2F_3][Sb_2F_{11}]$ under the Space Groups $P\bar{1}$ and $P1$

gas-phase $[OsO_2F_3][Sb_2F_{11}]$ (C_1)		crystal site (C_1)	unit cell[a] (C_i)		
			A_g	ν_1-ν_{51}, (–3R), 3T	Raman
$2(\nu_1$-ν_{51}, 3R, 3T)	A	A			
			A_u	ν_1-ν_{51}, 3R, (–3T)	IR

[a] The crystallographic space group is $P\bar{1}$ with $Z = 2$ structural units per unit cell.

gas-phase $[OsO_2F_3][Sb_2F_{11}]$ (C_1)		crystal site (C_1)	unit cell[a] (C_1)		
$2(\nu_1$-ν_{51}, 3R, 3T)	A	A	A	$2(\nu_1$-$\nu_{51})$, 3R (–3R), 3T (–3T)	Raman, IR

[a] The crystallographic space group is $P1$ with $Z = 2$ structural units per unit cell.

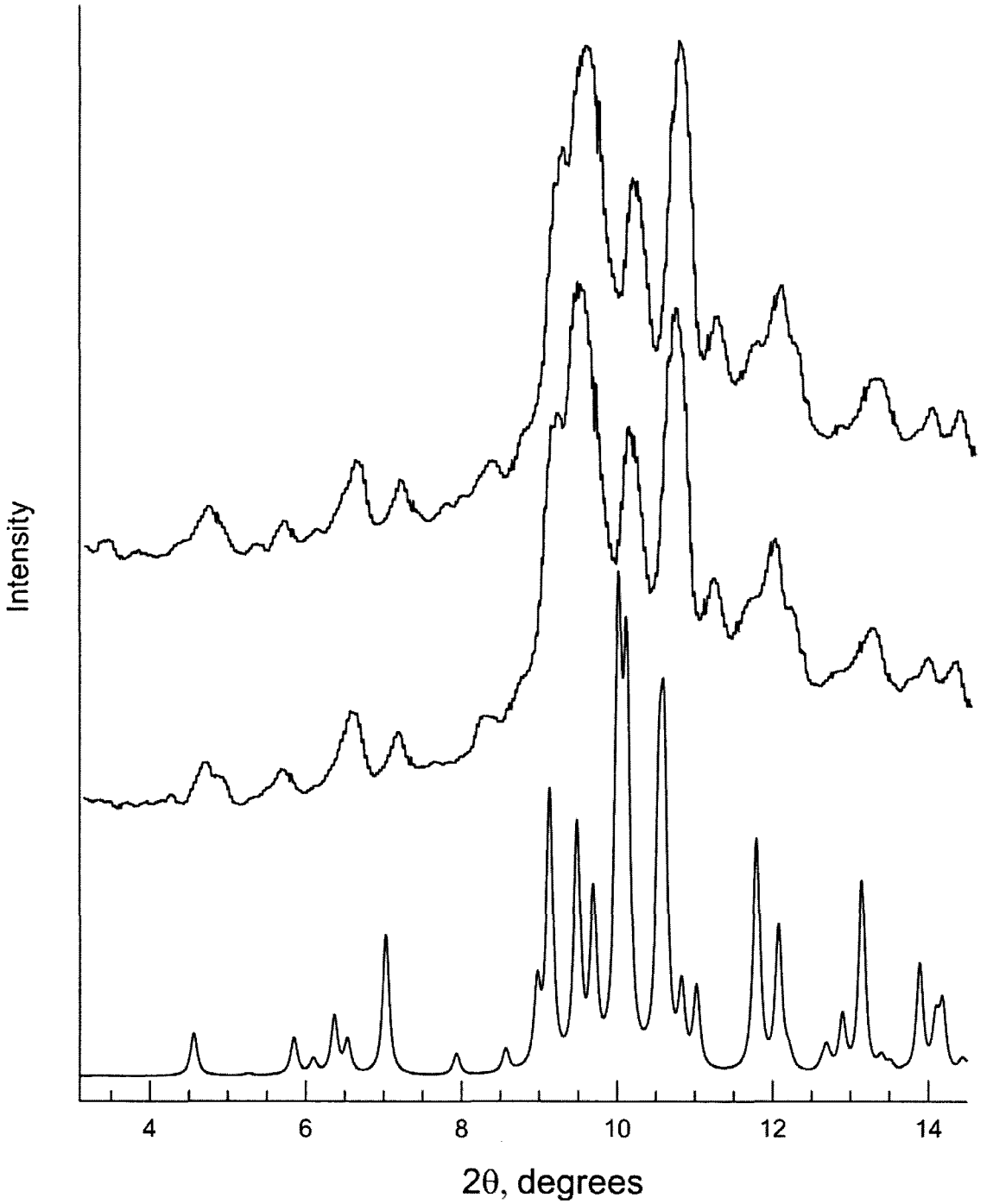

Figure 3.3. X-ray powder diffraction patterns of $[OsO_2F_3][Sb_2F_{11}]$ recorded on a microcrystalline sample mounted in a glass capillary at –173 (upper trace) and –150 °C (middle trace) and the powder pattern generated from the crystal structure of $[OsO_2F_3][Sb_2F_{11}]$ (bottom trace).

represents the true symmetry. Such a situation is illustrated by $[H_3O{\cdot}2XeF_2][AsF_6]$.[177]

Ion-pair formation results in pseudo-octahedral coordination about the osmium atom. The bands at 938/941 and 995/997 cm^{-1}, assigned to $\nu(OsO_1) - \nu(OsO_2)$ and $\nu(OsO_1) + \nu(OsO_2)$, respectively, were previously observed at 940 and 996 cm^{-1}, respectively, in frozen SbF_5 solution.[22] As in the case of *cis*-OsO_2F_4,[20] the in-phase $\nu(OsO_1) + \nu(OsO_2)$ mode is observed at higher frequency than the out-of-phase $\nu(OsO_1) - \nu(OsO_2)$ mode. In contrast with the coupled ν(OsO) modes calculated at the B3LYP level, those calculated at the SVWN level are only weakly coupled and are better described as isolated $\nu(OsO_1)$ and $\nu(OsO_2)$ stretches at this level of theory.

The bands at 702/706/709 and 716/718 cm^{-1}, previously assigned to $Sb_nF_{5n+1}^-$ modes[22] have been re-assigned to the in-phase $\nu(OsF_1) + \nu(OsF_2) + \nu(OsF_3)$ and out-of-phase $\nu(OsF_2) - \nu(OsF_3)$ stretches, respectively. Out-of-phase coupling of the $\nu(OsF_2) + \nu(OsF_3)$ mode to $\nu(OsF_1)$ gives rise to the $\nu(OsF_1) - [\nu(OsF_2) + \nu(OsF_3)]$ mode at 638 cm^{-1}. In general, the Os–O and Os–F stretching modes are in good agreement with those obtained for $OsO_2F_3^+$ in frozen SbF_5 solution, suggesting that the $OsO_2F_3^+$ cation is fluorine bridged to the $Sb_nF_{5n+1}^-$ anion and that Os(VIII) is six coordinate in the latter case.

Frequencies in the ranges 578–608 and 646–696 cm^{-1} are assigned to the Sb–F stretches of $Sb_2F_{11}^-$ and are in good agreement with those reported in the literature.[72, 176, 178-180] The prior solution Raman study[22] had assigned a very broad band at 522 cm^{-1} to the out-of-phase stretching mode of the Os---F_b---Sb fluorine bridge, $\nu(OsF_b) - \nu(SbF_b)$. In the present study, this band is resolved into two bands at 500 and 533 cm^{-1} which have

been re-assigned. The splitting arises from in-phase and out-of-phase coupling of the out-of-phase component of the Sb---F_9---Sb' stretching mode of $Sb_2F_{11}^-$, $\nu(Sb'F_9) - \nu(SbF_9)$, with $\nu(OsF_4) - \nu(SbF_4)$. These bridge mode frequencies are similar to the Os---F_b---Os out-of-phase stretching frequencies of $[\mu\text{-F}(cis\text{-}OsO_2F_3)_2][AsF_6]$ and $[\mu\text{-F}(cis\text{-}OsO_2F_3)_2][Sb_2F_{11}]$ (492 and 495 cm^{-1}, respectively). In several prior studies of $Sb_2F_{11}^-$ salts, the $\nu(SbF_9) - \nu(Sb'F_9)$ bands were only observed in the infrared spectra of the $Rh(CO_4)^+$ (489 cm^{-1}),[176] $Au(CO)_2^+$ (503 cm^{-1}),[179] and the $Pt(CO)_4^+$ (502 cm^{-1})[180] salts, which are in good agreement with the out-of-phase mode assigned in the present study (500 cm^{-1}). The low-frequency deformation modes (137-228 cm^{-1}) consist of coupled cation and anion modes whose frequencies are also in good agreement with the calculated values.

3.2.4. Computational Results.

The energy-minimized geometries of $[OsO_2F_3][Sb_2F_{11}]$ (C_1), $Sb_2F_{11}^-$ (C_1), $OsO_2F_3^+$ (C_{2v}) (Figure 3.4), and $[OsO_2F_3][SbF_6]$ (C_1) (Table A2 and Figure A2) were obtained at the SVWN and B3LYP levels of theory and resulted in stationary points with all frequencies real. The $OsO_2F_3^+$ cation has been previously calculated using NLDFT and LDFT methods[22] and the $Sb_2F_{11}^-$ anion has been calculated at the B3LYP level with the 3-21G* basis set.[175] For consistency and to enable comparisons to be made in the present study, all species have been calculated using more extensive basis sets and at the same levels of theory (see Section 2.13). All calculated $OsO_2F_3^+$ bond lengths are shorter than those previously calculated and are in better agreement with the experimental values

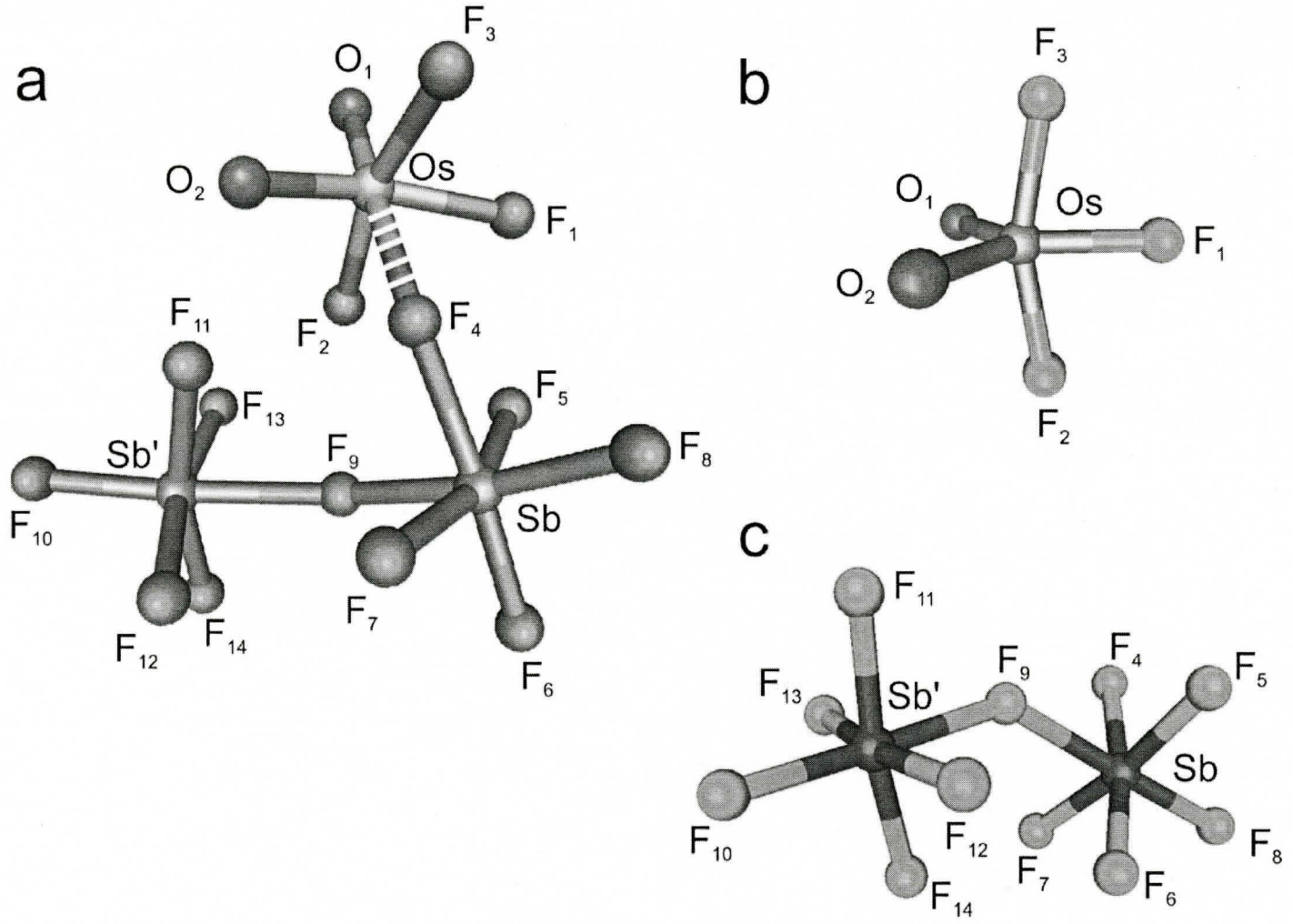

Figure 3.4. Calculated SVWN/SDDall(-PP) gas-phase geometries for (a) $[OsO_2F_3][Sb_2F_{11}]$ (C_1), (b) $OsO_2F_3^+$ (C_{2v}), and (c) $Sb_2F_{11}^-$ (C_1).

(Table 3.2). The frequencies calculated at the SVWN level provide slightly better agreement with experiment than at the B3LYP level, while the calculated geometries are in equally good agreement with experiment, therefore, only the SVWN values are referred to in the ensuing discussion.

3.2.4.1. Calculated Geometries.

The gas-phase geometry of $OsO_2F_3^+$ is predicted to be trigonal bipyramidal with two axial fluorine atoms and two oxygen atoms and one fluorine atom in the equatorial plane (Figure 3.4b). The coordination sphere of osmium in the $[OsO_2F_3][Sb_2F_{11}]$ ion pair is a distorted octahedron that results from a contact to the $Sb_2F_{11}^-$ anion by means of an Os---F_4–Sb bridge (Figure 3.4a). All of the calculated Os–O and Os–F bond lengths of the ion pair are elongated relative to those of the free cation as a result of electron density donation from the bridge fluorine, F_4, to Os (Table 3.2). Although the cation of the ion pair and free cation have markedly different calculated geometries, the F_2–Os–F_3 bond angles are bent away from O_1 and O_2 in both cases. The calculated ion-pair structure shows that the atoms in the equatorial plane, [O_2, F_3, F_1, F_2], are displaced away from the axial oxygen (O_1) towards the bridging fluorine atom (F_4) in accordance with the crystal structure.

The calculated Os–O_2 (1.696 Å) and Os–O_1 (1.708 Å) bond lengths are in good agreement with the experimental values (1.654(4) and 1.765(4) Å, respectively). The greater difference observed in the crystal structure is likely the result of short O···F contacts between O(2) and F(7C)/F(10D) of other nearest neighbor anions in the unit cell.

The Os–F bond lengths of the ion pair are overestimated relative to the experimental values but reproduce the observed trends. Upon ion-pair formation, the Os–F_1 bond length is significantly elongated when compared with that of the free cation because the pseudo-octahedral geometry of Os(VIII) places F_1 trans to O_2, whereas for the trigonal bipyramidal gas-phase geometry, F_1, O_1, and O_2 occupy the equatorial plane with F_1-Os-$O_{1,2}$ angles of 125.7°. The Os–F_2 (1.835 Å) and Os–F_3 (1.852 Å) bond lengths are longer in the gas-phase ion pair as a result of coordination to and electron donation by the F(4) atom of $Sb_2F_{11}^-$. The Os–$F_{2,3}$ bond lengths are non-equivalent presumably because the F_4---Os–F_2 (78.8°) angle is slightly more closed relative to the F_4---Os–F_3 (83.7°) angle. The Os---F_4 distance is somewhat underestimated (2.089 Å) when compared with the experimental value (2.190(3) Å). The bond lengths of the Os---F_4–Sb bridge are predicted to be similar, with a calculated Sb–F_4 bond length of 2.085 Å for the gas-phase ion pair, 1.958(3) Å for the ion-pair in the experimental structure, and 1.909 Å for the gas-phase $Sb_2F_{11}^-$ anion.

The calculated Sb–F bond lengths of the ion pair are all slightly longer than their experimental values. The asymmetry of the experimental Sb---F_9---Sb' bridge, Sb---F_9 (1.995(3) Å) and Sb'---F_9 (2.060(3) Å), is reproduced by the calculated Sb---F_9 (2.027 Å) and Sb'---F_9 (2.139 Å) bond lengths. When compared with the bond lengths of the free anion in the gas-phase, the Sb–F bond lengths of the ion pair are somewhat shorter because the net anion charge is diminished by bridge formation with the cation. The Sb---F bridge bond lengths of the gas-phase anion are symmetric (2.080 Å) and intermediate with respect to the calculated Sb---F_9---Sb' bridge bond lengths of the ion

pair. The Sb---F_9---Sb' bond angle of the ion pair is predicted to be significantly more closed (142.0°) than that in the crystal structure (170.0(2)°), which is likely a consequence of close packing in the crystal lattice (vide supra). The bridge angle of the free anion is more closed (133.7°) than that of the ion pair (142.0°) at the SVWN level, while at the B3LYP level, the free anion bond angle is somewhat more open (161.5°) when compared with that of the ion pair (158.2°).

Previous quantum-chemical calculations of the free $Sb_2F_{11}^-$ anion constrained the symmetry to D_{4h} with an Sb---F---Sb angle of 180° and an eclipsed conformation for the two SbF_4-planes.[175] In the current study, the use of C_1 as a starting symmetry allowed the Sb---F---Sb angle to bend and the SbF_4-planes to achieve a staggered conformation. Both structural changes led to better agreement between the observed and calculated bond lengths, angles, and vibrational frequencies. The larger Sb(1)---F(9)---Sb(2) angle in the crystal structure (170.0 (2)°) compared to the calculated gas-phase value (133.7)° is likely a consequence of interactions with the cation that accompany cubic close packing, which is indicative of the near-linear Sb(1)---F(9)---Sb(2) angle. The low frequency calculated for the Sb---F---Sb bend (23 cm^{-1}) underscores the deformability of this angle, and its susceptibility to crystal packing.

3.2.4.2. Charges, Valencies, and Bond Orders.

Natural bond orbital (NBO)[181-184] analyses were carried out for the SVWN- and B3LYP-optimized gas-phase structures of $OsO_2F_3^+$, $[OsO_2F_3][Sb_2F_{11}]$, $Sb_2F_{11}^-$ (Table 3.5), and $[OsO_2F_3][SbF_6]$ (Table A3).

Table 3.5. Natural Bond Orbital (NBO) Valencies, Bond Orders, and NPA Charges for $OsO_2F_3^+$, $[OsO_2F_3][Sb_2F_{11}]$, and $Sb_2F_{11}^-$

Charges

	$OsO_2F_3^+$ (C_{2v})		$[OsO_2F_3][Sb_2F_{11}]$ (C_1)		$Sb_2F_{11}^-$ (C_1)	
Atom	SVWN	B3LYP	SVWN	B3LYP	SVWN	B3LYP
Os	2.12	2.43	1.99	2.31		
O_1	–0.16	–0.21	–0.21	–0.23		
O_2	–0.16	–0.21	–0.18	–0.20		
F_1	–0.29	–0.36	–0.34	–0.41		
F_2	–0.25	–0.33	–0.29	–0.34		
F_3	–0.25	–0.33	–0.32	–0.38		
F_4			–0.58	–0.62	–0.64	–0.64
Sb			3.08	3.07	3.08	3.06
F_5			–0.61	–0.61	–0.64	–0.64
F_6			–0.61	–0.61	–0.65	–0.64
F_7			–0.60	–0.60	–0.65	–0.64
F_8			–0.62	–0.62	–0.66	–0.66
F_9			–0.67	–0.66	–0.66	–0.67
Sb′			3.08	3.05	3.08	3.06
F_{10}			–0.63	–0.63	–0.66	–0.66
F_{11}			–0.62	–0.62	–0.65	–0.64
F_{12}			–0.62	–0.62	–0.64	–0.64
F_{13}			–0.63	–0.65	–0.65	–0.64
F_{14}			–0.62	–0.63	–0.64	–0.64

Valencies

	$OsO_2F_3^+$ (C_{2v})		$[OsO_2F_3][Sb_2F_{11}]$ (C_1)		$Sb_2F_{11}^-$ (C_1)	
Atom	SVWN	B3LYP	SVWN	B3LYP	SVWN	B3LYP
Os	3.33	3.26	3.52	3.55		
O_1	0.95	0.96	0.95	0.96		
O_2	0.95	0.96	0.96	0.94		
F_1	0.54	0.52	0.50	0.47		
F_2	0.55	0.50	0.56	0.52		
F_3	0.55	0.50	0.53	0.50		
F_4			0.51	0.49	0.38	0.32
Sb			2.40	2.61	2.49	2.14
F_5			0.38	0.43	0.38	0.32
F_6			0.40	0.45	0.38	0.32
F_7			0.39	0.44	0.38	0.32
F_8			0.39	0.44	0.38	0.33
F_9			0.43	0.52	0.46	0.41
Sb′			2.45	2.62	2.49	2.14
F_{10}			0.40	0.44	0.38	0.33
F_{11}			0.39	0.42	0.38	0.32
F_{12}			0.40	0.42	0.38	0.32
F_{13}			0.37	0.38	0.38	0.32
F_{14}			0.38	0.41	0.38	0.32

Table 3.5. (Continued …)

	Bond Orders					
	$OsO_2F_3^+$ (C_{2v})		$[OsO_2F_3][Sb_2F_{11}]$ (C_1)		$Sb_2F_{11}^-$ (C_1)	
Bond	SVWN	B3LYP	SVWN	B3LYP	SVWN	B3LYP
Os–O_1	0.89	0.89	0.90	0.92		
Os–O_2	0.89	0.89	0.88	0.91		
Os–F_1	0.51	0.48	0.48	0.46		
Os–F_2	0.52	0.49	0.52	0.51		
Os–F_3	0.52	0.49	0.50	0.49		
Os---F_4			0.27	0.27		
Sb–F_4			0.26	0.26	0.44	0.38
Sb–F_5			0.44	0.49	0.44	0.38
Sb–F_6			0.45	0.50	0.44	0.38
Sb–F_7			0.45	0.50	0.44	0.38
Sb–F_8			0.44	0.49	0.43	0.38
Sb---F_9			0.39	0.37	0.27	0.24
Sb′---F_9			0.22	0.22	0.27	0.24
Sb′–F_{10}			0.45	0.49	0.43	0.38
Sb′–F_{11}			0.46	0.49	0.44	0.38
Sb′–F_{12}			0.46	0.49	0.44	0.38
Sb′–F_{13}			0.39	0.46	0.44	0.38
Sb′–F_{14}			0.44	0.48	0.44	0.38

The NBO analyses give NPA (Natural Population Analysis) charges of 2.12 and 1.99 for Os in $OsO_2F_3^+$ and $[OsO_2F_3][Sb_2F_{11}]$, respectively, and 3.08 for Sb in $[OsO_2F_3][Sb_2F_{11}]$ and $Sb_2F_{11}^-$. The average NPA charges of the oxygen ligands are significantly less negative than those of the fluorine ligands in both $OsO_2F_3^+$ and the $[OsO_2F_3][Sb_2F_{11}]$ ion pair, consistent with significant charge transfer from the filled oxygen p orbitals into the empty d orbitals of osmium. The fluorine atom charges of $Sb_2F_{11}^-$ are more negative than those of $OsO_2F_3^+$. The negative charge on F_4 is less than those of the remaining fluorine ligands bonded to Sb because F_4 is bridged to the highly electronegative Os(VIII) center. Overall, the charges are indicative of polar covalent bonds in all three species, with the most polar bonds occurring for the Sb–F and Sb---F bonds.

The average Os–O bond orders (0.89) are approximately double those of the average Os–F (0.50) bond orders, consistent with the formal double bond characters of the Os–O bonds which are consistent with the corresponding O and F valencies. The bond orders of Os---F_4 (0.27) and Sb---F_4 (0.26) in the ion pair are similar and indicate a strongly associated ion pair. The anion bridge bonds are asymmetric in the crystal structure, which is reflected in the calculated bond orders, Sb---F_9 (0.39) and Sb'---F_9 (0.22). The higher Sb---F_9 bond order results from electron density withdrawal from Sb by Os through the bridging F_4 atom (vide supra) which strengthens the Sb---F_9 bond and weakens the Sb'---F_9 bond, providing an Sb'–F_9 bond order that is half of the average terminal Sb–F and Sb'–F bond orders (0.45).

3.2.4.3. Thermochemistries of $[OsO_2F_3][PnF_6]$, $[OsO_2F_3][Sb_2F_{11}]$, $[\mu\text{-}F(OsO_2F_3)_2][PnF_6]$, and $[\mu\text{-}F(OsO_2F_3)_2][Sb_2F_{11}]$ (Pn = As, Sb).

Attempts to synthesize $[OsO_2F_3][SbF_6]$ from *cis*-OsO_2F_4 and SbF_5 under various conditions have proven unsuccessful (see Synthesis of $[OsO_2F_3][Sb_2F_{11}]$ and Attempted Synthesis of $[OsO_2F_3][SbF_6]$), resulting in the formation of either $[OsO_2F_3][Sb_2F_{11}]$ or $[\mu\text{-}F(OsO_2F_3)_2][Sb_2F_{11}]$. To account for the preferential formation of $Sb_2F_{11}^-$ salts, quantum-chemical calculations and volume-based lattice energies[185, 186] were used in conjunction with known thermodynamic quantities to estimate the standard enthalpies listed in Scheme 3.1.

The standard enthalpies were estimated by analyzing the corresponding Born-Haber cycles as exemplified for ΔH°_2 in Scheme 3.2. The enthalpies of fluoride ion abstraction from *cis*-OsO_2F_4 ($\Delta H^\circ_{-F^-}$), fluoride ion attachment ($\Delta H^\circ_{+F^-}$) to the Lewis acids MF_5 (M = Sb or As), association of the SbF_6^- ion with SbF_5 ($\Delta H^\circ_{+Sb_2F_{11}^-}$), and association of the $OsO_2F_3^+$ cation with *cis*-OsO_2F_4 ($\Delta H^\circ_{+Os_2O_4F_7^+}$) were calculated at the SVWN and B3LYP (Table 3.6) levels of theory. The SVWN and B3LYP values differ, but follow the same trends, with the B3LYP values expected to give more reliable energies.[187] Consequently, only the B3LYP values are referred to in the ensuing discussion.

The lattice enthalpies of the $OsO_2F_3^+$ and μ-$F(OsO_2F_3)_2^+$ salts (Table 3.7) were estimated by use of the volume-based method of Bartlett et al.[188] as generalized by Jenkins et al.[185, 186] in eq 3.6, where R is the gas constant (8.314 J K^{-1} mol^{-1}), V_m is the

ΔH°_1 $OsO_2F_{4(s)} + SbF_{5(l)} \longrightarrow [OsO_2F_3][SbF_6]_{(s)}$

ΔH°_2 $OsO_2F_{4(s)} + 2SbF_{5(l)} \longrightarrow [OsO_2F_3][Sb_2F_{11}]_{(s)}$

ΔH°_3 $2OsO_2F_{4(s)} + SbF_{5(l)} \longrightarrow [\mu\text{-}(OsO_2F_3)_2][SbF_6]_{(s)}$

ΔH°_4 $2OsO_2F_{4(s)} + 2SbF_{5(l)} \longrightarrow [\mu\text{-}(OsO_2F_3)_2][Sb_2F_{11}]_{(s)}$

ΔH°_5 $OsO_2F_{4(s)} + AsF_{5(g)} \longrightarrow [OsO_2F_3][AsF_6]_{(s)}$

ΔH°_6 $2OsO_2F_{4(s)} + AsF_{5(g)} \longrightarrow [\mu\text{-}(OsO_2F_3)_2][AsF_6]_{(s)}$

ΔH°_7 $2[OsO_2F_3][SbF_6]_{(s)} \longrightarrow [\mu\text{-}(OsO_2F_3)_2][Sb_2F_{11}]_{(s)}$

Scheme 3.1. Summary of Reactions for Which Standard Enthalpies Have Been Calculated.

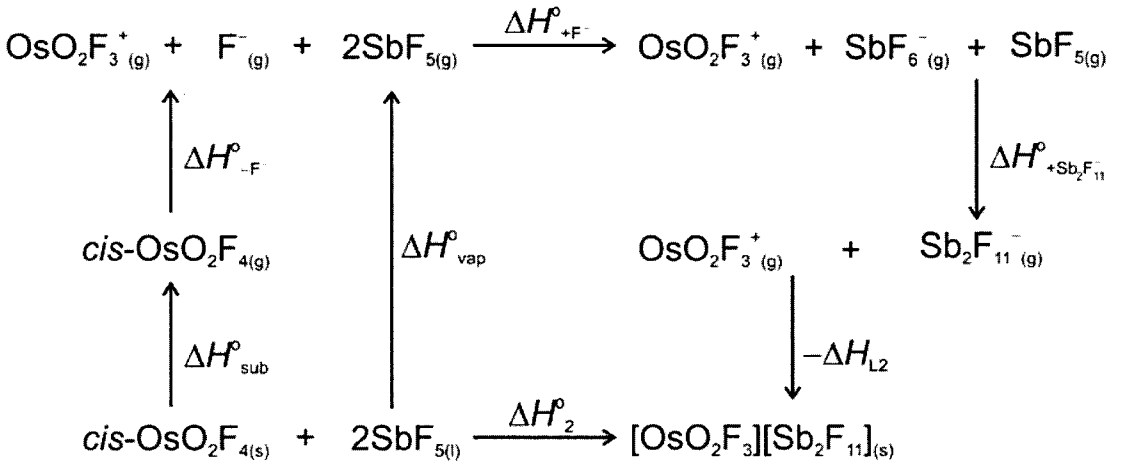

Scheme 3.2. Thermochemical cycle describing the formation of $[OsO_2F_3][Sb_2F_{11}]$.

Table 3.6. Gas-Phase Reaction Enthalpies for Fluoride Ion Transfer Reactions Involving *cis*-OsO_2F_4, SbF_5, and AsF_5

	ΔH^o (kJ mol^{-1})	
	SVWN[a]	B3LYP[b]
$OsO_2F_{4(g)} \longrightarrow OsO_2F_3^+{}_{(g)} + F^-_{(g)}$	699	918
$OsO_2F_{4(g)} + OsO_2F_3^+{}_{(g)} \longrightarrow \mu\text{–}F(OsO_2F_3)_2^+{}_{(g)}$	–182	–113
$SbF_{5(g)} + F^-_{(g)} \longrightarrow SbF_6^-{}_{(g)}$	–571	–464
$SbF_{5(g)} + SbF_6^-{}_{(g)} \longrightarrow Sb_2F_{11}^-{}_{(g)}$	–522	–132
$AsF_{5(g)} + F^-_{(g)} \longrightarrow AsF_6^-{}_{(g)}$	–190	–406

[a] Zero point energy-corrected enthalpies calculated using the SDDall basis set augmented for F, O, and Sb with two d-type polarization functions. [b] Zero point energy-corrected enthalpies calculated using the Stuttgart basis set with the f functional for Os and the aug-cc-pVTZ(-PP) basis sets were used for all other atoms.

Table 3.7. Estimated Volumes and Lattice Enthalpies of Salts Containing the $OsO_2F_3^+$ and μ-$F(OsO_2F_3)_2^+$ Cations

	Salt	V_m (nm^3)[a]	ΔH_L (kJ mol^{-1})[b]
ΔH_{L1}	$[OsO_2F_3][SbF_6]$	0.1627	538.5
ΔH_{L2}	$[OsO_2F_3][Sb_2F_{11}]$	0.26870(2)	472.3
ΔH_{L3}	$[\mu\text{-}F(OsO_2F_3)_2][SbF_6]$	0.2817	466.6
ΔH_{L4}	$[\mu\text{-}F(OsO_2F_3)_2][Sb_2F_{11}]$	0.3877(2)	430.5
ΔH_{L5}	$[OsO_2F_3][AsF_6]$	0.1517	548.6
ΔH_{L6}	$[\mu\text{-}F(OsO_2F_3)_2][AsF_6]$	0.2707	471.4

[a] The formula unit volumes, V_m, for $[OsO_2F_3][Sb_2F_{11}]$ (0.26870(2) nm^3) and $[\mu\text{-}F(OsO_2F_3)_2][Sb_2F_{11}]$ (0.3877(2) nm^3)[22] were obtained from their crystallographic unit cells at –173 °C. The volumes of SbF_6^- (0.121(12) nm^3) and AsF_6^- (0.110(7) nm^3) were obtained from Ref 185 and the volume of $Sb_2F_{11}^-$ (0.227 nm^3) was obtained from ref MG-031. The volumes of $OsO_2F_3^+$ (0.0417 nm^3) and μ-$(OsO_2F_3)_2^+$ (0.1607 nm^3) were estimated by subtraction of the SbF_6^- and $Sb_2F_{11}^-$ anion volumes, respectively, from V_m. The V_m values for the $[OsO_2F_3][SbF_6]$, $[\mu\text{-}F(OsO_2F_3)_2][SbF_6]$, $[OsO_2F_3][AsF_6]$, and $[\mu\text{-}F(OsO_2F_3)_2][AsF_6]$ salts were estimated from the sums of the respective cation and anion volumes. [b] The lattice enthalpies (ΔH_L) were calculated from eq 3.8 as described in Ref 186.

$$\Delta H_L = 2I\left(\frac{\alpha}{\sqrt[3]{V_m}} + \beta\right) + pRT \qquad (3.6)$$

volume of the salt, I is the ionicity of the salt (1), and α (117.3 mm kJ mol^{-1}), β (51.9 kJ mol^{-1}), and p (2) depend on the nature of the salt. In this formalism, ΔH_L, the lattice enthalpy, is defined as the energy required to break apart the crystal lattice and therefore has a positive value. The determination of the enthalpy of vaporization of SbF_5 (ΔH°_{vap}) is complicated by the polymeric nature of liquid SbF_5 and has been previously estimated to be 30.9 kJ mol^{-1}.[189-193] The determination of the enthalpy of sublimation of *cis*-OsO_2F_4 (ΔH°_{sub}) is prevented because *cis*-OsO_2F_4 decomposes near its melting point (90 °C).[20] Consequently, enthalpies of reaction, ΔH°, have been calculated incorporating values for all components of their Born-Haber cycles except ΔH°_{sub} of *cis*-OsO_2F_4 (Table 3.8).

The enthalpies of reaction for the formation of $OsO_2F_3^+$ and μ-$F(OsO_2F_3)_2^+$ salts can be calculated using thermochemical cycles similar to that given in Scheme 3.2 and are summarized by eq 3.7. Because ΔH°_{sub} of *cis*-OsO_2F_4 is unknown, direct comparisons

$$\Delta H^\circ_2 = 2\Delta H^\circ_{vap} + \Delta H^\circ_{sub} + \Delta H^\circ_{-F^-} + \Delta H^\circ_{+F^-} + \Delta H^\circ_{+SbF_6^-} - \Delta H_{L2} \qquad (3.7)$$

of the reaction enthalpies for a pair of reactions involving different molar amounts of *cis*-OsO_2F_4 in their reactions are not possible. For a pair of reactions having equimolar amounts of *cis*-OsO_2F_4 in common as a reactant, taking the difference in their reaction enthalpies leads to cancellation of the ΔH°_{sub} term and to the difference in their reaction enthalpies (Table 3.9).

Table 3.8. Reaction Enthalpies for the Formation of the AsF_6^-, SbF_6^-, and $Sb_2F_{11}^-$ Salts of $OsO_2F_3^+$ and μ-$F(OsO_2F_3)_2^+$

Reaction Enthalpies[a]	SVWN[b]	B3LYP[b]
ΔH°_1	$\Delta H_{sub} - 379$	$\Delta H_{sub} - 54.0$
ΔH°_2	$\Delta H_{sub} - 804$	$\Delta H_{sub} - 89.0$
ΔH°_3	$2\Delta H_{sub} - 490$	$2\Delta H_{sub} - 95.0$
ΔH°_4	$2\Delta H_{sub} - 944$	$2\Delta H_{sub} - 160$
ΔH°_5	$\Delta H_{sub} - 39.0$	$\Delta H_{sub} - 37.3$
ΔH°_6	$2\Delta H_{sub} - 144$	$2\Delta H_{sub} - 73.0$
ΔH°_7	–185	–52.1

[a] See Scheme 3.1 for the reaction details. [b] Values are in kJ mol^{-1}.

Table 3.9. Comparisons of ΔH° Values for Reactions that Lead to $OsO_2F_3^+$ and μ-$F(OsO_2F_3)_2^+$ Salt Formation

Standard Enthalpy Difference[a]	$\Delta(\Delta H^\circ)$ SVWN[b]	$\Delta(\Delta H^\circ)$ B3LYP[b]
$\Delta H^\circ_2 - \Delta H^\circ_1$	–424	–35.0
$\Delta H^\circ_1 - \Delta H^\circ_5$	–340	–16.7
$\Delta H^\circ_2 - \Delta H^\circ_5$	–765	–51.7
$\Delta H^\circ_4 - \Delta H^\circ_3$	–454	–65.1
$\Delta H^\circ_3 - \Delta H^\circ_6$	–346	–22.0
$\Delta H^\circ_4 - \Delta H^\circ_6$	–800	–87.1

[a] See Scheme 3.1 for the reaction details. [b] Values are in kJ mol^{-1}

Examination of Table 3.9 reveals that formation of $[OsO_2F_3][Sb_2F_{11}]$ and $[\mu\text{-}F(OsO_2F_3)_2][Sb_2F_{11}]$ are favored relative to $[OsO_2F_3][SbF_6]$ (–35.0 kJ mol^{-1}) and $[\mu\text{-}F(OsO_2F_3)_2][SbF_6]$ (–65.1 kJ mol^{-1}), in accordance with one's ability to isolate stable $[OsO_2F_3][Sb_2F_{11}]$ and $[\mu\text{-}F(OsO_2F_3)_2][Sb_2F_{11}]$[22] salts and inability to form the $[OsO_2F_3][SbF_6]$ and $[\mu\text{-}F(OsO_2F_3)_2][SbF_6]$ salts.

The standard enthalpies of reaction leading to the formation of the AsF_6^- salts of $OsO_2F_3^+$ and $\mu\text{-}F(OsO_2F_3)_2^+$ (ΔH°_5 and ΔH°_6, respectively) are less favorable when compared with their SbF_6^- and $Sb_2F_{11}^-$ analogues (Table 3.9). Direct comparisons of the standard enthalpies for the reactions of *cis*-OsO_2F_4 and AsF_5 that lead to the AsF_6^- salts of $OsO_2F_3^+$ and $\mu\text{-}F(OsO_2F_3)_2^+$, however, are also not possible because ΔH°_{sub} of *cis*-OsO_2F_4 is unknown. Although $[OsO_2F_3][AsF_6]$ is presently unknown, $[\mu\text{-}F(OsO_2F_3)_2][AsF_6]$ has been isolated and characterized by low-temperature Raman spectroscopy.[22] This salt has a significant AsF_5 dissociation vapor pressure (150 Torr, 23 °C) in accordance with its less negative enthalpy of reaction relative to those of the SbF_6^- and $Sb_2F_{11}^-$ analogues (Table 3.9).

Because an explicit comparison of the enthalpies of reaction for the formation of $[OsO_2F_3][SbF_6]$ and $[\mu\text{-}F(OsO_2F_3)_2][Sb_2F_{11}]$ is not possible, an alternative thermochemical cycle was considered (Scheme 3.3) that allowed the enthalpy for the interconversion of $[OsO_2F_3][SbF_6]$ and $[\mu\text{-}F(OsO_2F_3)_2][Sb_2F_{11}]$, ΔH°_7 (eq 3.8), to be estimated. The ΔH°_7 value (–52.1 kJ mol^{-1}) indicates that formation of $[\mu\text{-}F(OsO_2F_3)_2][Sb_2F_{11}]$ from $[OsO_2F_3][SbF_6]$ is also an exothermic process, again

$$\Delta H^{\circ}_7 = 2\Delta H_{L1} + \Delta H^{\circ}_{+OsO_2F_3^+} + \Delta H^{\circ}_{+SbF_6^-} - (\Delta H^{\circ}_{-F^-} + \Delta H^{\circ}_{+F^-} + \Delta H_{L4}) \quad (3.8)$$

underscoring why all attempts to synthesize $[OsO_2F_3][SbF_6]$ have led to $[\mu\text{-}F(OsO_2F_3)_2][Sb_2F_{11}]$ as the only isolable product.

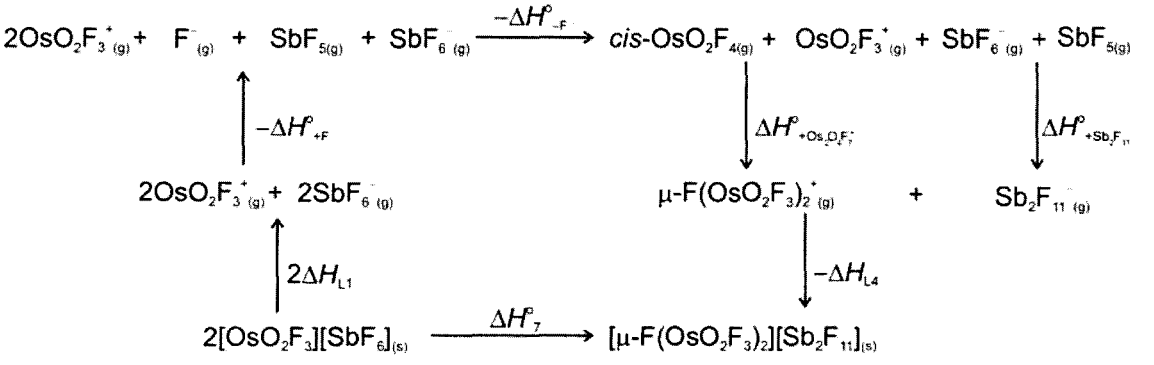

Scheme 3.3. Thermochemical cycle describing the conversion of $[OsO_2F_3][SbF_6]$ to $[\mu\text{-}F(OsO_2F_3)_2][Sb_2F_{11}]$.

A method for estimating the absolute standard entropy of a salt from its formula unit volume has been reported by Jenkins and Glasser (eq 3.9), where k is 1360 J K^{-1} mol^{-1} nm^{-3} and c is 15 JK^{-1} mol^{-1}.[194] The entropies calculated by this method for $[OsO_2F_3][SbF_6]$ and

$$S^{\circ}([Os_nO_{2n}F_{4n-1}][Sb_nF_{5n+1}]) = kV_m + c \quad (3.9)$$

$[\mu\text{-}F(OsO_2F_3)_2][Sb_2F_{11}]$ are 236 and 542 JK^{-1} mol^{-1}, respectively. The estimated ΔS° for the conversion of $[OsO_2F_3][SbF_6]$ to $[\mu\text{-}F(OsO_3F_2)_2][Sb_2F_{11}]$ (eq 3.10) is 69.7 JK^{-1} mol^{-1}, leading to a ΔG° value (eq 3.11) of –206 kJ mol^{-1} at the SVWN level and –72.8 kJ mol^{-1} at the B3LYP level. Gibbs free energies for the remaining reaction pairs in Table 3.9 cannot

$$2[OsO_2F_3][SbF_6]_{(s)} \longrightarrow [\mu\text{-}(OsO_2F_3)_2][Sb_2F_{11}]_{(s)} \quad (3.10)$$

$$\Delta G^{\circ} = \Delta H^{\circ} - T\Delta S^{\circ} \quad (3.11)$$

be evaluated because $S^{\circ}(SbF_{5(l)})$ is unknown. The only values available are those for the gas-phase monomer (353 JK^{-1} mol^{-1})[195] and the gas-phase tetramer (–35.5 JK^{-1} mol^{-1}).[192]

3.3. Conclusions

The $OsO_2F_3^+$ cation, previously observed in SbF_5 solution by ^{19}F NMR spectroscopy, has been fully structurally characterized in the solid state as its $Sb_2F_{11}^-$ salt. The $[OsO_2F_3][Sb_2F_{11}]$ structural unit is an ion pair in which a *cis*-dioxo $OsO_2F_3^+$ cation is fluorine bridged to an $Sb_2F_{11}^-$ anion, resulting in a pseudo-octahedral coordination sphere for Os(VIII). The Raman spectrum of the $Sb_2F_{11}^-$ salt has been fully assigned based on the calculated vibrational frequencies of the gas-phase $[OsO_2F_3][Sb_2F_{11}]$ ion pair. The gas-phase geometry and vibrational frequencies of $Sb_2F_{11}^-$ are in good agreement with the anion in $[OsO_2F_3][Sb_2F_{11}]$. The calculated vibrational frequencies of $Sb_2F_{11}^-$ are in better agreement with experiment than those previously reported, and provide more reliable vibrational assignments. Attempts to prepare $[OsO_2F_3][SbF_6]$ were unsuccessful and only resulted in the isolation of $[\mu\text{-}F(OsO_2F_3)_2][Sb_2F_{11}]$. Thermochemical calculations demonstrate that the standard enthalpies of reaction that lead to the $Sb_2F_{11}^-$ salts of $OsO_2F_3^+$ and $\mu\text{-}F(OsO_2F_3)_2^+$ are favored over the AsF_6^- and SbF_6^- salts, in accordance with failures to form $[OsO_2F_3][SbF_6]$ and $[\mu\text{-}F(OsO_2F_3)_2][SbF_6]$ in the present study.

CHAPTER 4

FLUORIDE ION ACCEPTOR PROPERTIES OF *cis*-OsO_2F_4; SYNTHESIS, RAMAN AND NMR SPECTROSCOPIC STUDY OF $OsO_2F_5^-$

4.1. Introduction

Presently, two oxide fluorides of Os(VIII) are known, namely, *fac*-OsO_3F_2[11] and *cis*-OsO_2F_4.[20] In the solid state, *fac*-OsO_3F_2 exists as a fluorine bridged polymer[11] or dimer.[18] For both *fac*-OsO_3F_2 and *cis*-OsO_2F_4, the geometry at the Os atom is pseudo-octahedral and the oxygen atoms are cis to one another. The *cis*-OsO_2F_4 molecule has been extensively characterized by ^{19}F NMR and electron diffraction.[20] Recently, the *cis*-dioxo geometry was also confirmed in the solid state by single-crystal X-ray diffraction (see Chapter 5).

Transition metal oxide fluorides in their highest oxidation states show a preference for a *cis*-dioxo arrangement which is well documented for *cis*-OsO_2F_4,[20] *cis*-$OsO_2F_3^+$,[139] *cis*-$F(cis\text{-}OsO_2F_3)_2^+$,[22] *cis*-$MoO_2F_2 \cdot 2THF$ (THF = tetrahydrofuran),[44] *cis*-$TcO_2F_4^-$,[47] *cis*-TcO_2F_3,[46] *cis*-ReO_2F_3,[45] *cis*-$ReO_2F_4^-$,[45] μ-$F(cis\text{-}ReO_2F_3)_2^-$,[45] and *cis*-$Re_3O_6F_{10}^-$.[45] This preference may be accounted for in terms of d-orbital participation and arises because the $d_{t_{2g}}$ orbitals of the d^0 transition metal have the correct symmetry to overlap with the p orbitals of oxygen, whereas the *trans*-dioxo isomer has only one p orbital per oxygen that has the correct symmetry to overlap with a single $d_{t_{2g}}$ orbital of the metal, causing the energies of the bonding $d\pi$-$p\pi$ orbitals of the *trans*-isomer to be higher in energy that those of the *cis*-isomer.[139]

Preliminary work from this laboratory investigated the fluoride ion acceptor properties of *cis*-OsO_2F_4.[28] The Cs^+, $N(CH_3)_4^+$, and NO^+ salts of $OsO_2F_5^-$ were studied by ^{19}F NMR and Raman spectroscopy. Based on the AX_4 coupling patterns observed in the ^{19}F NMR spectra, it was postulated that the anion observed was $OsO_2F_5^-$, and the geometry was based on a monocapped trigonal prism (structure I) in which four fluorine

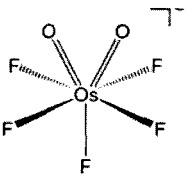

I

atoms occupy a square face, the oxygen atoms are *cis* to one another and occupy an edge, and the unique fluorine atom caps the square face of the prism. The chemical shifts of $OsO_2F_5^-$ were shown to have a large solvent dependence which was not extensively studied. However, each salt was characterized in a single solvent (Cs^+ in HF; $N(CH_3)_4^+$ in CH_3CN; and NO^+ in FNO) preventing any conclusions on the solvent dependency of the chemical shift to be drawn. The Raman spectra of the Cs^+, $N(CH_3)_4^+$, and NO^+ salts of what was assumed to be $OsO_2F_5^-$ were reported, with only preliminary assignments based on the frequency trends observed for other Os(VIII) oxide fluorides. A complete assignment of the vibrational modes was not possible at the time because the energy minimized geometry and vibrational frequencies had not been calculated, and therefore the solid-state geometry of $OsO_2F_5^-$ could not be unambiguously determined. The previous study also was not able to unambiguously discount the presence of $OsOF_5^-$ rather than $OsO_2F_5^-$, which is also expected to give an AX_4 spin-coupling pattern in the ^{19}F NMR spectrum.

The present work details the further characterization, by ^{19}F NMR and Raman spectroscopy, of the alleged $OsO_2F_5^-$ anion, which if correctly identified, would provide the first example of an oxide fluoride anion derived from *cis*-OsO_2F_4. Over the course of this work, the synthesis of the $OsOF_5^-$ anion was also attempted in order to distinguish between $OsO_2F_5^-$ and $OsOF_5^-$. An extensive computational study was carried out to assign the Raman and NMR spectra of the $OsO_2F_5^-$ anion based on the three possible seven-coordinate isomers predicted by the VSEPR rules, namely, the monocapped octahedron (MCO), monocapped trigonal prism (MCTP), and the pentagonal bipyramid (*cis*- and *trans*-PBP).

4.2. Results and Discussion

4.2.1. Synthesis of $[M][OsO_2F_5]$ ($M = Cs^+, N(CH_3)_4^+, NO^+$)

The reaction of an equimolar amount of *cis*-OsO_2F_4 with [Cs][F] was carried out at a temperature (90 °C) that was at the melting point of *cis*-OsO_2F_4 but lower than previously reported (150 °C),[28] yielding an orange powder presumed to have the formulation, $[Cs][OsO_2F_5]$ (eq 4.1). The Raman spectrum was in agreement with the previously reported spectrum.[28]

$$cis\text{-}OsO_2F_4 + [Cs][F] \xrightarrow{90\,^\circ C} [Cs][OsO_2F_5] \qquad (4.1)$$

In a separate synthesis, $[N(CH_3)_4][F]$ was reacted with an equimolar amount of *cis*-OsO_2F_4 in FNO solvent at –78 °C (eq 4.2) to produce an orange product formulated as

$$OsO_2F_4 + [N(CH_3)_4][F] \xrightarrow[-78\,^\circ C]{FNO} [N(CH_3)_4][OsO_2F_5] \qquad (4.2)$$

$[N(CH_3)_4][OsO_2F_5]$. The Raman spectrum of the product was shown to be in agreement with that reported previously.[28] Although the reaction was highly exothermic, the FNO solvent served to dissipate the heat of reaction. Prior attempts to prepare $[N(CH_3)_4][OsO_2F_5]$ in HF solution were unsuccessful because immediate decomposition occurred, which was attributed to the exothermic nature of the reaction and the apparent inability of HF solvent to effectively dissipate the heat of reaction.[28]

Attempts to grow crystals of $[Cs][OsO_2F_5]$ and $[N(CH_3)_4][OsO_2F_5]$ from their respective CH_3CN solutions did not yield crystalline salts of the $OsO_2F_5^-$ anion, but crystals of *cis*-$OsO_2F_4 \cdot [Cs][CH_2CN]$, *cis*-$OsO_2F_4 \cdot [Cs][CH_2CN] \cdot 0.3HF$, and *cis*-$OsO_2F_4 \cdot [N(CH_3)_4][CH_2CN]$ (eq 4.3) instead, indirectly confirming that $OsO_2F_5^-$ had been formed. For a full discussion of crystal growth procedures and structures, see Chapter 5.

$$[M][OsO_2F_5] + CH_3CN \xrightarrow{CH_3CN} cis\text{-}OsO_2F_4 + [M][CH_2CN] + HF \quad (4.3)$$

$$(M = Cs^+, N(CH_3)_4^+)$$

In FNO solvent, *cis*-OsO_2F_4 forms a deep red solution that exists in equilibrium with $[NO][OsO_2F_5]$ (eq 4.4). Attempts to isolate $[NO][OsO_2F_5]$ were, however,

$$cis\text{-}OsO_2F_4 + FNO \underset{FNO}{\overset{-78\ ^\circ C}{\rightleftharpoons}} [NO][OsO_2F_5] \quad (4.4)$$

unsuccessful because removal of FNO at –78 °C resulted in dissociation of $[NO][OsO_2F_5]$ back to FNO and *cis*-OsO_2F_4. Prior attempts to prepare $[NO_2][OsO_2F_5]$ from *cis*-OsO_2F_4 and FNO_2 did not lead to a reaction at either –78 (liquid) or 55 °C (under *ca.* 6 atm of FNO_2 gas).[28] The N–F bond of FNO is more polar than in FNO_2 and is likely the reason for the lack of reactivity of FNO_2. In addition, prior attempts to react *cis*-OsO_2F_4 and

$[N(CH_3)_4][F]$ in CHF_3 at −100 °C also resulted in no reaction because of the low solubility of *cis*-OsO_2F_4 in CHF_3.[28]

4.2.2. Synthesis of [M′][OsOF5] (M′ = Cs^+, NO^+)

The $OsOF_4$ sample used for the syntheses of $OsOF_5^-$ salts was prepared by two literature methods; (1) by hydrolysis of OsF_6 in HF at room temperature (eq 4.5);[36] and (2) by reaction of OsO_4 with OsF_6 at 180 °C in an metal vessel (eq 4.6).[41]

$$OsF_6 + H_2O \xrightarrow[25\ ^\circ C]{HF} OsOF_4 + 2HF \quad (4.5)$$

$$OsO_4 + 4OsF_6 \xrightarrow{180\ ^\circ C} 4OsOF_4 + Os + 4F_2 \quad (4.6)$$

Osmium oxide tetrafluoride synthesized by the first method, OsF_6 (eq 4.5) was allowed to react with either [Cs][F] in HF (eq 4.7) or neat FNO (eq 4.8). The products of

$$OsOF_4 + [Cs][F] \xrightarrow[25\ ^\circ C]{HF} [Cs][OsOF_5] \quad (4.7)$$

$$OsOF_4 + FNO \xrightarrow[25\ ^\circ C]{FNO} [NO][OsOF_5] \quad (4.8)$$

the reaction of [Cs][F] with $OsOF_4$ are slightly soluble in CH_3CN and HF solvents, whereas the product of the FNO with $OsOF_4$ reaction is slightly soluble in HF, FNO, and a mixture of HF and FNO (FNO/HF). The ^{19}F NMR spectra of all of these solutions revealed AX_4 coupling patterns corresponding to $OsO_2F_5^-$ (see Section 4.2.3.). Slow cooling of the CH_3CN solution yielded orange block-shaped crystals corresponding to $[Cs][OsO_3F_3]\cdot CH_3CN$ rather than the anticipated product (see Section 4.2.5). Attempts to grow crystals by slow cooling of HF, FNO, or FNO/HF solutions were unsuccessful.

Osmium oxide tetrafluoride synthesized by method (2) (eq 4.6) was also allowed to react with either [Cs][F] in HF (eq 4.7) or neat FNO (eq 4.8). Characterization of these products in HF or FNO, respectively by ^{19}F NMR spectroscopy again revealed AX_4

coupling patterns having the same chemical shifts and coupling constants as the samples prepared by the hydrolysis method. In addition to the AX_4 coupling pattern in HF solution, an A_2X_2 coupling pattern corresponding to *cis*-OsO_2F_4 that integrated to 9.1% of the AX_4 pattern of $OsO_2F_5^-$ was also observed. The products of these reactions were not isolated in the solid state, and therefore, dissolution of the products of either reaction in CH_3CN was not attempted.

It has been previously reported that when $OsOF_4$ dissolves in aqueous or alkaline media, it gives a yellow solution containing OsO_4; however, no other reaction products were identified.[37] In the present work, OsO_4, identified by Raman spectroscopy, and unidentified black products were observed in attempted reactions to form $[M'][OsOF_5]$. Disproportionation of $OsOF_4$ to form *cis*-OsO_2F_4 and a reduction product (eq 4.9) would

$$2OsOF_4 \longrightarrow \textit{cis}\text{-}OsO_2F_4 + \text{Osmium reduction product} \qquad (4.9)$$

be plausible in the current system although it was never possible to characterize a reduction product. Any *cis*-OsO_2F_4 that is formed can be expected to immediately react with the fluoride ion source to yield $OsO_2F_5^-$. Formation of $OsO_3F_3^-$ (vide supra) may possibly be explained if an excess of H_2O remained in the sample when $OsOF_4$ which was synthesized by hydrolysis of OsF_6. The residual H_2O could then react with $OsO_2F_5^-$ to form $OsO_3F_3^-$ (eq 4.10). Alternately, further disproportionation of $OsO_2F_5^-$ to OsF_7^- and $OsO_3F_3^-$ (eq 4.11) may also occur. There is no evidence that OsF_6 or OsF_7^- could be formed, and it likely would immediately decompose.

$$OsO_2F_5^- + H_2O \longrightarrow OsO_3F_3^- + HF \qquad (4.10)$$

$$2OsO_2F_5^- \longrightarrow OsO_3F_3^- + OsF_7^- \qquad (4.11)$$

4.2.3. NMR Spectroscopy

Table 4.1 lists the ^{19}F NMR parameters for solutions of $[M][OsO_2F_5]$ ($M = Cs^+$, $N(CH_3)_4^+$, and NO^+) and mixtures of $[M'][F]$ and $OsOF_4$ ($M' = Cs^+$ and NO^+) in CH_3CN (–30 to –38 °C), HF (–30 and –78 °C), FNO (–65 °C), and FNO/HF (–30 °C) solvents. The primary features of the ^{19}F NMR spectra of $[M][OsO_2F_5]$ (Figure 4.1) or $OsOF_4$ that had been reacted with $[M'][F]$ (Figure 4.2) in either CH_3CN, HF, FNO, or FNO/HF solvent were doublet and quintet patterns of the AX_4 spin system.

The ^{19}F chemical shifts and coupling constants of the AX_4 coupling pattern for different samples of $[M][OsO_2F_5]$ and $OsOF_4$ reacted with $[M'][F]$ recorded in the same solvents are similar (vide infra). Therefore, based on the NMR trends and the previously discussed propensity for Os(VI) of $OsOF_4$ to be oxidized to Os(VIII) (see Section 4.2.2), it was concluded that (1) the NMR samples only contained $OsO_2F_5^-$, and (2) there was no evidence for $OsOF_5^-$ resulting from the reaction of $OsOF_4$ with $[M'][F]$.

There are four possible seven-coordinate geometries for the $OsO_2F_5^-$ anion (see Section 4.2.6.2), *trans*-$OsO_2F_5^-$ based on a pentagonal bipyramid (*trans*-PBP) (Figure 4.3a) and three *cis*-$OsO_2F_5^-$ isomers based on a monocapped trigonal prism (MCTP) (Figure 4.4a), a pentagonal bipyramid (*cis*-PBP) (Figure 4.4b), and a monocapped octahedron (MCO) (Figure 4.4c). The only $OsO_2F_5^-$ isomer that is consistent with the observed AX_4 coupling pattern is the *cis*-dioxo monocapped trigonal prismatic isomer. The resonance corresponding to the four equivalent equatorial fluorine atoms is split into a doublet by the axial fluorine atom and the signal corresponding to the axial fluorine atom is split into a quintet by the four equivalent equatorial fluorine atoms.

Table 4.1. NMR Chemical Shifts and Spin-Spin Coupling Constants for *cis*-$OsO_2F_5^-$

starting material	solvent	T, °C	$\delta(^{19}F)$, ppm[a]	$^2J(^{19}F_1-^{19}F_2)$, Hz	$\Delta\delta(^{19}F)$, ppm
[Cs][F] + *cis*-OsO_2F_4	CH_3CN	–38	F_a 91.0 F_e 45.6	94	45.4
	HF[b]	–78	F_a –5.0 F_e –33.9	90	28.9
$[N(CH_3)_4][F]$ + *cis*-OsO_2F_4	CH_3CN[c]	–30	F_a 93.2 F_e 46.6	93	46.6
	HF[d]	–78	F_a –6.5 F_e –36.6	96	30.1
[NO][F] + *cis*-OsO_2F_4	HF[e]	–30	F_a –5.6 F_e –33.0	98	27.4
	FNO[f]	–65	F_a 79.8 F_e 37.4	96	42.4
	FNO + HF[g]	–30	F_a 0.2 F_e –23.0	99	23.0
[Cs][F] + $OsOF_4$	CH_3CN	–30	F_a 88.0 F_e 44.4	95	43.6
	HF	–30	F_a –5.2 F_e –35.7	97	30.5
[NO][F] + $OsOF_4$	HF	–32	F_a –5.5 F_e –33.6	98	28.1
	FNO + HF	–30	F_a 0.8 F_e –22.3	97	23.1

[a] The equatorial and axial fluorine atoms are denoted by F_e and F_a, respectively. [b] Two weak triplets (δ = 13.2 and 65.9 ppm; $^2J(^{19}F\text{-}^{19}F)$ = 131 Hz) resonances assigned to unreacted *cis*-OsO_2F_4 were observed. [c] A singlet (δ = 3.6 ppm; $^1J(^1H–^{13}C)$ = 82 Hz) in the proton spectrum is assigned to $N(CH_3)_4^+$. Weak unassigned peaks (s 144.8 ppm, d 108.0 ppm [J = 65 Hz], d 49.0 ppm [J = 76 Hz], q 41.0 ppm [J = 86 Hz], s 36.0 ppm, q 27 ppm [J = 106 Hz], m 20.9 ppm [J = 97 Hz], s(br) 12 ppm, d 10.9 ppm [J = 102 Hz], q 1.3 ppm [J = 79 Hz], d –1.0 ppm [J = 99 Hz], d –2.0 [J = 107 Hz], and d –4.8 ppm [J = 88 Hz], s(br) –6.9 ppm, where there abbreviations denote singlet (s), broad singlet (s(br)), doublet (d), quartet (q), and multiplet (m)) attributed to fluorinated CH_3CN decomposition products were also observed in the ^{19}F spectrum. [d] A quartet (δ = –63.0 ppm; J = 109 Hz) and doublet (δ = –70 ppm; J = 107 Hz) were observed. [e] A weak unassigned doublet (δ = –64.0 ppm; J = 108 Hz) and singlet (δ = –70.3 ppm) were also observed. [f] a broad peak at 79.2 ppm was also observed. [g] Two triplets (δ = 12.5 and 56.6 ppm; $^2J(^{19}F\text{-}^{19}F)$ = 139 Hz) resonances assigned to unreacted *cis*-OsO_2F_4 were observed.

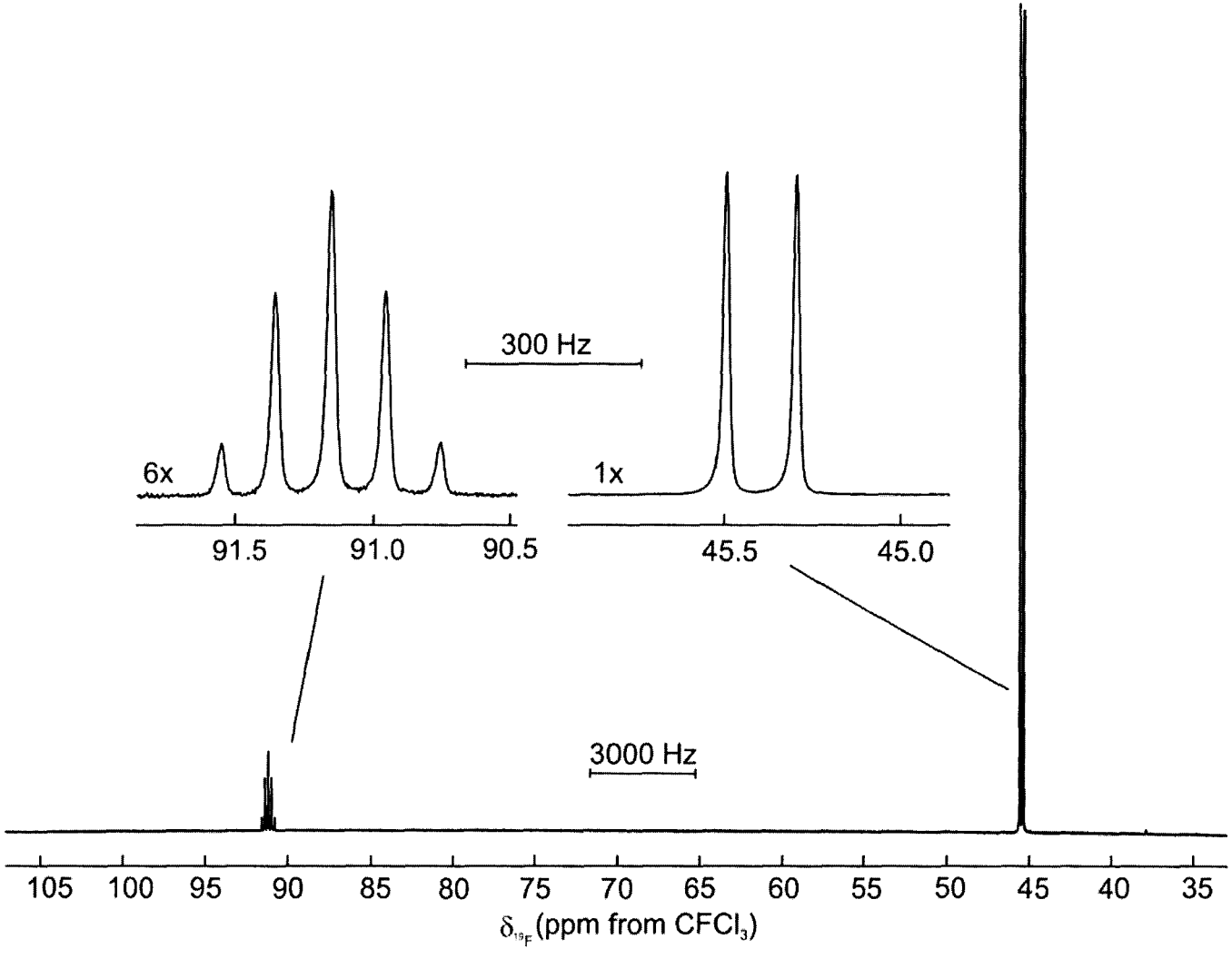

Figure 4.1. The ^{19}F NMR spectrum (470.409 MHz) of $[Cs][OsO_2F_5]$ in CH_3CN at –38 °C.

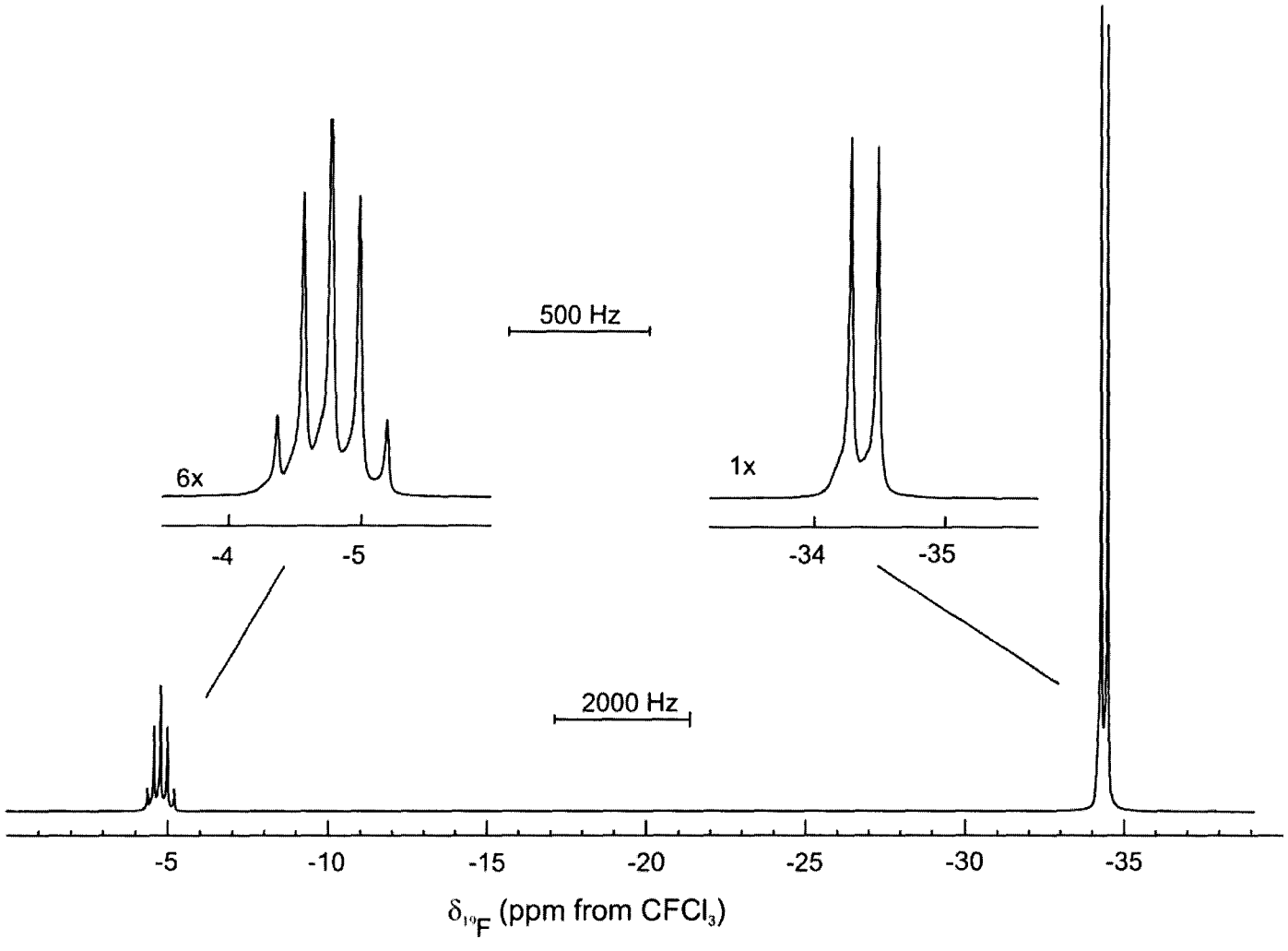

Figure 4.2. The ^{19}F NMR spectrum (470.409 MHz) of [Cs][$OsOF_5$] in HF at –30 °C.

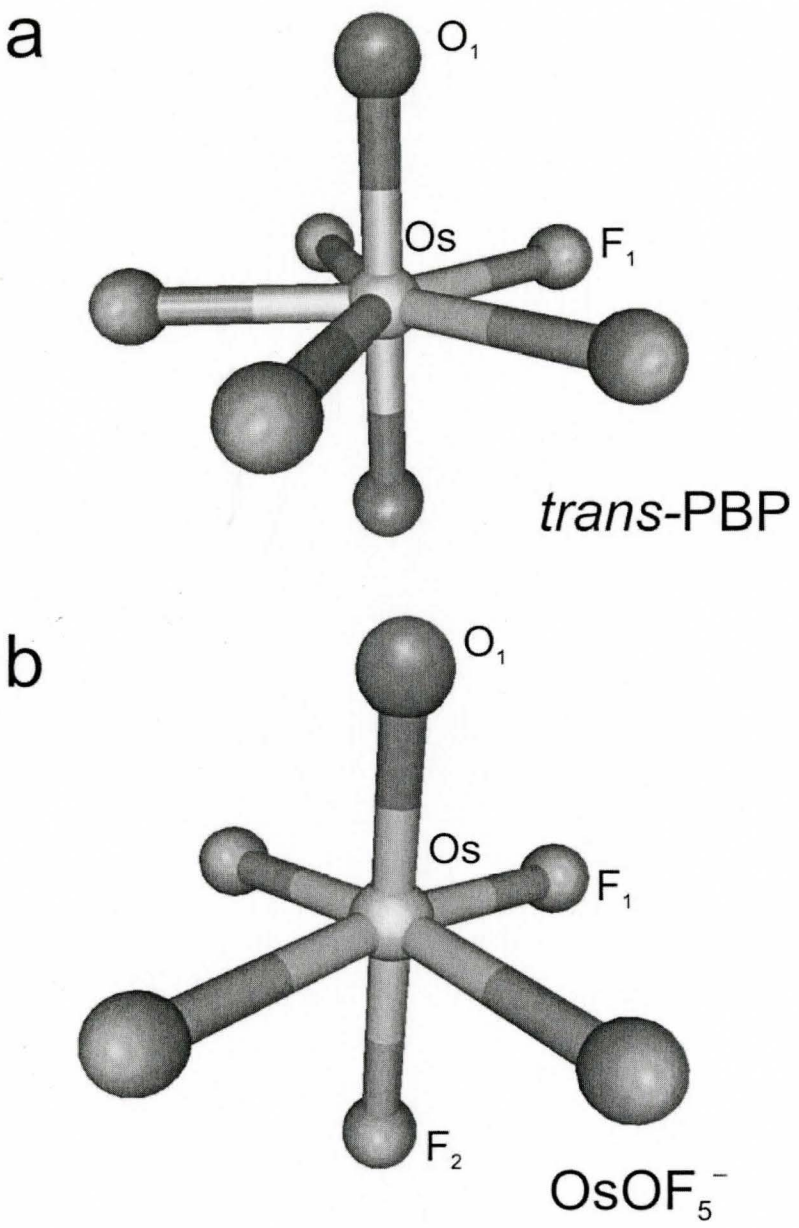

Figure 4.3. The calculated SVWN/SDDall gas-phase geometries for (a) *trans*-$OsO_2F_5^-$ (D_{5h}) and (b) $OsOF_5^-$ (C_{4v}).

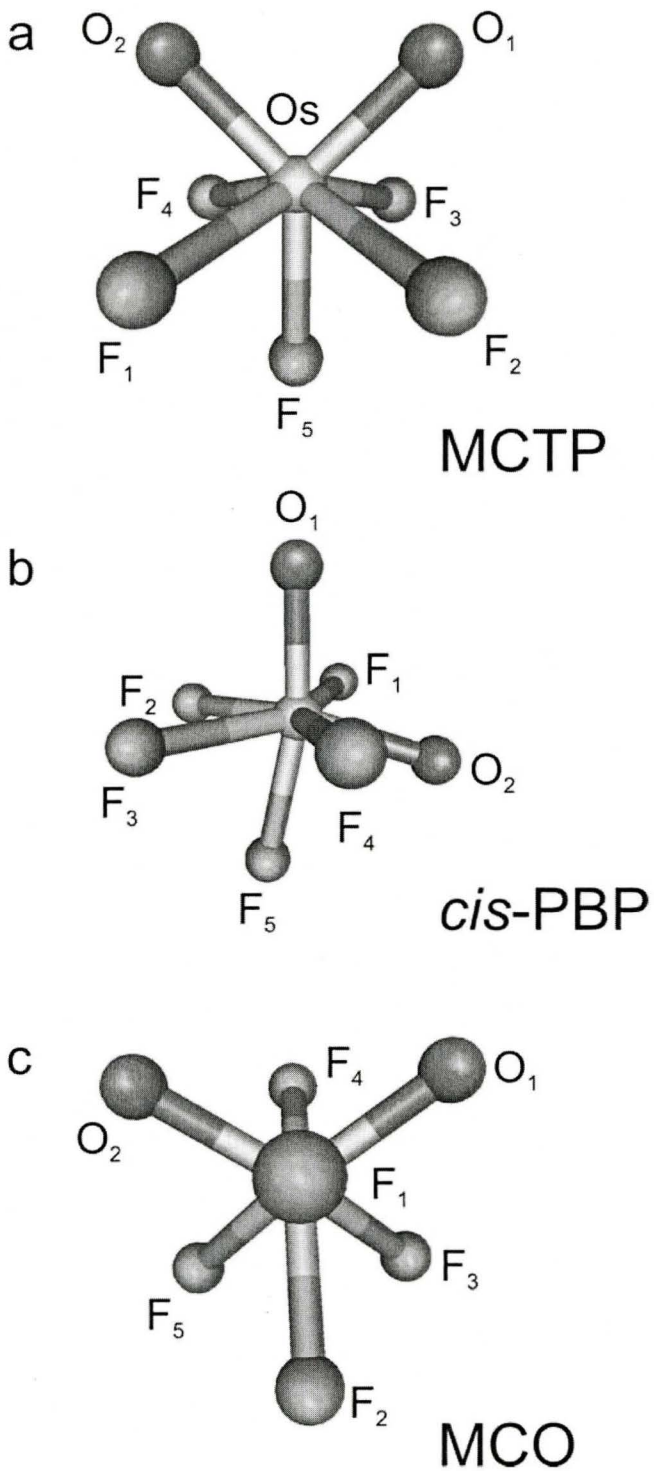

Figure 4.4. The calculated SVWN/SDDall gas-phase geometries for (a) monocapped trigonal prism (C_{2v}), (b) pentagonal bipyramid (C_s), and (c) monocapped octahedron (C_s) isomers of *cis*-$OsO_2F_5^-$.

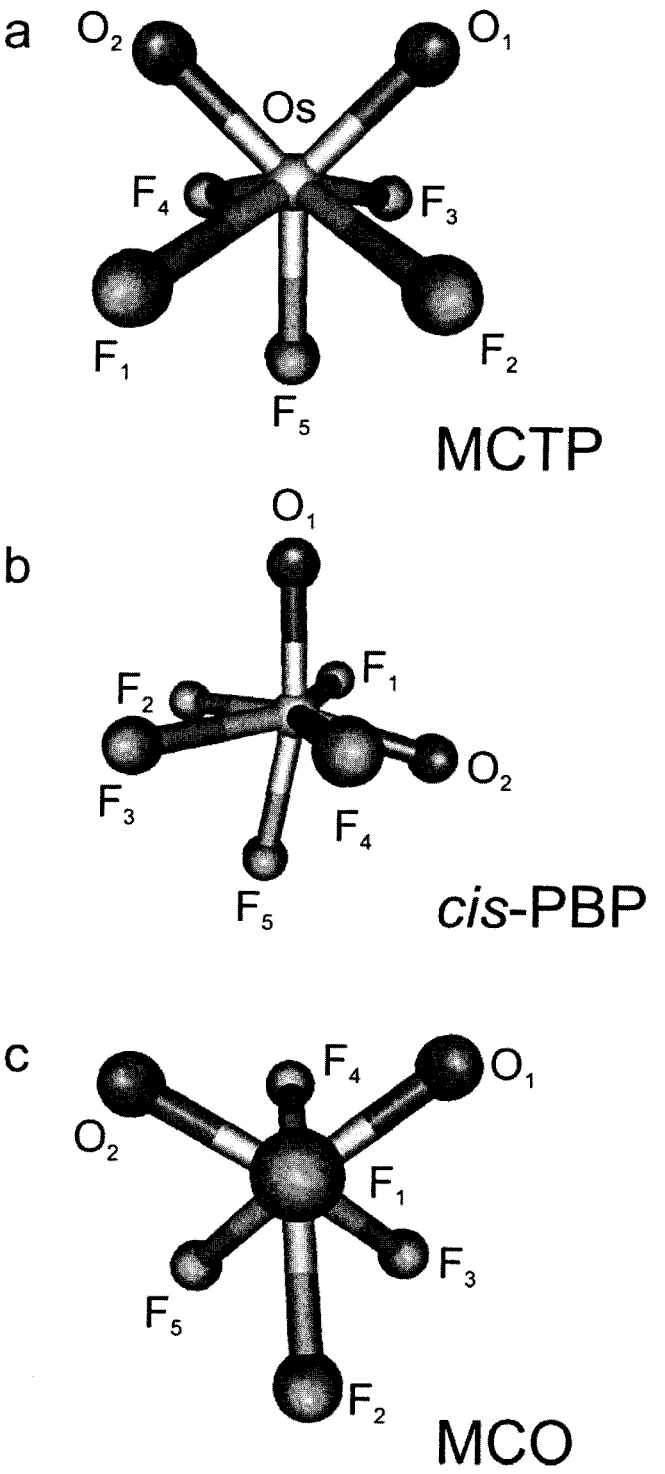

Figure 4.4. The calculated SVWN/SDDall gas-phase geometries for (a) monocapped trigonal prism (C_{2v}), (b) pentagonal bipyramid (C_s), and (c) monocapped octahedron (C_s) isomers of *cis*-$OsO_2F_5^-$.

The chemical shifts of the various *cis*-$OsO_2F_5^-$ salts are similar when recorded in the same solvent (see Table 4.1). However, different solvents result in significantly different chemical shifts. For example, the quintet associated with the [Cs][*cis*-OsO_2F_5] salt in CH_3CN solvent (91.0 ppm) is considerably less shielded than in HF solvent (–5.0 ppm) with the corresponding doublet (45.6 [CH_3CN] and –33.9 [HF] ppm) following the same trend. This chemical shift trend is also reproduced for the $N(CH_3)_4^+$ and NO^+ salts (see Table 4.1). It is interesting to note that the chemical shifts in the FNO/HF solvent mixture are intermediate with respect to the chemical shifts observed in pure HF and FNO solvents, again confirming that the dielectric constant of the solvent greatly influences the chemical shifts of the *cis*-$OsO_2F_5^-$ anion. The dependence of the chemical shift on solvent has been previously reported for KrF_2 and XeF_2. The chemical shift of KrF_2 (55.6 ppm[196]) and XeF_2 (–199.6 ppm[197]) in HF solvent are to lower frequency when compared to the chemical shifts in less polar solvent, BrF_5 (77.7[196] and –181.8 ppm,[196] respectively).

The chemical shift differences for the axial and equatorial fluorine environments of [Cs][OsO_2F_5] in CH_3CN solvent ($\Delta^{19}F(CH_3CN)$ = 45.4 ppm) is larger than in the more polar HF solvent ($\Delta^{19}F(HF)$ = 28.9 ppm). The same trend is reproduced for all other salts (see Table 4.1) in CH_3CN and HF solvents. It is noteworthy that in FNO solvent, the chemical shifts and chemical shift differences for [NO][OsO_2F_5] ($\delta(^{19}F_a)$ = 79.8, $\delta(^{19}F_e)$ = 37.4, $\Delta\delta(^{19}F)$ = 42.4 ppm) are much closer to those obtained in CH_3CN than those obtained in HF. The [$N(CH_3)_4$][ReO_2F_4] salt also shows a chemical shift dependence based on solvent which it is much more pronounced than for *cis*-$OsO_2F_5^-$.[45] In CH_3CN

solvent the chemical shift difference for the axial and equatorial environments ($\delta(^{19}F_a)$ = –53.8 and $\delta(^{19}F_e)$ –64.2 ppm) is much smaller than in HF solvent ($\delta(^{19}F_a)$ = –135.7 and $\delta(^{19}F_e)$ –30.7 ppm). Interestingly, in CH_3CN solvent, the axial resonance occurs to higher frequency than the equatorial resonance, whereas in HF solvent the equatorial resonance is to higher frequency.

The chemical shifts of [M][*cis*-OsO_2F_5] in HF solvent (M = Cs^+ [–5.0 and –33.9 ppm], $N(CH_3)_4^+$ [–6.5 and –36.6 ppm], and NO^+ [–5.6 and –33.0 ppm]) are to significantly lower frequency with respect to *cis*-OsO_2F_4 in HF solvent (63.3 and 15.8 ppm)[20] indicating that the fluorine ligands of *cis*-$OsO_2F_5^-$ are more shielded, consistent with anion formation.

In addition to the AX_4 spin coupling pattern, the ^{19}F NMR spectrum of [NO][OsO_2F_5] recorded in FNO/HF or HF contains an A_2X_2 spin coupling pattern corresponding to *cis*-OsO_2F_4. The relative molar ratio of $OsO_2F_5^-$ to *cis*-OsO_2F_4 in the FNO/HF solutions was determined from the integrated intensities of the AX_4 and A_2X_2 spin coupling patterns and ranged from 1:2.5 to 1:15, depending on the relative amounts of FNO and HF in the solvent mixture. As the amount of HF in the solvent increased, so did the intensity of the A_2X_2 signals. In contrast, only the AX_4 coupling pattern was observed in FNO solvent. The lack of peaks corresponding to *cis*-OsO_2F_4 in the FNO solution is consistent with the equilibrium depicted in eq 4.4, i.e. excess FNO forces the equilibrium to the right, favoring *cis*-$OsO_2F_5^-$, while in the FNO/HF solvent mixture or HF, the reaction is in equilibrium and both the product (*cis*-$OsO_2F_5^-$) and reactant (*cis*-OsO_2F_4) are present.

The coupling constant of the *cis*-$OsO_2F_5^-$ anion is similar for all salts in all solvents, ranging from 90 to 99 Hz, and is comparable to those of other *cis*-dioxo, d^0 transition metal oxide fluoride anions, $ReO_2F_4^-$ (87[45] or 89[198] Hz) and $TcO_2F_4^-$ (105 Hz).[47] The coupling constant of the parent compound, *cis*-OsO_2F_4 (138 Hz)[20] is larger than for the isoelectronic $ReO_2F_4^-$ and $TcO_2F_4^-$ anions as well as the *cis*-$OsO_2F_5^-$ anion, which is consistent with the more polar bonds of the anion relative to those of neutral *cis*-OsO_2F_4. As the positive charge on the central atom decreases, the bonding becomes more polar covalent so that the $^2J(^{19}F\text{-}^{19}F)$ coupling constant decreases. This behavior is further substantiated by $OsO_2F_3^+$ (164 Hz)[22] and *cis*-$WO_2F_4^{2-}$ (60 Hz).[199]

4.2.4. Raman Spectroscopy

The low-temperature Raman spectra of natural abundance and ^{18}O-enriched [Cs][*cis*-OsO_2F_5] are shown in Figure 4.5. The observed frequencies of [M][*cis*-OsO_2F_5] (M = Cs^+, $N(CH_3)_4^+$, and NO^+) and calculated frequencies and mode descriptions for *cis*-$OsO_2F_5^-$ are provided in Table 4.2, where the atom numbering scheme is given in Figure 4.4a. Spectral assignments for *cis*-$OsO_2F_5^-$ were made by comparison with the calculated frequencies and Raman intensities for the energy-minimized gas-phase geometries of the monocapped trigonal prismatic isomer of *cis*-$OsO_2F_5^-$ using SVWN and B3LYP methods. The SVWN geometry provides the best agreement for the benchmark, *cis*-OsO_2F_4 (see Section 4.2.6), and these values will be explicitly referred to in the ensuing discussion. The Raman spectrum of the $N(CH_3)_4^+$ salt is explicitly discussed in this section because it has been previously shown that $N(CH_3)_4^+$ salts have

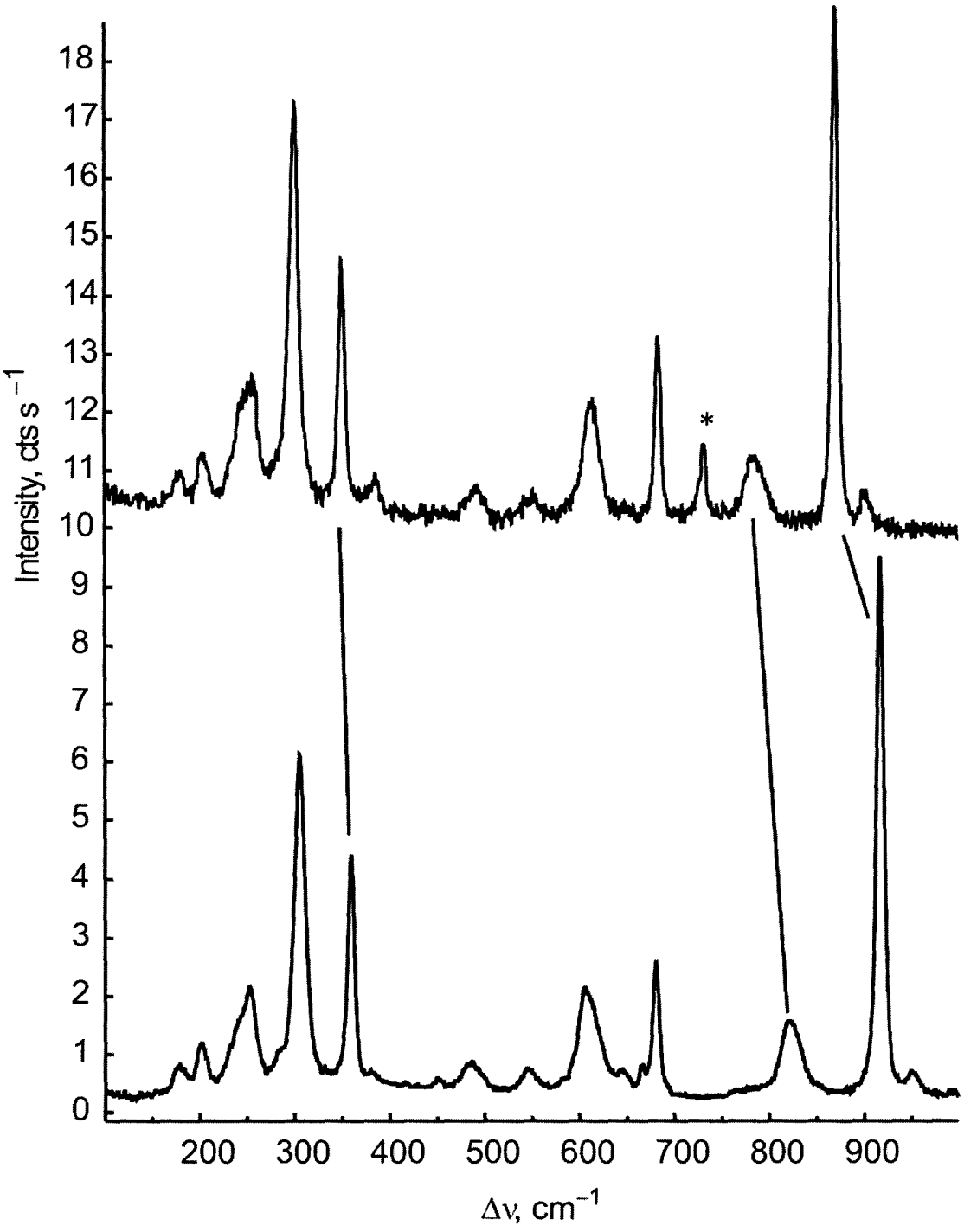

Figure 4.5. Raman spectra of $[Cs][OsO_2F_5]$ (bottom) and $[Cs][Os^{18}O_2F_5]$ (top) recorded at 25 °C using 785-nm (bottom) and 782-nm (top) excitation; the symbol denotes a FEP sample tube line (*).

Table 4.2. Experimental Raman Vibrational Frequencies and Intensities for $[Cs][OsO_2F_5]$, $[N(CH_3)_4][OsO_2F_5]$ and $[NO][OsO_2F_5]$ and Calculated Vibrational Frequencies and Infrared Intensities for $OsO_2F_5^-$

exptl			calcd[d]			$OsO_2F_5^-$ (monocapped trigonal prism)
Cs^+ [a,b]	$N(CH_3)_4^+$ [b,c]	NO^+ [b,c]	B3LYP[e]	SVWN[f]	SVWN[g]	assgnt (C_{2v})[h]
918(100)	920(100)	929(100) 926 sh	942(40)[91]	937(40)[86]	895(36)[80]	A_1 $\nu(OsO_1) + \nu(OsO_2)$
821(16)	826(16)	842(9) 832(18)	883(17)[154]	891(16)[148]	861(16)[134]	B_2 $\nu(OsO_1) - \nu(OsO_2)$
606(21) 594 sh	617(16)	584(38)	597(22)[95]	631(20)[96]	623(22)[90]	A_1 $\nu(OsF_1) + \nu(OsF_2) + \nu(OsF_3) + \nu(OsF_4) + \nu(OsF_5)$
545(7)	551(5)	573(51)[i]	554(2)[158]	594(2)[160]	585(2)[156]	B_1 $[\nu(OsF_1) + \nu(OsF_2)] - [\nu(OsF_3) + \nu(OsF_4)]$
			549(1)[18]	555(2)[14]	534(4)[9]	A_1 $[\nu(OsF_1) + \nu(OsF_2) + \nu(OsF_3) + \nu(OsF_4)] - [\nu(OsF_5)] + \delta(O_1OsO_2)$
485(8)	496(5)	517(4)	514(4)[0]	540(4)[0]	522(6)[0]	A_2 $[\nu(OsF_1) + \nu(OsF_3)] - [\nu(OsF_2) + \nu(OsF_4)] + \rho_t(O_1OsO_2)$
			489(3)[51]	527(3)[55]	517(4)[57]	B_2 $[\nu(OsF_1) + \nu(OsF_4)] - [\nu(OsF_2) + \nu(OsF_3)] + \rho_t(O_1OsO_2)$
			463(2)[10]	469(2)[4]	441(3)[2]	B_1 $\nu(OsF_5) + \delta(O_1OsO_2) - [\delta(F_1OsF_4) + \delta(F_2OsF_3)]$
450(5)			448(9)[<1]	470(7)[<1]	453(8)[<0.1]	A_1 $\rho_w(F_5OsO_1O_2) + \rho_w(F_1OsF_2) - \rho_w(F_3OsF_4)$
			373(<0.1)[18]	379(<1)[13]	353(<1)[11]	B_2 $\rho_r(F_5OsO_1O_2) + \rho_w(F_1OsF_4) - \rho_w(F_2OsF_3)$
			370(<1)[16]	374(<1)[17]	353(<1)[15]	A_1 $\delta_{umb}(OsF_1F_2F_3F_4) + \delta(O_1OsO_2)$
			362(<0.1)[40]	362(<1)[36]	335(<1)[26]	B_1 $\delta(F_1OsF_2) - \delta(F_3OsF_4) + \rho_w(F_5OsO_1O_2)$
381(6) 360(45)	364(31)	365sh	347(9)[0]	359(6)[0]	338(6)[0]	A_2 $\rho_t(F_1OsF_4) - \rho_t(F_2OsF_3) + \rho_t(O_1OsO_2)$
305(63)	310(sh) 304(45)	339 sh 310(40)[j]	334(4)[31]	339(3)[26]	316(3)[20]	B_2 $\delta(F_5OsO_1) - \delta(F_5OsO_2)$
			311(<1)[1]	311(<1)[1]	294(<1)[2]	B_1 $\delta(F_1OsF_2) - \delta(F_3OsF_4) - \rho_w(F_6OsO_1O_2)$
252(21)	254(12) 232(3)	264(26)	266(4)[3]	270(3)[2]	261(4)[1]	A_1 $\delta(F_1OsF_2) + \delta(F_3OsF_4)$
			54(2)[0]	73(1)[0]	61(1)[0]	A_2 $\rho_t(F_1OsF_2) + \rho_t(F_3OsF_4) + \rho_t(O_1OsO_2)$
			–103(<1)[2]	–102(<1)[1]	–97(<1)[1]	B_2 def.
200(11) 178(6)	201(10) 177(5)	209(14) 187(7)				lattice modes

[a] The Raman spectrum was recorded on microcrystalline solid in a quartz capillary at 25 °C using 785-nm excitation. [b] Frequencies are given in cm^{-1} and are relative intensities with the most intense band given as 100. The abbreviation (sh) denotes a shoulder. Bands were also observed at 949(7), 681(26), 667(7), 646(7) ($[Cs][OsO_2F_5]$); 977(4), 645(7) ($[N(CH_3)_4][OsO_2F_5]$); 967(7), 678(sh), 639(10) ($[NO][OsO_2F_5]$) cm^{-1} and are tentatively assigned to $OsOF_5^-$. Bands assigned to *cis*-OsO_2F_4 were observed at 943(330), 934(97), 683(18), 673(137), 578(47), 571(45), 402(213), 347(77), 342(97), and 321(40) in the spectrum of $[NO][OsO_2F_5]$. [c] The Raman spectrum was recorded on a microcrystalline solid sample in a FEP tube at –150 °C using 1064-nm excitation. [d] Values in parentheses denote calculated Raman intensities ($Å^4 u^{-1}$) and values in square brackets denote calculated infrared intensities (km mol^{-1}). [e] The B3LYP/Stuttgart basis set for Os and the aug-cc-pVTZ basis set for O and F were used. [f] The aug-cc-pVTZ basis set was used. [g] The SDDall basis set was used augmented for F and O with two d-type polarization functions. [h] Assignments are for the energy-minimized geometry calculated at the SVWN/SDDall level of theory. See Figure 4.4a for the atom labeling scheme. The symbols denote stretch (ν), bend (δ), twist (ρ_t), rock (ρ_r), wag (ρ_w), and umbrella (δ_{umb}). The abbreviation, def., denotes a deformation mode. [i] The band overlaps with a *cis*-OsO_2F_4 band. [j] The band overlaps with a FNO band

the weakest cation-anion interactions. Thus, the anion is expected to most closely resemble the gas-phase anion. Such an example is provided by the crystal structure of $[N(CH_3)_4][OsO_3F_3]$.[23]

The Os–O stretching frequencies of *cis*-$OsO_2F_5^-$ (826 and 920 cm^{-1}) bracket the calculated values (861 and 895 cm^{-1}). The Os–O stretching frequencies are also shifted to lower frequency than those of *cis*-OsO_2F_4 (933 and 943 cm^{-1}),[20] consistent with anion formation. The experimental frequency difference between the symmetric and asymmetric stretches (94 cm^{-1}) is much larger than the calculated difference (34 cm^{-1}). It is interesting to note that the experimental difference for *cis*-OsO_2F_4 (10 cm^{-1}) is also larger than the calculated difference (5 cm^{-1}, Table 5.4).

Examination of a series of *cis*-dioxo d^0 transition metal oxide fluorides reveals that there is a near-linear (R^2 = 87%) correlation between the O–M–O bond angle (M = Os, Re, Tc) and the difference in frequency between of the symmetric and asymmetric MO stretches (Table 4.3). The largest experimentally reported bond angle corresponds to *cis*-TcO_2F_3 (103.1°) and to a small frequency difference ($\Delta\nu$ = 11 cm^{-1}),[200] whereas the smallest experimentally reported bond angle occurs for [*cis*-OsO_2F_3][Sb_2F_{11}] (99.9(2)°), which displays the largest frequency difference ($\Delta\nu$ = 54 cm^{-1}).[139] The frequency difference observed for *cis*-$OsO_2F_5^-$ (94 cm^{-1}) is larger than for any species listed in Table 4.3, consequently, a O–Os–O bond angle that is much smaller than that of *cis*-$OsO_2F_3^+$ (99.9(2)°)[139] is anticipated. In support of this expectation, the calculated O–Os–O bond angle for the monocapped trigonal prismatic isomer is 89.2°.

Table 4.3. Correlation of the OMO Bond Angle with the Frequency Difference Between the Symmetric and Asymmetric MO Stretches for d^0 *cis*-dioxo Transition Metal Oxide Fluorides (M = Os, Re, Tc)

Molecule	$\Delta(\nu(MO))$,[a] cm^{-1}	OMO Bond Angle (°)	ref
cis-TcO_2F_3	11	103.1[a]	Re-031
cis-OsO_2F_4	13	103.5(25)	Os8-003
cis-$TcO_2F_3 \cdot SbF_5$	18[b]	103.3(3)	Re-008
cis-$ReO_2F_3 \cdot SbF_5$	21[c]	103.2(3)	Re-008
cis-$TcO_2F_3 \cdot XeO_2F_2$	26	101.5(8)	Re-008
[Li][*cis*-TcO_2F_4]	27	102.5(3)	Re-016
cis-ReO_2F_3	33[d]	102.3(4)	Re-013
[Li][*cis*-ReO_2F_4]	38	100.2(7)	Re-013
[*cis*-$F(OsO_2F_3)$][Sb_2F_{11}]	48[e]	101.4(6)	Os8-002
[*cis*-OsO_2F_3][Sb_2F_{11}]	54[f]	99.9(2)	Os8-023
[Cs][OsO_2F_5]	94	89.2[g]	

[a] Bond angle calculated from the average of the reported 104.5(5), 102.7(4), 103.3(4), and 102.4(5)° bond angles. [b] Calculated from $\nu_s(TcO_2)$ (995 cm^{-1}) and the average of $\nu_{as}(TcO_2)$ (982 and 972 cm^{-1}), [c] Calculated from $\nu_s(ReO_2)$ (1040 cm^{-1}) and the average of $\nu_{as}(ReO_2)$ (1025 and 1013 cm^{-1}), [d] Calculated from $\nu_s(ReO)$ (1025 cm^{-1}) and the average of $\nu_{as}(ReO)$ (994 and 990 cm^{-1}), [e] $\nu_s(OsO_b)$ (984 cm^{-1}) and $\nu_{as}(OsO_t)$ (936 cm^{-1}), [f] the average of $\nu_s(OsO)$ (997 and 995 cm^{-1}) and the average of $\nu_{as}(OsO)$ (946 and 938 cm^{-1}), [i] Calculated bond angle at the SVWN/SDDall level of theory for the monocapped trigonal prismatic isomer.

The observed totally symmetric Os–F stretch of $OsO_2F_5^-$ (617 cm^{-1}) is in good agreement with the calculated value (623 cm^{-1}) and is significantly lower in frequency when compared with that of *cis*-OsO_2F_4 (673 cm^{-1}).[20] The bands at 551 and 496 cm^{-1} are assigned to coupled equatorial stretching modes, three of which are coupled to (O_1OsO_2) bending modes and are in good agreement with the calculated values (585/534 and 522/517 cm^{-1}). All of these modes are shifted to lower frequency than the axial stretching modes of *cis*-OsO_2F_4 (680, 580, 572 cm^{-1}),[20] consistent with anion formation. Comparison of the equatorial Os–F stretches of *cis*-$OsO_2F_5^-$ with the axial stretches of *cis*-OsO_2F_4 is valid because, in both cases, the fluorine atoms are trans to fluorine atoms instead of oxygen atoms.

The low-frequency bending modes are in good agreement with those calculated at all levels and are also shifted to lower frequency when compared with those of *cis*-OsO_2F_4, again, consistent with anion formation.

The Raman spectrum of [NO][OsO_2F_5] was recorded as a precipitate under FNO solvent, and was always in admixture with *cis*-OsO_2F_4. The Os–O stretches of this salt (832, 842, 926, 929 cm^{-1}) are shifted to slightly higher frequency relative to the Cs^+ and $N(CH_3)_4^+$ salts, while the Os–F stretching modes, with the exception of the stretch at 573 cm^{-1} which overlaps with a *cis*-OsO_2F_4 band, are shifted to lower frequency. Overlap of the 573 cm^{-1} band does not allow for an accurate determination of the frequency of the *cis*-$OsO_2F_5^-$ mode. The shift in frequency of both the Os–F and Os–O stretching modes indicates that there is likely an interaction between the NO^+ cation and the fluorine atoms of the $OsO_2F_5^-$ anion resulting in a weaker Os–F bond and a stronger Os–O bond.

The stretching frequencies of the Cs^+ salt are similar to those of the $N(CH_3)_4^+$ salt but are shifted to slightly lower frequency, indicating that there is likely a slightly higher degree of interaction between the anion and cation than for the $N(CH_3)_4^+$ salt.

An ^{18}O-enriched sample of $[Cs][OsO_2F_5]$ was synthesized by a fusion reaction of *cis*-$Os^{18}O_2F_4$ with [Cs][F] (eq 4.1) in order to confirm the assignments of the Raman spectrum of $OsO_2F_5^-$. The spectrum of $Os^{18}O_2F_5^-$ is shown in Figure 4.5 and the observed and calculated frequencies and mode descriptions for *cis*-$OsO_2F_5^-$ and *cis*-$Os^{18}O_2F_5^-$ are provided in Table 4.4. The asymmetric and symmetric Os–O stretches of *cis*-$OsO_2F_5^-$ (820.8 and 917.6 cm^{-1}, respectively) shift to lower frequency upon ^{18}O-enrichment (781.6 and 870.5 cm^{-1}, respectively). These shifts ($\Delta\nu$ = –39.2 and –47.1 cm^{-1}, respectively) are well reproduced by the calculated values ($\Delta\nu$ = –42.7 and –47.7 cm^{-1}) and are slightly less than those of *cis*-OsO_2F_4 ($\Delta\nu_{as}$ = –47.7; $\Delta\nu_s$= –50.9 cm^{-1}). The low-frequency shifts of these modes confirm that they involve displacements of the oxygen ligands. Two Os–F stretches in the spectrum of $Os^{16}O_2F_5^-$ (485.3 and 545.6 cm^{-1}) have a small contribution from the $\delta(O_1OsO_2)$ and $\rho(O_1OsO_2)$ bending modes and do not shift appreciably in the spectrum of $Os^{18}O_2F_5^-$ (489.2 and 547.9 cm^{-1}). The totally symmetric Os–F stretch does not contain an appreciable contribution that involves oxygen displacement(s) and therefore does not shift appreciably upon enrichment ($\Delta\nu$ = 5.1 cm^{-1}).

4.2.5. X-ray Crystal Structure of $[Cs][OsO_3F_3]\cdot CH_3CN$

Details of data collection parameters and other crystallographic information are provided in Table 4.5 and geometric parameters are listed in Table 4.6. The crystal structure consists of well-isolated Cs^+ cations, $OsO_3F_3^-$ anions, and CH_3CN molecules

Table 4.4. Exeprimental Raman Vibrational Frequencies and Intensities for $[Cs][Os^{16/18}O_2F_5]$ and Calculated Vibrational Frequencies and Infrared Intensities for $Os^{16/18}O_2F_5^-$

exptl[a]		calcd[d]				assgnts (C_{2v})[g] (monocapped trigonal prism)
		SVWN[e]		B3LYP[f]		
$Os^{16}O_2F_5$[b]	$Os^{18}O_2F_5$[c]	$Os^{16}O_2F_5$	$Os^{18}O_2F_5$	$Os^{16}O_2F_5$	$Os^{18}O_2F_5$	
917.6(100)	870.5(100)	895.1(36)[80]	847.4(33)[73]	941.6(40)[91]	891.3(36)[82.8]	A_1 $\nu(OsO_1) + \nu(OsO_2)$
820.8(16)	781.6(13)	860.6(16)[134]	817.9(14)[129]	882.9(17)[154]	838.5(14)[147]	B_2 $\nu(OsO_1) - \nu(OsO_2)$
605.9(21), 594.5 sh	611.0(23)	622.6(22)[90]	622.4(21)[92]	597.4(22)[95]	596.5(21)[101]	A_1 $\nu(OsF_1) + \nu(OsF_2) + \nu(OsF_3) + \nu(OsF_4) + \nu(OsF_5)$
545.6(7)	547.9(6)	585.2(2)[156]	584(2)[158]	553.7(2)[158]	551.6(2)[165]	B_1 $[\nu(OsF_1) + \nu(OsF_2)] - [\nu(OsF_3) + \nu(OsF_4)]$
		534.5(4)[9]	525.4(5)[7]	548.9(1)[18]	530.6(2)[11]	A_1 $[\nu(OsF_1) + \nu(OsF_2) + \nu(OsF_3) + \nu(OsF_4)] - [\nu(OsF_5)] + \delta(O_1OsO_2)$
485.3(8)	489.2(7)	522.2(6)[0]	518.3(7)[0]	514.4(4)[0]	507.5(4)[0]	A_2 $[\nu(OsF_1) + \nu(OsF_3)] - [\nu(OsF_2) + \nu(OsF_4)] + \rho_t(O_1OsO_2)$
		516.6(4)[57]	514.0(4)[56]	488.6(3)[51]	485.5(3)[52]	B_2 $[\nu(OsF_1) + \nu(OsF_4)] - [\nu(OsF_2) + \nu(OsF_3)] + \rho_r(O_1OsO_2)$
		440.6(3)[2]	434.1(2)[<1]	463.2(2)[10]	455.7(2)[5]	B_1 $\nu(OsF_5) + \delta(O_1OsO_2) - [\delta(F_1OsF_4) + \delta(F_2OsF_3)]$
450.1(5)		452.8(8)[<0.1]	440.1(6)[<0.1]	447.8(9)[<1]	442.1(8)[<0.1]	A_1 $\rho_w(F_5OsO_1O_2) + \rho_w(F_1OsF_2) - \rho_w(F_3OsF_4)$
		353.2(<1)[11]	348.9(<1)[7]	372.9(<0.1)[18]	368.6(<1)[12]	B_2 $\rho_r(F_5OsO_1O_2) + \rho_w(F_1OsF_4) - \rho_w(F_2OsF_3)$
		352.8(<1)[15]	350.1(<1)[15]	370.1(<1)[16]	368.1(<1)[16]	A_1 $\delta_{umb}(OsF_1F_2F_3F_4) + \delta(O_1OsO_2)$
		335.4(<1)[26]	328.7(<1)[24]	361.7(<0.1)[40]	354.6(<0.1)[35]	B_1 $\delta(F_1OsF_2) - \delta(F_3OsF_4) + \rho_w(F_5OsO_1O_2)$
380.7(6), 360.2(45)	385.2(8), 349.7(49)	337.7(6)[0]	330.5(5)[0]	347.2(9)[0]	341.2(8)[0]	A_2 $\rho_t(F_1OsF_4) - \rho_t(F_2OsF_3) + \rho_t(O_1OsO_2)$
304.5(63)	301(79)	315.6(3)[20]	311.6(3)[22]	334.0(4)[31]	330.0(3)[34]	B_2 $\delta(F_5OsO_1) - \delta(F_5OsO_2)$
		294.3(<1)[2]	293.0(<1)[3]	310.9(<1)[1]	310.4(<1)[2]	B_1 $\delta(F_1OsF_2) - \delta(F_3OsF_4) - \rho_w(F_6OsO_1O_2)$
252.2(21)	251.8(28)	260.6(4)[1]	259.7(4)[1]	265.8(4)[3]	264.9(4)[2]	A_1 $\delta(F_1OsF_2) + \delta(F_3OsF_4)$
		60.6(1)[0]	59.5(1)[0]	53.8(2)[0]	52.6(2)[0]	A_2 $\rho_t(F_1OsF_2) + \rho_t(F_3OsF_4) + \rho_t(O_1OsO_2)$
		–97.0(<1)[1]	–96.3(<1)[1]	–103.5(<1)[2]	–102.7(<1)[2]	B_2 def.
199.8(11), 178.3(6)	201.1(11), 179(7)					lattice modes

[a] Frequencies are given in cm^{-1} and are relative intensities with the most intense band given as 100. The abbreviation (sh) denotes a shoulder. [b] The Raman spectrum was recorded on a microcrystalline solid in a quartz capillary at 25 °C using 785-nm excitation. Bands were also observed at 949(7), 681(26), 667(7), and 646(7) cm^{-1}. [c] The Raman spectrum was recorded on a microcrystalline solid in an FEP tube at 25 °C using 782-nm excitation. Bands were also observed at 899.8(7) and 683.7(35) cm^{-1}. [d] Values in parentheses denote calculated Raman intensities ($Å^4\,u^{-1}$) and values in square brackets

denote calculated infrared intensities (km mol^{-1}). [e] The SDDall basis set was used augmented for F and O with two d-type polarization functions. [f] The B3LYP/Stuttgart basis set for Os and the aug-cc-pVTZ basis set for O and F were used. [f] The aug-cc-pVTZ basis set was used. [h] Assignments are for the energy-minimized geometry calculated at the SVWN/SDDall level of theory. See Figure 4.4a for the atom labeling scheme. The symbols denote stretch (ν), bend (δ), twist (ρ_t), rock (ρ_r), wag (ρ_w), and umbrella (δ_{umb}). The abbreviation, def., denotes a deformation mode.

Table 4.5. Crystallographic Data for $[Cs][OsO_3F_3]\cdot CH_3CN$

	$[Cs][OsO_3F_3]\cdot CH_3CN$
chem formula	$OsO_3F_3C_2H_3NCs$
space group	$P2(1)/m$
a (Å)	5.4819(2)
b (Å)	6.0651(2)
c (Å)	12.2627(4)
β (deg)	90.480(1)
V (Å^3)	407.70(2)
molecules/unit cell	2
mol wt (g mol^{-1})	938.33
calcd density (g cm^{-3})	3.822
T (°C)	-173
μ (mm^{-1})	20.05
R_1[a]	0.0256
wR_2[b]	0.0373

[a] R_1 is defined as $\Sigma\|F_o\|-|F_c\|/\Sigma|F_o|$ for $I > 2\sigma(I)$. [b] wR_2 is defined as $\{\Sigma[w(F_o^2-F_c^2)^2]/\Sigma w(F_o^2)^2\}^{1/2}$ for $I > 2\sigma(I)$.

Table 4.6. Experimental Geometrical Parameters in $[Cs][OsO_3F_3]\cdot CH_3CN$

Bond Lengths (Å)		Bond Angles (°)			
Os(1)-O(1)	1.692(2)	O(1)-Os(1)-O(2)	101.65(7)	N(1)-C(1)-C(2)	179.4(3)
Os(1)-O(2)	1.731(1)	O(1)-Os(1)-F(1)	164.66(9)	C(1)-C(2)-H(1)	106(2)
Os(1)-F(1)	1.960(2)	O(1)-Os(1)-F(2)	89.80(7)	C(1)-C(2)-H(2)	111(2)
Os(1)-F(2)	1.959(1)	O(2)-Os(1)-O(2A)	99.76(9)	H(1)-C(2)-H(2)	107(2)
C(1)-C(2)	1.455(4)	O(2)-Os(1)-F(1)	88.11(6)		
C(1)-N(1)	1.136(4)	O(2)-Os(1)-F(2)	88.20(6)		
C(2)-H(1)	0.99(4)	O(2)-Os(1)-F(2A)	164.31(6)		
C(2)-H(2)	0.93(3)	F(1)-Os(1)-F(2)	78.60(5)		
		F(2)-Os(1)-F(2A)	81.09(7)		

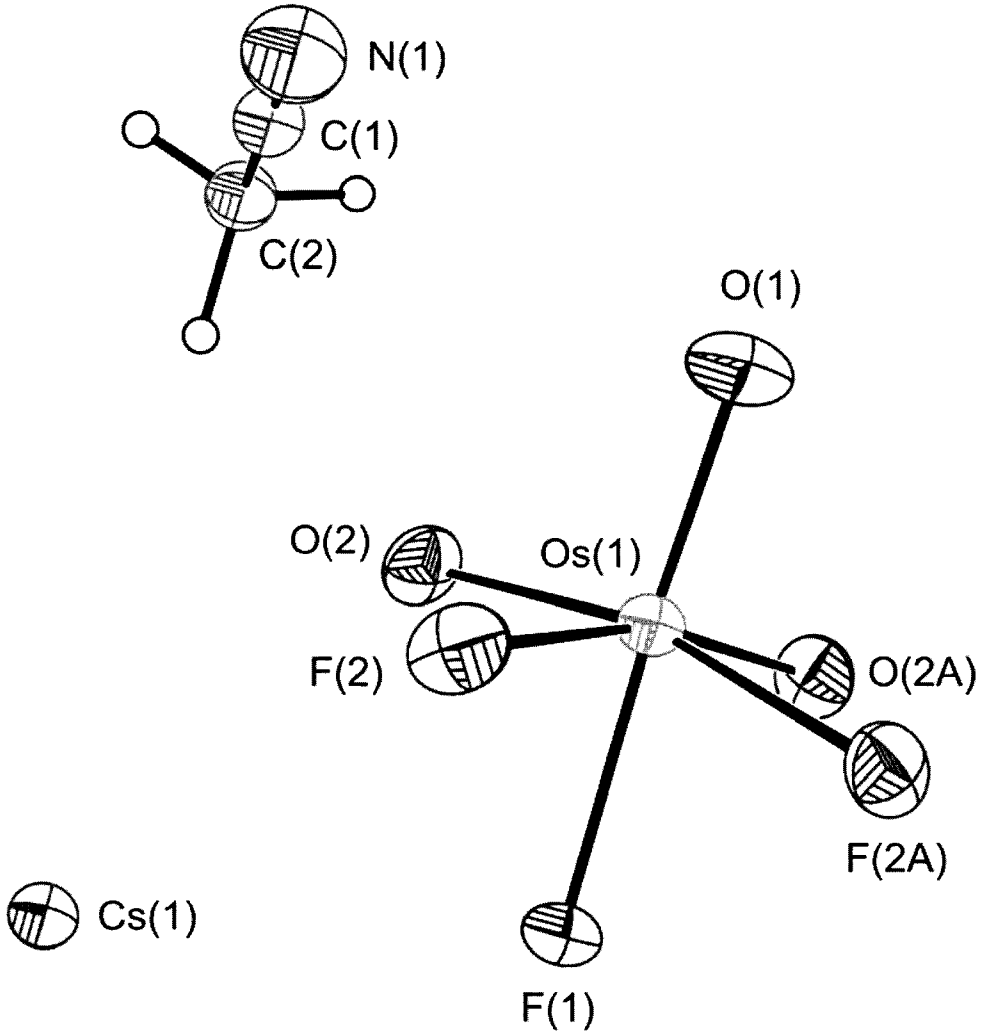

Figure 4.6. Structural unit in the X-ray crystal structure of $[Cs][OsO_3F_3]\cdot CH_3CN$ with thermal ellipsoids drawn at the 70% probability level.

(Figure 4.6). The Cs^+ and $OsO_3F_3^-$ ions are well isolated with the shortest contacts between the cation and anion being slightly over 3 Å. Each Cs^+ cation has twelve contacts to either fluorine, oxygen, or nitrogen atoms.

The Cs^+ cations, $OsO_3F_3^-$ anions and CH_3CN molecules stack in separate columns, without alternation, along the *a*- and *b*-axes (Figure B1). The Cs^+ cations, $OsO_3F_3^-$ anions and CH_3CN molecules alternate, in that order, in a column along the *c*-axis. The resulting O···F and O···C contacts between nearest-neighbor ion pairs are long[201] and near the sum of the van der Waals radii for oxygen and fluorine.[165, 202]

The $OsO_3F_3^-$ anion has a *fac*-trioxo geometry and the Os atom is displaced towards the centroid of the three facial oxygen atoms similar to the K^+,[26] $N(CH_3)_4^+$,[23] XeF_5^+,[203] and $Xe_2F_{11}^+$ [203] salts of $OsO_3F_3^-$. The geometrical parameters of the $OsO_3F_3^-$ anion are in good agreement with those reported for the K^+,[26] $N(CH_3)_4^+$,[23] XeF_5^+,[203] and $Xe_2F_{11}^+$ [203] salts. The Os(1)–O(2) bond length (1.731(1) Å) is longer than the Os(1)–O(1) bond length (1.692(2) Å) because of a short interaction between O(2) and Cs(1) (3.252(2) Å). In contrast, there is no short contact between O(1) and Cs(1). The Os–O(1) bond length is similar to those of the K^+ (1.698(2)Å),[26] $N(CH_3)_4^+$ (1.70(1) - 1.73(1) Å),[23] XeF_5^+ (1.692(3) - 1.701(3) Å),[203] and $Xe_2F_{11}^+$ (1.697(3), 1.703(2) Å)[203] salts. The Os–F(1,2) bond lengths (1.959(1), 1.960(2) Å) are similar to those of the $N(CH_3)_4^+$ salt (1.91(1) - 1.97(1) Å)[23] and are slightly elongated when compared with those of the K^+ salt (1.919(15) Å)[26] but they are not as long as those of the highly associated XeF_5^+ (2.006(2) - 2.028(2) Å)[203] and $Xe_2F_{11}^+$ (2.001(2) and 2.004(2) Å)[203] salts.

4.2.6. Computational Results

The AX_4 coupling pattern observed in the ^{19}F NMR spectra (see Section 4.2.3) is consistent with a MCTP (C_{2v}) isomer (Figure 4.4a). Consequently, this geometry was the starting geometry and optimized at the SVWN and B3LYP levels of theory resulting in stationary points with one negative frequency. The negative frequency was followed, and resulted in stationary points with a geometry corresponding to a *cis*-PBP (C_s) isomer (Figure 4.4b) with one negative frequency at the B3LYP level only. In the case of the B3LYP-optimized geometry, the negative frequency was once again followed and resulted in a stationary point with all frequencies real and a geometry corresponding to a MCO (C_s) isomer (Figure 4.4c). This geometry was then optimized at the SVWN level and again resulted in a stationary point with all frequencies real. It is worth noting that the three calculated geometries correspond to the three possible seven-coordinate *cis*-dioxo geometries predicted by the valence shell electron pair repulsion (VSEPR) model of molecular geometry.

The calculated geometries for *trans*-$OsO_2F_5^-$ (D_{5h}, *trans*-PBP) and $OsOF_5^-$ (C_{4v}) (Figure 4.3) were optimized at the SVWN and B3LYP levels of theory and resulted in stationary points with all frequencies real. The energy-minimized geometries and vibrational frequencies for *cis*-OsO_2F_4 (C_{2v})[18] were also calculated to serve as benchmarks and for comparison with *cis*-$OsO_2F_5^-$. Overall, the SVWN/SDDall geometry and frequencies provided the best agreement for *cis*-OsO_2F_4 (see Chapter 5) and are therefore used in the following discussions.

4.2.6.1. Relative Stabilities of the $OsO_2F_5^-$ Isomers

The relative gas-phase reaction enthalpies and Gibbs free energies were calculated for each isomer at the SVWN and B3LYP levels (Table 4.7). The calculated enthalpies reveal that the *cis*-PBP (1.7 kJ mol^{-1}), MCO (0 kJ mol^{-1}), and *trans*-PBP (6.9 kJ mol^{-1}) isomers are all similar in energy and are favored when compared with the MCTP isomer (47.0 kJ mol^{-1}). It is reasonable to assume that in solution or in the solid state, these relatively small barriers could be easily overcome, making it possible to observe the MCTP isomer in solution (See Section 4.2.3.) and in the solid state (See Section 4.2.4.).

The most stable gas-phase isomer, MCO, could rearrange in solution through a *cis*-PBP intermediate to a MCTP isomer (Scheme 4.1). Isomerization of the MCO to the *cis*-PBP involves movement of the O_1 atom to a position on the pseudo 5-fold axis. This displacement would result in movement of the F_2 atom into the equatorial plane to form the *cis*-PBP isomer. Rearrangement of the *cis*-PBP to the MCTP would occur when the O_2 atom moves above the equatorial plane, displacing the O_1 atom away from it. The remaining equatorial fluorine atoms would reposition so as to minimize their mutual repulsions.

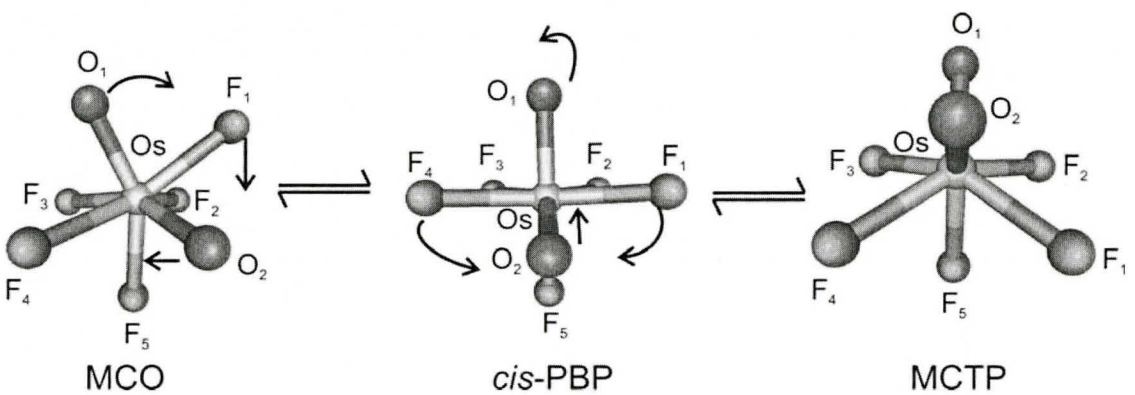

Scheme 4.1. Possible Isomerization Pathways for $OsO_2F_5^-$

Table 4.7. Calculated Relative Gas Phase ΔG and ΔH Values for the Monocapped Trigonal Prism (MCTP), Pentagonal Bipyramid (*cis*-PBP), Monocapped Octahedron (MCO), and *trans*-$OsO_2F_5^-$ (*trans*-PBP) Iomers, and for the Inter-Conversion of the MCTP, *cis*-PBP, MCO, and *trans*-PBP Isomers.[a]

	SVWN[c]		SVWN[d]		B3LYP[e]	
Isomer[b]	ΔH	ΔG	ΔH	ΔG	ΔH	ΔG
MCO	0.00	0.00	0.00	0.00	0.00	0.00
cis-PBP	1.73	6.16	4.69	–3.43	4.26	7.51
trans-PBP	6.89	11.80	4.24	9.10	6.10	7.51
MCTP	46.97	53.12	51.71	57.42	56.70	61.74

	SVWN[c]		SVWN[d]		B3LYP[e]	
Isomers	ΔH	ΔG	ΔH	ΔG	ΔH	ΔG
cis-PBP to MCTP	45.23	46.96	47.02	60.85	52.44	54.23
MCO to MCTP	46.97	53.12	51.71	57.42	56.70	61.74
MCO to *cis*-PBP	1.74	6.16	4.69	3.43	4.26	7.51
MCTP to *trans*-PBP	–40.07	–41.32	–47.47	–48.31	–50.60	–51.22
cis-PBP to *trans*-PBP	5.16	5.64	–0.45	12.53	1.84	3.01
MCO to *trans*-PBP	6.89	11.80	4.25	9.11	6.10	10.52

[a] Zero-point corrected values for each member of an isomer pair were used. Energies are given in kJ mol^{-1}. [b] Relative ΔH and ΔG values with the MCO isomer set to 0. [c] The SDDall basis set was used augmented for F and O with two d-type polarization functions. [d] The aug-cc-pVTZ(-PP) basis sets were used for all atoms. [e] The Stuttgart basis set was used for Os with the f functional. The aug-cc-pVTZ basis sets were used for fluorine and oxygen.

4.2.6.2. Calculated Geometries

4.2.6.2.1. $OsO_2F_5^-$ (MCTP, *cis*-PBP, MCO, *trans*-PBP)

The bond length and bond angle trends calculated for the optimized geometries of the MCTP (Figure 4.4a), *cis*-PBP (Figure 4.4b), and MCO (Figure 4.4c) (Table 4.8) are reproduced and are similar at all levels of theory. The Os–O and Os–F bond lengths of all three isomers are elongated when compared with the corresponding Os–O and Os–F bond lengths of *cis*-OsO_2F_4, consistent with anion formation and more polar-covalent bonding in the anion.

The MCTP geometry (C_{2v}) (Figure 4.4a) has four fluorine atoms in the equatorial plane, two *cis*-oxygen atoms above the plane which are trans to the capping fluorine atom that is located below the equatorial plane. The four equatorial fluorine atoms have equivalent Os–F bond lengths (1.948 Å) that are slightly longer than the Os–F bond length of the capping fluorine atom (1.924 Å). The shorter capping Os–F bond length is a result of the *trans*-influence of the Os–O double bonds.

The four equatorial fluorine atoms are bent away from the Os–O double bond domains towards the capping fluorine atom, F_5, so that the F_5–Os–$F_{1\text{-}4}$ angle (74.8°) is more closed. The equatorial fluorine atoms are not symmetric around the Os atom. The F_1–Os–F_4 bond angle, which is bisected by the Os–O_2 bond is much larger (98.9°) than the F_1–Os–F_2 bond angle that is not bisected by an Os-O bond (73.1°). This opening of the F_1–Os–F_4 bond angle is due to the proximity of the Os–O_2 double bond domain, which increases the repulsion between the fluorine atoms. The O_1–Os–O_2 bond angle (89.2°) is close to 90° but is significantly more closed when compared with the calculated

Table 4.8. Calculated Geometrical Parameters for the Monocapped Trigonal Prismatic, Pentagonal Bipyramidal, and Monocapped Octahedral Isomers of *cis*-$OsO_2F_5^-$

	Bond Lengths (Å)								
	Monocapped Trigonal Prism (C_{2v})[a]			Pentagonal Bipyramid (C_s)[b]			Monocapped Octahedron (C_s)[c]		
	B3LYP[d]	SVWN[e]	SVWN[f]	B3LYP[d]	SVWN[e]	SVWN[f]	B3LYP[d]	SVWN[e]	SVWN[f]
Os–O_1	1.710	1.709	1.740	1.696	1.696	1.729	1.695	1.695	1.726
Os–O_2				1.700	1.698	1.730			
Os–F_1	1.961	1.925	1.948	1.987	1.948	1.971	2.032	1.984	1.998
Os–F_2				1.944	1.915	1.935	1.890	1.869	1.894
Os–F_3							1.955	1.924	1.948
Os–F_4							1.968	1.930	1.956
Os–F_5	1.927	1.903	1.924	1.932	1.908	1.936			
	Bond Angles(°)								
O_1–Os–O_2	89.4	89.0	89.2	106.5	107.1	107.9	110.0	110.5	110.8
O_1–Os–F_1	127.0	127.1	127.2	87.0	86.7	86.5	78.1	78.3	78.6
O_1–Os–F_2	76.5	76.6	76.6	91.8	91.9	92.0	115.6	115.6	115.7
O_1–Os–F_3							82.9	81.2	82.8
O_1–Os–F_4							152.9	152.7	152.2
O_1–Os–F_5	135.3	135.5	135.4	168.9	168.6	168.1	81.3	81.2	81.0
O_2–Os–F_1				76.2	76.3	76.1			
O_2–Os–F_2				140.1	139.8	139.3			
O_2–Os–F_5				84.6	84.3	84.0			
F_1–Os–F_2	72.9	73.1	73.1	69.6	69.7	69.9	70.1	70.1	70.3
F_1–Os–F_3	149.9	149.8	149.6	141.3	141.4	141.9	128.7	128.6	128.9
F_1–Os–F_4	99.2	98.9	98.8	148.7	148.4	147.6	143.6	143.6	143.6
F_1–Os–F_5	75.0	74.9	74.8	95.9	96.3	96.7			
F_2–Os–F_3				71.8	71.8	72.1	76.4	76.3	76.2
F_2–Os–F_4				141.3	141.4	141.9	146.3	146.3	146.1
F_2–Os–F_5				79.2	78.9	78.5			
F_3–Os–F_4							77.2	77.3	77.2
F_3–Os–F_5							76.4	76.2	75.7

[a] See Figure 4.4a for the atom labeling scheme. [b] See Figure 4.4b for the atom labeling scheme. [c] See Figure 4.4c for the atom labeling scheme. [d] The Stuttgart basis set was used for Os with the f functional. The aug-cc-pVTZ basis sets were used for fluorine and oxygen. [e] The aug-cc-pVTZ(-PP) basis sets were used for all atoms. [f] The SDDall basis set was used augmented for F and O with two d-type polarization functions.

structure of *cis*-OsO_2F_4 (101.4°). This is likely a result of the four equatorial fluorine atoms that cannot be significantly displaced because of the presence of the capping F_5 atom.

The *cis*-PBP isomer (Figure 4.4b) has one oxygen and four fluorine atoms in the equatorial plane with one apical fluorine and one apical oxygen atom so that the two oxygen atoms are cis to one another. The equatorial plane of the pentagonal bipyramid is distorted, with a O_1–Os–O_2 bond angle (107.9°) that is significantly larger than the O_1–Os–$F_{1,2}$ bond angles (86.5 and 92.0°, respectively). This distortion arises from the greater repulsion interactions that occur between the Os–O double bond domains than between the Os–F single bond domains. Displacement of the O_2 atom below the equatorial plane results in displacement of the $F_{1,4}$ atoms out of that plane so as to minimize the $F_{1,4}\cdots O_2$ interactions. The apical F_5 atom is not on the pseudo 5-fold axis, so that it avoids the double bond domain of the Os–O_2 bond, giving a O_1–Os–F_5 bond angle (168.9°) that deviates significantly from 180°.

The Os–$F_{1,4}$ bond lengths (1.948 Å) are slightly longer than the $F_{2,3}$ bond lengths (1.935 Å) as a result of the close proximity of the $F_{1,4}$ atoms to the O_2 and O_1 atoms, with the O_1–Os–$F_{1,4}$ bond angles (86.5°) being more closed with respect to the O_1–Os–$F_{2,3}$ bond angles (92.0°). The apical Os–F_5 bond length (1.936 Å) is comparable to the Os–$F_{2,3}$ bond lengths because the F_5 atom is approximately trans to O_1 and the $F_{2,3}$ atoms are nearly trans to O_2.

The MCO isomer (Figure 4.4c) has two *cis*-oxygen atoms and four fluorine atoms in a pseudo-octahedral arrangement with one capping fluorine atom (F_1). The pseudo-

octahedron is severely distorted by the capping fluorine atom which is located in the $O_1O_2F_2$-face. The O_1, O_2, and F_2 atoms are pushed away from their ideal octahedral positions by the capping fluorine atoms causing the O_1–Os–O_2 (110.8°) and the $O_{1,2}$–Os–F_2 (115.7°) bond angles to be much more open relative to the O_1–Os–O_2 (101.4°) and O_1–Os–F_3 (93.9°) bond angles of *cis*-OsO_2F_4 (Figure 5.6a). The $F_3F_4F_5$-face is slightly closed, with the $F_{3,5}$–Os–F_4 (76.2°) and F_3–Os–F_5 (75.7°) bond angles more closed than the F_1–Os–F_3 (85.2°) and F_1–Os–F_2 (79.3°) bond angles of *cis*-OsO_2F_4. The capping fluorine atom is located somewhat closer to the F_2 atom because of the greater steric repulsion of the osmium oxygen double bond domains as opposed to the osmium F_1 single bond domain.

The Os–F_1 bond length (1.998 Å) involving the capping fluorine atom is, as expected, the longest of all the Os–F bonds, while the Os–F_2 bond is the shortest (1.894 Å). The short Os–F_2 bond presumably results because the F_2 atom is not trans to either an O or a fluorine atom and thus the *trans*-influence on that bond is expected to be minimal. The remaining Os–F bond lengths are similar (1.956 and 1.948 Å) and intermediate with respect to the Os–F_1 and Os–F_2 bond lengths.

The *trans*-PBP isomer (Figure 4.3a and Table 4.9) is based on a D_{5h} pentagonal bipyramid with two axial oxygen atoms (180°), and five coplanar equatorial fluorine atoms. The Os–O bond length (1.762 Å) is longer than for any of the *cis*-dioxo isomers (vide supra), while the Os–F bond length (1.924 Å) is intermediate with respect to those of the *cis*-dioxo isomers.

Table 4.9. Calculated Geometrical Parameters for *trans*-$OsO_2F_5^-$ and $OsOF_5^-$

	trans-$OsO_2F_5^-$ (D_{5h})[a]			$OsOF_5^-$ (C_{4v})[b]		
	Bond Lengths (Å)					
	B3LYP[c]	SVWN[d]	SVWN[e]	B3LYP[c]	SVWN[d]	SVWN[e]
Os–O_1	1.734	1.732	1.762	1.666	1.667	1.697
Os–F_1	1.930	1.899	1.924	1.930	1.902	1.920
Os–F_2				1.895	1.872	1.897
	Bond Angles (°)					
O_1–Os–O_2	180.0	180.0	180.0			
O_1–Os–F_1	90.0	90.0	90.0	95.5	95.9	96.2
O_1–Os–F_2				180.0	180.0	180
F_1–Os–F_2	72.0	72.0	72.0	84.5	84.1	89.3
F_1–Os–F_3	144.0	144.0	144.0	89.5	89.4	83.8
F_1–Os–F_4				169.0	168.3	167.5

[a] See Figure 4.3a for the atom labeling scheme. [b] See Figure 4.3b for the atom labeling scheme. [c] The Stuttgart basis set was used for Os with the f functional. The aug-cc-pVTZ basis sets were used for fluorine and oxygen. [d] The aug-cc-pVTZ(-PP) basis sets were used for all atoms. [e] The SDDall basis set was used augmented for F and O with two d-type polarization functions.

4.2.6.2.2. $OsOF_5^-$

The $OsOF_5^-$ anion is octahedral with C_{4v} symmetry (Figure 4.3b and Table 4.9). The Os–F_2 bond length (1.897 Å) trans to the axial oxygen atom is shorter than the Os–F_1 bond length (1.920 Å) for the four equatorial fluorine atoms contrary to the valence shell electron repulsion (VSEPR) model. For $OsOF_5^-$, the fluorine atoms in the equatorial planes bend away from the axial oxygen atom so that the O_1–Os–F_1 bond angle (96.2°) is much larger than 90° due to the greater steric requirements of the oxygen double bond domain compared to a fluorine single bond.

4.2.6.3. Calculated Frequencies

The vibrational frequencies and intensities of the MCTP, *cis*-PBP, MCO (Table 4.10), *trans*-PBP, and $OsOF_5^-$ (Table 4.11) have been calculated at the B3LYP and SVWN levels of theory. This was done to demonstrate that the only isomer present in the Raman spectrum of $OsO_2F_5^-$ was the MCTP isomer (see Section 4.2.4).

The MCO and *trans*-PBP isomers show small differences between the symmetric and asymmetric $\nu(OsO_2)$ stretches ($\Delta\nu$ = 11 and 7 cm^{-1}, respectively) when compared with the experimental difference ($\Delta\nu$ = 95 cm^{-1}). As a result, the presence of the MCO and *trans*-PBP isomers can be ruled out.

The *cis*-PBP isomer can also be ruled out because the intensities of the symmetric and asymmetric $\nu(OsO_2)$ stretches are predicted to be nearly equivalent, whereas the symmetric stretch in the experimental spectrum is much more intense than the asymmetric stretch.

Table 4.10. Calculated Frequencies and Intensities for the Monocapped Trigonal Prismatic, Pentagonal Bipyramidal, and Monocapped Octahedral Isomers of *cis*-$OsO_2F_5^-$ [a]

Monocapped Trigonal Prism (C_{2v})[b]				Pentagonal Bipyramid (C_s)[c]				Monocapped Octahedron (C_s)[d]			
B3LYP[e]	SVWN[f]	SVWN[g]		B3LYP[e]	SVWN[f]	SVWN[g]		B3LYP[e]	SVWN[f]	SVWN[g]	
942(40)[91]	937(40)[86]	895(36)[80]	A_1	974(33)[119]	966(28)[122]	936(23)[123]	A'	970(43)[62]	960(43)[58]	920(41)[55]	A'
883(17)[154]	891(16)[148]	861(16)[134]	B_2	946(26)[128]	942(28)[107]	907(30)[84]	A'	969(12)[174]	963(11)[159]	931(12)[142]	A"
597(22)[95]	631(20)[96]	623(22)[90]	A_1	599(17)[123]	632(17)[114]	616(19)[102]	A'	619(17)[109]	649(17)[104]	630(19)[96]	A'
554(2)[158]	594(2)[160]	585(2)[156]	B_1	547(<1)[146]	587(<1)[181]	578(<1)[179]	A"	557(2)[169]	599(1)[172]	588(2)[168]	A'
549(1)[18]	555(2)[14]	534(4)[9]	A_1	531(8)[56]	565(8)[54]	547(10)[54]	A'	510(3)[35]	540(4)[42]	525(5)[41]	A"
514(4)[0]	540(4)[0]	522(6)[0]	A_2	523(<1)[39]	538(<1)[2]	517(1)[<1]	A"	498(4)[14]	531(4)[17]	517(6)[18]	A'
489(3)[51]	527(3)[55]	517(4)[57]	B_2	486(4)[6]	519(4)[11]	505(8)[13]	A'	474(8)[2]	498(4)[2]	489(6)[4]	A'
463(2)[10]	469(2)[4]	441(3)[2]	B_1	447(8)[3]	463(6)[2]	440(5)[1]	A'	438(3)[2]	451(3)[1]	424(3)[1]	A'
448(9)[<1]	470(7)[<1]	453(8)[<0.1]	A_1	403(8)[<1]	426(7)[<1]	412(8)[<0.1]	A"	431(6)[11]	331(5)[7]	410(5)[4]	A"
373(<0.1)[18]	379(<1)[13]	353(<1)[11]	B_2	383(6)[7]	383(5)[6]	361(6)[4]	A'	354(5)[10]	363(4)[10]	345(4)[9]	A'
370(<1)[16]	374(<1)[17]	353(<1)[15]	A_1	354(1)[15]	361(1)[19]	338(1)[10]	A"	342(3)[10]	349(3)[8]	329(3)[8]	A'
362(<0.1)[40]	362(<1)[36]	335(<1)[26]	B_1	328(<1)[17]	335(<1)[20]	315(<1)[16]	A'	321(2)[21]	330(2)[22]	313(2)[16]	A'
347(9)[0]	359(6)[0]	338(6)[0]	A_2	322(4)[59]	336(3)[50]	316(4)[45]	A"	320(<1)[7]	329(<0.1)[9]	306(<1)[7]	A"
334(4)[31]	339(3)[26]	316(3)[20]	B_2	313(2)[40]	321(1)[32]	301(2)[29]	A'	303(3)[59]	314(1)[58]	294(1)[47]	A'
311(<1)[1]	311(<1)[1]	294(<1)[2]	B_1	261(1)[3]	265(1)[2]	247(1)[3]	A'	303(4)[31]	311(3)[22]	289(3)[22]	A"
266(4)[3]	270(3)[2]	261(4)[1]	A_1	227(<0.1)[10]	235(<1)[7]	224(<1)[6]	A"	276(<1)[<1]	283(<0.1)[<1]	257(<1)[1]	A"
54(2)[0]	73(1)[0]	61(1)[0]	A_2	95(1)[2]	103(1)[2]	102(1)[2]	A'	159(<1)[4]	157(<1)[3]	152(<1)[3]	A'
–103(<1)[2]	–102(<1)[1]	–97(<1)[1]	B_2	–37(<1)[3]	5(<1)[3]	–31(<1)[3]	A"	79(<1)[<1]	76(<1)[<1]	58(<1)[<1]	A"

[a] Values in parentheses denote calculated Raman Intensities ($Å^4\ u^{-1}$) and values in square brackets denote calculated infrared intensities (km mol^{-1}). [b] See Figure 4.4a for the atom labeling scheme. [c] See Figure 4.4b for the atom labeling scheme. [d] See Figure 4.4c for the atom labeling scheme. [e] The Stuttgart basis set was used for Os with the f functional. The aug-cc-pVTZ basis sets were used for fluorine and oxygen. [f] The aug-cc-pVTZ(-PP) basis sets were used for all atoms. [g] The SDDall basis set was used augmented for F and O with two d-type polarization functions.

Table 4.11. Calculated Frequencies and Intensities for *trans*-$OsO_2F_5^-$ and $OsOF_5^-$ [a]

trans-$OsO_2F_5^-$ (D_{5h})[b]				$OsOF_5^-$ (C_{4v})[c]			
B3LYP[d]	SVWN[e]	SVWN[f]		B3LYP[d]	SVWN[e]	SVWN[f]	
927(0)[256]	921(0)[241]	897(0)[211]	A_2''	1051(36)[148]	1036(33)[139]	1004(33)[138]	A_1
945(56)[0]	930(55)[0]	890(55)[0]	A_1'				
				634(21)[100]	659(20)[84]	652(25)[74]	A_1
594(29)[0]	625(24)[0]	612(26)[0]	A_1'	589(<0.1)[236]	623(<0.1)[215]	624(<0.1)[212]	E
578(0)[178]	614(0)[185]	608(0)[180]	E_1'	570(8)[0]	603(8)[0]	598(11)[0]	B_2
				548(6)[44]	576(6)[43]	570(8)[44]	A_1
501(1)[0]	524(1)[0]	512(2)[0]	E_2'				
417(7)[0]	434(5)[0]	419(5)[0]	E_2'				
373(6)[0]	369(5)[0]	346(6)[0]	E_1''				
329(0)[8]	332(0)[8]	311(0)[8]	A_2''				
308(0)[30]	318(0)[37]	298(0)[29]	E_1'	307(3)[4]	303(3)[2]	293(4)[2]	E
				282(<1)[10]	280(<0.1)[10]	269(<0.1)[11]	E
				250(<1)[26]	248(<1)[23]	238(<1)[23]	A_1
181(0)[0]	179(0)[0]	169(0)[0]	E_2''	183(<1)[0]	183(<1)[0]	174(<1)[0]	B_2
				160(1)[12]	155(<1)[12]	146(1)[11]	E
				178(3)[0]	139(3)[0]	142(3)[0]	B_1
122(0)[39]	140(0)[37]	115(0)[36]	E_1'				

[a] Values in parentheses denote calculated Raman Intensities ($Å^4$ u^{-1}) and values in square brackets denote calculated infrared intensities (km mol^{-1}). [b] See Figure 4.3a for the atom labeling scheme. [c] See Figure 4.3b for the atom labeling scheme. [d] The Stuttgart basis set was used for Os with the f functional. The aug-cc-pVTZ basis sets were used for fluorine and oxygen. [e] The aug-cc-pVTZ(-PP) basis sets were used for all atoms. [f] The SDDall basis set was used augmented for F and O with two d-type polarization functions.

Only one Os–O stretching mode (1004 cm^{-1}) is predicted for the $OsOF_5^-$ anion which occurs to higher frequency of the two OsO_2 modes calculated for the $OsO_2F_5^-$ isomers (See Tables 4.10 and 4.11). It is proposed that the weak modes observed at 949 (Cs^+), 977 ($N(CH_3)_4^+$), and 967 (NO^+) cm^{-1} may correspond to the ν(OsO) mode of $OsOF_5^-$. The totally symmetric $\nu(OsF_1) + \nu(OsF_2)$ stretching mode (652 cm^{-1}) of $OsOF_5^-$ is predicted to occur at higher frequency than the totally symmetric mode of the MCTP isomer (623 cm^{-1}). It is proposed that the weak modes observed at 646 (Cs^+), 645 ($N(CH_3)_4^+$), and 639 (NO^+) cm^{-1} may correspond to the totally symmetric Os–F mode in $OsOF_5^-$.

4.2.6.4. Charges, Valencies, and Bond Orders

The NBO analyses were carried out for the optimized gas-phase geometries of the MCTP, *cis*-PBP, MCO (Table B1), *trans*-PBP, and $OsOF_5^-$ (Table B2). The NBO analyses give natural population analysis (NPA) charges for Os that are similar for all Os(VIII) compounds (1.93 to 1.99) and are similar to that of *cis*-OsO_2F_4 (1.96) (Table 5.6), while the $OsOF_5^-$ anion has a smaller charge (1.87) owing to the lower formal oxidation state of osmium. The NPA charges of the fluorine (–0.39 to –0.50) and oxygen (–0.35 to –0.46) atoms are more negative compared to the fluorine (–0.36 and –0.38) and oxygen (–0.23) atoms of *cis*-OsO_2F_4, which is consistent with the negative charge of the anion. The negative charges on the light atoms and positive charges of the osmium atom indicate that the bonds formed with the osmium atom are polar covalent. Overall, the negative charges on the light atoms of the $OsOF_5^-$ anion (–0.45, –0.51, and –0.36) are somewhat more

negative than those of the $OsO_2F_5^-$ anion owing to the reduced number of ligands on the Os(VI) anion.

The Os–O bond orders of all species (0.76 to 0.91) are approximately twice the Os–F bond orders (0.37 to 0.45). The relative bond orders are consistent with the formal bond orders of two for the Os–O bonds and one for the Os–F bonds. The Os–F_5 bond order (0.41) of the MCTP isomer is very similar to the Os–$F_{1\text{-}4}$ bond orders (0.40). The Os–$F_{1,4}$ bond orders (0.39) of the *cis*-PBP isomer may be marginally less than the Os–$F_{2,3}$ (0.41) and Os–F_5 (0.41) bond orders because the F_1 and F_4 atoms are repelled by the *cis*-dioxo group creating a longer Os–$F_{1,4}$ bond length (see Section 4.2.6).

The largest Os–F bond order for the MCO isomer occurs for the Os–F_2 bond (0.45). The F_2 atom is located in the same plane as the oxygen atoms and is not affected by the *trans*-influence of the oxygen atoms, while the $F_{3,4,5}$ atoms are in a plane below the oxygen and capping fluorine (F_1) atoms and, as a result, have somewhat lower bond orders (0.40 and 0.39). The capping F_1 atom has the smallest Os–F bond order (0.37) and the longest bond length of all of the fluorine atoms because of greater steric repulsions involving the capping atom.

The Os–F_1 bond order (0.41) of the $OsOF_5^-$ anion is less than the Os–F_2 bond order (0.44) owing to the increased steric repulsions in the equatorial plane which increase the Os–F_1 bond length as opposed to the axial Os–F_2 bond.

4.3. Conclusions

The *cis*-$OsO_2F_5^-$ anion has been synthesized as its Cs^+, $N(CH_3)_4^+$, and NO^+ salts and represents the only example of an anion derived from *cis*-OsO_2F_4. The AX_4 coupling pattern observed in the ^{19}F NMR spectra is assigned to *cis*-dioxo monocapped trigonal prismatic isomer $OsO_2F_5^-$. This isomer has four equatorial fluorine atoms, one capping fluorine atom and two *cis*-dioxo oxygen atoms trans to the capping fluorine atom. The Raman spectra have also been fully assigned based on the calculated geometry, frequencies, and intensities of the monocapped trigonal prismatic isomer. The calculated gas-phase reaction enthalpies for the interconversion of the possible seven-coordinate isomers of $OsO_2F_5^-$ were determined and reveal that all of the isomers are relatively similar in energy with the monocapped octahedron being favored and the monocapped trigonal prism being least favored. However, the energy differences for interconversion between the *cis*-dioxo isomers are relatively small and may be expected to be influenced by the solvent medium. The attempted synthesis of $OsOF_5^-$ from $OsOF_4$ revealed that osmium was easily oxidized to the +8 oxidation state yielding *cis*-$OsO_2F_5^-$.

CHAPTER 5

X-RAY CRYSTAL STRUCTURE AND RAMAN SPECTRA OF *cis*-OsO_2F_4 AND THE CH_2CN^- ANION

5.1. Introduction

Osmium dioxide tetrafluoride, *cis*-OsO_2F_4, is one of the two neutral oxide fluorides of Os(VIII) that are known, the other being OsO_3F_2 ((*fac*-$OsO_3F_2)_\infty$;[19] $(OsO_3F_2)_2$[18]). It is synthesized by reaction of OsO_4 or OsO_3F_2 with KrF_2 in anhydrous HF (eqs 5.1 and 5.2) and is a deep magenta-colored solid.[13] The *cis*-dioxo geometry of

$$OsO_4 + 2KrF_2 \xrightarrow[25\ ^\circ C]{HF} cis\text{-}OsO_2F_4 + 2Kr + O_2 \quad (5.1)$$

$$OsO_3F_2 + KrF_2 \xrightarrow[25\ ^\circ C]{HF} cis\text{-}OsO_2F_4 + Kr + \tfrac{1}{2}O_2 \quad (5.2)$$

cis-OsO_2F_4 has been confirmed by ^{19}F NMR, vibrational spectroscopy, and gas-phase electron diffraction.[20] The ^{19}F NMR spectrum of *cis*-OsO_2F_4 consists of an A_2X_2 spin coupling pattern and, in addition, provides a rare example of an Os(VIII) species for which ^{187}Os satellites are observed. The ^{187}Os chemical shift (1431 ± 10 ppm) was also determined by inverse correlation using ^{19}F as the observed nuclide.[20] The X-ray crystal structure of *cis*-OsO_2F_4 has previously been reported, but was severely disordered and twinned and did not allow for a definitive assignment of one O and one F atom, therefore an accurate determination of the geometrical parameters was not possible.[11]

The present work describes four X-ray crystal structures that contain isolated *cis*-OsO_2F_4 molecules in which the positions of the oxygen and fluorine atoms are unambiguously assigned. Three of these structures provide the first examples of non-

coordinated CH_2CN^- anions. In an separate study, the $[K][CH_2CN]$ salt was also synthesized and the anion was characterized by Raman spectroscopy. The optimized structures of *cis*-OsO_2F_4, *cis*-$Os^{18}O_2F_4$, and CH_2CN^- have been obtained and used to aid in the assignments of the Raman spectra.

5.2. Results and Discussion

5.2.1. Syntheses of $[M][OsO_2F_5]$ ($M = Cs^+$ and $N(CH_3)_4^+$)

The salt, $[Cs][OsO_2F_5]$, was synthesized by the direct fusion of *cis*-OsO_2F_4 (m.p. 90 °C)[20] with powdered [Cs][F] above 90 °C forming an orange powder (eq 5.3) as previously described (See Chapter 4), whereas the $[N(CH_3)_4][OsO_2F_5]$ salt was synthesized by reaction $[N(CH_3)_4][F]$ with *cis*-OsO_2F_4 in liquid FNO at –78 °C (eq 5.4) as previously described (See Chapter 4).

$$cis\text{-}OsO_2F_4 + [Cs][F] \xrightarrow{90\ ^\circ C} [Cs][OsO_2F_5] \quad (5.3)$$

$$cis\text{-}OsO_2F_4 + [N(CH_3)_4][F] \xrightarrow[-78\ ^\circ C]{FNO} [N(CH_3)_4][OsO_2F_5] \quad (5.4)$$

5.2.2. Syntheses of *cis*-OsO_2F_4·$[Cs][CH_2CN]$·0.3HF, *cis*-OsO_2F_4·$[Cs][CH_2CN]$ and *cis*-OsO_2F_4·$[N(CH_3)_4][CH_2CN]$

Crystalline *cis*-OsO_2F_4·$[Cs][CH_2CN]$·0.3HF was obtained from a solution of $[Cs][OsO_2F_5]$ dissolved in CH_3CN and was obtained as orange plates that grew over a period of 11 h as the solution was slowly cooled from 0 to –35 °C. Crystalline *cis*-OsO_2F_4·$[Cs][CH_2CN]$ was obtained from an CH_3CN solution containing 1 mol of $[Cs][OsO_2F_5]$ and 1 mol of [Cs][F], which deposited as red plates over a period of 3h at 0 °C. Crystalline *cis*-OsO_2F_4·$[N(CH_3)_4][CH_2CN]$ was obtained from an CH_3CN solution

of $[N(CH_3)_4][OsO_2F_5]$ and grew as red needles by slow cooling of the CH_3CN solution from –15 to –28 °C over a period of 13 h.

The formation of the CH_2CN^- anion likely occurs by a mechanism in which $OsO_2F_5^-$ dissociates to form the weak Lewis acid *cis*-OsO_2F_4 and F^- (eq 5.5) followed by proton abstraction from the CH_3CN solvent by F^- to form HF and CH_2CN^- (eq 5.6). This is similar

$$OsO_2F_5^- \longrightarrow \textit{cis}\text{-}OsO_2F_4 + F^- \qquad (5.5)$$

$$F^- + CH_3CN \xrightarrow{CH_3CN} CH_2CN^- + HF \qquad (5.6)$$

to anhydrous $[N(CH_3)_4][F]$, so called "naked fluoride", which is able to abstract a fluoride ion from CH_3CN, initially forming CH_2CN^- (eq 5.6),[54] which subsequently reacts with an additional CH_3CN molecule and a proton to form the condensation product, $(H_2N)(H_3C)C{=}C(H)(CN)$ (eq 5.7).[53]

$$CH_2CN^- + H^+ + CH_3CN \xrightarrow{CH_3CN} (H_2N)(H_3C)C{=}C(H)(CN) \qquad (5.7)$$

5.2.3. *cis*-OsO_2F_4 Crystal Growth

Crystalline *cis*-OsO_2F_4 forms thin hexagonal platelets when obtained by vacuum sublimation or by slow growth from HF and is prone to multiple twinning. For this reason, a non-disordered single crystal structure has not been reported. The previously reported crystal structure was determined from crystals grown by sublimation,[11] which were twinned. Moreover, the structure also suffered from a positional disorder. Repeated attempts, in the present work, to grow single crystals by slowly cooling of an HF solution of *cis*-OsO_2F_4 also yielded multiply twinned crystals.

An ordered single-crystal structure of *cis*-OsO_2F_4 was obtained from crystals that had been grown over a period of 4 days by the co-sublimation of *cis*-OsO_2F_4 and XeF_6

from a melt (45 °C) comprised of a ca. 1:5 stoichiometric ratio *cis*-OsO_2F_4 dissolved in XeF_6. Crystals of *cis*-OsO_2F_4 grew as purple hexagonal plates and XeF_6 grew as colorless blocks in the cooler portions of the reactor while the solution in the bottom of the FEP vessel was maintained at 45 °C. As crystal growth proceeded, some of the purple plates became encased in colorless blocks of XeF_6. Examination of the crystals under a microscope revealed that the purple plates encased in XeF_6 were of better quality than the crystals that were not encased, which was likely a result of the outer XeF_6 layer preventing further growth of *cis*-OsO_2F_4, therefore limiting the degree of twinning. The encased purple crystals were carefully broken out of the larger XeF_6 crystal at low temperature in the crystal mounting apparatus (See Section 2.11.2) and proved to be suitable for a single-crystal X-ray structure determination.

5.2.4. Synthesis of [K][CH_2CN]

The salt, [K][CH_2CN], was prepared by a method similar to that used to synthesize [Na][CH_2CN],[55] i.e., by reacting [K][$((CH_3)_3Si)_2N$] with CH_3CN in $(CH_3CH_2)_2O$ (eq 5.8).[55]

$$[K][((CH_3)_3Si)_2N] + CH_3CN \xrightarrow[-65\ ^{o}C]{Et_2O} [K][CH_2CN] + ((CH_3)_3Si)_2NH \qquad (5.8)$$

The ^1H NMR spectrum of [K][CH_2CN] recorded in liquid NH_3 consisted of a singlet ($\delta(^1H)$ = 1.68 ppm) assigned to the CH_2CN^- anion. This peak is shifted to higher frequency compared to that of [Li][CH_2CN] in DMSO (1.15 ppm)[60] and [Na][CH_2CN] in pyridine (0.93 ppm).[55] The ^{13}C NMR spectrum recorded in liquid NH_3 consisted of a singlet ($\delta(^{13}C)$ = 47.6 ppm) which is assigned to the terminal CH_2 group which was not

reported in the earlier studies. The $^{1}J(^{1}H\text{-}^{13}C)$ coupling constant was not observed in either the ^{1}H or ^{13}C spectra.

5.2.5. X-ray Crystal Structures of *cis*-OsO_2F_4·[Cs][CH_2CN], *cis*-OsO_2F_4·[Cs][CH_2CN]·0.3HF, *cis*-OsO_2F_4·[$N(CH_3)_4$][CH_2CN], and *cis*-OsO_2F_4

Details of data collection parameters and other crystallographic information are provided in Table 5.1. Selected bond lengths and bond angles for *cis*-OsO_2F_4 and CH_2CN^- are listed in Tables 5.2 and 5.3, respectively. A complete list of bond lengths and bond angles are provided in Table C1.

The crystal structure of *cis*-OsO_2F_4 has been previously reported and did not allow confirmation of the *cis*-dioxo geometry or an accurate determination of bond lengths and bond angles. This resulted from crystal twinning, absorption problems associated with thin plates, and inability to distinguish between $P6_1$ and $P6_5$ for the space group of the unit cell.[11]

The present *cis*-OsO_2F_4 crystal used for data collection and refinement (Figure 5.1a) was doubly twinned (merohedral and racemic) but not disordered so that the geometrical parameters are accurately determined. The positions of the oxygen and fluorine atoms were located from the difference map and were assigned based on their relative bond lengths and angles. The *cis*-OsO_2F_4 units pack (Figure 5.1b) in columns along the *a*- and *b*-axes and with a distorted right-handed helical chain orientation of six *cis*-OsO_2F_4 molecules along the *c*-axis similar to the previously published structure.[11]

Table 5.1. Crystallographic Data for *cis*-OsO_2F_4·[Cs][CH_2CN], *cis*-OsO_2F_4·[$N(CH_3)_4$][CH_2CN], *cis*-OsO_2F_4·[Cs][CH_2CN]·*n*HF, and *cis*-OsO_2F_4

	cis-OsO_2F_4·[Cs][CH_2CN]	*cis*-OsO_2F_4·[$N(CH_3)_4$][CH_2CN]	*cis*-OsO_2F_4·[Cs][CH_2CN]·0.3HF	*cis*-OsO_2F_4
chem formula	$Os_8O_{16}F_{32}C_{16}H_{16}N_8Cs_8$	$Os_2O_4F_8C_{12}H_{28}N_4$	$Os_8O_{16}F_{35.3}C_{16}H_{19.3}N_8Cs_8$	$Os_6O_{12}F_{24}$
space group	$C_{2/m}$	$P\bar{1}$	C_m	$P6(5)$
a (Å)	12.1015(8)	7.9103(4)	11.0712(5)	4.8915(4)
b (Å)	12.1461(8)	7.9355(4)	12.2469(5)	4.8915(4)
c (Å)	11.3504(8)	9.4939(5)	12.1389(5)	27.229(3)
α (deg)	90	106.961(3)	90	90
β (deg)	103.133(4)	91.832(3)	90.540(2)	90
γ (deg)	90	90.376(3)	90	120
V (Å^3)	1624.7(2)	596.66(6)	1645.8(1)	564.2(1)
molecules/unit cell	8	2	8	6
mol wt (g mol^{-1})	3769.25	824.78	3817.27	1789.20
calcd density (g cm^{-3})	3.852	2.404	3.851	5.266
T (°C)	-173	-173	-173	-173
μ (mm^{-1})	20.14	11.23	19.89	33.89
R_1[a]	0.0352	0.0387	0.0442	0.0483
wR_2[b]	0.0528	0.0841	0.1118	0.0575

[a] R_1 is defined as $\Sigma \| F_o | - | F_c \| / \Sigma | F_o |$ for $I > 2\sigma(I)$. [b] wR_2 is defined as $\{\Sigma[w(F_o^2\text{-}F_c^2)^2]/\Sigma w(F_o^2)^2\}^{½}$ for $I > 2\sigma(I)$.

Table 5.2. Selected Experimental Geometrical Parameters for *cis*-OsO_2F_4 in the X-ray Crystal Structures of *cis*-OsO_2F_4·[Cs][CH_2CN], *cis*-OsO_2F_4·[$N(CH_3)_4$][CH_2CN], *cis*-OsO_2F_4·[Cs][CH_2CN]·0.3HF, and *cis*-OsO_2F_4 and Calculated Geometrical Parameters for *cis*-OsO_2F_4[a]

	exptl					calcd		
	cis-OsO_2F_4·[Cs][CH_2CN]		*cis*-OsO_2F_4·[$N(CH_3)_4$][CH_2CN]	*cis*-OsO_2F_4·[Cs][CH_2CN]·0.3HF	*cis*-OsO_2F_4	SVWN[b]	B3LYP[c]	PBE1PBE[c]
			Bond Lengths (Å)					
Os(1)-O(1)	1.696(3)	1.698(4)	1.756(3)	1.724(10)	1.704(10)	1.717	1.688	1.673
Os(1)-O(2)		1.713(5)	1.670(4)	1.688(12)	1.684(11)			
Os(1)-F(1)	1.958(2)	1.966(4)	1.956(3)	1.948(8)	1.916(8)	1.892	1.887	1.872
Os(1)-F(2)		1.945(3)	1.937(3)	1.958(8)	1.914(8)			
Os(1)-F(3)	1.890(3)	1.889(2)	1.911(2)	1.909(8)	1.839(10)	1.858	1.857	1.840
Os(1)-F(4)	1.886(3)		1.865(3)	1.888(8)	1.837(8)			
			Bond Angles (°)					
O(1)-Os(1)-O(2)	107.3(2)	106.9(2)	105.1(2)	109.8(5)	102.8(7)	101.4	100.8	100.9
O(1)-Os(1)-F(1)	88.2(1)	87.2(2)	86.0(2)	86.5(4)	89.4(4)	89.6	89.6	89.6
O(1)-Os(1)-F(2)	164.5(1)	163.7(2)	165.2(2)	164.6(4)	168.9(6)	168.9	169.6	169.5
O(1)-Os(1)-F(3)	92.6(1)	92.70(8)	90.5(1)	91.8(5)	93.6(6)	93.9	93.9	94.0
O(1)-Os(1)-F(4)	92.4(1)		92.4(2)	92.0(4)	94.3(4)			
O(2)-Os(1)-F(1)		165.9(2)	168.6(2)	163.7(4)	167.8(6)			
O(2)-Os(1)-F(2)		89.4(2)	89.6(2)	85.7(4)	88.4(4)			
O(2)-Os(1)-F(3)		92.27(8)	92.2(2)	93.0(4)	95.1(4)			
O(2)-Os(1)-F(4)			95.7(2)	93.2(5)	93.7(5)			
F(1)-Os(1)-F(2)	76.4(2)	76.5(2)	79.2(1)	78.1(3)	79.5(5)	79.3	80.0	79.9
F(1)-Os(1)-F(3)	86.5(1)	86.94(9)	84.8(1)	93.2(5)	84.1(5)	85.2	85.3	85.2
F(1)-Os(1)-F(4)	86.8(1)		86.5(1)	87.1(3)	85.1(4)			
F(2)-Os(1)-F(3)		86.51(8)	87.7(1)	86.2(3)	85.0(3)			
F(2)-Os(1)-F(4)			87.3(1)	88.0(5)	85.1(5)			
F(3)-Os(1)-F(4)	171.5(2)	171.6(2)	170.6(1)	171.1(3)	166.6(6)	167.5	167.8	167.5

[a] See Figure 5.6a for the atom labeling scheme of one *cis*-OsO_2F_4 molecule, and Table C1 for a complete listing of bond lengths and bond angles. [b] The SDDall basis set augmented for F and O with two d-type polarization functions was used. [c] The Stuttgart basis set with the f functional was used for Os and the aug-cc-pVTZ basis sets were used for all other

Table 5.3. Selected Experimental Geometrical Parameters for CH_2CN^- in the X-ray Crystal Structures of *cis*-OsO_2F_4·[Cs][CH_2CN], *cis*-OsO_2F_4·[$N(CH_3)_4$][CH_2CN], and *cis*-OsO_2F_4·[Cs][CH_2CN]·0.3HF and the Calculated Geometrical Parameters for CH_2CN^- [a]

	exptl					calcd			
	cis-OsO_2F_4·[Cs][CH_2CN]	*cis*-OsO_2F_4·[$N(CH_3)_4$][CH_2CN]	*cis*-OsO_2F_4·[Cs][CH_2CN]·0.3HF			B3LYP[b]	B3LYP[c]	PBE1PBE[b]	PBE1PBE[c]
			Bond Lengths (Å)						
C(1)–C(2)	1.449(7)	1.469(6)	1.48(3)	1.42(3)	1.42(3)	1.400	1.380	1.396	1.379
C(2)–N(1)	1.136(6)	1.144(6)	1.15(3)	1.15(3)	1.15(3)	1.182	1.179	1.181	1.178
C(1)–H(1A)	0.81(6)	0.905	0.83	1.09	0.97	1.099	1.082	1.098	1.083
C(1)–H(1B)	0.81(6)	0.928	1.50	1.09	0.97				
N(1)···F(13)			1.57(4)	1.61(6)	1.28(6)				
			Bond Angles (deg)						
C(1)–C(2)–N(1)	179.7(6)	179.1(5)	175(2)	175(2)	178(2)	176.2	178.3	176.3	178.2
H(1A)–C(1)–H(1B)	102(6)	109.5	135.0	80.9	78.8	113.7	117.6	111.6	117.5
H(1A)–C(1)–C(2)	116(5)	102.5	113.2	108.8	117.7	110.9	119.3	113.9	118.9
H(1B)–C(1)–C(2)	107(5)	106.1	110.6	108.8	117.7				
C(2)–N(1)···F(13)			97(2)	121(3)	94(3)				

[a] See Figure 5.6b for the atom labeling scheme and Table C1 for a complete listing of bond lengths and bond angles. [b] The 6-21G* basis set was used. [c] The aug-cc-pVTZ basis set was used

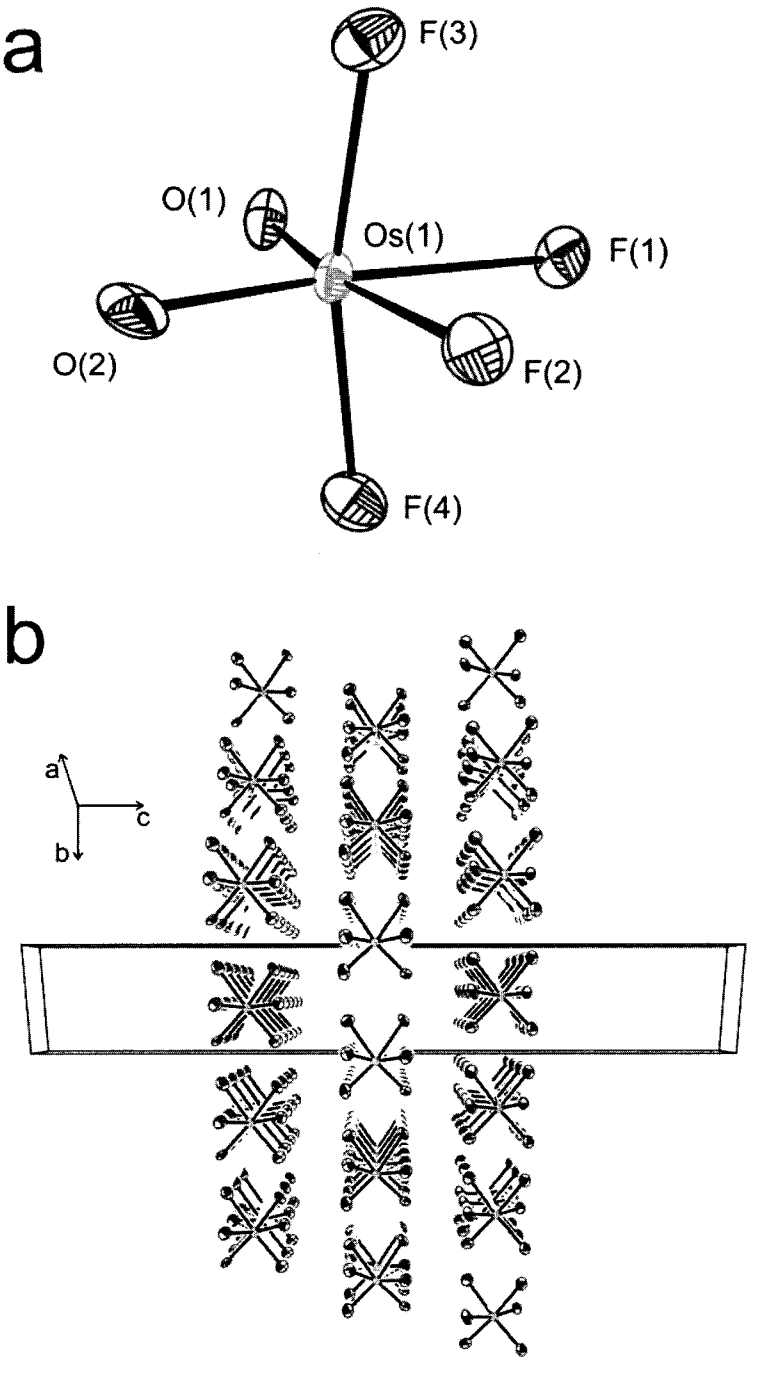

Figure 5.1. (a) Structural unit in the X-ray crystal structure of *cis*-OsO_2F_4 with thermal ellipsoids drawn at the 50% probability level. (b) The crystallographic unit cell of *cis*-OsO_2F_4 viewed along the *a*-axis.

The *cis*-OsO_2F_4 molecules are well isolated and the resulting intermolecular contacts are long and near the sums of the van der Waals radii.[165, 204]

The asymmetric units of the *cis*-OsO_2F_4·[Cs][CH_2CN] (Figure 5.2a), *cis*-OsO_2F_4·[Cs][CH_2CN]·0.3HF (Figure 5.3), and *cis*-OsO_2F_4·[$N(CH_3)_4$][CH_2CN] (Figure 5.2b) consist of well isolated *cis*-OsO_2F_4, CH_2CN^-, and M^+ units (M^+ = Cs^+, $N(CH_3)_4^+$), and the packing (Figures C1-C3) in each structure is similar.[205] The *cis*-OsO_2F_4·[$N(CH_3)_4$][CH_2CN] structure displays significant hydrogen bonding between the protons on CH_2CN^- and an oxygen and a fluorine atom of *cis*-OsO_2F_4 (H(6A)---O(1), 2.568; H(6B)---F(4), 2.497 Å). All of the other intermolecular contacts are long and near the sums of the van der Waals radii.[165, 206-208]

The structure of *cis*-OsO_2F_4·[Cs][CH_2CN]·0.3HF also contains three short N···F contacts (1.606(60), 1.569(36), and 1.280(67) Å) between the CH_2CN^- anion and the HF molecules. Determination of the fluorine atom position is hampered because it is partially occupied. As a result, it is not possible to specify the hydrogen position of the HF molecule. It is therefore not possible to discuss the position of the HF molecule in an unambiguous fashion. The presence of the HF molecule confirms the mechanism proposed for formation of CH_2CN^- (eqs 5.5 and 5.6). This structure is unique because there are no free HF molecules in the crystal lattices of *cis*-OsO_2F_4·[Cs][CH_2CN] and *cis*-OsO_2F_4·[$N(CH_3)_4$][CH_2CN]; the HF corresponding to these products is likely retained solution.

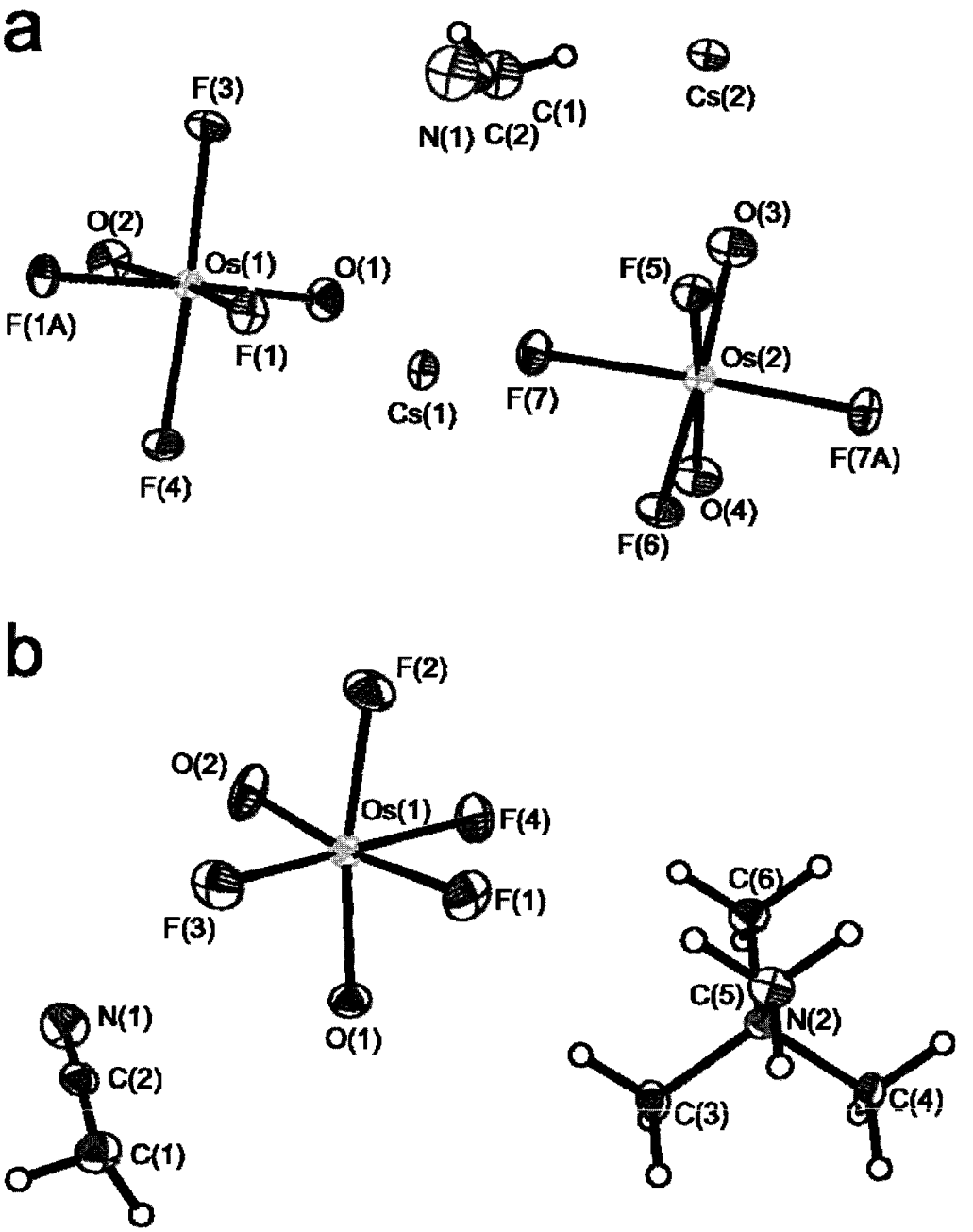

Figure 5.2. Structural units in the X-ray crystal structures of (a) *cis*-OsO_2F_4·[Cs][CH_2CN] and (b) *cis*-OsO_2F_4·[$N(CH_3)_4$][CH_2CN] with thermal ellipsoids drawn at the 50% probability level.

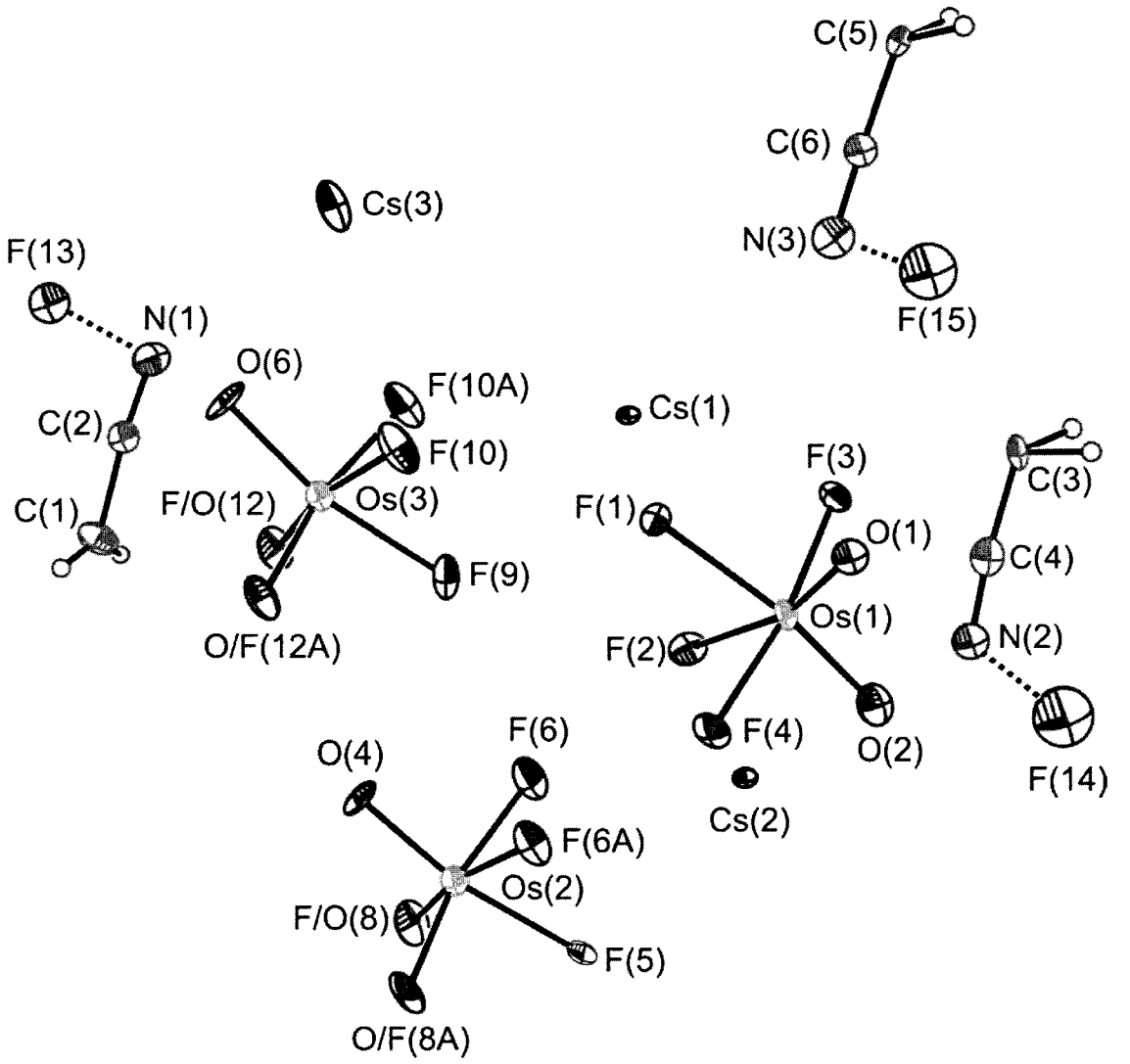

Figure 5.3. Structural unit in the X-ray crystal structure of *cis*-OsO_2F_4·[Cs][CH_2CN]·0.3HF with thermal ellipsoids drawn at the 50% probability level.

5.2.5.1. *cis*-OsO_2F_4

The OsO_2F_4 molecules in the crystal structures of *cis*-OsO_2F_4, *cis*-OsO_2F_4·[Cs][CH_2CN], *cis*-OsO_2F_4·[Cs][CH_2CN]·0.3HF, and *cis*-OsO_2F_4·[$N(CH_3)_4$][CH_2CN] are pseudo-octahedral with *cis*-dioxo geometries consistent with the previously published gas-phase electron diffraction structure,[20] and other d^0 transition metal oxide fluorides such as *cis*-$OsO_2F_3^+$,[139] *cis*-F(*cis*-$OsO_2F_3)_2^+$,[22] *cis*-MoO_2F_2·2THF (THF = tetrahydrofuran),[44] *cis*-$TcO_2F_4^-$,[47] *cis*-TcO_2F_3,[46] *cis*-ReO_2F_3,[45] *cis*-$ReO_2F_4^-$,[45] μ-F(*cis*-$ReO_2F_3)_2^-$,[45] and *cis*-$Re_3O_6F_{10}^-$ [45] and has been previously discussed in detail.[139]

The *cis*-OsO_2F_4·[Cs][CH_2CN]·0.3HF structure contains three distinct *cis*-OsO_2F_4 molecules, two of which have symmetry imposed 50:50 positional disorders between an oxygen and an axial fluorine atom. The disordered Os–O/F bond length (1.774 (10) Å) is intermediate with respect to the Os–O(1,2) (1.688(12) and 1.724(10) Å) and the axial Os–F(3,4) bond lengths (1.909(8) and 1.888(8) Å, respectively) of the non-disordered *cis*-OsO_2F_4 molecule in *cis*-OsO_2F_4·[Cs][CH_2CN]·0.3HF. For the purpose of the current discussion, only the ordered *cis*-OsO_2F_4 molecule will be discussed in detail.

With the exception of *cis*-OsO_2F_4·[$N(CH_3)_4$][CH_2CN], the Os–O bond lengths for each *cis*-OsO_2F_4 molecule are equal within $\pm 3\sigma$ (see Table 5.2) and are elongated when compared with those of the gas-phase electron diffraction structure (1.674(4) Å).[20] The *cis*-OsO_2F_4 molecule of *cis*-OsO_2F_4·[$N(CH_3)_4$][CH_2CN] has Os–O bond lengths that differ significantly (1.670(4) and 1.756(3) Å). The O(1) atom hydrogen bonds to the protons of CH_2CN^- (H(6A)···O(1), 2.568 Å) and $N(CH_3)_4^+$ (O(1)···H(1A), 2.686 Å,

O(1)···H(3A), 2.655 Å). These hydrogen bonding interactions withdraw electron density from the oxygen atom and elongate the Os–O(1) bond. The shorter Os–O(2) bond length is attributed to greater electron donation from the oxygen *p*-orbitals to the *d*-orbital of the Os atom that results in elongation of the Os–O(1) bond.

In all four structures, the Os–F(1,2) bonds trans to Os–O bonds are longer than the Os–F(3,4) bonds cis to Os–O bonds, in accordance with the electron diffraction study[20] and other d^0 *cis*-dioxo transition metal oxide fluoride species such as *cis*-$OsO_2F_3^+$,[139] *cis*-MoO_2F_2·2THF (THF = tetrahydrofuran),[44] *cis*-$TcO_2F_4^-$,[47] *cis*-TcO_2F_3,[46] *cis*-ReO_2F_3,[45] and *cis*-$ReO_2F_4^-$[45] and has been previously discussed in detail for the isovalent $TcO_2F_4^-$ anion (Tc–F(3,4), 1.876(3); Tc–F(1,2), 1.986(3) Å).[47] The Os–F(3,4) bond lengths in the X-ray crystal structure of *cis*-OsO_2F_4 (1.837(8) and 1.839(10) Å) are similar to those in the electron diffraction study (1.843(3) Å) while the Os–F(1,2) bonds (1.914(8) and 1.916(8) Å) are slightly elongated (1.883(3) Å).[20] It is interesting to note that the Os–F bond lengths determined from the X-ray crystal structure of *cis*-OsO_2F_4 are all shorter than the corresponding Os–F bond lengths for the *cis*-OsO_2F_4 molecules in the *cis*-OsO_2F_4·[Cs][CH_2CN], *cis*-OsO_2F_4·[Cs][CH_2CN]·0.3HF, and *cis*-OsO_2F_4·[$N(CH_3)_4$][CH_2CN] structures.

The *cis*-OsO_2F_4·[$N(CH_3)_4$][CH_2CN] structure contains short cation-anion contacts between the O atoms and the H atoms of CH_2CN^- or $N(CH_3)_4^+$ (vide supra) resulting in a difference in the Os–F(1,2) bond lengths. The Os–F(1) bond trans to the short Os–O(2) bond (1.937(3) Å) is longer than the Os–F(2) bond trans to the longer Os–O(1) bond (1.956(3) Å). The difference in the Os–F(1,2) bond length is likely also influenced by the

F(3,4)···H contacts with the anion and cation in the unit cell where F(4) has only one contact to a proton (F(4)···H(1BA) 2.371 Å), resulting in a shorter Os–F bond length than for F(3) which has two contacts to protons (F(3)···H(2BA/4BA) 2.377/2.376 Å).

The F(3)–Os–F(4) bond angles of all four structures bend away from the oxygen atoms (see Table 5.2) and are similar to the bond angle obtained from the gas-phase electron diffraction study (170(4)°).[20] Similar deviations from 180° have also been observed for *cis*-$OsO_2F_3^+$ (159.6(2)°),[139] μ-F(*cis*-$OsO_2F_3)_2^+$ (161.2(10)°),[22] *cis*-$ReO_2F_4^-$ (162.9(6)°),[45] μ-F(*cis*-$ReO_2F_3)_2^{2-}$ (159.9(5)°),[45] *cis*-$Re_3O_6F_{10}^-$ (159.2(3)°),[45] and *cis*-$TcO_2F_4^-$ (164.2(3)°),[47] and can be accounted for based on stronger bond pair-bond pair repulsions between the Os–F(3,4) bond pairs and the Os–O(1,2) double bond pairs than between the Os–F(3,4) bond pairs and the Os–F(1,2) bond pairs.[47]

The light atoms of *cis*-OsO_2F_4 in all four structures form distorted octahedral coordination spheres about their respective osmium atoms. Although there is significant variation in the bond lengths around the osmium atoms, the light atom octahedra are relatively undistorted (Figure C4), as shown by the nearest neighbor-ligand atom contacts (Table C2). The Os atom is located in the O(1)O(2)F(1)F(2)-planes of the *cis*-OsO_2F_4·[Cs][CH_2CN], *cis*-OsO_2F_4·[$N(CH_3)_4$][CH_2CN], *cis*-OsO_2F_4·[Cs][CH_2CN]·0.3HF and *cis*-OsO_2F_4 structures (coplanar to within ±0.0009, 0.028, 0.0002, and 0.0033 Å, respectively) and is symmetrically displaced towards both oxygen atoms (0.1716 and 0.1716 Å; 0.188 and 0.122 Å; 0.184 and 0.171 Å; 0.167 and 0.168 Å, respectively), with the orthogonal [O(1), F(2), F(3), F(4)]- and [O(2), F(1), F(3), F(4)]-planes bisecting each other, similar to that of *cis*-$OsO_2F_3^+$ (0.314 Å).[139]

5.2.5.2. CH_2CN^-

The CH_2CN^- anion co-crystallized in the structures of *cis*-OsO_2F_4·[Cs][CH_2CN], *cis*-OsO_2F_4·[Cs][CH_2CN]·0.3HF, and *cis*-OsO_2F_4·[$N(CH_3)_4$]-[CH_2CN] providing the first instances in which the structure of the isolated CH_2CN^- anion has been crystallographically determined. The CH_2CN^- anion is a reactive intermediate in condensation reactions involving nitriles,[55] and has been used in organic synthesis as a nucleophile[56] or as a ligand in organometallic chemistry where it is C-coordinated (e.g., $P(CH_2CN)_3$,[57] $[(Ph_3P)_2N][Ir(CO)_2(CH_2CN)_2]$,[58] and $[Li(THF)][Zn_3(CH_2CN)_3(LiBr)(NP(CH_3)_3)_4]$[59]).

In all three structures, the C–C (1.449(7), 1.56(2), and 1.469(6) Å, respectively) and C–N (1.136(6), 1.10(3), and 1.144(6) Å, respectively) bond lengths are similar and, with the exception of *cis*-OsO_2F_4·[Cs][CH_2CN]·0.3HF, are equal to within ±3σ. The C–C and C–N bond lengths are in good agreement with those of free CH_3CN (1.54(2); 1.16(1) Å)[209] and other co-crystallized CH_3CN molecules (eg., $OsO_3F_2(NCCH_3)$·CH_3CN (1.437(5); 1.140(4) Å)[155] and $ReO_3F(NCCH_3)_2$·CH_3CN (1.451(7); 1.136(7) Å))[45] as well as for CH_2CN^- ligands (e.g., $P(CH_2CN)_3$ (1.457(2); 1.142(2) Å),[57] $Ir(CO)_2(CH_2CN)_2$ (1.45(1); 1.114(9) Å),[58] and $Zn_3(CH_2CN)_3(LiBr)(NPMe_3)_4^-$ (1.38(2) and 1.16(2) Å)[59]).

The N–C–C bond angle of CH_2CN^- is, as expected, linear, (179.7(6), 176(2), and 179.1(5), respectively) and is consistent with free CH_3CN (180°),[209] other co-crystallized CH_3CN molecules (e.g., $OsO_3F_2(NCCH_3)$·CH_3CN, 178.6(3)[155] and $ReO_3F(NCCH_3)_2$·CH_3CN, 178.9(9)°[45]), and C-coordinated CH_2CN^- ligands (e.g., $P(CH_2CN)_3$ (179.2(9)°),[57] $Ir(CO)_2(CH_2CN)_2$ (178(1)°),[58] and

$Zn_3(CH_2CN)_3(LiBr)(NPMe_3)_4^-$ (175(2) °)[59]). The C–H bond lengths (av. 0.93 Å) and H–C–H bond angles (av. 92.8 °) are in good agreement with each other and the calculated values with the exception of C(1)–H(1B) (1.50 Å) because there is a short hydrogen bond to an HF molecule (H(1B)···F(14A) 1.78 Å) which results in the H(1A)–C(1)–H(1B) bond angle being more open (135 °) than for any other CH_2CN^- anion.

5.2.6. Raman Spectroscopy

The low-temperature (–150 °C) Raman spectra of natural abundance and ^{18}O- enriched *cis*-OsO_2F_4 are shown in Figure 5.4. The Raman spectrum of [K][CH_2CN] is shown in Figure 5.5. The observed and calculated frequencies and mode descriptions for *cis*-OsO_2F_4 and CH_2CN^- are provided in Tables 5.4, and 5.5 where the atom numbering schemes are given in Figures 5.6a and 5.6b.

5.2.6.1. *cis*-OsO_2F_4

The Raman spectrum of *cis*-OsO_2F_4 has been previously assigned under C_{2v} symmetry[20] and has been used as a computational benchmark for other Os(VIII) oxide fluoride systems.[18, 139, 155, 203] The present work details the observed and calculated frequencies of ^{18}O-enriched *cis*-OsO_2F_4 and its comparison with that of natural abundance *cis*-OsO_2F_4. The Raman spectra of OsO_4 and $Os^{18}O_4$ have been recorded and used as a benchmark for the vibrational frequencies of the OsO_2 group and for $^{16/18}Os$ isotopic shifts.

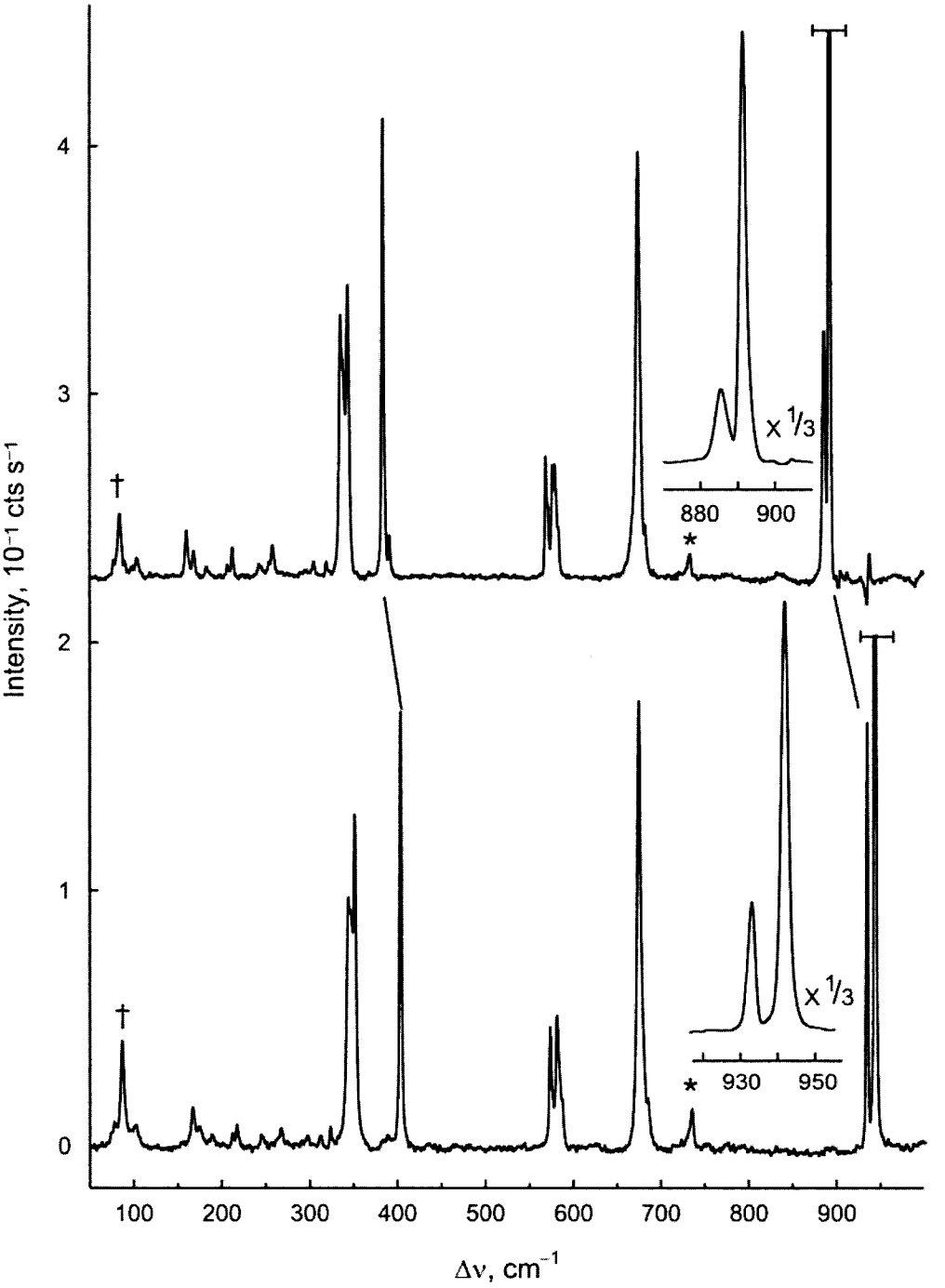

Figure 5.4. Raman spectra of *cis*-OsO_2F_4 (bottom) and *cis*-$Os^{18}O_2F_4$ (top) recorded at –150 °C using 1064-nm excitation; the symbols denote FEP sample tube lines (*) and an instrumental artifact (†).

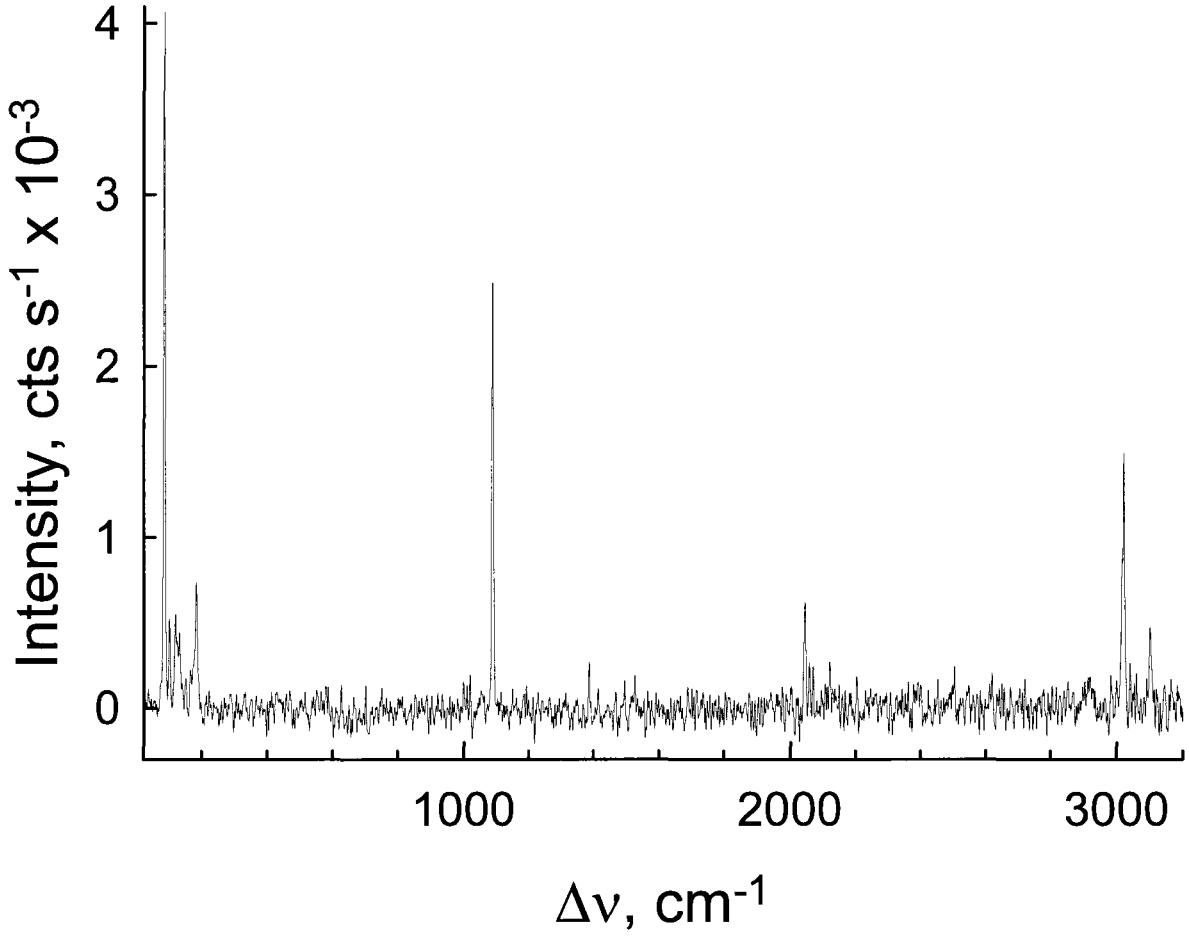

Figure 5.5. Raman spectrum of [K][CH_2CN] recorded in a 4-mm-o.d. glass tube at −150 °C using 1064-nm excitation.

Table 5.4. Experimental and Calculated Raman Frequencies and Intensities for *cis*-OsO_2F_4 and *cis*-$Os^{18}O_2F_4$

exptl[a]		calcd[b]						assgnts (C_{2v})[e]
cis-OsO_2F_4	*cis*-$Os^{18}O_2F_4$	*cis*-OsO_2F_4	*cis*-$Os^{18}O_2F_4$	*cis*-OsO_2F_4	*cis*-$Os^{18}O_2F_4$	*cis*-OsO_2F_4	*cis*-$Os^{18}O_2F_4$	
		SVWN[c]		PBE1PBE[d]		B3LYP[d]		
942.1(100)	891.2(100)	972.7(31)[57]	920.3(27)[53]	1057.2(37)[67]	1000.2(33)[62]	1018.7(36)[63]	963.8(33)[58]	$\nu_{sym}(OsO_2)$
933.1(31)	885.4(15)	968.5(13)[90]	919.0(11)[85]	1028.3(14)[119]	975.6(12)[112]	992.6(14)[109]	941.8(12)[103]	$\nu_{as}(OsO_2)$
683.3(sh)	682.5(3)	702.7(<1)[166]	702.6(<1)[166]	708.2(19)[84]	708.2(19)[84]	684.4(21)[78]	684.4(21)[78]	$\nu_{as}(OsF_3)$
672.7(59)	673.6(29)	692.1(24)[50]	692.0(24)[50]	703.5(<0.1)[209]	703.3(<0.1)[210]	682.7(<0.1)[197]	682.4(<0.1)[198]	$\nu_{sym}(OsF_3) + \nu_{sym}(OsF_1)$
577.7(17)	578.8(7)	632.2(12)[35]	632.1(12)[34]	635.9(6)[40]	635.8(6)[40]	615.9(8)[35]	615.8(8)[35]	$\nu_{sym}(OsF_3) - \nu_{sym}(OsF_1)$
570.1(14)	568.6(8)	612.2(11)[55]	611.5(12)[54]	621.2(6)[74]	620.6(6)[73]	602.8(8)[68]	602.1(8)[67]	$\nu_{as}(OsF_1)$
401.6(38)	383.3(31)	383.6(5)[1]	367.0(5)[1]	425.7(5)[1]	407.4(4)[1]	415.8(5)[2]	397.9(4)[1]	$\delta(O_1OsO_1')$
349.9(31)	343.2(20)	329.8(4)[3]	323.0(4)[1]	355.7(4)[0]	349.2(4)[0]	347.5(4)[0]	341.1(4)[0]	$\delta(F_1OsF_1') + \delta(F_3OsF_3')$
342.0(31)	335.0(18)	329.0(5)[0]	322.9(5)[0]	355.2(4)[4]	348.5(3)[1]	347.2(4)[4]	340.2(4)[2]	$\delta(OOsF_1) + \delta(F_1OsF_1')$
321.4(1)	318.7(1)	312.4(<1)[11]	310.2(<1)[11]	337.4(<1)[12]	335.4(<1)[12]	329.4(<1)[12]	327.6(<1)[12]	$\rho_r(F_3OsF_3')$
304.4 (1)	304.2(1)	298.0(1)[19]	293.4(1)[18]	321.5(1)[25]	316.4(<1)[24]	316.6(1)[24]	311.5(1)[23]	$\rho_t(O_1OsO_1')$
265.1 (2)	257.6(2)	252.6(<0.1)[36]	247.6(<0.1)[36]	268.0(<0.1)[45]	262.2(<1)[44]	266.4(<0.1)[43]	260.9(<0.1)[43]	$\rho_r(F_1OsF_1')$
215.1 (1)	211.8(2)	217.7(<1)[1]	216.1(<1)[1]	236.1(<1)[2]	234.7(<1)[2]	230.3(<1)[2]	228.9(<1)[2]	$\delta(F_1OsF_1') - \delta(F_3OsF_3')$
165.6 (3)	159.8(2)	185.9(<1)[<1]	183.1(<1)[1]	203.3(<1)[1]	200.2(<1)[1]	200.5(<1)[1]	197.5(<1)[1]	$\delta(OOsF_1) - \delta(F_3OsF_3')$
104.0(sh)	103.6(1)	100.4(<1)[0]	97.9(<1)[0]	108.9(<1)[0]	106.0(<1)[0]	111.3(<1)[0]	108.4(<1)[0]	$\rho_t(F_1OsF_1')$

[a] The Raman spectrum was recorded on a microcrystalline solid sample in a FEP tube at –150 °C using 1064-nm excitation. Experimental Raman intensities are given in parentheses and are relative intensities with the most intense band given as 100. [b] Values in parentheses denote calculated Raman intensities ($Å^4\,u^{-1}$) and values in square brackets denote calculated infrared intensities (km mol^{-1}). [c] The SDDall basis set was used augmented for F and O with two d-type polarization functions. [d] The Stuttgart basis set was used for Os with the f functional. The aug-cc-pVTZ basis sets were used for fluorine and oxygen. [e] The atom labeling scheme refers to the Figure 5.6a. The abbreviations denote stretch (ν), asymmetric (as), symmetric (sym), bend (δ), twist (ρ_t) and rock (ρ_r).

Table 5.5. Experimental Raman Frequencies and Intensities for [K][CH_2CN] and Calculated Frequencies, Intensities and Assignments for CH_2CN^-

exptl			calcd[e]				assgnt (C_s)[h]
Raman	IR[b]		B3LYP		PBE1PBE		
[a]	[c]	[d]	[f]	[g]	[f]	[g]	
3099(19)	3260 s	3350 m	3046(92)[120]	3190(105)[37]	3101(90)[100]	3216(100)[34]	A", $\nu_{as}(CH_2)$
3021(60)	3130 br	3250 m	3006(132)[66]	3121(260)[20]	3050(130)[53]	3141(221)[20]	A', $\nu_s(CH_2)$
	2240 s						
2038(25)	2160 s	2200 s	2209(40)[231]	2138(543)[691]	2236(40)[244]	2168(429)[680]	A', ν(CN)
	2050 s						
		1610 s					
1386(10)		1250 m	1485(23)[1]	1424(18)[7]	1477(20)[1]	1413(15)[7]	A', δ(HCH)
1086(100)		900 m	1051(13)[14]	1075(27)[30]	1072(14)[15]	1089(33)[30]	A', ν(CC)
			1113(6)[1]	1034(12)[<1]	1105(6)[1]	1028(9)[<1]	A", ρ_r(HCH)
		615 m,br	611(4)[58]	566(20)[1]	618(3)[47]	576(12)[1]	A', $\delta(CCN)_{oop}$
		532 m,br 472 m,br	463(2)[7]	436(1)[4]	467(2)[7]	440(1)[4]	A", $\delta(CCN)_{oop} + \rho_r$(HCH)
183(30)		280 m	523(10)[142]	214(201)[240]	502(10)[166]	231(152)[236]	A', ρ_w(HCH)
129(17)							
122(16)							
118(22)							lattice modes
100(20)							

[a] The Raman spectrum was recorded on a microcrystalline solid sample in a glass tube at 24 °C using 1064-nm excitation. Experimental Raman intensities are given in parentheses and are relative intensities with the most intense band given as 100. [b] The abbreviations denote strong (s) and broad (br). [c] From Ref 55. [d] From Ref 60 [e] Values in parentheses denote calculated Raman intensities ($Å^4\,u^{-1}$) and values in square brackets denote calculated infrared intensities (km mol^{-1}). [f] The 6-21G* basis set was used. [g] The aug-cc-pVTZ basis set was used [h] Assignments are for the energy-minimized geometry calculated at the PBE1PBE/aug-cc-pVTZ level of theory. See Figure 5.6b for the atom labeling scheme. The symbols denote stretch (ν), bend (δ), rock (ρ_r), wag (ρ_w) and out-of-plane (oop).

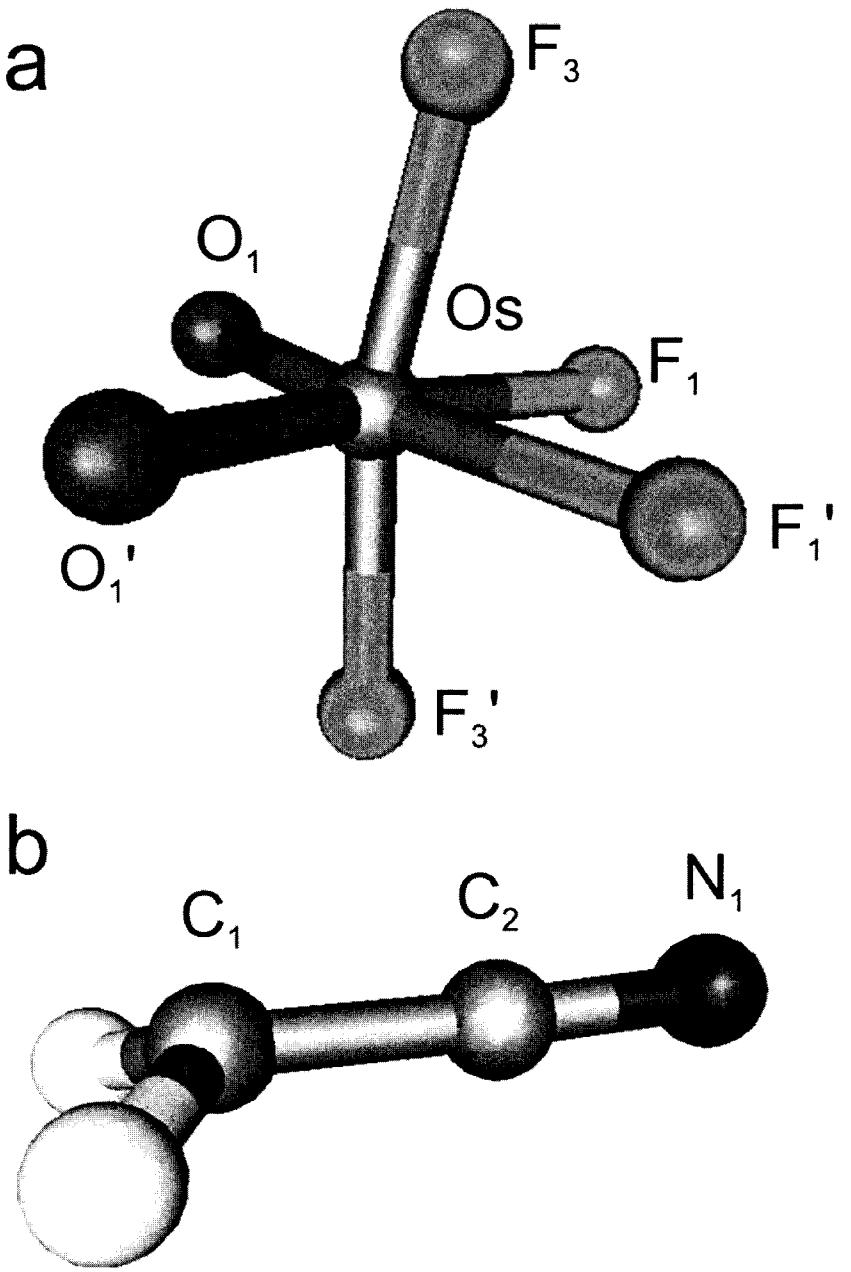

Figure 5.6. Gas-phase geometries calculated at the B3LYP level of theory for (a) *cis*-OsO_2F_4 (C_{2v}) and (b) CH_2CN^- (C_s).

The Raman spectrum of ^{18}O-enriched *cis*-OsO_2F_4 is similar to that of the natural abundance *cis*-OsO_2F_4 with the modes involving ^{18}O atoms shifted to lower frequency. The shift is most pronounced for the OsO_2 stretches which shift from 942.1 to 891.2 cm^{-1} for $\nu_s(OsO_2)$ and from 933.1 to 885.4 cm^{-1} for $\nu_{as}(OsO_2)$. These isotopic shifts ($\Delta\nu_s$= –50.9; $\Delta\nu_{as}$ = –47.7 cm^{-1}) are reproduced at all levels of theory ($\Delta\nu_s$ = –52.4 [SVWN]; –57.0 [PBE1PBE]; –54.9 [B3LYP]; $\Delta\nu_{as}$ = –49.5 [SVWN]; –52.7 [PBE1PBE]; –50.8 [B3LYP] cm^{-1}) and are comparable to the shifts observed and calculated for OsO_4 ($\Delta\nu_s$ = –54.9 [exptl]; –56.6 [SVWN]; –58.6 [B3LYP]; $\Delta\nu_{as}$ = –55.5 [exptl]; –50.1 [SVWN]; –50.9 [B3LYP] cm^{-1}) (see Section 5.2.7.3) The Os–F stretching modes are not significantly affected by ^{18}O-enrichment as expected (683.3/672.7/577.7/570.1 [$Os^{16}O_2F_4$]; 682.5/673.6/578.8/568.6 [$Os^{18}O_2F_4$] cm^{-1}).

Of the bending modes, $\delta(O_1OsO_1')$ shows the largest $^{16/18}O$ isotopic shift ($\Delta\nu$ = –18.3 cm^{-1}). The remaining bending modes do not show large shifts (< 8 cm^{-1}) because the oxygen atom displacements are not large components of the vibrational modes.

5.2.6.2. CH_2CN^-

The infrared spectrum of [A][CH_2CN] (A = Li[60] and Na[55]) has been previously reported, however, spectral assignments were not provided. In the present study, the Raman spectrum is reported and spectral assignments were made by comparison with the calculated frequencies and infrared and Raman intensities for the energy-minimized geometries of CH_2CN^- and the previously reported experimental infrared frequencies and intensities.

The CH_2CN^- (C_s) anion possesses nine fundamental vibrational modes belonging to the irreducible representations, 6A' + 3A", all of which are predicted to be Raman and infrared active. The calculated stretching modes are slightly overestimated when compared to experiment.

The symmetric (3021 cm^{-1}) and asymmetric (3099 cm^{-1}) stretching frequencies of the CH_2 group are in good agreement with the previously published infrared values for [A][CH_2CN] (A = Li, 3250 and 3350;[60] Na, 3130 and 3260 cm^{-1},[55] respectively). Both stretches are shifted to higher frequencies when compared with the symmetric and asymmetric CH_3 stretches of CH_3CN (2938 and 2999 cm^{-1}, respectively),[155] consistent with the removal of a proton which strengthens the remaining C–H bonds. The ν(CN) stretching band (2038 cm^{-1}) occurs at lower frequency than that of the Li^+ (2200 cm^{-1})[60] and Na^+ (2240/2160/2050 cm^{-1})[55] salts and free CH_3CN (2248 cm^{-1}).[155] The ν(CC) stretching mode (1086 cm^{-1}) has only been previously observed for the Li^+ salt (900 cm^{-1})[60] and is shifted to higher frequency relative to that of free CH_3CN (922 cm^{-1}).[155] The low-frequency shift of the C–N stretch and the high-frequency shift of the C–C stretch are consistent with the resonance structures depicted in Scheme 5.1, whereby the negative charge is distributed between the terminal N and C atoms and, as a result, the C–C bond is strengthened and the C–N bond weakened. The only observed bending mode, δ(HCH) (1386 cm^{-1}) is comparable to that of free CH_3CN (1376 cm^{-1}) and occurs at higher frequency relative to [Li][CH_2CN] (1250 cm^{-1}). The two bending modes that are predicted to have the highest intensities, δ(HCH) (1386 cm^{-1}) and ρ_w(HCH)

(183 cm^{-1}) are observed, whereas the $\rho_r(HCH)$, $\delta(CCN)_{oop}$, and $\delta(CCN)_{oop} + \rho_r(HCH)$ bends are predicted to be weak, and are not observed.

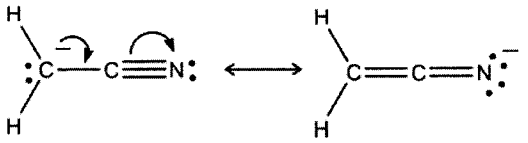

Scheme 5.1. Resonance structures for CH_2CN^-.

5.2.7. Computational Results

The calculated geometries of *cis*-OsO_2F_4 (Figure 5.6a, Table 5.2) and CH_2CN^- (Figure 5.6b, Table 5.3) were optimized under C_{2v} and C_s symmetries, respectively at the SVWN, B3LYP, PBE1PBE and B3LYP, PBE1PBE levels of theory, respectively, and resulted in stationary points with all frequencies real. The vibrational modes of the B3LYP structure provide the best approximation and these values are referred to in the ensuing discussion. The energy-minimized geometries and vibrational frequencies of OsO_4 and $Os^{18}O_4$ were calculated to serve as benchmarks for the isotopic enrichment study, while CH_3CN (C_{3v}) was calculated to serve as a benchmark and for comparison with CH_2CN^-. The values B3LYP/aug-cc-pVTZ are, overall, in better agreement with experiment for CH_2CN^- than the remaining levels, and will therefore be referred to in the ensuing discussion.

5.2.7.1. Calculated Geometries

5.2.7.1.1. *cis*-OsO_2F_4

The geometrical parameters of the *cis*-OsO_2F_4 molecule in the crystal structure of *cis*-OsO_2F_4 are used for comparison with the calculated parameters in the ensuing discussion. The present calculated structures provide more accurate geometrical

parameters and vibrational frequencies than those previously calculated.[20] The *cis*-OsO_2F_4 structure does not contain any co-crystallized molecules and is in good agreement with the structures of other *cis*-OsO_2F_4 molecules obtained in this study from structures containing the CH_2CN^- anion (see Section 5.2.5.1). The calculated Os–O_1 (1.688 Å), Os–F_1 (1.887 Å), and Os–F_3 (1.857 Å) bond lengths are comparable to the experimental Os–O(1/2) (1.68(1) – 1.70(1) Å), Os–F(1/2) (1.914(8) – 1.916(8) Å), and Os–F(3/4) (1.837(8) – 1.84(1) Å) bond lengths, with the largest discrepancy occurring for the Os–F_1 bond length. This underestimation likely results because the calculations fail to model secondary bonding interactions that are present in the crystal structure.

The O_1–Os–O_1' bond angle is calculated to be slightly more closed (100.8°) when compared with the experimental (102.8(7)°). In contrast, the calculated F_1–Os–F_1' (79.9°) and F_3–Os–F_3' (167.5°) bond angles are in good agreement with experiment (79.5(5) and 166.6(6)°, respectively), reproducing the displacement of the fluorine atoms away from the oxygen double bond domains.

5.2.7.1.2. CH_2CN^-

The present calculated geometrical parameters of CH_2CN^- agree well with the experimental results and the previously calculated geometries.[210-212] The geometrical parameters are explicitly compared with those of the CH_2CN^- anion in *cis*-OsO_2F_4·[Cs][CH_2CN] because of the lower number of intermolecular interactions in that structure (see Section 5.2.5.2).

The C–N bond length (1.181 Å) is somewhat overestimated compared to the experimental value (1.136(6) Å), whereas the C–C bond length (1.380 Å) is significantly

underestimated (1.449(7) Å). This bond length trend is consistent with a predicted stronger C–C and a weaker C–N bond, consistent with the vibrational assignments (see Section 5.2.6.2.). The C–C–N bond angle (178.3°) is close to linear, and is in good agreement with experiment (179.7(6)°). The C–H bond length is significantly overestimated (1.082 Å) compared to the experimental values (0.81(6) Å) while the H–C–H and H–C–C bond angles are more open (117.6 and 119.3°, respectively).

5.2.7.2. Charges, Valencies, and Bond Orders

Natural Bond Orbital (NBO)[181-184] analyses were carried out for the gas-phase geometries of *cis*-OsO_2F_4 optimized at the SVWN, B3LYP, and PBE1PBE levels (Table C3) and CH_2CN^- optimized at the B3LYP and PBE1PBE levels (Table C4).

5.2.7.2.1. *cis*-OsO_2F_4

The NBO analyses give a natural population analysis (NPA) charge of 2.27 for osmium. The NPA charges of all of the light atoms are negative indicating that the bonds formed with the osmium atom are polar covalent. The slightly larger negative charge on the equatorial fluorine atom, F_1 (–0.44), as compared to the axial fluorine atom, F_3 (–0.41), is consistent with the osmium atom withdrawing less charge from the equatorial fluorine atom than the axial one, consistent with the longer bond length (see Calculated Geometries).

The Os–O bond order (0.89) is nearly twice those of the Os–F bonds (F_1, 0.45 and F_3, 0.45) which is consistent with the double bond character of the Os–O bond as compared to the single bond between fluorine and osmium. The Os–F_3 bond order is greater than the Os–F_1 bond order which is again consistent with a stronger Os–F bond trans to fluorine

when compared with a Os–F bond trans to oxygen, which results from the *trans*-influence of oxygen.

5.2.7.2.2. CH_2CN^-

The NPA charges of the atoms in CH_2CN^- alternate along the CCNH chain indicating that the bonding in the anion is polar covalent. The negative charge is located on the terminal C_1 (–0.97) and N_1 (–0.63) atoms, which is consistent with the resonance structure proposed in Scheme 5.1. The C–C (1.24) and C–N (1.86) bond orders are also in accordance with the proposed resonance structure.

5.2.7.3. Isotopic Enrichment of OsO_4

The vibrational spectrum of OsO_4 has been reported and assigned in the gas,[213, 214] liquid,[215] and solid phases[215, 216] and the gas-phase spectrum of $Os^{18}O_4$[213, 214] has also been reported. The present work (Figure 5.7) is in very good agreement with the prior work but also provides the first instance in which the site symmetry lowering was able to be observed as three distinct $\nu_{as}(OsO)$ bands were observed in the solid state. The prior reports have not resolved the broad band assigned to $\nu_{as}(OsO)$[215] and/or only two of these components were resolved.[216] The site symmetry lowering is also present for the double degenerate $\delta_s(OsO_4)$ mode and triply degenerate $\rho_w(OsO_2) + \rho_r(OsO_2)$ modes where only one mode is not resolved. The intramolecular force constants (Urey-Bradley,[213, 217] orbital valence,[213] and valence stretching[218]) for OsO_4 have also been previously determined and the vibrational modes have been calculated, however, they have not been previously calculated and assigned using quantum-chemical methods. The vibrational frequencies of $Os^{16}O_4$ and $Os^{18}O_4$ (Table 5.6) were calculated at the SVWN and B3LYP levels to serve as a benchmark

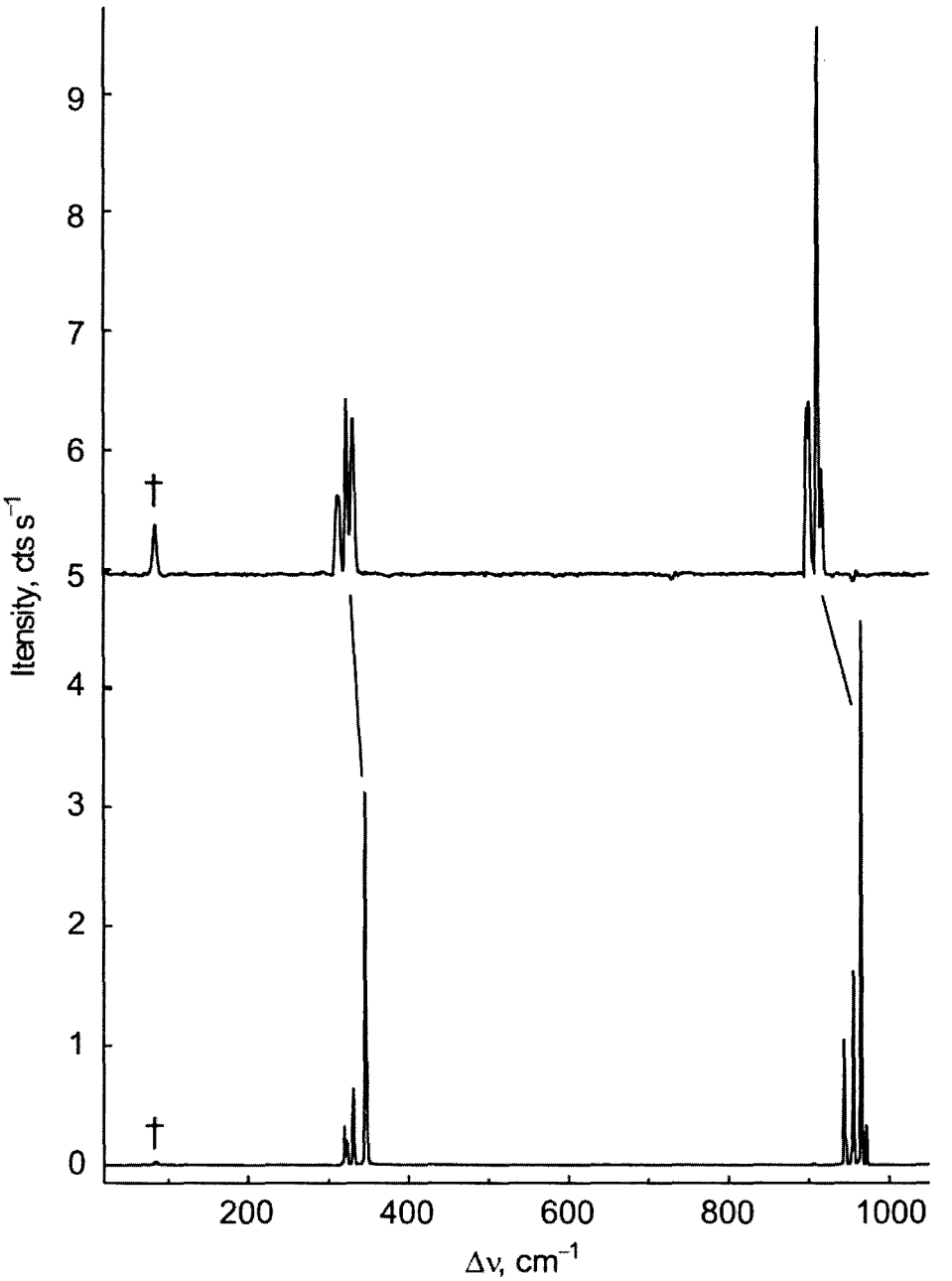

Figure 5.7. Raman spectra of OsO_4 (bottom) and $Os^{18}OF_4$ (top) recorded at –150 °C using 1064-nm excitation; the symbol denotes an instrumental artifact (†).

Table 5.6. Experimental Raman Frequencies and Intensities for OsO_4 and $Os^{18}O_4$ and Calculated Frequencies, Intensities and Assignments for OsO_4 and $Os^{18}O_4$

exptl[a]		calcd[b]				assgnts
		SVWN[d]		B3LYP[e]		
OsO_4	$Os^{18}O_4$	OsO_4	$Os^{18}O_4$	OsO_4	$Os^{18}O_4$	T_d
964.7(100)	909.8(100)	986.2(46)[0]	929.6(31)[0]	1022.9(50)[0]	964.3(45)[0]	A_1, $\nu_s(OsO_4)$
971.6(7) 955.3(37) 943.7(24)	916.1(19) 899.7(31) 896.9(30)	981.1(13)[99]	931.0(11)[89]	999.1(12)[135]	948.2(11)[123]	T_2, $\nu_{as}(OsO_4)$
346.9(70) 330.9(15)	330.4(28) 322.1(31)	332.0(6)[0]	312.9(6)[0]	346.6(6)[0]	326.7(5)[0]	E, $\delta_s(OsO_4)$
323.0(4) 320.1(7)	313.0(sh) 311.6(14)	326.1(2)[3]	310.1(2)[3]	347.7(2)[5]	330.7(2)[5]	T_2, $\rho_w(OsO_2) + \rho_r(OsO_2)$

[a] The Raman spectrum was recorded on a microcrystalline solid sample in a FEP tube at −150 °C using 1064-nm excitation. Experimental Raman intensities are given in parentheses and are relative intensities with the most intense band given as 100. [b] Values in parentheses denote calculated Raman intensities ($Å^4\ u^{-1}$) and values in square brackets denote calculated infrared intensities (km mol^{-1}). [c] Assignments are for the energy-minimized geometry calculated at the SVWN level of theory. The symbols denote symmetric (s), asymmetric (as), stretch (ν), bend (δ), rock (ρ_r), and wag (ρ_w). [d] The SDDall basis set was used augmented for F and O with two d-type polarization functions. [e] The Stuttgart basis set was used for Os with the f functional. The aug-cc-pVTZ basis sets were used for fluorine and oxygen.

for those of *cis*-$Os^{16}O_2F_4$ and *cis*-$Os^{18}O_2F_4$. The calculated isotopic shifts of the $\nu_s(OsO)$ and $\nu_{as}(OsO)$ stretches (–56.6 and –50.1 [SVWN]; –58.6 and –50.9 [B3LYP] cm^{-1}) closely approximate the experimental shifts (–54.9 and –55.6 cm^{-1}). The $\delta_s(OsO_4)$ (–19.1 [SVWN]; –19.9 [B3LYP] cm^{-1}) and $\rho_w(OsO_2) + \rho_r(OsO_2)$ (–16.0 [SVWN]; –17.0 [B3LYP] cm^{-1}) bending modes show much smaller shifts, in good agreement with the experimental results (–16.5 and –10.0 cm^{-1}, respectively).

5.3. Conclusions

The crystal structures of *cis*-$OsO_2F_4 \cdot [Cs][CH_2CN] \cdot 0.3HF$, *cis*-$OsO_2F_4 \cdot [Cs][CH_2CN]$, *cis*-$OsO_2F_4 \cdot [N(CH_3)_4][CH_2CN]$, and *cis*-$OsO_2F_4$ have been obtained, providing the first examples of non-disordered *cis*-OsO_2F_4 molecules providing more precise determinations of its geometrical parameters. The solid-state structure has a pseudo-octahedral, *cis*-dioxo arrangement, and the fluorine atoms trans to oxygen atoms have shorter bond lengths than those trans to fluorine. The compounds, *cis*-$OsO_2F_4 \cdot [Cs][CH_2CN] \cdot 0.3HF$, *cis*-$OsO_2F_4 \cdot [Cs][CH_2CN]$, and *cis*-$OsO_2F_4 \cdot [N(CH_3)_4][CH_2CN]$, were formed by abstraction of a proton from CH_3CN by $OsO_2F_5^-$, yielding CH_2CN^- and *cis*-OsO_2F_4 and the appropriate cation. In addition to *cis*-OsO_2F_4, the crystal structures also contain co-crystallized linear CH_2CN^- anions which provided the crystal structures of this anion for the first time. In a separate synthesis, $[K][CH_2CN]$ was formed and its Raman spectrum was assigned based on the calculated vibrational frequencies of CH_2CN^-. Quantum-chemical calculations have been used to model the gas-phase geometries of both *cis*-OsO_2F_4 and CH_2CN^-.

CHAPTER 6

SYNTHESIS AND X-RAY CRYSTAL STRUCTURE OF $(OsO_3F_2)_2 \cdot 2XeOF_4$ AND THE RAMAN SPECTRUM OF $(OsO_3F_2)_\infty$, $(OsO_3F_2)_2$, AND $(OsO_3F_2)_2 \cdot 2XeOF_4$

6.1. Introduction

Polymeric $(OsO_3F_2)_\infty$ was first synthesized in 1957 by reaction of OsO_4 with BrF_3.[25] However, only the melting point and elemental analyses were reported. Three distinct phases of $(OsO_3F_2)_\infty$ were subsequently identified by X-ray powder diffraction: a low-temperature (< 90 °C) α-phase (monoclinic), a β-phase (orthorhombic) at intermediate temperatures (90–130 °C), and a γ-phase (orthorhombic) at high temperatures (> 130 °C).[19] Single crystals of OsO_3F_2 were obtained by sublimation under static vacuum at 130 °C in a sapphire tube, which resulted in the X-ray crystal structure determination of the low-temperature monoclinic phase (space group $P2_1/c$).[11] The structure consists of an infinite chain in which the pseudo-octahedral Os(VIII) atoms are bridged by fluorine atoms that are trans to oxygen atoms and the three oxygen atoms are in a facial arrangement.

The vibrational characterization of OsO_3F_2 has also been carried out for both the matrix-isolated monomer and $(OsO_3F_2)_\infty$. The infrared[14, 15] and Raman[14] spectra of monomeric OsO_3F_2, obtained in both argon and nitrogen matrices at 12 K, are consistent with a trigonal bipyramidal geometry (D_{3h} symmetry) in which the three oxygen atoms lie in the equatorial plane and the fluorine atoms are in axial positions. Although incompletely assigned, the Raman spectra[16, 17, 19] of solid OsO_3F_2 are consistent with the

low-temperature fluorine-bridged polymeric structure obtained from the single-crystal X-ray structure.[11]

The present chapter details the syntheses and structural characterizations by Raman spectroscopy of a new low-temperature phase of OsO_3F_2, namely $(OsO_3F_2)_2$, and its $XeOF_4$ adduct, $(OsO_3F_2)_2 \cdot 2XeOF_4$, which has also been characterized by single-crystal X-ray diffraction. The Raman spectrum of the low-temperature monoclinic α-phase, $(OsO_3F_2)_\infty$, and its assignments are also reported.

6.2. Results and Discussion

6.2.1. Syntheses of $(OsO_3F_2)_2 \cdot 2XeOF_4$ and $(OsO_3F_2)_2$.

Polymeric OsO_3F_2 slowly dissolved in $XeOF_4$ at room temperature forming a deep orange solution. The ^{19}F NMR spectrum at 30 °C consisted of an exchange-broadened $XeOF_4$ solvent line [$\delta(^{19}F) = 96.0$ ppm, $\Delta\nu_{1/2} = 1800$ Hz] and trace amounts of *cis*-OsO_2F_4 [$\delta(^{19}F) = 68.8$ ppm (t) and 18.5 ppm(t), $^2J(^{19}F-^{19}F) = 138$ Hz)] and XeO_2F_2 [$\delta(^{19}F) = 107.2$ ppm, $\Delta\nu_{1/2} = 521$ Hz]. Fluorine-19 exchange between OsO_3F_2 and $XeOF_4$ solvent not only resulted in broadening of the $XeOF_4$ solvent line, but prevented observation of the fluorine-on-osmium environments of the solute and the ^{129}Xe satellites of the solvent and of XeO_2F_2. The formation of trace amounts of *cis*-OsO_2F_4 and XeO_2F_2 resulted from oxygen/fluorine metathesis between $(OsO_3F_2)_\infty$ and $XeOF_4$ solvent (eq 6.1).

$$^1/_\infty(OsO_3F_2)_\infty + XeOF_4 \xrightarrow[30\ ^\circ C]{XeOF_4} OsO_2F_4 + XeO_2F_2 \qquad (6.1)$$

The sample composition was also monitored at intervals by Raman spectroscopy as $XeOF_4$ was removed under dynamic vacuum at 0 °C (Table D1). The Raman spectrum

of the initial frozen solution was comprised of bands that arose from a mixture of $XeOF_4$ and $(OsO_3F_2)_2{\cdot}2XeOF_4$. Removal of excess $XeOF_4$ at 0 °C yielded an orange solid corresponding to $(OsO_3F_2)_2{\cdot}2XeOF_4$ (eq 6.2). Slow cooling of a solution of

$$^2/_\infty(OsO_3F_2)_\infty + 2XeOF_4 \xrightarrow[25\ ^\circ C]{XeOF_4} (OsO_3F_2)_2{\cdot}2XeOF_4 \qquad (6.2)$$

$(OsO_3F_2)_2{\cdot}2XeOF_4$ in $XeOF_4$ from 25 to 0 °C resulted in light orange needle-shaped crystals of $(OsO_3F_2)_2{\cdot}2XeOF_4$ which were characterized by single-crystal X-ray diffraction (*vide infra*) and which had a Raman spectrum identical to that of the bulk compound. The $(OsO_3F_2)_2{\cdot}2XeOF_4$ adduct was stable at 25 °C for up to 5 h, after which time dissociation to $(OsO_3F_2)_\infty$ and $XeOF_4$ (eq 6.3) was detectable by Raman

$$(OsO_3F_2)_2{\cdot}2XeOF_4 \xrightarrow{25\ ^\circ C} {}^2/_\infty(OsO_3F_2)_\infty + 2XeOF_4 \qquad (6.3)$$

spectroscopy. Upon further pumping under dynamic vacuum at 0 °C, $(OsO_3F_2)_2{\cdot}2XeOF_4$ slowly lost $XeOF_4$ to give a yellow powder corresponding to $(OsO_3F_2)_2$ (eq 6.4), which

$$(OsO_3F_2)_2{\cdot}2XeOF_4 \xrightarrow[0\ ^\circ C]{vac} (OsO_3F_2)_2 + 2XeOF_4 \qquad (6.4)$$

was confirmed by Raman spectroscopy (Table D1). Raman spectroscopy established that the dimer was stable indefinitely at 0 °C, but transformed over a period of 2 h at 25 °C to an orange powder corresponding to the monoclinic polymeric phase, $(OsO_3F_2)_\infty$ (eq 6.5).[19]

$$\infty(OsO_3F_2)_2 \xrightarrow{25\ ^\circ C} 2(OsO_3F_2)_\infty \qquad (6.5)$$

6.2.2. X-ray Crystal Structure of $(OsO_3F_2)_2{\cdot}2XeOF_4$. Details of data collection parameters and other crystallographic information are provided in Table 6.1. Bond lengths and bond angles are listed in Table 6.2.

Table 6.1. Summary of Crystal Data and Refinement Results for $(OsO_3F_2)_2 \cdot 2XeOF_4$

chem formula	$Os_2O_8F_{12}Xe_2$
space group	$P\bar{1}$ (2)
a (Å)	5.0808(6)
b (Å)	7.7446(9)
c (Å)	9.2133(11)
α (deg)	80.012(4)
β (deg)	83.659(4)
γ (deg)	89.217(4)
V (Å^3)	354.8(1)
molecules/unit cell	1
mol wt (g mol^{-1})	999.00
calcd density (g cm^{-3})	24.675
T (°C)	–173
μ (mm^{-1})	22.76
R_1[a]	0.0408
wR_2[b]	0.0988

[a] R_1 is defined as $\Sigma \| F_o | - | F_c \| \Sigma | F_o |$ for $I > 2\sigma(I)$. [b] wR_2 is defined as $[\Sigma[w(F_o^2 - F_c^2)^2]/\Sigma w(F_o^2)^2]^{1/2}$ for $I > 2\sigma(I)$.

Table 6.2. Experimental and Calculated Geometrical Parameters for $(OsO_3F_2)_2 \cdot 2XeOF_4$ and Calculated Geometrical Parameters for $(OsO_3F_2)_2$, $XeOF_4$, and $(OsO_3F_2)_2 \cdot 2XeOF_4$

Bond Lengths (Å)								
$(OsO_3F_2)_2 \cdot 2XeOF_4$					$(OsO_3F_2)_2$		$XeOF_4$	
exptl [a]		calcd (C_1) [b]			calcd (C_{2h})		calcd (C_{4v})	
			SVWN [c]	B3LYP [d]	SVWN [c]	B3LYP [d]	SVWN [c]	B3LYP [e]
Os(1)–O(1)	1.703(6)	Os–O_1	1.721	1.688	1.715	1.689		
Os(1)–O(2)	1.684(6)	Os–O_2	1.703	1.683	1.709	1.686		
Os(1)–O(3)	1.685(6)	Os–O_3	1.704	1.683	1.709	1.686		
Os(1)---F(1)	2.117(5)	Os---F_1	2.146	2.147	2.114	2.152		
Os(1)–F(2)	1.927(5)	Os–F_2	1.915	1.921	1.892	1.892		
Os(1)---F(1A)	2.107(4)	Os---F_1'	2.093	2.143	2.114	2.152		
Xe(1)···F(2)	2.757(5)	Xe···F_2	2.735	2.968				
Xe(1)–O(4)	1.709(6)	Xe–O_4	1.750	1.742			1.749	1.742
Xe(1)–F(3)	1.907(5)	Xe–F_3	1.953	1.953			1.951	1.949
Xe(1)–F(4)	1.918(5)	Xe–F_4	1.971	1.953			1.951	1.949
Xe(1)–F(5)	1.912(5)	Xe–F_5	1.949	1.952			1.951	1.949
Xe(1)–F(6)	1.913(5)	Xe–F_6	1.976	1.956			1.951	1.949
Xe(1)···O(1A)	3.983(6)	Xe···O_1'	2.872	3.829				
		Bond Angles (deg)						
O(1)–Os(1)–O(2)	102.0(3)	O_1–Os–O_2	102.7	102.5	102.4	102.2		
O(1)–Os(1)–O(3)	102.1(3)	O_1–Os–O_3	102.7	102.4	102.4	102.2		
O(1)–Os(1)---F(1)	85.3(2)	O_1–Os---F_1	82.2	83.8	82.9	83.0		
O(1)–Os(1)–F(2)	157.4(3)	O_1–Os–F_2	152.9	155.1	152.8	154.2		
O(1)–Os(1)---F(1A)	85.3(2)	O_1–Os---F_1'	83.8	83.8	82.9	83.0		
O(2)–Os(1)–O(3)	105.1(3)	O_2–Os–O_3	105.6	105.3	105.3	105.2		
O(2)–Os(1)---F(1)	159.8(2)	O_2–Os---F_1	162.6	159.8	160.7	160.3		
O(2)–Os(1)–F(2)	91.8(3)	O_2–Os–F_2	94.5	92.5	93.9	93.4		
O(2)–Os(1)---F(1A)	91.5(2)	O_2–Os---F_1'	93.7	92.2	91.4	92.1		
O(3)–Os(1)---F(1)	91.5(3)	O_3–Os---F_1	89.3	91.8	91.4	92.1		
O(3)–Os(1)–F(2)	91.2(3)	O_3–Os–F_2	92.4	92.5	93.9	93.4		
O(3)–Os(1)---F(1A)	159.8(2)	O_3–Os---F_1'	157.4	159.4	160.7	160.3		
F(1)---Os(1)–F(2)	76.1(2)	F_1---Os–F_2	75.6	75.8	75.0	75.8		
F(1)---Os(1)---F(1A)	70.2(2)	F_1---Os---F_1'	70.0	69.2	70.7	69.5		

Table 6.2. (continued ...)

F(2)–Os(1)---F(1A)	76.5(2)	F_2–Os---F_1'	74.2	75.7	75.0	75.8		
Os(1)---F(1)---Os(1A)	109(1)	Os---F_1---Os'	110.0	110.8	109.3	110.5		
F(2)···Xe(1)···O(1A)	43.2(1)	F_2···Xe···O_1'	55.4	45.4				
F(2)···Xe(1)–F(3)	82.2(2)	F_2···Xe–F_3	105.7	97.2				
F(2)···Xe(1)–F(4)	96.4(2)	F_2···Xe–F_4	69.9	78.3				
F(2)···Xe(1)–F(5)	93.8(2)	F_2···Xe–F_5	70.4	85.3				
F(2)···Xe(1)–F(6)	83.8(2)	F_2···Xe–F_6	105.6	90.1				
F(2)···Xe(1)–O(4)	171.6(2)	F_2···Xe–O_4	154.6	170.3				
O(4)–Xe(1)–F(3)	90.8(3)	O_4–Xe–F_3	92.5	92.2			92.6	92.6
O(4)–Xe(1)–F(4)	90.6(3)	O_4–Xe–F_4	91.8	92.3			92.6	92.6
O(4)–Xe(1)–F(5)	90.8(3)	O_4–Xe–F_5	92.7	92.4			92.6	92.6
O(4)–Xe(1)–F(6)	91.5(3)	O_4–Xe–F_6	91.9	92.3			92.6	92.6
O(4)–Xe(1)···O(1A)	128.5(2)	O_4–Xe···O_1'	149.9	142.7				
F(3)–Xe(1)–F(4)	178.6(2)	F_3–Xe–F_4	175.6	175.5			180	174.8
F(3)–Xe(1)–F(5)	90.0(2)	F_3–Xe–F_5	89.3	90.0			89.9	89.9
F(3)–Xe(1)–F(6)	89.0(2)	F_3–Xe–F_6	89.5	90.1			89.9	89.9
F(3)–Xe(1)···O(1A)	55.6(2)	F_3–Xe···O_1'	68.3	65.6				
F(4)–Xe(1)–F(5)	90.1(2)	F_4–Xe–F_5	89.3	89.9			89.9	89.9
F(4)–Xe(1)–F(6)	90.9(2)	F_4–Xe–F_6	91.6	89.7			89.9	89.9
F(4)–Xe(1)···O(1A)	123.3(2)	F_4–Xe···O_1'	108.2	110.5				
F(5)–Xe(1)–F(6)	177.5(2)	F_5–Xe–F_6	175.3	175.4			180	174.8
F(5)–Xe(1)···O(1A)	122.7(2)	F_5–Xe···O_1'	109.3	116.0				
F(6)–Xe(1)···O(1A)	54.9(2)	F_6–Xe···O_1'	66.0	60.0				
Xe(1)···F(2)–Os(1)	163.2(2)	Xe···F_2–Os	123.2	158.6				
Xe(1)···O(1A)–Os(1)	142.6(3)	Xe···O_1'–Os'	121.0	146.1				

[a] For the atom labeling scheme, see Figure 6.1a. [b] For the atom labeling scheme, see Figure 6.6b. [c] SDDall basis set augmented for F, O, and Xe with two d-type polarization functions by Huzinaga.[151] [d] Stuttgart basis set for Os augmented with one f-type polarization functional.[152] aug-cc-pVTZ basis sets for all other atoms. [e] The aug-cc-pVTZ basis set.

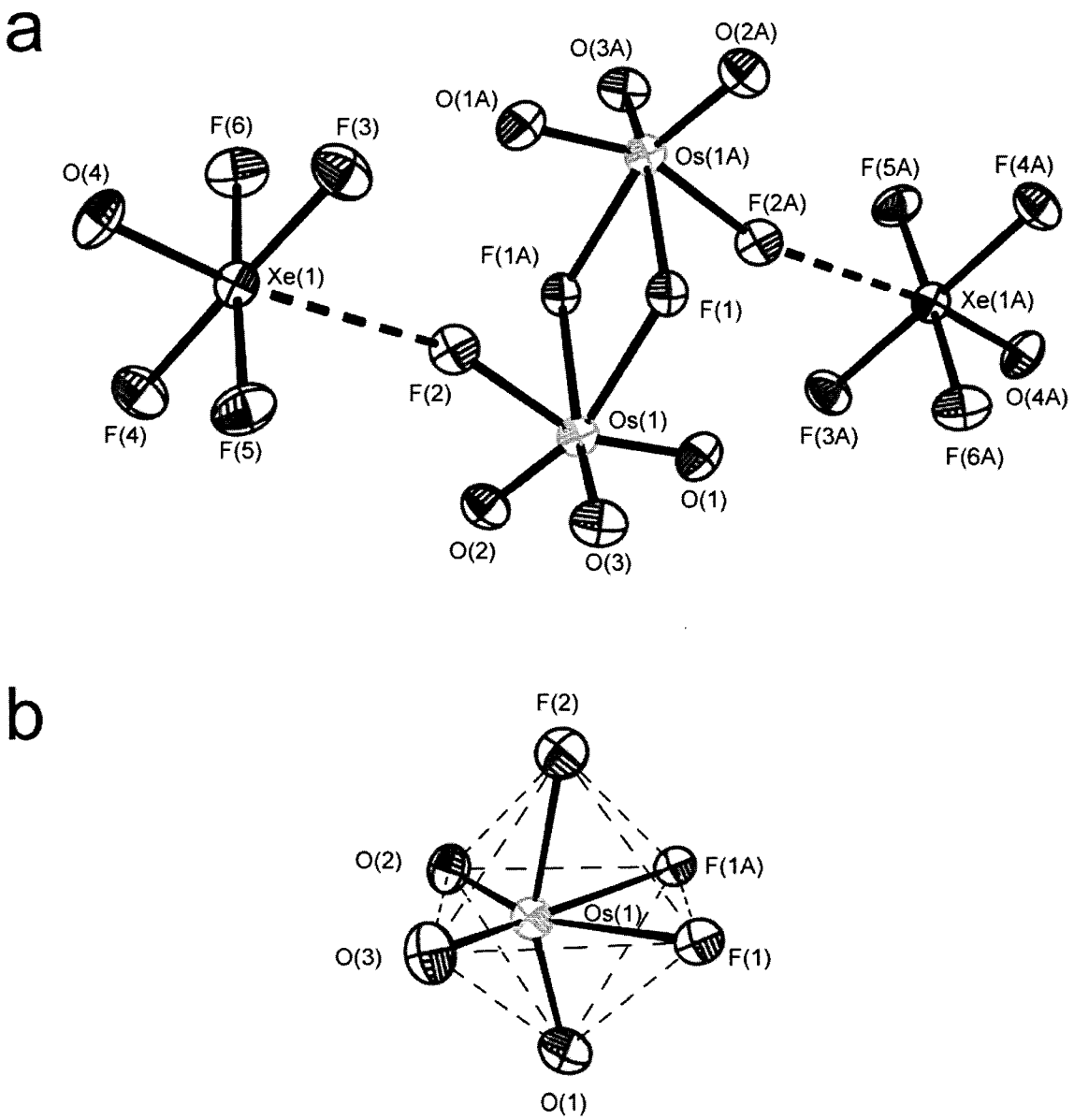

Figure 6.1. (a) Structural unit in the X-ray crystal structure of $(OsO_3F_2)_2 \cdot 2XeOF_4$ with thermal ellipsoids drawn at the 70% probability level. (b) Visualization of the octahedron formed by the light atoms of the OsO_3F_3 unit.

The structure consists of $(OsO_3F_2)_2 \cdot 2XeOF_4$ units that are stacked along the *a*-axis but alternate along the *b*- and *c*-axes so that the $XeOF_4$ and OsO_3F_2 molecules face one another in adjacent columns parallel to these axes (Figure D1). The resulting intermolecular contacts are long and are near the sums of the van der Waals radii.[165, 219] The OsO_3F_2 molecules are bridged to one another through two fluorine atoms, F(1) and F(1A), that are formally contributed by each OsO_3F_2 molecule. The remaining fluorine ligand of each OsO_3F_2 unit bridges through xenon to a $XeOF_4$ molecule (Figure 6.1a). The primary coordination spheres of the osmium atoms consist of three oxygen and three fluorine atoms in a facial arrangement, providing a distorted octahedral environment around osmium (Figure 6.1b). The preference for the *fac*-trioxo structure has been previously discussed for other d^0 transition metal trioxo species such as $(OsO_3F_2)_\infty$,[11] $OsO_3F_3^-$,[23] $[OsO_3F][HF][SbF_6]$,[21] ReO_3F,[49] and $ReO_3F(CH_3CN)_2 \cdot CH_3CN$.[45] The occurrence of the bridging fluorine atoms trans to oxygen atoms is also observed in $(OsO_3F_2)_\infty$[11] and other transition metal oxide fluorides, e.g., μ-F(*cis*-$OsO_2F_3)_2^+$,[22] polymeric $MO_2F_3 \cdot SbF_5$ (M = Tc, Re),[46] μ-F$(TcOF_4)_2^+$,[158] μ-F$(ReOF_4)_2^+$,[157] μ-F(*cis*-$ReO_2F_3)_2^-$,[45] $Re_3O_6F_{10}^-$,[45] $(WOF_4)_4$,[171] and $(MoOF_4)_\infty$.[220] The *trans*-position of the bridging fluorine ligand is attributed to the *trans*-influence of the doubly bonded oxygen ligand which results from the inability of the fluorine ligand to compete as effectively as an oxygen ligand for the $d_{t_{2g}}$ orbitals of osmium.[47]

The Os–O bonds are equal to within $\pm 3\sigma$ and only the Os(1)–O(2,3) bond lengths (1.685(6) Å) are within $\pm 3\sigma$ of those of the polymeric phase (1.688(1) and 1.678(1) Å), whereas the Os(1)–O(1) bond (1.703(6) Å) is significantly shorter than the terminal bond

of $(OsO_3F_2)_\infty$ (1.727(1) Å). The fluorine bridges have bond lengths that are equal within $\pm 3\sigma$ (Os(1)–F(1), 2.117(5) Å and Os(1)---F(1A), 2.107(4) Å) and are very similar to those observed for $(OsO_3F_2)_\infty$ (2.126(1) and 2.108(1) Å).[11] The remaining fluorine ligand, F(2), coordinates to Xe(1), forming a Os(1)–F(2)···Xe(1) bridge in which the Xe(1)···F(2) contact (2.757(5) Å) is significantly less than the sum of the van der Waals radii for F and Xe (3.63 Å).[165] The Os(1)–F(2) bond length (1.927(5) Å) is longer than the terminal Os–F bond in the polymeric phase (1.879(1) Å)[11] but is significantly shorter than the Os---F bridge bonds in $(OsO_3F_2)_2$. The Os(1)–F(2) bond length is, in fact, similar to those of the more polar Os–F bonds in the $OsO_3F_3^-$ anion (1.97(1)–1.91(1) Å),[23] and is rendered more basic by the trans influence of the Os(1)–O(1) bond.

The light atoms of $(OsO_3F_2)_2$ form a distorted octahedral coordination sphere about each osmium atom. Although there is significant variation in the bond lengths around the osmium atoms, the light atom octahedra are relatively undistorted (Figure 6.1b), as shown by the nearest neighbor-ligand atom contacts.[221] The O(1)–Os(1)–F(2) angle (157.4(3)°) is bent away from the Os(1)–O(2,3) double bond domain towards the less repulsive Os(1)---F(1,1A) bridge bonds. The F(1), F(1A), O(2), and O(3) atoms are coplanar within ±0.0001 Å, with the osmium atom lying 0.161 Å out of this plane, and displaced towards O(1). The O(2)–Os(1)–O(3) angle (105.1(3)°) is considerably more open as a result of greater repulsion between the Os–O double bond domains, whereas the F(1)---Os(1)---F(1A) angle (70.2(2)°) is considerably more closed because of weaker repulsions between the longer and more polar Os---F bridge bond domains. The F(1A), F(2), O(1), O(3) [F(1), F(2), O(1), O(2)] atoms are coplanar within ±0.02 [±0.02] Å, and

the osmium atom is displaced 0.262 [0.265] Å out of this plane towards O(2) [O(3)]. The displacement of the osmium atom occurs along the pseudo three-fold axis towards the facial oxygen ligands, which is consistent with the metal atom displacements observed for $(OsO_3F_2)_\infty$,[11] $ReCl_3O_3^{2-}$,[222] and $OsO_3F_3^-$ [23] and for the *cis*-dioxo species *cis*-OsO_2F_4,[20] μ-F(*cis*-$OsO_2F_3)_2^+$,[22] *cis*-$ReO_2F_4^-$,[45] and *cis*-$TcO_2F_4^-$.[47] In the latter cases, the central metal atom (M) is displaced towards the *cis*-oxygen ligands along the axis bisecting the O–M–O angle.

The $XeOF_4$ molecule has been structurally well characterized by ^{19}F NMR,[99] photoelectron,[100] Raman,[101] and gas-phase microwave spectroscopy,[102-104] and by single-crystal X-ray diffraction.[95] Xenon oxide tetrafluoride has been shown to have a square pyramidal geometry based on a AX_4YE VSEPR arrangement, with an axial oxygen atom, four co-planar fluorine atoms in equatorial positions, and an axial valence electron lone pair. The long F(2)···Xe(1) contact in the present structure has no perceptible effect on the geometry of $XeOF_4$ which retains its square-based pyramidal geometry, providing geometric parameters (Table 6.2) that are in good agreement with those reported previously.[95, 103, 104] The only other crystal structure containing the $XeOF_4$ molecule is $[XeF_5][SbF_6]\cdot XeOF_4$.[95] The xenon atom of the $XeOF_4$ molecule in this structure has a short Xe···F contact with a fluorine atom of the SbF_6^- anion but has no contacts with the XeF_5^+ cation. This fluorine bridge interaction also does not significantly distort the square-pyramidal geometry of the $XeOF_4$ molecule nor does it result in significant elongation of the Sb–F bridge bond. In the present structure, the primary Xe–F bond lengths range between 1.907(5) and 1.918(5) Å and are equal within ±3σ. The O–Xe–F

bond angles are in the range 90.6(3) to 91.5(3)° and are equal within ±3σ, indicating that the repulsive effect of the oxygen double bond domain is comparable to that of the electron lone pair. This is consistent with the crystal structure of $[XeF_5][SbF_6]\cdot XeOF_4$[95] as well as with gas-phase microwave and electron diffraction studies of $XeOF_4$.[104]

6.2.3 Raman Spectroscopy.

The low-temperature, solid-state Raman spectra of $(OsO_3F_2)_\infty$, $(OsO_3F_2)_2$, and $(OsO_3F_2)_2\cdot 2XeOF_4$ are shown in Figures 6.2, 6.3, and 6.4, respectively. The observed and calculated frequencies and assignments for $(OsO_3F_2)_\infty$ and for $(OsO_3F_2)_2$ and $(OsO_3F_2)_2\cdot 2XeOF_4$ are listed in Tables 6.3 and 6.4, respectively, where the atom numbering schemes are given in Figures 6.5, 6.6a, and 6.6b, respectively. Spectral assignments for $(OsO_3F_2)_2$ and $(OsO_3F_2)_2\cdot 2XeOF_4$ were made by comparison with the calculated frequencies and Raman intensities (Table 6.4) for the energy-minimized gas-phase geometries of $(OsO_3F_2)_2$, $XeOF_4$, and $(OsO_3F_2)_2\cdot 2XeOF_4$ and by comparison with the experimental frequencies of $XeOF_4$[101] (Table D2). The vibrational assignments for $(OsO_3F_2)_\infty$ were made by comparison with the calculated frequencies and assignments of the presently unknown $(\mu\text{-}FOsO_3F_2)_2OsO_3F^-$ anion (Tables 6.3 and D3). The central OsO_3F_3 group of $(\mu\text{-}FOsO_3F_2)_2OsO_3F^-$ is comprised of two *cis*-bridged fluorine atoms, one terminal fluorine atom, and a *fac*-OsO_3 moiety, providing a good approximation of the repeat unit in the fluorine-bridged polymer. Moreover, the formal charge of the anion is evenly dispersed over the light atoms (see Table D4) and is not expected to have a significant effect on the vibrational frequencies of the central OsO_3F_3 group.

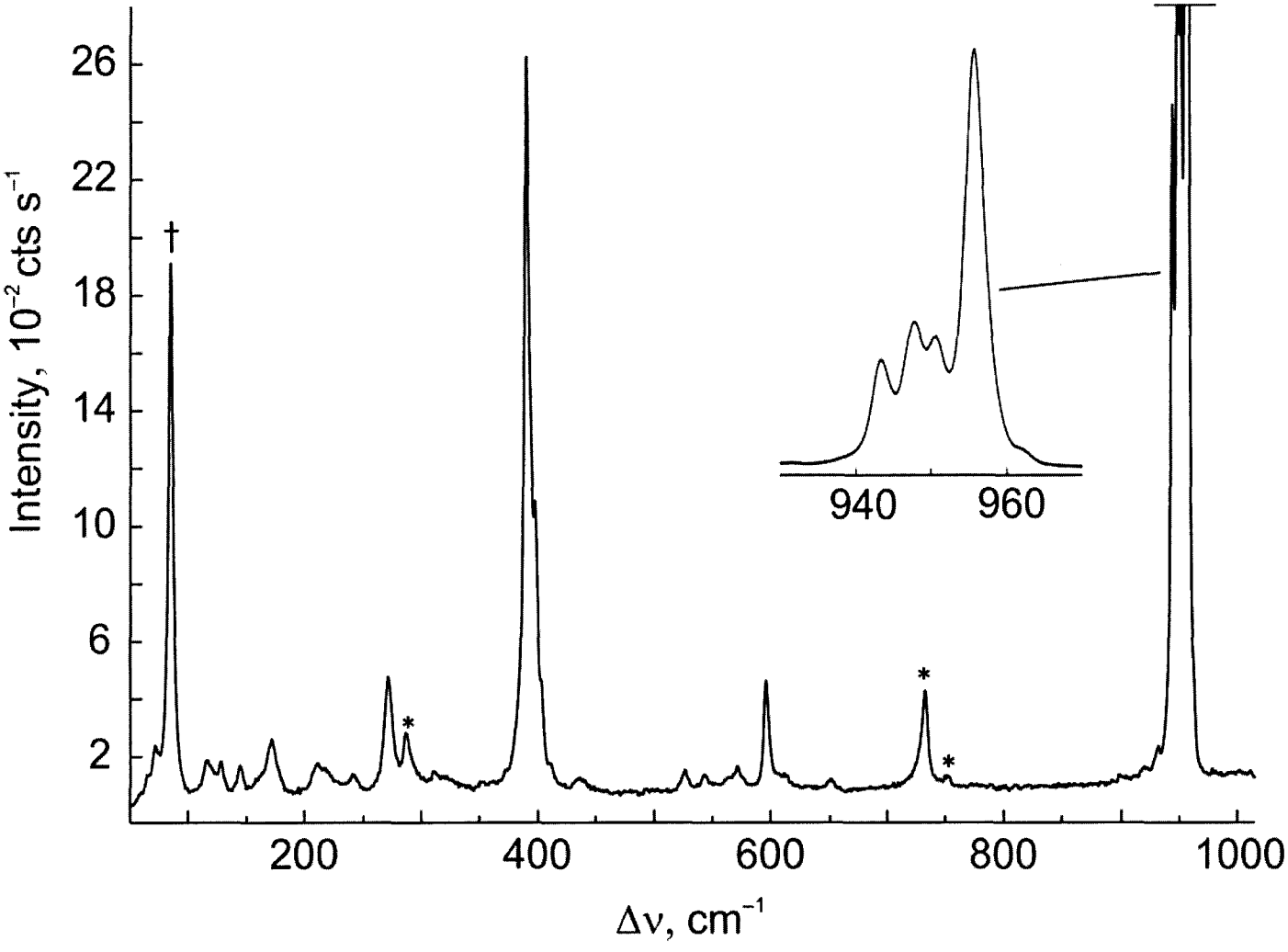

Figure 6.2. Raman spectrum of $(OsO_3F_2)_\infty$ recorded at –150 °C using 1064-nm excitation; the symbols denote FEP sample tube lines (*) and an instrumental artifact (†).

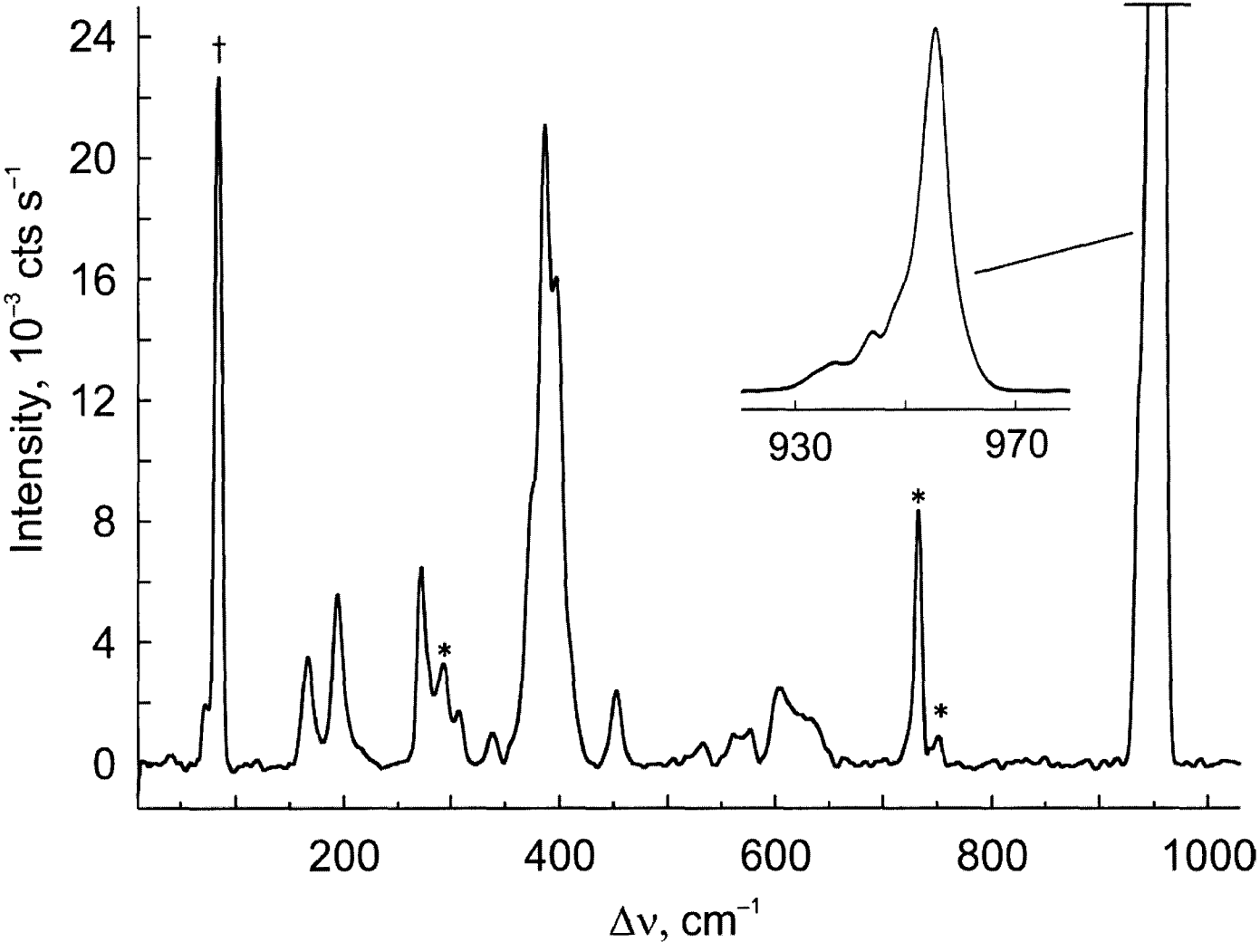

Figure 6.3. Raman spectrum of $(OsO_3F_2)_2$ recorded at –150 °C using 1064-nm excitation; the symbols denote FEP sample tube lines (*) and an instrumental artifact (†).

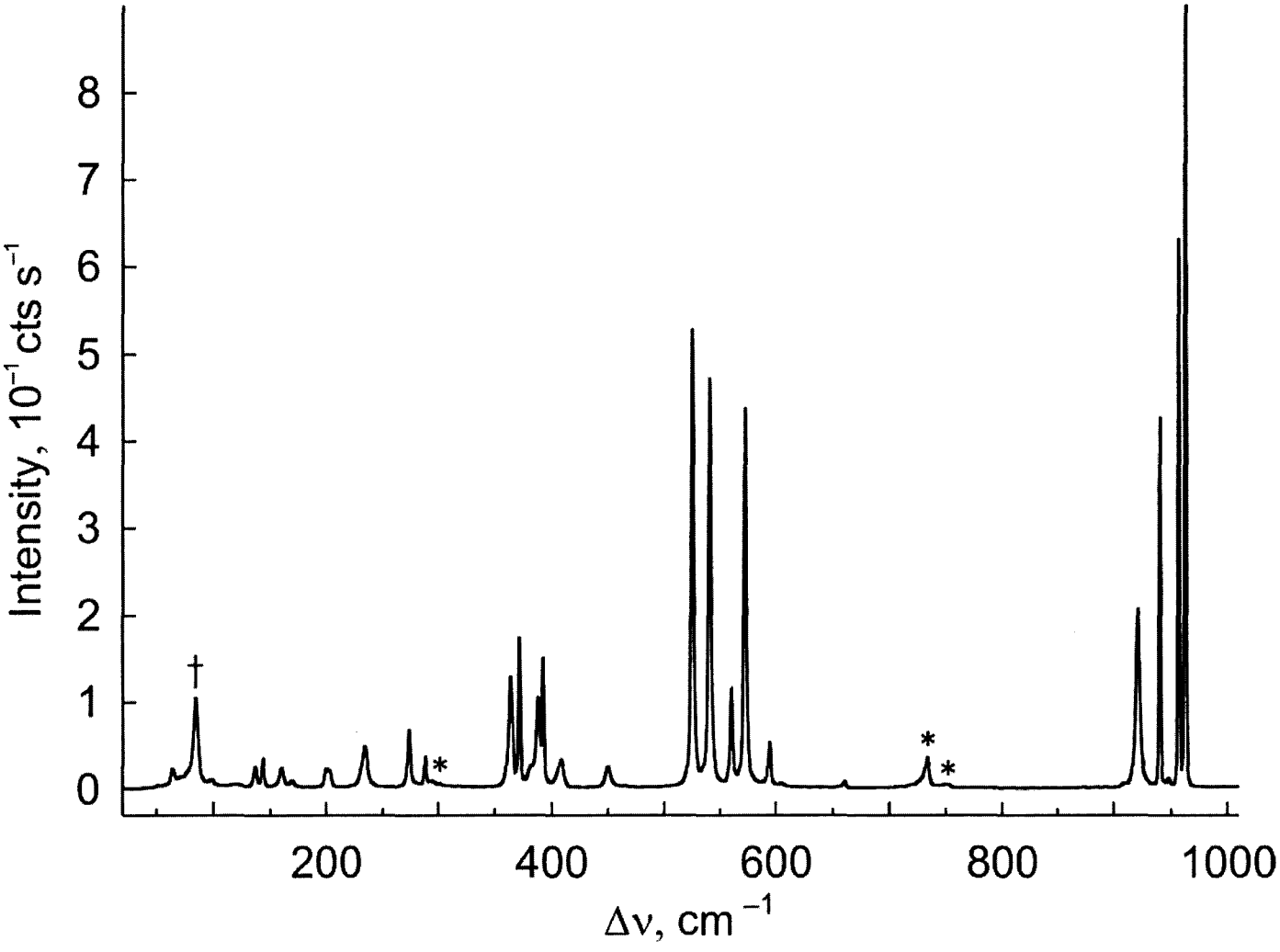

Figure 6.4. Raman spectrum of $(OsO_3F_2)_2 \cdot 2XeOF_4$ recorded at –150 °C using 1064-nm excitation; the symbols denote FEP sample tube lines (*) and an instrumental artifact (†).

Table 6.3. Raman Frequencies, Intensities, and Assignments for $(OsO_3F_2)_\infty$, and Calculated Vibrational Frequencies and Intensities for $(\mu\text{-}FOsO_3F_2)_2OsO_3F^-$

$(OsO_3F_2)_\infty$			$(\mu\text{-}FOsO_3F_2)_2OsO_3F^-$ $(C_1)^d$		
Exptl			calcd		assgnts[e]
[a]	[b]	[c]	SVWN	B3LYP	
953(100)	944vs	957(100)	971(158)[44]	1014(97)[39]	$\nu(Os_bO_{t1}) + \nu(Os_bO_{t2}) + \nu(Os_bO_t)$
			970(48)[35]	1008(56)[54]	
			966(2)[97]	1007(72)[67]	
		952(28)	965(10)[217]	994(13)[191]	$\nu(Os_bO_{t1}) - \nu(Os_bO_{t2}) + \nu(Os_bO_t)_{small}$
947(28)		949(33)	964(19)[223]	992(12)[167]	$\nu(Os_bO_{t1}) + \nu(Os_bO_{t2})_{small} - \nu(Os_bO_t)$
			961(86)[108]	985(29)[49]	
			955(27)[39]	983(17)[336]	
			952(21)[15]	980(13)[127]	
941(22)	934mw	945(30)	945(22)[105]	977(10)[69]	$[\nu(Os_bO_t) + \nu(Os_1O_2) + \nu(Os_2O_4)] - [\nu(Os_bO_{t1}) + \nu(Os_1O_1) + \nu(Os_2O_5)]$
748(<1)					
725(<1)					
662(2)					
644(2)	633w	610(2)	652(14)[104]	614(2)[182]	$\nu(Os_bF_t) - [\nu(Os_1F_1) + \nu(Os_1F_2) + \nu(Os_2F_4) + \nu(Os_2F_5)]_{small}$
			628(8)[105]	607(<1)[145]	
596(2)	613mw	596(6)	621(14)[90]	598(17)[7]	$\nu(Os_bF_t) + [\nu(Os_1F_1) + \nu(Os_1F_2) + \nu(Os_2F_4) + \nu(Os_2F_5)]_{small}$
588(2)			567(4)[67]	545(4)[50]	
			560(7)[47]	542(3)[38]	
		413(2)	509(13)[100]	471(5)[73]	$[\nu(Os_bF_{b1}) + \nu(Os_bF_{b2})] - [\nu(Os_1F_{b1}) + \nu(Os_2F_{b2})]$
428(<1) br	449w	404(4)	477(4)[97]	443(<1)[140]	$[\nu(Os_bF_{b1}) + \nu(Os_2F_{b2})] - [\nu(Os_bF_{b2}) + \nu(Os_1F_{b1})]$
			391(13)[3]	416(3)[3]	
			388(7)[2]	415(2)[3]	
	397m	398(10)	381(5)[5]	405(3)[6]	$\delta(Os_bO_tO_{t1}O_{t2})_{oop}$
		394(11)	378(6)[1]	401(7)[7]	$\delta(O_{t1}Os_bO_{t2})$
389(18)	387m	389(29)	373(5)[5]	398(3)[8]	$\delta(O_tOs_bO_{t2}) - \delta(O_tOs_bO_{t1})$
			372(3)[6]	392(7)[4]	
			369(6)[2]	391(7)[3]	
			365(5)[7]	389(2)[27]	
			362(6)[14]	383(2)[36]	
			349(1)[12]	349(<1)[18]	$\rho_w(F_{b1}Os_bF_{b2}) + \delta(F_4Os_2F_5)$
			339(<1)[11]	337(1)[7]	deformation mode
318(<1)		324(2)	314(<1)[13]	336(<1)[9]	$\delta(Os_bF_tF_{b1}F_{b2})_{oop} + \delta(O_1Os_1O_2) - \delta(F_1Os_1F_2)$

Table 6.3. (continued ...)

$(OsO_3F_2)_\infty$			$(\mu\text{-}FOsO_3F_2)_2OsO_3F^-$ (C_1)[d]		
exptl			calcd		assgnts[e]
a	b	c	SVWN	B3LYP	
		313(1)	310(1)[9]	318(1)[41]	$\rho_w(F_4Os_2O_4) + \rho_w(F_4Os_2F_{b2})$
		301(1)	303(1)[18]	306(2)[14]	deformation modes
283(<1)		287(3)	284(5)[15]	293(1)[18]	
271(3)	269w	273(5)	277(4)[11]	282(2)[5]	$\delta(F_tOs_bO_t) + \rho_r(O_1Os_1O_3) + \rho_w(F_1Os_1F_2) + \rho_w(F_4Os_2F_5) + \rho_t(O_6Os_2O_4)$
		262 sh	269(5)[10]	278(2)[9]	deformation modes
			250(1)[10]	267(1)[16]	
		245(1)	237(3)[51]	234(1)[36]	$\rho_t(F_{b2}Os_bF_t) + \rho_t(F_{b1}Os_bF_t) + \rho_r(O_tOs_bO_{t1})$
	235w	223(2)	235(<1)[38]	214(1)[27]	$\delta(F_{b1}Os_bF_{b2}) + \rho_w(F_tOs_bO_t)$
212(2)		214(2)	218(1)[14]	207(<1)[234]	$\rho_r(F_{b1}Os_bF_{b2}) - \rho_r(O_{t1}Os_bO_{t2}) + \delta(O_4Os_2F_4) + \rho_r(O_5Os_2O_6)$
	190w	176(4)	182(1)[3]	168(<1)[2]	deformation modes
		163(1)	169(1)[1]	166(<1)[1]	
	156w	150(2)	147(<1)[3]	155(<1)[20]	
		135(2)	144(<1)[1]	146(<1)[<1]	$\rho_t(O_{t1}Os_bO_{t2}) + \rho_w(O_tOs_bF_t)$
			134(1)[1]	130(<1)[1]	deformation modes
		120(2)	120(<1)[1]	128(<1)[2]	
		91(2)	109(<1)[<1]	110(<1)[3]	
			95(<0.1)[4]	66(<1)[1]	
			84(<0.1)[<1]	44(<1)[<1]	
			81(<0.1)[1]	37(<1)[<1]	
			65(<0.1)[<1]	19(<0.1)[1]	
			52(<1)[<1]	16(<1)[<1]	
			44(<1)[<1]	14(<0.1)[1]	
			39(<1)[1]	7(<0.1)[1]	

[a] From Ref 17. [b] From Ref 16. The abbreviations denote very strong (vs), medium (m), medium weak (mw), and weak (w) intensities. [c] The Raman spectrum was recorded on a microcrystalline sample in a FEP tube at −150 °C using 1064-nm excitation. The experimental Raman intensities given in parentheses are relative intensities with the most intense band given as 100. The abbreviation, n.o., denotes not observed. [d] SVWN/SDDall. B3LYP/Stuttgart cc-pVTZ. Values in parentheses denote calculated Raman intensities (amu $Å^{-4}$) and values in square brackets denote calculated infrared intensities (km mol^{-1}). [e] Assignments are for the energy-minimized geometry calculated at the B3LYP level; only the mode assignments that involve the central $Os_bO_tO_{t1}O_{t2}F_tF_{b1}F_{b2}$ unit are provided. See Table D3 for a complete set of assignments. See Figure 6.5 for the atom labeling scheme. The abbreviations denote stretch (ν), bend (δ), umbrella (δ_{umb}), twist (ρ_t), wag (ρ_w), and rock (ρ_r).

Table 6.4. Calculated and Experimental Vibrational Frequencies, Intensities, and Assignments for $(OsO_3F_2)_2$ and $(OsO_3F_2)_2{\cdot}2XeOF_4$

exptl[a]		calcd[d]				assgnts (C_1)[e]
$(OsO_3F_2)_2$[b]	$(OsO_3F_2)_2{\cdot}2XeOF_4$[c]	$(OsO_3F_2)_2$ (C_{2h})		$(OsO_3F_2)_2{\cdot}2XeOF_4$ (C_i)		$(OsO_3F_2)_2{\cdot}2XeOF_4$
		SVWN	B3LYP	SVWN	B3LYP	
n.o.	n.o.	994(0)[166]	1029(0)[85]	997(0)[100]	1035(0)[73]	$[\nu(OsO_1) + \nu(OsO_2) + \nu(OsO_3)] - [\nu(Os'O_1') + \nu(Os'O_3') + \nu(Os'O_2')]$
955(100)	962(100)	990(114)[0]	1031(116)[0]	1000(162)[0]	1037(114)[0]	$\nu(OsO_1) + \nu(OsO_2) + \nu(OsO_3) + \nu(Os'O_1') + \nu(Os'O_2') + \nu(Os'O_3')$
n.o.	948(1)	986(0)[126]	1018(0)[225]	1003(0)[117]	1025(0)[181]	$[\nu(OsO_2) + \nu(Os'O_3')] - [\nu(OsO_3) + \nu(Os'O_2')]$
948 sh 944(16) }	957(39)	986(51)[0]	1010(50)[0]	996(36)[0]	1017(40)[0]	$[\nu(OsO_2) + \nu(Os'O_2')] - [\nu(OsO_3) + \nu(Os'O_3')]$
n.o.	n.o.	979(0)[128]	1007(0)[230]	962(0)[158]	1011(0)[269]	$\nu(OsO_1) - \nu(Os'O_1')$
937(7)	940(47)	972(27)[0]	1001(23)[0]	954(136)[0]	1005(42)[0]	$\nu(OsO_1) + \nu(Os'O_1')$
	921(12)			902(191)[0]	890(74)[0]	$\nu(XeO_4) + \nu(Xe'O_4')$
	911(1)			901(0)[111]	890(0)[77]	$\nu(XeO_4) - \nu(Xe'O_4')$
n.o.		649(0)[130]	632(0)[162]			$\nu(OsF_2) - \nu(Os'F_2')$
	n.o.			616(0)[304]	594(0)[456]	$[\nu(OsF_2) - \nu(Os'F_2')] + [\nu(Xe'F_2') - \nu(XeF_2)]$
604(1) br		630(17)[0]	616(10)[0]			$\nu(OsF_2) + \nu(Os'F_2')$
	n.o.			588(0)[333]	585(0)[472]	$[\nu(XeF_3 + XeF_5) + \nu(Xe'F_4' + Xe'F_6')] - [\nu(XeF_4 + XeF_6) + \nu(Xe'F_3' + Xe'F_5')]$
	594(6)			601(36)[0]	585(6)[0]	$[\nu(XeF_4 + XeF_5) + \nu(Xe'F_4' + Xe'F_5')] - [\nu(XeF_3 + XeF_6) + \nu(Xe'F_3' + Xe'F_6')]$
	n.o.			594(0)[416]	584(0)[366]	$[\nu(XeF_4 + XeF_5) + \nu(Xe'F_3' + Xe'F_6')] - [\nu(XeF_3 + XeF_6) + \nu(Xe'F_4' + Xe'F_5')]$
	560(12)			589(11)[0]	584(1)[0]	$[\nu(XeF_5) + \nu(Xe'F_5')] - [\nu(XeF_6) + \nu(Xe'F_6')]$
	572(48)			579(8)[0]	571(28)[0]	$[\nu(OsF_2) + \nu(Os'F_2')] - [\nu(XeF_2) + \nu(Xe'F_2')]$
	n.o.			536(0)[11]	546(0)[3]	$\nu(XeF_{4e}) - \nu(Xe'F_{4e}')$
	540(51)			536(78)[0]	544(80)[0]	$\nu(XeF_{4e}) + \nu(Xe'F_{4e}')$
	525(58)			506(23)[0]	505(34)[0]	$[\nu(XeF_3 + XeF_4) + \nu(Xe'F_3' + Xe'F_4')] - [\nu(XeF_5 + XeF_6) + \nu(Xe'F_5' + Xe'F_6')]$
	n.o.			508(0)[11]	505(0)[<1]	$[\nu(XeF_3 + XeF_4) + \nu(Xe'F_5' + Xe'F_6')] - [\nu(XeF_5 + XeF_6) + \nu(Xe'F_3' + Xe'F_4')]$

Table 6.4. (continued ...)

453(1) br	450(3)	450(3)[0]	441(3)[0]	457(3)[0]	447(2)[0]	$\nu(OsF_1) + \nu(Os'F_1) + \nu(Os'F_1') + \nu(OsF_1')$
n.o.	n.o.	394(0)[5]	421(0)[55]	440(0)[44]	420(0)[58]	$\delta(O_1OsF_1) - \delta(O_1'Os'F_1')$
n.o.	n.o.	449(0)[170]	413(0)[109]	396(0)[4]	413(0)[45]	$[\delta(OsO_1O_2O_3) - \delta(Os'O_1'O_2'O_3')] + [\nu(OsF_1) + \nu(OsF_1')] - [\nu(Os'F_1) + \nu(Os'F_1')]$
409(2)	409(4)	376(7)[0]	412(5)[0]	413(8)[0]	413(5)[0]	$[\delta(O_1OsO_2) + \delta(O_1'Os'O_2')] + [\nu(OsF_1) + \nu(Os'F_1')] - [\nu(Os'F_1) + \nu(OsF_1')]$
399 sh 396(9)	392(16)	381(7)[0]	408(6)[0]	380(25)[0]	407(6)[0]	$\delta(OsO_1O_2O_3) + \delta(Os'O_1'O_2'O_3')$
n.o.	n.o.	374(0)[9]	398(0)[3]	378(0)[6]	400(0)[2]	$[\delta(O_1OsO_2) - \delta(O_1'Os'O_2')] + [\delta(O_2'Os'O_3') - \delta(O_2OsO_3)]$
386(13)	388(11)	361(6)[0]	383(5)[0]	377(22)[0]	383(4)[0]	$\delta(O_2OsO_3) + \delta(O_2'Os'O_3')$
376(5)	379(19)	415(1)[0]	374(3)[0]	365(9)[0]	375(4)[0]	$[\nu(OsF_1) + \nu(Os'F_1')] - [\nu(OsF_1') + \nu(Os'F_1)] + \delta(O_3OsF_2) + \delta(O_3'Os'F_2')$
n.o.	381(3)	359(0)[13]	380(0)[39]	364(0)[6]	380(0)[25]	$\delta(O_2OsO_3) - \delta(O_2'Os'O_3')$
337(1)	n.o.	344(0)[10]	353(0)[14]	341(0)[10]	348(0)[16]	$\delta(F_1OsF_2) - \delta(F_1'Os'F_2')$
n.o.	n.o.	355(0)[22]	334(0)[37]	356(0)[19]	337(0)[27]	$[\nu(OsF_1) + \nu(Os'F_1)] - [\nu(OsF_1') + \nu(Os'F_1')]$
	n.o.			308(0)[6]	327(0)[7]	$\delta(O_4XeF_5) - \delta(O_4'Xe'F_5')$
	361 sh 364(14)			311(5)[0]	327(6)[0]	$\delta(O_4XeF_3) + \delta(O_4'Xe'F_3')$
				308(5)[0]	327(5)[0]	$\delta(O_4XeF_5) + \delta(O_4'Xe'F_5')$
	n.o.			310(0)[5]	327(0)[7]	$\delta(O_4XeF_3) - \delta(O_4'Xe'F_3')$
308(1)	304(1)	299(<1)[0]	302(<1)[0]	310(3)[0]	300(<1)[0]	$\rho_t(F_1OsF_1')$
n.o.	n.o.	271(0)[5]	284(0)[3]	284(0)[14]	281(0)[2]	$[\rho_r(O_2OsO_3) - \rho_r(O_2'Os'O_3')] + [\rho_w(O_1OsF_2) - \rho_w(O_1'Os'F_2')]$
271(4)	288(4)	278(5)[0]	280(4)[0]	282(5)[0]	277(5)[0]	$\delta(O_1OsF_2) + \delta(O_1'Os'F_2')$
	282(1)			241(0)[128]	263(0)[80]	$\delta_{umb}(XeF_{4e}) - \delta_{umb}(Xe'F_{4e}')$
n.o.	n.o.	243(0)[63]	250(0)[94]	254(0)[42]	243(0)[130]	$\delta(O_1OsF_2) - \delta(O_1'Os'F_2')$
	240 sh 235(5)			249(3)[0]	264(1)[0]	$\delta_{umb}(XeF_{4e}) + \delta_{umb}(Xe'F_{4e}')$
	203(2)			188(3)[0]	209(4)[0]	$\delta(F_4XeF_5) + \delta(F_3XeF_6) + \delta(F_4'Xe'F_5') + \delta(F_3'Xe'F_6')$
	n.o.			187(0) [<1]	209(0)[<0.1]	$[\delta(F_4XeF_5) + \delta(F_3XeF_6)] - [\delta(F_4'Xe'F_5') + \delta(F_3'Xe'F_6')]$
192(3)	201(3)	201(1)[0]	206(1)[0]	199(2)[0]	205(1)[0]	$\rho_r(OsO_1O_2O_3F_2) + \rho_r(Os'O_1'O_2'O_3'F_2')$
166(2)	170(1)	177(1)[0]	172(<1)[0]	205(2)[0]	178(<1)[0]	$[\rho_w(O_1OsF_2) + \rho_w(O_1'Os'F_2')] + \rho_r(F_1OsF_1')$
	n.o.			182(0)[<1]	173(0)[<0.1]	$[\rho_t(F_3XeF_5) + \rho_t(F_3'Xe'F_5')] - [\rho_t(F_4XeF_6) + \rho_t(F_4'Xe'F_6')]$

Table 6.4. (continued …)

	160(3)			182(<1)[0]	171(<1)[0]	$[\rho_t(F_3XeF_5) + \rho_t(F_4'Xe'F_6')] - [\rho_t(F_4XeF_6) + \rho_t(F_3'Xe'F_5')]$
	n.o.			132(0)[1]	151(0)[<1]	$[\delta(F_3XeF_5) + \delta(F_4'Xe'F_6')] - [\delta(F_4XeF_6) + \delta(F_3'Xe'F_5')]$
	154 sh			130(1)[0]	151(<1)[0]	$[\delta(F_3XeF_5) + \delta(F_3'Xe'F_5')] - [\delta(F_4XeF_6) + \delta(F_4'Xe'F_6')]$
				142(1)[0]	150(<1)[0]	$[\delta(F_3XeF_6) + \delta(F_3'Xe'F_6')] - [\delta(F_4XeF_5) + \delta(F_4'Xe'F_5')]$
	n.o.			139(0)[2]	150(0)[<1]	$[\delta(F_3XeF_6) + \delta(F_4'Xe'F_5')] - [\delta(F_4XeF_5) + \delta(F_3'Xe'F_6')]$
n.o.	143(4)	140(1)[0]	135(1)[0]	141(2)[0]	136(1)[0]	breathing of $(OsO_3F_2)_2$
n.o.	121(1)	117(0)[<0.1]	117(0)[<1]	153(0)[1]	122(0)[1]	$\rho_t(OsO_2O_3F_2) - \rho_t(Os'O_2'O_3'F_2')$
n.o.	118(1)	109(0)[2]	108(0)[2]	123(0)[4]	109(0)[2]	$\rho_r(OsO_1O_2O_3F_1F_2) - \rho_r(Os'O_1'O_2'O_3'F_1'F_2')$
n.o.	102 sh	92(0)[<0.1]	99(0)[<0.1]	119(0)[<1]	101(0)[<0.1]	$\rho_t(OsO_1O_2O_3) - \rho_t(Os'O_1'O_2'O_3')$
	98(1)	82(<1)[0]	75(<1)[0]	103(4)[0]	74(<1)[0]	$\rho_r(O_2OsO_3) + \rho_r(O_2'Os'O_3')$
	64(2)			106(4)[0]	45(1)[0]	coupled $XeOF_4$ and $(OsO_3F_2)_2$ modes
	n.o.			99(0)[<1]	39(0)[1]	
	n.o.			82(<1)[0]	34(1)[0]	
	n.o.			63(0)[3]	32(0)[1]	
	n.o.			83(1)[0]	26(1)[0]	
	n.o.			78(0)[<1]	26(0)[<1]	
	n.o.			49(<1)[0]	13(<1)[0]	
	n.o.			36(<1)[0]	10(<1)[0]	
	n.o.			30(0) [<0.1]	9(0)[<0.1]	
	n.o.			67(<1)[0]	9(<1)[0]	
	n.o.			48(0)[<1]	8(0)[<1]	
	n.o.			23(0)[<1]	4(0)[<1]	

Table 6.4. (continued ...)

[a] The Raman spectrum was recorded on a microcrystalline solid sample in a FEP tube at −150 °C using 1064-nm excitation. Experimental Raman intensities are given in parentheses and are relative intensities with the most intense band given as 100. The abbreviations denote shoulder (sh), broad (br), and not observed (n.o.). [b] Bands were also observed at 276(sh), 280(sh), and 288(sh) cm^{-1} but are unassigned. [c] Bands were also observed at 136(3), 274(7), 605(1), and 661(1) cm^{-1} but are unassigned. [d] SVWN/SDDall. Values in parentheses denote calculated Raman intensities (amu $Å^{-4}$) and values in square brackets denote calculated infrared intensities (km mol^{-1}). [e] Assignments are for the energy-minimized geometry calculated at the B3LYP level. See Figure 6.6a for the atom labeling scheme of $(OsO_3F_2)_2$. See Figure 6.6b for the atom labeling scheme of $(OsO_3F_2)_2 \cdot 2XeOF_4$. The abbreviations denote stretch (ν), bend (δ), twist (ρ_t), wag (ρ_w), rock (ρ_r), and umbrella (δ_{umb}). The atoms F_3, F_4, F_5, F_6 and F_3', F_4', F_5', F_6' are represented as F_{4e} and F_{4e}', respectively.

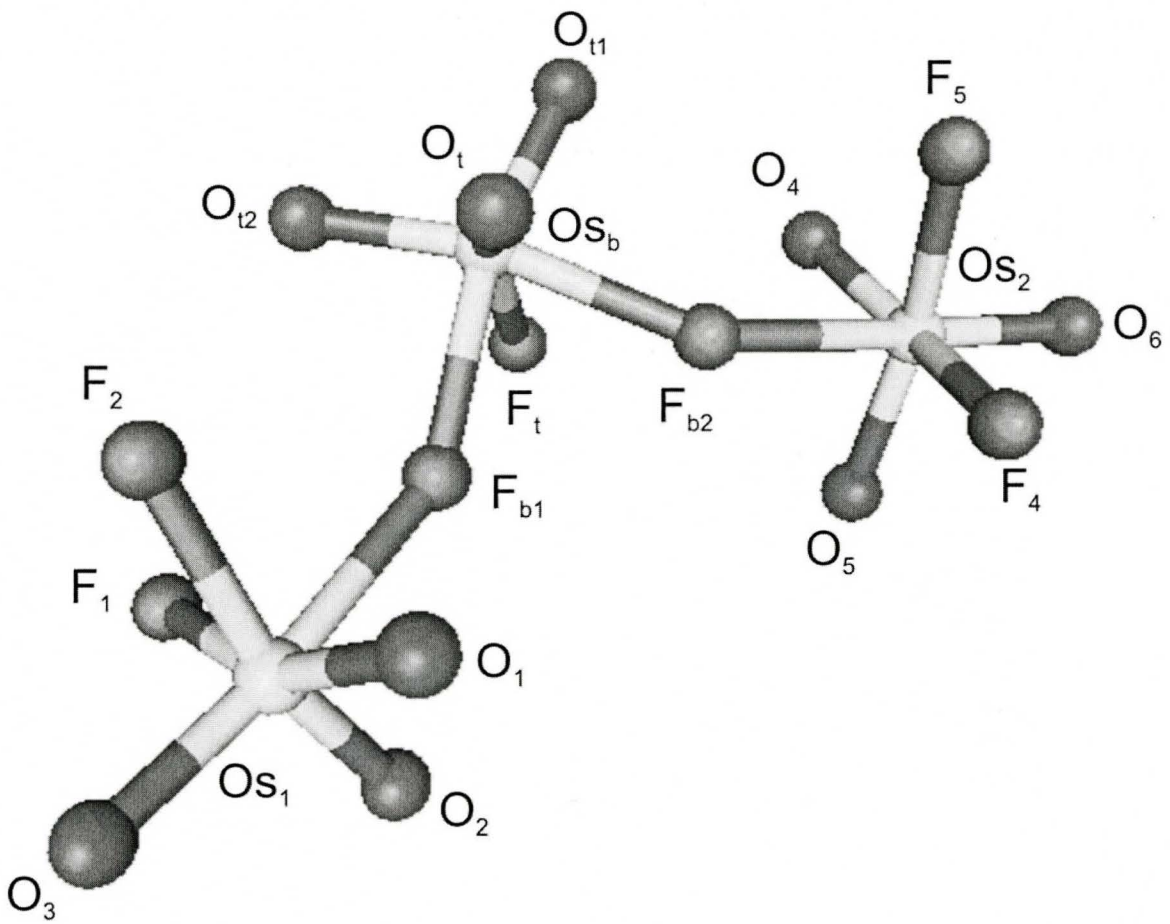

Figure 6.5. Calculated B3LYP gas-phase geometry for $(\mu\text{-}FOsO_3F_2)_2OsO_3F^-$ (C_1).

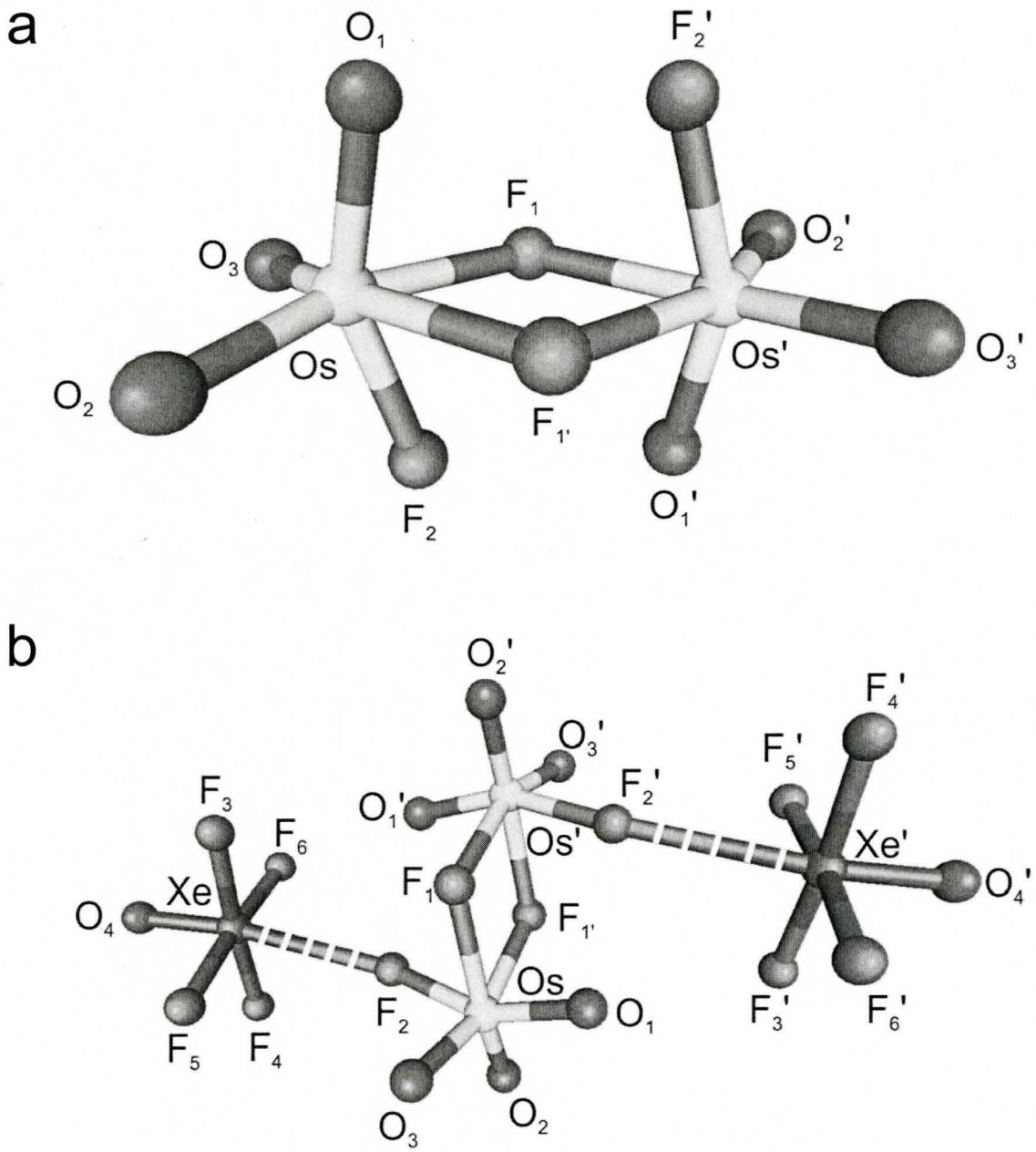

Figure 6.6. Calculated B3LYP gas-phase geometries for (a) $(OsO_3F_2)_2$ (C_{2h}) and (b) $(OsO_3F_2)_2 \cdot 2XeOF_4$ (C_i).

6.2.3.1. $(OsO_3F_2)_\infty$

The infrared and Raman spectra of matrix-isolated OsO_3F_2 monomer[14, 15] and the Raman spectrum of the low-temperature polymeric phase, $(OsO_3F_2)_\infty$,[16, 17] have been previously reported. The vibrational bands of matrix-isolated OsO_3F_2 were fully assigned under D_{3h} symmetry and the $^{16}O/^{18}O$ isotopic shifts for the $Os^{16}O_3F_2$, $Os^{16}O_2{}^{18}OF_2$, $Os^{16}O^{18}O_2F_2$, and $Os^{18}O_3F_2$ isotopomers were used to calculate the principal and the interaction force constants and to confirm the vibrational assignments.[14] Two prior vibrational studies of $(OsO_3F_2)_\infty$[16, 17] are at considerable variance with each other and with the present study (Table 6.3). The Raman spectrum of $(OsO_3F_2)_\infty$ has been re-examined in the present study, providing frequencies and intensities that were reproducible over multiple preparations of $(OsO_3F_2)_\infty$ using different synthetic procedures (see Ref 11 and eqs 6.3 and 6.5). In addition, more precise descriptions and assignments of the vibrational modes, based on the calculated vibrational frequencies and atomic displacements for $(\mu\text{-}FOsO_3F_2)_2OsO_3F^-$, are also reported. The SVWN and B3LYP frequencies (Table 6.3) agree well with each other and for the purpose of this discussion, the B3LYP frequencies are explicitly referred to in the subsequent discussion.

Four well-resolved bands occur at 945, 949, 952, and 957 cm^{-1} in the $(OsO_3F_2)_\infty$ spectrum that are assigned to coupled Os_b–O stretching modes. The calculated frequencies associated with the central OsO_3F_3 unit of the $(\mu\text{-}FOsO_3F_2)_2OsO_3F^-$ anion (977, 992, 994, and 1014 cm^{-1}) are overestimated with respect to those of $(OsO_3F_2)_\infty$ but well reproduce the experimental trend. The Os–O stretching frequencies are overestimated by similar amounts for the benchmark, *cis*-OsO_2F_4 (Table D5).

The infinite chain OsO_3F_2 polymer contains two fluorine environments, a terminal (F_t) and a bridging (F_b) environment. The Os_b–F_t stretching bands (596 and 610 cm^{-1}) are weak and are in good agreement with the coupled Os_b–F_t stretching modes calculated for (μ-$FOsO_3F_2)_2OsO_3F^-$ (598 and 614 cm^{-1}). The stretching bands involving Os_b–$F_{b(1,2)}$ (404 and 413 cm^{-1}) are also weak, but their frequencies are not modeled as well by (μ-$FOsO_3F_2)_2OsO_3F^-$, with the predicted values occurring at much higher frequencies (443 and 471 cm^{-1}, respectively). As anticipated, the Os_b–F_t stretching modes occur at higher frequencies than those involving Os_b–$F_{b(1,2)}$, in accord with the shorter bond length of Os_b–F_t (1.879(1) Å) relative to that of Os_b–F_b (2.126(1) Å).[11]

A limited number of the calculated bending modes (146, 214, 234, 398, 401, and 405 cm^{-1}) are exclusively associated with the central OsO_3F_3 unit and have been explicitly assigned, i.e., the bands at 389, 394, and 398 cm^{-1} can be reliably associated with O–Os_b–O bending modes. Detailed descriptions were not attempted for the remaining bending modes because the central OsO_3F_3 and terminal OsO_3F_2 units are extensively coupled. Because $(OsO_3F_2)_\infty$ does not have significant contributions from terminal groups, the highly coupled bending modes of the central OsO_3F_3 and terminal OsO_3F_2 units in (μ-$FOsO_3F_2)_2OsO_3F^-$ are inappropriate models for the bending modes in $(OsO_3F_2)_\infty$.

6.2.3.2. $(OsO_3F_2)_2$ and $(OsO_3F_2)_2 \cdot 2XeOF_4$.

Under C_1 symmetry, all vibrational modes (30 A for $(OsO_3F_2)_2$ and 66 A for $(OsO_3F_2)_2 \cdot 2XeOF_4$) are predicted to be both infrared- and Raman-active. Although correlation of the gas-phase adduct symmetry (C_i) to the crystal site symmetry (C_1) results

in no additional band splittings, correlation of the site symmetry to the centrosymmetric unit cell symmetry (C_i with $Z = 1$) results in equal apportioning of the vibrational modes between A_g and A_u symmetries (Table D6). Thus, 33 of the 66 A modes of $(OsO_3F_2)_2 \cdot 2XeOF_4$ are Raman-active A_g modes and 33 are infrared-active A_u modes under the unit cell symmetry. In accord with the factor-group analysis, 37 vibrational bands were observed in the Raman spectrum. The calculated frequencies at the SVWN and B3LYP levels are in good agreement with each other. The degree of coupling between the $(OsO_3F_2)_2$ and $XeOF_4$ modes varies with the level of theory, with stronger coupling occurring at the SVWN level. The predominant components in the mode descriptions, however, are the same at both levels and are therefore used as the basis for discussion. The differences arise because the Xe atom of the $XeOF_4$ molecule is coordinated to $F(2)/F_2$ of $(OsO_3F_2)_2$ in both the experimental and B3LYP geometries, while the Xe atom is coordinated to both $F(2)/F_2$ and $O(1A)/O_1'$ of $(OsO_3F_2)_2$ in the SVWN geometry (see Calculated Geometries). Because the B3LYP geometry better reproduces the experimental geometry, the B3LYP frequencies and corresponding mode descriptions are referred to in the following discussion.

The Os–O stretching frequencies of $(OsO_3F_2)_2$ and $(OsO_3F_2)_2 \cdot 2XeOF_4$ (Table 6.4) are comparable to those of $(OsO_3F_2)_\infty$. The Os–O stretching modes of $(OsO_3F_2)_2 \cdot 2XeOF_4$ are not coupled to any of the $XeOF_4$ modes and are only slightly shifted to higher frequency relative to those of $(OsO_3F_2)_2$.

The Os–$F_{(2,2')}$ and Xe–$F_{(2,2')}$ bridge stretching modes of the fluorine bridge are coupled, giving rise to two modes, ($[\nu(OsF_2) - \nu(Os'F_2')] + [\nu(Xe'F_2') - \nu(XeF_2)]$) and

([$\nu(OsF_2)$ + $\nu(Os'F_2')$] – [$\nu(Xe'F_2')$ + $\nu(XeF_2)$]). Only the latter mode is observed at 572 cm^{-1} as a strong band, which is in good agreement with the calculated frequency (571 cm^{-1}) and strong intensity. The frequency of this mode is shifted to lower frequency when compared with that of the [$\nu(OsF_2)$ + $\nu(Os'F_2')$] mode in $(OsO_3F_2)_2$, observed at 604 cm^{-1} as a broad, low-intensity band. The experimental frequency difference upon going from the dimer to the adduct (32 cm^{-1}) is in reasonable agreement with the calculated shift (45 cm^{-1}). A similar shift (38 cm^{-1}) was calculated for the modes involving [$\nu(OsF_2)$ – $\nu(Os'F_2')$].

In contrast, and as expected, all stretching mode descriptions and frequencies that involve Os–$F_{(1,1')}$ are nearly identical for both $(OsO_3F_2)_2$ and $(OsO_3F_2)_2{\cdot}2XeOF_4$. The in-phase mode, [$\nu(OsF_1)$ + $\nu(Os'F_1)$ + $\nu(Os'F_1')$ + $\nu(OsF_1')$], appears as a weak band at 453 and 450 cm^{-1}, respectively. The out-of-phase mode, [$\nu(OsF_1)$ + $\nu(Os'F_1')$] – [$\nu(Os'F_1)$ + $\nu(OsF_1')$], is significantly coupled with bending modes, giving rise to bands at 376 and 409 cm^{-1} for the dimer and at 379 and 409 cm^{-1} for the adduct. The frequency at 409 cm^{-1} is in very good agreement with the Os_b–F_b frequencies of $(OsO_3F_2)_\infty$ (404, 413 cm^{-1}).

Most of the O–Os–O, F–Os–O, and F–Os–F bending modes are not coupled or are very weakly coupled to the F–Xe–F and F–Xe–O bending modes of the $(OsO_3F_2)_2{\cdot}2XeOF_4$ adduct and are generally in very good agreement with the calculated values, as well as with the experimental and calculated values for $(OsO_3F_2)_2$ and $(OsO_3F_2)_\infty$.

The $XeOF_4$ molecules adducted to $(OsO_3F_2)_2$ are rendered non-equivalent because the C_i site symmetry of the adduct results in lowering of the free molecule symmetry from

C_{4v} to local C_1 symmetry and removal of the degeneracies of the E vibrational modes. In addition, all $XeOF_4$ vibrational modes are coupled to each other but, for the most part, do not exhibit significant coupling with the $(OsO_3F_2)_2$ modes, except in the case noted above.

Both the symmetric (921 cm^{-1}) and asymmetric (911 cm^{-1}) Xe–O stretching modes of $(OsO_3F_2)_2 \cdot 2XeOF_4$ occur at higher frequencies than the calculated values (890 and 890 cm^{-1}, respectively, Table 6.4). The Xe–O stretching modes are shifted to lower frequency than that of the experimental and calculated gas-phase $XeOF_4$ molecule[101] (927 and 928 cm^{-1}, respectively, Table D2), in accordance with coordination of the Lewis acidic $XeOF_4$ molecule.

6.2.4. Computational Results.

The geometries of $(OsO_3F_2)_2$ and $(OsO_3F_2)_2 \cdot 2XeOF_4$ (Figure 6.6) optimized under C_{2h} and C_i symmetries, respectively, and resulted in stationary points with all frequencies real. The starting geometries for both energy minimizations were the crystallographic geometries. Although $(OsO_3F_2)_2$ optimized to C_{2h} symmetry, the geometry is very close to C_i symmetry, which is reflected in the atom labeling scheme used in Figure 6.6a. The energy-minimized geometries and vibrational frequencies of the benchmarks, $XeOF_4$ (C_{4v}) and *cis*-OsO_2F_4 (C_{2v}) (Tables D2 and D5, respectively) were also calculated. The geometry of the $XeOF_4$ molecule has been energy minimized using the SVWN/SDDall and B3LYP/aug-cc-pVTZ methods and provides geometrical parameters and frequencies that are similar to the experimental values of $XeOF_4$[101] and $(OsO_3F_2)_2 \cdot 2XeOF_4$.

The energy-minimized geometry of the presently unknown $(\mu\text{-}FOsO_3F_2)_2OsO_3F^-$ anion was obtained for C_1 symmetry (Table D7), resulting in a stationary point with all frequencies real. Descriptions of the vibrational modes are provided in Table D3. The vibrational modes and frequencies of the $(\mu\text{-}FOsO_3F_2)_2OsO_3F^-$ anion were used to aid the vibrational assignments of the infinite-chain polymer, $(OsO_3F_2)_\infty$. The central OsO_3F_3 group of the anion provided a satisfactory model for the OsO_3F_3 group of the polymer. Moreover, the formal negative charge of the anion is essentially equally distributed among all of the electronegative light atoms (see Table D4) so that the formal negative charge may be expected to have a minimal effect on the geometrical parameters and vibrational frequencies associated with the OsO_3F_3 group.

6.2.4.1. Calculated Geometries

6.2.4.1.1. $(OsO_3F_2)_2$ and $(OsO_3F_2)_2 \cdot 2XeOF_4$

The energy-minimized geometries calculated at the SVWN/SDDall (Figure D2) and B3LYP/Stuttgart(Os) aug-cc-pVTZ (Xe, O, F) levels (Figure 6.6b) for $(OsO_3F_2)_2 \cdot 2XeOF_4$ only differ by the relative positions of the $XeOF_4$ molecules in relation to the $(OsO_3F_2)_2$ dimer, with the B3LYP geometry more closely reproducing the experimental interaction between $(OsO_3F_2)_2$ and $XeOF_4$. The experimental (2.757(5) Å) and SVWN (2.735 Å) Xe···F_2 bond lengths are in close agreement, whereas the B3LYP bond length is slightly longer (2.968 Å). In contrast, the B3LYP (3.829 Å) and SVWN (2.872 Å) Xe···O_1' contact distances are both shorter than the experimental distance (3.983(6) Å). The Xe atom of the $XeOF_4$ molecule is nearly equidistant from O_1' and F_2 at the SVWN level, whereas it is much closer to F(2)/F_2 for the experimental and B3LYP

geometries. The Xe···F(2)/F_2–Os bond angles for the experimental (163.2(2)°), B3LYP (158.6°), and SVWN (123.2°) geometries also reflect the shorter Xe···F(2)/F_2 distance.

The calculated $(OsO_3F_2)_2$ and $(OsO_3F_2)_2 \cdot 2XeOF_4$ geometries are in good agreement with the experimental geometry of the dimer unit in $(OsO_3F_2)_2 \cdot 2XeOF_4$, although the Os–O bond lengths are slightly overestimated in the calculated structures. Both calculated structures provide good estimates for the Os---F_1 bond lengths whereas the calculated Os–F_2 bond length of $(OsO_3F_2)_2$ is underestimated when compared with the experimental and calculated values for $(OsO_3F_2)_2 \cdot 2XeOF_4$. This is likely attributable to the significant interaction that occurs between F_2 and Xe in $(OsO_3F_2)_2 \cdot 2XeOF_4$. The Os–$O_1$ and Os'–O_1' bond lengths of $(OsO_3F_2)_2 \cdot 2XeOF_4$ calculated at the SVWN level (1.721 Å) are longer than the B3LYP (1.688 Å) and experimental (1.703(6) Å) values because of the much shorter $O_{1,1}$'···Xe(') contacts in the SVWN geometry. The absence of an interaction between O_1 and Xe in the experimental structure is also consistent with the similar calculated and experimental Os–O_1 bond lengths found for $(OsO_3F_2)_2$.

In both the calculated and experimental structures of $(OsO_3F_2)_2$ and $(OsO_3F_2)_2 \cdot 2XeOF_4$, the light atoms of the $(OsO_3F_2)_2$ dimer lie in two dihedral planes; one comprised of atoms O_2,O_3,Os,F_1,F_1',Os',O_2',O_3', and the other comprised of atoms F_2,Os,O_1,O_1',Os',F_2'. In the case of the O_1–Os–F_2 and O_1'–Os'–F_2' bond angles, both are bent towards the fluorine bridge atoms, F_1 and F_1' (Figure 6.6).

The shorter $O_{(1,1')}$···Xe(') bond length obtained for the SVWN geometry results in a O_4–Xe···F_2 bond angle that is more closed than in the B3LYP and experimental geometries (154.6, 170.3 and 171.6(2)°, respectively). In both the SVWN and B3LYP

geometries, the O_4–Xe···O_1' bond angle is calculated to be larger than in the experimental structure (149.9, 142.7 and 128.5(2)°, respectively), with the difference likely due to crystal packing. In the geometry calculated at the SVWN level, the Xe atom is essentially equidistant from the F_2 atom and the O_1' atom, while in the B3LYP geometry, the Xe atom lies along a line coincident with the Os–F_2 bond that has no significant interaction with O_1', in agreement with the crystal structure. In both calculated structures, the Xe–F and Xe–O bond lengths of the $XeOF_4$ molecule are slightly overestimated and the angle formed between O_4 and the plane defined by the F_3, F_4, F_5, F_6 atoms is also slightly overestimated.

6.2.4.1.2. $(\mu\text{-}FOsO_3F_2)_2OsO_3F^-$

The structure of the $(\mu\text{-}FOsO_3F_2)_2OsO_3F^-$ anion, optimized at the B3LYP (Figure 6.5) and SVWN (values in square brackets) levels (Table D7), has both terminal OsO_3F_2 units orientated so that the Os_1---F_{b1}---Os_b---F_{b2}---Os_2 backbone forms a shallow W-shaped arrangement. The Os_1---F_{b1}---Os_b (144.7 [129.8]) and Os_2---F_{b2}---Os_b (144.4° [128.8]) bridge bond angles are bent away from each other, as a result, $\angle Os_1Os_bOs_2$ is significantly greater than 90° (106.5° [116.4]).

The Os_1---F_{b1} and Os_2---F_{b2} bridge bond lengths of the terminal OsO_3F_3 units (av., 2.194 Å) are elongated with respect to the terminal $Os_{(1,2)}$–F bond lengths (av., 1.922 Å). The bridging Os_b---F_{b1} and Os_b---F_{b2} bond lengths (av., 2.072 Å) and the terminal Os_b–F_t bond (1.904 Å) are shorter than the respective bridging $Os_{1,2}$---F_b and terminal $Os_{1,2}$–$F_{1,2,4,5}$ bond lengths. In contrast with the experimental Os–O bond lengths of $(OsO_3F_2)_\infty$ (1.727(1), 1.688(1), and 1.678(1) Å),[Os8-001] the calculated Os_b–$O_{(t,t1,t2)}$ bond

lengths of (μ-$FOsO_3F_2)_2OsO_3F^-$ are nearly equal and are not significantly influenced by the *trans*-fluorine ligands. It is noteworthy that the *trans*-influence on the Os–O bond lengths is observed for the experimental structure of $(OsO_3F_2)_2{\cdot}2XeOF_4$ but was not apparent in the calculated structures of $(OsO_3F_2)_2$ and $(OsO_3F_2)_2{\cdot}2XeOF_4$.

6.2.4.2. Charges, Valencies, and Bond Orders.

The NBO[181-184] analyses were carried out for the SVWN- and B3LYP-optimized gas-phase geometries of $(OsO_3F_2)_2$ and $(OsO_3F_2)_2{\cdot}2XeOF_4$ and are similar (Table D8). Because the B3LYP geometry better reproduces the experimental geometry than the SVWN geometry (see Section 6.2.4.1), only the B3LYP results are referred to in the ensuing discussion.

The NBO analyses give natural charges of 2.19 and 2.18 for Os in $(OsO_3F_2)_2$ and $(OsO_3F_2)_2{\cdot}2XeOF_4$, respectively, and 3.13 for Xe in $(OsO_3F_2)_2{\cdot}2XeOF_4$. The natural charge of the Xe atom is approximately half of its formal oxidation number and the oxygen and fluorine atoms are also close to half of their respective formal oxidation numbers, indicating that the bonding in $(OsO_3F_2)_2$ and $(OsO_3F_2)_2{\cdot}2XeOF_4$ is, as expected, polar covalent. The Os---F_1 bridge bond order (0.23, 0.23) is approximately half that of the terminal Os–F_2 bond (0.43, 0.40) for both $(OsO_3F_2)_2$ and $(OsO_3F_2)_2{\cdot}2XeOF_4$, respectively, which is consistent with equivalent bonding of the F_1 bridging fluorine atom to both osmium atoms.

With the exception of F_2, the Os–O and Os–F bond orders of $(OsO_3F_2)_2$ and $(OsO_3F_2)_2{\cdot}2XeOF_4$ are comparable. The Os–F_2 bond order for $(OsO_3F_2)_2{\cdot}2XeOF_4$ (0.40) is slightly lower when compared with that of $(OsO_3F_2)_2$ (0.43), and is attributable to

coordination of F_2 to the Xe atom of $XeOF_4$. The Xe···F_2 bond order corresponding to this weak fluorine bridge interaction is only 0.04.

6.3. Conclusions.

The $(OsO_3F_2)_2 \cdot 2XeOF_4$ adduct has been synthesized by reaction of $(OsO_3F_2)_\infty$ with $XeOF_4$ solvent and is comprised of the doubly fluorine bridged $(OsO_3F_2)_2$ dimer and two $XeOF_4$ molecules which interact with the terminal fluorine ligands of the dimer by means of fluorine bridges between the Xe(VI) and Os(VIII) atoms. The $XeOF_4$ molecule retains its square pyramidal geometry and the primary coordination spheres of the osmium atoms are *fac*-OsO_3F_3 arrangements in which the oxygen ligands are cis to one another and the bridging fluorine atoms are trans to an oxygen ligand. The adduct is stable at room temperature for up to 5 h, slowly dissociating to $(OsO_3F_2)_\infty$ and $XeOF_4$. The $(OsO_3F_2)_2$ dimer has been isolated by removal of $XeOF_4$ from $(OsO_3F_2)_2 \cdot 2XeOF_4$ under dynamic vacuum and represents a new low-temperature phase of OsO_3F_2. Upon standing at 25 °C, the dimer undergoes an irreversible phase transition to the α-phase of $(OsO_3F_2)_\infty$, a polymeric chain structure. The vibrational modes and the Raman spectrum of $(OsO_3F_2)_\infty$ have been assigned in detail with the aid of quantum-chemical calculations of the presently unknown trinuclear μ–$F(OsO_3F_2)_2OsO_3F^-$ anion. Because the negative formal charge was found to be essentially uniformly dispersed over all the light atoms, the vibrational modes of the central OsO_3F_3 moiety of this anion proved to be a good model for the assignment of the vibrational modes of the OsO_3F_3 moieties in the infinite chain polymer, $(OsO_3F_2)_\infty$.

CHAPTER 7

SYNTHESES AND MULTI-NMR STUDY OF *fac*- AND *mer*-$OsO_3F_2(NCCH_3)$ AND THE X-RAY CRYSTAL STRUCTURE ($n = 2$) AND RAMAN SPECTRUM ($n = 0$) OF *fac*-$OsO_3F_2(NCCH_3)\cdot nCH_3CN$

7.1 Introduction

The Lewis acid behavior of $(OsO_3F_2)_\infty$ has been established by the syntheses of the Ag^+,[25] Cs^+,[24, 25] K^+,[24, 25] Na^+,[24] $N(CH_3)_4^+$,[23] NO^+,[23] Rb^+,[24] XeF_5^+,[203] and $Xe_2F_{11}^+$ [203] salts of *fac*-$OsO_3F_3^-$ from their respective fluorides. The facial geometry of $OsO_3F_3^-$ was determined from the vibrational spectra of the Cs^+, K^+, Rb^+, and Na^+ salts[24] and was confirmed by the X-ray crystal structure and Raman spectra of $[N(CH_3)_4][OsO_3F_3]$[23] and $[M][OsO_3F_3]$ ($M = XeF_5^+$, $Xe_2F_{11}^+$).[203]

Acetonitrile forms Lewis base adducts with high-oxidation state d^0 transition metal fluorides $[CH_3CN\cdot MF_4(NCl)]$ (M = Mo,[223] W[44]), oxide fluorides $MoOF_4(NCCH_3)$,[224] $ReO_2F_3(NCCH_3)$,[45] $TcO_2F_3(NCCH_3)$,[47] and $WOF_4(NCCH_3)$,[225] as well as with the sulfide fluoride, $WSF_4(NCCH_3)$.[226] The crystal structures of $[CH_3CN\cdot MF_4(NCl)]$ (M = Mo,[223] W[44]) and $ReO_3F(NCCH_3)_2\cdot CH_3CN$[45] have CH_3CN coordinated to the d^0 metal through the nitrogen electron lone pair to give a linear M---N–C–C arrangements. Both CH_3CN ligands of $ReO_3F(NCCH_3)_2\cdot CH_3CN$[45] coordinate cis to one another and trans to two of the three facial oxygen atoms. The only examples of Os(VIII) coordinated to nitrogen are adducts of OsO_4, e.g., $OsO_4(NH_3)$,[227] $OsO_4(NC_5H_5)$,[228] $OsO_4(NC_7H_{13})$,[229] and OsO_4L (L = NC_9H_7, $N_2C_8H_6$, and 1,2-$C_4H_4N_2$),[228] as well as nitrido-derivatives, e.g., $[A][OsO_3N]$ (A = $(C_6H_5)_4As^+$,[230]

Cs^+,[231] K^+,[232, 233] and H^+ [227]), $OsNCl_3(PPh_3)_2$,[234] and $OsO_2(OH)N$.[235] Prior to this work, there were no examples of nitrogen bases coordinated to Os(VIII) oxide fluorides known.

The current work describes the synthesis and characterization by multi-NMR and Raman spectroscopy, and single-crystal X-ray diffraction of *fac*-$OsO_3F_2(NCCH_3)$. The *mer*-$OsO_3F_2(NCCH_3)$ isomer in which the oxygen atoms are in a meridional arrangement and the CH_3CN ligand is coordinated trans to fluorine has also been characterized in solution by multi-NMR spectroscopy along with *fac*-$OsO_3F_2(NCCH_3)$.

7.2. Results and Discussion

7.2.1. Syntheses of *fac*-$OsO_3F_2(NCCH_3)$, *fac*-$OsO_3F_2(NCCH_3)\cdot n CH_3CN$ ($n \geq 2$), and *mer*-$OsO_3F_2(NCCH_3)$.

Osmium trioxide difluoride, $(OsO_3F_2)_\infty$, dissolves in CH_3CN at –40 °C according to eq 7.1 to give an orange-brown solution. Removal of excess CH_3CN under dynamic

$$OsO_3F_2 + CH_3CN \xrightarrow[-40\ ^\circ C]{CH_3CN} fac\text{-}OsO_3F_2(NCCH_3) \qquad (7.1)$$

vacuum at –40 °C initially yielded yellow-brown *fac*-$OsO_3F_2(NCCH_3)\cdot n CH_3CN$, which was confirmed by X-ray crystallography and Raman spectroscopy (Table E1). Acetonitrile in the crystal lattice was removed by continued pumping for 3 h at –40 °C to yield yellow-brown *fac*-$OsO_3F_2(NCCH_3)$ (see Section 7.2.3) which did not dissociate after a further 3 h of pumping at –40 °C. The unsolvated complex is stable at room temperature for at least several days and is very soluble in CH_3CN at –40 °C and slightly soluble in SO_2ClF at –40 and –80 °C. The solution NMR spectra (see Section 7.2.4) revealed the presence of *fac*-$OsO_3F_2(NCCH_3)$ as the major product, but also the presence

of *mer*-$OsO_3F_2(NCCH_3)$. Removal of excess SO_2ClF under dynamic vacuum at –80 °C yielded only *fac*-$OsO_3F_2(NCCH_3)$ (Table E1).

7.2.2. X-ray Crystal Structure of *fac*-$OsO_3F_2(NCCH_3)\cdot 2CH_3CN$.

Details of the data collection parameters and other crystallographic information are provided in Table 7.1 Bond lengths and bond angles are listed in Table 7.2.

The crystal structure (Figure 7.1a) is comprised of monomeric OsO_3F_2 coordinated to a CH_3CN molecule through the nitrogen atom to give pseudo-octahedral coordination at osmium. In addition, there are two uncoordinated, symmetry-related CH_3CN molecules in the asymmetric unit. The $OsO_3F_2(NCCH_3)$ adduct possesses a *fac*-trioxo arrangement about osmium in which the nitrogen atom of CH_3CN is coordinated trans to an oxygen atom. Preference for the *fac*-trioxo arrangement has been well documented and is consistent with other d^0 transition metal trioxo species such as the related Os(VIII) and Re(VII) species, $(OsO_3F_2)_\infty$,[11] $(OsO_3F_2)\cdot 2XeOF_4$,[18] $OsO_3F_3^-$,[23, 203] $[XeF_5][\mu\text{-}F(OsO_3F_2)_2]$,[203] $[OsO_3F][HF][SbF_6]$,[21] ReO_3F,[49] and $ReO_3F(CH_3CN)_2\cdot CH_3CN$,[45] and has been previously discussed.[23]

The crystal lattice consists of *fac*-$OsO_3F_2(NCCH_3)$ and CH_3CN molecules stacked along the *b*- and *c*-axes which alternate along the *a*-axis (Figure E1). In the *a*,*b*-plane, the adduct molecule reverses orientation between successive layers, with the free CH_3CN molecules alternating their orientations in a similar manner. The resulting intermolecular contacts are long and are near the sums of the van der Waals radii of the contacting atoms.[165, 236]

Table 7.1. Summary of Crystal Data and Refinement Results for *fac*-$OsO_3F_2(NCCH_3)\cdot 2CH_3CN$

chem formula	$C_6F_2H_9N_3O_3Os$
space group	*Pnma* (No. 62)
a (Å)	7.7995(2)
b (Å)	14.7327(4)
c (Å)	9.5210(2)
V (Å^3)	1095.2(1)
molecules/unit cell	4
mol wt (g mol^{-1})	1597.45
calcd density (g cm^{-3})	2.425
T (^{o}C)	–173
μ (mm^{-1})	11.68
R_1[a]	0.0178
wR_2[b]	0.0413

[a] R_1 is defined as $\Sigma\| F_o | - | F_c \| / \Sigma | F_o |$ for $I > 2\sigma(I)$. [b] wR_2 is defined as $\{\Sigma[w(F_o^2-F_c^2)^2]/\Sigma w(F_o^2)^2\}^{1/2}$ for $I > 2\sigma(I)$.

Table 7.2. Experimental Geometrical Parameters for *fac*-$OsO_3F_2(NCCH_3)\cdot 2CH_3CN$ and Calculated Geometrical Parameters for *fac*-$OsO_3F_2(NCCH_3)$, *mer*-$OsO_3F_2(NCCH_3)$, and CH_3CN

exptl[a]		calcd						
fac-$OsO_3F_2(NCCH_3)\cdot 2CH_3CN$			*fac*-$OsO_3F_2(NCCH_3)$ (C_1)		*mer*-$OsO_3F_2(NCCH_3)$ (C_1)		CH_3CN (C_{3v})	
			SVWN[b]	B3LYP[c]	SVWN[b]	B3LYP[c]	SVWN[b]	B3LYP[d]
bond lengths (Å)								
Os–O(1)	1.704(2)	Os–O_1	1.727	1.701	1.760	1.736		
		Os–O_2	1.727	1.701	1.728	1.705		
Os–O(2)	1.696(2)	Os–O_3	1.712	1.687	1.760	1.736		
Os–F(1)	1.940(1)	Os–F_1	1.922	1.922	1.863	1.857		
		Os–F_2	1.922	1.922	1.968	1.972		
Os---N(1)	2.206(3)	Os---N	2.260	2.386	2.114	2.175		
N(1)–C(1)	1.140(5)	N–C_1	1.169	1.142	1.167	1.140	1.181	1.149
C(1)–C(2)	1.437(5)	C_1–C_2	1.443	1.449	1.440	1.447	1.451	1.455
C(2)–H	0.980	C_2–H	1.108	1.089	1.108	1.089	1.108	1.089
N(2)–C(3)	1.140(4)							
C(3)–C(4)	1.456(4)							
C(4)–H	0.94(4)							
bond angles (deg)								
O(1)–Os–O(1A)	101.5(1)	O_1–Os–O_2	100.9	100.7	101.5	101.4		
O(1)–Os–O(2)	102.60(8)	O_1–Os–O_3	103.4	103.5	101.5	100.4		
O(1)–Os–F(1)	87.79(8)	O_1–Os–F_1	87.6	87.3	88.5	90.5		
O(1)–Os–F(1A)	159.89(8)	O_1–Os–F_2	156.1	155.6	79.3	79.5		
O(1)–Os---N(1)	84.08(7)	O_1–Os---N_1	82.9	82.0	91.0	88.9		

O(1A)–Os–O(2)	102.60(8)	O_2–Os–O_3	103.4	103.5	156.9	158.7		
O(1A)–Os–F(1)	159.89(8)	O_2–Os–F_1	156.1	155.6	88.5	90.5		
O(1A)–Os–F(1A)	87.79(8)	O_2–Os–F_2	87.6	87.3	79.3	79.5		
O(1A)–Os---N(1)	84.08(7)	O_2–Os---N_1	82.9	82.0	91.0	88.9		
O(2)–Os–F(1)	92.52(8)	O_3–Os–F_1	96.2	96.8	100.1	100.0		
O(2)–Os–F(1A)	92.52(8)	O_3–Os–F_2	96.2	96.8	155.8	158.4		
O(2)–Os---N(1)	169.2(1)	O_3–Os---N_1	169.9	171.2	82.4	83.1		
F(1)–Os–F(1A)	78.27(9)	F_1–Os–F_2	76.7	76.9	104.1	101.5		
F(1)–Os---N(1)	79.16(7)	F_1–Os---N_1	75.9	76.3	177.5	176.9		
F(1A)–Os---N(1)	79.16(7)	F_2–Os---N_1	75.9	76.3	73.4	75.4		
Os---N(1)–C(1)	178.7(2)	Os---N_1–C_1	170.5	173.7	173.6	174.3		
N(1)–C(1)–C(2)	178.6(3)	N_1–C_1–C_2	179.3	179.7	179.1	179.5		
C(1)–C(2)–H	109.5	C_1–C_2–H	110.0	110.3	110.0	109.3		
H–C(2)–H	109.5	H–C_2–H	108.5	109.0	108.5	109.4		
N(2)–C(3)–C(4)	178.6(3)						180	180
C(3)–C(4)–H(4A)	111(3)						110.8	110.2
C(3)–C(4)–H(4B)	109(2)						108.1	108.8
C(3)–C(4)–H(4C)	109(2)							
H(4A)–C(4)–H(4B)	109(3)							
H(4A)–C(4)–H(4C)	115(3)							
H(4B)–C(4)–H(4C)	104(3)							

[a] For the atom labeling scheme, see Figure 7.1a. [b] The SDDall basis set, augmented for F and O with two d-type polarization functions by Huzinaga, was used.[151] [c] The Stuttgart basis set for Os augmented with one f-type polarization functional was used;[152] The aug-cc-pVTZ basis sets were used for all other atoms. [d] The aug-cc-pVTZ basis set was used.

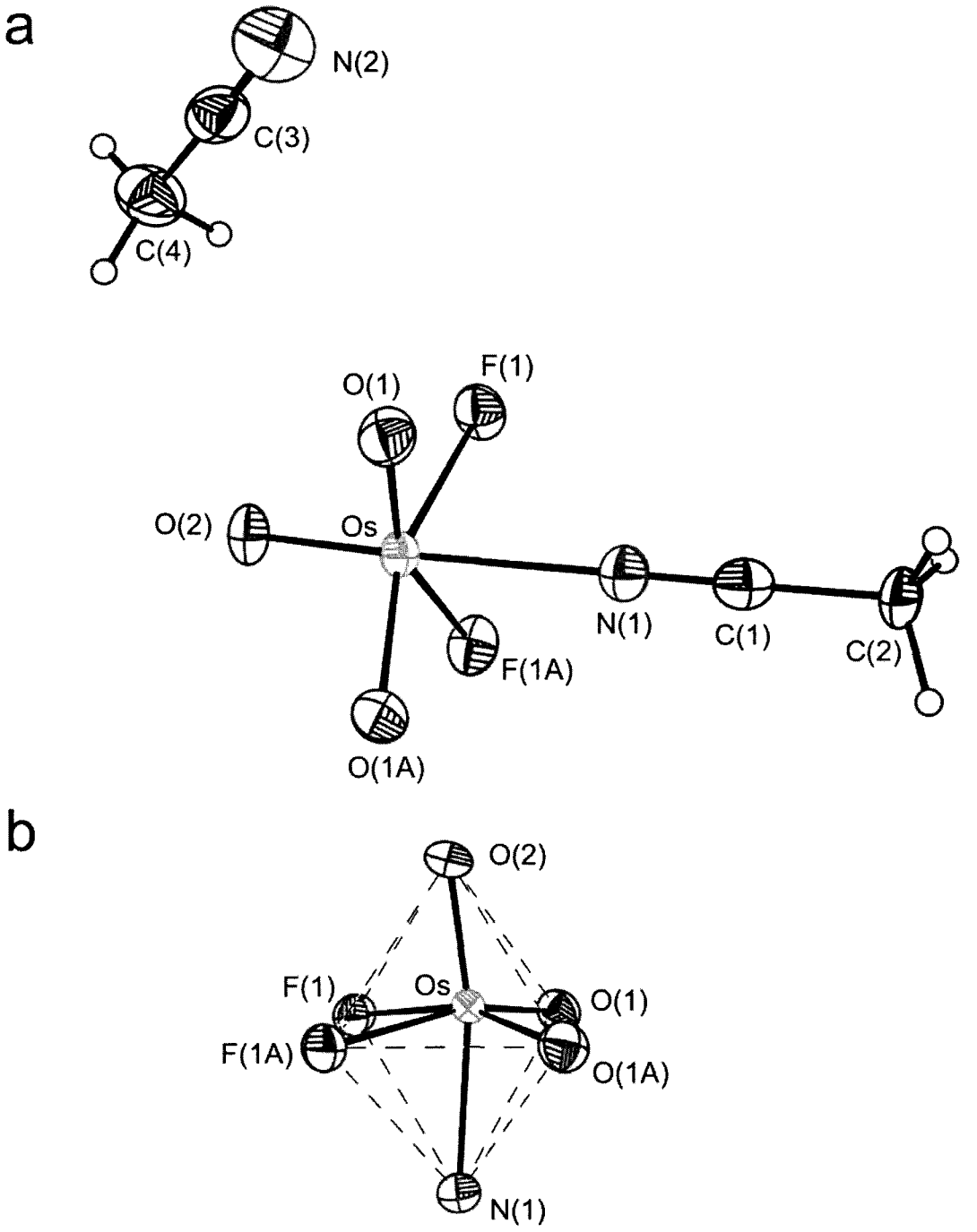

Figure 7.1. (a) Structural unit in the X-ray crystal structure of *fac*-$OsO_3F_2(NCCH_3)\cdot 2CH_3CN$ with thermal ellipsoids drawn at the 70% probability level. (b) The octahedron formed by the light atoms of the OsO_3F_2N-unit.

The C–N (1.140(5) Å) and C–C (1.437(5) Å) bond lengths of the adducted CH_3CN molecule are comparable to those of the co-crystallized CH_3CN solvent molecules (1.140(4) and 1.450(4) Å, respectively) and both bond lengths are similar to those of $ReO_3F(NCCH_3)_2$ (C–C 1.451(7), C–N 1.136(7) Å).[45] The C–N triple bond length is in good agreement with the previously calculated additive covalent radii for C (0.60 Å) and N (0.54 Å).[237]

The Os---N bond length (2.206(3) Å) is shorter than the metal-nitrogen bond lengths of the d^0 rhenium and tungsten adducts, $ReO_3F(NCCH_3)_2 \cdot CH_3CN$ (2.294(4) Å),[45] $WF_6(NC_5H_4F)$ (2.294(9) Å),[238] $WOF_4(NC_5H_4F)$ (2.39(1) Å),[238] and $WOF_4(NC_5H_5)$ (2.246(8) Å).[239] The nitrogen atom is trans to an oxygen atom which is consistent with the latter adducts and fluorine-bridged oxide fluoride compounds where the weakly bonded bridging fluorine atom is trans to an oxygen atom; e.g., $(OsO_3F_2)_\infty$,[11] $(OsO_3F_2)_2 \cdot 2XeOF_4$,[18] μ-$F(OsO_3F_2)_2^-$,[203] $F(cis\text{-}OsO_2F_3)_2^+$,[22] polymeric $MO_2F_3 \cdot SbF_5$ (M = Re, Tc),[46] μ-$F(TcOF_4)_2^+$,[158] μ-$F(ReOF_4)_2^+$,[157] μ-$F(cis\text{-}ReO_2F_3)_2^+$,[45] $Re_3O_6F_{10}^-$,[47] $(WOF_4)_4$,[171] and $(MoOF_4)_\infty$.[220] The *trans*-influence of oxygen results in bonding of the nitrogen and fluorine atoms trans to oxygen atoms because the CH_3CN and fluorine σ-donor ligands do not compete as effectively as the π-donor oxygen ligands for the osmium $d_{t_{2g}}$ orbitals.[47]

All Os–O bonds are *cis* to one another and the bond lengths are equal to within $\pm 3\sigma$ (1.704(2) and 1.696(2) Å) and are in the same range as those of other neutral *fac*-trioxo osmium(VIII) compounds such as $(OsO_3F_2)_\infty$ (1.688(1), 1.678(1), and 1.727(1) Å),[11] and $(OsO_3F_2)_2 \cdot 2XeOF_4$ (1.703(6), 1.685(6) and 1.685(6) Å).[18] Although the Os–N

bond is longer than the Os–F bonds (vide infra), the Os–O(2) bond does not show significant shortening, indicating that, like fluorine, CH_3CN does not compete as effectively with oxygen as a donor to osmium(VIII). The Os–F(1,1A) bonds (1.940(1) Å) are longer than the terminal Os–F bond in $(OsO_3F_2)_\infty$ (1.879(1) Å),[11] but are similar to those of the $OsO_3F_3^-$ anion (1.97(1)–1.91(1) Å),[23] suggesting that the adducted CH_3CN molecule donates sufficient electron density to the osmium atom to significantly weaken the Os–F bonds (see Section 7.2.6).

The ligand atoms of *fac*-$OsO_3F_2(NCCH_3)$ form a distorted octahedral coordination sphere around osmium. Although there is significant variation in the bond lengths around the osmium atom, the octahedron formed by the light atoms is relatively undistorted (Figure 7.1b), as shown by the range of nearest neighbor-ligand atom contacts.[240] The F(1), F(1A), O(1), and O(1A) [F(1), N(1), O(1A), and O(2)] {F(1A), N(1), O(1), and O(2)} atoms are coplanar to within ±0.001 [0.03] {0.03} Å, and the osmium atom lies 0.255 [0.256] {0.159} Å out of this plane, towards O(2) [O(1)] {O(1A)}. All three planes are orthogonal to one another to within ±0.3°. The Os–O(2) and Os---N(1) bonds bend away from the Os–O(1,1A) bonds towards the Os–F(1,1A) bonds at an angle of 169.2(1)°. The displacement of the osmium atom towards the *fac*-OsO_3 group is similar to the metal atom displacements observed in $(OsO_3F_2)_\infty$,[11] $(OsO_3F_2)_2{\cdot}2XeOF_4$,[18] $ReCl_3O_3^{2-}$,[222] $OsO_3F_3^-$,[23, 203] and μ-$F(OsO_3F_2)_2^-$ [203] and to those in the *cis*-dioxo-metal oxide fluoride species *cis*-OsO_2F_4,[20] $F(cis\text{-}OsO_2F_3)_2^+$,[22] $OsO_2F_3^+$,[139] *cis*-$ReO_2F_4^-$,[45] and *cis*-$TcO_2F_4^-$,[47] where the central metal atom is symmetrically displaced along the line bisecting the O–M–O angle toward the oxygen ligands of the *cis*-MO_2 group.

7.2.3. Raman Spectroscopy.

The low-temperature Raman spectrum of *fac*-$OsO_3F_2(NCCH_3)$ (Figure 7.2) is very similar to that of *fac*-$OsO_3F_2(NCCH_3)\cdot n CH_3CN$, where $n \geq 2$ (Figure E2), with the exception of the vibrational bands of uncoordinated CH_3CN. With few exceptions, the bands in both spectra are split into two components. The Raman spectrum of *fac*-$OsO_3F_2(NCCH_3)$ isolated from SO_2ClF showed a small amount of free CH_3CN as an impurity (Table E1). The assigned Raman spectrum is that of the unsolvated product, *fac*-$OsO_3F_2(NCCH_3)$, whereas the crystal structure is that of the solvated product, *fac*-$OsO_3F_2(NCCH_3)\cdot 2CH_3CN$. Consequently, a factor-group analysis could not be carried out to unambiguously confirm that the additional splittings in the Raman spectra of *fac*-$OsO_3F_2(NCCH_3)$ and *fac*-$OsO_3F_2(NCCH_3)\cdot n CH_3CN$ arise from vibrational coupling within the unit cell. The factor-group analysis for *fac*-$OsO_3F_2(NCCH_3)\cdot 2CH_3CN$ (Table E2), however, predicts that the vibrational bands are split into two components, suggesting that the unit cells of *fac*-$OsO_3F_2(NCCH_3)$, *fac*-$OsO_3F_2(NCCH_3)\cdot n CH_3CN$, and *fac*-$OsO_3F_2(NCCH_3)\cdot 2CH_3CN$ are closely related, or identical for the solvated adducts, i.e., $n = 2$.

The observed and calculated frequencies of *fac*-$OsO_3F_2(NCCH_3)$ at both the SVWN and B3LYP levels of theory and their assignments are listed in Table 7.3. The spectral assignments were made by comparison with the calculated frequencies and Raman intensities (Table 7.3) of the energy-minimized geometries of *fac*-$OsO_3F_2(NCCH_3)$ and CH_3CN (see Section 7.2.6). The calculated vibrational frequencies obtained at the SVWN and B3LYP levels are in good agreement. The mode

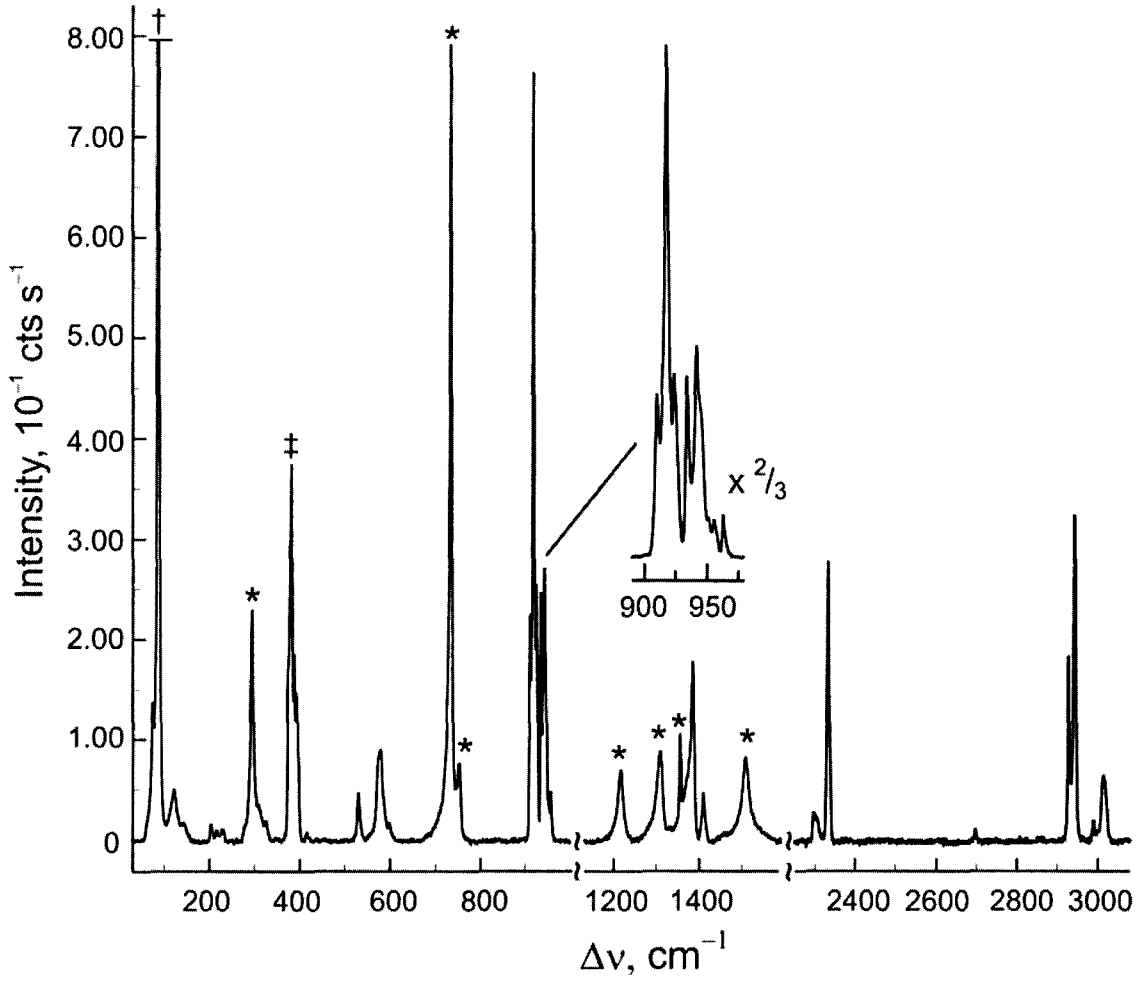

Figure 7.2. Raman spectrum of *fac*-$OsO_3F_2(NCCH_3)$ recorded at –150 °C using 1064-nm excitation; the symbols denote FEP sample tube lines (*), a band that overlaps with an FEP sample tube line (‡), and an instrumental artifact (†).

Table 7.3. Calculated and Experimental Raman Frequencies, Intensities, and Assignments for *fac*-$OsO_3F_2(NCCH_3)$

exptl[a]		calcd				assgnts (C_1)[f]
fac-$OsO_3F_2(NCCH_3)$	CH_3CN	*fac*-$OsO_3F_2(NCCH_3)$		CH_3CN		
		SVWN[b,c]	B3LYP[c,d]	SVWN[b,c]	B3LYP[c,e]	
3014(8), 2990(2)	2999(54)	3072(81)[3] 3071(74)[3]	3125(67)[<1] 3125(64)[1]	3065(64)[<1]	3115(58)[1]	$\nu_{as}(CH_3)$
2944(43), 2929(24) 2697(1)[g]	2938(97)	2976(230)[4]	3052(239)[<1]	2972(144)[1]	3048(195)[3]	$\nu_s(CH_3)$
2332(36) 2296(3)[h]	2248(100)	2322(245)[67]	2422(184)[78]	2247(50)[8]	2363(81)[11]	ν(CN)
1410(6)	1457(11) 1454(7)	1425(20)[24]	1467(6)[12]	1439(21)[20]	1475(5)[10]	$\delta_{as}(CH_3)$
1385(24)	1425(3) 1420(4)	1425(19)[24]	1467(6)[12]			
1356(14)	1376(15) 1371(3)	1394(34)[27]	1411(12)[2]	1397(18)[22]	1413(6)[2]	$\delta_s(CH_3)$
1041(1), 1029(1)	1042(1)	1043(<1)[10] 1040(<0.1)[10]	1063(<1)[4] 1061(<1)[4]	1048(<1)[6]	1063(<1)[2]	$\rho_r(CH_3)$
956(6), 952(sh)	922(20)	988(5)[16]	1020(60)[95]	948(5)[1]	928(5)[1]	ν(CC)[i]
945(sh), 942(36)		951(37)[64]	989(23)[125]			$\nu(OsO_1) + \nu(OsO_2)$
934(33), 924(34)		949(14)[117]	975(14)[150]			$\nu(OsO_1) - \nu(OsO_2)$
918(100), 910(30)		983(47)[117]	948(8)[9]			$\nu(OsO_3)$[j]
598(2)		624(10)[98]	609(8)[115]			$\nu(OsF_1) + \nu(OsF_2)$
529(7)		564(7)[52]	547(4)[51]			$\nu(OsF_1) - \nu(OsF_2)$
	400(3)	410(2)[<1]	421(<1)[1]			$\delta(NCC)_{oop}$
415(1)	395(12) 392(9) 386(5)	408(2)[<1]	422(1)[3]	375(4)[<1]	382(1)[1]	$\delta(NCC)_{ip}$
396(sh), 392(19)		387(4)[2]	417(3)[2]			$\delta(O_1OsO_2) + \delta(F_1OsF_2)$
388(50)[k]		369(5)[13]	392(1)[12]			$\delta(OsO_1O_2O_3)$
378(40), 374(sh)		361(6)[5]	386(6)[6]			$\rho_t(O_1OsO_2) + \delta(O_2OsO_3)$
326(2)		319(<1)[10]	338(<1)[10]			$\delta(O_1OsO_2) - \delta(F_1OsF_2) + \delta(NCC)_{ip\ small}$
309(4)		281(2)[13]	289(2)[17]			$\delta(OsF_1F_2O_3)$
277(sh)		278(2)[17]	291(2)[20]			$\rho_r(O_1OsO_2) - \rho_r(F_1OsF_2) + \delta(NCC)_{oop}$

232(1), 228(1)		217(<1)[<1]	211(<1)[<1]	δ(Os---NC)$_{ip}$
216(1)		214(<1)[<1]	209(<1)[1]	δ(Os---NC)$_{oop}$
204(2)		203(1)[16]	149(<1)[17]	ν(Os---N)
143(2)		174(<1)[<0.1]	174(<1)[<0.1]	$\rho_t(F_1OsF_2) - \rho_t(O_2OsO_1)$
		49(2)[5]	50(1)[4]	ρ_w(NCC)$_{ip}$
121(7)		49(2)[4]	50(2)[4]	ρ_w(NCC)$_{oop}$
n.o.		14(<0.1)[<0.1]	5(<0.1)[<0.1]	$\rho_t(CH_3)$
230(1)	116(18)			
119(sh)	108(13)			lattice modes
114(11)	102(15)			
106(8)	96(32)			

[a] The Raman spectrum was recorded on a microcrystalline solid in a FEP sample tube at −150 °C using 1064-nm excitation. Raman intensities are given in parentheses and are relative intensities with the most intense band given as 100. The abbreviation (sh) denotes a shoulder. [b] SVWN/SDDall. [c] Values in parentheses denote calculated Raman intensities ($Å^4\ u^{-1}$) and values in square brackets denote calculated infrared intensities (km mol^{-1}). [d] B3LYP/Stutt-f (Os) aug-cc-pVTZ (H, C, N, F). [e] B3LYP/aug-cc-pVTZ (H,C,N). [f] Assignments are based on the B3LYP calculated geometry. The atom labeling scheme refers to Figure 7.6a for *fac*-$OsO_3F_2(NCCH_3)$ and the plane of symmetry is defined by the O_2, O_3, Os, F_1, and N atoms. The abbreviations denote stretch (ν), bend (δ), torsion (ρ_t), wag (ρ_w), rock (ρ_r), out-of-plane (oop) and in-plane (ip). [g] Overtone band corresponding to 2 x 1356 cm^{-1}. [h] Combination band corresponding to 1356 + 956 cm^{-1}. [i] At the SVWN level, the mode description is $\nu(C_1C_2) - \nu(OsO_3)_{small}$. [j] At the SVWN level, the mode description is $\nu(OsO_3) + \nu(C_1C_2)_{small}$. [k] The band overlaps with a FEP sample tube band.

descriptions are based on the atomic displacements obtained for the optimized B3LYP geometry.

The bands at 924, 934 and at 942, 945 cm^{-1} are assigned to the out-of-phase $\nu(OsO_1) - \nu(OsO_2)$ and the in-phase $\nu(OsO_1) + \nu(OsO_2)$ stretching modes. The modes are shifted to lower frequency when compared with the corresponding modes in $(OsO_3F_2)_\infty$ (945, 949, 952, 957 cm^{-1}),[18] in accordance with donation of electron density from the nitrogen atom to the osmium atom which weakens the Os–O bonds. The Os–O stretching modes occur to higher frequency than those of $OsO_3F_3^-$ (908, 912, 920 cm^{-1}),[23] consistent with the lower base strength of CH_3CN relative to that of the fluoride ion. Based on the vibrational displacements obtained at the B3LYP level, the relatively strong bands at 910 and 918 cm^{-1} are assigned to the $\nu(OsO_3)$ stretching mode, however, at the SVWN level, the $\nu(OsO_3)$ stretch weakly couples in an in-phase manner with $\nu(C_1C_2)$ of the CH_3CN ligand bonded trans to O_3. The in-phase $\nu(OsF_1) + \nu(OsF_2)$ (598 cm^{-1}) stretching mode occurs to higher frequency than its out-of-phase counterpart, $\nu(OsF_1) - \nu(OsF_2)$ (529 cm^{-1}), in agreement with the calculated values (609 and 547 [B3LYP] cm^{-1}, respectively). The in-phase stretch is very similar to the in-phase stretch of $(OsO_3F_2)_\infty$ (596 cm^{-1})[18] and is shifted to higher frequency than in $OsO_3F_3^-$ (573 cm^{-1}),[23] consistent with a neutral species. The out-of-phase stretching mode is intermediate within the span of asymmetric Os–F stretching modes observed for $(OsO_3F_2)_\infty$ (610 cm^{-1})[18] and $OsO_3F_3^-$ (504 cm^{-1}).[23] Its intermediacy is consistent with that observed for the Os–O stretching modes (vide supra). The Os---N stretching band at 204 cm^{-1} is weak and intermediate with respect to the M---N stretching frequencies of other CH_3CN adducts such as

$TcO_2F_3(NCCH_3)$ (217 cm^{-1}),[47] $[ReO_2F_2(CH_3CN)_2][SbF_6]$ (264 cm^{-1}),[46] and $ReO_2F_3(NCCH_3)$ (252 cm^{-1}).[45]

The ν(CN) stretching band of the coordinated CH_3CN molecule (2332 cm^{-1}) occurs at significantly higher frequency than that of free CH_3CN (2248 cm^{-1}). The high-frequency shift is consistent with donation of electron density by the nitrogen ligand atom to osmium, which strengthens the C–N bond as a result of nitrogen rehybridization to give more s character to the CN σ-bond.[241] Thus, backbonding from Os(VIII) into the π* orbitals of the CN group is not important because it would lead to a decrease in Δν(CN). The calculated complexation shifts at the SVWN (Δν(CN), 75 cm^{-1}) and B3LYP (Δν(CN), 59 cm^{-1}) levels are in good agreement with the experimental complexation shift (Δν(CN), 84 cm^{-1}). The bands at 952 and 956 cm^{-1} are assigned to ν(CC) of coordinated CH_3CN at the B3LYP level, which weakly in-phase and out-of-phase couple with $\nu(OsO_3)$ at the SVWN level (vide supra). The ν(CC) band shifts to higher frequency at the SVWN and B3LYP levels upon coordination (exptl., Δν(CC), 34 cm^{-1}; calcd., Δν(CC), 40 and 19 cm^{-1}, respectively), indicating a strengthened C–C bond. The experimental complexation shifts for ν(CN) and ν(CC) and their trends are similar to those of $TcO_2F_3(NCCH_3)$ (Δν(CN), 49; Δν(CC), 18 cm^{-1})[47] and $ReO_2F_3(NCCH_3)$ (Δν(CN), 75; Δν(CC), 22 cm^{-1}),[45] suggesting similar Lewis acid strengths for monomeric OsO_3F_2, TcO_2F_3, and ReO_2F_3. The C–H bonds are little affected by coordination to osmium, with the experimental and calculated CH_3 group frequencies showing no significant complexation shifts.

There are four modes associated with the in-plane and out-of-plane δ(NCC) bending modes (relative to the [O2, O3, Os, F1, N]-plane). The $\delta(NCC)_{ip}$ bend is observed at 415 cm^{-1}, while the $\delta(NCC)_{oop}$ bend is predicted to occur at higher frequency, but could not be observed. The remaining out-of-plane and in-plane bending modes are both weakly coupled to O–Os–O and F–Os–F bends to give bands at 277 and 326 cm^{-1}, respectively. The in-plane (232 cm^{-1}) and out-of-plane (216 cm^{-1}) δ(Os---NC) bending modes are to higher frequency than the Re---NC bending modes in $ReO_2F_3(NCCH_3)$ (174 and 154 cm^{-1}).[45]

7.2.4. NMR Spectroscopy.

Table 7.4 lists the ^{1}H, ^{13}C, ^{15}N, and ^{19}F NMR parameters for *fac*-$OsO_3F_2(^{14}NCCH_3)$ in CH_3CN solvent (–40 °C), *fac*- and *mer*-$OsO_3F_2(^{14}NCCH_3)$ in SO_2ClF solvent (–40 and –80 °C) and *fac*- and *mer*-$OsO_3F_2(^{15}NCCH_3)$ in SO_2ClF solvent (–84 °C).

7.2.4.1. *fac*-$OsO_3F_2(NCCH_3)$.

The ^{19}F NMR spectrum of *fac*-$OsO_3F_2(^{14}NCCH_3)$ in CH_3CN solvent at –40 °C consists of a singlet at –99.6 ppm, which is less shielded than the ^{19}F environment of $OsO_3F_3^-$ in CH_3CN solvent (–116.8 ppm)[23] and considerably more shielded than both ^{19}F environments of *cis*-OsO_2F_4 (15.8 and 63.3 ppm) in anhydrous HF solvent.[20] This is consistent with a decrease in the number of strongly electron withdrawing fluorine ligands and the addition of the electron donating nitrogen and oxygen ligands. The ^{19}F chemical shift is intermediate with respect to those of $WOF_4(NCCH_3)$ (–68.5 ppm)[225] and $MoOF_4(NCCH_3)$ (–147.4 ppm)[224] recorded at –30 °C in CH_3CN. The ^{1}H NMR spectrum

Table 7.4. NMR Chemical Shifts and Spin-Spin Coupling Constants for *fac*-$OsO_3F_2(^{14/15}NCCH_3)$ and *mer*-$OsO_3F_2(^{14/15}NCCH_3)$

			chemical shifts, ppm				coupling constants, Hz			
species	solvent	T (°C)	$\delta(^{19}F)^a$	$\delta(^{15}N)$	$\delta(^{13}C)^b$	$\delta(^1H)$	$^2J(^{19}F_1\text{-}^{19}F_2)^a$	$^1J(^{15}N\text{-}^{19}F_1)^a$	$^1J(^{13}C\text{-}^1H)$	$^1J(^{19}F\text{-}^{187}Os)^c$
fac-$OsO_3F_2(^{14}NCCH_3)$	CH_3CN	–40	–99.6[d]			2.55[e]			126.1	
fac-$OsO_3F_2(^{14}NCCH_3)$	SO_2ClF^f	–40	–93.6			2.66			137.9	
fac-$OsO_3F_2(^{14}NCCH_3)$	SO_2ClF^f	–80	–96.1			1.76			139.5	41.2
fac-$OsO_3F_2(^{15}NCCH_3)^g$	SO_2ClF^f	–84	–96.8	–197.3	2.24 (CH_3)	2.02		21.4	139.8	
mer-$OsO_3F_2(^{14}NCCH_3)$	SO_2ClF^f	–40	–44.4 F_2 –13.1 F_1			3.12	134.3		142.8	
mer-$OsO_3F_2(^{14}NCCH_3)$	SO_2ClF^f	–80	–46.1 F_2 –15.4 F_1			2.71	135.0		145.3	
mer-$OsO_3F_2(^{15}NCCH_3)^g$	SO_2ClF^f	–84	–48.0 F_2 –17.9 F_1	–258.6	3.15 (CH_3)	3.04	134.3	18.3	140.4	

[a] The equatorial and axial fluorine atoms are denoted by F_1 and F_2, respectively. [b] The ^{13}C resonances of *fac*-$OsO_3F_2(^{14}NCCH_3)$ and *mer*-$OsO_3F_2(^{14}NCCH_3)$ could not be observed. [c] The $^1J(^{19}F\text{-}^{187}Os)$ coupling constant could only be observed for *fac*-$OsO_3F_2(^{14}NCCH_3)$ in SO_2ClF solvent (–80 °C). [d] Weak doublet (46.9 ppm) and quintet (95.2 ppm) ($^2J(^{19}F\text{-}^{19}F)$ = 92 Hz) resonances assigned to $OsO_2F_5^-$ were observed in the ^{19}F spectrum. [e] Acetonitrile solvent was observed in the ^1H spectrum at 2.01 ppm, $^1J(^1H\text{-}^{13}C)$ = 137 Hz]. [f] Resonances assigned to SO_2ClF solvent, SO_2F_2 solvent impurity (parentheses), and weak unassigned resonances (braces) were observed in the ^{19}F spectra [–40 °C: 98.9 (32.7) {–70.5, –72.0, –76.6}; –80 °C: 98.5 (32.7) {–70.7, –72.2, –76.7}; –84 °C: 98.7 (32.7) {69.0, –72.1, –73.1, –76.6} ppm]. Resonances assigned to HF impurity (a doublet) and free CH_3CN (parentheses) were observed in the ^1H spectra [–40 °C: 6.16 ppm, $^1J(^1H\text{-}^{19}F)$ = 496 Hz (1.94 ppm, $^1J(^1H\text{-}^{13}C)$ = 131 Hz); –80 °C: 6.69 ppm, 487 Hz (1.26 ppm, $^1J(^1H\text{-}^{13}C)$ = 130 Hz); –84 °C: 7.19 ppm, $^1J(^1H\text{-}^{13}C)$ = 47 Hz (1.51 ppm, $^1J(^1H\text{-}^{13}C)$ = 136 Hz)]. [g] Unreacted $CH_3C^{15}N$ was also observed in the $^{13}C\{^1H\}$ (117.50 [CN] and 0.86 [CH_3] ppm) and ^{15}N (–138.3 ppm) spectra.

at –40 °C is a singlet corresponding to complexed CH_3CN at 2.55 ppm ($^1J(^1H–^{13}C)$ = 126.1 Hz) which is shifted to higher frequency than the ^1H resonance of CH_3CN solvent (2.06 ppm, $^1J(^1H–^{13}C)$ = 136.1 Hz), consistent with Lewis acid-base adduct formation. The complexation shift (0.49 ppm) is comparable to that of $TcO_2F_3(NCCH_3)$ in CH_3CN solvent (0.37 ppm).[47]

The ^{19}F NMR spectrum of *fac*-$OsO_3F_2(^{14}NCCH_3)$ in SO_2ClF solvent at –80 (–40) °C is a singlet at –97.6 (–93.6) ppm with ^{187}Os (I = ½; natural abundance, 1.64%) satellites corresponding to $^1J(^{187}Os–^{19}F)$ = 41.2 Hz. The $^{187}Os–^{19}F$ coupling constant is greater than that observed for the $OsO_3F_3^-$ anion (32 Hz),[23] and is consistent with greater Os–F bond covalency in the neutral adduct, and is similar to one of the two $^1J(^{187}Os-^{19}F)$ couplings observed for *cis*-OsO_2F_4 (35.1 and 59.4 Hz).[20] In the latter case, the smaller coupling constant was tentatively assigned to $^1J(^{187}Os-^{19}F_a)$ where the fluorine ligands are trans to one another, and the larger coupling was assigned to $^1J(^{187}Os-^{19}F_e)$, where the fluorine ligands are trans to oxygen ligands. The F atoms are trans to O atoms for both $OsO_3F_3^-$ and $OsO_3F_2(NCCH_3)$, suggesting that the $^1J(^{187}Os-^{19}F)$ coupling and ^{19}F chemical shift assignments for *cis*-OsO_2F_4 should be interchanged. The low-frequency ^{19}F resonance of *cis*-OsO_2F_4 (15.8 ppm; $^1J(^{187}Os–^{19}F)$, 35.1 Hz) should be re-assigned to the two equatorial fluorine ligands trans to oxygen and the high-frequency ^{19}F resonance (63.3 ppm $^1J(^{187}Os–^{19}F)$, 59.4 Hz) should be re-assigned to the mutually trans axial fluorine ligands. The re-assignment is now consistent with the range of $^1J(^{187}Os–^{19}F)$ coupling constants for fluorine trans to oxygen in other Os(VIII) oxide fluorides; namely, *cis*-OsO_2F_4, *fac*-$OsO_3F_2(NCCH_3)$, and *fac*-$OsO_3F_3^-$. Smaller $^1J(M-^{19}F)$ coupling constants

for fluorine trans to oxygen relative to those for fluorine trans to fluorine have also been reported for $WO_2F_4^{2-}$ [199] and $TcO_2F_4^-$.[47] A ^{15}N-enriched sample of *fac*-$OsO_3F_2(^{15}NCCH_3)$ in SO_2ClF solvent resulted in splitting of the *fac*-$OsO_3F_2(^{15}NCCH_3)$ ^{19}F resonance at –96.8 ppm into a doublet ($^2J(^{19}F–^{15}N)$, 21.4 Hz, Figure 7.3), confirming that a single CH_3CN molecule is coordinated to osmium and that both fluorine ligands are chemically equivalent.

The ^{15}N NMR resonance of *fac*-$OsO_3F_2(^{15}NCCH_3)$ (Figure 7.4) at –197.3 ppm is a triplet ($^2J(^{15}N–^{19}F)$ = 21.4 Hz) which is consistent with splitting of the ^{15}N resonance by coupling to two chemically equivalent fluorine nuclei. The ^{15}N resonance of the complexed $CH_3C^{15}N$ ligand is shifted by 59.0 ppm to lower frequency when compared with that of free $CH_3C^{15}N$ (–138.3 ppm) in SO_2ClF solvent.

The ^1H NMR spectra of *fac*-$OsO_3F_2(^{14}NCCH_3)$ and *fac*-$OsO_3F_2(^{15}NCCH_3)$ (Figure 7.5) recorded in SO_2ClF solvent at –80 (–40) °C are singlets at 1.76 (2.66) ppm ($^1J(^1H–^{13}C)$, 139.5 (137.9) Hz) and 2.02 ppm ($^1J(^1H–^{13}C)$, 139.8 Hz), respectively. The ^1H complexation shifts for the ^{14}N (0.50 ppm) and ^{15}N (0.51 ppm) isotopomers are comparable to that observed for $ReO_2F_3(NCCH_3)$ in SO_2ClF (0.59 ppm).[45] A singlet was observed at 2.24 ppm in the $^{13}C\{^1H\}$ NMR spectrum of *fac*-$OsO_3F_2(^{15}NCCH_3)$ (–80 °C) which resulted from the methyl carbon of the coordinated CH_3CN ligand, representing a 1.59 ppm complexation shift relative to free CH_3CN (0.65 ppm), also observed in the same sample. The ^{13}C resonances of complexed CH_3CN could not be observed in CH_3CN solvent presumably because they overlap with the solvent peaks.

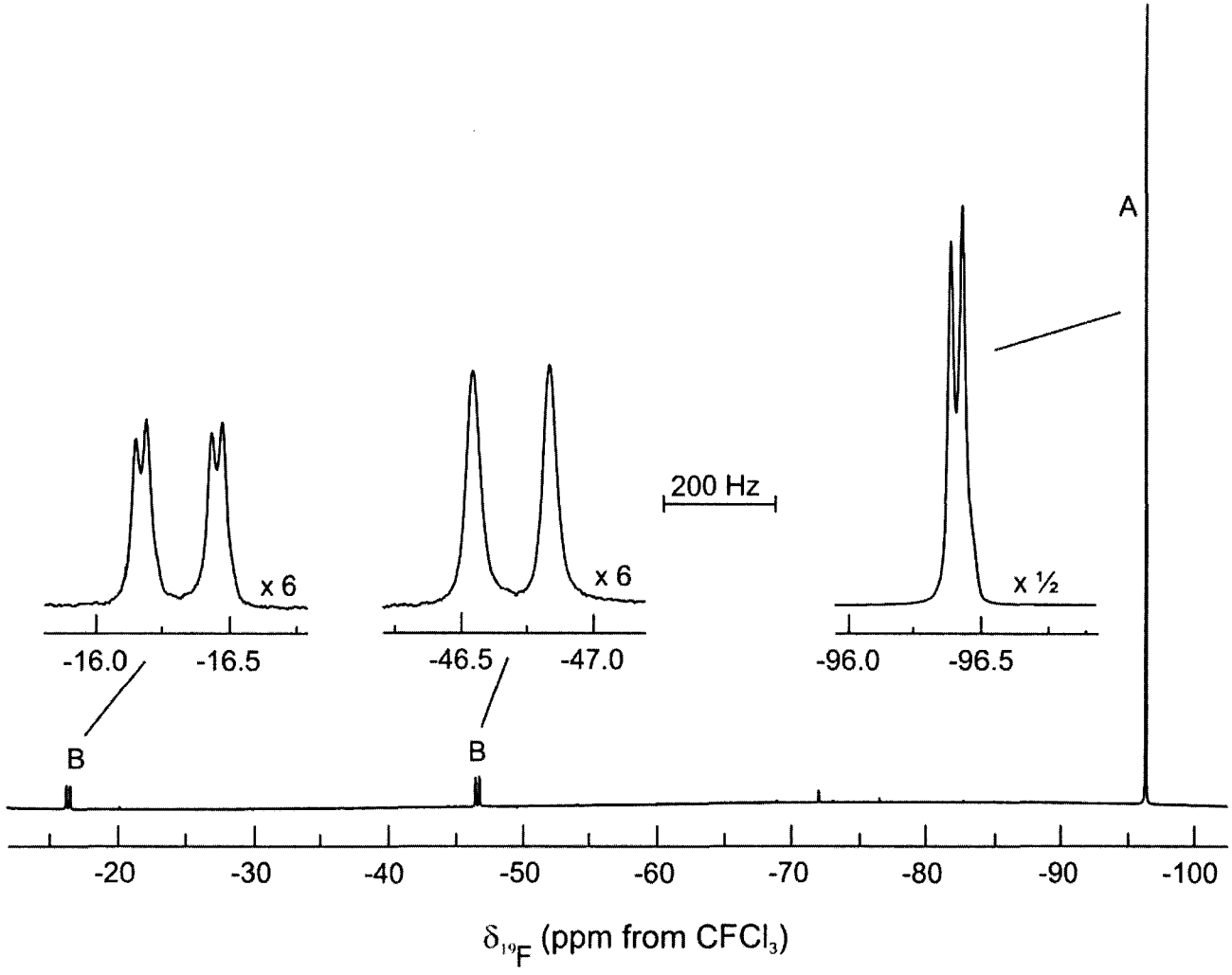

Figure 7.3. ^{19}F NMR spectra (470.409 MHz) of ^{15}N-enriched *fac*-$OsO_3F_2(NCCH_3)$ (A) and *mer*-$OsO_3F_2(NCCH_3)$ (B) in SO_2ClF solvent at –80 °C.

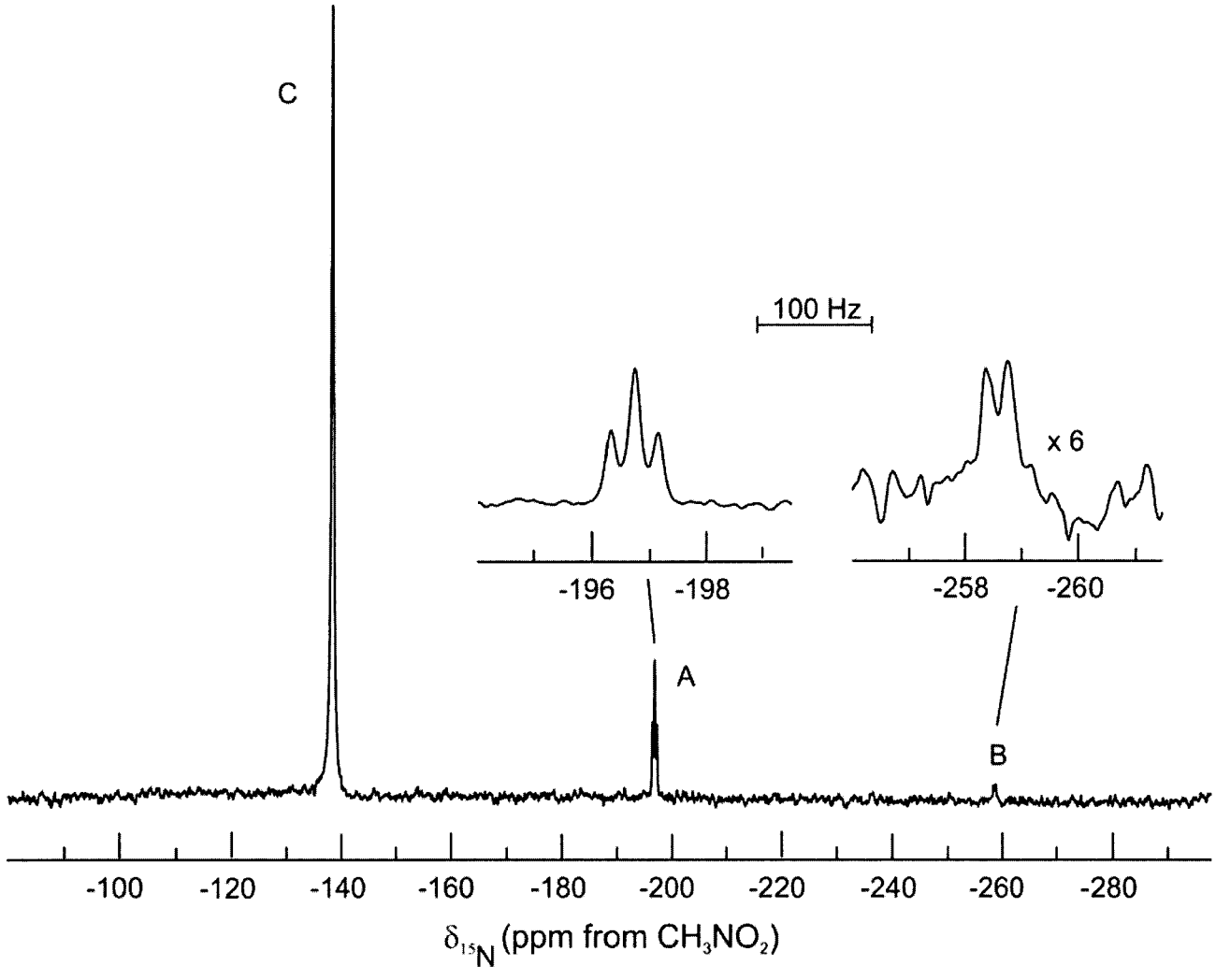

Figure 7.4. ^{15}N NMR spectra (50.693 MHz) of ^{15}N-enriched *fac*-$OsO_3F_2(NCCH_3)$ (A), *mer*-$OsO_3F_2(NCCH_3)$ (B), and free CH_3CN (C) in SO_2ClF solvent at –80 °C.

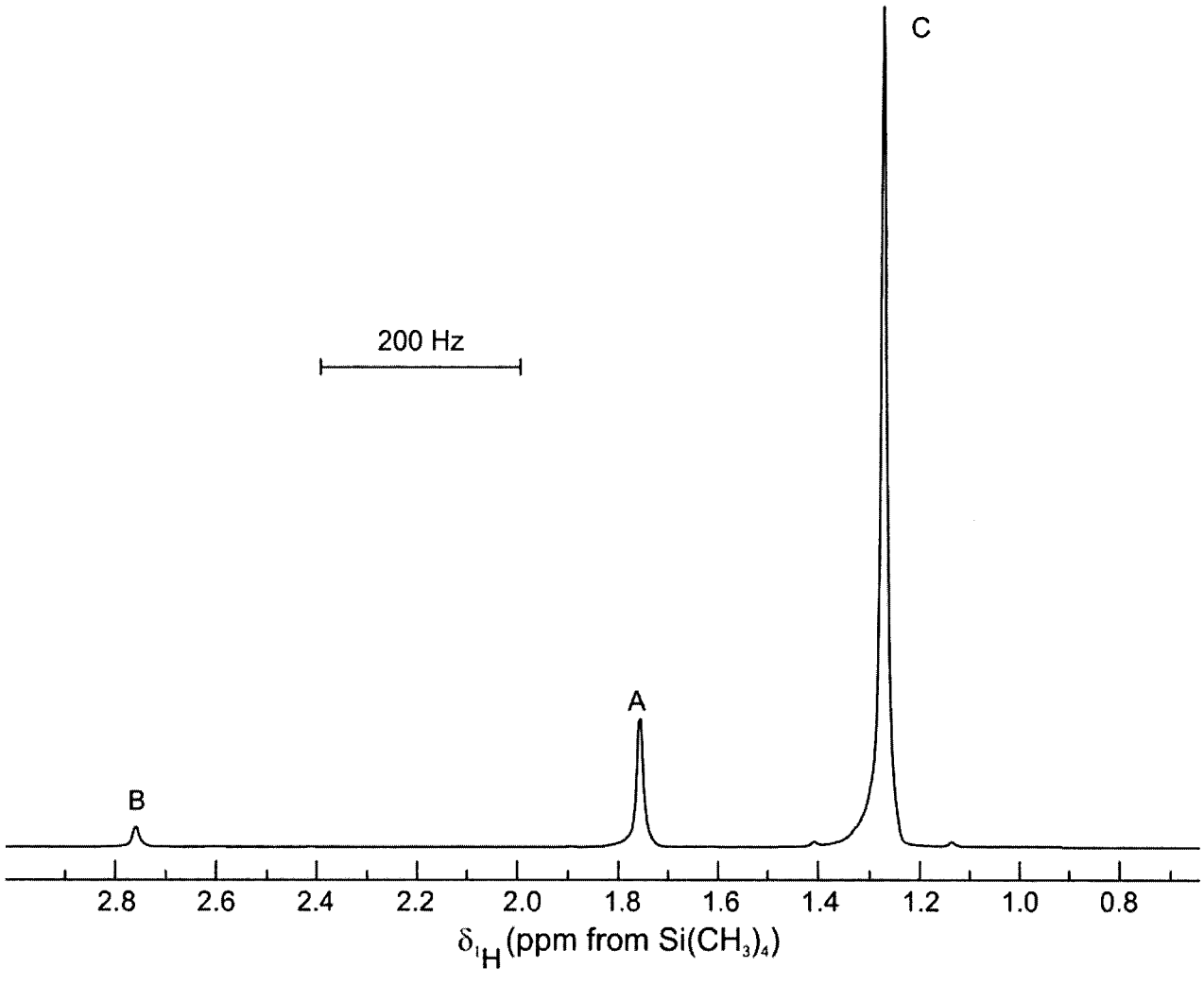

Figure 7.5. ^{1}H NMR spectra (500.138 MHz) of ^{15}N-enriched *fac*-$OsO_3F_2(NCCH_3)$ (A), *mer*-$OsO_3F_2(NCCH_3)$ (B), and free CH_3CN (C) in SO_2ClF solvent at –80 °C.

7.2.4.2. *mer*-$OsO_3F_2(NCCH_3)$.

The ^{19}F NMR spectra of *mer*-$OsO_3F_2(^{14}NCCH_3)$ at –40 [–80] °C in SO_2ClF solvent consisted of two weak doublets assigned to the equatorial (–13.1 [–15.4] ppm) and axial (–44.4 [–46.1] ppm) fluorine environments with $^2J(^{19}F_1–^{19}F_2)$ = 134.3 [135.0] Hz, which is similar to the two-bond fluorine-fluorine coupling constant of *cis*-OsO_2F_4 (138.3 Hz).[20] The ^{19}F NMR spectrum of *mer*-$OsO_3F_2(^{15}NCCH_3)$, recorded at –84 °C, consisted of a weak doublet of doublets at –17.9 ppm assigned to F_1 and a weak doublet, of equal intensity, at –48.0 ppm assigned to F_2 with $^2J(^{19}F_1–^{19}F_2)$ = 134.3 Hz and $^2J(^{15}N\text{-}^{19}F_1)$ = 18.3 Hz (Figure 7.3). The $^2J(^{15}N\text{-}^{19}F_2)$ coupling was not resolved.

The ^{15}N NMR spectrum of the ^{15}N enriched *mer*-$OsO_3F_2(NCCH_3)$ (Figure 7.4) consisted of a doublet at –258.6 ppm which resulted from coupling to the equatorial fluorine ($^2J(^{15}N–^{19}F_1)$ = 18.3 Hz), however, as in the ^{19}F NMR spectrum, the $^2J(^{15}N–^{19}F_2)$ coupling to the axial fluorine was not resolved.

Two-bond coupling constants are known to have a bond angle dependence, with the coupling constant increasing with increasing bond angle so that a *trans*-^2J coupling is generally larger in magnitude than a *cis*-^2J coupling.[242] The $^2J(^{15}N\text{-}^{19}F_1)$ coupling constant is therefore expected to be larger than $^2J(^{15}N\text{-}^{19}F_2)$. The only splitting observed on the resonance at –17.9 ppm has therefore been assigned to $^2J(^{15}N\text{-}^{19}F_1)$ assuming that the $^2J(^{15}N\text{-}^{19}F_2)$ coupling on the resonance at –48.0 ppm is smaller and therefore could not be resolved.

The ^1H NMR spectrum recorded in SO_2ClF (Figure 7.5) is a singlet at 3.12 ppm (–40 °C, $^1J(^1H–^{13}C)$ = 142.8 Hz) and at 3.04 ppm (–80 °C, $^1J(^1H–^{13}C)$ = 140.4 Hz). The

complexation shift (av., 1.53 ppm) is significantly greater than that observed for *fac*-$OsO_3F_2(NCCH_3)$ (av., 0.51 ppm), in accordance with the shorter calculated Os---N bond length (see Section 7.2.6.1). The $^{13}C\{^1H\}$ NMR spectrum consists of a singlet at 2.39 ppm for the methyl carbon of the coordinated CH_3CN ligand, however, a ^{13}C signal could not be observed for the cyano carbon of the natural abundance sample at either temperature.

7.2.5. Reaction Pathways Leading to *fac*- and *mer*-$OsO_3F_2(NCCH_3)$.

In addition to *fac*-$OsO_3F_2(NCCH_3)$ (Structure II), two other $OsO_3F_2(NCCH_3)$ isomers are possible in which the oxygen ligands have *mer*-arrangements. These meridional isomers are distinguished by coordination of CH_3CN trans to a F atom (*mer*-$OsO_3F_2(NCCH_3)$, Structure III) and by coordination of CH_3CN trans to an O atom (*mer'*-$OsO_3F_2(NCCH_3)$, Structure IV). Solution NMR studies and the solid-state Raman spectrum and a single-crystal X-ray structure reveal that only the *fac*-isomer is observed in the solid state and in CH_3CN solution, whereas a mixture of *fac*- and *mer*-$OsO_3F_2(NCCH_3)$ is observed in SO_2ClF solvent where the *fac*-isomer is strongly favored over the *mer*-isomer. No experimental evidence for the *mer'*-isomer was obtained. The ensuing discussion proposes likely pathways that lead to the *mer*- and *fac*-isomers and account for the absence of the *mer'*-isomer.

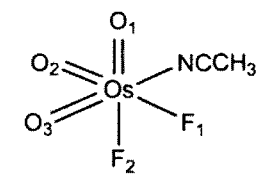

fac-$OsO_3F_2(NCCH_3)$

II

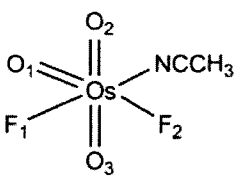

mer-$OsO_3F_2(NCCH_3)$

III

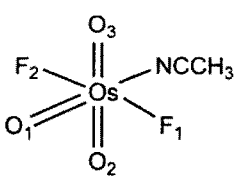

mer'-$OsO_3F_2(NCCH_3)$

IV

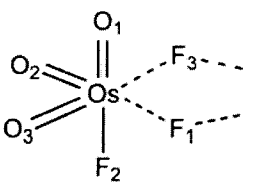

$(OsO_3F_2)_x$

V

In the solid state, $(OsO_3F_2)_\infty$ is a fluorine-bridged polymer in which the Os atoms are pseudo-octahedrally coordinated, having a *fac*-trioxo arrangement and two bridging F atoms and one terminal F atom that are trans to O atoms (Structure V). The Os---$F_{1,3}$ bridge bonds can be regarded as half bonds relative to the terminal Os–F_2 bond of the $(OsO_3F_2)_\infty$ polymer. Thus, the fluorine bridge ligand is the only viable leaving group for displacement by CH_3CN.[18] When $(OsO_3F_2)_\infty$ is dissolved in CH_3CN, the direction of solvent attack must be along a pseudo three-fold axis along which a $d_{t_{2g}}$ metal orbital points. The preferred face for attack will be the least sterically hindered face of the pseudo-octahedron which is comprised of two bridging fluorine ligands and an oxygen ligand, and leads exclusively to the *fac*-isomer (Scheme 7.1a). Dissociation of *fac*-$OsO_3F_2(NCCH_3)$ to the trigonal bipyramidal *cis*-OsO_3F_2 intermediate is suppressed in CH_3CN solvent so that isomerization to *mer*-$OsO_3F_2(NCCH_3)$ is prevented (Scheme 7.1b). Isomerization occurs, however, when $OsO_3F_2(NCCH_3)$ is formed in SO_2ClF solvent because the equilibrium leading to *cis*-OsO_3F_2 (C_s) is no longer suppressed, allowing CH_3CN to recombine by coordination in the trigonal plane of *cis*-OsO_3F_2 at (a) the sterically least congested sites between the equatorial fluorine ligand and an oxygen ligand to give *fac*-$OsO_3F_2(NCCH_3)$ (Scheme 7.1c) or at (b) the sterically most congested and least favored site between two oxygen ligands to give *mer*-$OsO_3F_2(NCCH_3)$ (Scheme 7.1d). Thus, the pathway that leads to *fac*-$OsO_3F_2(NCCH_3)$ in SO_2ClF is twice as likely as that which leads to *mer*-$OsO_3F_2(NCCH_3)$. The experimental isomer ratios are not statistical (*fac*/*mer* = 2), but are significantly skewed towards the *fac*-isomer due to steric and electronic effects which also favor the *fac*-isomer. In SO_2ClF solvent, a plausible path

from *fac*-$OsO_3F_2(NCCH_3)$ and *mer*-$OsO_3F_2(NCCH_3)$ to *mer*'-$OsO_3F_2(NCCH_3)$ commences with dissociation of *fac*- or *mer*-$OsO_3F_2(NCCH_3)$ to *cis*-OsO_3F_2 (C_s) followed by intramolecular ligand exchange by means of Berry pseudo-rotation to give the *cis,trans*-OsO_3F_2 (C_{2v}) and *eq*-OsO_3F_2 (D_{3h}) intermediates (Scheme 7.1e). Recombination by CH_3CN coordination to *cis,trans*-OsO_3F_2 in the trigonal plane between one of the F atoms and the O atom affords *mer*-$OsO_3F_2(NCCH_3)$ (Scheme 7.1f) whereas coordination between the two F atoms affords *mer*'-$OsO_3F_2(NCCH_3)$ (Scheme 7.1g), which is sterically more favorable, but statistically less favorable. The calculated relative stabilities of *cis*-OsO_3F_2 (C_s) and *eq*-OsO_3F_2 (D_{3h}) are similar with *cis*-OsO_3F_2 (C_s) being slightly more stable (5.7 kJ mol^{-1}) at the B3LYP level of theory and *eq*-OsO_3F_2 (D_{3h}) being slightly more stable (3.1 kJ mol^{-1}) at the SVWN level of theory. Attempts to optimize the structure of the *cis, trans*-OsO_3F_2 (C_{2v}) intermediate failed at both the SVWN and B3LYP levels of theory, yielding only *eq*-OsO_3F_2 (D_{3h}) as the optimized structure. To ensure failure to optimize the *cis*-, *trans*-OsO_3F_2 (C_{2v}) intermediate was notbasis set dependent, a further attempt was made at the B3LYP level using the aug-cc-pVTZ(-PP) basis set for Os. Once again the optimization only gave the *eq*-OsO_3F_2 (D_{3h}) geometry. Thus, there is apparently no pathway that converts *cis*-OsO_3F_2 to *cis, trans*-OsO_3F_2 by means of Berry pseudo-rotation. Although the stabilities of *cis*-OsO_3F_2 and *eq*-OsO_3F_2 are very similar, the non-existence of the *cis, trans*-OsO_3F_2 intermediate renders isomerization pathways f–h in Scheme 7.1 untenable. Alternative rearrangements by dissociative mechanisms would be predicated on the dissociation of the *cis*-OsO_3F_2 to OsO_3F^+ and F^-, which; however, would present a formidable barrier, with gas-phase

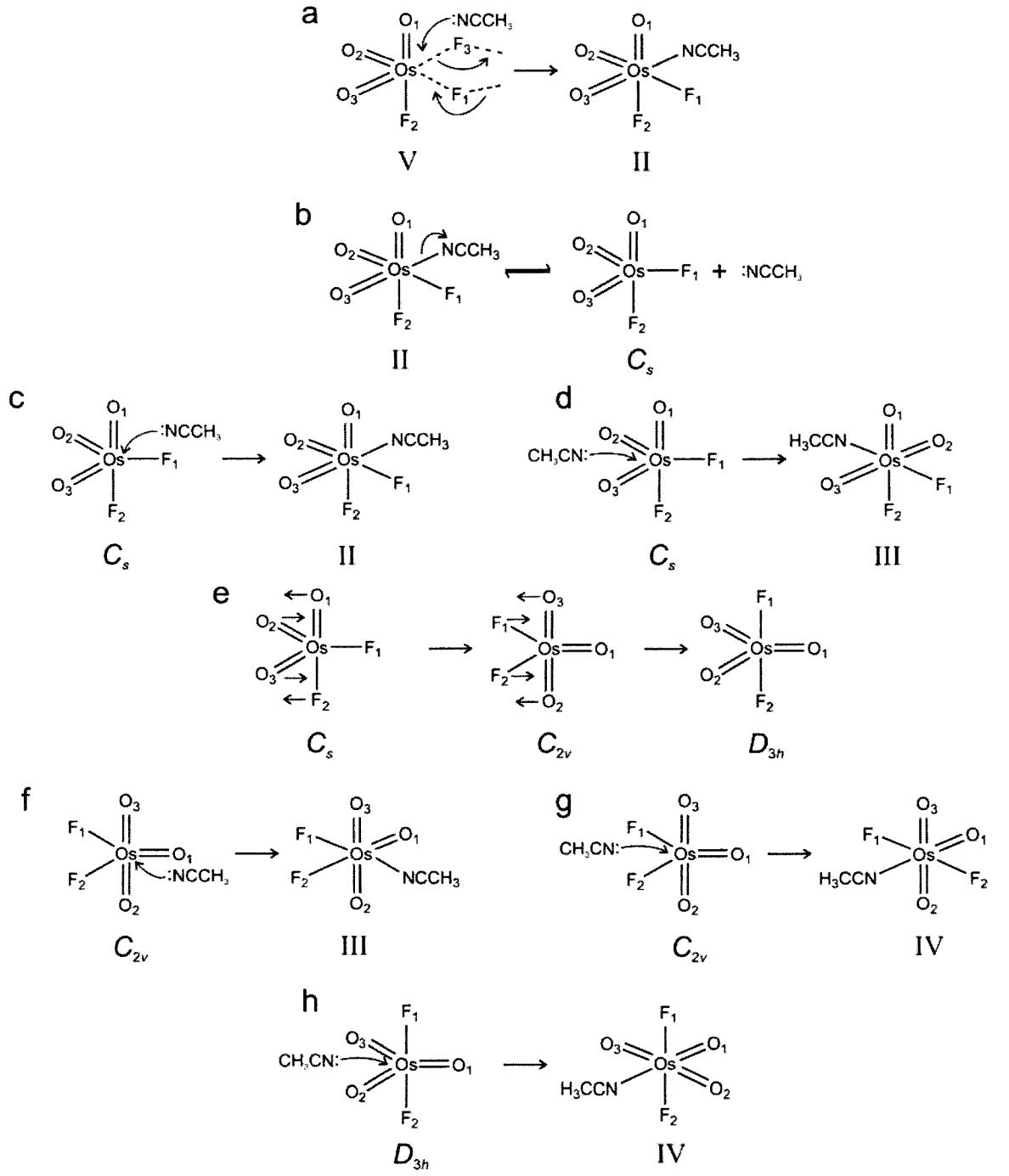

Scheme 7.1. Reaction pathways that account for the formation of the experimentally observed *fac*- and *mer*-$OsO_3F_2(NCCH_3)$ isomers and the absence of *mer'*-$OsO_3F_2(NCCH_3)$.

dissociation energies of 948 (SVWN) and 872 (B3LYP) kJ mol^{-1}. Moreover, a dissociative mechanism would not be viable under the present basic solvent conditions because OsO_3F^+ can only be generated by fluoride ion abstraction using strong Lewis acid fluoride ion acceptors.[21]

The reaction pathways in Scheme 7.1 suggest that the most abundant isomer should be *fac*-$OsO_3F_2(NCCH_3)$, consistent with the CH_3CN solution NMR studies and isolation of this isomer from CH_3CN solution. The weaker resonances in SO_2ClF solution have a splitting pattern and abundance consistent with *mer*-$OsO_3F_2(NCCH_3)$. The above considerations account for why the *fac*-isomer was always present in significantly higher concentration than the *mer*-isomer in SO_2ClF solution and why *mer'*-$OsO_3F_2(NCCH_3)$ is not observed.

7.2.6. Computational Results.

The calculated geometries of *fac*- and *mer*-$OsO_3F_2(NCCH_3)$ (Figure 7.6) optimized under C_1 symmetry at the SVWN [B3LYP] levels of theory and resulted in stationary points with all frequencies real. The starting geometry for *fac*-$OsO_3F_2(NCCH_3)$ was the crystallographic geometry and the starting geometry for *mer*-$OsO_3F_2(NCCH_3)$ was obtained by interchanging the positions of one oxygen and one fluorine atom in the optimized geometry of *fac*-$OsO_3F_2(NCCH_3)$. The energy-minimized geometries (Table 7.2 and Figure E3) and vibrational frequencies (Table 7.3) of CH_3CN (C_{3v}) and *cis*-OsO_2F_4 (C_{2v})[18] were also calculated to serve as benchmarks and for comparison with *fac*- and *mer*-$OsO_3F_2(NCCH_3)$.

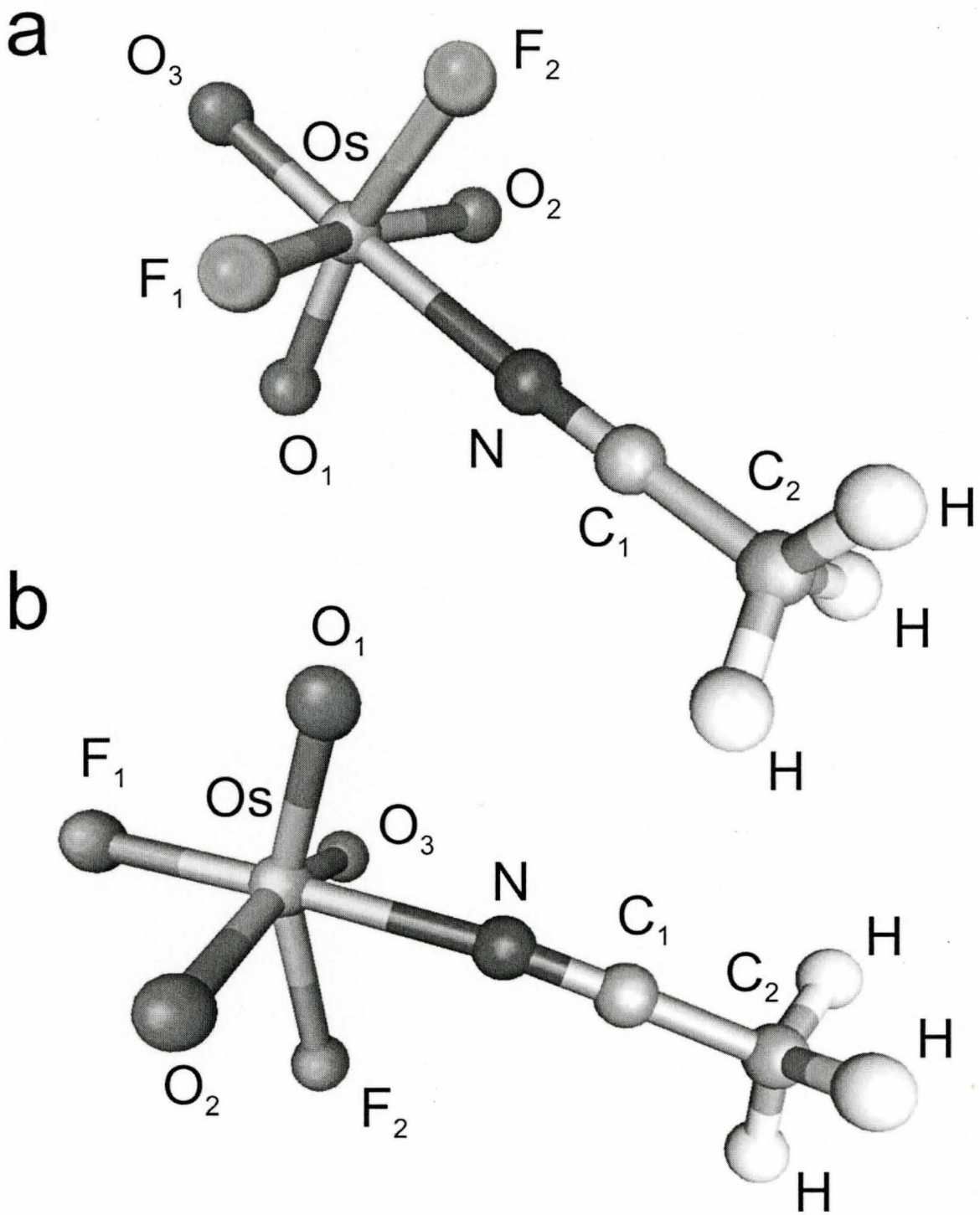

Figure 7.6. The calculated SVWN/SDDall gas-phase geometries for (a) *fac*-$OsO_3F_2(NCCH_3)$ (C_1), (b) *mer*-$OsO_3F_2(NCCH_3)$ (C_1).

7.2.6.1. Calculated Geometries.

7.2.6.1.1. *fac*-$OsO_3F_2(NCCH_3)$.

The calculated geometries of *fac*-$OsO_3F_2(NCCH_3)$ (Figure 7.6a) are in good agreement with the experimental geometry. Overall, the B3LYP values provide slightly better agreement with the experimental bond lengths, although the Os---N bond length (2.260 [2.386] Å) is overestimated when compared with the experimental value (2.205(3) Å). The Os–O bond lengths (1.727, 1,712 [1.701, 1.687] Å) are in good agreement with the experimental values (1.707(2), 1.704(2), 1.699(2) Å), however, the calculations overestimate the bond length differences between bonds that are trans to F and those that are trans to O. The Os–F bond lengths (1.922 [1.922] Å) are slightly underestimated when compared with the experimental values (1.939(2) Å). The experimental bond angles are all well reproduced by both methods, the largest discrepancy being the Os---N–C bond angle, which is calculated to be 170.5 [173.7]° instead of the almost linear experimental value of 178.4(2)°. The deviation from linearity for the calculated structure is likely a result of the CH_3CN ligand being repelled by the Os–O double bond domain towards the Os–F single bond domain. The near-linear Os---N–C bond angle in the crystal structure is attributed to crystal packing because this angle is very deformable as suggested by the low calculated Os---N–C bending frequencies (214 and 217 cm^{-1}). The N–C and C–C bond lengths of the adducted CH_3CN molecule are slightly shorter than those predicted for the free CH_3CN molecule, in agreement with experiment.

7.2.6.1.2. *mer*-$OsO_3F_2(NCCH_3)$.

The energy-minimized geometry of *mer*-$OsO_3F_2(NCCH_3)$ (Figure 7.6b) has a pseudo-octahedral osmium coordination sphere in which the nitrogen atom of CH_3CN is coordinated trans to a fluorine atom (Os–N, 2.114 [2.175] Å). The O_2 and O_3 atoms are equidistant from the osmium atom (1.760 [1.736] Å) with a somewhat shorter Os–O_1 bond length (1.728 [1.705] Å). The longer Os–$O_{2,3}$ bond lengths result from the mutual trans influences of the oxygen ligands, whereas the shorter Os–O_1 bond length results because O_1 is trans to a fluorine ligand, F_2. The F_1 atom is trans to the CH_3CN ligand, resulting in a Os–F_1 bond length (1.863 [1.857] Å) that is shorter than the Os–F_2 bond length (1.968 [1.972] Å). The longer Os–F_2 bond length results from the greater trans influence of O_1 when compared with that of the CH_3CN ligand. The N---Os–$O_{2,3}$ bond angles are equal (91.0 [88.9]°) and more open than the N---Os–O_1 (84.2 [83.1]°) and N---Os–F_2 (73.4 [75.4]°) bond angles.

The N–C and C–C bond lengths of the adducted CH_3CN molecule are slightly shorter than those calculated for the free CH_3CN molecule, in accordance with the relatively short Os---N bond length (2.114 [2.175] Å), and are comparable to those of the *fac*-isomer (vide supra).

7.2.6.2. Charges, Valencies, and Bond Orders.

The NBO analyses were carried out for the SVWN- and B3LYP-optimized gas-phase geometries of *fac*-$OsO_3F_2(NCCH_3)$, *mer*-$OsO_3F_2(NCCH_3)$, and CH_3CN. The NBO results are given in Table E3. The SVWN and B3LYP results are similar for the

experimentally observed *fac*- and *mer*-$OsO_3F_2(NCCH_3)$ isomers; therefore, only the SVWN results are referred to in the ensuing discussion.

The NBO analyses give natural population analysis (NPA) charges for Os of 1.83 and 1.76 in *fac*- and *mer*-$OsO_3F_2(NCCH_3)$, respectively. The NPA charges of the oxygen, fluorine, and nitrogen ligand atoms are negative with charges that are somewhat less than –0.50, indicating that the bonds formed with the osmium atom are polar covalent.

The Os–O bond orders (fac, 0.84 and mer, 0.81) are approximately twice the Os–F bond order (fac 0.42 and 0.42 and mer 0.50 and 0.40). The Os–N bond orders indicate that the Os---N bonds have significant covalent character. The Os–N bond order of the *fac*-isomer (0.29) is significantly less than the Os–N bond order of the *mer*-$OsO_3F_2(NCCH_3)$ isomer (0.40), indicating that the latter Os–N bond is expected to be stronger than that of the *fac*-$OsO_3F_2(NCCH_3)$ isomer, consistent with its shorter calculated bond length (vide supra) and coordination of the CH_3CN ligand trans to a fluorine ligand.

The charges on the N atoms of the adducted CH_3CN ligands (fac, –0.41 and mer, –0.37) are more negative than that of the free ligand (–0.31), whereas the charges on the C_1 atoms (fac, 0.49 and mer, 0.53) are more positive than that of CH_3CN (0.28). The C–N bond orders (1.76 and 1.74, respectively) are less than that of the free ligand (1.84). The charge differences and C–N bond orders indicate that the adducted ligand is polarized by the electronegative Os(VIII) center and that significant electron density has migrated from the formal C–N triple bond to the N atom. As expected, the charges, valencies, and bond orders of the CH_3 group do not change significantly upon adduct formation.

7.2.6.3. Calculated Frequencies.

The vibrational frequencies, intensities, and assignments for *fac*- and *mer*-$OsO_3F_2(NCCH_3)$ were calculated at the SVWN and B3LYP levels (Table 7.5) and confirm that the assignments of the experimental vibrational frequencies are consistent with *fac*-$OsO_3F_2(NCCH_3)$ (see Section 7.2.3).

The *fac*- and *mer*-isomers cannot be differentiated based solely on the CH_3CN ligand frequencies. The calculated frequencies between 1040 and 3072 cm^{-1} are assigned to the adducted CH_3CN molecule and are comparable for the *mer*- and *fac*-isomers and are in good agreement with the experimental frequencies of the *fac*-isomer.

The presence of *mer*-$OsO_3F_2(NCCH_3)$ is discounted for the following reasons: (1) The calculated ν(CC) and ν(OsO) stretching frequencies of *fac*- and *mer*-$OsO_3F_2(NCCH_3)$ occur between 949–988 cm^{-1} and 888–1002 cm^{-1}, respectively, whereas the experimental ν(CC) and ν(OsO) stretches occur between 910–956 cm^{-1}. The frequency range of the *fac*-isomer is significantly narrower than that of the *mer*-isomer and more consistent with the experimental frequency range. (2) The bands associated with the Os–F stretches are coupled in the case of the *fac*-$OsO_3F_2(NCCH_3)$ isomer, giving rise to in-phase, $\nu(OsF_1) + \nu(OsF_2)$, and out-of-phase, $\nu(OsF_1) - \nu(OsF_2)$, modes with frequencies calculated at 564 and 624 cm^{-1}, respectively. In contrast, Os–F stretches of *mer*-$OsO_3F_2(NCCH_3)$ are not coupled, with $\nu(OsF_2)$ and $\nu(OsF_1)$ calculated at 531 and 663 cm^{-1}. When compared with the experimental ν(OsF) stretching frequencies of the *fac*-isomer (529 and 598; Δν, 68 cm^{-1}), the calculated difference between the two ν(OsF) modes of the *mer*-$OsO_3F_2(NCCH_3)$ isomer (Δν, 132 cm^{-1}) is much greater. Overall, the

Table 7.5. Calculated Vibrational Frequencies (cm^{-1}), Intensities,[a] and Assignments for *fac*- and *mer*-$OsO_3F_2(NCCH_3)$

fac-$OsO_3F_2(NCCH_3)$		*mer*-$OsO_3F_2(NCCH_3)$		assgnts (C_1)[d]
SVWN[b]	B3LYP[c]	SVWN[b]	B3LYP[c]	
3072(81)[3]	3125(67)[<1]	3070(78)[6]	3126(63)[2]	$\nu_{as}(CH_3)$
3071(74)[3]	3125(64)[1]	3072(84)[5]	3127(67)[2]	
2976(230)[4]	3052(239)[<1]	2975(251)[10]	3052(246)[3]	$\nu_s(CH_3)$
2322(245)[67]	2422(184)[78]	2348(321)[87]	2447(222)[113]	$\nu(CN)$
1425(20)[24]	1467(6)[12]	1421(18)[25]	1463(5)[13]	$\delta_{as}(CH_3)$
1425(19)[24]	1467(6)[12]	1421(20)[25]	1463(6)[13]	
1394(34)[27]	1411(12)[2]	1394(39)[30]	1409(14)[2]	$\delta_s(CH_3)$
1043(<1)[10]	1063(<1)[4]	1038(<1)[11]	1058(<1)[5]	$\rho_r(CH_3)$
1040(<0.1)[10]	1061(<1)[4]	1040(<1)[11]	1061(<1)[4]	
		1003(7)[5][e]	957(23)[31]	$\nu(CC) + \nu(OsO_1)$
988(5)[16][f]	1020(60)[95]			$\nu(CC)$
		932(30)[84][g]	974(21)[46]	$\nu(OsO_1) - \nu(CC)$
983(47)[117][h]	947(8)[9]			$\nu(OsO_3)$
		882(44)[15][i]	916(37)[43]	$\nu(OsO_2) + \nu(OsO_3)$
951(37)[64]	989(23)[125]			$\nu(OsO_1) + \nu(OsO_2)$
		889(3)[163]	916(2)[198]	$\nu(OsO_2) - \nu(OsO_3)$
949(14)[117]	975(14)[150]			$\nu(OsO_1) - \nu(OsO_2)$
		678(21)[123]	663(18)[133]	$\nu(OsF_1)$
624(10)[98]	609(8)[115]			$\nu(OsF_1) + \nu(OsF_2)$
564(7)[52]	547(4)[51]			$\nu(OsF_1) - \nu(OsF_2)$
		542(9)[53]	531(8)[63]	$\nu(OsF_2)$
410(2)[<1]	421(<1)[1]	433(3)[2]	446(1)[3]	$\delta(NCC)_{oop}$
408(2)[<1]	422(1)[3]	411(2)[<0.1]	435(2)[<1]	$\delta(NCC)_{ip}$
		397(6)[<1]	431(4)[<1]	$\delta(O_2OsF_2) + \delta(O_1OsO_3)$
387(4)[2]	417(3)[2]			$\delta(O_1OsO_2) + \delta(F_1OsF_2)$
		335(4)[<1]	343(5)[<1]	$\delta(O_2OsF_1) - \delta(O_3OsF_1)$
369(5)[13]	392(1)[12]			$\delta(OsO_1O_2O_3)$
361(6)[5]	386(6)[6]			$\rho_t(O_1OsO_2) + \delta(O_2OsO_3)$
		323(1)[4]	350(<1)[5]	$\rho_w(F_2OsO_1)$
319(<1)[10]	338(<1)[10]			$\delta(O_1OsO_2) - \delta(F_1OsF_2)$
		312(4)[15]	336(3)[23]	$\delta(O_1OsF_1) + \rho_w(O_2OsO_3)$
		296(3)[22]	306(3)[28]	$\delta(OsO_1F_1F_2)$
281(2)[13]	289(2)[17]			$\delta(OsO_3F_1F_2)$
203(1)[16]	149(<1)[17]	274(<1)[3]	235(,1)[20]	$\nu(Os\text{---}N)$
278(2)[17]	291(2)[20]			$\rho_r(O_1OsO_2) - \rho_r(F_1OsF_2)$
217(<1)[<1]	211(<1)[<1]	260(<1)[32]	264(,1)[25]	$\delta(Os\text{---}NC)_{ip}$
214(<1)[<1]	209(<1)[1]	210(<0.1)[<1]	226(<0.1)[<0.1]	$\delta(Os\text{---}NC)_{oop}$
		194(3)[15]	213(2)[14]	coupled deformation mode
174(<1)[<0.1]	174(<1)[<0.1]			$\rho_t(F_1OsF_2) - \rho_t(O_2OsO_1)$
		89(2)[4]	71(1)[3]	coupled deformation mode
49(2)[5]	50(1)[4]	61(2)[4]	59(<1)[3]	$\rho_r(NCCN)_{ip}$
49(2)[4]	50(2)[4]	59(<1)[<1]	57(2)[3]	$\rho_r(NCCN)_{oop}$
9(<0.1)[<0.1]	5(<0.1)[<0.1]	55(3)[<0.1]	14(<0.1)[<0.1]	$\rho_t(CH_3)$

[a] Values in parentheses denote calculated Raman intensities ($Å^4\ u^{-1}$) and values in square brackets denote calculated infrared intensities (km mol^{-1}). [b] SVWN/SDDall. [c] B3LYP/Stutt-Fl (Os) aug-cc-pVTZ (H, C, N, F). [d] Assignments are based on the B3LYP geometry for both compounds. The atom labeling scheme refers to Figure 7.6 and the plane of symmetry is defined by the O_2, O_3, Os, F_1, and N atoms. The abbreviations denote stretch (ν), bend (δ),

torsion (ρ_t), wag (ρ_w), rock (ρ_r), out-of-plane (oop) and in-plane (ip). [e] At the SVWN level, the mode description is $\nu(C_1C_2)$. [f] At the SVWN level, the mode description is $\nu(C_1C_2) - \nu(OsO_3)_{small}$. [g] At the SVWN level, the mode description is $\nu(OsO_1)$. [h] At the SVWN level, the mode description is $\nu(OsO_3) + \nu(C_1C_2)_{small}$. [i] At the SVWN level, the mode description is $\nu(OsO_1) - \nu(OsO_2) + \nu(OsO_3)$.

Table 7.6. Calculated Gas-Phase ΔH and ΔG (kJ mol^{-1}) Values for the Conversion of *fac*-$OsO_3F_2(NCCH_3)$ to *mer*-$OsO_3F_2(NCCH_3)$[a]

	ΔH		ΔG	
T (K)	SVWN	B3LYP	SVWN	B3LYP
298.15	114.24	121.24	115.23	123.39
233.15	114.46	121.20	117.83	122.92
193.15	114.43	121.18	117.24	122.62

[a] Zero-point energy corrected values for each member of an isomer pair were used.

calculated frequencies of *fac*-$OsO_3F_2(NCCH_3)$ provide the best overall agreement with the experimental spectrum.

7.2.6.4. Relative Stabilities of *fac*-$OsO_3F_2(NCCH_3)$ and *mer*-$OsO_3F_2(NCCH_3)$.

The reaction enthalpies and Gibbs free energies were calculated for the conversion of *fac*-$OsO_3F_2(NCCH_3)$ to *mer*-$OsO_3F_2(NCCH_3)$ at the SVWN and B3LYP levels of theory at 298, 233, and 193 K (Table 7.6). The calculated enthalpy changes demonstrate that the *fac*-isomer is preferred over the *mer*-isomer by 114.4(1) (SVWN) and 121.2(3) (B3LYP) kJ mol^{-1}, which is consistent with the experimental findings. As expected for an isomerization, the ΔG values at the SVWN (–115.2 to –117.8 kJ mol^{-1}) and B3LYP levels (–122.6 to –123.4 kJ mol^{-1}) do not show a large entropy dependence with little variation in ΔG with temperature.

7.3. Conclusions

Fluorine-19 NMR spectroscopy reveals that dissolution of $(OsO_3F_2)_\infty$ in CH_3CN solvent exclusively yields exclusively *fac*-$OsO_3F_2(NCCH_3)$ and single-crystal X-ray diffraction has shown that crystallization from CH_3CN solvent at –45 °C yields *fac*-$OsO_3F_2(NCCH_3)\cdot 2CH_3CN$. The F_2O_3OsN-moiety in the X-ray crystal structure of *fac*-$OsO_3F_2(NCCH_3)\cdot 2CH_3CN$ is pseudo-octahedral with the three oxygen ligands in a facial arrangement and the CH_3CN ligand nitrogen coordinated to osmium. The CH_3CN solvent molecules in the crystal lattice can be removed under dynamic vacuum at –40 °C to yield unsolvated *fac*-$OsO_3F_2(NCCH_3)$. The *fac*- and *mer*- isomers of $OsO_3F_2(NCCH_3)$ were observed in SO_2ClF solvent and confirmed by their spin-spin coupling patterns in

their low-temperature ^{19}F and ^{15}N NMR spectra. The Raman spectra of the solids isolated from CH_3CN and SO_2ClF solutions are identical and are attributed to *fac*-$OsO_3F_2(NCCH_3)$. The vibrational assignments of *fac*-$OsO_3F_2(NCCH_3)$ were confirmed by the calculated vibrational frequencies which show better agreement with the experimental results than the calculated values for *mer*-$OsO_3F_2(NCCH_3)$. Thermochemical calculations are consistent with experiment, showing that the *fac*-isomer is favored over the *mer*-isomer by ca. 118 kJ mol^{-1}. Quantum-chemical calculations and the proposed reaction pathways account for why *fac*-$OsO_3F_2(NCCH_3)$ is observed exclusively in CH_3CN solvent and why a mixture of *fac*- and *mer*-$OsO_3F_2(NCCH_3)$ isomers is observed in SO_2ClF, with the *fac*-isomer dominating in the latter case. The proposed reaction pathways also account for the absence of *mer'*-$OsO_3F_2(NCCH_3)$.

CHAPTER 8

SYNTHESES, RAMAN SPECTRA, AND X-RAY CRYSTAL STRUCTURES OF $[XeF_5][\mu\text{-}F(OsO_3F_2)_2]$ AND $[M][OsO_3F_3]$ ($M = XeF_5^+, Xe_2F_{11}^+$)

8.1. Introduction

Polymeric $(OsO_3F_2)_\infty$ has been previously shown to behave as a fluoride-ion acceptor towards strong fluoride ion donors, forming the $OsO_3F_3^-$ anion as its K^+,[24-26] Cs^+,[24-26] Ag^+,[25] Rb^+,[24] Na^+,[24] NO^+,[23] and $N(CH_3)_4^+$ [23] salts. The infrared and Raman spectra of $OsO_3F_3^-$ have been assigned to the *fac*-isomer (C_{3v} symmetry)[23, 24] and an EXAFS study also assigned a facial geometry to the $OsO_3F_3^-$ anion in its K^+ salt.[26] The single-crystal X-ray structure of $[N(CH_3)_4][OsO_3F_3]$[23] also established that the $OsO_3F_3^-$ anion of this salt has a facial geometry.

A recent study of the reaction of $(OsO_3F_2)_\infty$ with $XeOF_4$ has led to the molecular adduct, $(OsO_3F_2)_2{\cdot}2XeOF_4$ which, prior to the present study, was the only example of a Xe(VI)/Os(VIII) compound.[18] Failure to abstract a fluoride ion from $XeOF_4$ to form a $XeOF_3^+$ salt of $OsO_3F_3^-$ is in accordance with the lower gas-phase fluoride ion affinity of OsO_3F_2 (348.5 kJ mol^{-1}) relative to that of SbF_5 (495.0 kJ mol^{-1}).[243] Moreover, only $XeOF_3^+$ salts derived from one of the strongest fluoride ion acceptors known, SbF_5, have been synthesized, namely, $[XeOF_3][SbF_6]$[68, 130, 244] and $[XeOF_3][Sb_2F_{11}]$.[244-246] The fluoride ion acceptor strength of $(OsO_3F_2)_\infty$ toward polar-covalent fluorides is diminished relative to that of gas-phase OsO_3F_2 because the fluoride ion donor must be sufficiently

fluoro-basic to disrupt the Os---F---Os bridge bonds of the polymeric solid-state structure of $(OsO_3F_2)_\infty$.[11]

In contrast, XeF_6 is the strongest fluoride ion donor among the binary fluorides of xenon,[69] and forms a large number of XeF_5^+ and $Xe_2F_{11}^+$ salts with a variety of Lewis acid fluorides having a wide range of fluoride ion acceptor strengths. The XeF_5^+ and $Xe_2F_{11}^+$ cations are extensively associated with their anions through fluorine bridge contacts. In the present study, the reactivity of $(OsO_3F_2)_\infty$ with the moderately strong fluoride ion donor, XeF_6, is investigated. The syntheses and characterizations by Raman spectroscopy and single-crystal X-ray diffraction of $[XeF_5][\mu\text{-}F(OsO_3F_2)_2]$, $[XeF_5][OsO_3F_3]$, and $[Xe_2F_{11}][OsO_3F_3]$ are described and provide the first examples of noble-gas cations stabilized by metal oxide fluoride anions. The X-ray crystal structures of these strongly ion-paired salts and their Raman spectra are compared within the series and with the gas-phase ion-pair geometries and vibrational spectra that have been arrived at by quantum-chemical calculations.

8.2. Results and Discussion

8.2.1. Syntheses and Crystal Growth of $[XeF_5][\mu\text{-}F(OsO_3F_2)_2]$, $[XeF_5][OsO_3F_3]$, and $[Xe_2F_{11}][OsO_3F_3]$.

The $[XeF_5][\mu\text{-}F(OsO_3F_2)_2]$, $[XeF_5][OsO_3F_3]$, and $[Xe_2F_{11}][OsO_3F_3]$ salts were synthesized by direct reaction of XeF_6 and $(OsO_3F_2)_\infty$ at temperatures ranging from 25 to 50 °C and the extent of reaction was monitored by low-temperature (−150 °C) Raman spectroscopy.

A 2:1 molar ratio of OsO_3F_2 and XeF_6 was allowed to react at room temperature (25 °C), initially forming an orange liquid which solidified as the reaction progressed. To ensure complete reaction, the resulting microcrystalline orange solid, $[XeF_5][\mu\text{-}F(OsO_3F_2)_2]$, was heated at 50 °C for 1 h but showed no physical changes or change in the Raman spectrum (eq 8.1). When dissolved in HF at 25 °C, the fluoride ion

$$2OsO_3F_2 + XeF_6 \xrightarrow{50^{\circ}C} [XeF_5][\mu\text{-}F(OsO_3F_2)_2] \quad (8.1)$$

affinity of HF was sufficient to abstract a fluoride ion from $\mu\text{-}F(OsO_3F_2)_2^-$ to form $(OsO_3F_2)_\infty$, XeF_6, and $F^-\cdot n$HF (eq 8.2). In HF solution, XeF_6 ionizes to XeF_5^+ and $F^-\cdot n$HF (eq 8.3).[247] In $XeOF_4$ solvent at 25 °C, $[XeF_5][\mu\text{-}F(OsO_3F_2)_2]$ reacted to form $(OsO_3F_2)_2\cdot 2XeOF_4$[18] and XeF_6 (eq 8.4) which was verified by Raman spectroscopy after removal of the solvent at –40 °C.

$$[XeF_5][\mu\text{-}F(OsO_3F_2)_2] + n\text{HF} \xrightarrow{HF} 2OsO_3F_2 + XeF_6 + F^-\cdot n\text{HF} \quad (8.2)$$

$$XeF_5^+ + F^-\cdot n\text{HF} \overset{HF}{\rightleftharpoons} XeF_6 \quad (8.3)$$

$$[XeF_5][\mu\text{-}F(OsO_3F_2)_2] + 2XeOF_4 \xrightarrow{XeOF_4} (OsO_3F_2)_2\cdot 2XeOF_4 + XeF_6 \quad (8.4)$$

When molten $[XeF_5][\mu\text{-}F(OsO_3F_2)_2]$ was cooled from 50 to 25 °C over a period of 1 h, light orange, block-shaped crystals of $[XeF_5][\mu\text{-}F(OsO_3F_2)_2]$ formed which were suitable for single-crystal X-ray diffraction. The Raman spectrum of the recrystallized compound was identical to that of the bulk microcrystalline compound used for recrystallization.

A 1:1 molar ratio of OsO_3F_2 and XeF_6 was fused at 25 °C, yielding an intense orange liquid that slowly solidified at 0 °C to give an orange crystalline mass that

corresponded to $[XeF_5][OsO_3F_3]$ (eq 8.5). The sample was remelted and slowly cooled

$$XeF_6 + OsO_3F_2 \longrightarrow [XeF_5][OsO_3F_3] \quad (8.5)$$

over a period of 1 h from 5 to 0 °C, forming light orange block-shaped crystals that were suitable for single-crystal X-ray diffraction. The Raman spectra of the initial crystalline solid and of the remelted crystalline solid were identical.

The reaction of $(OsO_3F_2)_\infty$ with two molar equivalents of XeF_6 yielded an orange, microcrystalline powder corresponding to $[Xe_2F_{11}][OsO_3F_3]$ (eq 8.6), which melted at

$$2XeF_6 + OsO_3F_2 \xrightarrow{25\ ^\circ C} [Xe_2F_{11}][OsO_3F_3] \quad (8.6)$$

40–45 °C to give an intense orange liquid. Cooling of the melt to 25 °C resulted in crystalline $[Xe_2F_{11}][OsO_3F_3]$. Crystalline $[Xe_2F_{11}][OsO_3F_3]$, suitable for single-crystal X-ray diffraction, was obtained by heating a mixture of 4.6 equivalents of XeF_6 and one equivalent of OsO_3F_2 at 45 °C, whereupon XeF_6 melted and reacted with OsO_3F_2 to form an intense orange liquid. Cooling of the reaction mixture to 15 °C over a period of 12 h resulted in the growth of light orange needle-shaped crystals of $[Xe_2F_{11}][OsO_3F_3]$ and colorless block-shaped crystals of XeF_6. The latter was shown to be a monoclinic phase ($P2_1/c$, $Z = 32$) of XeF_6[61, 63] based on its unit cell parameters. Crystals grown from the XeF_6 melt had the same unit cell parameters as crystals grown from a 2:1 stoichiometric mixture of XeF_6 : OsO_3F_2.

The salts, $[XeF_5][\mu\text{-}F(OsO_3F_2)_2]$, $[XeF_5][OsO_3F_3]$, and $[Xe_2F_{11}][OsO_3F_3]$, are stable at room temperature for up to 24 h, however, when heated at 50 °C under ca. 1 atm of dry N_2 for periods exceeding 2 h, crystals of XeF_6 sublimed out of the heated zone and condensed on the cooler walls of the reaction vessel. Although XeF_6 is oxophilic towards

a number of metal oxides and oxide fluorides,[45, 85, 200] fluoride/oxide metathesis, indicated by $XeOF_4$ formation and strong Xe–O stretching bands at 902 and 908 cm^{-1} in the solid,[18] was not detected in the course of monitoring the aforementioned syntheses by Raman spectroscopy.

8.2.2. X-ray Crystal Structures of $[XeF_5][\mu\text{-}F(OsO_3F_2)_2]$, $[XeF_5][OsO_3F_3]$, and $[Xe_2F_{11}][OsO_3F_3]$.

Details of data collection parameters and other crystallographic information are provided in Table 8.1. The bond lengths and bond angles of $[XeF_5][\mu\text{-}F(OsO_3F_2)_2]$ are listed in Table 8.2 and those of $[XeF_5][OsO_3F_3]$ and $[Xe_2F_{11}][OsO_3F_3]$ are listed in Table 8.3. The ion pairs of all three structures are well isolated from one another (Figures 8.1a - 8.3a), although an inter-ion pair contact (O(1B)···Xe(1)) occurs in the $[Xe_2F_{11}][OsO_3F_3]$ structure, with long intermolecular contacts between adjacent ion pairs in $[XeF_5][\mu\text{-}F(OsO_3F_2)_2]$,[248] $[XeF_5][OsO_3F_3]$,[249] and $[Xe_2F_{11}][OsO_3F_3]$[250] near the sums of the van der Waals radii[165] of the contacting atoms.

The structures consist of discrete $[XeF_5][\mu\text{-}F(OsO_3F_2)_2]$, $[XeF_5][OsO_3F_3]$, and $[Xe_2F_{11}][OsO_3F_3]$ ion pairs (Figures 8.1–8.3, respectively) whose geometries are well reproduced by gas-phase quantum-chemical calculations (see Sectopm 8.2.4). The $\mu\text{-}F(OsO_3F_2)_2^-$ anions and XeF_5^+ cations stack, without alternation, along the *b*- and *c*-axes (Figure F1), and the $[XeF_5][\mu\text{-}F(OsO_3F_2)_2]$ ion pairs alternate along the *a*-axis. The anions and cations of $[XeF_5][OsO_3F_3]$ form layers in which the cations and anions alternate along the *a*- and *b*-axes and the ion pairs stack, without alternation, along the *c*-axis (Figure F2), so that the Xe···Os internuclear axes are orthogonal to each other

Table 8.1. Summary of Crystal Data and Refinement Results for $[XeF_5][\mu\text{-}F(OsO_3F_2)_2]$, $[XeF_5][OsO_3F_3]$, and $[Xe_2F_{11}][OsO_3F_3]$

	$[XeF_5][\mu\text{-}F(OsO_3F_2)_2]$	$[XeF_5][OsO_3F_3]$	$[Xe_2F_{11}][OsO_3F_3]$
chem formula	$Os_8O_{24}F_{40}Xe_4$	$Os_8O_{24}F_{64}Xe_8$	$Os_4O_{12}F_{56}Xe_8$
space group	*Pnma* (62)	$P4_2/n$ (86)	*Pnma* (62)
a (Å)	12.672(1)	16.8876(3)	9.2479(3)
b (Å)	11.444(1)	16.8876(3)	15.1769(5)
c (Å)	7.5818(7)	5.3414(2)	8.1192(2)
V (Å^3)	1099.6(2)	1523.3(1)	1139.46(6)
molecules/unit cell	4	8	4
mol wt (g mol^{-1})	1633.40	4172.00	3067.20
calcd density (g cm^{-3})	4.819	4.548	4.470
T (°C)	–173	–173	–173
μ (mm^{-1})	26.28	21.24	17.24
R_1[a]	0.0273	0.0356	0.0249
wR_2[b]	0.0486	0.0729	0.0603

[a] R_1 is defined as $\Sigma\|\|F_o\|-\|F_c\|\|/\Sigma|F_o|$ for $I > 2\sigma(I)$. [b] wR_2 is defined as $\{\Sigma[w(F_o^2-F_c^2)^2]/\Sigma w(F_o^2)^2\}^{1/2}$ for $I > 2\sigma(I)$.

Table 8.2. Experimental and Calculated Geometrical Parameters for $[XeF_5][\mu\text{-}F(OsO_3F_2)_2]$

exptl[a]		calcd[b]					
$[XeF_5][\mu\text{-}F(OsO_3F_2)_2]$		$[XeF_5][\mu\text{-}F(OsO_3F_2)_2]$		$\mu\text{-}F(OsO_3F_2)_2^-$		XeF_5^+	
		(C_{2v})		(C_2)		(C_{4v})	
		SVWN[c]	B3LYP[d]	SVWN[c]	B3LYP[d]	SVWN[c]	B3LYP[e]
Bond Lengths (Å)							
Os(1)–F(1)	1.978(1)	1.975	1.980	1.919	1.927		
Os(1)–F(2)	1.962(1)	1.975	1.980	1.908	1.925		
Os(1)---F(3)	2.1179(5)	2.115	2.147	2.121	2.157		
Os(1)–O(1)	1.698(2)	1.712	1.690	1.729	1.701		
Os(1)–O(2)	1.701(2)	1.712	1.690	1.730	1.702		
Os(1)–O(3)	1.692(2)	1.708	1.690	1.723	1.699		
Xe(1)···F(1)	2.622(1)	2.461	2.643				
Xe(1)···F(2)	2.663(1)	2.461	2.644				
Xe(1)–F(4)	1.822(2)	1.890	1.881			1.844	1.840
Xe(1)–F(5)	1.848(1)	1.922	1.898			1.877	1.871
Xe(1)–F(6)	1.848(2)	1.916	1.902			1.877	1.871
Xe(1)–F(7)	1.852(2)	1.916	1.902			1.877	1.871
Xe(1)–F(5A)	1.848(1)	1.922	1.898			1.877	1.871
Bond Angles (deg)							
F(1)–Os(1)–F(2)	75.71(6)	74.2	74.4	77.6	77.6		
F(1)–Os(1)---F(3)	79.18(7)	77.0	77.4	78.2	78.3		
F(1)–Os(1)–O(1)	160.07(7)	156.6	157.1	158.6	159.1		
F(1)–Os(1)–O(2)	87.72(8)	88.2	88.5	87.6	88.0		
F(1)–Os(1)–O(3)	91.39(8)	93.1	93.2	94.9	94.1		
F(2)–Os(1)---F(3)	77.22(7)	77.0	77.4	79.4	77.8		
F(2)–Os(1)–O(1)	88.99(7)	88.2	88.5	88.4	88.0		
F(2)–Os(1)–O(2)	156.62(7)	156.6	157.1	158.3	158.7		
F(2)–Os(1)–O(3)	94.56(8)	93.1	93.2	95.0	94.4		
F(3)---Os(1)–O(1)	85.10(8)	84.2	84.2	83.5	83.9		
F(3)---Os(1)–O(2)	83.62(8)	84.2	84.2	82.0	84.0		
F(3)--Os(1)–O(3)	168.71(9)	167.5	168.1	171.9	170.0		
O(1)–Os(1)–O(2)	102.72(9)	103.7	103.2	100.8	101.1		
O(1)–Os(1)–O(3)	102.67(9)	103.3	103.0	102.3	102.2		
O(2)–Os(1)–O(3)	102.34(9)	103.3	103.0	102.1	102.2		
F(1)···Xe(1)···F(2)	54.44(4)	57.9	53.8				
F(1)···Xe(1)–F(4)	136.53(6)	135.7	136.9				
F(1)···Xe(1)–F(5)	70.03(5)	70.3	69.8				
F(1)···Xe(1)–F(5A)	130.36(5)	130.2	130.9				
F(1)···Xe(1)–F(6)	126.07(6)	128.1	125.4				
F(1)···Xe(1)–F(7)	71.09(6)	70.6	71.9				
F(2)···Xe(1)–F(4)	135.95(6)	135.7	136.9				
F(2)···Xe(1)–F(5)	68.19(6)	130.2	130.9				
F(2)···Xe(1)–F(5A)	131.94(6)	70.3	69.8				
F(2)···Xe(1)–F(6)	71.81(6)	70.6	71.9				
F(2)···Xe(1)–F(7)	124.98(6)	128.1	125.4				
F(4)–Xe(1)–F(5)	77.96(5)	77.6	77.8			83.1	83.5
F(4)–Xe(1)–F(5A)	77.96(5)	77.6	77.8			83.1	83.5
F(4)–Xe(1)–F(6)	79.7(1)	78.5	79.4			83.1	83.5
F(4)–Xe(1)–F(7)	79.3(1)	78.5	79.4			83.1	83.5
F(5)–Xe(1)–F(5A)	155.91(9)	155.1	155.6			166.2	167.0
F(5)–Xe(1)–F(6)	87.67(5)	87.5	87.8			89.2	89.3
F(5)–Xe(1)–F(7)	87.98(5)	87.5	87.8			89.2	89.3
F(5A)–Xe(1)–F(6)	87.67(5)	87.5	87.8			89.2	89.3
F(5A)–Xe(1)–F(7)	87.98(5)	87.5	87.8			89.2	89.3
F(6)–Xe(1)–F(7)	159.0(1)	157.0	158.9			166.2	167.0

Os(1)---F(3)---Os(1A)	155.5(1)	150.9	155.4	143.0	140.7
Os(1)–F(1)···Xe(1)	114.94(6)	113.8	115.6		
Os(1)–F(2)···Xe(1)	113.83(6)	113.8	115.6		

[a] See Figure 8.1a for the atom labeling scheme. [b] See Figure 8.8a for the atom labeling scheme, where F(5A) and Os(1A) correspond to F_5' and Os', respectively, for the symmetry-related atoms. [c] The SDDall(-PP) basis set augmented for F, O, and Xe with two d-type polarization functions. [d] The Stuttgart basis set was used for Os with the f functional. The aug-cc-pVTZ(-PP) basis sets were used for all other atoms. [e] The aug-cc-pVTZ(-PP) basis sets.

Table 8.3. Experimental and Calculated Geometrical Parameters for $[XeF_5][OsO_3F_3]$ and $[Xe_2F_{11}][OsO_3F_3]$

	$[XeF_5][OsO_3F_3]$[a]			$[Xe_2F_{11}][OsO_3F_3]$[b]		
	exptl	calcd (C_s)		exptl	calcd (C_s)	
		SVWN[c]	B3LYP[d]		SVWN[c]	B3LYP[d]
		Bond Lengths (Å)				
Os–F(1)	2.011(2)	2.032	2.052	2.004(2)	2.018	2.072
Os–F(2)	2.006(2)	2.032	2.052	2.001(2)	2.033	1.949
Os–F(3)	2.028(2)	1.999	1.990			
Os–O(1)	1.701(3)	1.711	1.688	1.703(2)	1.711	1.689
Os–O(2)	1.701(3)	1.711	1.688	1.697(3)	1.710	1.690
Os–O(3)	1.692(3)	1.711	1.689			
Xe(1)···F(1)	2.514(2)	2.373	2.460	2.504(2)	2.370	2.404
Xe(1)···F(2)	2.521(2)	2.373	2.460	2.800(2)	2.613	3.197
Xe(1)···F(3)[e]	2.468(2)	2.420	2.606	2.2953(9)	2.244	2.295
Xe(1)–F(4)	1.819(2)	1.890	1.879	1.830(2)	1.893	1.884
Xe(1)–F(5)	1.866(2)	1.923	1.911	1.859(2)	1.921	1.913
Xe(1)–F(6)	1.862(2)	1.924	1.912	1.873(2)	1.939	1.922
Xe(1)–F(7)	1.866(2)	1.924	1.912	1.873(2)	1.928	1.920
Xe(1)–F(8)	1.864(2)	1.923	1.911	1.862(2)	1.918	1.914
Xe(1)···O(1B)				3.353(2)		
		Bond Angles (deg)				
F(1)–Os–F(2)	74.4(1)	73.2	73.8	75.77(7)	73.9	76.0
F(1)–Os–F(3/1A)	74.6(1)	72.9	73.8	78.96(9)	76.3	77.8
F(1)–Os–O(1/1A)	159.4(1)	158.7	159.8	162.72(9)	160.2	163.8
F(1)–Os–O(2)	89.8(1)	89.5	89.7	88.5(1)	88.5	84.8
F(1)–Os–O(3/1)	89.3(1)	88.4	87.6	88.31(8)	88.6	88.7
F(2)–Os–F(3/1A)	74.8(1)	72.9	73.8	75.77(7)	73.9	76.0
F(2)–Os–O(1/1A)	88.8(1)	89.5	89.7	89.88(9)	89.7	92.2
F(2)–Os–O(2)	158.6(1)	158.7	159.8	159.5(1)	157.5	155.1
F(2)–Os–O(3/1)	90.8(1)	88.4	87.6	89.88(9)	89.7	92.2
F(3/1A)–Os–O(1/1A)	89.8(1)	90.3	90.8	88.31(8)	88.6	88.7
F(3/1A)–Os–O(2)	87.3(1)	90.3	90.8	88.5(1)	88.5	84.8
F(3/1A)–Os–O(3/1)	160.7(1)	156.5	156.7	162.72(9)	160.2	163.8
O(1/1A)–Os–O(2)	103.0(2)	104.0	103.7	102.9(1)	104.1	103.1
O(1/1A)–Os–O(3/1)	102.9(2)	103.9	103.4	101.4(1)	102.8	103.0
O(2)–Os–O(3/1)	103.6(2)	103.9	103.4	102.9(1)	104.1	103.1
F(1)···Xe(1)···F(2)	57.69(8)	61.4	60.0	54.90(6)	58.3	50.1
F(1)···Xe(1)···F(3)[e]	58.87(8)	60.0	57.2	75.37(7)	72.4	71.6
F(1)···Xe(1)–F(4)	140.0(1)	147.4	148.3	139.68(7)	140.3	142.6
F(1)···Xe(1)–F(5)	71.6(1)	111.7	112.0	127.31(7)	128.5	124.3
F(1)···Xe(1)–F(6)	124.4(1)	130.1	128.3	74.43(7)	75.6	75.3
F(1)···Xe(1)–F(7)	128.3(1)	84.6	84.5	72.47(6)	70.7	73.4
F(1)···Xe(1)–F(8)	74.5(1)	71.5	72.4	125.60(7)	123.1	123.5
F(2)···Xe(1)···F(3)	58.84(8)	60.0	57.2	61.55(7)	62.4	59.1
F(2)···Xe(1)–F(4)	145.5(1)	147.4	148.3	135.39(8)	135.1	138.0
F(2)···Xe(1)–F(5)	129.0(1)	71.5	72.4	72.43(8)	70.3	74.3
F(2)···Xe(1)–F(6)	116.6(1)	84.6	84.5	67.94(6)	69.1	66.8
F(2)···Xe(1)–F(7)	71.8(1)	130.1	128.3	126.22(7)	128.1	122.3
F(2)···Xe(1)–F(8)	81.1(1)	111.7	112.0	132.84(7)	131.1	132.5
F(3)···Xe(1)–F(4)[e]	150.6(1)	137.2	139.3	144.56(9)	145.9	145.6
F(3)···Xe(1)–F(5)[e]	91.6(1)	128.2	126.8	79.08(9)	82.2	78.3
F(3)···Xe(1)–F(6)[e]	71.95(9)	71.8	72.4	129.45(8)	130.8	125.9
F(3)···Xe(1)–F(7)[e]	104.9(1)	71.8	72.4	118.10(9)	112.2	117.8
F(3)···Xe(1)–F(8)[e]	129.5(1)	128.2	126.8	72.96(8)	71.8	74.1
F(4)–Xe(1)–F(5)	79.5(1)	79.7	79.9	79.43(9)	80.1	80.3

F(4)–Xe(1)–F(6)	79.5(1)	79.1	79.5	77.45(8)	78.0	79.0
F(4)–Xe(1)–F(7)	79.8(1)	79.1	79.5	79.10(9)	80.4	80.4
F(4)–Xe(1)–F(8)	79.2(1)	79.7	79.9	78.48(9)	78.6	79.2
F(5)–Xe(1)–F(6)	86.3(1)	87.5	88.1	88.24(9)	89.9	86.8
F(5)–Xe(1)–F(7)	158.9(1)	158.3	159.1	158.37(8)	160.0	160.6
F(5)–Xe(1)–F(8)	91.3(1)	84.5	85.1	88.1(1)	87.9	89.8
F(6)–Xe(1)–F(7)	86.3(1)	92.7	91.4	88.65(8)	90.6	91.0
F(6)–Xe(1)–F(8)	158.6(1)	158.3	159.1	155.91(8)	156.6	158.2
F(7)–Xe(1)–F(8)	88.3(1)	87.5	88.1	85.12(8)	83.8	85.1
Os–F(1)···Xe(1)				119.39(7)	117.2	131.2
Os–F(2)···Xe(1)				107.48(6)	107.0	102.1
Xe(1)---F(3)---Xe(2)				135.9(1)	129.3	152.2

[a] See Figure 8.2a for the atom labeling scheme. [b] See Figure 8.3a for the atom labeling scheme. [c] The SDDall(-PP) basis set, augmented for F, O, and Xe with two d-type polarization functions, was used. [d] The Stuttgart basis set was used for Os with the f functional. The aug-cc-pVTZ(-PP) basis sets were used for all other atoms. [e] The atom labeling scheme refers to the structure of $[XeF_5][OsO_3F_3]$. In the case of $[Xe_2F_{11}][OsO_3F_3]$ the Xe(1)···F(3) notation should read as Xe(1)---F(3).

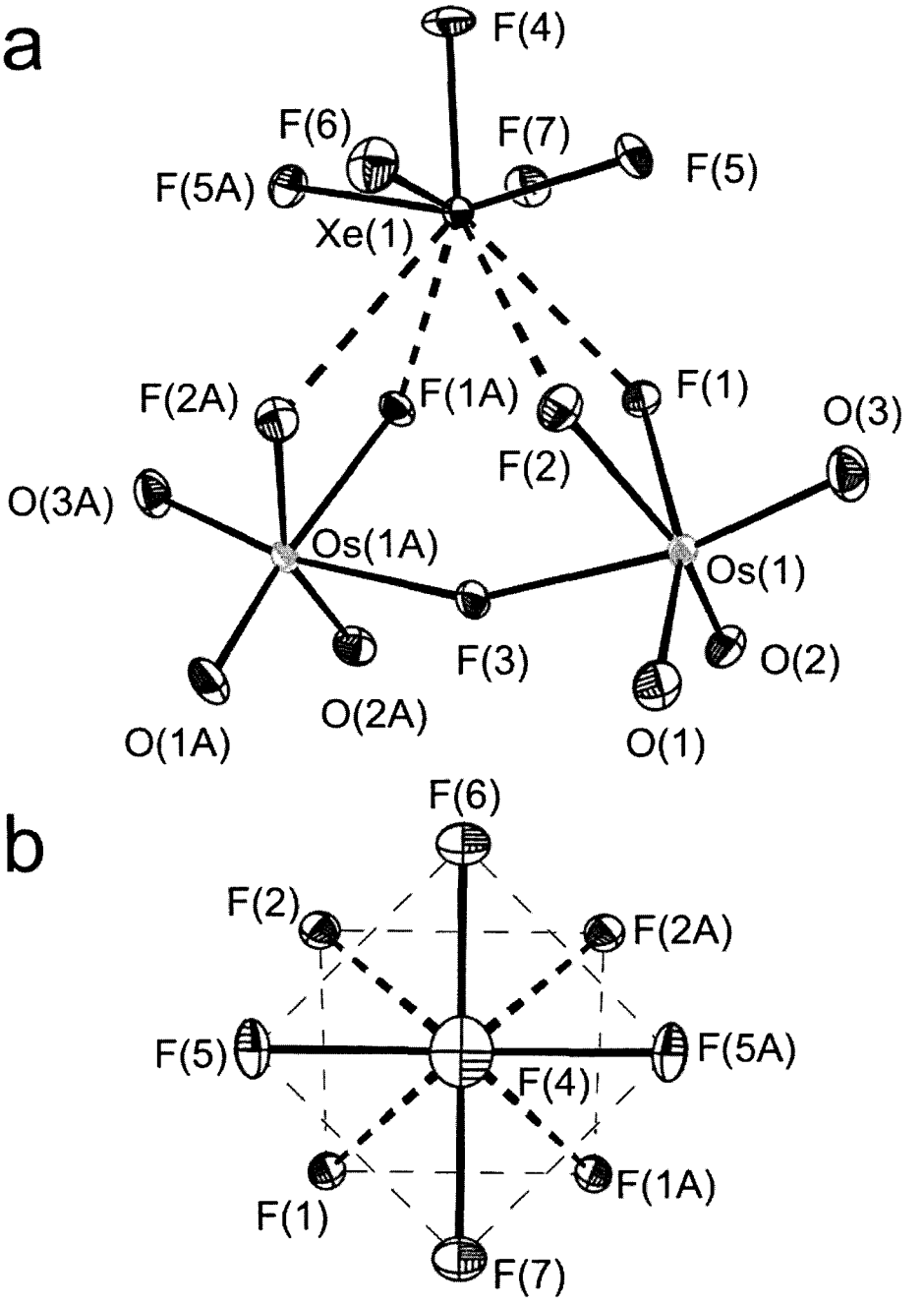

Figure 8.1. Depictions of (a) the structural unit in the X-ray crystal structure of $[XeF_5][\mu\text{-}F(OsO_3F_2)_2]$ with thermal ellipsoids drawn at the 70% probability level, and (b) the primary and secondary coordination spheres of xenon in XeF_5^+ showing the four secondary bonding interactions between xenon and the terminal fluorine atoms of $\mu\text{-}F(OsO_3F_2)_2^-$.

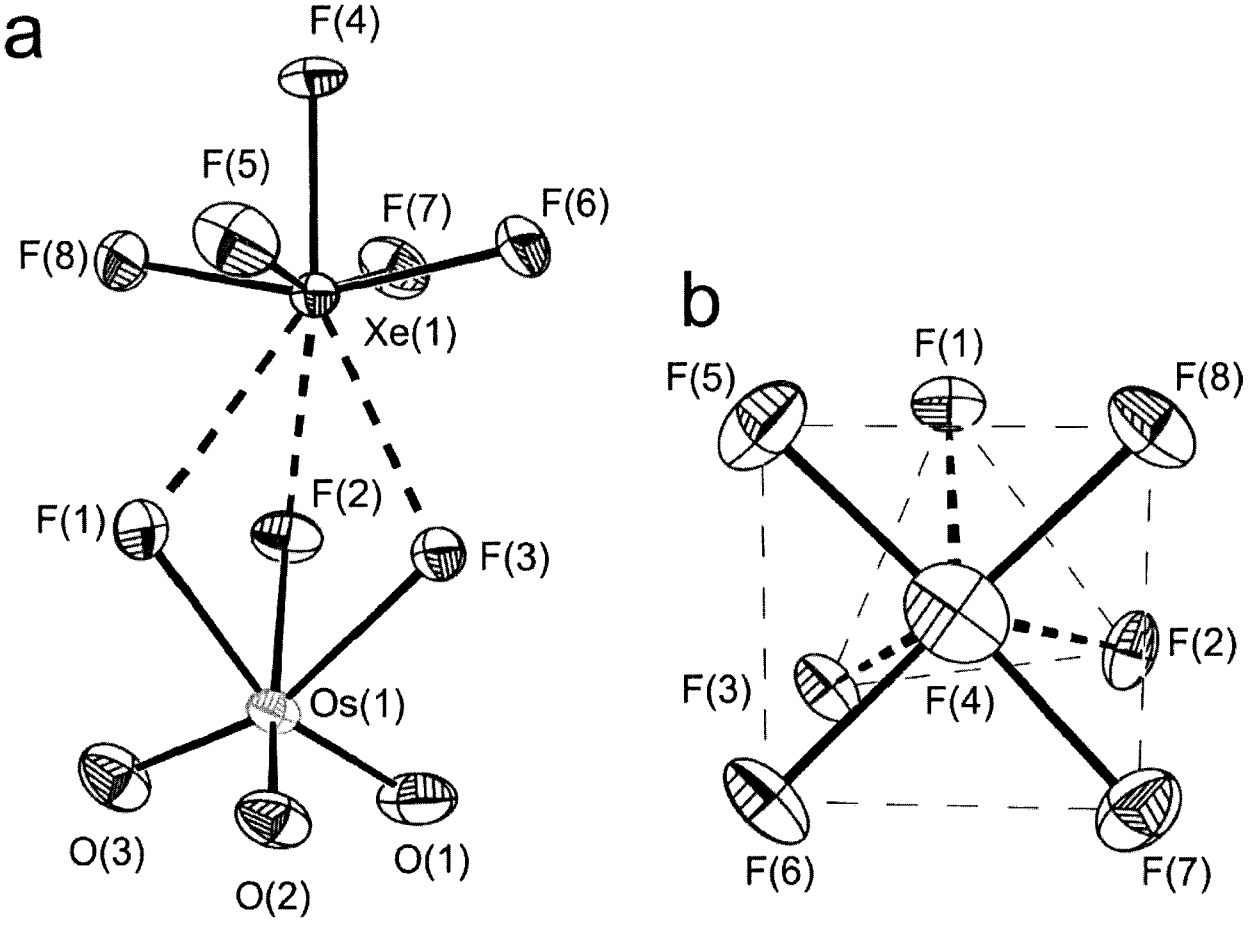

Figure 8.2. Depictions of (a) the structural unit in the X-ray crystal structure of $[XeF_5][OsO_3F_3]$ with thermal ellipsoids drawn at the 70% probability level, and (b) the primary and secondary coordination spheres of xenon in XeF_5^+ showing the three secondary bonding interactions between xenon and the three facial fluorine atoms of $OsO_3F_3^-$.

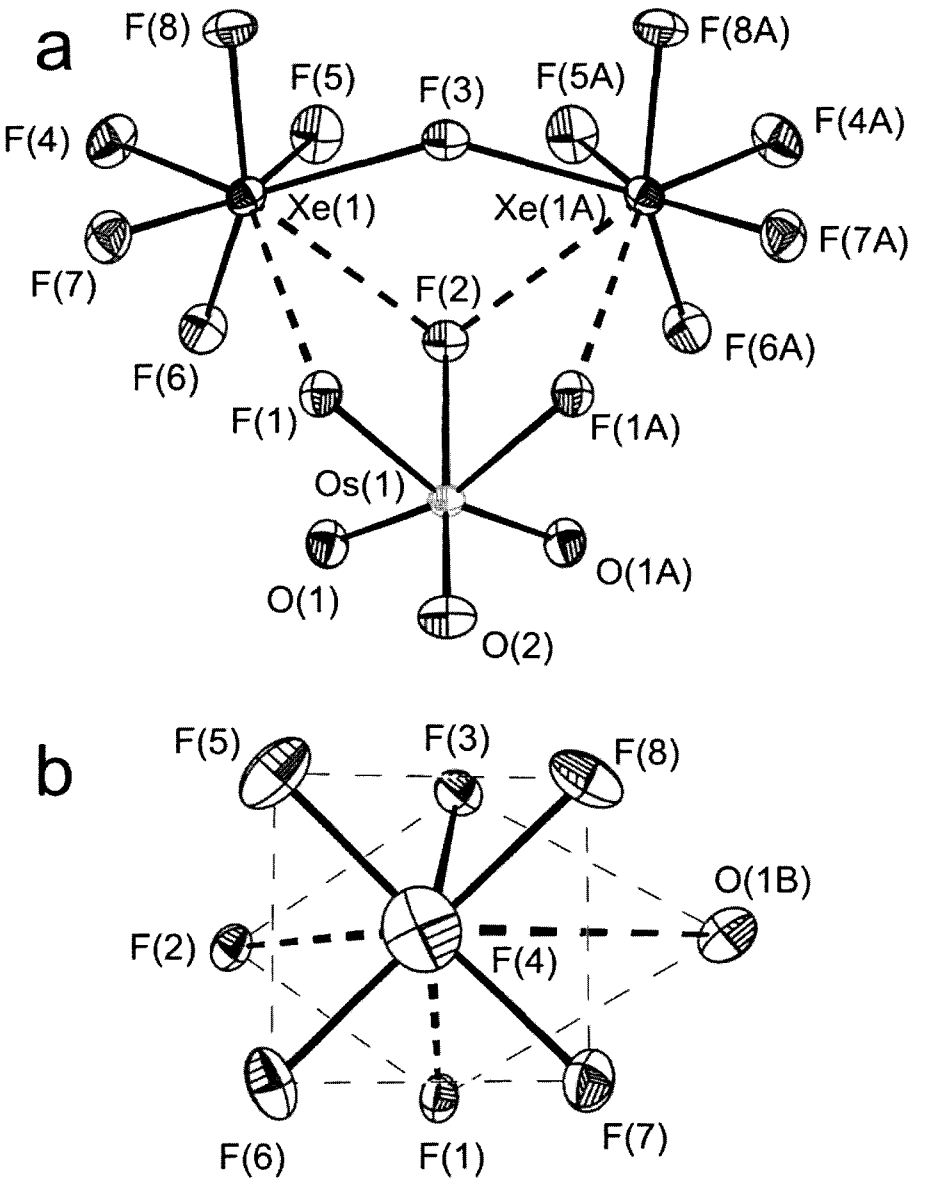

Figure 8.3. Depictions of (a) the structural unit in the X-ray crystal structure of $[Xe_2F_{11}][OsO_3F_3]$ with thermal ellipsoids drawn at the 70% probability level, and (b) the primary and secondary coordination spheres of xenon in the XeF_5-units of $Xe_2F_{11}^+$ showing the secondary bonding interactions between one oxygen atom and three fluorine atoms of $OsO_3F_3^-$ and one xenon atom of $Xe_2F_{11}^+$.

within adjacent columns in the *ab*-plane. The $[Xe_2F_{11}][OsO_3F_3]$ ion pairs stack in layers along the *c*-axis (Figure F3) and are offset such that the anions and cations are alternately stacked one on top of each other along the *a*- and *b*-axes.

8.2.2.1. $OsO_3F_3^-$ and μ-$F(OsO_3F_2)_2^-$.

The primary coordination spheres of the osmium atoms in $[XeF_5][\mu\text{-}F(OsO_3F_2)_2]$, $[XeF_5][OsO_3F_3]$, and $[Xe_2F_{11}][OsO_3F_3]$ consist of three oxygen and three fluorine atoms in facial arrangements, providing distorted octahedral environments around the osmium atoms (Figures 8.1-8.3). The preference for the *fac*-trioxo arrangement has been previously discussed for other d^0 osmium trioxo-species such as $(OsO_3F_2)_\infty$,[11] $OsO_3F_3^-$,[23] $(OsO_3F_2)_2{\cdot}2XeOF_4$,[18] and $[OsO_3F][HF][SbF_6]$.[21] The OsO_3F_2-groups of μ-$F(OsO_3F_2)_2^-$ are symmetry related, and therefore only one OsO_3F_2-group is discussed.

The $[XeF_5][\mu\text{-}F(OsO_3F_2)_2]$ salt is the first example of the fluorine-bridged μ-$F(OsO_3F_2)_2^-$ anion (Figure 8.1a). The Os–O bond lengths are equal to within $\pm3\sigma$ (1.698(2), 1.701(2), 1.692(2) Å) and are similar to those of the $OsO_3F_3^-$ anion (vide infra). The F(3) atom bridges the OsO_3F_2-groups, resulting in a bridge bond length (Os(1)---F(3), 2.1179(5) Å) that is similar to the Os---F bridge bond lengths in $(OsO_3F_2)_\infty$ (2.126(1), 2.108(1) Å)[11] and $(OsO_3F_2)_2{\cdot}2XeOF_4$ (2.117(5), 2.107(4) Å).[18] The Os–F(1) and Os–F(2) bond lengths (1.978(1) and 1.962(1) Å, respectively) are significantly shorter than the Os–F bonds of the $OsO_3F_3^-$ anions in the $Xe_2F_{11}^+$ and XeF_5^+ salts (vide infra). When compared with other terminal Os–F bond lengths of the related fluorine-bridged species $(OsO_3F_2)_\infty$ (1.879(1) Å)[11] and $(OsO_3F_2)_2{\cdot}2XeOF_4$ (1.927(5) Å),[18] the Os–F bonds of the $OsO_3F_3^-$ and μ-$F(OsO_3F_2)_2^-$ anions are elongated as a result of

increased negative charge on the oxygen ligands of the anions. The terminal fluorine atoms of μ-$F(OsO_3F_2)_2^-$, F(1)/F(1A) and F(2)/F(2A), form bridge contacts to xenon of the XeF_5^+ cation, constraining the symmetry-related OsO_2F_2-equatorial planes of μ-$F(OsO_3F_2)_2^-$ so that they are eclipsed. Although the Os(1)---F(3)---Os(1A) bridge bond angle (155.5(1)°) is significantly bent, which allows the four fluorine ligands to chelate the XeF_5^+ cation, it is significantly more open than in the related Os(VIII) compounds, $(OsO_3F_2)_\infty$ (143.9(2)°)[11] and $(OsO_3F_2)_2 \cdot 2XeOF_4$ (109(1)°),[18] owing to the steric requirements of the XeF_5^+ cation.

The geometrical parameters of the $OsO_3F_3^-$ anions in the present study (Figures 8.2 and 8.3) are in good agreement with those reported for the K^+ [26] and $N(CH_3)_4^+$ [23] salts. The Os–O bond lengths are equal, within $\pm 3\sigma$, for $[Xe_2F_{11}][OsO_3F_3]$ (1.703(2), 1.697(3) Å) and $[XeF_5][OsO_3F_3]$ (1.701(3), 1.701(3), 1.692(3) Å), and are in good agreement with the values reported for $[K][OsO_3F_3]$ (1.698(2) Å, EXAFS),[26] $[N(CH_3)_4][OsO_3F_3]$ (1.70(1)–1.73(1) Å),[23] $(OsO_3F_2)_\infty$ (1.678(1)–1.727(1) Å),[11] and $(OsO_3F_2)_2 \cdot 2XeOF_4$ (1.684(6)–1.703(6) Å).[18] The Os–F bond lengths of $[Xe_2F_{11}][OsO_3F_3]$ (2.004(2), 2.001(2) Å) and $[XeF_5][OsO_3F_3]$ (2.011(2), 2.006(2), 2.028(2) Å) are also in good agreement with each other, but are somewhat elongated compared to those of $[N(CH_3)_4][OsO_3F_3]$ (1.97(1), 1.91(1), 1.94(1) Å)[23] and $[K][OsO_3F_3]$ (1.919(15) Å),[26] which is attributed to significant Xe···F intra-ion pair contacts with the XeF_5^+ and $Xe_2F_{11}^+$ cations (vide infra).

The light atoms of $OsO_3F_3^-$ and μ-$F(OsO_3F_2)_2^-$ form relatively undistorted octahedral coordination spheres about the osmium atoms (Figure 8.4) as shown by their

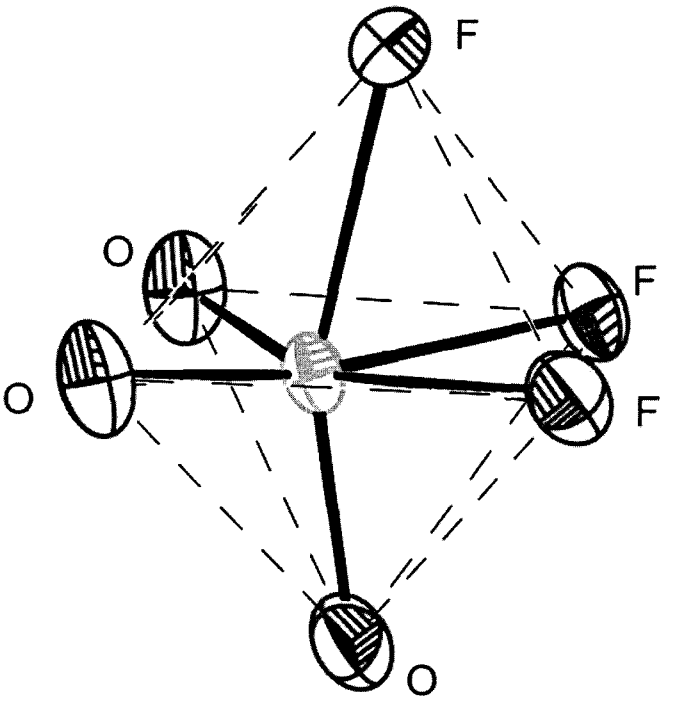

Figure 8.4. The primary coordination sphere formed by the light atoms of the OsO_3F_3-units in $[XeF_5][\mu\text{-}F(OsO_3F_2)_2]$, $[XeF_5][OsO_3F_3]$, and $[Xe_2F_{11}][OsO_3F_3]$.

nearest-neighbor inter-ligand atom contacts (Table F1). The displacements of the osmium atoms towards the centroid of the three facial oxygen atoms are similar to the metal atom displacements observed for other Os(VIII) compounds, which have been previously discussed in detail for $(OsO_3F_2)_\infty$,[11] $(OsO_3F_2)_2 \cdot 2XeOF_4$,[18] and $OsO_3F_3^-$.[23]

8.2.2.2. XeF_5^+ and $Xe_2F_{11}^+$.

The XeF_5^+ cations of $[XeF_5][\mu\text{-}F(OsO_3F_2)]$ (Figure 8.1) and $[XeF_5][OsO_3F_3]$ (Figure 8.2) are based on pseudo-octahedral AX_5E VSEPR arrangements of bond pairs (X) and lone pairs (E) which give rise to a square-pyramidal geometry. The $Xe_2F_{11}^+$ cation of $[Xe_2F_{11}][OsO_3F_3]$ (Figure 8.3) is comprised of two XeF_5^+ cations bridged by a common fluoride ion such that the trajectories of the fluorine bridge interactions with the xenon atoms approach opposite the axial fluorine ligands and from beneath the equatorial planes of the XeF_5-groups so that the axial lone pairs of the xenon atoms are avoided. The four fluorine atoms that comprise the base of the square pyramid are coplanar within ±0.245, ±0.004, and ±0.021 Å in $[XeF_5][\mu\text{-}F(OsO_3F_2)]$, $[XeF_5][OsO_3F_3]$, and $[Xe_2F_{11}][OsO_3F_3]$, respectively, and the respective apical fluorine atoms are located 1.460, 1.478, and 1.461 Å above the equatorial plane and the xenon atoms lie 0.362, 0.341, and 0.369 Å below that plane.

The secondary bonding interactions that occur between the cations and anions in all three structures have contact distances that are significantly less than the sum of the xenon and fluorine van der Waals radii,[165] resulting in xenon atoms that are eight-coordinate in $[XeF_5][OsO_3F_3]$ (Figure 8.2b) and nine-coordinate in $[XeF_5][\mu\text{-}F(OsO_3F_2)]$ (Figure 8.1b) and $[Xe_2F_{11}][OsO_3F_3]$ (Figure 8.3b). The light atom interatomic distances

associated with the xenon coordination spheres are similar, with the distances between the apical fluorine and four equatorial fluorine atoms of the XeF_5-groups being slightly shorter than the average F···F/O contact distances (Table F1). All secondary cation-anion contacts are between the fluorine atoms of the anion and the xenon atoms, except in the case of $[Xe_2F_{11}][OsO_3F_3]$ where an oxygen atom of a neighboring $OsO_3F_3^-$ anion in the unit cell provides an additional short contact to a xenon atom. The anion contacts in all three salts occur from beneath the equatorial planes of the XeF_5-units so as to avoid the valence electron lone pair position in the manner described for $[XeF_5][RuF_6]$.[93]

The three long contacts to the XeF_5^+ cation in $[XeF_5][OsO_3F_3]$ occur through the facial fluorine atoms, F(1,2,3), of the anion (Figure 8.2b), forming a tripod beneath the square base of the XeF_5^+ cation, having very similar Xe···F contact distances (2.514(2), 2.521(2), and 2.468(2) Å, respectively). The shortest contact, Xe(1)···F(3), is likely a consequence of crystal packing and is reflected in the longer Os–F(3) bond (2.028(2) Å) and shorter Os–O(3) bond (1.692(3) Å) that is trans to Os–F(3). The xenon atom is located 2.064 Å above the F(1,2,3)-plane which is parallel, to within ±5.2°, to the equatorial F(5,6,7,8)-plane of the XeF_5^+ cation. Eight-coordinate xenon has also been observed in other XeF_5^+ salts, e.g., $[XeF_5]_2[PdF_6]$,[91] $[XeF_5][AsF_6]$,[76] and $[XeF_5]_2[NiF_6]$.[88] These examples also contain three long Xe···F cation-anion contacts that originate from within the ion pair.

Nine coordinate xenon atom of XeF_5^+ in $[XeF_5][\mu\text{-}F(OsO_3F_2)]$ (Figure 8.1b) results from four short contacts with the terminal fluorine atoms of the anion (two from each OsO_3F_2-group) which again contact xenon from beneath the square plane of the

cation and avoid the valence electron lone pair. The contact distances are comparable (Xe···F(1,1A) (2.622(1) Å) and Xe···F(2,2A) (2.663(1) Å)), with the xenon atom located 1.909 Å above the plane defined by the four contacting atoms of the anion, F(1,1A,2,2A). The four contacting fluorine atoms are coplanar by symmetry and this plane is parallel (±0.1°) to the equatorial F(5,5A,6,7)-plane of XeF_5^+.

The secondary contacts of the nine-coordinate xenon atoms of $[Xe_2F_{11}][OsO_3F_3]$ (Figure 8.3b), do not all originate from within the same ion pair. In the case of Xe(1), two contacts are with terminal fluorine atoms, F(1) and F(2), of the $OsO_3F_3^-$ anion, one is with the bridging F(3) atom of the $Xe_2F_{11}^+$ cation, and the remaining contact is with O(1B) (3.353(2) Å) of another $OsO_3F_3^-$ anion in the unit cell. The Xe(1)···F(2) contact distance (2.800(2) Å) is relatively long when compared with Xe(1)···F(1) (2.504(2) Å) because F(2) is equivalently coordinated to both Xe(1) and Xe(1A), whereas F(1) forms a single short contact with Xe(1). The Xe(1) atom is located 1.916 Å above the near parallelogram-shaped arrangement of F(1), F(2), F(3), O(1B) atoms, which are coplanar to within ±0.0260 Å and parallel to the F(5,6,7,8)-plane to within ±2.0°.

The planes of contacting atoms and the equatorial fluorine atoms of the XeF_5-groups in $[XeF_5][\mu\text{-}F(OsO_3F_2)_2]$ (Figure 8.1b) and $[Xe_2F_{11}][OsO_3F_3]$ (Figure 8.3b) have near-staggered conformations. The xenon coordination spheres may be described as distorted monocapped square antiprisms having dihedral angles between the basal fluorine atom planes of the XeF_5-groups and planes of contacting atoms that are close to 45° (49.0° for the F(4,5,7)Xe(1)- and F(1,3,4)Xe(1)-planes and 42.9° for the O(1B)F(2,4)Xe(1)- and F(4,6,8)Xe(1)-planes of $[Xe_2F_{11}][OsO_3F_3]$; 41.4° for the

F(4,5,5A)Xe(1)- and F(1,2A,4)Xe(1)-planes and 48.6° for the F(1A,2,4)Xe(1)- and F(4,6,7)Xe(1)-planes of $[XeF_5][\mu\text{-}F(OsO_3F_2)_2]$). The near-staggered arrangements provide the closest packed arrangements for the fluorine atoms of the equatorial XeF_4-planes and the light atoms that comprise the secondary coordination sphere. In contrast, the equatorial XeF_4-planes of $Xe_2F_{11}^+$ are eclipsed because they are constrained by symmetry.

Nine-coordinate xenon occurs in other XeF_5^+ and $Xe_2F_{11}^+$ salts, e.g., $[XeF_5][SbF_6]\cdot XeOF_4$,[95] $[XeF_5][AsF_6]$,[76] $[XeF_5][PtF_6]$,[92] $[XeF_5][RuF_6]$,[93] $[XeF_5][AgF_4]$,[71] $[Xe_2F_{11}][AuF_6]$,[80] and $[Xe_2F_{11}]_2[NiF_6]$.[89] The xenon coordination in $[Xe_2F_{11}][OsO_3F_3]$ is similar to that of the AuF_6^- salt where the secondary coordination sphere of xenon also arises from one inter- and two intra-ion pair contacts within the unit cell. The nine-coordination to xenon in $[XeF_5][\mu\text{-}F(OsO_3F_2)]$ is, however, unique because it is the only XeF_5^+ salt known to have four secondary fluorine contacts to a XeF_5^+ cation that originate solely from the anion of its ion pair.

With the exception of Xe(1)···F(2) in $[Xe_2F_{11}][OsO_3F_3]$ (2.800(2) Å), the Xe···F contact distances in all three salts are shorter than those in $(OsO_3F_2)_2\cdot 2XeOF_4$ (2.757(5) Å),[18] which is accompanied by significant charge transfer from the anion to the cation (see Section 8.2.4).

8.2.3. Raman Spectroscopy.

The low-temperature Raman spectra of $[XeF_5][\mu\text{-}F(OsO_3F_2)_2]$, $[XeF_5][OsO_3F_3]$, and $[Xe_2F_{11}][OsO_3F_3]$ are shown in Figures 8.5-8.7, respectively. The observed and calculated frequencies and mode descriptions for $[XeF_5][\mu\text{-}F(OsO_3F_2)_2]$, $[XeF_5][OsO_3F_3]$, and $[Xe_2F_{11}][OsO_3F_3]$ are provided in Tables 8.4-8.6, respectively, where the atom

numbering schemes are given in Figure 8.8. Spectral assignments for $[XeF_5][\mu\text{-}F(OsO_3F_2)_2]$, $[XeF_5][OsO_3F_3]$, and $[Xe_2F_{11}][OsO_3F_3]$ were made by comparison with the calculated frequencies and Raman intensities for the energy-minimized gas-phase geometries of their ion pairs, which are in good agreement with experiment at the SVWN and B3LYP levels of theory.

Examination of Tables 8.4-8.6 reveals that several bands in the Raman spectra of $[XeF_5][\mu\text{-}F(OsO_3F_2)_2]$, $[XeF_5][OsO_3F_3]$, and $[Xe_2F_{11}][OsO_3F_3]$ are split into two bands. Factor-group analyses (Tables F2-F4) were therefore undertaken to account for these splittings, and are based on analyses of the ion pairs in the crystal structures of these salts.

The atomic positions of the xenon and osmium atoms in the crystal structures of $[Xe_2F_{11}][OsO_3F_3]$ and $[XeF_5][\mu\text{-}F(OsO_3F_2)_2]$ (see Section 8.2.2) reveal that the $[XeF_5][\mu\text{-}F(OsO_3F_2)_2]$ and $[Xe_2F_{11}][OsO_3F_3]$ ion pairs are located on mirror planes. Under C_s symmetries, all vibrational modes, 27A' + 24A" for $[XeF_5][\mu\text{-}F(OsO_3F_2)_2]$ and 29A' + 25A" for $[Xe_2F_{11}][OsO_3F_3]$, are predicted to be both infrared- and Raman-active. Correlations of the gas-phase ion-pair symmetries to the crystal site symmetries (C_s) results in no additional splitting of the vibrational bands. Correlation of their site symmetries to the unit cell symmetry (D_{2h}) results in equal apportioning of the A' vibrational modes between Raman-active A_g and B_{2g} and infrared-active B_{1u} and B_{3u} symmetries and equal apportioning of the A" vibrational modes between Raman-active B_{1g} and B_{3g} and infrared-active A_u and B_{2u} symmetries for both salts (Table F2 and F4, respectively). Consequently, the vibrational bands in the Raman spectrum are predicted to be split, but this splitting is only resolved on two Raman bands of the $[Xe_2F_{11}][OsO_3F_3]$

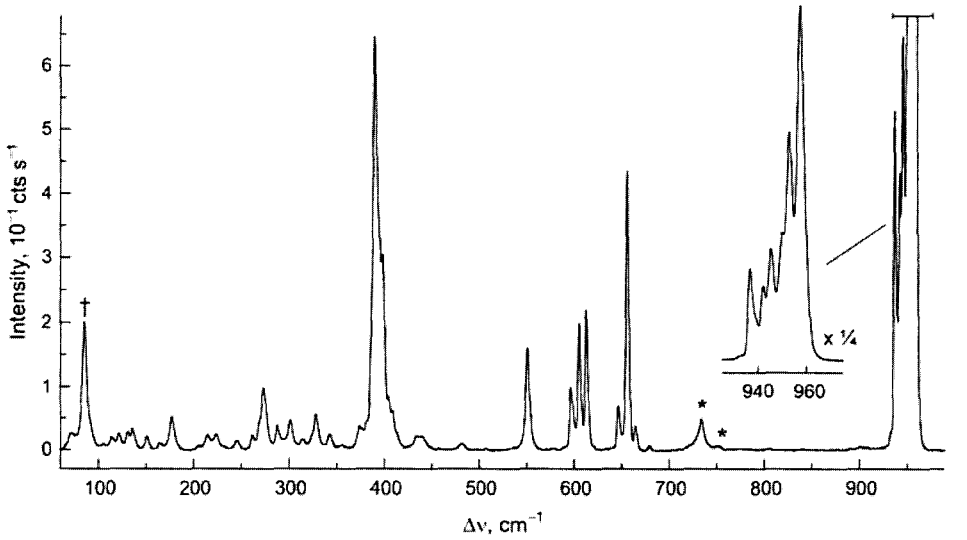

Figure 8.5. Raman spectrum of $[XeF_5][\mu\text{-}F(OsO_3F_2)_2]$ recorded at –150 °C using 1064-nm excitation; the symbols denote FEP sample tube lines (*) and an instrumental artifact (†).

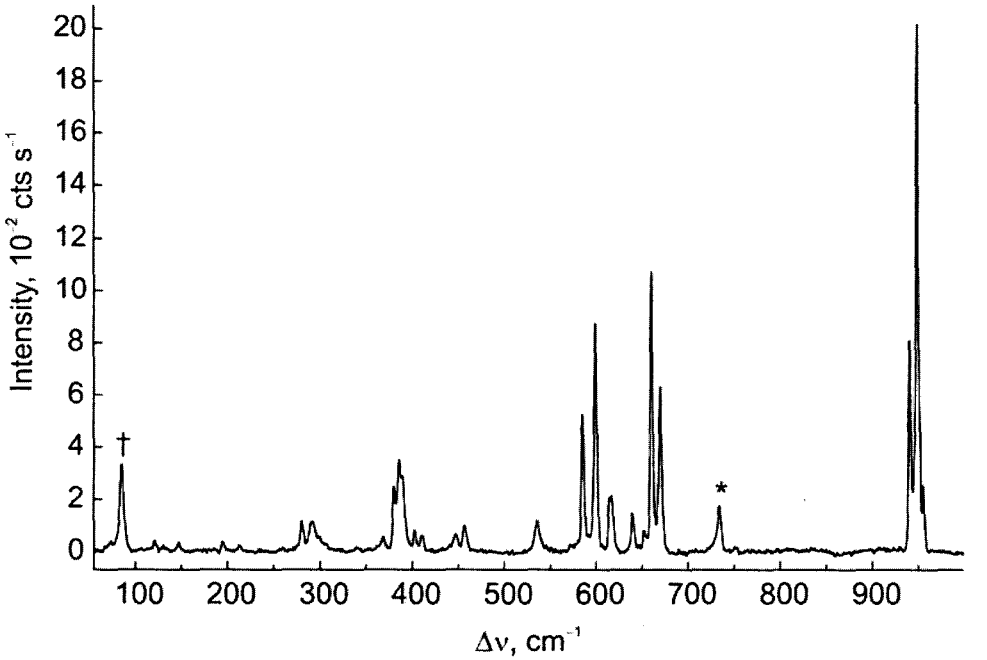

Figure 8.6. Raman spectrum of $[XeF_5][OsO_3F_3]$ recorded at –150 °C using 1064-nm excitation; the symbols denote FEP sample tube lines (*) and an instrumental artifact (†).

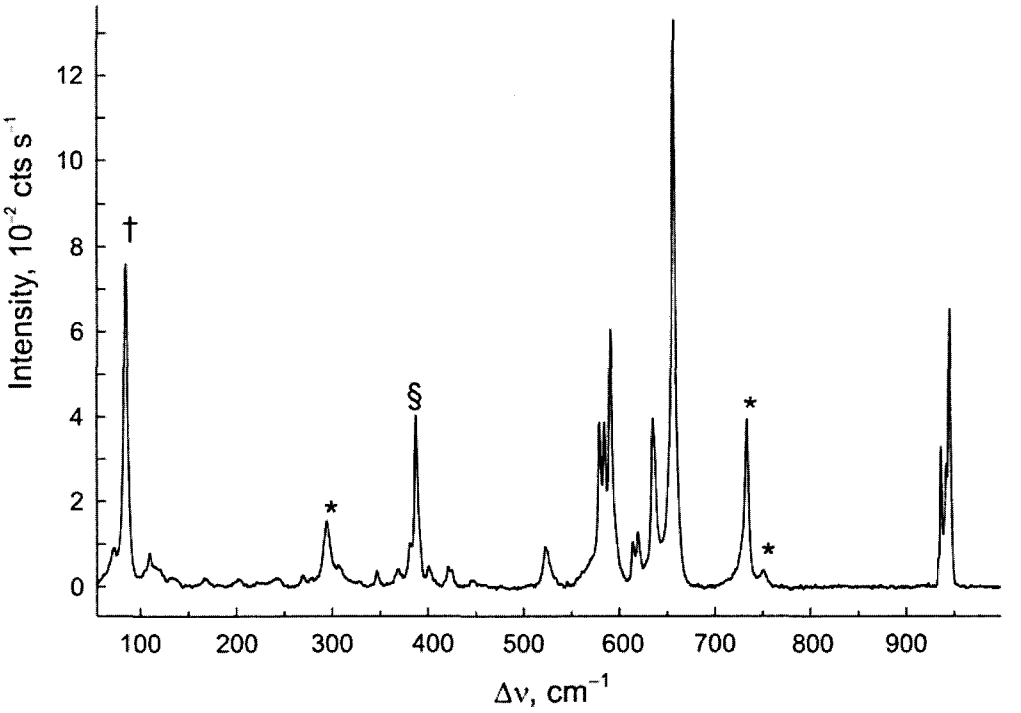

Figure 8.7. Raman spectrum of $[Xe_2F_{11}][OsO_3F_3]$ recorded at –150 °C using 1064-nm excitation; the symbols denote FEP sample tube lines (*), an instrumental artifact (†), and overlap of a $[Xe_2F_{11}][OsO_3F_3]$ line with a FEP sample tube line (§).

Table 8.4. Experimental Raman and Calculated Frequencies, Intensities, and Assignments for $[XeF_5][\mu\text{-}F(OsO_3F_2)_2]$

exptl[a]	calcd[b]		assgnts (C_{2v})[e]
	SVWN[c]	B3LYP[d]	
957(100)	991(85)[21]	1027(124)[10]	A_1, $\nu(OsO_3) + \nu(Os'O_3')$
953(64)	986(2)[141]	1024(<0.1)[93]	B_2, $\nu(OsO_3) - \nu(Os'O_3')$
950(35)	981(82)[111]	1008(34)[165]	A_1, $\nu(OsO_1) + \nu(OsO_2) + \nu(Os'O_1') + \nu(Os'O_2')$
945(31)	983(33)[152]	1006(34)[216]	B_1, $[\nu(OsO_1) + \nu(Os'O_1')] - [\nu(OsO_2) + \nu(Os'O_2')]$
942(20)	978(11)[0]	1003(8)[82]	B_2, $[\nu(OsO_1) + \nu(OsO_2)] - [\nu(Os'O_1') + \nu(Os'O_2')]$
936(25) 933(sh)	979(5)[0]	1001(3)[0]	A_2, $[\nu(OsO_1) + \nu(Os'O_2')] - [\nu(OsO_2) + \nu(Os'O_1')]$
680(2)	630(10)[172]	637(7)[174]	B_1, $\nu(XeF_6) - \nu(XeF_7)$
664(2)	619(5)[204]	627(6)[186]	B_2, $\nu(XeF_5) - \nu(XeF_5')$
656(21)	622(58)[54]	621(87)[52]	A_1, $\nu(XeF_4)$
646(3)	589(10)[209]	574(7)[80]	A_1, $\nu(XeF_4) + \nu(OsF_1) + \nu(OsF_2) + \nu(Os'F_1') + \nu(Os'F_2')$
612(10)	561(20)[34]	563(13)[44]	A_1, $\nu(XeF_6) + \nu(XeF_7)$
605(9)	573(2)[251]	551(3)[273]	B_2, $[\nu(OsF_1) + \nu(OsF_2) + \nu(OsF_3)] - [\nu(Os'F_1') + \nu(Os'F_2') + \nu(Os'F_3)]$
596(5)	552(41)[68]	550(42)[168]	A_1, $\nu(XeF_5) + \nu(XeF_5')$
550(8)	497(1)[7]	470(1)[15]	B_1, $[\nu(OsF_1) + \nu(Os'F_1')] - [\nu(OsF_2) + \nu(Os'F_2')]$
480(<1)	477(1)[0]	454(1)[0]	A_2, $[\nu(OsF_1) + \nu(Os'F_2')] - [\nu(OsF_2) + \nu(Os'F_1')]$
441(1)	473(<1)[21]	452(<1)[25]	B_2, $\nu(OsF_3) - \nu(Os'F_3)$
433(1)	398(5)[47]	406(6)[1]	A_1, $\delta(F_1OsF_2) + \delta(F_1'Os'F_2') + [\delta(O_1OsO_2) + \delta(O_1'Os'O_2')]_{small}$
409(2)	387(1)[25]	404(2)[7]	B_2, $[\delta(O_1OsO_2) + \delta(F_1OsF_2)] - [\delta(O_1'Os'O_2') + \delta(F_1'Os'F_2')]$
405(4)	375(<1)[5]	399(<1)[6]	B_1, $\rho_t(O_1OsO_2) + \delta(O_1OsO_3) + \rho_t(O_1'Os'O_2') + \delta(O_1'Os'O_3')$
398(14)	371(2)[1]	398(1)[2]	A_1, $\delta_{umb}(OsO_1O_2O_3) + \delta_{umb}(Os'O_1'O_2'O_3')$
390(31)	371(9)[0]	395(8)[0]	A_2, $[\rho_t(O_1OsO_2) + \delta(O_1OsO_3)] - [\rho_t(O_1'Os'O_2') + \delta(O_1'Os'O_3')]$
	367(3)[19]	394(<1)[29]	B_2, $\delta_{umb}(OsO_1O_2O_3) - \delta_{umb}(Os'O_1'O_2'O_3')$
382(2)	361(2)[1]	387(3)[23]	B_2, $\delta(F_4XeF_5) - \delta(F_4XeF_5')$
374(1)	350(1)[6]	371(1)[8]	B_1, $\delta(F_4XeF_6) - \delta(F_4XeF_7)$
342(1)	362(3)[41]	368(1)[32]	A_1, $\delta(O_1OsO_2) + \delta(O_1'Os'O_2') + \nu(OsF_3) + \nu(Os'F_3)$
	337(<1)[<1]	337(1)[72]	A_1, $\delta_{umb}(XeF_1F_2F_1'F_2') + \delta(F_5XeF_5') - [\nu(OsF_3) + \nu(Os'F_3)]$
327(2)	331(1)[9]	328(4)[13]	B_2, $[\delta(O_1OsO_2) + \delta(F_1'Os'F_2')] - [\delta(O_1'Os'O_2') + \delta(F_1OsF_2)]$
315(1)	313(1)[78]	320(<1)[92]	A_1, $\rho_w(F_5'XeF_5) + \rho_w(F_6XeF_7) + \nu(OsF_3) + \nu(Os'F_3)$
	314(<1)[16]	319(<1)[20]	B_1, $\rho_t(O_1OsO_2) + \rho_t(O_1'Os'O_2') + \rho_r(F_1OsF_2) + \rho_r(F_1'Os'F_2') + \delta(OsF_3Os')$
301(2)	290(1)[0]	281(1)[<0.1]	A_2, $\rho_t(O_1OsO_2) + \rho_r(F_1OsF_2) - [\rho_t(O_1'Os'O_2') + \rho_r(F_1'Os'F_2')]$
288(2)	266(2)[18]	267(1)[4]	A_1, $\delta(O_3OsF_3) + \delta(O_3'Os'F_3)$
274(4)	247(1)[0]	267(1)[0]	A_2, $\delta(F_5XeF_7) + \delta(F_6XeF_5')$
268(sh)	287(<1)[1]	259(<1)[8]	B_1, $\delta(F_1XeF_1') - \delta(F_2XeF_2') + \delta(OsF_3Os')$

262(1)	262(1)[51]	258(1)[75]	B_2, $\rho_w(F_1OsF_2) + \rho_w(F_1'Os'F_2')$
245(1)	241(<1)[<1]	249(<0.1)[<0.1]	A_1, $\rho_t(F_5XeF_6) + \rho_t(F_5'XeF_7)$
224(1)	212(<0.1)[<1]	217(<0.1)[<0.1]	B_1, $\rho_w(F_5XeF_5') + \delta(OsF_3Os') + \rho_t(F_1OsF_2) - \rho_t(F_1'OsF_2')$
217(1)	180(<0.1)[<1]	198(<0.1)[1]	B_2, $\delta(F_6XeF_7)$
207(<1)	183(<1)[0]	190(<0.1)[0]	A_2, $\rho_t(F_1OsF_2) + \rho_t(F_2'Os'F_1')$
177(2)	172(<1)[<0.1]	185(<1)[<0.1]	B_1, B_2, $[XeF_5][\mu\text{–}F(OsO_3F_2)]$ def.
165(<1)	140(<1)[4]	140(1)[8]	
150(1)	154(8)[2]	132(1)[13]	A_1, $[XeF_5][\mu\text{–}F(OsO_3F_2)]$ breathing mode
136(1)	130(<1)[0]	129(<0.1)[0]	A_2, $\mu\text{–}F(OsO_3F_2)^-$ def.
130(1)	123(1)[2]	114(<1)[2]	B_2, $[XeF_5][\mu\text{–}F(OsO_3F_2)]$ def.
121(1)	124(1)[<0.1]	106(1)[<0.1]	B_1, $\mu\text{–}F(OsO_3F_2)^-$ breathing mode
114(1)	127(<1)[<0.1]	110(<1)[<0.1]	A_1, $\rho_r(F_4XeF_6) + \rho_r(F_4XeF_7)$
92(sh)	105(<1)[1]	93(<1)[6]	A_1, $[XeF_5][\mu\text{–}F(OsO_3F_2)]$ breathing mode
	95(<0.1)[0]	81(<0.1)[0]	A_2, $[XeF_5][\mu\text{–}F(OsO_3F_2)]$ def.
	99(<0.1)[<0.1]	63(<0.1)[<1]	B_1, $\mu\text{–}F(OsO_3F_2)$ def.
	69(<0.1)[<1]	57(<0.1)[<1]	
	59(<0.1)[<0.1]	47(<0.1)[1]	A_2, B_2, $[XeF_5][\mu\text{–}F(OsO_3F_2)]$ def.
	72(<0.1)[0]	33(<0.1)[0]	

[a] The Raman spectrum was recorded on a microcrystalline solid sample in a FEP tube at –150 °C using 1064-nm excitation. Experimental Raman intensities are given in parentheses and are relative intensities with the most intense band given as 100. The abbreviations denote shoulder (sh). [b] Values in parentheses denote calculated Raman intensities ($Å^4\,u^{-1}$) and values in square brackets denote calculated infrared intensities (km mol^{-1}). [c] SVWN/SDDall(-PP). [d] B3LYP/Stuttgart (Os) aug-cc-pVTZ(-PP) (Xe, O, F) [e] Assignments are for the energy-minimized geometry calculated at the SVWN level of theory. See Figure 8.8a for the atom labeling scheme. The symbols denote stretch (ν), bend (δ), twist (ρ_t), rock (ρ_r), wag (ρ_w), and umbrella (δ_{umb}). The abbreviation, def., denotes a deformation mode.

Table 8.5. Experimental Raman and Calculated Frequencies, Intensities, and Assignments for $[XeF_5][OsO_3F_3]$

exptl[a]	calcd[b]		assgnts (C_s)
	SVWN[c]	B3LYP[d]	
955(12), 951(sh)	986(22)[84]	1008(23)[120]	A", $\nu(OsO_1) - \nu(OsO_2)$
948(100), 946(sh)	983(55)[51]	1025(59)[53]	A', $\nu(OsO_1) + \nu(OsO_2) + \nu(OsO_3)$
940(39)	985(27)[81]	1006(20)[120]	A', $\nu(OsO_1) + \nu(OsO_2) - \nu(OsO_3)$
654(sh), 652(4)	625(8)[202]	621(8)[208]	A", $[\nu(XeF_5) + \nu(XeF_6)] - [\nu(XeF_7) + \nu(XeF_8)]$
670(32)	624(11)[197]	620(7)[204]	A', $[\nu(XeF_5) + \nu(XeF_8)] - [\nu(XeF_6) + \nu(XeF_7)]$
660(53)	622(58)[148]	619(86)[120]	A', $\nu(XeF_4)$
617(11), 615(10)	572(16)[12]	569(22)[6]	A', $\nu(XeF_4) - [\nu(XeF_5) + \nu(XeF_6) + \nu(XeF_7) + \nu(XeF_8)]$
599(44)	556(13)[<0.1]	551(16)[<0.1]	A", $[\nu(XeF_5) + \nu(XeF_7)] - [\nu(XeF_6) + \nu(XeF_8)]$
585(27)	551(20)[149]	537(13)[171]	A', $\nu(OsF_1) + \nu(OsF_2) + \nu(OsF_3)$
457(5)	458(2)[7]	443(2)[12]	A', $[\nu(OsF_1) + \nu(OsF_2)] - \nu(OsF_3)$
447(3)	445(2)[7]	419(3)[7]	A", $\nu(OsF_1) - \nu(OsF_2)$
411(3)	374(3)[4]	397(3)[3]	A", $\rho_t(O_1OsO_3) - \delta(O_2OsO_3)$
402(4)	364(2)[25]	396(3)[3]	A', $\delta_{umb}(OsO_1O_2O_3)$
390(14), 386(18)	371(3)[4]	393(4)[5]	A', $\delta(O_1OsO_2)$
380(12)	399(1)[195]	370(1)[181]	A', $\nu(Xe\cdots F_1) + \nu(Xe\cdots F_2) + \nu(Xe\cdots F_3)$
369(3)	336(2)[6]	361(1)[7]	A", $\delta(F_4XeF_5F_6) - \rho_w(F_7XeF_8)$
	333(2)[7]	360(1)[19]	A', $\delta(F_4XeF_5F_8) - \rho_w(F_6XeF_7)$
291(6)	289(2)[31]	318(3)[61]	A', $\delta_{umb}(XeF_5F_6F_7F_8)$
299(3)	314(<1)[5]	305(<1)[19]	A", $\rho_t(O_2OsO_3) + \rho_t(F_1XeF_2) + \rho_t(F_2XeF_3)$
	277(<1)[6]	292(<1)[30]	A', $\rho_w(F_1OsF_2) - [\delta(O_3OsF_3) + \rho_w(O_1OsO_2)]$
	284(<1)[6]	282(1)[1]	A", $\rho_t(F_1OsF_2) + \rho_w(F_1OsF_3)$
280(6)	309(2)[12]	278(1)[2]	A', $\delta(F_1OsF_2) + \delta(F_3OsO_3) + \nu(XeF_3)$
213(1)	234(2)[<1]	257(2)[<1]	A', $\delta(F_5XeF_8) + \delta(F_6XeF_7)$
	219(<0.1)[<0.1]	231(<0.1)[<0.1]	A", $\rho_t(F_5XeF_6) + \rho_t(F_7XeF_8)$
195(2)	172(<1)[<1]	191(<1)[<1]	A", $\delta(F_5XeF_6) - \delta(F_7XeF_8)$
146(2)	167(1)[1]	183(<1)[<1]	A', $\delta(F_5XeF_8) - \delta(F_6XeF_7)$
	147(<0.1)[<0.1]	163(<0.1)[<0.1]	A", $\rho_{twist}(OsO_1O_2O_3) - \rho_{twist}(OsF_1F_2F_3)$
130(1)	149(2)[4]	133(1)[13]	A', $[XeF_5][OsO_3F_3]$ breathing
120(2)	112(<1)[<0.1]	112(<1)[<0.1]	A", $[XeF_5][OsO_3F_3]$ def.
	102(<1)[<1]	103(<1)[1]	A', $\rho_w(F_4XeF_5F_8) + \rho_w(F_6XeF_7)$
	88(<0.1)[<0.1]	68(<0.1)[<1]	A", $\rho_t(O_1OsO_2) + \rho_t(F_1OsF_2) + \rho_t(O_3OsF_3)$
	89(<1)[<0.1]	50(<0.1)[<1]	A', $\rho_w(O_1OsO_2) + \rho_t(O_3OsF_3) - \rho_w(F_1OsF_2)$
	7(<0.1)[<0.1]	21(<0.1)[<0.1]	A", $[XeF_5][OsO_3F_3]$ def.

[a] The Raman spectrum was recorded on a microcrystalline solid sample in a FEP tube at −150 °C using 1064-nm excitation. Experimental Raman intensities are given in parentheses and are relative intensities with the most intense band given as 100. The abbreviations denote shoulder (sh). Bands were also observed at 536(6) and 639(7) cm^{-1} but were not assigned. [b] Values in parentheses denote calculated Raman intensities ($Å^4$ u^{-1}) and values in square brackets denote calculated infrared intensities (km mol^{-1}). [c] SVWN/SDDall(-PP). [d] B3LYP/Stuttgart (Os) aug-cc-pVTZ(-PP) (Xe, O, F). [e] Assignments are for the energy-minimized geometry calculated at the B3LYP level of theory. See Figure 8.8b for the atom labeling scheme. The symbols denote stretch (ν), bend (δ), twist (ρ_t), rock (ρ_r), wag (ρ_w), and umbrella (δ_{umb}). The abbreviation, def., denotes a deformation mode.

Table 8.6. Experimental Raman and Calculated Frequencies, Intensities, and Assignments for $[Xe_2F_{11}][OsO_3F_3]$

exptl[a]	calcd[b]		assgnts (C_s)[e]
	SVWN[c]	B3LYP[d]	
945(49)	982(59)[43]	1023(58)[50]	A', $\nu(OsO_1) + \nu(OsO_2) + \nu(OsO_1')$
942(21)	983(13)[81]	1006(19)[132]	A", $\nu(OsO_1) - \nu(OsO_1')$
936(24) 933(sh)	986(33)[76]	1001(21)[111]	A', $\nu(OsO_1) + \nu(OsO_1') - \nu(OsO_2)$
	635(8)[248]	622(28)[251]	A', $[\nu(Xe_1F_5) + \nu(Xe_1'F_5')] - [\nu(Xe_1F_7) + \nu(Xe_1'F_7')]$
656(100)	624(105)[192]	620(131)[134]	A', $\nu(Xe_1F_4) + \nu(Xe_1F_5) + \nu(Xe_1F_6) + \nu(Xe_1F_4') + \nu(Xe_1'F_5') + \nu(Xe_1'F_6')$
635(28)	626(23)[283]	615(39)[399]	A', $[\nu(Xe_1F_4) + \nu(Xe_1F_6) + \nu(Xe_1'F_4') + \nu(Xe_1'F_6')] - [\nu(Xe_1F_8) + \nu(Xe_1'F_8')]$
620(8)	613(12)[37]	609(25)[14]	A", $[\nu(Xe_1F_4) + \nu(Xe_1F_5)] - [\nu(Xe_1'F_4') + \nu(Xe_1'F_5')]$
613(6)	612(21)[196]	607(14)[121]	A", $[\nu(Xe_1F_4) + \nu(Xe_1F_7) + \nu(Xe_1F_8) + \nu(Xe_1'F_5') + \nu(Xe_1'F_6')] - [\nu(Xe_1F_5) + \nu(Xe_1F_6) + \nu(Xe_1'F_4') + \nu(Xe_1'F_7') + \nu(Xe_1'F_8')]$
	604(6)[147]	599(1)[192]	A", $[\nu(Xe_1F_4) + \nu(Xe_1F_6) + \nu(Xe_1'F_8')] - [\nu(Xe_1F_8) + \nu(Xe_1'F_4') + \nu(Xe_1'F_6')]$
	569(3)[<1]	568(7)[11]	A", $[\nu(Xe_1F_3)] + \nu(Xe_1F_5) + \nu(Xe_1F_6) + \nu(Xe_1F_7)] - [\nu(Xe_1'F_3) + \nu(Xe_1'F_5') + \nu(Xe_1'F_6') + \nu(Xe_1'F_7')]$
591(44)	573(22)[33]	567(20)[52]	A', $[\nu(OsF_1) + \nu(OsF_2) + \nu(OsF_1') + \nu(Xe_1F_4) + \nu(Xe_1'F_4')] - [\nu(Xe_1F_5) + \nu(Xe_1F_6) + \nu(Xe_1F_7) + \nu(XeF_8) + \nu(Xe_1'F_5') + \nu(Xe_1'F_6') + \nu(Xe_1'F_7') + \nu(Xe_1'F_8')]$
585(27)	529(33)[109]	551(21)[111]	A', $\nu(OsF_2)$
580(27)	554(13)[29]	544(23)[3]	A', $[\nu(Xe_1F_5) + \nu(Xe_1F_7) + \nu(Xe_1'F_5') + \nu(Xe_1'F_7')] - [\nu(Xe_1F_6) + \nu(Xe_1F_8) + \nu(Xe_1'F_6') + \nu(Xe_1'F_8')]$
	549(5)[<0.1]	542(8)[<1]	A", $[\nu(Xe_1F_5) + \nu(Xe_1F_7) + \nu(Xe_1'F_6') + \nu(Xe_1'F_8')] - [\nu(Xe_1F_6) + \nu(Xe_1F_8) + \nu(Xe_1'F_5') + \nu(Xe_1'F_7')]$
448(1)	435(2)[3]	434(3)[137]	A', $\nu(OsF_1) + \nu(OsF_1') - \nu(OsF_2)$
426(2) 422(3)	453(<1)[113]	412(2)[95]	A", $\nu(OsF_1) - \nu(OsF_1') + \rho_t(O_1OsO_1') + \delta(O_2OsO_1')$
401(3)	379(3)[32]	400(2)[4]	A', $\rho_w(O_1OsO_1') + \rho_r(O_2OsF_2)$
386(30)[f]	381(4)[3]	394(4)[23]	A', $\delta(O_1OsO_1')$
381(7)	384(4)[110]	388(1)[80]	A", $\rho_t(O_1OsO_1') + \rho_t(F_1OsF_1') - \rho_t(O_2OsF_2)$
369(2)	344(1)[3]	366(<1)[13]	A', $[\delta(F_4Xe_1F_6) + \delta(F_4'Xe_1'F_6')] - [\delta(F_4Xe_1F_8) + \delta(F_4'Xe_1'F_8')]$
	342(1)[61]	365(1)[4]	A", $[\delta(F_3Xe_1F_8) + \delta(F_4Xe_1F_6)] - [\delta(F_3Xe_1'F_8') + \delta(F_4'Xe_1'F_6')]$
	362(1)[37]	349(<1)[39]	A', $\delta(OsF_1F_2F_1')$
	319(<1)[8]	347(<1)[62]	A", $[\delta(F_4Xe_1F_7) + \delta(F_3Xe_1F_5)] - [\delta(F_3'Xe_1'F_5') + \delta(F_4'Xe_1'F_7')]$
347(2)	322(3)[7]	344(1)[1]	A', $[\delta(F_4Xe_1F_5) + \delta(F_4'Xe_1'F_5')] - [\delta(F_4Xe_1F_7) + \delta(F_4'Xe_1'F_7')]$
	370(2)[132]	329(<0.1)[268]	A", $\nu(XeF_3) - \nu(Xe_1'F_3) + \rho_t(F_1OsF_1') + \rho_w(F_2OsO_2)$
	335(2)[9]	322(7)[12]	A', $\delta_{umb}(Xe_1F_{4e}) + \delta_{umb}(Xe_1'F_{4e}') + \nu(Xe_1F_3) + \nu(Xe_1'F_3')$
	308(2)[18]	312(1)[92]	A", $\delta_{umb}(Xe_1F_{4e}) - \delta_{umb}(Xe_1'F_{4e}')$
306(3)	313(4)[11]	299(6)[19]	A', $\delta(F_1OsF_1') + \delta(F_2OsO_2)$
	300(<1)[26]	276(<1)[118]	A', $\nu(Xe_1F_3) - \nu(Xe_1'F_3) + \rho_t(O_1OsO_1') + \rho_t(F_1OsF_1')$
	284(2)[28]	257(1)[7]	A', $\rho_w(F_3Xe_1F_7) + \rho_w(F_3Xe_1'F_7') + \delta_r(F_1OsF_1')$
269(2)	254(1)[7]	256(4)[13]	A', $\delta(F_5Xe_1F_8) + \delta(F_6Xe_1F_7) + \delta(F_5'Xe_1'F_8') + \delta(F_6'Xe_1'F_7') + \delta(Xe_1F_3Xe_1')$
242(1)	265(2)[46]	251(4)[9]	A", $[(\delta(F_5Xe_1F_8) + \delta(F_6Xe_1F_7)] - [\delta(F_5'Xe_1'F_8') + \delta(F_6'Xe_1'F_7')] + \rho_w(F_1OsF_2)$
	239(<0.1)[<1]	241(<1)[9]	A", $Xe_2F_{11}^+$ def.

	237(2)[1]	237(1)[2]	A', $\delta(F_1OsF_1') - \delta(O_2OsF_2) + \rho_t(F_5Xe_1F_6) + \rho_w(F_5'Xe_1'F_6') + \delta(Xe_1F_3Xe_1')$
	224(1)[<1]	224(1)[16]	A', $\delta(O_2OsF_2) - \delta(F_1OsF_1') + \delta(F_6Xe_1F_7) + \delta(F_6'Xe_1'F_7') + \delta(Xe_1F_3Xe_1')$
	212(<0.1)[2]	216(<1)[7]	A", $Xe_2F_{11}^+$ def.
203(1)	205(<1)[1]	202(1)[15]	A", $[Xe_2F_{11}][OsO_3F_3]$ def.
	196(1)[3]	197(<0.1)[<1]	A', $[\delta(F_5Xe_1F_6) + \delta(F_5'Xe_1'F_6')] - [\delta(F_7Xe_1F_8) + \delta(F_7'Xe_1'F_8')] + [\rho_w(F_3Xe_1F_4) + \rho_w(F_3Xe_1'F_4')]$
	176(<1)[1]	194(<1)[<0.1]	A", $[\rho_w(F_4Xe_1F_6) + \rho_t(F_5Xe_1F_7)] - [\rho_w(F_4'Xe_1'F_6') + \rho_t(F_5'Xe_1'F_7')]$
	153(<1)[<1]	171(<0.1)[<1]	A", $[Xe_2F_{11}][OsO_3F_3]$ def.
167(1)	153(2)[1]	170(<1)[1]	A', $\rho_w(F_6Xe_1F_8) - \rho_w(F_6'Xe_1'F_8') + \delta(F_3Xe_1F_7) - \delta(F_3Xe_1'F_7')$
	167(1)[1]	147(2)[1]	A', $Xe_2F_{11}^+$ def.
135(1)	133(<1)[1]	134(1)[12]	A', $[Xe_2F_{11}][OsO_3F_3]$ breathing
	124(<1)[4]	115(1)[5]	
110(4)	124(1)[1]	100(1)[1]	
	104(<1)[<1]	97(1)[<0.1]	
	111(<1)[<0.1]	91(1)[1]	
	112(<1)[<0.1]	73(<1)[1]	
	89(<1)[<1]	66(<1)[<1]	$[Xe_2F_{11}][OsO_3F_3]$ def.
	45(<0.1)[<0.1]	60(<1)[<1]	
	25(<1)[<0.1]	44(<0.1)[<1]	
	96(<1)[<1]	34(<0.1)[<0.1]	
	77(1)[<0.1]	30(1)[<1]	
	63(<0.1)[<0.1]	15(<0.1)[<0.1]	

[a] The Raman spectrum was recorded on a microcrystalline sample in a FEP sample tube at –150 °C using 1064-nm excitation. Experimental Raman intensities are given in parentheses and are relative intensities with the most intense band given as 100. The abbreviations denote shoulder (sh). A band was also observed at 523(6) cm^{-1} but was not assigned. [b] Values in parentheses denote calculated Raman intensities ($Å^4$ u^{-1}) and values in square brackets denote calculated infrared intensities (km mol^{-1}). [c] SVWN/SDDall(-PP). [d] B3LYP/Stuttgart (Os) aug-cc-pVTZ(-PP) (Xe, O, F) [e] Assignments are for the energy-minimized geometry calculated at the B3LYP level of theory. See Figure 8.8c for the atom labeling scheme. The symbols denote stretch (ν), bend (δ), twist (ρ_t), rock (ρ_r), wag (ρ_w), umbrella (δ_{umb}), and F_5, F_6, F_7, F_8 (F_{4e}). The abbreviation, def., denotes a deformation mode. [f] The band overlaps with a FEP sample tube band, the intensity is not corrected.

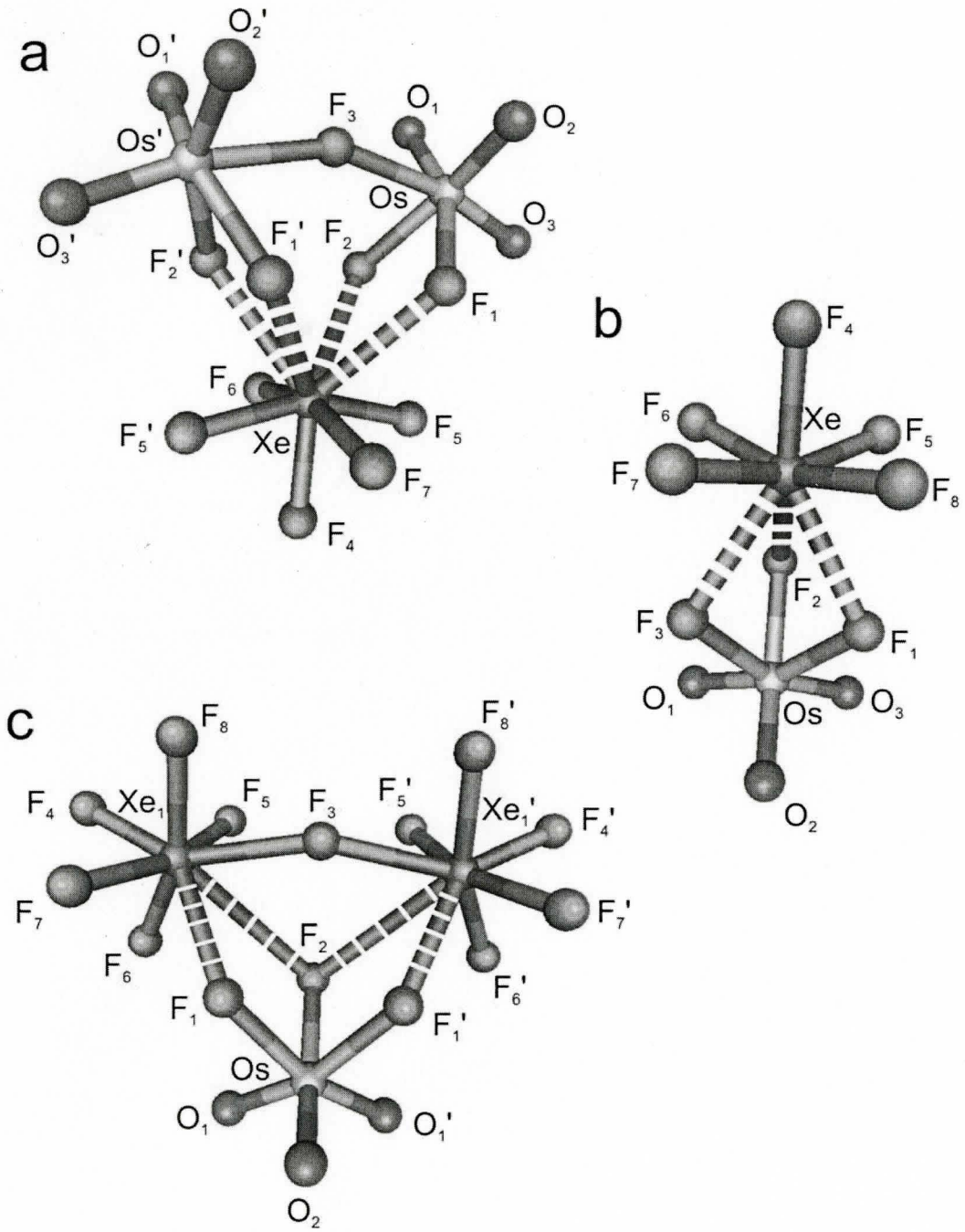

Figure 8.8. Calculated gas-phase geometries at the B3LYP level of theory for (a) $[XeF_5][\mu\text{-}F(OsO_3F_2)_2]$ (C_{2v}), (b) $[XeF_5][OsO_3F_3]$ (C_s), and (c) $[Xe_2F_{11}][OsO_3F_3]$ (C_s).

salt, namely, 933/936 and 422/426 cm^{-1}.

All vibrational modes of $[XeF_5][OsO_3F_3]$ (19A' + 14A") are predicted to be both infrared- and Raman-active under C_s symmetry. Correlation of the gas-phase ion-pair symmetry of $[XeF_5][OsO_3F_3]$ (C_s) to the crystal site symmetry (C_1) results in lowering of the A' and A" symmetries to A symmetry, and correlation of the site symmetry to the unit cell symmetry (C_{4h} with $Z = 4$) results in equal apportioning of the vibrational modes among the Raman-active A_g, B_g, and E_g symmetries and infrared-active A_u, B_u, and E_u symmetries (Table F3). Therefore, each Raman band is predicted to be factor-group split into A_g, B_g, and E_g components. These splittings are only manifested for the bands at 951/955, 946/948, 652/654, 615/617, and 386/390 cm^{-1}, with the third component remaining unresolved.

The mode descriptions provided in Tables 8.4-8.6 show that the cation and anion modes are, for the most part, weakly coupled within their respective ion pairs, with the low-frequency deformation modes displaying the greatest degree of coupling.

8.2.3.1 $OsO_3F_3^-$ and μ-$F(OsO_3F_2)_2^-$.

The vibrational modes of $OsO_3F_3^-$ in $[N(CH_3)_4][OsO_3F_3]$ have been previously assigned under C_{3v} symmetry, consistent with a weakly ion-paired anion.[23] The present assignments for $OsO_3F_3^-$ in the XeF_5^+ and $Xe_2F_{11}^+$ salts are in overall good agreement with the previous assignments, however, strong cation-anion fluorine bridge contacts result in significant vibrational coupling between the anion and the cation modes. These differences are the main focus of the ensuing discussion.

The Os–O stretching frequencies of $[XeF_5][\mu\text{-}F(OsO_3F_2)_2]$ (933–957 cm^{-1}), $[XeF_5][OsO_3F_3]$ (940–955 cm^{-1}), and $[Xe_2F_{11}][OsO_3F_3]$ (933–945 cm^{-1}) are shifted to higher frequencies when compared with those of the $OsO_3F_3^-$ anion in $[M][OsO_3F_3]$ (M = $N(CH_3)_4^+$ [908–920 cm^{-1}];[23] NO^+ [920–934 cm^{-1}];[23] Cs^+ [915–932 cm^{-1}];[24] Rb^+ [918–928 cm^{-1}];[24] K^+ [916–932 cm^{-1}];[24] and Na^+ [920–935 cm^{-1}][24]). The high-frequency shifts are in accordance with the presence of several short cation-anion contacts that withdraw negative charge from the anion, leading to more covalent Os–O bonds than in the $N(CH_3)_4^+$, NO^+, and the alkali metal salts. The Os–O stretching modes of $[XeF_5][OsO_3F_3]$ are shifted to somewhat higher frequencies than those of $[Xe_2F_{11}][OsO_3F_3]$ because secondary bonding interactions with the smaller XeF_5^+ cation are stronger than with the more weakly Lewis acidic $Xe_2F_{11}^+$ cation (see Section 8.2.2). As expected, the Os–O stretching region of $\mu\text{-}F(OsO_3F_2)_2^-$ is more complex than that of $OsO_3F_3^-$ because of vibrational coupling between the two OsO_3F_3-units. The frequencies of $\mu\text{-}F(OsO_3F_2)_2^-$ are in better agreement with those of their counterparts in the neutral species $(OsO_3F_2)_\infty$ (934–957 cm^{-1}),[14, 17, 18] $(OsO_3F_2)_2$ (937–955 cm^{-1}),[18] and $(OsO_3F_2)_2{\cdot}2XeOF_4$ (940–962 cm^{-1}),[18] than with those of $OsO_3F_3^-$ (Tables 8.5 and 8.6) owing to greater dispersion of negative charge in $\mu\text{-}F(OsO_3F_2)_2^-$.

The frequency ranges associated with the terminal Os–F stretching modes of $[XeF_5][\mu\text{-}F(OsO_3F_2)_2]$ (480–646 cm^{-1}), $[XeF_5][OsO_3F_3]$ (447–585 cm^{-1}), and $[Xe_2F_{11}][OsO_3F_3]$ (422–591 cm^{-1}) salts are similar to the Os–F stretching frequencies of the $OsO_3F_3^-$ anion in its $[M][OsO_3F_3]$ salts (M = $N(CH_3)_4^+$ [504, 573 cm^{-1}];[23] NO^+ [555 cm^{-1}];[23] Cs^+ [482, 565 cm^{-1}];[24] Rb^+ [490, 568 cm^{-1}];[24] K^+ [478, 490, 570 cm^{-1}];[24] Na^+

[460, 490, 580 cm^{-1}][24]), and occur at lower frequencies than those of the neutral species, $(OsO_3F_2)_\infty$ [596, 610 cm^{-1}] and $(OsO_3F_2)_2$ [604 cm^{-1}].[18] The 646 ($[XeF_5][\mu\text{-}F(OsO_3F_2)_2]$) and 591 ($[Xe_2F_{11}][OsO_3F_3]$) cm^{-1} bands involve coupled terminal Os–F and Xe–F stretches which result in shifts to higher frequency when compared with the pure terminal Os–F stretching frequencies of $[XeF_5][\mu\text{-}F(OsO_3F_2)_2]$ and $[Xe_2F_{11}][OsO_3F_3]$.

The symmetric Os–F stretches of the terminal OsF_2 groups of $[XeF_5][\mu\text{-}F(OsO_3F_2)_2]$ (646 cm^{-1}) are in-phase coupled with the axial Xe–F stretch which is shifted to significantly higher frequency than the symmetric Os–F stretch of $[XeF_5][OsO_3F_3]$ (585 cm^{-1}) and $[Xe_2F_{11}][OsO_3F_3]$ (591 cm^{-1}). The in-phase terminal Os–F stretch of $[Xe_2F_{11}][OsO_3F_3]$ is weakly coupled to all of the terminal Xe–F stretches of the $Xe_2F_{11}^+$ cation whereas the symmetric Os–F stretch of the OsF_3 moiety of $[XeF_5][OsO_3F_3]$ is not significantly coupled to any other mode, and is in good agreement with the symmetric terminal Os–F stretching modes of $[N(CH_3)_4][OsO_3F_3]$ (573 cm^{-1}),[23] $(OsO_3F_2)_\infty$ (596 cm^{-1}),[18] and $(OsO_3F_2)_2$ (604 cm^{-1}).[18]

The asymmetric fluorine bridge stretching mode, $\nu(OsF_3) - \nu(Os'F_3)$ (441 cm^{-1}), of the $\mu\text{-}F(OsO_3F_2)_2^-$ anion is not significantly coupled to any other mode and is comparable to the two asymmetric fluorine bridge stretching modes of $(OsO_3F_2)_\infty$ (404, 413 cm^{-1}).[18] Upon anion formation, a shift to lower frequency relative to those of $(OsO_3F_2)_\infty$ would be expected for this mode, however, this is not observed and can be attributed to significant withdrawal of electron density from F_1 and F_2 by the XeF_5^+ cation which strengthens the Os---F bridge bonds. In contrast, the symmetric $\nu(OsF_3) + \nu(Os'F_3)$ stretch is in-phase coupled to the $\rho_w(F_5'XeF_5) + \rho_w(F_6XeF_7)$ bending mode (313 [SVWN]

and 320 [B3LYP] cm^{-1}) and is out-of-phase coupled to the $\delta_{umb}(XeF_1F_2F_1'F_2')$ + $\delta(F_5XeF_5')$ (337 [SVWN], 337 [B3LYP] cm^{-1}) bending mode of XeF_5^+. Only the in-phase coupled mode was observed at 315 cm^{-1}. The $\nu(OsF_3)$ + $\nu(Os'F_3)$ stretch is also in-phase coupled to the $\delta(O_1OsO_2)$ + $\delta(O_1'Os'O_2')$ mode of μ-$F(OsO_3F_2)_2^-$ (342 cm^{-1}). These modes are shifted to lower frequency than the pure $\nu(OsF_3)$ – $\nu(Os'F_3)$ mode as a consequence of coupling with lower frequency OOsO deformation modes.

The asymmetric $\nu(OsF_1)$ + $\nu(OsF_2)$ – $\nu(OsF_3)$ modes of $[XeF_5][OsO_3F_3]$ (457 cm^{-1}) and $[Xe_2F_{11}][OsO_3F_3]$ (448 cm^{-1}) have similar frequencies and are not significantly coupled to other vibrational modes. The $\nu(OsF_1)$ – $\nu(OsF_2)$ stretching mode of $[XeF_5][OsO_3F_3]$ (447 cm^{-1}) also is not coupled to any other mode and occurs at higher frequency than the $\nu(OsF_1)$ – $\nu(OsF_1')$ + $\rho_r(O_1OsO_1')$ + $\delta(O_2OsO_1')$ mode of $[Xe_2F_{11}][OsO_3F_3]$ (426/422 cm^{-1}) as a result of coupling with lower frequency OOsO and FXeF bending modes.

8.2.3.2. XeF_5^+

Because vibrational assignments for the XeF_5^+ cation under C_{4v} symmetry have been previously reported for other salts, e.g., AsF_6^-,[65, 78, 251] AuF_6^-,[65] BF_4^-,[65, 78] GaF_4^-,[72] NiF_6^{2-},[88] PdF_6^{2-},[65] PtF_6^-,[65] RuF_6^-,[65] and are in good agreement with the present values for the μ-$F(OsO_3F_2)_2^-$ (C_{2v} ion-pair symmetry, Table 8.4) and $OsO_3F_3^-$ (C_s ion-pair symmetry, Table 8.5) salts, no detailed discussion of their vibrational assignments is provided. It is noteworthy that the bands at 280 and 380 cm^{-1} in the Raman spectrum of $[XeF_5][OsO_3F_3]$ are associated with the secondary bonding interactions between the cation and the anion,

and are assigned to the coupled $\delta(F_1OsF_2) + \delta(F_3OsO_3) + \nu(Xe\cdots F_3)$ and the $\nu(Xe\cdots F_1) + \nu(Xe\cdots F_2) + \nu(Xe\cdots F_3)$ modes, respectively.

8.2.3.3. $Xe_2F_{11}^+$

The vibrational modes of $Xe_2F_{11}^+$ have not been assigned in detail in prior vibrational studies, e.g., the AsF_6^-,[65] PF_6^-,[65] PbF_6^{2-},[90] PdF_6^{2-},[90] SnF_6^-,[90] and VF_6^- [98] salts. The present assignments provide a more detailed description of the vibrational modes of $Xe_2F_{11}^+$ under C_s symmetry (Table 8.6).

Among the most noteworthy features of the $Xe_2F_{11}^+$ Raman spectrum of $[Xe_2F_{11}][OsO_3F_3]$ are the Xe–F stretching frequencies which occur between 580 and 656 cm^{-1}, and are comparable with other $Xe_2F_{11}^+$ salts. The band at 591 cm^{-1} is assigned to extensively coupled Xe–F and Os–F stretches involving the three facial Os–F bond stretches and the ten primary Xe–F bond stretches of the XeF_5-units (Table 8.6). The most intense Xe–F stretching band at 656 cm^{-1} is assigned to the $[\nu(Xe_1F_4) + \nu(Xe_1F_5) + \nu(Xe_1F_6)] + [\nu(Xe_1'F_4') + \nu(Xe_1'F_5') + \nu(Xe_1'F_6')]$ stretching mode and is in good agreement with the most intense cation band of other $Xe_2F_{11}^+$ salts, e.g., AsF_6^- (663 cm^{-1}),[65] PF_6^- (666 cm^{-1}),[65] PbF_6^{2-} (650 cm^{-1}),[90] PdF_6^{2-} (651 cm^{-1}),[90] SnF_6^{2-} (657 cm^{-1}),[90] and VF_6^- (655 cm^{-1}).[98] The Xe_1---F_3---Xe_1' bridge stretches are predicted to be weak and to occur at 370, 335, and 300 (SVWN) and 329, 322, and 276 (B3LYP) cm^{-1}, but could not be observed. In the present case, the symmetric $\nu(Xe_1F_3) + \nu(Xe_1'F_3)$ bridge stretch is in-phase coupled to the $\delta_{umb}(XeF_{4e}) + \delta_{umb}(Xe_1'F_{4e}')$ bending mode, whereas the asymmetric $\nu(Xe_1F_3) - \nu(Xe_1'F_3)$ bridge stretch is in-phase coupled to both the

$\rho_t(F_1OsF_1') + \rho_w(F_2OsO_2)$ and $\rho_t(O_1OsO_1') - \rho_t(F_1OsF_1')$ bending modes. The three modes are predicted to occur between 300-370 (SVWN) and 276–329 (B3LYP) cm^{-1}.

8.2.4. Computational Results.

The structures of $[XeF_5][\mu\text{-}F(OsO_3F_2)_2]$ (C_{2v}), $[XeF_5][OsO_3F_3]$ (C_s), $[Xe_2F_{11}][OsO_3F_3]$ (C_s), XeF_5^+ (C_{4v}), $Xe_2F_{11}^+$ (C_s), $OsO_3F_3^-$ (C_{3v}), and $\mu\text{-}F(OsO_3F_2)_2^-$ (C_2) (Figures 8.8, F4 and F5) were optimized using SVWN and B3LYP methods under the specified symmetries and resulted in stationary points with all frequencies real. The geometrical parameters and vibrational frequencies were benchmarked, as previously described, using *cis*-OsO_2F_4 and $XeOF_4$.[18]

8.2.4.1. Calculated Geometries.

The calculated ion-pair geometries of $[XeF_5][\mu\text{-}F(OsO_3F_2)_2]$ (Table 8.2), $[XeF_5][OsO_3F_3]$, and $[Xe_2F_{11}][OsO_3F_3]$ (Table 8.3) are in good agreement with the experimental geometries, with slightly better agreement for the Xe–F bond lengths at the B3LYP level, and for the Os–F and Os–O bond lengths of the $[XeF_5][OsO_3F_3]$ and $[Xe_2F_{11}][OsO_3F_3]$ salts at the SVWN level. The calculations confirm that the gas-phase ion pairs are stable entities and all trends in their crystal structures are reproduced by the calculated ion-pair geometries, with the largest discrepancies occurring for the Xe···F contact distances. In all cases, the SVWN calculations predict slightly shorter secondary bonding interactions than the B3LYP calculations (Tables 8.2 and 8.3).

The calculated geometries of the $[XeF_5][\mu\text{-}F(OsO_3F_2)_2]$ and $[XeF_5][OsO_3F_3]$ ion pairs are in better agreement with their experimental geometries than $[Xe_2F_{11}][OsO_3F_3]$, underscoring that both ion pairs are well isolated in their crystal structures, showing no

inter-ion pair contacts. The experimental Os---F_3---Os' bridge bond lengths of $[XeF_5][\mu\text{-}F(OsO_3F_2)_2]$ (2.1179(5) Å) are particularly well modeled by both the B3LYP (2.147 Å) and SVWN (2.115 Å) structures. The Os---F_3---Os' bridge bond angle (155.5(1)°) is also very well reproduced at the B3LYP (155.4°) and SVWN (150.9°) levels. For this structure, the Xe···F contact distances calculated at the B3LYP (2.643 and 2.644 Å) level better reproduce the experimental values (2.622(1) and 2.663(1) Å) than those calculated at the SVWN level (2.461 and 2.461 Å).

The calculated structure of the $[Xe_2F_{11}][OsO_3F_3]$ ion pair does not take into account the additional Xe···O inter-ion pair contact (vide supra) and consequently does not reproduce the experimental ion-pair geometry as well. The tri-coordination of F(2) is reproduced, but the $Xe_1\cdots F_2$ and $Xe_2\cdots F_2$ contact distances at the B3LYP level (3.197 and 3.197 Å) are significantly longer than the SVWN (2.613 and 2.613 Å) and the experimental (2.800(2) Å) values.

The geometries of the isolated gas-phase cations and anions have also been calculated in order to assess the effects of ion pairing on the primary bond lengths and angles. The fluorine atoms of the ion-paired $OsO_3F_3^-$ anions strongly coordinate to xenon, elongating the Os–F bonds (av. 2.022, SVWN; 2.031, B3LYP Å) when compared with those of the gas-phase $OsO_3F_3^-$ anion (1.950, SVWN; 1.961, B3LYP Å) (Table F5). As a result, the Os–O bond lengths of the ion pair are significantly shorter (av. 1.711, SVWN; 1.689, B3LYP Å) than those of the free anion (1.737, SVWN; 1.711, B3LYP Å). The same trends are observed for $\mu\text{-}F(OsO_3F_2)_2^-$ (Table 8.2), i.e., the Os–O bond lengths are shortened and the Os–$F_{1,2}$ bond lengths are elongated upon coordination to XeF_5^+. The

Os---F---Os bond angle of the free μ-$F(OsO_3F_2)_2^-$ anion is more closed (143.0°, SVWN; 140.7°, B3LYP) relative to that of the gas-phase ion pair (150.9°, SVWN; 155.4°, B3LYP) because chelation of the XeF_5^+ cation through xenon contacts with the fluorine ligands of the anion results in compression of this angle. In contrast, the Xe---F---Xe bond angle of the free $Xe_2F_{11}^+$ cation is more open (141.8°, SVWN; 171.2°, B3LYP) than in $[Xe_2F_{11}][OsO_3F_3]$ (129.3°, SVWN; 152.2°, B3LYP), which is again attributed to coordination of the anion fluorine ligands to xenon, leading to compression of the Xe---F---Xe angle in the chelate relative to that of the free $Xe_2F_{11}^+$ cation. The Xe–F bond lengths of the free XeF_5^+ (Table 8.2) and $Xe_2F_{11}^+$ (Table F6) cations are slightly shorter than in their respective ion pairs as a consequence of the extra electron density donated to the xenon cation by the anion, resulting in longer, more polar primary Xe–F bonds in the ion pairs (see below for anion-cation charge drift values).

8.2.4.2. Charges, Valencies, and Bond Orders.

The Natural Bond Orbital (NBO) analyses were carried out for the optimized B3LYP [SVWN] gas-phase geometries of $[XeF_5][\mu\text{-}F(OsO_3F_2)_2]$, $[XeF_5][OsO_3F_3]$, $[Xe_2F_{11}][OsO_3F_3]$ (Table 8.7), XeF_5^+, $Xe_2F_{11}^+$ (Table F7), $OsO_3F_3^-$, and μ-$F(OsO_3F_2)_2^-$ (Table F8).

The NPA (Natural Population Analysis) gave positive charges of 2.19 [1.88], 2.17 [1.87], and 2.18 [1.87] for osmium and 3.29 [3.05], 3.28 [3.04], and 3.29 [3.06] for xenon in the $[XeF_5][\mu\text{-}F(OsO_3F_2)_2]$, $[XeF_5][OsO_3F_3]$, and $[Xe_2F_{11}][OsO_3F_3]$ ion pairs, respectively. The negative charges of the light atoms indicate that the bonding in the ion pairs is polar covalent. The average charges of the oxygen ligands are less negative than

Table 8.7. Natural Bond Orbital (NBO) Valencies, Bond Orders and NPA Charges for $[XeF_5][\mu\text{-}F(OsO_3F_2)_2]$, $[XeF_5][OsO_3F_3]$, and $[Xe_2F_{11}][OsO_3F_3]$

Atom	$[XeF_5][\mu\text{-}F(OsO_3F_2)_2]$[a]		$[XeF_5][OsO_3F_3]$[b]		$[Xe_2F_{11}][OsO_3F_3]$[c]	
	SVWN[d]	B3LYP[e]	SVWN[d]	B3LYP[e]	SVWN[d]	B3LYP[e]
	NPA charges [valencies]					
Os	1.880 [3.554]	2.187 [3.527]	1.866 [3.585]	2.174 [3.559]	1.867 [3.549]	2.178 [3.566]
O_1	–0.312 [0.914]	–0.372 [0.909]	–0.310 [0.916]	–0.372 [0.913]	–0.303 [0.922]	–0.373 [0.913]
O_2	–0.312 [0.914]	–0.372 [0.909]	–0.313 [0.916]	–0.375 [0.910]	–0.304 [0.917]	–0.376 [0.904]
O_3	–0.303 [0.918]	–0.369 [0.916]	–0.310 [0.916]	–0.372 [0.913]		
F_1	–0.496 [0.513]	–0.581 [0.432]	–0.519 [0.499]	–0.610 [0.427]	–0.524 [0.502]	–0.628 [0.423]
F_2	–0.496 [0.513]	–0.581 [0.432]	–0.504 [0.506]	–0.582 [0.438]	–0.557 [0.526]	–0.571 [0.442]
F_3	–0.546 [0.561]	–0.626 [0.435]	–0.519 [0.499]	–0.610 [0.427]	–0.600 [0.389]	–0.697 [0.340]
Xe	3.054 [2.723]	3.288 [2.704]	3.041 [2.649]	3.280 [2.712]	3.055 [2.639]	3.290 [2.694]
F_4	–0.469 [0.369]	–0.472 [0.400]	–0.469 [0.383]	–0.476 [0.409]	–0.470 [0.379]	–0.480 [0.412]
F_5	–0.493 [0.398]	–0.504 [0.433]	–0.489 [0.400]	–0.513 [0.438]	–0.484 [0.404]	–0.517 [0.421]
F_6	–0.486 [0.403]	–0.502 [0.440]	–0.492 [0.398]	–0.515 [0.429]	–0.499 [0.385]	–0.522 [0.433]
F_7	–0.486 [0.403]	–0.502 [0.440]	–0.492 [0.398]	–0.515 [0.429]	–0.488 [0.406]	–0.512 [0.434]
F_8	–0.493 [0.398]	–0.504 [0.433]	–0.489 [0.400]	–0.513 [0.438]	–0.490 [0.397]	–0.521 [0.429]
			bond orders			
Os–O_1	0.855	0.872	0.861	0.876	0.862	0.877
Os–O_2	0.855	0.872	0.860	0.873	0.858	0.868
Os–O_3	0.863	0.877	0.861	0.876		
Os–F_1	0.366	0.349	0.325	0.297	0.330	0.288
Os–F_2	0.366	0.349	0.351	0.344	0.325	0.380
Os–F_3	0.250	0.214	0.325	0.297		
Xe···F_1	0.127	0.078	0.159	0.125	0.154	0.141
Xe···F_2	0.127	0.078	0.141	0.088	0.096	0.022
Xe···F_3[f]			0.159	0.125	0.203	0.182
Xe–F_4	0.453	0.501	0.457	0.504	0.456	0.500
Xe–F_5	0.437	0.474	0.433	0.469	0.439	0.465
Xe–F_6	0.441	0.478	0.412	0.469	0.421	0.459
Xe–F_7	0.441	0.478	0.412	0.469	0.439	0.466
Xe–F_8	0.437	0.474	0.433	0.469	0.431	0.462

[a] See Figure 8.8a for the atom labeling scheme. [b] See Figure 8.8b for the atom labeling scheme. [c] See Figure 8.8c for the atom labeling scheme. [d] The SDDall(-PP) basis set augmented for F, O, an,d Xe with two d-type polarization functions, was used. [e] The Stuttgart basis set was used for Os with the f functional. The aug-cc-pVTZ(-PP) basis sets were used for all other atoms. [f] The atom labeling scheme refers to the structure of $[XeF_5][\mu\text{-}F(OsO_3F_2)]$ and $[XeF_5][OsO_3F_3]$. In the case of $[Xe_2F_{11}][OsO_3F_3]$ the Xe···F_3 notation should read as Xe---F_3.

the average charges of the fluorine ligands in both the anions and cations, which is consistent with significant charge transfer from the filled oxygen p orbitals into the empty d orbitals of osmium. Overall, the fluorine ligands of the anions are more negative than those of the cations, which is consistent with the net charges of the cation and anion.

The Xe---F_3 bridge bond orders of $[Xe_2F_{11}][OsO_3F_3]$ (0.18 [0.20]) and the Os---F_3 bond orders of $[XeF_5][\mu\text{-}F(OsO_3F_2)_2]$ (0.21 [0.25]) are significantly less than those of the terminal Xe–F (av. 0.46-0.50 [0.41-0.46]) and Os–F (av. 0.29-0.38 [0.32-0.37]) bonds of either salt because the bridging fluorine atoms are equally shared between the two electropositive heavy atoms. Although the Xe---F_3 and Os---F_3 bridge bond orders are similar, the average terminal Xe–F bond orders of XeF_5^+ and $Xe_2F_{11}^+$ are more than double the bridging Xe---F_3 bond order in $Xe_2F_{11}^+$. In contrast, the average terminal Os–F bond orders of $OsO_3F_3^-$ and $\mu\text{-}F(OsO_3F_2)_2^-$ are less than twice the Os---F_3 bridge bond order. The difference is attributable to significantly higher positive charges on the xenon atoms than on the osmium atoms (Table 8.7), which result in lower negative charges on the fluorine atoms of the xenon cations and more covalent Xe–F bonds than for fluorine bonded to osmium.

The Os–O bond orders of both ion pairs are similar (0.87–0.88 [0.86–0.86]) but slightly greater than those of the free anions (0.85–86 [0.81–0.83]). The Os–F bond orders (0.29–0.38 [0.32–0.37]) are also similar but less than those of the free anions (0.38–0.41 [0.39–0.42]). Both features result from significant fluorine bridge interactions between the fluorine ligands of osmium and xenon atoms of the ion pairs. The somewhat higher Os–O bond orders compensate for the negative charge drift onto the cation via the

secondary bonding interactions. The calculated negative charge drifts from anion to cation within the ion pair reflect this trend: $[XeF_5][\mu\text{-}F(OsO_3F_2)_2]$, 0.19 [0.37]; $[XeF_5][OsO_3F_3]$, 0.25 [0.39]; $[Xe_2F_{11}][OsO_3F_3]$, 0.23 [0.37].

Other than the Xe---F_3 bridge bond orders of $Xe_2F_{11}^+$, the secondary Xe···F bond orders range from 0.02 [0.10] for the F_2 atom of $[Xe_2F_{11}][OsO_3F_3]$ to 0.12 [0.16] for the F_1 and F_3 atoms of $[XeF_5][OsO_3F_3]$. The lower Xe···F_2 bond order results from the interaction of F_2 with both xenon atoms of the $Xe_2F_{11}^+$ cation. The higher Xe···$F_{1,3}$ bond orders of $[XeF_5][OsO_3F_3]$ when compared with the Xe···$F_{1,2}$ bond orders of $[XeF_5][\mu\text{-}F(OsO_3F_2)_2]$ correlate with the higher positive charge on xenon that results from only eight primary and secondary contacts to xenon instead of nine as in the remaining two ion pairs (see Section 8.2.4.1).

The axial and equatorial Xe–F bond orders of XeF_5^+ and $Xe_2F_{11}^+$ are only slightly altered upon coordination of either cation to $OsO_3F_3^-$. The equatorial Xe–F bond orders for all three ion pairs are similar (0.47–0.48 [0.41–0.44]) and are only slightly less than those of free XeF_5^+ and $Xe_2F_{11}^+$ (0.48–0.49 [0.48]). The axial Xe–F bonds of the ion pairs have significantly higher bond orders (0.50 [0.45–0.46]) than the equatorial Xe–F bonds. The axial Xe–F bond orders of the ion pairs are similar to those of the free cations calculated at the B3LYP level (0.51–0.53), but at the SVWN level they are somewhat higher for the free cations (0.50–0.52). The lower Xe–F bond orders for all of the ion pairs relative to those of free XeF_5^+ and $Xe_2F_{11}^+$ are in accord with the calculated anion-cation charge drifts (vide supra).

8.3. Conclusions

The $[XeF_5][\mu\text{-}F(OsO_3F_2)_2]$, $[XeF_5][OsO_3F_3]$, and $[Xe_2F_{11}][OsO_3F_3]$ salts have been synthesized by the reactions of stoichiometric mixtures of XeF_6 and $(OsO_3F_2)_\infty$. All three salts are room-temperature stable but dissociate back to the starting materials after prolonged heating at 50 °C. The salts provide the only examples of noble-gas cations that are stabilized by metal oxide fluoride anions and the first example of a salt of the fluorine-bridged $\mu\text{-}F(OsO_3F_2)_2^-$ anion. All three salts exist as discrete ion pairs in which the fluorine ligands of the osmium oxide fluoride anions mainly interact by means of secondary bonding interactions with the xenon atoms of the cations. Ion-pairing results in nine-coordination at the xenon atoms of $[XeF_5][\mu\text{-}F(OsO_3F_2)_2]$ and $[Xe_2F_{11}][OsO_3F_3]$ and eight-coordination at the xenon atom of $[XeF_5][OsO_3F_3]$. The primary coordination spheres of the osmium atoms of $\mu\text{-}F(OsO_3F_2)_2^-$ and $OsO_3F_3^-$ are pseudo-octahedral with facial arrangements of oxygen and fluorine ligands. The $OsO_3F_3^-$ anions have geometrical parameters that are closer to those of neutral trioxo Os(VIII) species, indicating that the XeF_5^+ and $Xe_2F_{11}^+$ cations withdraw significant electron density from the anion by means of their secondary bonding interactions. Quantum-chemical calculations have been used to model the ion pairs and their component ions and provide energy-minimized geometries that are in very good agreement with the experimental structures. The Raman spectra of all three salts have been fully assigned based on the calculated vibrational modes.

CHAPTER 9

SYNTHESES AND STRUCTURES OF THE MOLECULAR ADDITION COMPOUNDS, $XeOF_4 \cdot NgF_2$ (Ng = Xe or Kr)

9.1. Introduction

The noble-gas difluorides, NgF_2, behave as fluoride ion donors towards strong fluoride ion acceptors such as AsF_5, SbF_5, and BiF_5 forming NgF^+ salts having short terminal Ng–F bonds.[110, 126, 252-256] In such cases, a fluoride ion of NgF_2 is essentially transferred to form the corresponding fluoro-anion conjugate base of the Lewis acid. A fluorine ligand of the anion, F_b, however, interacts with the NgF^+ cation by means of a long Ng---F_b fluorine bridge bond, forming an ion pair, e.g. $F–Kr^+---F–AsF_5^-$.[126]

Coordination of a weak to moderate strength, oxidatively resistant Lewis acid to a fluorine atom of XeF_2 occurs without "complete" fluoride ion transfer. A considerable number of metal cations fulfill this criterion, and their XeF_2 coordination complexes have been synthesized and structurally characterized, but there are no examples of metal cation coordination complexes with KrF_2. A recent review has outlined progress in this area[257] and recently the $[M(XeF_2)_5][PF_6]_2$ (M = Ca, Cd),[105] $[Pb_3(XeF_2)_{11}][PF_6]_6$,[120] $[M(XeF_2)_3][PF_6]_2$ (M = Sr, Pb),[120] $[Sr_3(XeF_2)_{10}][PF_6]_6$,[120] $[Ba(XeF_2)_5][AsF_6]_2$,[113] and $[Ba(XeF_2)_4][PF_6]_2$[117] complexes have been synthesized. In these instances, coordination of the XeF_2 ligand can either be terminal or bridging. Terminal XeF_2 ligands interact through only one fluorine atom resulting in lengthening of the bridge bond and contraction of the terminal bond. Bridging XeF_2 ligands occur as two types, symmetric or asymmetric. The symmetrically bridged structures resemble network structures and have

equivalent Xe–F bond lengths. Structures containing asymmetrically bridged XeF_2 also have single contacts to each fluorine atom of the XeF_2 molecule which are inequivalent and render the Xe–F bonds asymmetric.

Examples of XeF_2 coordinated to moderate strength Lewis acid transition metal oxide fluorides have also been reported. Adducts of XeF_2 with MOF_4 (M = Mo and W), $XeF_2 \cdot nMOF_4$ (n = 1–4) are known, and have been characterized by solution ^{19}F and ^{129}Xe NMR spectroscopy,[121, 122] and Raman spectroscopy.[122, 123] The M---F–Xe bridge bonds in these complexes have been shown to be non-labile by ^{19}F and ^{129}Xe NMR spectroscopy at low temperatures in BrF_5 and SO_2ClF solvents and it has been found that there is isomerization between oxygen- and fluorine-bridged XeF groups for $XeF_2 \cdot nWOF_4$ (n = 2, 3) to form W–O–XeF linkages in SO_2ClF. The only crystal structure that has been determined for this class of compounds is that of $WOF_4 \cdot XeF_2$, in which XeF_2 is fluorine bridged to tungsten.[258]

Examples are known in which XeF_2 coordinates to non-metal centers and are represented by $2XeF_2 \cdot [XeF_5][AsF_6]$, $XeF_2 \cdot [XeF_5][AsF_6]$, and $XeF_2 \cdot 2([XeF_5][AsF_6])$, where XeF_2 coordinates to the Xe(VI) atom of XeF_5^+.[79] The X-ray crystal structure has recently been reported for $[BrOF_2][AsF_6] \cdot 2XeF_2$[118] and $[BrOF_2][AsF_6] \cdot KrF_2$[124] which have also been structurally characterized by Raman spectroscopy. Both adducts contain XeF_2 molecules that are homoleptically coordinated to bromine(V) through fluorine.

The molecular addition compound, $XeOF_4 \cdot XeF_2$ has been previously synthesized and its Raman spectrum and X-ray powder pattern have been obtained.[75] The Raman spectrum was assigned as the sum of the XeF_2 and $XeOF_4$ component spectra. The

$XeOF_4 \cdot XeF_2$ compound was proposed to be isostructural with $IF_5 \cdot XeF_2$ because both IF_5 and $XeOF_4$ are square pyramidal with a lone pair occupying the open face of the square pyramid.[114]

In contrast, there are few examples of KrF_2 coordination complexes. The known adducts are formed with MOF_4 (M = Cr,[125] Mo,[123] and W[123]) transition metal centers which have been characterized by ^{19}F NMR and vibrational spectroscopy. The only crystal structures of KrF_2 adducts are those of $[Kr_2F_3][SbF_6]_2 \cdot KrF_2$[126] and $[BrOF_2][AsF_6] \cdot 2KrF_2$.[124] These adducts provide examples of terminally bridged KrF_2 molecules. Currently there are no examples of structures that contain bridged KrF_2 molecules.

The research presented in Chapter 8 details the fluoride ion donor properties of XeF_6 towards OsO_3F_2. Xenon hexafluoride is the strongest fluoride ion donor among the binary xenon fluorides, XeF_2, XeF_4, and XeF_6. If was also of interest to investigate the fluoride ion acceptor properties of OsO_3F_2 toward XeF_2; however, in both HF and $XeOF_4$ solvents no reaction was observed. Instead, the $XeF_2/XeOF_4$ system gave rise to a molecular addition compound $XeOF_4 \cdot XeF_2$. The present chapter details the syntheses and characterization by single-crystal X-ray diffraction and Raman spectroscopy of $XeOF_4 \cdot XeF_2$ and $XeOF_4 \cdot KrF_2$. Although the $XeOF_4 \cdot NgF_2$ compounds are molecular addition compounds, they will generally be referred to as adducts for simplicity. Quantum-chemical calculations have been used to aid in the assignments of the vibrational modes of the $XeOF_4 \cdot NgF_2$ adducts.

9.2 Results and Discussion

9.2.1. Syntheses and Crystal Growth of $XeOF_4 \cdot NgF_2$ (Ng = Xe or Kr).

The adduct, $XeOF_4 \cdot XeF_2$, was synthesized using the previously described procedure (eq 9.1).[75] Slow cooling of a solution of XeF_2 dissolved in $XeOF_4$ to –36 °C resulted in growth of colorless plates. A small amount of $XeOF_4$ solution froze on the

$$XeOF_4 + XeF_2 \xrightarrow[25\ ^\circ C]{XeOF_4} XeOF_4 \cdot XeF_2 \qquad (9.1)$$

crystals upon isolation and crystals suitable for single-crystal X-ray diffraction were isolated by mechanically separating them from the frozen $XeOF_4$.

Reaction of $XeOF_4$ with KrF_2 at low temperature (–20 °C) resulted in the formation of an adduct corresponding to $XeOF_4 \cdot nKrF_2$ (eq 9.2) where n is shown to be 1

$$XeOF_4 + nKrF_2 \xrightarrow[-20\ ^\circ C]{} XeOF_4 \cdot nKrF_2 \quad (n = 1, > 1) \qquad (9.2)$$

(see Section 9.2.3) or > 1 (see Section 9.2.4). Isolation of the adduct, however, was not possible because pumping at either –20 or –40 °C resulted in removal of both $XeOF_4$ and KrF_2. Colorless needles corresponding to $XeOF_4 \cdot KrF_2$ were grown by slow cooling of the solution to –41 °C. Crystals suitable for single-crystal X-ray diffraction were isolated by mechanically separating them from excess frozen $XeOF_4$ that encased the crystals.

Reaction of $XeOF_4$ with excess KrF_2 at –20 °C initially resulted in the formation of a mixture of phases that have not yet been conclusively identified (see Section 9.2.4). This mixture was warmed to –20 °C and the reaction was monitored by Raman spectroscopy over a period of 12 h until the spectrum remained unchanged and corresponded to a mixture of unreacted KrF_2 and $XeOF_4 \cdot nKrF_2$ where $n > 1$.

9.2.2. NMR Spectroscopy.

Table 9.1 lists the ^{19}F and ^{129}Xe NMR parameters of NgF_2 (Ng = Xe, Kr) dissolved in $XeOF_4$ solvent (–35 °C). In both cases, $XeOF_4$ was always in excess so that the XeF_2 solution had a concentration of ca. 0.234 mol L^{-1} while KrF_2 was ca. 0.328 mol L^{-1}. There is no evidence for a discrete interaction and both NgF_2 and $XeOF_4$ fail to show spin-spin couplings or significant chemical shift changes that correspond to coordination and are indicative of labile Xe(VI)---F–Ng(II) interactions in solution. The ^{19}F chemical shift of XeF_2 (–183.0 ppm) is similar to that of XeF_2 observed in BrF_5 at either 26 and –20 °C (–181.8 ppm)[196] and the ^{129}Xe chemical shift (–1606 ppm) is similar to that recorded in HF at 25 °C (–1592 ppm)[68] and is shifted to somewhat lower frequency than in BrF_5 solvent at –40 °C (–1708 ppm).[68] The $^1J(^{129}Xe\text{-}^{19}F)$ coupling constant of XeF_2 in $XeOF_4$ solvent (5630 Hz) is similar to that of XeF_2 in BrF_5 at 26, –20, and –40 °C (5616,[196] 5650,[196] and 5583 Hz,[68] respectively) and in HF at 25 °C (5652 Hz).[68] The ^{19}F chemical shift of KrF_2 in $XeOF_4$ solvent (64.4 ppm) is similar to the chemical shift observed for KrF_2 in BrF_5 solvent at –50 °C (67.9 ppm) and is intermediate with respect to those obtained in BrF_5 (77.7 ppm) and HF (55.6 ppm) solvents at 25 °C.[196]

The ^{19}F and ^{129}Xe chemical shifts and the $^1J(^{129}Xe\text{-}^{19}F)$ coupling constants of $XeOF_4$ in the XeF_2 (98.1 and 6.5 ppm, 1120 Hz, respectively) and KrF_2 (97.7 and 7.8 ppm, 1111 Hz, respectively) adducts are similar and are comparable to those of pure liquid $XeOF_4$ recorded at 24 °C (100.3 and 0.0 ppm, 1128 Hz, respectively).[259]

Table 9.1. NMR Chemical Shifts and Spin-Spin Coupling Constants for XeF_2 and KrF_2 Recorded in $XeOF_4$ Solvent at –35 °C

		Chemical Shifts, ppm		Coupling Constants, Hz
Solute	Species	$\delta(^{19}F)^a$	$\delta(^{129}Xe)^b$	$^1J(^{129}Xe\text{-}^{19}F)$
XeF_2	$XeOF_4$	98.1	6.5	1120
	XeF_2	–183.0	–1606	5630
KrF_2	$XeOF_4$	97.7	7.8	1111
	KrF_2	64.4		

[a] Resonances assigned to traces of XeF_4 [XeO_2F_2] {HF} impurities were observed for the XeF_2 mixture (–18.4 ppm ($^1J(^{19}F\text{-}^{129}Xe)$ = 3848 Hz), [101.1 ppm ($^1J(^{19}F\text{-}^{129}Xe)$ = 1180 Hz)], {–188.7 ppm}) and the KrF_2 mixture (–18.9 ppm ($^1J(^{19}F\text{-}^{129}Xe)$ = 3850 Hz) {–188.5 ppm ($^1J(^1H\text{-}^{19}F)$ = 536 Hz)}). [b] Resonances assigned to traces of XeF_4 [XeO_2F_2] impurities were observed for the XeF_2 mixture (287 ppm ($^1J(^{19}F\text{-}^{129}Xe)$ = 3848 Hz) [127 ppm ($^1J(^{19}F\text{-}^{129}Xe)$ = 1180 Hz)]) and the KrF_2 mixture (292 ppm ($^1J(^{19}F\text{-}^{129}Xe)$ = 3850 Hz)).

9.2.3. X-ray Crystal Structures of $XeOF_4 \cdot NgF_2$ (Ng = Xe or Kr).

Details of data collection parameters and other crystallographic information are provided in Table 9.2. Bond lengths and bond angles for $XeOF_4 \cdot NgF_2$ are listed in Tables 9.3 and 9.4, respectively. The unit cell parameters for $XeOF_4 \cdot XeF_2$ are in good agreement with those obtained from the X-ray powder diffraction study (a = 7.56(2), c = 11.36(3) Å, V = 647 Å^3, Z = 4, 20 °C).[75]

9.2.3.1. Packing and Intermolecular Contacts.

The $XeOF_4 \cdot XeF_2$ adduct crystallizes in the $I4/m$ space group. The structure of $XeOF_4 \cdot XeF_2$ consists of $XeOF_4$ and XeF_2 units that stack along the a- and b- axes but alternate along the c-axis. The Xe–O bonds of the $XeOF_4$ molecules alternate directions by 180° in columns along the a- and c-axes so that in the b,c-plane, either the Xe–O bonds or the xenon lone pairs of the $XeOF_4$ molecules face one another (Figure G1). The XeF_2 ligands pack along the a- and c-axes alternating their orientations by 180°. There are four XeF_2 molecules that have close contacts with the Xe atom of $XeOF_4$ (Figure 9.1a). In turn, each fluorine atom of the XeF_2 molecule has a close contact with the Xe atoms of two $XeOF_4$ molecules (Figure 9.1b). The X-ray crystal structure confirms that the adduct is isostructural with $IF_5 \cdot XeF_2$.[114] The Xe···F contact distances in $XeOF_4 \cdot XeF_2$ (3.239(4) Å) are comparable to the I···F contact distances in $IF_5 \cdot XeF_2$ (3.142(7) Å), but are somewhat less than the sums of their respective Xe (3.63 Å)/I (3.45 Å) and F van der Waals radii.[165] Symmetric coordination of four XeF_2 molecules results in the preservation of the local C_{4v} symmetry of the $XeOF_4$ molecule, whereas symmetric coordination of one XeF_2 molecule to four $XeOF_4$ molecules results in local C_i symmetry at XeF_2, thus retaining the

Table 9.2. Summary of Crystal Data and Refinement Results for $XeOF_4 \cdot XeF_2$ and $XeOF_4 \cdot KrF_2$

chem formula	$Xe_8O_4F_{24}$	$Xe_2Kr_2F_{12}O_2$
space group	*I*4/*m* (87)	$P\bar{1}$ (2)
a (Å)	7.502(1)	6.760(5)
b (Å)	7.502(1)	7.229(5)
c (Å)	11.193(4)	7.891(5)
α (deg)	90	96.501(5)
β (deg)	90	114.352(5)
γ (deg)	90	113.813(5)
V (Å^3)	630.0(6)	302.8(3)
molecules/unit cell	4	2
mol wt (g mol^{-1})	1570.40	690.20
calcd density (g cm^{-3})	4.139	3.785
T (°C)	–173	–173
μ (mm^{-1})	10.81	13.00
R_1[a]	0.0257	0.0289
wR_2[b]	0.0395	0.0700

[a] R_1 is defined as $\Sigma \| F_o | - | F_c \| / \Sigma | F_o |$ for $I > 2\sigma(I)$. [b] wR_2 is defined as $\{\Sigma[w(F_o^2\text{-}F_c^2)^2]/\Sigma w(F_o^2)^2\}^{1/2}$ for $I > 2\sigma(I)$.

Table 9.3. Experimental Bond Lengths and Angles in $XeOF_4 \cdot XeF_2$ and Calculated Bond Lengths and Angles in $2XeOF_4 \cdot XeF_2$ and $XeOF_4 \cdot 4XeF_2$

$XeOF_4 \cdot XeF_2$[a]		$2XeOF_4 \cdot XeF_2$[b]				$XeOF_4 \cdot 4XeF_2$[c]		
			calcd (C_{2v})[d]			calcd (C_4)[d]		
exptl			SVWN	B3LYP	PBE1PBE	SVWN	B3LYP	PBE1PBE
		Bond Lengths (Å)						
Xe(1)–O(1)	1.729(7)	Xe_1–O_1	1.738	1.742	1.725	1.741	1.744	1.727
Xe(1)–F(1)	1.900(3)	Xe_1–$F_{1,2}$	1.959	1.960	1.935	1.954	1.953	1.928
		Xe_1–$F_{3,4}$	1.943	1.952	1.925			
Xe(1)···F(5)	3.239(4)	Xe_1···F_5	2.647	2.880	2.890	2.920	3.446	3.357
Xe(2)–F(5)	2.104(5)	Xe_2–F_5	2.015	2.024	1.999	2.024	2.031	2.006
		Xe_2–F_6				1.984	2.004	1.979
		Bond Angles (deg)						
O(1)–Xe(1)–F(1)	89.2(1)	O_1–Xe_1–F_1	92.4	92.2	91.6	89.3	90.8	90.3
		O_1–Xe_1–F_3	92.8	92.4	91.8			
O(1)–Xe(1)···F(5)	141.13(8)	O_1–Xe_1···F_5	157.8	162.0	158.0	140.2	139.5	139.4
F(1)–Xe(1)–F(1C)	89.99(0)	F_1–Xe_1–F_2	87.5	88.9	88.8	90.0	90.0	90.0
F(1)–Xe(1)–F(1B)	178.3(2)	F_1–Xe_1–F_3	174.5	175.4	176.5	178.6	178.4	179.4
		F_1–Xe_1–F_4	90.5	90.2	90.2			
F(1)–Xe(1)···F(5)	60.6(1)	F_1–Xe_1···F_5	71.9	75.1	73.0	63.4	60.6	61.4
		F_1–Xe_1···F_7				64.0	63.5	63.4
		F_1–Xe_1···F_9				117.8	118.0	118.1
		F_1–Xe_1···F_{11}				117.2	115.2	116.1
		F_3–Xe_1–F_4	91.0	90.4	90.6			
		F_3–Xe_1···F_5	102.6	100.2	103.6			
F(5)–Xe(2)–F(5A)	180.00(0)	F_5–Xe–F_5'	180.0	180.0	180.0	178.0	179.0	179.0
Xe(1)···F(5)–Xe(2)	116.8(1)	Xe_1···F_5–Xe_2	113.8	127.5	122.7	117.6	116.6	117.3

[a] For the atom labeling scheme see Figure 9.1a. [b] For the atom labeling scheme see Figure 9.7b. [c] For the atom labeling scheme see Figure 9.7a. [d] The aug-cc-pVTZ(-PP) basis sets were used.

Table 9.4. Experimental Bond Lengths and Bond Angles in $XeOF_4 \cdot KrF_2$ and Calculated Bond Lengths and Angles in $2XeOF_4 \cdot KrF_2$ and $XeOF_4 \cdot 2KrF_2$

$XeOF_4 \cdot KrF_2$[a]			$2XeOF_4 \cdot KrF_2$[b]			$XeOF_4 \cdot 2KrF_2$[c]		
exptl			calcd (C_{2h})[d]			calcd (C_1)[d]		
			SVWN	B3LYP	PBE1PBE	SVWN	B3LYP	PBE1PBE
			Bond Lengths (Å)					
Xe(1)–O(1)	1.711(2)	$Xe_1–O_1$	1.738	1.742	1.725	1.740	1.743	1.726
Xe(1)–F(1)	1.913(3)	$Xe_1–F_1$	1.956	1.959	1.933	1.958	1.958	1.933
Xe(1)–F(2)	1.906(2)	$Xe_1–F_2$				1.958	1.958	1.933
Xe(1)–F(3)	1.901(2)	$Xe_1–F_3$	1.942	1.950	1.924	1.958	1.958	1.933
Xe(1)–F(4)	1.893(2)	$Xe_1–F_4$				1.958	1.958	1.933
Xe(1)···F(5)	2.962(2)	$Xe_1···F_5$	2.688	2.935	2.943	2.674	2.975	2.957
Xe(1)···F(6)	3.009(3)	$Xe_1···F_7$				2.674	2.975	2.957
Xe(1)···F(5B)	3.470(3)							
Xe(1)···F(2A)	3.661(2)							
Kr(1)–F(5)	1.896(3)	$Kr–F_5$	1.883	1.898	1.868	1.905	1.914	1.884
		$Kr–F_6$				1.851	1.876	1.846
Kr(2)–F(6)	1.889(2)	$Kr–F_7$				1.905	1.914	1.884
		$Kr–F_8$				1.851	1.876	1.846
			Bond Angles (deg)					
O(1)–Xe(1)–F(1)	89.4(1)	$O_1–Xe_1–F_1$	92.5	92.2	91.6	91.3	91.3	90.9
O(1)–Xe(1)–F(2)	89.4(1)					91.3	91.3	90.8
O(1)–Xe(1)–F(3)	89.7(1)	$O_1–Xe_1–F_3$	92.8	92.4	91.8	91.3	91.3	90.9
O(1)–Xe(1)–F(4)	90.1(1)					91.3	91.3	90.8
O(1)–Xe(1)···F(5)	151.6(1)	$O_1–Xe_1···F_5$	157.1	160.6	157.0	152.3	151.6	150.8
O(1)–Xe(1)···F(6)	148.5(1)	$O_1–Xe_1···F_7$				152.3	151.6	150.8
O(1)–Xe(1)···F(5B)	130.5(1)							
O(1)–Xe(1)···F(2A)	122.4(1)							
F(1)–Xe(1)–F(2)	89.2(1)	$F_1–Xe_1–F_2$	87.5	88.8	88.8	90.5	90.0	90.1
F(1)–Xe(1)–F(3)	178.96(7)	$F_1–Xe_1–F_3$	174.5	175.3	176.4	177.4	177.5	178.3

F(1)–Xe(1)–F(4)	88.82(9)	F_1–Xe_1–F_4	90.5	90.2	90.2	89.5	89.9	89.9
F(1)–Xe(1)···F(5)	66.53(8)	F_1–Xe_1···F_5	71.3	74.1	72.3	69.5	69.1	69.0
F(1)–Xe(1)···F(6)	115.95(8)	F_1–Xe_1···F_7				108.1	108.5	109.4
F(2)–Xe(1)–F(3)	91.39(9)	F_2–Xe_1–F_3	90.5	90.2	90.2	89.5	89.9	89.9
F(2)–Xe(1)–F(4)	177.98(9)	F_2–Xe_1–F_4	174.5	175.3	176.4	177.4	177.5	178.3
F(2)–Xe(1)···F(5)	75.17(8)	F_2–Xe_1···F_5	71.3	74.1	72.3	108.1	108.5	109.4
F(2)–Xe(1)···F(6)	107.84(8)	F_2–Xe_1···F_7				69.5	69.1	69.0
F(3)–Xe(1)–F(4)	90.57(9)	F_3–Xe_1–F_4	91.0	90.4	90.5	90.5	90.0	90.1
F(3)–Xe(1)···F(5)	114.11(8)	F_3–Xe_1···F_5	103.1	101.2	104.2	108.1	108.5	109.4
F(3)–Xe(1)···F(6)	65.05(8)	F_3–Xe_1···F_7				69.5	69.1	69.0
F(4)–Xe(1)···F(5)	104.45(9)	F_4–Xe_1···F_5	103.1	101.2	104.2	69.5	69.1	69.0
F(4)–Xe(1)···F(6)	65.05(8)	F_4–Xe_1···F_7				108.1	108.5	109.4
F(5)–Kr(1)–F(5A)	180.0(1)	F_5–Kr_1–F_5'	180.0	180.0	180.0	178.8	179.3	179.4
F(6)–Kr(2)–F(6A)	180.0(2)	F_7–Kr_2–F_8				178.8	179.3	179.4
Kr(1)–F(5)···Xe(1)	123.4(1)	Kr_1–F_5···Xe_1	110.3	121.7	118.3	111.0	118.9	117.5
Kr(2)–F(6)···Xe(1)	145.4(1)	Kr_2–F_7···Xe_1				111.0	118.9	117.5

[a] For the atom labeling scheme see Figure 9.2a. [b] For the atom labeling scheme see Figure 9.8a. [c] For the atom labeling scheme see Figure 9.8b. [d] The aug-cc-pVTZ(-PP) basis sets were used.

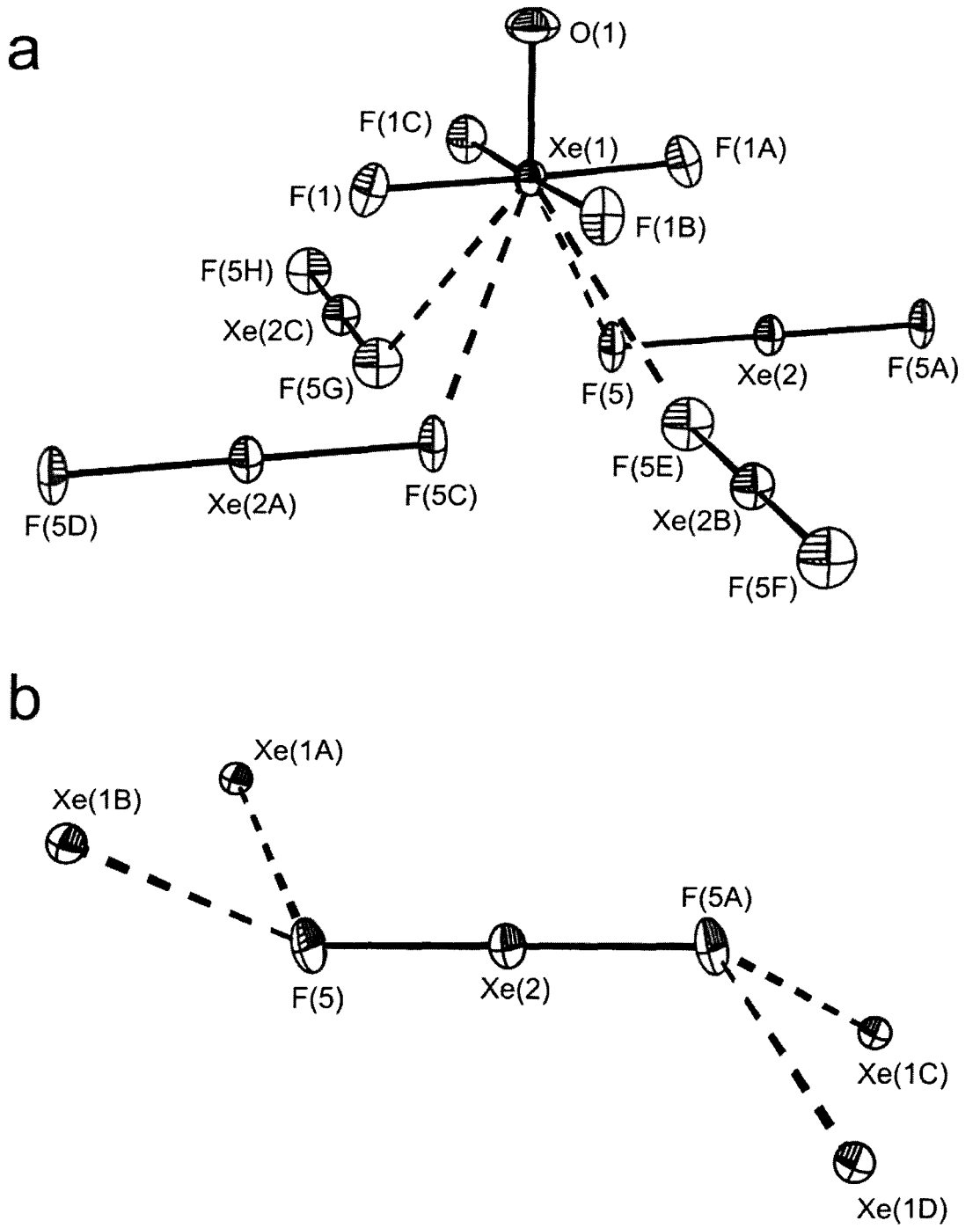

Figure 9.1. A depiction of the coordination spheres of the (a) $XeOF_4$ molecule and (b) XeF_2 molecule in the X-ray crystal structure of $XeOF_4 \cdot XeF_2$ with thermal ellipsoids drawn at the 50% probability level.

center of symmetry in XeF_2.

In contrast to the highly symmetric $XeOF_4 \cdot XeF_2$ structure, $XeOF_4 \cdot KrF_2$ crystallizes in the $P\bar{1}$ space group and thus has significantly different structural features. The $XeOF_4 \cdot KrF_2$ adduct contains two crystallographically independent KrF_2 molecules. The $XeOF_4$ and KrF_2 molecules stack along the *a*- and *b*- axes and occupy separate planes that bisect the *b,c*-plane and contain the *a*-axis (Figure G2). Within their respective planes, the $XeOF_4$ and KrF_2 molecules alternate their orientations by 180°. The $XeOF_4$ and KrF_2 molecules form a layer in the *a,b*-plane so that columns of $XeOF_4$ molecules alternate with two crystallographically independent KrF_2 molecules along the *c*-axis. As a result, each Xe atom of the $XeOF_4$ molecules has a short contacts to two KrF_2 molecules (2.962(2) and 3.009(3) Å), and one longer contact to a single KrF_2 molecule (3.470(3) Å). There is also a second long contact to Xe which occurs with F(2A) of an adjacent $XeOF_4$ molecule (3.661(2) Å) (Figure 9.2a), which, when included in the coordination sphere of Xe, renders Xe nine-coordinate. Both of the long contacts to Xe are close to the sum of the F and Xe van der Waals radii,[165] but the shorter contacts are ca. 0.65 Å less than this sum. Each fluorine atom of $Kr(1)F_2$ has two short contacts with the xenon atoms of two symmetry related $XeOF_4$ molecules while each fluorine atom of $Kr(2)F_2$ has only one short contact with one $XeOF_4$ molecule (Figure 9.2b). The remaining intermolecular contacts for $XeOF_4 \cdot XeF_2$[260] and $XeOF_4 \cdot KrF_2$[261] are long and near the sum of the Xe and F van der Waals radii.[165]

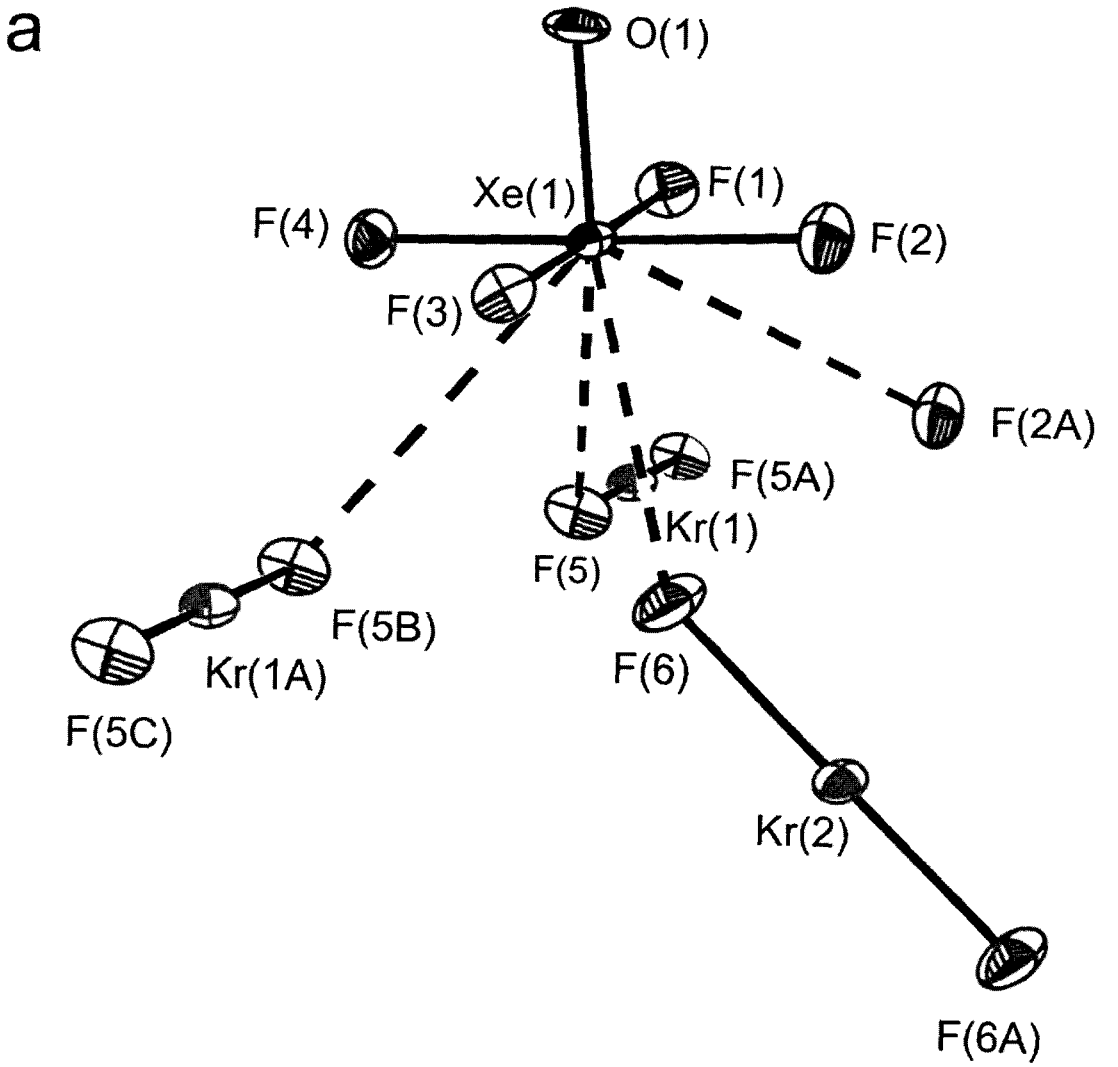

Figure 9.2. (continued ...)

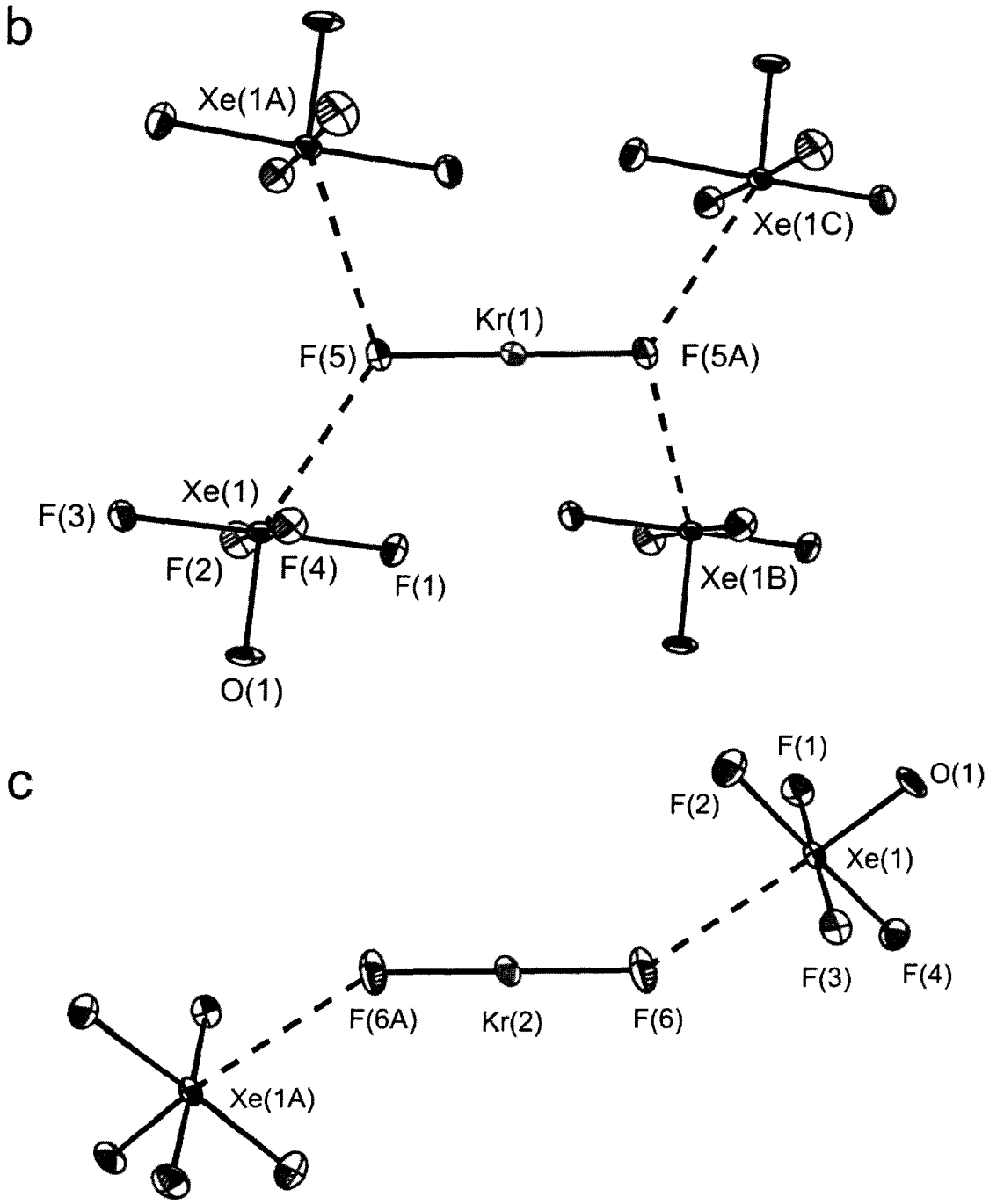

Figure 9.2 A depiction of the coordination spheres of the (a) $XeOF_4$ molecule and (b) and (c) KrF_2 molecules in the X-ray crystal structure of $XeOF_4 \cdot KrF_2$ with thermal ellipsoids drawn at the 50% probability level.

9.2.3.2. $XeOF_4$.

The $XeOF_4$ molecules in both of the NgF_2 adducts are based on a pseudo-octahedral AX_4YE VSEPR arrangement of bond pairs (X), double bond pairs (Y), and lone pairs (E) which gives rise to a square-pyramidal geometry. The four fluorine atoms that comprise the base of the square pyramid are coplanar as imposed by symmetry for $XeOF_4 \cdot XeF_2$ and are coplanar within ±0.003 Å for α-$XeOF_4 \cdot KrF_2$, with the respective apical oxygen atoms located 1.701 and 1.700 Å above the equatorial plane and the xenon atom lying 0.028 and 0.011 Å below that plane.

The secondary bonding interactions that occur between the $XeOF_4$ and NgF_2 molecules in each structure have contact distances that are significantly less than the sum of the xenon and fluorine van der Waals radii,[165] resulting in nine coordinate xenon atoms (Figure 9.3). The light atom interatomic distances associated with the xenon coordination spheres are similar, with the distances between the oxygen and four fluorine atoms being slightly shorter than the average overall interatomic distances (Table G1). The contacts in both structures occur from beneath the equatorial planes of the $XeOF_4$ molecules so as to avoid the valence electron lone pair position in the manner described for $[XeF_5][RuF_6]$,[93] $[XeF_5][OsO_3F_3]$,[203] and $[XeF_5][\mu\text{-}F(OsO_3F_2)_2]$.[203]

The secondary contacts for $XeOF_4 \cdot XeF_2$ are from the F(5) atom of four symmetry-equivalent XeF_2 molecules and the Xe atom is located 2.522 Å above the F(5,5C,5E,5G)-plane. This plane is coplanar by symmetry and is parallel to the equatorial F(1,1A,1B,1C)-plane. Secondary contacts to the Xe atom of the $XeOF_4 \cdot KrF_2$ structure are from the F(5), F(5B), F(6), and F(2A) atoms which form a near parallelogram-shaped

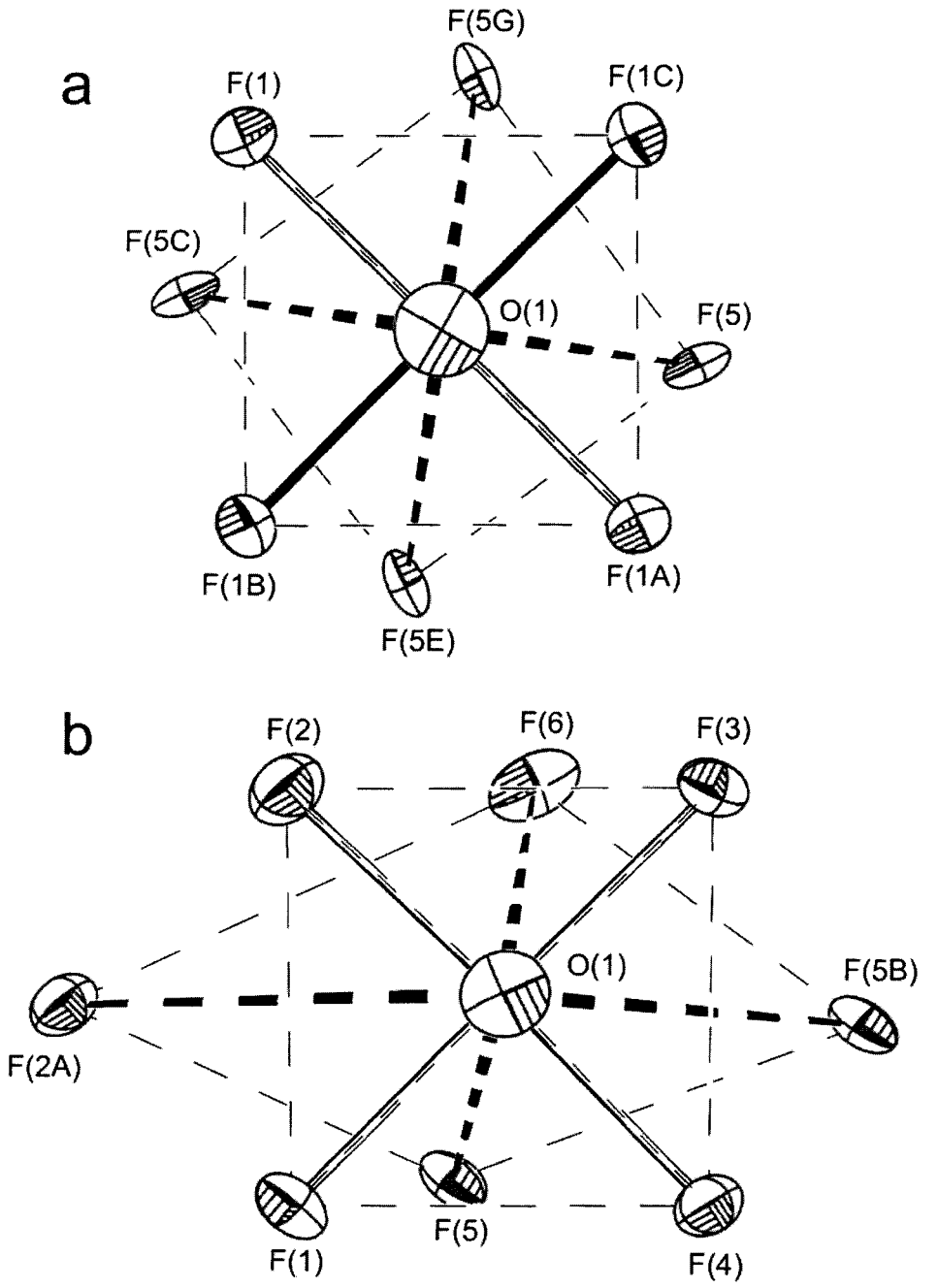

Figure 9.3. Visualization of the coordination sphere formed by the light atoms of the XeF_9 unit of (a) $XeOF_4 \cdot XeF_2$ and (b) $XeOF_4 \cdot KrF_2$

plane. The Xe(1) atom is located 2.351 Å above the (F5,F5B,F6,F2A)-plane which is coplanar to within ±0.232 Å and parallel to the F(1,2,3,4)-plane to within ±2.9°.

The planes of contacting atoms and the equatorial fluorine atoms in $XeOF_4 \cdot NgF_2$ have near-staggered conformations. The xenon coordination spheres may be described as distorted monocapped square antiprisms having dihedral angles, ψ, between the basal fluorine atom planes of the $XeOF_4$ molecules and planes of contacting atoms that are close to 45° (36.8° for the F(5,5C)Xe(1)O(1)- and F(1,1A)Xe(1)O(1)-planes and 53.2° for the F(5G,5E)Xe(1)O(1)- and F(1,1A)Xe(1)O(1)-planes of $XeOF_4 \cdot XeF_2$; 46.4° for the F(1,3)Xe(1)O(1)- and F(2A,5B)Xe(1)O(1)-planes and 33.5° for the F(1,3)Xe(1)O(1)- and F(5,6A)Xe(1)O(1)-planes of $XeOF_4 \cdot KrF_2$). The Xe–F bond lengths of the $XeOF_4$ molecule in both the XeF_2 and KrF_2 complexes (1.900(3) and av. 1.903(3) Å, respectively) are not significantly affected by the long secondary Xe(VI)···F contacts and are similar to those of other structures containing adducted $XeOF_4$ such as $[XeF_5][SbF_6] \cdot XeOF_4$ (1.890(2) and 1.895(2) Å)[95] and $(OsO_3F_2)_2 \cdot 2XeOF_4$ (av. 1.912(5) Å)[18] as well as the gas-phase microwave (1.95(5) Å)[102] and electron diffraction (1.901(3) Å)[104] structures of $XeOF_4$. The Xe–O bond length in the XeF_2 adduct (1.729(7) Å) is comparable within ±3σ to that of $XeOF_4 \cdot KrF_2$ (1.711(2) Å) and is similar to those of $[XeF_5][SbF_6] \cdot XeOF_4$ (1.713(3) Å),[95] $(OsO_3F_2)_2 \cdot 2XeOF_4$ (av 1.709(6) Å),[18] and $XeOF_4$ (microwave, 1.70(5)[102]; electron diffraction, 1.71(1)[104] Å).

9.2.3.3. XeF_2 and KrF_2

The XeF_2 molecule in the crystal structure of $XeOF_4 \cdot XeF_2$ is linear by symmetry with a Xe–F bond length of 2.014(5) Å. The Xe–F bond lengths are slightly elongated

when compared with those of free XeF_2 which has been determined by X-ray diffraction (1.999(4) Å),[262] neutron diffraction (2.00(1) Å),[263] and in the gas phase (1.9791(1)[264] and 1.977965(5)[265] Å) determined by vibrational spectroscopy, and is comparable to the Xe–F bond lengths in the X-ray crystal structures of other compounds containing symmetrically coordinated XeF_2 molecules such as $IF_5 \cdot XeF_2$ (2.018(9) Å),[114] $2[XeF_5][AsF_6] \cdot XeF_2$ (2.01(2) Å),[79] $XeF_4 \cdot XeF_2$ (2.010(6) Å),[116] and $[Ba(XeF_2)_5][AsF_6]_2$ (1.994(9), 2.005(5), and 1.995(5) Å).[117]

The two crystallographically independent KrF_2 molecules in the crystal structure of $XeOF_4 \cdot KrF_2$ are both linear by symmetry with Kr–F bond lengths (1.896(3) and 1.889(2) Å) in good agreement with those of α-KrF_2 (1.894(5) Å),[126] β-KrF_2 (1.89(2) Å),[266] and the co-crystallized KrF_2 molecule in the structure of $[Kr_2F_3]_2[SbF_6]_2 \cdot KrF_2$ (1.881(4) and 1.887(4) Å).[126] The Kr-F bond lengths are intermediate when compared to those of the asymmetrically coordinated $[BrOF_2][AsF_6] \cdot 2KrF_2$[124] adduct (1.943(4) and 1.933(3); 1.840(5) and 1.847(3) Å) and the Kr–F and Kr---F bond lengths of KrF^+ and $Kr_2F_3^+$ salts such as $[KrF][AuF_6]$ (1.76(1) and 2.16(1) Å, respectively),[252] $[KrF][SbF_6]$ (1.765(3) and 2.140(3) Å, respectively),[126] and $[Kr_2F_3][AsF_6]$ (av. 1.796(6) and 2.048(5) Å, respectively).[126] The intermediate bond length in the current structure clearly indicates a molecular adduct of KrF_2 rather than formation of a KrF^+ salt.

9.2.4. Raman Spectroscopy

Reaction of XeF_2 with a 10-fold excess $XeOF_4$ leads to the synthesis of the molecular addition compound $XeOF_4 \cdot XeF_2$, while reaction of KrF_2 with $XeOF_4$ leads to a mixture of phases, two of which have been preliminarily identified as $XeOF_4 \cdot KrF_2$ and

$XeOF_4 \cdot nKrF_2$ (see Section 9.2.1.). The low-temperature, solid-state Raman spectra of $XeOF_4 \cdot XeF_2$, $XeOF_4 \cdot KrF_2$, and $XeOF_4 \cdot nKrF_2$ are shown in Figures 9.4, 9.5, and 9.6, respectively. The observed frequencies and mode descriptions for $XeOF_4 \cdot XeF_2$, $XeOF_4 \cdot KrF_2$, and $XeOF_4 \cdot nKrF_2$ are listed in Tables 9.5, 9.6, and 9.7, respectively. Spectral assignments and mode descriptions for $XeOF_4 \cdot XeF_2$ and $XeOF_4 \cdot KrF_2$ were made by comparison with the experimental and calculated frequencies of gas-phase (Table G2)[163] and solid (Figure G3) $XeOF_4$, XeF_2 (Table G3),[267] and KrF_2 (Table G3)[103] along with the calculated frequencies and mode descriptions for the unknown adducts $2XeOF_4 \cdot NgF_2$ (C_{2h}) (Table G4) (Ng = Kr, Xe), $XeOF_4 \cdot 2KrF_2$ (C_4) (Table 9.7), and $XeOF_4 \cdot 4XeF_2$ (C_1) (Table G5). The adducts were calculated to provide a close approximation of the local symmetry of the $XeOF_4$ ($XeOF_4 \cdot 2KrF_2$ and $XeOF_4 \cdot 4XeF_2$) or NgF_2 ($2XeOF_4 \cdot NgF_2$) molecules in the crystal, allowing for an estimate of the degree of intra- and intermolecular vibrational coupling and account for the frequency shifts compared with $XeOF_4$ and XeF_2. The spectral assignments and mode descriptions for $XeOF_4 \cdot nKrF_2$ were made by comparison with the calculated frequencies and mode descriptions for $XeOF_4 \cdot 2KrF_2$. The geometric parameters and benchmarks of the structures calculated at the PBE1PBE level provided the best overall agreement with experiment (See Section 9.2.5) and are referred to explicitly.

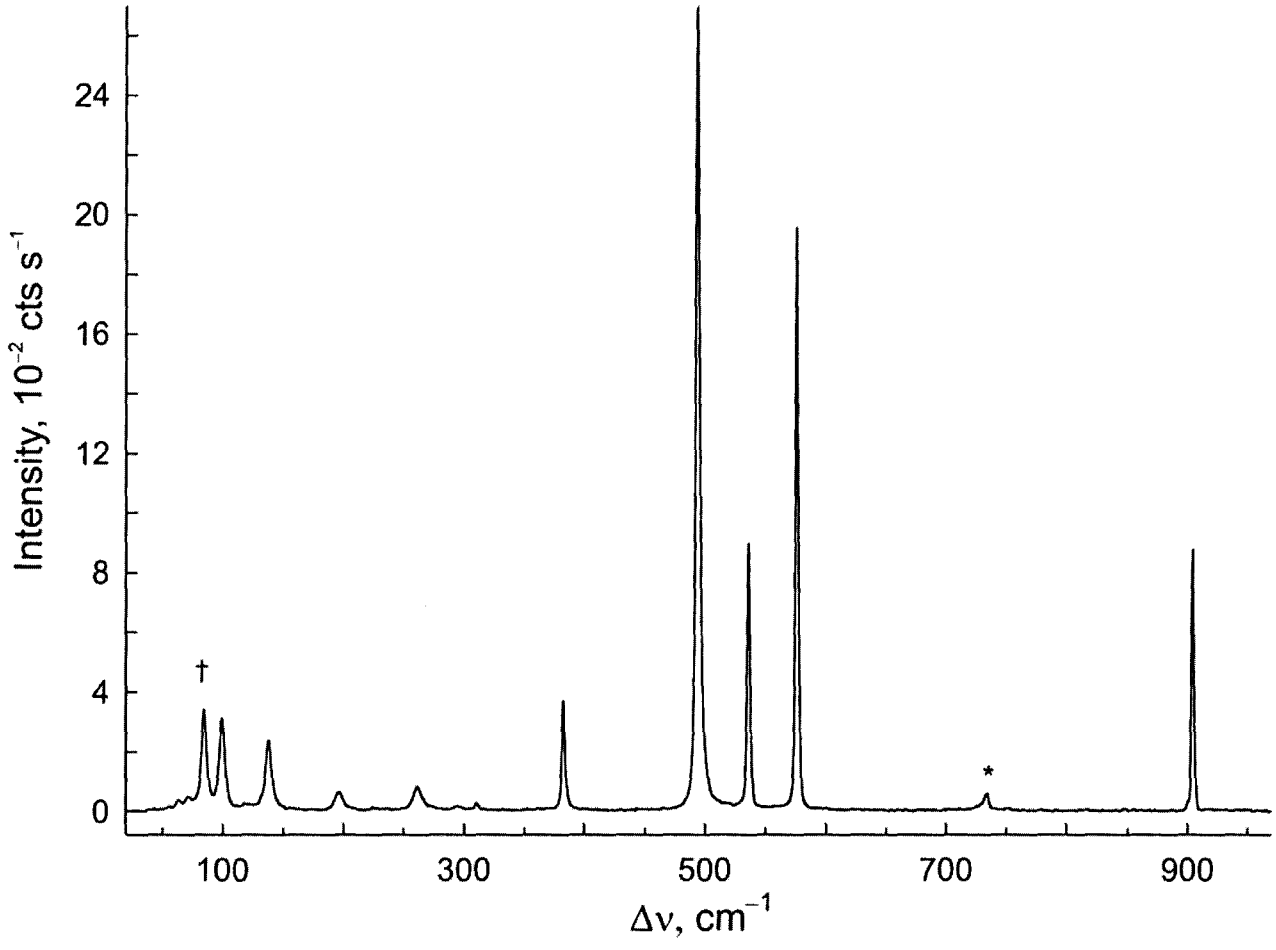

Figure 9.4. Raman spectrum of $XeOF_4 \cdot XeF_2$ recorded at –150 °C using 1064-nm excitation; the symbols denote FEP sample tube lines (*) and an instrumental artifact (†).

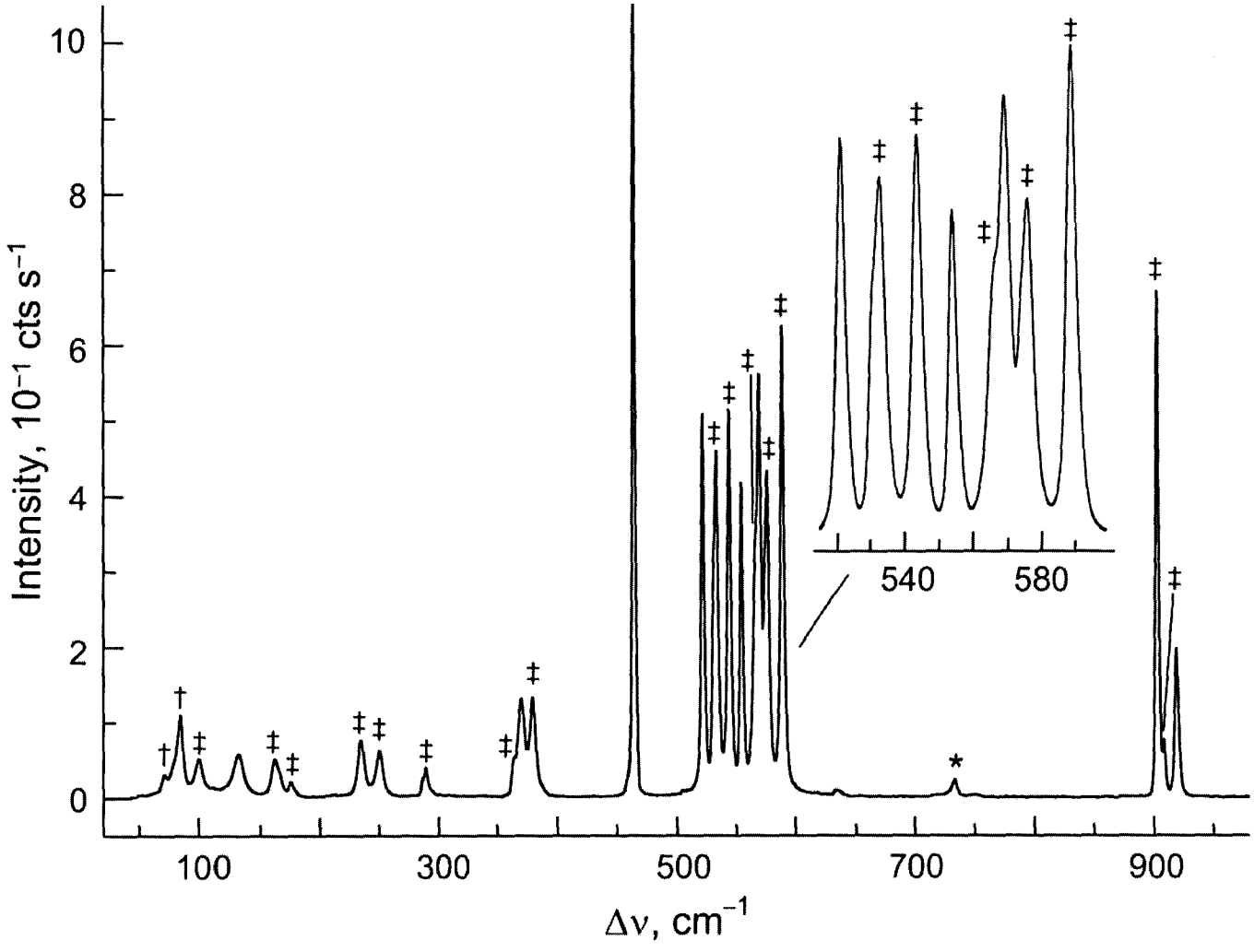

Figure 9.5. Raman spectrum of $XeOF_4 \cdot KrF_2$ recorded at –150 °C using 1064-nm excitation; the symbols denote FEP sample tube lines (*), an instrumental artifact (†), and excess $XeOF_4$ (‡).

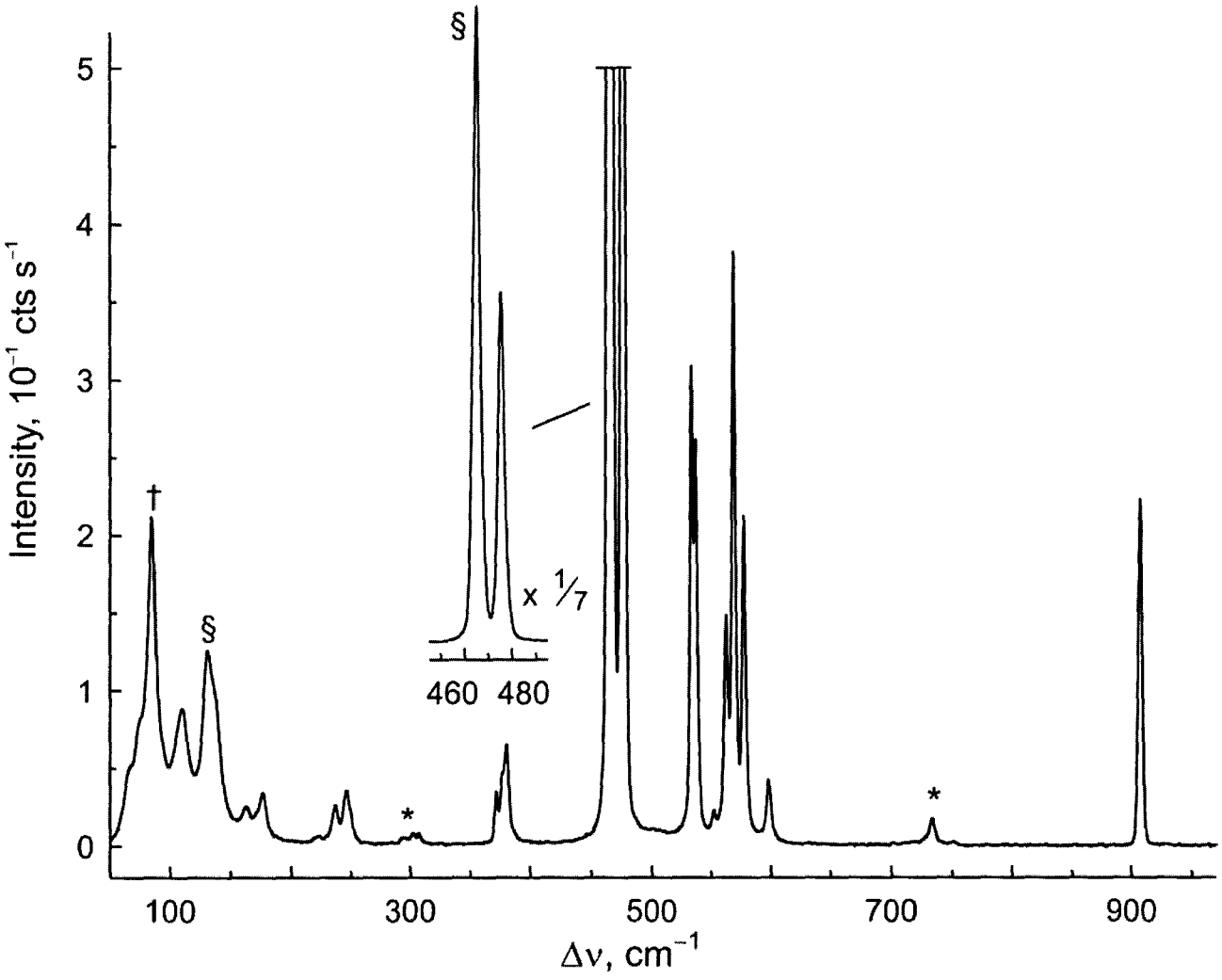

Figure 9.6. Raman spectrum of $XeOF_4 \cdot nKrF_2$ recorded at –150 °C using 1064-nm excitation; the symbols denote FEP sample tube lines (*), an instrumental artifact (†), and excess KrF_2 (§).

Table 9.5. Raman Frequencies and Intensities for $XeOF_4$, XeF_2, and $XeOF_4 \cdot XeF_2$ and Assignments for $XeOF_4 \cdot 4XeF_2$ and $2XeOF_4 \cdot XeF_2$

exptl		assgnts[a]
$XeOF_4$[b]	$XeOF_4 \cdot XeF_2$[d]	$XeOF_4 \cdot 4XeF_2$ (C_4)[e]
928(m)	904(30)	A, $\nu(Xe_1O_1)$
609(vw)		E, $\nu(Xe_1F_1) - \nu(Xe_1F_3)$ / $\nu(Xe_1F_2) - \nu(Xe_1F_4)$
577(vs)	575(72)	A, $\nu_s(Xe_1F_{4e})$
543(w)	536(33)	B, $[\nu(Xe_1F_1) + \nu(Xe_1F_2)] - [\nu(Xe_1F_4) + \nu(Xe_1F_3)]$[f] B, $[\nu(Xe_1F_1) + \nu(Xe_1F_2)] - [\nu(Xe_1F_4) + \nu(Xe_1F_3)]$[f]
360(w)	383(14)	E, $\delta(O_1Xe_1F_1F_4)$ / $\delta(O_1Xe_1F_2F_3)$
286(m)	262(3)	A, $\delta_{umb}(Xe_1F_{4e})$
225(w)	196(2)	B, $\delta(F_1Xe_1F_2) + \delta(F_3Xe_1F_4)$[f] B, $\delta(F_1Xe_1F_2) + \delta(F_3Xe_1F_4)$[f]
161(w)		E, $\delta(F_1Xe_1F_3)$ / $\delta(F_2Xe_1F_4)$
	99(12)	E, $\rho_r(XeOF_4)$
		B, $\rho_t(F_1Xe_1F_2) - \rho_t(F_3Xe_1F_4)$
		A, $\rho_t(Xe_1F_{4e})$
XeF_2[c]		$2XeOF_4 \cdot XeF_2$ (C_{2h})[g]
	i.a.	B_u $\nu(Xe_2F_5) - \nu(Xe_2F_5')$
	i.a.	B_u $\nu(Xe_2F_5) - \nu(Xe_2F_5')$[h]
497(100)	494(100)	A_g $\nu(Xe_2F_5) + \nu(Xe_2F_5')$
	i.a.	B_u $\delta(F_5Xe_2F_5')$[h]
	i.a.	B_u $\delta_{ip}(F_5Xe_2F_5')$
	i.a.	A_u $\delta_{oop}(F_5Xe_2F_5')$
	138(9)	A_g $\rho_r(F_5Kr_1F_5')_{ip}$

[a] The abbreviations denote stretch (ν), symmetric (s) bend (δ), twist (ρ_t), umbrella (δ_{umb}), in-plane (ip), out-of-plane (oop), F(1)F(1A)F(1B)F(1C) (F_{4e}). [b] From Ref 101. The abbreviations denote very strong (vs), medium (m), weak (w), and very weak (vw). [c] From Ref 267. [d] The Raman spectrum was recorded on a microcrystalline solid sample in a FEP tube at −150 °C using 1064-nm excitation. Experimental Raman intensities are given in parentheses and are relative intensities with the most intense band given as 100. The abbreviations denote shoulder (sh), broad (br), inactive (i.a.) and not observed (n.o.). A weak band was also observed at 310(1) cm^{-1} but is unassigned. [e] See Figure 9.7a for the atom labeling scheme. See Table G5 for complete mode descriptions and calculated frequencies for $XeOF_4 \cdot 4XeF_2$. [f] Coupled to the $[\nu(Xe_2F_5) + \nu(Xe_4F_9)] - [\nu(Xe_3F_7) + \nu(Xe_5F_{11})]$ mode in the calculated $XeOF_4 \cdot 4XeF_2$ structure. [g] See Figure 9.7b for the atom labeling scheme. See Table G4 for the complete mode descriptions and calculated frequencies for $2XeOF_4 \cdot XeF_2$. [h] Coupled to $XeOF_4$ modes in the calculated $2XeOF_4 \cdot XeF_2$ structure.

Table 9.6. Raman Frequencies and Intensities for $XeOF_4$, KrF_2, and $XeOF_4 \cdot KrF_2$ and Assignments for $XeOF_4 \cdot 2KrF_2$ and $2XeOF_4 \cdot KrF_2$

exptl		assgnts[a]
$XeOF_4$[b]	$XeOF_4 \cdot KrF_2$[c]	$XeOF_4 \cdot 2KrF_2$ (C_1)[d]
928(m)	918(19)	$\nu(Xe_1O_1)$
577(vs)	568(51)	$\nu(Xe_1F_1) + \nu(Xe_1F_2) + \nu(Xe_1F_3) + \nu(Xe_1F_4)$
609(vw)	554(38)	$[\nu(Xe_1F_1) + \nu(Xe_1F_4)] - [\nu(Xe_1F_2) + \nu(Xe_1F_3)]$
543(w)	531 sh	$[\nu(Xe_1F_1) + \nu(Xe_1F_2)] - [\nu(Xe_1F_3) + \nu(Xe_1F_4)]$
	521(47)	$[\nu(Xe_1F_1) + \nu(Xe_1F_3)] - [\nu(Xe_1F_2) + \nu(Xe_1F_4)]$
360(w)	370(12)	$\delta(Xe_1F_1F_2O_1) + \delta(Xe_1F_3F_4O_1)$
		$\delta(Xe_1F_1F_4O_1) + \delta(Xe_1F_2F_3O_1)$
286(m)	287 sh	$\delta_{umb}(Xe_1F_1F_2F_3F_4)$
		$\delta(F_1Xe_1F_4) + \delta(F_2Xe_1F_3)$
225(w)	212(1)	$\rho_t(F_1Xe_1F_2) + \rho_t(F_3Xe_1F_4)$
161(w)		$\delta(F_1Xe_1F_4) - \delta(F_2Xe_1F_3)$
		$\delta(F_1Xe_1F_2) - \delta(F_3Xe_1F_4)$
KrF_2[e]		$2XeOF_4 \cdot KrF_2$[f]
	i.a.	$B_u\ \nu(Kr_1F_5) - \nu(Kr_1F_5')$
	i.a.	$B_u\ \nu(Kr_1F_5) - \nu(Kr_1F_5')$[g]
462(100)	463(100)	$A_g\ \nu(Kr_1F_5) + \nu(Kr_1F_5')$
	i.a.	$B_u\ \delta(F_5Kr_1F_5')$[g]
	i.a.	$B_u\ \delta_{ip}(F_5Kr_1F_5')$
	i.a.	$A_u\ \delta_{oop}(F_5Kr_1F_5')$
	132(1)	$A_g\ \rho_r(F_5Kr_1F_5')_{ip}$

[a] The abbreviations denote stretch (ν), bend (δ), twist (ρ_t), rock (ρ_r), umbrella (δ_{umb}), and out-of-plane (oop). [b] From Ref 101. The abbreviations denote very strong (vs), medium (m), weak (w), and very weak (vw). [c] The Raman spectrum was recorded on a microcrystalline solid sample in a FEP tube at −150 °C using 1064-nm excitation. Experimental Raman intensities are given in parentheses and are relative intensities with the most intense band given as 100. The abbreviations denote shoulder (sh) and inactive (i.a.). Bands assigned to free solid $XeOF_4$ were observed at 908, 902, 588, 576, 566, 543, 532, 379, 289, 250, 234, 176, 166, 162, and 100 cm^{-1}. [d] See Figure 9.8a for the atom labeling scheme. See Table G4 for complete mode descriptions and calculated frequencies for $XeOF_4 \cdot 2KrF_2$. [e] From Ref 268. [f] See Figure 9.8b for the atom labeling scheme. See Table 9.7 for the complete mode descriptions and calculated frequencies for $2XeOF_4 \cdot KrF_2$. [g] Coupled to contributions from the adducted $XeOF_4$ molecule in $2XeOF_4 \cdot KrF_2$.

Table 9.7. Experimental Raman and Calculated Vibrational Frequencies (cm^{-1}), Intensities, and Assignments for $XeOF_4 \cdot nKrF_2$

exptl[a]	calcd[b]			assgnts (C_1)[c]
	SVWN	B3LYP	PBE1PBE	
908(14)	917(47)[51]	888(34)[35]	935(30)[39]	$\nu(Xe_1O_1)$
578(13)	610(4)[2]	586(5)[9]	613(10)[5]	$[\nu(Kr_1F_5) + \nu(Kr_2F_7)] - [\nu(Kr_1F_6) + \nu(Kr_2F_8)]$
551(1)	578(<1)[480]	577(<0.1)[54]	603(<0.1)[6]	$[\nu(Xe_1F_1) + \nu(Xe_1F_4)] - [\nu(Xe_1F_2) + \nu(Xe_1F_3)]$
	578(<1)[220]	575(<0.1)[255]	600(<0.1)[268]	$[\nu(Xe_1F_1) + \nu(Xe_1F_2)] - [\nu(Xe_1F_3) + \nu(Xe_1F_4)]$
598(2)	593(<1)[402]	566(<1)[910]	593(<1)[1014]	$[\nu(Kr_1F_5) + \nu(Kr_2F_8)] - [\nu(Kr_1F_6) + \nu(Kr_2F_7)]$
568(25), 562(10)	535(15)[3]	537(29)[2]	568(24)[2]	$\nu(Xe_1F_1) + \nu(Xe_1F_2) + \nu(Xe_1F_3) + \nu(Xe_1F_4)$
536(17), 533(20)	496(14)[0]	496(20)[0]	526(18)[0]	$[\nu(Xe_1F_1) + \nu(Xe_1F_3)] - [\nu(Xe_1F_2) + \nu(Xe_1F_4)]$
475(100)	499(290)[1]	488(229)[1]	519(195)[1]	$\nu(Kr_1F_5) + \nu(Kr_1F_6) + \nu(Kr_2F_7) + \nu(Kr_2F_8)$
	493(2)[58]	484(5)[55]	514(3)[79]	$[\nu(Kr_1F_5) + \nu(Kr_1F_6)] - [\nu(Kr_2F_7) + \nu(Kr_2F_8)]$
380(4)	320(2)[2]	336(2)[4]	355(2)[5]	$\delta(Xe_1F_1F_2O_1) + \delta(Xe_1F_3F_4O_1)$
377 sh	321(2)[3]	335(2)[4]	355(2)[5]	$\delta(Xe_1F_1F_4O_1) + \delta(Xe_1F_2F_3O_1)$
250 sh	274(3)[2][d]	276(1)[25]	292(1)[28]	$\delta_{umb}(Xe_1F_1F_2F_3F_4)$
	259(<0.1)[81][e]	247(<1)[59]	261(<1)[57]	$\delta(F_5Kr_1F_6) + \delta(F_7Kr_2F_8)$
246(2)	263(2)[14]	246(1)[5]	260(1)[7]	$\delta(F_5Kr_1F_6) - \delta(F_7Kr_2F_8)$
237(2)	242(<1)[0]	237(<1)[<0.1]	251(<1)[<0.1]	$\rho_w(F_5Kr_1F_6) - \rho_w(F_7Kr_2F_8)$
	240(<0.1)[14]	237(<0.1)[18]	251(<0.1)[18]	$\rho_w(F_5Kr_1F_6) + \rho_w(F_7Kr_2F_8)$
176(2)	194(2)[<1]	208(2)[1]	215(2)[1]	$\delta(F_1Xe_1F_4) + \delta(F_2Xe_1F_3)$
	191(<1)[0]	189(<0.1)[0]	201(<0.1)[0]	$\rho_t(F_1Xe_1F_2) + \rho_t(F_3Xe_1F_4)$
163(2)	172(1)[9]	161(1)[4]	165(1)[3]	$\delta(F_1Xe_1F_4) - \delta(F_2Xe_1F_3)$
	132(<1)[1]	146(<1)[<1]	148(<1)[<1]	$\delta(F_1Xe_1F_2) - \delta(F_3Xe_1F_4)$
110(6)	122(7)[3]	94(8)[1]	95(7)[1]	def.
136(7)	130(2)[<1]	91(1)[1]	92(1)[1]	$\rho_t(F_5Kr_1F_6) + \rho_t(F_7Kr_2F_8)$
	118(<1)[<0.1]	89(<1)[<0.1]	91(<1)[<0.1]	def.
	79(1)[3]	43(3)[5]	49(2)[5]	
	59(2)[0]	46(4)[0]	47(3)[0]	$\rho_r(F_5Kr_1F_6) + \rho_r(F_7Kr_2F_8)$
	68(<1)[<0.1]	41(<1)[<0.1]	40(<1)[<0.1]	def.
	56(2)[2]	28(1)[2]	30(1)[2]	
	34(<1)[<1]	18(<1)[<1]	18(<1)[<1]	
	43(1)[0]	16(1)[0]	18(1)[<0.1]	
	26(<0.1)[<1]	12(<1)[<1]	10(<1)[<1]	

[a] The Raman spectrum was recorded on a microcrystalline solid sample in a FEP tube at −150 °C using 1064-nm excitation. Experimental Raman intensities are given in parentheses and are relative intensities with the most intense band given as 100. The abbreviation denotes shoulder (sh). Bands assigned to KrF_2 were observed at 465 and 131 cm^{-1}. [b] Values in parentheses denote calculated Raman intensities ($Å^4\ u^{-1}$) and values in square brackets denote calculated infrared intensities (km mol^{-1}). The aug-cc-pVTZ(-PP) basis sets were used. [c] Assignments are based on the PBE1PBE geometry. The atom labeling scheme refers to Figure 9.8b and the plane of symmetry is defined by the $Xe_1F_1F_2F_3F_4$ atoms. The abbreviations denote stretch (ν), bend (δ), torsion (ρ_t), wag (ρ_w), rock (ρ_r), and $XeOF_4 \cdot 2KrF_2$ deformation mode (def.). [d] At the SVWN level, the mode is out-of-phase coupled to $\delta(F_5Kr_1F_6) + \delta(F_7Kr_1F_8)$. [e] At the SVWN level, the mode is in-phase coupled to $\delta_{umb}(Xe_1F_1F_2F_3F_4)$.

9.2.4.1. $XeOF_4 \cdot XeF_2$.

The Raman spectrum of the $XeOF_4 \cdot XeF_2$ adduct (Figure 9.4) has been previously reported,[75] but the present work provides an in-depth assignment and description of the vibrational modes based on knowledge of the crystal structure. The spectrum is relatively simple and is comprised of nine bands indicating that there is no symmetry reduction for either $XeOF_4$ or XeF_2 upon adduct formation. The previous study noted that the Raman spectrum was essentially a composite spectrum of $XeOF_4$ and XeF_2 and it was therefore assigned to a $XeOF_4 \cdot XeF_2$ molecular addition compound.

In the crystal structure, the coordination sphere of XeF_2 is symmetric, giving rise to two crystallographically equivalent Xe–F bond lengths (vide supra). Therefore, as in free XeF_2, only the band derived from the symmetric Xe–F stretch, i.e. $\nu(Xe_2F_5) + \nu(Xe_2F_5')$ is Raman active (494 cm^{-1}) with a frequency similar to that of free XeF_2 (497 cm^{-1}).[267] The slight shift relative to that of free XeF_2 is indicative of adduct formation. Although the Xe–F stretch is overestimated for free XeF_2 (534 cm^{-1}), the small shift to lower frequency is reproduced for $2XeOF_4 \cdot XeF_2$ (523 cm^{-1}). A small complexation shift has also been observed for $IF_5 \cdot XeF_2$ (493 cm^{-1})[269] and $2[XeF_5][AsF_6] \cdot XeF_2$ (496 cm^{-1}),[79] and is more pronounced for $[Ag(XeF_2)_2][AsF_6]$ (501 and 508 cm^{-1}),[111] $[Ba(XeF_2)_5][SbF_6]_2$ (521 cm^{-1}),[112] and $[M(XeF_2)_3][AsF_6]_2$ (M = Pb (514 cm^{-1}) and Sr (531 cm^{-1})).[115] It is noteworthy that the calculated values for $\nu(XeF_5) - \nu(XeF_5')$ (535 cm^{-1}) and $\delta(F_5XeF_5')$ (220 and 238 cm^{-1}) are in good agreement with the experimental infrared values of free XeF_2 (555 and 213 cm^{-1}, respectively). Only two modes at 576 and 282 cm^{-1} reveal intermolecular vibrational coupling between the $XeOF_4$

and XeF_2 molecules, and are both predicted to be Raman inactive. The band at 138 cm^{-1} is assigned to the $\rho_r(F_5XeF_5')$ bend associated with the coordinated XeF_2 molecule.

The $XeOF_4$ molecule in the crystal structure is also symmetrically coordinated and has local C_{4v} symmetry. The Xe–O stretch of $XeOF_4$ in $XeOF_4 \cdot XeF_2$ (904 cm^{-1}) is shifted to lower frequency relative to that of the gas-phase molecule (928 cm^{-1}).[101] The calculated shift of the ν(XeO) stretch of $XeOF_4 \cdot 4XeF_2$ (930 cm^{-1}) relative to that calculated for $XeOF_4$ (936 cm^{-1}) (see Table G2), is smaller that what is observed experimentally. The observed $\nu_s(Xe_1F_{4e})$ band (575 cm^{-1}) is comparable to that in the free molecule (577 cm^{-1}),[101] whereas in $XeOF_4 \cdot 4XeF_2$, the calculated $\nu_s(Xe_1F_{4e})$ (569 cm^{-1}) mode is predicted to be shifted relative to that of free $XeOF_4$ (583 cm^{-1}). The band at 536 cm^{-1} is assigned to the asymmetric Xe–F stretching mode and is shifted to lower frequency compared to that of gaseous $XeOF_4$ (543 cm^{-1}). Although only one band is observed experimentally (536 cm^{-1}), calculation for the energy-minimized structure of $XeOF_4 \cdot 4XeF_2$ predict that the asymmetric $[\nu(Xe_1F_1) + \nu(Xe_1F_2)] - [\nu(Xe_1F_3) + \nu(Xe_1F_4)]$ stretch is a component of two modes, being coupled in-phase (522 cm^{-1}) and out-of-phase (530 cm^{-1}) to the $[\nu(Xe_2F_5) + \nu(Xe_4F_9)] - [\nu(Xe_3F_7) + \nu(Xe_5F_{11})]$ mode of the adducted XeF_2 molecules, with the calculated band at 522 cm^{-1} being predicted to be significantly more intense in the Raman spectrum than the calculated band at 530 cm^{-1}. A similar discrepancy is also observed for the deformation mode, $\delta(F_1Xe_1F_2) + \delta(F_3Xe_1F_4)$, which is observed as a single band (196 cm^{-1}) shifted to lower frequency than that of gaseous $XeOF_4$ (225 cm^{-1}); whereas the calculated model predicts a split band (209 and 218 cm^{-1}) because of coupling to XeF_2; these two modes are shifted to lower frequency relative to

$XeOF_4$ (219 cm^{-1}), in agreement with the experimental trend. This indicates that although the calculated model does not perfectly reproduce the experimental spectrum, it does provide a very close approximation of the local symmetry at the $XeOF_4$ center. The only band in the present structure that was not observed in either the spectrum of gaseous $XeOF_4$ or solid XeF_2 is at 99 cm^{-1} and has been assigned to the $\rho_r(XeOF_4)$ mode.

9.2.4.2. $XeOF_4 \cdot KrF_2$.

The Raman spectrum of $XeOF_4 \cdot KrF_2$ (Figure 9.5) also contained excess $XeOF_4$. A pure sample of $XeOF_4 \cdot KrF_2$ could not be isolated because both $XeOF_4$ and $XeOF_4 \cdot KrF_2$ are removed under dynamic vacuum at –20 or –40 °C (vide supra). The ratio of the bands in the Raman spectrum assigned to $XeOF_4 \cdot KrF_2$ and free $XeOF_4$ was constant after dynamic pumping on the sample at 0 °C for 2 h. The sample composition was similar to that used for crystal growth and it is reasonable to assume that the bands, other than those associated with $XeOF_4$, can be associated with the $XeOF_4 \cdot KrF_2$ molecular addition compound characterized by X-ray crystallography.

The crystal structure of $XeOF_4 \cdot KrF_2$ consists of two symmetry-independent KrF_2 molecules. The Kr–F bond lengths of each KrF_2 molecule are similar (1.896(3) and 1.889(2) Å) and do not differ significantly from the α-phase of KrF_2 (1.894(5) Å).[126] As such, the Kr–F stretch of the adducted KrF_2 molecule (463 cm^{-1}) is not significantly shifted when compared with that of solid KrF_2 (462 cm^{-1}).[268] The calculated symmetric Kr–F stretch of the $2XeOF_4 \cdot KrF_2$ adduct (520 cm^{-1}) also does not show a large complexation shift when compared with that of the calculated gas-phase KrF_2 (525 cm^{-1}) molecule, consistent with the small variation in the calculated Kr–F bond length for the

$2XeOF_4 \cdot KrF_2$ and KrF_2 structures (1.868 and 1.861 Å, respectively). The complexation shift of the present adduct is much less than those of $MOF_4 \cdot KrF_2$ adducts (M = Cr, 486 cm^{-1};[125] Mo, 479 and 462 cm^{-1};[123] W, 469 and 450 cm^{-1} [123]) indicating that the bonding in the present structure differs significantly from those of $MOF_4 \cdot KrF_2$. The only other band associated with the adducted KrF_2 molecule is the $\rho_r(F_5Kr_1F_5')_{ip}$ bend (132 cm^{-1}) which is not observed for the gas-phase molecule.

The vibrational modes associated with the adducted $XeOF_4$ molecule are more complex than those of the gas-phase molecule. The Xe–O stretch (918 cm^{-1}) of the adduct is shifted to lower frequency when compared with that of gaseous $XeOF_4$ (928 cm^{-1}), consistent with the formation of an adduct. The Xe–O stretch calculated for the $XeOF_4 \cdot 2KrF_2$ adduct (935 cm^{-1}) does not show a significant complexation shift when compared with that calculated for the gas-phase $XeOF_4$ molecule (936 cm^{-1}). The absence of a shift likely occurs because the $XeOF_4 \cdot 2KrF_2$ model does not take into account all of the secondary bonding interactions that are present in the crystal structure. The Xe–F stretching region is much more complex and is consistent with a lowering of the C_{4v} symmetry of the gas-phase free molecule to C_1 of the calculated $XeOF_4 \cdot 2KrF_2$ adduct. This results in four distinct Xe–F stretches which are all observed in the present spectrum. The symmetric Xe–F stretching mode (568 cm^{-1}) is shifted to lower frequency when compared to that of free $XeOF_4$ (577 cm^{-1}), similar to the shift observed for the Xe–O stretch. There are relatively few low-frequency modes observed in the present spectrum which may result from overlap with bands from excess $XeOF_4$ that could not be resolved.

9.2.4.3. $XeOF_4 \cdot n KrF_2$.

The reaction of excess KrF_2 with $XeOF_4$ leads to a mixture of phases, one of which has been identified as $XeOF_4 \cdot n KrF_2$. The spectrum corresponding to $XeOF_4 \cdot n KrF_2$ (Figure 9.6) also contains two bands that are tentatively assigned to uncomplexed KrF_2. This new spectrum, which differs significantly different from that of $XeOF_4 \cdot KrF_2$, reveals a new phase in which the coordination of the KrF_2 molecule is not consistent with the coordination in the crystal structure. The Raman spectrum is in good agreement with the calculated frequencies and intensities of $XeOF_4 \cdot 2KrF_2$ which contains end-on coordinated KrF_2 molecules.

The two fluorine atoms on each KrF_2 molecule are rendered non-equivalent because end-on coordination to $XeOF_4$ results in four predicted Kr–F stretching modes, three of which are observed. The most intense band in the spectrum is assigned to the symmetric Kr–F stretch (475 cm^{-1}) which is overestimated compared to the calculated structure (519 cm^{-1}). This band is shifted to higher frequency when compared with that of free KrF_2 (462 cm^{-1}) and is similar to the shift of the most intense Kr–F stretch observed for $[BrOF_2][AsF_6] \cdot 2KrF_2$ (472 cm^{-1}) which contains two end-on coordinated KrF_2 molecules. The complexation shift of $XeOF_4 \cdot n KrF_2$ is also similar to that observed for the $MOF_4 \cdot KrF_2$ adducts (M = Cr, 486 cm^{-1};[125] Mo, 479 and 462 cm^{-1};[123] W, 469 and 450 cm^{-1} [123]) indicating that the bonding in these adducts is similar.

The remaining three Kr–F stretching modes are out-of-phase coupled. Two are observed in the present spectrum (578 and 598 cm^{-1}) and are comparable to those of the $MOF_4 \cdot KrF_2$ adducts (M = Mo, 566 and 579 cm^{-1};[123] W, 571 and 581 cm^{-1} [123]) but appear

at much higher frequency than those of the $[BrOF_2][AsF_6]\cdot 2KrF_2$ (533 and 549 cm^{-1})[124] and $CrOF_4\cdot KrF_2$ adducts (550 cm^{-1}).[125] This indicates that the bonding in $XeOF_4\cdot nKrF_2$ is likely to be more similar to $MOF_4\cdot KrF_2$ (M = Mo, W) than to $[BrOF_2][AsF_6]\cdot 2KrF_2$ and $CrOF_4\cdot KrF_2$.

The observed Xe–O stretch of the adduct (908 cm^{-1}) is shifted to lower frequency when compared with that of gaseous $XeOF_4$ (928 cm^{-1}).[101] The low-frequency shift is consistent with donation of electron density from the KrF_2 molecules to the Xe atom of $XeOF_4$ weakening the Xe–O bond. The calculated Xe–O stretch of $XeOF_4\cdot nKrF_2$ (935 cm^{-1}), however, does not mirror this trend when compared with the Xe–O stretch of $XeOF_4$ (935 cm^{-1}), indicating that the model adduct does not completely account for all of the secondary bonding interactions. The symmetric Xe–F stretch (562/568 cm^{-1}) is shifted to lower frequency when compared to that of the gas-phase $XeOF_4$ (577 cm^{-1})[101] molecule or $XeOF_4\cdot XeF_2$ (575 cm^{-1}) adduct (vide supra). The calculated structure of $XeOF_4\cdot 2KrF_2$ adduct predicts a shift of the symmetric Xe–F stretch (568 cm^{-1}) to lower frequency relative to that of gaseous $XeOF_4$ (583 cm^{-1}) which is in agreement with the present findings. The remaining Xe–F stretches (533/536, and 551 cm^{-1}) are assigned to asymmetric Xe–F stretches which are in good agreement with the calculated structure. These bands appear in the same range as the two asymmetric Xe–F stretches of $XeOF_4$ (543 and 609 cm^{-1})[101] and the one stretch observed for $XeOF_4\cdot XeF_2$ (536 cm^{-1}) (vide supra).

9.2.5. Computational Results.

The energy-minimized geometries of $2XeOF_4 \cdot NgF_2$ (C_{2v}) (Ng = Xe, Kr) (Figure 9.7b and 9.8b), $XeOF_4 \cdot 2KrF_2$ (C_1), and $XeOF_4 \cdot 4XeF_2$ (C_4) (Figure 9.7a) were obtained at the SVWN, B3LYP and PBE1PBE levels of theory and resulted in stationary points with all frequencies real, except for $2XeOF_4 \cdot XeF_2$ and $XeOF_4 \cdot 4XeF_2$ which had two imaginary frequencies at the B3LYP level. The energy-minimized geometries and vibrational frequencies for $XeOF_4$(C_{4v}), (Table G6) XeF_2 ($D_{\infty h}$), and KrF_2 ($D_{\infty h}$) (Table G7), were also obtained at the SVWN, B3LYP and PBE1PBE levels of theory for use as benchmarks.

The structure of $XeOF_4 \cdot 2NgF_2$ was calculated to mimic the local NgF_2 environment in the crystal structures of $XeOF_4 \cdot NgF_2$. In the crystal structures, the XeF_2 molecule is symmetrically coordinated to two $XeOF_4$ molecules; the KrF_2 molecule is symmetrically coordinated to two or four $XeOF_4$ molecules, and in all cases, the local symmetry (including the Xe···F bridge interactions with $XeOF_4$) of the NgF_2 molecule is C_s (see X-ray Crystallography). In $2XeOF_4 \cdot NgF_2$, the NgF_2 molecule is symmetrically coordinated to two $XeOF_4$ molecules providing a local environment for the NgF_2 molecule that is a good approximation of that in the crystal structure. The $XeOF_4 \cdot 4XeF_2$ and $XeOF_4 \cdot 2KrF_2$ structures were calculated to mimic the local environment of $XeOF_4$ in the crystal structure of $XeOF_4 \cdot NgF_2$. In $XeOF_4 \cdot XeF_2$, each $XeOF_4$ molecule has four short contacts to fluorine atoms of an adjacent XeF_2 molecule, whereas in $XeOF_4 \cdot KrF_2$, the $XeOF_4$ molecule has two short contacts to KrF_2 molecules and two additional long contacts (see Section 9.2.3). The $XeOF_4 \cdot 2KrF_2$ structure was also used as a model for the

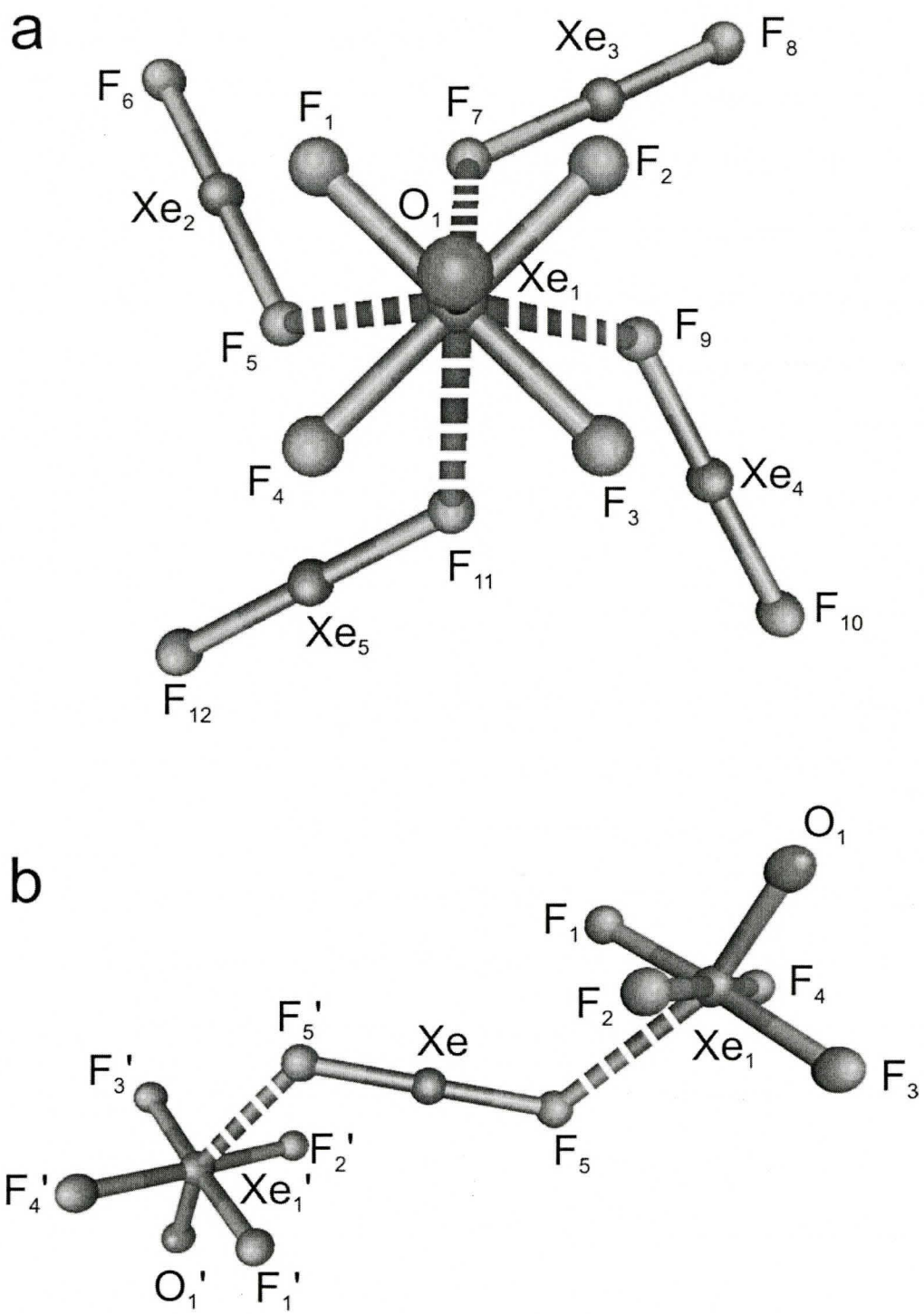

Figure 9.7. Calculated PBE1PBE/aug-cc-pVTZ(-PP) gas-phase geometry for (a) $XeOF_4 \cdot 4XeF_2$ (C_4) and (b) $2XeOF_4 \cdot XeF_2$ (C_{2h}).

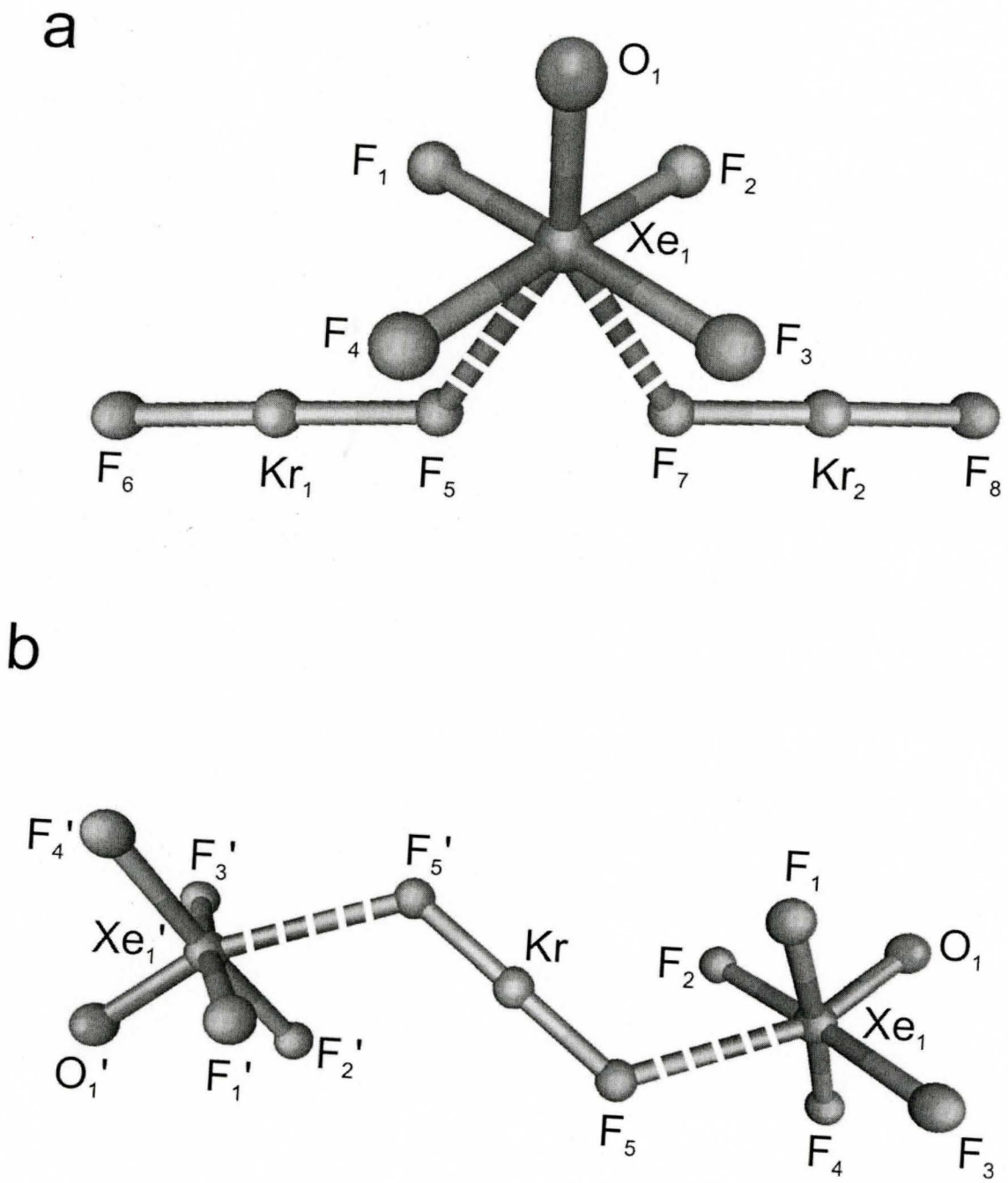

Figure 9.8. Calculated PBE1PBE/aug-cc-pVTZ(-PP) gas-phase geometry for (a) $XeOF_4 \cdot 2KrF_2$ (C_1) and (b) $2XeOF_4 \cdot KrF_2$ (C_{2h}).

structure of $XeOF_4 \cdot nKrF_2$. In $XeOF_4 \cdot 4XeF_2$ (C_4 symmetry), the XeF_2 molecules are symmetrically coordinated to the $XeOF_4$ molecule giving a good approximation of $XeOF_4 \cdot XeF_2$ in the crystal structure. The $XeOF_4 \cdot 2KrF_2$ structure (C_1 symmetry) only takes into account two short KrF_2 contacts, but still provides a good approximation of the $XeOF_4$ molecule in the crystal structure.

9.2.5.1. Calculated Geometries

The energy-minimized geometries for $2XeOF_4 \cdot NgF_2$ (Ng = Xe, Kr) (Table 9.3 and 9.4), $XeOF_4 \cdot 4XeF_2$ (Table 9.3), and $XeOF_4 \cdot 2KrF_2$ (Table 9.4) are similar at all levels, although the SVWN geometries predict significantly shorter Xe---F contacts. Although identical trends are expected at all levels, the values calculated at the PBE1PBE level provide the best overall agreement with experiment and are explicitly referred to.

9.2.5.1.1. $2XeOF_4 \cdot NgF_2$ (Ng = Xe, Kr).

The $Xe_1–F_5$ (1.999 Å) and Kr–F_5 (1.868 Å) bond lengths are slightly underestimated when compared with experiment (2.104(5) and 1.896(3) Å, respectively). As expected and observed in the experimental structures, they are slightly elongated when compared with the calculated free molecule (1.986 and 1.861 Å, respectively).

The Xe···F_5 contact length (2.890 Å) in $2XeOF_4 \cdot XeF_2$ is significantly underestimated when compared with experiment (3.239(4) Å). The discrepancy may be linked to the simplified model which involves one $XeOF_4$ group per fluorine atom, instead of two $XeOF_4$ groups per fluorine atom in the experimental structure, resulting in a shorter calculated $Xe_1 \cdots F_5$ contact. In contrast, the $Xe_1 \cdots F_5$ contact (2.943 Å) in

$2XeOF_4 \cdot KrF_2$ is in very good agreement with the two short contacts in the crystal structure of $XeOF_4 \cdot KrF_2$ (2.962(2) and 3.009(3) Å).

The $Xe_1–F_{1,2}$ (1.935 and 1.933 Å, respectively) bond lengths of the $XeOF_4$ molecule are slightly elongated when compared with those of $Xe_1–F_{3,4}$ (1.925 and 1.924 Å, respectively). The asymmetry in the bond lengths results in the calculated structure having C_{2v} symmetry instead of local C_{4v} symmetry observed in the crystal structure. The Xe–F bond lengths of $XeOF_4 \cdot NgF_2$ (Ng = Xe, 1.900(3); Kr, 1.893(2) Å) and those calculated for $XeOF_4$ (1.924 Å) do not show this asymmetry.

9.2.5.1.2. $XeOF_4 \cdot 4XeF_2$ and $XeOF_4 \cdot 2KrF_2$.

The calculated $Xe_1–O_1$ and $Xe_1–F_1$ bond lengths of $XeOF_4 \cdot 4XeF_2$ (1.727 and 1.928 Å) and $XeOF_4 \cdot 2KrF_2$ (1.726 and 1.933 Å) are in good agreement with the experimental values for $XeOF_4 \cdot XeF_2$ (1.729(7) and 1.900(3) Å), $XeOF_4 \cdot KrF_2$ (1.711(2) and 1.893 to 1.913(3) Å), and the gas-phase microwave (1.70(5) and 1.95(5) Å) and electron diffraction (1.71(1) and 1.901(3) Å) structures of $XeOF_4$, respectively and with the calculated values for free $XeOF_4$ (1.726 and 1.924 Å). The calculated $O_1–Xe_1–F_1$ bond angles of $XeOF_4 \cdot 4XeF_2$ (90.3°) and $XeOF_4 \cdot 2KrF_2$ (90.9°) are close to 90°, in agreement with the experimental bond angles of $XeOF_4 \cdot XeF_2$ (89.2(1)°) and $XeOF_4 \cdot KrF_2$ (89.4(1) to 90.1(1)°). This near 90° bond angle contrasts with the O–Xe–F bond angles calculated for gas-phase $XeOF_4$ (92.0°). The slightly smaller bond angle results from the increased steric repulsion between the equatorial fluorine atoms of $XeOF_4$ and the fluorine atoms of the coordinated NgF_2 molecules.

The $Xe_1\cdots F_5$ contacts of $XeOF_4{\cdot}4XeF_2$ (3.357 Å) and $XeOF_4{\cdot}2KrF_2$ (2.957 Å) are in good agreement with experiment for $XeOF_4{\cdot}XeF_2$ (3.239(4) Å) and $XeOF_4{\cdot}KrF_2$ (2.962(2) and 3.009(3) Å) although the asymmetry of the Xe···F contacts in the crystal structure of $XeOF_4{\cdot}KrF_2$ is not reproduced by the calculated structure of $XeOF_4{\cdot}2KrF_2$. The Ng–F_5 bond lengths of the adducted NgF_2 molecules are rendered non-equivalent because of coordination to $XeOF_4$. The adducted Ng–F_5 bond lengths (Xe_2, 2.006 Å and Kr_1, 1.884 Å) are underestimated when compared with the experimental values (Xe_2, 2.104(5) Å and Kr_1, 1.896(3) Å). Both bond lengths are longer than those of the calculated gas-phase NgF_2 molecules (Xe, 1.986 and Kr, 1.861 Å).

The Ng–F_5---Xe_1 bond angle of $XeOF_4{\cdot}4XeF_2$ (122.7°) is slightly more open than that of $XeOF_4{\cdot}2KrF_2$ (117.5°). The increased Xe–F_5---Xe angle in $XeOF_4{\cdot}4XeF_2$ compared to the experimental structure (116.8(1)°) is likely a result of additional intermolecular contacts in the crystal structure that are not taken into account in the present model. To the contrary, the Kr–F---Xe angle for $XeOF_4{\cdot}2KrF_2$ is more closed than in the experimental structure (123.4(1) and 145.4(1)°), which is likely a result of the higher coordination in the crystal structure causing more repulsion between fluorine atoms of each KrF_2 molecule.

The calculated NgF_2 molecules have near-linear F–Ng–F bond angles (Xe_2, 179.0 and Kr_1, 174.4°) which are comparable to those in the crystal structures (Xe, 180.00(0) and Kr, 178.96(7)°).

9.2.5.2. Charges, Valencies, and Bond Orders.

The Natural Bond Orbital (NBO)[181-184] analyses were carried out for the SVWN-, B3LYP-, and PBE1PBE-optimized gas-phase geometries of $2XeOF_4 \cdot NgF_2$ (Ng = Xe, Kr) (Table G8), $XeOF_4 \cdot 4XeF_2$, $XeOF_4 \cdot 2KrF_2$ (Table G9) $XeOF_4$ (Table G10), XeF_2, and KrF_2 (Table G11). Although all values are similar and because the PBE1PBE geometries better reproduce the experimental geometries (see Section 9.2.5.1), only the PBE1PBE values are explicitly referred to in the ensuing discussion.

The natural population analyses (NPA) give positive charges of 3.17, 3.16, 3.18 and 3.18 for the Xe_1 of the $XeOF_4$ molecule in the structures of $2XeOF_4 \cdot XeF_2$, $2XeOF_4 \cdot KrF_2$, $XeOF_4 \cdot 4XeF_2$, and $XeOF_4 \cdot 2KrF_2$, respectively. The charges on the Ng atoms are 1.26, 1.06, 1.24, 1.05, respectively, with the smaller charges being associated with the Kr atoms. The F_5 atoms directly bonded to the Ng atom in $2XeOF_4 \cdot NgF_2$ (Ng = Xe, Kr), have a charge of –0.63 and –0.53, respectively. The charges reveal that the Xe–F bond is more polar as compared to that of the Kr–F bond in agreement with the increased electronegativity of Kr as opposed to Xe. The fluorine and oxygen atoms all have a negative charge indicating that the bonding in the $XeOF_4$ and NgF_2 molecules is polar covalent.

The Xe–O (0.93) and Xe–F (0.39) bond orders in all structures are the same and suggest very little influence due to the different coordination motifs of the $XeOF_4$ molecules in the four structures. These values are also very close to those of gaseous $XeOF_4$ (0.94 and 0.40, respectively), indicating that association of the NgF_2 molecules does not greatly affect the bond orders of the $XeOF_4$ molecule.

The Ng–F bond orders of the symmetrically coordinated XeF_2 (0.31) and KrF_2 (0.32) molecules of $2XeOF_4 \cdot NgF_2$ (Ng = Xe, Kr, respectively) are very similar to those of the free XeF_2 (0.29) and KrF_2 (0.31) molecules. The Ng–F bond orders in the $XeOF_4 \cdot 4XeF_2$ and $XeOF_4 \cdot 2KrF_2$ structures are asymmetric (XeF_2, 0.28 and 0.31; KrF_2, 0.29 and 0.34, respectively), and the smaller Ng–F bond order is associated with the adducted fluorine atom.

The Xe_1---F bond orders in all four structures are all less that 0.04, indicating that the interactions between $XeOF_4$ and NgF_2 are weak. The Xe_1---F bond order in $2XeOF_4 \cdot NgF_2$ does not change upon coordination of XeF_2 (0.03) or (0.03). In contrast, the Xe_1---F bond order in the $XeOF_4 \cdot 4XeF_2$ structure (0.01) is significantly less that that of $XeOF_4 \cdot 2KrF_2$ (0.03), and is likely a result of the bonding being distributed between four molecules for $XeOF_4 \cdot 4XeF_2$ rather than two for $XeOF_4 \cdot 2KrF_2$.

9.3. Conclusions.

The $XeOF_4 \cdot NgF_2$ (Ng = Xe, Kr) addition compounds have been synthesized by reaction of NgF_2 with $XeOF_4$. The $XeOF_4 \cdot KrF_2$ structure provides the first example of a compound containing a bridging KrF_2 molecule, and the first example of a mixed Xe/Kr noble-gas compound. In the solid state, the $XeOF_4 \cdot NgF_2$ addition compounds are formulated as 1:1 adducts. The NgF_2 molecules are symmetrically coordinated to two or four $XeOF_4$ molecules. The Xe atoms of both $XeOF_4$ molecules are nine-coordinate, including three or four contacts to NgF_2 molecules, and the coordination sphere of Xe is based on a monocapped square antiprism. The ^{19}F and ^{129}Xe NMR spectra of solutions of

NgF_2 in $XeOF_4$ do not show any evidence for an associated compound in solution. The calculated structures of $2XeOF_4 \cdot NgF_2$, $XeOF_4 \cdot 2KrF_2$, and $XeOF_4 \cdot 4XeF_2$ have been used to provide close approximations of the local environments of the NgF_2 and $XeOF_4$ molecules in the experimental structures. The vibrational modes of both molecular addition compounds have been described based on these calculated structures, with little vibrational coupling between the $XeOF_4$ and NgF_2 molecules. A different phase of a $XeOF_4 \cdot nKrF_2$ addition compound has also been synthesized and assigned based on the calculated structure for $XeOF_4 \cdot 2KrF_2$.

CHAPTER 10

CONCLUSIONS AND DIRECTIONS FOR FUTURE WORK

10.1. Conclusions

The chemistry of osmium in the plus eight oxidation state was significantly extended in the present work. The fluoride ion donor and acceptor properties of *cis*-OsO_2F_4 were further investigated through the synthesis and full structural characterization of [*cis*-OsO_2F_3][Sb_2F_{11}] and the spectroscopic characterization of the *cis*-$OsO_2F_5^-$ anion. The previously known *cis*-$OsO_2F_3^+$ cation exists in the solid state as a closely associated ion pair with the $Sb_2F_{11}^-$ rendering the coordination sphere of the Os atom pseudo-octahedral with a *cis*-dioxo arrangement.

The *cis*-$OsO_2F_5^-$ anion has been shown to exist as a monocapped trigonal prism both in the solid state by Raman spectroscopy and in solution by ^{19}F NMR spectroscopy. Attempts to crystallize the anion were unsuccessful, but did yield a series of *cis*-OsO_2F_4·[M][CH_2CN] structures (M = Cs^+ and $N(CH_3)_4^+$) which result from abstraction of a proton from the CH_3CN solvent by a fluoride ion donated by *cis*-$OsO_2F_5^-$ to form *cis*-OsO_2F_4, CH_2CN^-, and HF. The crystal structure of *cis*-OsO_2F_4·[Cs][CH_2CN]·0.3HF offers further substantiation for this reaction pathway because the HF molecule is present in the crystal structure. Each of these structures provides the first examples of non-disordered *cis*-OsO_2F_4 molecule and the first crystal structures containing an isolated CH_2CN^- anion. The *cis*-OsO_2F_4 molecule was also crystallized independently from a XeF_6 melt. All of the structures confirm the *cis*-dioxo

octahedral geometry for *cis*-OsO_2F_4 and provide the most precise geometric parameters available for *cis*-OsO_2F_4.

Reactions of *fac*-OsO_3F_2 with the Xe(VI) compounds XeF_6 and $XeOF_4$ led to the syntheses of $[Xe_2F_{11}][OsO_3F_3]$, $[XeF_5][OsO_3F_3]$, $[XeF_5][\mu\text{-}F(OsO_3F_2)_2]$, and $(OsO_3F_2)_2{\cdot}2XeOF_4$. The $[Xe_2F_{11}][OsO_3F_3]$, $[XeF_5][OsO_3F_3]$, and $[XeF_5][\mu\text{-}F(OsO_3F_2)_2]$ salts were synthesized by means of stoichiometric reactions between XeF_6 and *fac*-OsO_3F_2. The crystal structures consist of highly associated ion pairs. The xenon atoms in the $[Xe_2F_{11}][OsO_3F_3]$ and $[XeF_5][\mu\text{-}F(OsO_3F_2)_2]$ salts are each 9-coordinate with the light atoms forming a distorted mono-capped square antiprism arrangement. The $[XeF_5][\mu\text{-}F(OsO_3F_2)_2]$ salt is unique because it is the only example of a 9-coordinate xenon atom in which all nine contacts to xenon are within a single ion pair whereas all other examples in the literature contain both intra- and inter-ion pair contacts. The xenon atom of the $[XeF_5][OsO_3F_3]$ salt is 8-coordinate, and all contacts are also within the ion pair.

Dissolution of *fac*-OsO_3F_2 in $XeOF_4$ solvent led to the isolation of the fluorine bridged (*fac*-$OsO_3F_2)_2{\cdot}2XeOF_4$ adduct upon removal of the solvent. The $(OsO_3F_2)_2$ dimer is coordinated to $XeOF_4$ through a short fluorine bridge rendering both the OsO_3F_3 units and $XeOF_4$ molecule octahedral. The $(OsO_3F_2)_2$ dimer was isolated by removal of the adducted $XeOF_4$ under dynamic vacuum and was characterized by Raman spectroscopy. The dimer rearranges back to the polymer when held at 25 °C for 1 h. Attempts to crystallize the dimer from CH_3CN solvent led to *fac*-$OsO_3F_2(NCCH_3){\cdot}2CH_3CN$. Characterization of the $OsO_3F_2(NCCH_3)$ adduct in SO_2ClF solution reveals the presence

of both the *fac*- and *mer*- isomers providing a rare example of a *mer*-trioxo d^0 transition metal compound.

The study of noble-gas difluoride molecular addition compounds of $XeOF_4$ was carried out for XeF_2 and KrF_2. The characterization of the $XeOF_4 \cdot XeF_2$ adduct confirmed the previous findings but provided the first complete assignment of the Raman spectrum and its crystal structure. The $XeOF_4 \cdot KrF_2$ adduct was also synthesized but crystallizes in a different space group and contains two crystallographically independent KrF_2 molecules. For both $XeOF_4 \cdot NgF_2$ (Ng = Kr or Xe) the Xe atoms of the $XeOF_4$ atoms are 9-coordinate with the XeF_2 adduct having four long contacts to XeF_2 molecules, while for the KrF_2 adduct there are three contacts to KrF_2 molecules and one to an adjacent $XeOF_4$ molecule. In all cases, both fluorine atoms of NgF_2 molecules are coordinated to one or more different $XeOF_4$ molecules.

10.2. Directions for Future Work

The $OsO_3F_2(NCCH_3)$ adduct synthesized in the present work suggests that the syntheses of other nitrogen base adducts of Os(VIII) oxide fluorides should be possible. One avenue of research would be to attempt the reaction of other nitrogen bases such as NSF_3 (eq 10.1) and HCN (eq 10.2) with OsO_3F_2 either as neat solutions at low

$$OsO_3F_2 + NSF_3 \xrightarrow{NSF_3} OsO_3F_2(NSF_3) \qquad (10.1)$$

$$OsO_3F_2 + HCN \longrightarrow OsO_3F_2(NCH) \qquad (10.2)$$

temperature in HF solvent to form the $OsO_3F_2(NSF_3)$ and $OsO_3F_2(NCH)$ complexes. If formed, the $OsO_3F_2(NSF_3)$ adduct would represent a rare Os---N–S linkage. In HF

solvent, the $OsO_3F_2(NSF_3)$ adduct may undergo solvolysis at higher temperatures in HF solvent to first form $OsO_3F_2(N(H)SF_4)$ (eq 10.3) and subsequently $OsO_3F_2(N(H_2)SF_5)$ (eq 10.4). A second possible direction would be to attempt the dissolution of $[OsO_3F][PnF_6]$

$$OsO_3F_2(NSF_3) + HF \xrightarrow{HF} OsO_3F_2(N(H)SF_4) \quad (10.3)$$

$$OsO_3F_2(N(H)SF_4) + 2HF \xrightarrow{HF} OsO_3F_2(N(H_2)SF_5) \quad (10.4)$$

(Pn = As, Sb) or $[OsO_3F][Sb_3F_{16}]$ in CH_3CN to form the adduct cation, $OsO_3F(NCCH_3)_2^+$ (eq 10.5). While the OsO_3F^+ cation is likely to be aggressively oxidizing, if this reaction

$$[OsO_3F][PnF_6] + 2CH_3CN \xrightarrow{CH_3CN} [OsO_3F(NCCH_3)_2][PnF_6] \quad (10.5)$$

is carried out at low-temperature it may be possible to stabilize the adduct cation. By analogy to the *fac*- and *mer*-$OsO_3F_2(NCCH_3)$ adducts, the $OsO_3F(NCCH_3)_2^+$ may exist as a mixture of *fac*- and *mer*-isomers.

Attempts to react OsO_4 with XeF_6 as an extension of the $[Xe_nF_{5n+1}][OsO_3F_3]$ (n = 1, 2) salts that were synthesized in the present work should be attempted. There are three possible reaction pathways that such a reaction could take: (1) Xenon hexafluoride is known to fluorinate the transition metal oxide fluorides MO_3F (M = Re,[45] Tc[200]) to form MO_2F_3 (eq 10.6) and, by analogy, XeF_6 may fluorinate OsO_4 to form OsO_3F_2 (eq 10.7) which would represent a new synthetic pathway to *fac*-OsO_3F_2. (2) Osmium

$$MO_3F + XeF_6 \xrightarrow{HF} MO_2F_3 + XeOF_4 \qquad (M = Re, Tc) \quad (10.6)$$

$$OsO_4 + XeF_6 \longrightarrow OsO_3F_2 + XeOF_4 \quad (10.7)$$

tetroxide is known to act as a fluoride ion acceptor towards [Cs][F],[24] $[N(CH_3)_4][F]$,[23] and [Rb][F][24] and XeF_6 can act as a fluoride ion donor, therefore, it may be possible to form a $[Xe_nF_{5n+1}][OsO_4F]$ (n = 1,2) salt (eq 10.8). (3) There may be no reaction but rather an

adduct such as $OsO_4 \cdot 2XeF_6$ could be formed (eq 10.9). If the second or third reaction

$$XeF_6 + OsO_4 \longrightarrow [XeF_5][OsO_4F] \quad (10.8)$$

$$2XeF_6 + OsO_4 \longrightarrow OsO_4 \cdot 2XeF_6 \quad (10.9)$$

pathways proves viable, it would be very interesting to determine the geometries of such compounds to see if the Os atoms are octahedral or trigonal bipyramidal and what kind of interaction they would have with the Xe atoms. Also it would be interesting to determine the coordination sphere around each xenon atoms.

The pentafluorooxotellurate ($OTeF_5$) group has been previously used as a substitute for fluorine in high-oxidation state oxo-compounds such as $ReO_2(OTeF_5)_3$,[270] $ReO(OTeF_5)_5$,[271] $MoO(OTeF_5)_4$,[272] $OsO(OTeF_5)_4$[272] and $WO(OTeF_5)_4$.[273] The syntheses of the $OTeF_5$ analogues of *fac*-OsO_3F_2, *cis*-OsO_2F_4, the OsO_4F^- and the *fac*-$OsO_3F_3^-$ anions by reaction of either $B(OTeF_5)_3$ or $[N(CH_3)_4][OTeF_5]$ (eqs 10.10-10.13) should be possible.

$$3\textit{fac}\text{-}OsO_3F_2 + 2B(OTeF_5)_3 \longrightarrow 3OsO_3(OTeF_5)_2 + 2BF_3 \quad (10.10)$$

$$3\textit{cis}\text{-}OsO_2F_4 + 4B(OTeF_5)_3 \longrightarrow 3\textit{cis}\text{-}OsO_2(OTeF_5)_4 + 4BF_3 \quad (10.11)$$

$$OsO_4 + [N(CH_3)_4][OTeF_5] \longrightarrow [N(CH_3)_4][OsO_4(OTeF_5)] \quad (10.12)$$

$$OsO_3(OTeF_5)_2 + [N(CH_3)_4][OTeF_5] \longrightarrow [N(CH_3)_4][OsO_3(OTeF_5)_3] \quad (10.13)$$

This series of compounds should provide an interesting structural study to determine if the large $OTeF_5$ ligands are able to alter the predominant *cis*- or *fac*-trioxo arrangement of all other Os(VIII) compounds.

Synthesis of the highest oxide fluoride of Os(VIII), $OsOF_6$, should be attempted. A computational study on the stability of $OsOF_6$ predicts that it should be stable towards all unimolecular gas-phase decomposition channels, however, it should be unstable

towards bimolecular channels.[187] Based on the predicted thermodynamic stability of $OsOF_6$ it may be possible to synthesize it at low temperatures. Reaction of *cis*-OsO_2F_4 with the strongest oxidizers KrF_2 and $[KrF][AsF_6]$ does not proceed, but it may be possible to use KrF_2 or KrF^+ to oxidize the $OsO_2F_5^-$ (eq 10.14) or $OsOF_5^-$ (eq 10.15)

$$KrF_2 + [Cs][OsO_2F_5] \longrightarrow [Cs][OsOF_7] + Kr + \tfrac{1}{2}O_2 \qquad (10.14)$$

$$KrF_2 + [Cs][OsOF_5] \longrightarrow [Cs][OsOF_7] + Kr \qquad (10.15)$$

anions to form an $OsOF_7^-$ salt because of the inherent greater stabilities of anions when compared with cations and neutral species. Another possible route to $OsOF_6$ would be to oxidize the known Os(VII) compound $OsOF_5$[274] with KrF_2 (eq 10.16) which could provide a direct route to $OsOF_6$.

$$OsOF_5 + KrF_2 \longrightarrow OsOF_6 + Kr + \tfrac{1}{2}F_2 \qquad (10.16)$$

REFERENCES

1. Gerken, M.; Schrobilgen, G. J. *Osmium(VIII) Chemistry*. in *Inorganic Chemistry Highlights*. Meyer, G.; Naumann, D.; Wesemann, L. Eds.; Wiley-VCH Verlag GmbH: Weinheim, Germany, **2005**, *14*, pp. 243-266
2. Ahlert, S.; Klein, W.; Jepsen, O.; Gunnarsson, O.; Anderson, O. K.; Jansen, M. *Angew. Chem., Int. Ed. Engl.* **2003**, *42*, 4322-4325.
3. Ahlert, S.; Diekhöner, L.; Sordan, R.; Kern, K.; Jansen, M. *Chem. Commun.* **2004,** 462-463.
4. Mercer, E. E.; Farrar, D. T. *Can. J. Chem.* **1969**, *47*, 581–586.
5. Gunn, S. R. *J. Am. Chem. Soc.* **1965**, *87*, 2290–2291.
6. Hamilton, W. C.; Ibers, J. A.; Mackenzie, D. R. *Science* **1963**, *141*, 532–534.
7. Zalkin, A.; Forrester, J. D.; Templeton, D. H.; Williamson, S. M.; Koch, C. W. *Science* **1963**, *142*, 501–502.
8. Zalkin, A.; Forrester, J. D.; Templeton, D. H. *Inorg. Chem.* **1964,** 3, 1417–1421.
9. Ibers, J. A.; Hamilton, W. C.; MacKenzie, D. R. *Inorg. Chem.* **1964**, *3*, 1412–1416.
10. Zalkin, A.; Forrester, J. D.; Templeton, D. H.; Williamson, S. M.; Koch, C. W. *J. Am. Chem. Soc.* **1964**, *86*, 3569–3571.
11. Bougon, R.; Buu, B.; Seppelt, K. *Chem. Ber.* **1993**, *126*, 1331–1336.
12. Bougon, R. *J. Fluorine Chem.* **1991**, *53*, 419–427.
13. Christe, K. O.; Bougon, R. *J. Chem. Soc., Chem. Commun.* **1992**, 1056–1056.
14. Beattie, I. R.; Blayden, H. E.; Crocombe, R. A.; Jones, P. J.; Ogden, J. S. *J. Raman Spectrosc.* **1976**, *4*, 313–322.

15. Hope, E. G.; Levason, W.; Ogden, J. S. *J. Chem. Soc., Dalton Trans.* **1988**, 61–65.

16. Beattie, I. R.; Livingston, K. M. S.; Reynolds, D. J.; Ozin, G. A. *J. Chem. Soc. A.* **1970**, 1210–1216.

17. Falconer, W. E.; Disalvo, F. J.; Griffiths, J. E.; Stevie, F. A.; Sunder, W. A.; Vasile, M. J. *J. Fluorine Chem.* **1975**, *6*, 499–520.

18. Hughes, M. J.; Mercier, H. P. A.; Schrobilgen, G. J. *Inorg. Chem.* **2009**, *48*, 4478–4490.

19. Nghi, N.; Bartlett, N. *C. R. Acad. Sci.* **1969**, *269*, 756–759.

20. Christe, K. O.; Dixon, D. A.; Mack, H. G.; Oberhammer, H.; Pagelot, A.; Sanders, J. C. P.; Schrobilgen, G. J., *J. Am. Chem. Soc.* **1993**, *115*, 11279–11284.

21. Gerken, M.; Dixon, D. A.; Schrobilgen, G. J., *Inorg. Chem.* **2002**, *41*, 259–277.

22. Casteel, W. J.; Dixon, D. A.; Mercier, H. P. A.; Schrobilgen, G. J. *Inorg. Chem.* **1996**, *35*, 4310–4322.

23. Gerken, M.; Dixon, D. A.; Schrobilgen, G. J. *Inorg. Chem.* **2000**, *39*, 4244–4255.

24. Jones, P. J.; Levason, W.; Tajik, M. *J. Fluorine Chem.* **1984**, *25*, 195–201.

25. Hepworth, M. A.; Robinson, P. L. *J. Inorg. Nucl. Chem.* **1957**, *4*, 24–29.

26. Brewer, S. A.; Brisdon, A. K.; Holloway, J. H.; Hope, E. G.; Levason, W.; Ogden, J. S.; Saad, A. K. *J. Fluorine Chem.* **1993,** 60, 13–17.

27. Behnam Azad, B. Synthesis and Structural Studies of the Osmium(VIII) Anion, $OsO_2F_5^-$. B. Sc. Thesis, McMaster University, Hamilton, ON, 2005.

28. Gerken, M. Syntheses and Characterization of XeO_4 and Oxide Fluorides of Xenon(VIII), Osmium(VIII), Iodine(VIII), and Xenon(II). Ph.D. Thesis, McMaster University, Hamilton, ON, 2000.

29. Burbank, R. D. *J. Appl. Crystallogr.* **1974**, *7*, 41–44.

30. Burns, R. C.; O'Donnell, T. A. *Inorg. Synth.* **1986**, *24*, 79–81.

31. Weinstock, B.; Malm, J. G. *J. Am. Chem. Soc.* **1958**, *80*, 4466–4468.

32. Weinstock, B.; Claassen, H. H.; Malm, J. G., *J. Chem. Phys.* **1960**, *32*, 181–185.

33. Moffitt, W.; Goodman, G. L.; Fred, M.; Weinstock, B. *Mol. Phys.* **1959**, *2*, 109–122.

34. Vovna, V. I.; Dudin, A. S.; Lopatin, S. N.; Rakov, E. G. *Koord. Khim.* **1980**, *6*, 1580–1584.

35. Drews, T.; Supel, J.; Hagenbach, A.; Seppelt, K. *Inorg. Chem.* **2006**, *45*, 3782–3788.

36. Selig, H.; Sunder, W. A.; Disalvo, F. A.; Falconer, W. E. *J. Fluorine Chem.* **1978**, *11*, 39–50.

37. Burns, R. C.; Odonnell, T. A.; Waugh, A. B. *J. Fluorine Chem.* **1978**, *12*, 505–517.

38. Falconer, W. E.; Burbank, R. D.; Jones, G. R.; Sunder, W. A.; Vasile, M. J., *J. Chem. Soc., Chem. Commun.* **1972**, 1080–1081.

39. Alexeichuk, I. S.; Ugarov, V. V.; Rambidi, N. G.; Legasov, V. A.; Sokolov, V. B., *Dokl. Akad. Nauk* **1981**, *257*, 625–628.

40. Sunder, W. A.; Stevie, F. A. *J. Fluorine Chem.* **1975**, *6*, 449–463.

41. Shorafa, H.; Seppelt, K. *Z. Anorg. Allg. Chem.* **2007**, *633*, 543–547.

42. Shustorovich, E. M.; Buslaev, I. A. *Inorg. Chem.* **1976**, *15*, 1142–1147.

43. Lyne, P., D.; Mingos, D. M., P. *J. Chem. Soc., Dalton Trans.* **1995**, 1635–1643.

44. Rhiel, M.; Wocadlo, S.; Massa, W.; Dehnicke, K. *Z. Anorg. Allg. Chem.* **1996**, *622*, 1195–1199.

45. Casteel, W. J.; Dixon, D. A.; LeBlond, N.; Lock, P. E.; Mercier, H. P. A.; Schrobilgen, G. J. *Inorg. Chem.* **1999**, *38*, 2340–2358.

46. LeBlond, N.; Dixon, D. A.; Schrobilgen, G. J. *Inorg. Chem.* **2000**, *39*, 2473–2487.

47. Casteel, W. J.; Dixon, D. A.; LeBlond, N.; Mercier, H. P. A.; Schrobilgen, G. J. *Inorg. Chem.* **1998**, *37*, 340–353.

48. Leimkühler, M.; Mattes, R. *J. Solid State Chem.* **1986**, *65*, 260–264.

49. Supel, J.; Marx, R.; Seppelt, K. *Z. Anorg. Allg. Chem.* **2005**, *631*, 2979–2986.

50. Abrahams, S. C.; Marsh, P.; Ravez, J. *J. Chem. Phys.* **1987**, *87*, 6012–6020.

51. Gillespie, R. J.; Bytheway, I.; Tang, T. H.; Bader, R. F. W. *Inorg. Chem.* **1996**, *35*, 3954–3963.

52. Boatz, J. A.; Christe, K. O.; Dixon, D. A.; Fir, B. A.; Gerken, M.; Gnan, R. Z.; Mercier, H. P. A.; Schrobilgen, G. J. *Inorg. Chem.* **2003**, *42*, 5282–5292.

53. Christe, K. O.; Wilson, W. W.; Wilson, R. D.; Bau, R.; Feng, J.-a. *J. Am. Chem. Soc.* **1990**, *112*, 7619–7625.

54. Christe, K. O.; Wilson, W. W. *J. Fluorine Chem.* **1990,** 47, 117-120.

55. Kruger, C. *J. Organomet. Chem.* **1967,** 9, 125–134.

56. Rossi, L.; Feroci, M.; Inesi, A. *Mini-Reviews in Organic Chemistry* **2005**, *2*, 79–90.

57. Dahl, O.; Larsen, S. *J. Chem. Res.* **1979**, 396–397.

58. Porta, F.; Ragaini, F.; Cenini, S. *Organometallics* **1990**, *9*, 929–935.

59. Krieger, M.; Gould, R. O.; Dehnicke, K., *Z. Anorg. Allg. Chem.* **2002**, *628*, 1289–1293.

60. Das, R.; Wilkie, C., A. *J. Am. Chem. Soc.* **1972**, *94*, 4555–4557.

61. Burbank, R. D.; Jones, G. R. *Science* **1971**, *171*, 485–487.

62. Burbank, R. D.; Jones, G. R. *J. Am. Chem. Soc.* **1974**, *96*, 43–48.

63. Hoyer, S.; Emmler, T.; Seppelt, K. *J. Fluorine Chem.* **2006**, *127*, 1415–1422.

64. Schreiner, F.; Osborne, D. W.; Malm, J. G.; McDonald, G. N. *J. Chem. Phys.* **1969**, *51*, 4838–4851.

65. Adams, C. J.; Bartlett, N. *Isr. J. Chem.* **1978**, *17*, 114–125.

66. Gasner, E. J.; Claassen, H. H. *Inorg. Chem.* **1967**, *6*, 1937–1938.

67. Seppelt, K.; Rupp, H. H. *Z. Anorg. Allg. Chem.* **1974**, *409*, 331–337.

68. Schrobilgen, G. J.; Holloway, J. H.; Granger, P.; Brevard, C. *Inorg. Chem.* **1978**, *17*, 980–987.

69. Bartlett, N.; Sladky, F. O. *J. Am. Chem. Soc.* **1968**, *90*, 5316–5317.

70. Lutar, K.; Jesih, A.; Žemva, B. *Rev. Chim. Miner.* **1986**, *23*, 565–571.

71. Lutar, K.; Jesih, A.; Leban, I.; Žemva, B.; Bartlett, N. *Inorg. Chem.* **1989**, *28*, 3467–3471.

72. Žemva, B.; Milićev, S.; Slivnik, J. *J. Fluorine Chem.* **1978**, *11*, 519–526.

73. Selig, H. *Science* **1964**, *144*, 537.

74. Pullen, K. E.; Cady, G. H. *Inorg. Chem.* **1967**, *6*, 2267–2268.

75. Bartlett, N.; Wechsberg, M. *Z. Anorg. Allg. Chem.* **1971**, *385*, 5–17.

76. Bartlett, N.; DeBoer, B. G.; Hollander, F. J.; Sladky, F. O.; Templeton, D. H.; Zalkin, A. *Inorg. Chem.* **1974**, *13*, 780–785.

77. Gillespie, R. J.; Schrobilgen, G. J. *Inorg. Chem.* **1974**, *13*, 765–770.

78. Christe, K. O.; Curtis, E. C.; Wilson, R. D. *J. Inorg. Nucl. Chem. Suppl.* **1976**, *12*, 159–165.

79. Žemva, B.; Jesih, A.; Templeton, D. H.; Zalkin, A.; Cheetham, A. K.; Bartlett, N. *J. Am. Chem. Soc.* **1987**, *109*, 7420–7427.

80. Leary, K.; Zalkin, A.; Bartlett, N. *Inorg. Chem.* **1974**, *13*, 775–779.

81. Leary, K.; Bartlett, N. *Chem. Commun.* **1972**, 903–904.

82. Žemva, B. *Croat. Chem. Acta* **1988**, *61*, 163–187.

83. Lutar, K.; Borrmann, H.; Žemva, B. *Inorg. Chem.* **1998**, *37*, 3002–3006.

84. Emara, A. A. A.; Schrobilgen, G. J. *Inorg. Chem.* **1992**, *31*, 1323–1332.

85. Fele Beuermann, M.; Milićev, S.; Lutar, K.; Žemva, B. *Eur. J. Solid State Inorg. Chem.* **1994**, *31*, 545–556.

86. Mallouk, T. E.; Desbat, B.; Bartlett, N. *Inorg. Chem.* **1984**, *23*, 3160–3166.

87. Žemva, B.; Milićev, S.; Slivnik, J. *J. Fluorine Chem.* **1978**, *11*, 545–553.

88. Jesih, A.; Lutar, K.; Leban, I.; Žemva, B. *Eur. J. Solid State Inorg. Chem.* **1991**, *28*, 829–840.

89. Jesih, A.; Lutar, K.; Leban, I.; Žemva, B. *Inorg. Chem.* **1989**, *28*, 2911–2914.

90. Žemva, B.; Jesih, A. *J. Fluorine Chem.* **1984**, *24*, 281–289.

91. Leary, K.; Templeton, D. H.; Zalkin, A.; Bartlett, N. *Inorg. Chem.* **1973**, *12*, 1726–1730.

92. Bartlett, N.; Einstein, F.; Stewart, D. F.; Trotter, J. *J. Chem. Soc. A.* **1967**, 1190–1193.

93. Bartlett, N.; Gennis, M.; Gibler, D. D.; Morrell, B. K.; Zalkin, A. *Inorg. Chem.* **1973**, *12*, 1717–1721.

94. Gard, G. L.; Cady, G. H. *Inorg. Chem.* **1964**, *3*, 1745–1747.

95. Pointner, B. E.; Suontamo, R. J.; Schrobilgen, G. J. *Inorg. Chem.* **2006**, *45*, 1517–1534.

96. Pullen, K. E.; Cady, G. H. *Inorg. Chem.* **1966**, *5*, 2057–2059.

97. Desmarteau, D. D.; Eisenberg, M. *Inorg. Chem.* **1972**, *11*, 2641–2644.

98. Jesih, A.; Žemva, B.; Slivnik, J. *J. Fluorine Chem.* **1982**, *19*, 221–226.

99. Brown, T. H.; Whipple, E. B.; Verdier, P., H. *J. Chem. Phys.* **1963**, *38*, 3029–3030.

100. Brundle, C. R.; Jones, G. R. *J. Electron Spectrosc. Relat. Phenom.* **1973**, *1*, 403–407.

101. Tsao, P.; Cobb, C. C.; Claassen, H. H. *J. Chem. Phys.* **1971**, *54*, 5247.

102. Martins, J.; Wilson, E. B., Jr. *J. Chem. Phys.* **1964**, *41*, 570–571.

103. Martins, J. F.; Wilson, E. B. J. *J. Mol. Spectrosc.* **1968**, *26*, 410–417.

104. Jacob, E. J.; Thompson, H. B.; Bartell, L. S. *J. Mol. Struct.* **1971**, *8*, 383–394.

105. Bunic, T.; Tavcar, G.; Tramsek, M.; Žemva, B. *Inorg. Chem.* **2006**, *45*, 1038–1042.

106. Tramsek, M.; Benkič, P.; Žemva, B. *Inorg. Chem.* **2004**, *43*, 699–703.

107. Tramsek, M.; Lork, E.; Mews, R.; Žemva, B. *J. Solid State Chem.* **2001**, *162*, 243–249.

108. Elliott, H. S. A.; Lehmann, J. F.; Mercier, H. P. A.; Jenkins, H. D. B.; Schrobilgen, G. J. *Inorg. Chem.* **2010**, *49*, 8504-8523.

109. McRae, V. M.; Peacock, R. D.; Russell, D. R.. *J. Chem. Soc., Chem. Commun.* **1969**, 62–63.

110. Zalkin, A.; Ward, D. L.; Biagioni, R. N.; Templeton, D. H.; Bartlett, N. *Inorg. Chem.* **1978**, *17*, 1318-1322.

111. Hagiwara, R.; Hollander, F.; Maines, C.; Bartlett, N. *Eur. J. Solid State Inorg. Chem.* **1991**, *28*, 855–866.

112. Turičnik, A.; Benkič, P.; Žemva, B. *Inorg. Chem.* **2002**, *41*, 5521–5524.

113. Gerken, M.; Hazendonk, P.; Iuga, A.; Nieboer, J.; Tramsek, M.; Goreshnik, E.; Žemva, B.; Zheng, S.; Autschbach, J. *Inorg. Chem.* **2007**, *46*, 6069–6077.

114. Jones, G. R.; Burbank, R. D.; Bartlett, N. *Inorg. Chem.* **1970**, *9*, 2264–2268.

115. Tramsek, M.; Benkič, P.; Žemva, B. *Solid State Sciences* **2002**, *4*, 9–14.

116. Burns, J. H.; Ellison, R. D.; Levy, H. A. *Acta Crystallogr.* **1965**, *18*, 11–16.

117. Bunic, T.; Tramsek, M.; Goreshnik, E.; Žemva, B. *Solid State Sciences* **2008**, *10*, 1511–1516.

118. Brock, D. S.; Casalis de Pury, J. J.; Mercier, H. P. A.; Schrobilgen, G. J. *Inorg. Chem.* **2010**, *49*, 6673-6689.

119. Benkič, P.; Tramsek, M.; Žemva, B. *Solid State Sciences* **2002**, *4*, 1425–1434.

120. Bunic, T.; Tramsek, M.; Goreshnik, E.; Tavcar, G.; Žemva, B. *Inorg. Chem.* **2007**, *46*, 5276–5282.

121. Holloway, J. H.; Schrobilgen, G. J. *Inorg. Chem.* **1980**, *19*, 2632–2640.

122. Holloway, J. H.; Schrobilgen, G. J.; Taylor, P. *J. Chem. Soc., Chem. Commun.* **1975**, 40–41.

123. Holloway, J. H.; Schrobilgen, G. J. *Inorg. Chem.* **1981**, *20*, 3363–3368.

124. Brock, D. S.; Casalis de Pury, J. J.; Mercier, H. P. A.; Schrobilgen, G. J.; Silvi, B. *J. Am. Chem. Soc.* **2010**, *132*, 3533-3542.

125. Christe, K. O.; Wilson, W. W.; Bougon, R. A. *Inorg. Chem.* **1986**, *25*, 2163–2169.

126. Lehmann, J. F.; Dixon, D. A.; Schrobilgen, G. J. *Inorg. Chem.* **2001**, *40*, 3002–3017.

127. Winfield, J. M. *J. Fluorine Chem.* **1984**, *25*, 91–98.

128. Vogel, A. I. *Practical Organic Chemistry*. Longmans, Green and Co. LTD: London, 1948; pp 161.

129. Brauer, G., *Handbook of Preparative Inorganic Chemsitry*. 2nd ed.; Academic Press Inc: New York, 1965; Vol. 2, pp 1859.

130. Mercier, H. P. A.; Sanders, J. C. P.; Schrobilgen, G. J.; Tsai, S. S. *Inorg. Chem.* **1993**, *32*, 386–393.

131. Bezmel'nitsyn, V. N.; Legasov, V. A.; Chaivanov, B. B. *Dokl. Akad. Nauk* **1977**, *235*, 96–98.

132. Kinkead, S. A.; FitzPatrick, J. R.; Foropoulos, J. J.; Purson, J. D., *Inorganic Fluorine Chemistry, Towards the 21st Century,* Thrasher, J. S. Strauss, S. H. Eds; ACS Symposium Series 555; American Chemical Society: Washington D.C., 1994,

133. Chernick, C. L.; Malm, J. G. *Inorg. Synth.* **1966**, *8*, 259–260.

134. Schumacher, G. A.; Schrobilgen, G. J. *Inorg. Chem.* **1984**, *23*, 2923–2929.

135. Syvret, R. G.; Mitchell, K. M.; Sanders, J. C. P.; Schrobilgen, G. J. *Inorg. Chem.* **1992**, *31*, 3381-3385.

136. Fir, B. A. X-ray Crystal Structures of Xe(II)-N and Xe(II)-O Bonded Compounds, and the Syntheses of $OTeF_5$ Derivatives of As(III) and Sb(III). M. Sc. Thesis, McMaster, Hamilton, ON, 1999.

137. Bilir, V. Preparation and Characterization of $[C_6F_5Xe][OTeF_5]$ and $XeOF_2$. Duisburg-Essen., Hamilton, ON, 2005.

138. Brock, D. S.; Bilir, V.; Mercier, H. P.; Schrobilgen, G. J. *J. Am. Chem. Soc.* **2007**, *129*, 3598–3611.

139. Hughes, M. J.; Mercier, H. P. A.; Schrobilgen, G. J. *Inorg. Chem.* **2010**, *49*, 271–284.

140. *SMART, release 5.611, and SAINT, release 6.02;* Siemens Energy and Automotive Analytical Instrumentation Inc.: Madison, WI, 1999.

141. Sheldrick, G. M., *SADABS (Siemens Area Detector Absorption Corrections)*, version 2.10; Siemens Analytical X-ray Instruments Inc.; Madison, WI, 2004.

142. *APEX2*, Release 2.0–2; Bruker AXS Inc.: Madison, WI, 2005.

143. Sheldrick, G. M., *SHELXTL-Plus*, release 6.14; Siemens Analytical X-ray Instruments, Inc.; Madison, WI, 2000-2003.

144. Farrugia, L. J. *J. Appl. Crystallogr.* **1999**, *32*, 837–838.

145. *GADDS: General Area Detector Diffraction System*, V4.1.29 Smith, K. L.; Jin, Z.; Chambers, J. L.; He, B.; Preckwinkel U.; Moran P. D., Eds.; Bruker: Madison WI. 2007

146. Macrae, C. F.; Edgington, P. R.; McCabe, P.; Pidcock, E.; Shields, G. P.; Taylor, R.; Towler, M.; J., v. d. S.; Wood, P. A. *J. Appl. Crystallogr.* **2006**, *39*, 452–457.

147. *TOPAS V3: General profile and structure analysis software for powder diffraction data. - User's Manual*; Bruker AXS, Karlsruhe, Germany, 2005

148. Frisch, M. J.; Trucks, G. W.; Schlegel, H. B.; Scuseria, G. E.; Robb, M. A.; Cheeseman, J. R.; Zakrzewski, V. G.; Montgomery, J. A., Jr.; Stratmann, R. E.; Burant, J. C.; Dapprich, S.; Millam, J. M.; Daniels, A. D.; Kudin, K. N.; Strain, M. C.; Farkas, O.; Tomasi, J.; Barone, V.; Cossi, M.; Cammi, R.; Mennucci, B.; Pomelli, C.; Adamo, C.; Clifford, S.; Ochterski, J.; Petersson, G. A.; Ayala, P. Y.; Cui, Q.; Morokuma, K.; Salvador, P.; Dannenberg, J. J.; Malick, D. K.; Rabuck, A. D.; Raghavachari, K.; Foresman, J. B.; Cioslowski, J.; Ortiz, J. V.; Baboul, A. G.; Stefanov, B. B.; Liu, G.; Liashenko, A.; Piskorz, P. K., I.; Gomperts, R.; Martin, R. L.; Fox, D. J.; Keith, T.; Al-Laham, M. A.; Peng, C. Y.; Nanayakkara, A.; Challacombe, M.; Gill, P. M. W.; Johnson, B.; Chen, W.; Wong, M. W.; Andres, J. L.; Gonzalez, C.; Head-Gordon, M.; Replogle, E. S.; Pople, J. A., *Gaussian 98*, Revision A.11; Gaussian, Inc.; Pittsburgh, PA, 2003.

149. Frisch, M. J.; Trucks, G. W.; Schlegel, H. B.; Scuseria, G. E.; Robb, M. A.; Cheeseman, J. R.; Montgomery, J. A.; Vreven, J. T.; Kudin, K. N.; Burant, J. C.; Millam, J. M.; Iyengar, S. S.; Tomasi, J.; Barone, V.; Mennucci, B.; Cossi, M.; Scalmani, G.; Rega, N.; Petersson, G. A.; Nakatsuji, H.; Hada, M.; Ehara, M.; Toyota, K.; Fukuda, R.; Hasegawa, J.; Ishida, M.; Nakajima, T.; Honda, Y.; Kitao, O.; Nakai, H.; Klene, M.; Li, X.; Knox, J. E.; Hratchian, H. P.; Cross, J. B.; Adamo,

C.; Jaramillo, J.; Gomperts, R.; Stratmann, R. E.; Yazyev, O.; Austin, A. J.; Cammi, R.; Pomelli, C.; Ochterski, J. W.; Ayala, P. Y.; Morokuma, K.; Voth, G. A.; Salvador, P.; Dannenberg, J. J.; Zakrzewski, V. G.; Dapprich, S.; Daniels, A. D.; Strain, M. C.; Farkas, O.; Malick, D. K.; Rabuck, A. D.; Raghavachari, K.; Foresman, J. B.; Ortiz, J. V.; Cui, Q.; Baboul, A. G.; Clifford, S.; Cioslowski, J.; Stefanov, B. B.; Liu, G.; Liashenko, A.; Piskorz, P.; Komaromi, I.; Martin, R. L.; Fox, D. J.; Keith, T.; Al-Laham, M. A.; Peng, C. Y.; Nanayakkara, A.; Challacombe, M.; Gill, P. M. W.; Johnson, B.; Chen, W.; Wong, M. W.; Gonzalez, C.; Pople, J. A., *Gaussian 03* Revision B.04; Gaussian, Inc.; Pittsburgh, PA, 2003.

150. Frisch, M. J.; Trucks, G. W.; Schlegel, H. B.; Scuseria, G. E.; Robb, M. A.; Cheeseman, J. R.; Scalmani, G.; Barone, V.; Mennucci, G. A.; Petersson, B.; Nakatsuji, H.; Caricato, M.; Li, X.; Hratchian, H. P.; Izmaylov, A. F.; Bloino, J.; Zheng, G.; Sonnenberg, J. L.; Hada, M.; Ehara, M.; Toyota, K.; Fukuda, R.; Hasegawa, J.; Ishida, M.; Nakajima, T.; Honda, Y.; Kitao, O.; Nakai, H.; Vreven, T.; Montgomery, J. A. J.; Peralta, J. E.; Ogliaro, F.; Bearpark, M.; Heyd, J. J.; Brothers, E.; Kudin, K. N.; Staroverov, V. N.; Kobayashi, R.; Normand, J.; Raghavachari, K.; Rendell, A.; Burant, J. C.; Iyengar, S. S.; Tomasi, J.; Cossi, M.; Rega, N.; Millam, J. M.; Klene, M.; Knox, J. E.; Cross, J. B.; Bakken, V.; Adamo, C.; Jaramillo, J.; Gomperts, R.; Stratmann, R. E.; Yazyev, O.; Austin, A. J.; Cammi, R.; Pomelli, C.; Ochterski, J. W.; Martin, R. L.; Morokuma, K.; Zakrzewski, V. G.; Voth, G. A.; Salvador, P.; Dannenberg, J. J.; Dapprich, S.; Daniels, A. D.; Farkas,

O.; Foresman, J. B.; Ortiz, J. V.; Cioslowski, J.; Fox, D. J., *Gaussian 09*, Revision A.02: Gaussian, Inc.; Wallingford CT, 2009.

151. Huzinaga, S.; Andzelm, J.; Kolobukowski, M.; Radzio-Andzelm, E.; Sakai, Y.; Tatewaki, H., *Gaussian Basis Sets for Molecular Calculations*. Physical Science Data 16; Elsevier: Amsterdam, 1984.
152. Ehlers, A. W.; Bohme, M.; Dapprich, S.; Gobbi, A.; Hollwarth, A.; Jonas, V.; Kohler, K. F.; Stegmann, R.; Veldkamp, A.; Frenking, G. *Chem. Phys. Lett.* **1993**, *208*, 111–114.
153. Feller, D., *J. Comput. Chem.* **1996**, *17*, 1571-1586.
154. Schuchardt, K. L.; Didier, B. T.; Elsethagen, T.; Sun, L.; Gurumoorthi, V.; Chase, J.; Li, J.; Windus, T. L. *J. Chem. Inf. Model.* **2007**, 47.
155. Hughes, M. J.; Gerken, M.; Mercier, H. P. A.; Schrobilgen, G. J. *Inorg. Chem.* **2010**, *49*, 4768-4780.
156. *GaussView*, release 3.0; Gaussian Inc.: Pittsburgh, PA, 2003.
157. Schrobilgen, G. J.; Holloway, J. H.; Russell, D. R. *J. Chem. Soc., Dalton Trans.* **1984**, 1411–1415.
158. LeBlond, N.; Mercier, H. P. A.; Dixon, D. A.; Schrobilgen, G. J. *Inorg. Chem.* **2000**, *39*, 4494–4509.
159. Supel, J.; Abram, U.; Hagenbach, A.; Seppelt, K. *Inorg. Chem.* **2007**, *46*, 5591–5595.
160. McKee, D. E.; Zalkin, A.; Bartlett, N. *Inorg. Chem.* **1973**, *12*, 1713–1717.
161. Drews, T.; Seppelt, K. *Angew. Chem., Int. Ed. Engl.* **1997**, *36*, 273–274.

162. Lind, M. D.; Christe, K. O. *Inorg. Chem.* **1972**, *11*, 608–612.

163. Hwang, I.-C.; Seidel, S.; Seppelt, K. *Angew. Chem., Int. Ed. Engl.* **2003**, *42*, 4392–4395.

164. Vij, A.; Wilson, W. W.; Vij, V.; Tham, F. S.; Sheehy, J. A.; Christe, K. O. *J. Am. Chem. Soc.* **2001**, *123*, 6308–6313.

165. Bondi, A. *J. Phys. Chem.* **1964**, *68*, 441–451.

166. The long contacts within the sum of the van der Waals radii in $[OsO_2F_3][Sb_2F_{11}]$ are: F(1)···F(1A) (2.659(7) Å), F(1)···F(8B) (2.727(5) Å), F(1)···F(5A) (2.769(5) Å), O(2)···F(7C) (2.763(5) Å), F(7)···F(7C) (2.771(7) Å), F(8)···F(8B) (2.801(8) Å), and O(2)···F(10D) (2.808(4) Å), The corresponding sums of the van der Waals radii (taken from ref 165) are: F···F (2.94 Å) and O···F (2.99 Å).

167. The *cis*-dioxo geometry has d_{xy}, d_{yz}, and d_{xz} orbitals with correct symmetries for overlap with the p orbitals of oxygen, whereas the *trans*-dioxo geometry has one p orbital per oxygen ligand that has the correct symmetry to compete for a single d_{t2g} orbital on the metal. This causes the orbital energies of the *trans*-isomer to be higher than those of the *cis*-isomer, making the *cis*-isomer more favorable.

168. Edwards, A. J.; Jones, G. R.; Steventon, B. R. *Chem. Commun.* **1967**, 462–464.

169. The interatomic distances for the light atoms forming the coordination spheres of the Os atoms in $[OsO_2F_3][Sb_2F_{11}]$ are: O(1)···F(1,2,3) 2.659(6), 2.645(5), 2.654(5) Å; O(1)···O(2) 2.618(6) Å; F(4)···F(1,2,3) 2.564(5), 2.564 (5), 2.590(4) Å; F(1)···F(2,3) 2.499(5), 2.473(5) Å; O(2)···F(2,3) 2.521(5), 2.494(5) Å.

170. Hwang, I.-C.; Seppelt, K. *Inorg. Chem.* **2003**, *42*, 7116–7122.

171. Edwards, A. J.; Jones, G. R. *J. Chem. Soc. A* **1968**, 2074–2078.

172. Edwards, A. J.; Jones, G. R. *J. Chem. Soc. A* **1970**, 1891–1894.

173. Edwards, A. J.; Jones, G. R. *J. Chem. Soc. A* **1970**, 1491–1497.

174. Edwards, A. J. *J. Chem. Soc., Dalton Trans.* **1972**, 2325–2328.

175. Sham, I. H. T.; Patrick, B. O.; von Ahsen, B.; von Ahsen, S.; Willner, H.; Thompson, R. C.; Aubke, F. *Solid State Sciences* **2002**, *4*, 1457–1463.

176. Ahsen, B.; Bach, C.; Berkei, M.; Kockerling, M.; Willner, H.; Hagele, G.; Aubke, F. *Inorg. Chem.* **2003**, *42*, 3801–3814.

177. Gerken, M.; Moran, M. D.; Mercier, H. P. A.; Pointner, B. E.; Schrobilgen, G. J.; Hoge, B.; Christe, K. O.; Boatz, J. A. *J. Am. Chem. Soc.* **2009**, *131*, 13474–13489.

178. Al-Mukhtar, M.; Holloway, J. H.; Hope, E. G.; Schrobilgen, G. J. *J. Chem. Soc., Dalton Trans.* **1991**, 2831.

179. Willner, H.; Schaebs, J.; Hwang, G.; Mistry, F.; Jones, R.; Trotter, J.; Aubke, F., *J. Am. Chem. Soc.* **1992**, *114*, 8972–8980.

180. Benkič, P.; Jenkins, H. D. B.; Ponikvar, M.; Mazej, Z. *Eur. J. Inorg. Chem.* **2006**, 1084–1092.

181. Reed, A. E.; Weinstock, R. B.; Weinhold, F. *J. Chem. Phys.* **1985,** *83*, 735–746.

182. Glendening, E. D.; Reed, A. E.; Carpenter, J. E.; Weinhold, F. In *NBO Version 3.1*, Gaussian Inc.: Pittsburgh, PA, 1990.

183. Reed, A. E.; Curtiss, L. A.; Weinhold, F. *Chem. Rev.* **1998**, *88*, 899–926.

184. Glendening, E. D.; Badenhoop, J. K.; Reed, A. E.; Carpenter, J. E.; Bohmann, C. M.; Morales, C. M.; Weinhold, F., In *NBO Version 5.0*, Theoretical Chemical Institute, University of Wisconsin: Madison WI, 2001.

185. Jenkins, H. D. B. *Inorg. Chem.* **1999**, *38*, 3609–3620.

186. Jenkins, H. D. B.; Tudela, D.; Glasser, L. *Inorg. Chem.* **2002**, *41*, 2364–2367.

187. Riedel, S.; Kaupp, M. *Inorg. Chem.* **2006**, *45*, 10497–10502.

188. Bartlett, N.; Yeh, S.; Kourtakis, K.; Mallouk, T. *J. Fluorine Chem.* **1984**, *26*, 97–116.

189. Shair, R. C.; Schurig, W. F. *Ind. Eng. Chem.* **1951**, *43*, 1624–1627.

190. Brunvoll, J.; Ischenko, A. A.; Miakshin, I. N.; Romanov, G. V.; Spiridonov, V. P.; Strand, T. G.; Sukhoverkhov, V. F. *Acta Chem. Scand.* **1980**, *34*, 733–737.

191. Bougon, R.; Bui Huy, T.; Burgess, J.; Christe, K. O.; Peacock, R. D. *J. Fluorine Chem.* **1982**, *19*, 263–277.

192. Fawcett, J.; Holloway, J. H.; Peacock, R. D.; Russell, D. K. *J. Fluorine Chem.* **1982**, *20*, 9–12.

193. Lehmann, J. F.; Riedel, S.; Schrobilgen, G. J. *Inorg. Chem.* **2008**, *47*, 8343–8356.

194. Jenkins, H. D. B.; Glasser, L. *Inorg. Chem.* **2003**, *42*, 8702–8708.

195. Nagarajan, G. *Bull. Soc. Chim. Belg.* **1962**, *71*, 324–328.

196. Gillespie, R. J.; Schrobilgen, G. J. *Inorg. Chem.* **1976**, *15*, 22–31.

197. Gillespie, R. J.; Netzer, A.; Schrobilgen, G. J. *Inorg. Chem.* **1974**, *13*, 1455–1459.

198. Bolshakov, A. M.; Glushkova, M. A.; Buslaev, I. A. *Dokl. Akad. Nauk* **1983**, *273*, 1134–1137.

199. Buslaev, Y. A.; Petrosyants, S. P. *J. Struct. Chem.* **1969**, *10*, 983–985.

200. Mercier, H. P. A.; Schrobilgen, G. J. *Inorg. Chem.* **1993**, *32*, 145–151.

201. The long contacts within the sum of the van der Waals radii in $[Cs][OsO_3F_3]\cdot CH_3CN$ are: F(1)···O(1B) (3.044(3) Å), C(1)···O(1) (3.012(3) Å), and C(2)···O(2) (3.148(3) Å). There are no short F···F, F···N, F···C or O···N contacts. The shortest contacts to Cs+ are: (F(1)···Cs(1) (3.1617(2) Å), F(2)···Cs(1C) (3.035(1) Å), F(2)···Cs(1D) (3.066(1) Å) and O(2)···Cs(1) (3.252(2) Å)). The corresponding sums of the van der Waals radii (taken from Refs 165 and 202) are: F···F (2.94 Å), F···O (2.99 Å), F···N (3.02 Å), F···C (3.17 Å), O···N (3.07 Å), O···C (3.22 Å), N···C (3.25 Å), Cs···F (4.90 Å), Cs···O (4.95 Å), Cs···N (4.98 Å), Cs···C (5.13 Å).

202. Mantina, M.; Chamberlin, A. C.; Valero, R.; Cramber, C. J.; Truhlar, D. G. *J. Phys. Chem.* **2009**, *113*, 5806–5812.

203. Hughes, M. J.; Mercier, H. P. A.; Schrobilgen, G. J. *Inorg. Chem.* **2010**, *49*, 3501-3515.

204. The ranges of long contacts in *cis*-OsO_2F_4 are: F(3)···F(4B) (2.85(1) Å) to F(2)···F(3A) (3.00(2) Å), F(2)···O(1D) (2.76(1) Å) to F(2)···O(2A) (3.04(2) Å), O(1)···O(2) (2.98(1) Å). The corresponding sums of the van der Waals radii (taken from Ref 165) are: F···F (2.94 Å), O···F (2.99 Å), and O···O(3.04 Å). .

205. The *cis*-$OsO_2F_4\cdot[Cs][CH_2CN]$ (Figure C1) structure packs along the *c*-axis so that the cis-OsO_2F_4 and CH_2CN^- units alternate within a column and the Cs^+ cations form a layer between the rows of the *cis*-OsO_2F_4 and CH_2CN^- units. The

cis-OsO_2F_4·[Cs][CH_2CN]·0.3HF (Figure C2) structure packs so that *cis*-OsO_2F_4 and Cs^+ units alternate within a column and the CH_2CH^- and HF molecules alternate within an adjacent column. The *cis*-OsO_2F_4·[$N(CH_3)_4$][CH_2CN] (Figure C3) structure packs so that the *cis*-OsO_2F_4, CH_2CN^-, and $N(CH_3)_4^+$ units stack in columns along the *a*-, *b*-, and *c*-axes and are offset so that columns of *cis*-OsO_2F_4, CH_2CN^-, and $N(CH_3)_4^+$ units are adjacent to one another.

206. The ranges of long contacts in *cis*-OsO_2F_4·[Cs][CH_2CN] are: F(3)···F(8B) (3.099(5) Å), F(4)···O(3C) (2.926(6) Å) to F(3)···O(4B) (3.157(5) Å), F(4)···C(2G) (3.219(4) Å) to F(4)···C(1G) (3.390(6) Å), O(3)···O(3F) (2.77(1) Å), O(1)···C(1D) (3.189(8) Å) to O(1)···C(1E) (3.421(6) Å), N(1)···N(1G) (3.131(9) Å). The Cs atoms are each 12-coordinate with the range of contacts between Cs(1)···F(1) (2.998(2) Å) to Cs(2)···N(1H) (3.564(4) Å). There are no short F···N, O···C, O···N, C···C, or C···N contacts. The corresponding sums of the van der Waals radii (taken from Ref 165) are: F···F (2.94 Å), F···O (2.99 Å), F···C (3.17 Å), F···N (3.02 Å), O···O (3.04 Å), O···C (3.22 Å), O···N (3.07 Å), C···C (3.40 Å), C···N (3.25 Å), N···N (3.10 Å).

207. The ranges of long contacts in *cis*-OsO_2F_4·[$N(CH_3)_4$][CH_2CN] are: F(3)···F(3A) (3.212(6) Å), F(3)···O(2A) (3.061(5) Å) to F(3)···O(1A) (3.082(4) Å), F(4)···C(6C) (3.274(6) Å) to F(1)···C(1B) (3.395(5) Å), O(2)···O(2E) (3.282(7) Å), O(1)···C(5) (3.234(6) Å) to O(1)···C(6D) (3.359(6) Å), C(1)···C(5D) (3.366(6) Å), C(4)···N(2A) (3.083(6) Å) to C(2)···N(2F) (3.315(7) Å). There are no short F···N, O···N, or N···N contacts. The corresponding sums of the van der Waals radii (taken from Ref 165)

are: F···F (2.94 Å), F···O (2.99 Å), F···C (3.17 Å), F···N (3.02 Å), O···O (3.04 Å), O···C (3.22 Å), O···N (3.07 Å), C···C (3.40 Å), C···N (3.25 Å), N···N (3.10 Å).

208. The ranges of long contacts in *cis*-OsO_2F_4·[Cs][CH_2CN]·0.3HF are: F(12)···F(13A) (3.12(3) Å) to F(3)···F(13B) (3.26(4) Å), F(1)···O(2C) (3.01(2) Å) to F(5)···O(6D) (3.23(2) Å), F(15)···C(3) (2.60(6) Å) to F(13)···C(4E) (3.35(3) Å), O(12)···C(2) (3.01(2) Å) to O(1)···C(1F) (3.37(2) Å), O(4)···N(1G) (3.26(1) Å) to O(8)···N(1A) (3.33(2) Å). The Cs atoms are each 12-coordinate with the range of contacts between Cs(2)···F(2) (3.001(7) Å) to Cs(2)···O(2) (3.66(1) Å). There are no short F···N, O···O, O···N, C···C, C···N, or N···N contacts. The corresponding sums of the van der Waals radii (taken from Ref 165) are: F···F (2.94 Å), F···O (2.99 Å), F···C (3.17 Å), F···N (3.02 Å), O···O (3.04 Å), O···C (3.22 Å), O···N (3.07 Å), C···C (3.40 Å), C···N (3.25 Å), N···N (3.10 Å).

209. Brockway, L. O. *J. Am. Chem. Soc.* **1936**, *58*, 2516–2518.

210. Kaneti, J.; Schleyer, P. v. R.; Clark, T.; Kos, A. J.; Spitznagel, G. W.; Andrade, J. G.; Moffat, J. B. *J. Am. Chem. Soc.* **1986**, *108*, 1481-1492.

211. Hiraoka, K.; Mizuse, S.; Yamabe, S.; Nakatsuji, Y. *Chem. Phys. Lett.* **1988**, *148*, 497-501.

212. Gutsev, G. L.; Adamowicz, L. *Chem. Phys. Lett.* **1995**, *246*, 245-250.

213. Srivastava, B. B.; Dublish, A. K.; Pandey, A. N.; Mithal, A. K. *Z. Naturforsch., A: Phys. Sci.* **1972**, *27*, 1213-1216.

214. Shimanouchi, T. *J. Phys. Chem. Ref. Data* **1977**, *6*, 993-1102.

215. Davidson, G.; Logan, N.; Morris, A. *Chem. Commun.* **1968**, 1044-1046.

216. Grinter, R.; Zimmerman, R. L.; Thomas, M. D. *J. Mol. Spectrosc.* **1984**, *107*, 12-20.

217. Huston, J. L.; Claassen, H. H. *J. Chem. Phys.* **1970**, *52*, 5646-5648.

218. McDowell, R. S.; Goldblatt, M. *Inorg. Chem.* **1971**, *10*, 625-630.

219. Long contact ranges are: F(6)···F(5A) (2.903(8) Å) to F(1)···F(5B) (3.135(7) Å); F(6)···O(3C) (2.810(8) Å) to F(6)···O(4D) (3.155(8) Å); O(2)···O(4E) (2.954(9) Å) to O(2)···O(3A) (3.168(8) Å); Xe(1)···F(4F) (3.545(6) Å) to Xe(1)···F(5A) (3.684(5) Å); and Xe(1)···O(3C) (3.715(6) Å) to Xe(1)···O(2F) (3.720(6) Å). The corresponding sums of the van der Waals radii are: F···F (2.94 Å), F···O (2.99 Å), O···O (3.04 Å), Xe···F (3.63 Å) and Xe···O (3.68 Å); Ref 165.

220. Edwards, A. J.; Steventon, B. R. *J. Chem. Soc. A.* **1968**, 2503–2510.

221. The interatomic distances for the light atoms forming the coordination spheres of the Os atoms in $(OsO_3F_2)_2 \cdot 2XeOF_4$ are: O(1)···O(2,3) 2.634(9), 2.634(9) Å; O(1)···F(1,1A) 2.606(8), 2.600(7) Å; O(2)···O(3) 2.674(8) Å; O(2)···F(1A,2) 2.731(7), 2.599(9) Å; O(3)···F(1,2) 2.740(8), 2.587(8) Å; and F(1A)···F(1,2) 2.428 (9), 2.501(7) Å. .

222. Lis, T. *Acta Crystallogr., Sect. C* **1983**, *39*, 961–962.

223. Fenske, D.; Volp, K.; Dehnicke, K. *Z. Naturforsch., B: Chem. Sci.* **1987**, *42*, 1398–1402.

224. Buslaev, I. A.; Kokunov, Y. V.; Bochkaryova, V. A.; Shustorovich, E. M. *J. Inorg. Nucl. Chem.* **1972**, *34*, 2861–2865.

225. Buslaev, I. A.; Kokunov, Y. V.; Bochkareva, V. A. *J. Struct. Chem.* **1972**, *13*, 560–575.

226. Nieboer, J.; Hillary, W.; Yu, X.; Mercier, H. P. A.; Gerken, M. *Inorg. Chem.* **2009**, *48*, 11251–11258.

227. Hair, M. L.; Robinson, P. L. *J. Chem. Soc.* **1960**, 2775–2776.

228. Griffith, W. P.; Rossetti, R. *J. Chem. Soc., Dalton Trans.* **1972**, 1449–1453.

229. Griffith, W. P.; Skapski, A. C.; Woode, K. A.; Wright, M. P. *Inorg. Chim. Acta* **1978**, *31*, L413–L414.

230. Muller, V. A.; Bollmann, F.; Baran, E. J. *Z. Anorg. Allg. Chem.* **1969**, *370*, 238–247.

231. Pastuszak, R.; L'Haridon, P.; Marchand, R.; Laurent, Y. *Acta Crystallogr., Sect. B* **1982**, *38*, 1427–1430.

232. Clifford, A. F.; Kobayashi, C. S. *Inorg. Synth.* **1960**, *6*, 204–208.

233. Scmidt, M. H.; Flemming, V.; Muller, A. *Spectrochim. Acta, Part A* **1975**, *31*, 1913–1919.

234. Griffith, W. P.; Pawson, D. *J. Chem. Soc., Chem. Commun.* **1973**, 418–419.

235. Griffith, W. P. *J. Chem. Soc.* **1965**, 3694–3697.

236. The long contacts in *fac*-$OsO_3F_2{\cdot}NCCH_3$ are: F(2)···O(2A) (2.988(3) Å), F(1)···H(5B) (2.469 Å) to F(2)···H(3C) (2.740 Å), O(1)···O(3D) (2.897(3) Å), O(3)···H(9D) (2.557 Å) to O(3)···H(1E) (2.861 Å), O(3)···C(2E) (3.094(4) Å), N(3)···H(1F) (2.601 Å), N(3)···C(1F) (3.206(5) Å) to N(3)···C(2G) (3.434(5) Å), and C(1)···C(5F) (3.471(5) Å). The corresponding sums of the van der Waals radii (taken from Ref 165) are: [F···F (2.94 Å), F···O (2.99 Å), F···N (3.02 Å), F···H (2.67 Å), F···C (3.17 Å), O···O (3.04 Å), O···N (3.07 Å), O···H (2.72 Å), O···C (3.22 Å),

N···N (3.10 Å), N···H (2.75 Å), N···C (3.25 Å), H···H (2.40 Å), H···C (2.90 Å) and C···C (3.40 Å)]

237. Pyykkö, P.; Riedel, S.; Patzschke, M. *Chem. –Eur. J.* **2005**, *11*, 3511-3520.

238. Arnaudet, L.; Bougon, R.; Buu, B.; Lance, M.; Nierlich, M.; Vigner, J. *Inorg. Chem.* **1993**, *32*, 1142–1146.

239. Arnaudet, L.; Bougon, R.; Ban, B.; Charpin, P.; Isabey, J.; Lance, M.; Nierlich, M.; Vigner, J. *Inorg. Chem.* **1989**, *28*, 257–262.

240. The interatomic distances for the light atoms that comprise the coordination spheres of the Os atoms in fac-$OsO_3F_2 \cdot NCCH_3$ are: O(1)···O(2,3) 2.638(3), 2.655(3) Å; O(1)···F(1) 2.538(3) Å; O(1)···N(1) 2.647(4) Å; O(2)···O(3) 2.658(3); O(2)···F(2) 2.534(3) Å; O(2)···N(1) 2.646(4) Å; O(3)···F(1,2) 2.633(3), 2.636(3); and N(1)···F(1,2) 2.645(3), 2.647(3) Å.

241. Purcell, K. F.; Drago, R. S. *J. Am. Chem. Soc.* **1966**, *88*, 919–924.

242. Mason, J., *Multinuclear NMR*, 2nd ed.; Plenum Press: New York, 1987; pp 639.

243. Christe, K. O.; Dixion, D. A. Recent Progress on the Christe/Dixon Quantitative Scale of Lewis Acidity. Presented at the 92nd Canadian Society for Chemistry Conference, Hamilton, On. May-June 2009.

244. Gillespie, R. J.; Landa, B.; Schrobilgen, G. J. *Inorg. Chem.* **1976**, *15*, 1256–1263.

245. McKee, D. E.; Adams, C. J.; Zalkin, A.; Bartlett, N. *J Chem. Soc., Chem. Commun.* **1973**, 26–28.

246. Gillespie, R. J.; Landa, B.; Schrobilgen, G. J. *J. Chem. Soc., Chem. Commun.* **1972**, 607–609.

247. Hyman, H. H.; Quarterman, L. A. Hydrogen Fluoride Solutions Containing Xenon Difluoride, Xenon Tetrafluoride and Xenon Hexafluoride. In *Noble-Gas Compounds*; Hyman, H. H., Ed.; University of Chicago Press: Chicago, 1963; pp 275–278.

248. The ranges of long contacts in $[XeF_5][\mu\text{-}F(OsO_3F_2)_2]$ are: F(5)···F(5B) (2.626(3) Å) to F(3)···F(7C) (3.103(3) Å); O(2)···F(12D) (2.748(2) Å) to O(1)···F(2E) (3.127(3) Å); O(2)···O(6) (2.866(3) Å) to O(3)···O(5F) (3.164(3) Å); Xe(1)···F(5G) (4.374(2) Å); Xe(1)···O(4H) (3.909(2) Å); Os(1)···F(9) (3.402(2) Å); Os(1)···O(5F) (3.671(2) Å). The corresponding sums of the van der Waals radii (taken from Ref 165) are: F···F (2.94 Å), F···O (2.99 Å), O···O (3.04 Å), Xe···F(3.63 Å), and Xe···O (3.68 Å).

249. The ranges of long contacts in $[XeF_5][OsO_3F_3]$ are: F(3)···F(4A) (2.843(4) Å) to F(3)···F(4B) (3.171(4) Å); O(3)···O(3C) (2.874(8) Å) to O(1)···O(2D) (3.205(5) Å); O(2)···F(2E) (2.695(4) Å) to O(2)···F(7A) (3.280(43) Å); Xe(1)···F(3F) (3.787(2) Å) to Xe(1)···F(5D) (3.926(3) Å); There are no short Xe···O contacts. The corresponding sums of the van der Waals radii (taken from Ref 165) are: F···F (2.94 Å), O···O (3.04 Å), F···O (2.99 Å), and Xe···F(3.63 Å).

250. The ranges of long contacts in $[Xe_2F_{11}][OsO_3F_3]$ are: F(7)···F(10B) (2.715(3) Å) to F(6)···F(10B) (3.110(3) Å); F(11)···O(2C) (2.897(4) Å) to F(3)···O(3A) (3.161(3) Å); Xe(1)···F(4D) (3.817(2) Å) to Xe(2)···F(10B) (3.820(2) Å); Xe(1)···O(1A) (3.355(2) Å) to Xe(2)···O(3A) (3.356(2) Å); There are no short O···O contacts. The corresponding sums of the van der Waals radii (taken from Ref 165) are: F···F (2.94 Å), F···O (2.99 Å), Xe···F(3.63 Å), and Xe···O (3.68 Å).

251. Landa, B. Laser Raman Spectroscopic Investigations of Some Fluoroxenon Compounds. Ph. D. Thesis, McMaster University, Hamilton On, 1974.

252. Lehmann, J. F.; Schrobilgen, G. J. *J. Fluorine Chem.* **2003**, *119*, 109–124.

253. Sladky, F. O.; Bulliner, P. A.; Bartlett, N. *J. Chem. Soc. A.* **1969**, 2179-2188.

254. Gillespie, R. J.; Landa, B. *Inorg. Chem.* **1973**, *12*, 1383-1389.

255. Frlec, B.; Holloway, J. H. *J. Chem. Soc., Dalton Trans.* **1975**, 535-540.

256. Gillespie, R. J.; Martin, D.; Schrobilgen, G. J. *J. Chem. Soc., Dalton Trans.* **1980**, 1898-1903.

257. Tramsek, M.; Žemva, B. *J. Fluorine Chem.* **2006**, *127*, 1275–1284.

258. Tucker, P. A.; Taylor, P. A.; Holloway, J. H.; Russell, D. R. *Acta Crystallogr., Sect. B.* **1975**, *31*, 906–908.

259. Birchall, T.; Myers, R. D.; Waard, H.; Schrobilgen, G. J. *Inorg. Chem.* **1982**, *21*, 1068–1073.

260. The ranges of long intermolecular contacts in $XeOF_4 \cdot XeF_2$ are: F(1)···F(1A) (2.88(2) Å); O(1)···O(1B) (2.69(1) Å); Xe(1)···F(5C) (3.239(4) Å); there are no short Xe···Xe, O···F, or Xe···O contacts. The corresponding sums of the van der Waals radii (taken from Ref 165) are: F···F (2.94 Å), F···O (2.99 Å), O···O (3.04 Å), Xe···F(3.63 Å), and Xe···O (3.68 Å).

261. The ranges of long intermolecular contacts in $XeOF_4 \cdot KrF_2$ are: F(3)···F(6D) (2.801(3) Å) to F(1)···F(1C) (3.265(4) Å); O(1)···O(1E) (3.206(8) Å); O(1)···F(4F) (3.204(4) Å) to O(1)···F(5G) (3.295(4) Å); Kr(1)···O(1H) (3.356(3) Å) to Kr(2)···O(1J) (3.476(4) Å); Kr(2)···F(1) (3.171(3) Å) to Kr(1)···F(2I) (3.292(3) Å);

there are no short Xe···Xe or Xe···O contacts and short Xe···F contacts are discussed in the text. The corresponding sums of the van der Waals radii (taken from Ref 165) are: F···F (2.94 Å), F···O (2.99 Å), O···O (3.04 Å), Kr···F (3.49 Å), Kr···O (3.54 Å), Xe···F(3.63 Å), and Xe···O (3.68 Å).

262. Lehmann, J. F. Crystallographic, Spectroscopic, and Theoretical Studies of Fluoro-Kr(II), Xe(II), Au(V), and Halogen(VII) Compounds; and New Synthetic Developments in Bromine(VII) Oxide Fluoride Chemistry. Ph. D. Thesis, McMaster University, Hamilton, Ontario, Canada, 2004.
263. Levy, H. A.; Agron, P. A. *J. Am. Chem. Soc.* **1963**, *85*, 241–242.
264. Brassington, N. J.; Edwards, H. G. M.; Long, D. A. *J. Chem. Soc., Farady Trans. 2* **1978**, *74*, 1208–1213.
265. Burger, H.; Kuna, R.; Ma, S.; Breidung, J.; Thiel, W. *J. Chem. Phys.* **1994**, *101*, 1–14.
266. Burbank, R. D.; Falconer, W. E.; Sunder, W. A. *Science* **1972**, *178*, 1285–1286.
267. Agron, P. A.; Begun, G. M.; Levy, H. A.; Mason, A. A.; Jones, C. G.; Smith, D. F. *Science* **1963**, *139*, 842–844.
268. Claassen, H. H.; Goodman, G. L.; Malm, J. G.; Schreiner, F. *J. Chem. Phys.* **1965**, *42*, 1229–1232.
269. Sladky, F. O.; Bartlett, N. *J. Chem. Soc. A.* **1969**, 2188–2189.
270. Casteel, W. J.; MacLeod, D. M.; Mercier, H. P. A.; Schrobilgen, G. J. *Inorg. Chem.* **1996**, *35*, 7279–7288.
271. Turowsky, L.; Seppelt, K. *Z. Anorg. Allg. Chem.* **1990**, *590*, 37–47.

272. Huppmann, P.; Labischinski, H.; Lentz, D.; Pritzkow, H.; Seppelt, K. *Z. Anorg. Allg. Chem.* **1982**, *487*, 7–25.

273. Turowsky, L.; Seppelt, K. *Z. Anorg. Allg. Chem.* **1990**, *590*, 23–36.

274. Shorafa, H.; Seppelt, K. *Inorg. Chem.* **2006**, *45*, 7929–7934.

APPENDIX A

CHAPTER 3: FLUORIDE ION DONOR PROPERTIES OF *cis*-OsO_2F_4; SYNTHESIS, RAMAN SPECROSCOPIC STUDY, AND X-RAY CRYSTAL STRUCTURE OF $[OsO_2F_3][Sb_2F_{11}]$

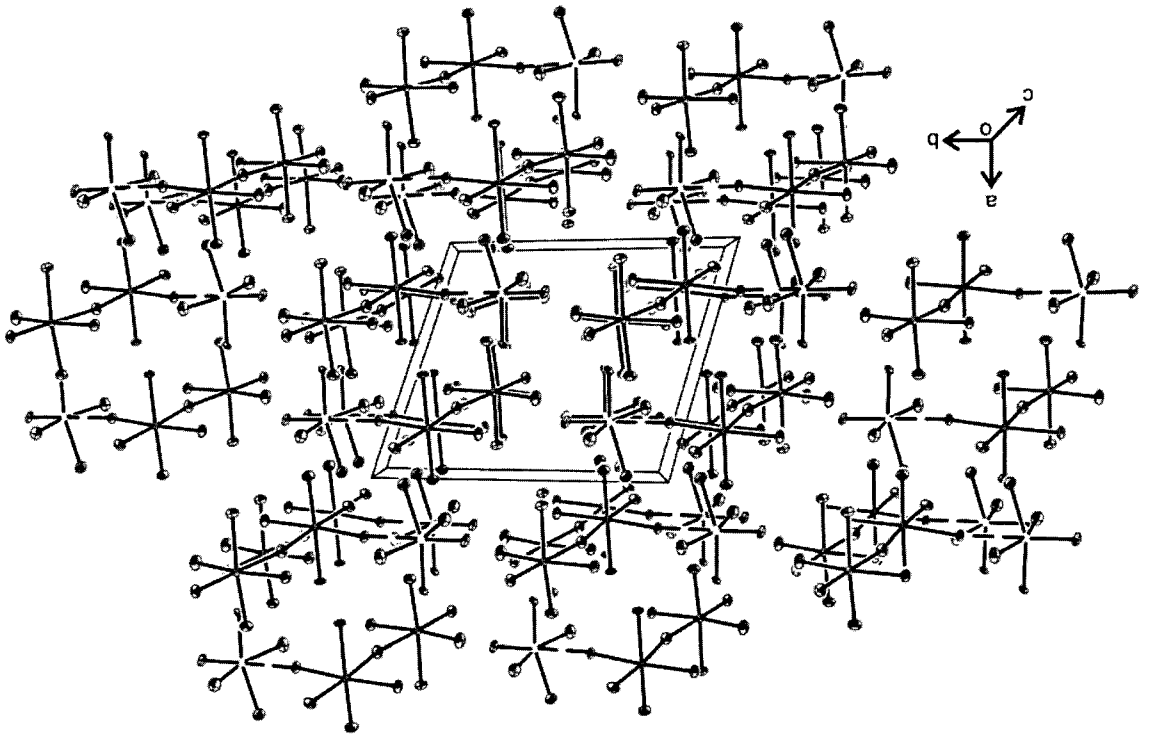

Figure A1. View of $[OsO_2F_3][Sb_2F_{11}]$ crystallographic unit cell along the *c*-axis.

Table A1. Calculated Vibrational Frequencies and Assignments for $[OsO_2F_3][SbF_6]$

SVW[a,b]	B3LYP[a,c]	assgnts (C_1)[d]
998(63)[83]	1040(69)[57]	$\nu(OsO_1)$
980(60)[23]	1016(11)[91]	$\nu(OsO_2)$
726(2)[134]	709(<1)[201]	$\nu(OsF_2) - \nu(OsF_3)$
702(72)[42]	698(26)[77]	$\nu(OsF_2) + \nu(OsF_3) + \nu(OsF_1)$
668(12)[80]	680(2)[88]	$[\nu(SbF_9) + \nu(SbF_6)] - [\nu(SbF_5) + \nu(SbF_8)]$
665(16)[73]	678(1)[67]	$[\nu(SbF_9) + \nu(SbF_8)] - [\nu(SbF_5) + \nu(SbF_6)]$
659(12)[104]	672(5)[106]	$\nu(SbF_5) + \nu(SbF_9)$
647(12)[34]	636(8)[33]	$\nu(OsF_1) - \nu(OsF_2) + \nu(OsF_3)$
609(28)[27]	626(28)[21]	$\nu(SbF_6) + \nu(SbF_8) + \nu(SbF_4)$
557(12)[30]	584(3)[1]	$[\nu(SbF_9) + \nu(SbF_8)] - [\nu(SbF_7) + \nu(SbF_5)]$
478(38)[92]	474(6)[153]	$\nu(OsF_4) - \nu(SbF_4)$
399(16)[1]	416(9)[3]	$\delta(O_1OsO_2) + \nu(OsF_4) + \nu(SbF_4)$
371(1)[16]	353(<1)[14]	$\delta(O_1OsO_2) - \nu(OsF_4) + \nu(SbF_4)$
355(5)[4]	363(3)[1]	$\delta(O_2OsF_2) + \delta(F_1OsF_3)$
316(5)[2]	338(4)[2]	$\delta(O_1OsF_2) + \delta(F_1OsF_3)$
293(1)[9]	308(1)[5]	$\rho_w(O_2OsF_1) + \rho_w(F_2OsF_3)$
283(<1)[20]	292(<0.1)[48]	$\rho_w(O_1OsO_2) + \rho_w(F_1OsF_4)$
266(6)[24]	280(1)[2]	deformation mode $[OsO_2F_3][SbF_6]$
255(3)[17]	267(<1)[35]	
250(4)[16]	259(1)[36]	
241(3)[63]	264(<1)[15]	$\delta(F_5SbF_8) - \delta(F_7SbF_6)$
227(7)[71]	228(<1)[180]	deformation modes $[OsO_2F_3][SbF_6]$
212(4)[6]	214(1)[3]	
194(3)[9]	208(1)[5]	
188(1)[4]	198(<1)[7]	
169(1)[1]	172(<1)[<1]	
145(1)[2]	130(<0.1)[<0.1]	
135(<1)[1]	128(<1)[5]	
109(<1)[<1]	102(<1)[1]	
111(<1)[<1]	102(<0.1)[<1]	
83(<0.1)[<1]	48(<1)[1]	
56(<1)[<1]	31(<0.1)[<1]	
27(<1)[<1]	10(<0.1)[<0.1]	

[a] Values in parentheses denote calculated Raman intensities (amu $Å^{-4}$) and values in square brackets denote calculated infrared intensities (km mol^{-1}). [b] SVWN/SDDall(-PP). [c] B3LYP/Stuttgart aug-cc-pVTZ(-PP). [d] See Figure A2 for the atom labeling scheme. The abbreviations denote stretch (ν) and bend (δ).

Table A2. Calculated Geometrical Parameters for $[OsO_2F_3][SbF_6]$

Bond Lengths (Å)			Bond Angles (°)					
	SVWN[a]	B3LYP[b]		SVWN[a]	B3LYP[b]		SVWN[a]	B3LYP[b]
Os–F_1	1.876	1.868	O_1–Os–O_2	102.8	101.7	F_4–Sb–F_5	83.3	83.6
Os–F_2	1.840	1.840	O_1–Os–F_1	95.7	94.4	F_4–Sb–F_6	176.8	178.1
Os–F_3	1.847	1.840	O_1–Os–F_2	96.5	96.1	F_4–Sb–F_7	81.0	81.6
Os–O_1	1.702	1.676	O_1–Os–F_3	98.2	96.1	F_4–Sb–F_8	81.4	81.6
Os–O_2	1.709	1.679	O_1–Os---F_4	161.4	172.4	F_4–Sb–F_9	84.1	83.6
Os---F_4	2.042	2.020	O_2–Os–F_1	161.3	163.8	F_5–Sb–F_6	98.3	97.7
Sb–F_4	2.136	2.205	O_2–Os–F_2	94.3	94.1	F_5–Sb–F_7	164.0	165.2
Sb–F_5	1.895	1.885	O_2–Os–F_3	92.6	94.1	F_5–Sb–F_8	87.6	89.2
Sb–F_6	1.884	1.877	O_2–Os---F_4	84.7	85.8	F_5–Sb–F_9	91.1	89.9
Sb–F_7	1.908	1.897	F_1–Os–F_2	85.3	84.1	F_6–Sb–F_7	97.3	97.0
Sb–F_8	1.932	1.897	F_1–Os–F_3	82.8	84.1	F_6–Sb–F_8	95.8	97.0
Sb–F_9	1.892	1.885	F_1–Os---F_4	76.8	78.0	F_6–Sb–F_9	98.7	97.7
			F_2–Os–F_3	161.9	163.6	F_7–Sb–F_8	87.2	88.0
			F_2–Os---F_4	81.0	83.2	F_7–Sb–F_9	90.2	89.2
			F_3–Os---F_4	83.0	83.2	F_8–Sb–F_9	165.5	165.2
			Os---F_4–Sb_1	126.6	140.8			

[a] The SDDall basis set, augmented for F, O, and Sb with two d-type polarization functions, was used. [b] The Stuttgart basis set was used for Os with the f functional. The aug-cc-pVTZ(-PP) basis sets were used for all other atoms.

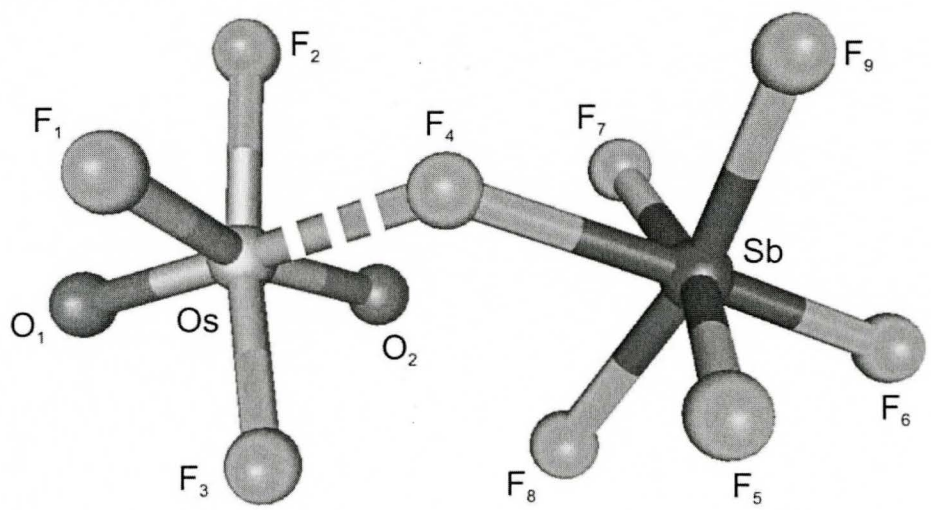

Figure A2. Calculated SVWN/SDDall(-PP) gas-phase geometry for $[OsO_2F_3][SbF_6]$.

Table A3. Natural Bond Orbital (NBO) Valencies, Bond Orders, and Natural Population Analysis (NPA) Charges for $[OsO_2F_3][SbF_6]$

	charges		valencies			bond orders	
	SVWN	B3LYP	SVWN	B3LYP		SVWN	B3LYP
Os	1.97	2.27	3.47	3.49	$Os–O_1$	0.87	0.90
O_1	–0.22	–0.25	0.92	0.93	$Os–O_2$	0.87	0.89
O_2	–0.18	–0.20	0.95	0.93	$Os–F_1$	0.45	0.45
F_1	–0.36	–0.42	0.48	0.46	$Os–F_2$	0.49	0.48
F_2	–0.31	–0.38	0.52	0.50	$Os–F_3$	0.50	0.49
F_3	–0.30	–0.36	0.53	0.50	$Os---F_4$	0.30	0.28
F_4	–0.55	–0.58	0.51	0.49	$Sb–F_4$	0.23	0.24
Sb	3.06	3.02	2.45	0.43	$Sb–F_5$	0.45	0.48
F_5	–0.62	–0.62	0.40	0.42	$Sb–F_6$	0.46	0.49
F_6	–0.62	–0.62	0.41	0.44	$Sb–F_7$	0.44	0.46
F_7	–0.63	–0.63	0.39	0.40	$Sb–F_8$	0.41	0.44
F_8	–0.62	–0.63	0.37	0.39	$Sb–F_9$	0.45	0.48
F_9	–0.62	–0.62	0.41	0.43			

APPENDIX B

CHAPTER 4: FLUORIDE ION ACCEPTOR PROPERTIES OF *cis*-OsO_2F_4; SYNTHESIS, RAMAN AND NMR SPECTROSCOPIC STUDY OF $OsO_2F_5^-$

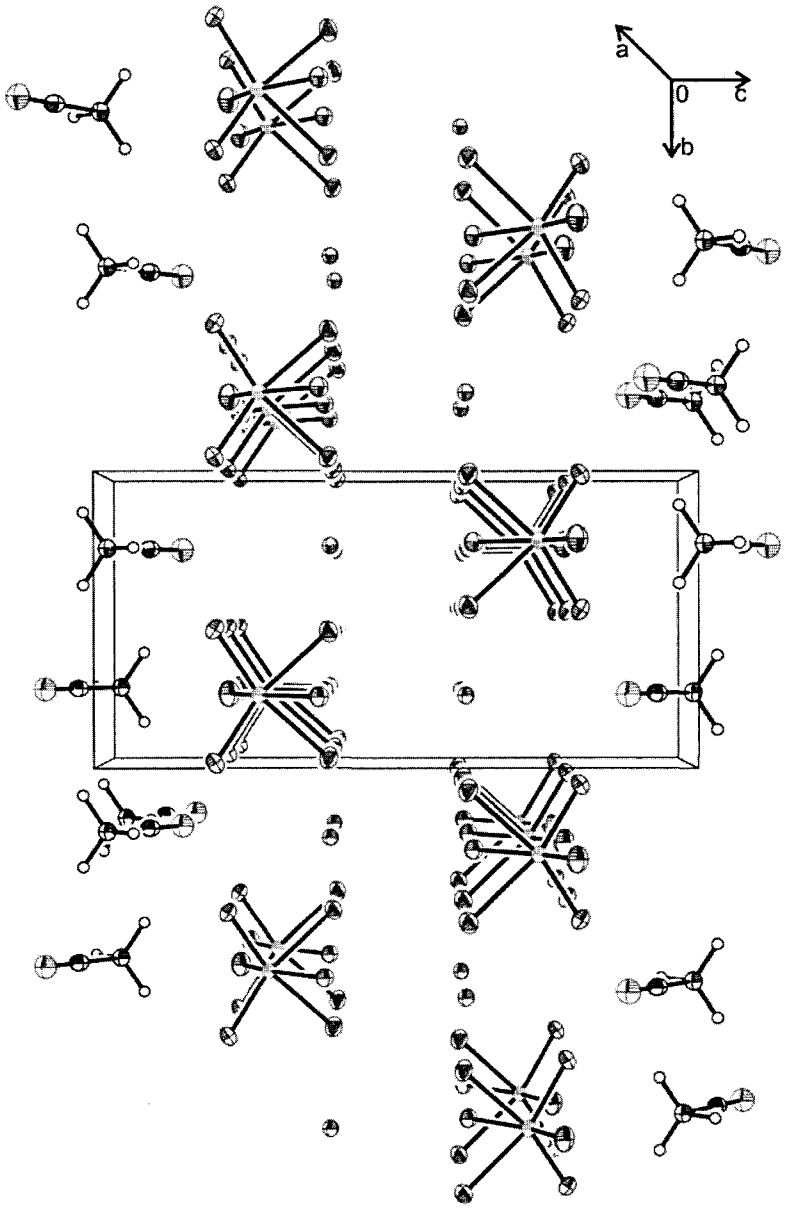

Figure B1. View of the crystallographic unit cell of $[Cs][OsO_3F_3]\cdot CH_3CN$ along the *a*-axis.

Table B1. Natural Bond Orbital NPA Charges, Valencies and Bond Orders for the Monocapped Trigonal Prismatic, Pentagonal Bipyramidal, and Monocapped Octahedral Isomers of *cis*-$OsO_2F_5^-$

	Monocapped Trigonal Prism (C_{2v})[a]			Pentagonal Bipyramid (C_s)[b]			Monocapped Octahedron (C_s)[c]		
	B3LYP[d]	SVWN[e]	SVWN[f]	B3LYP[d]	SVWN[e]	SVWN[f]	B3LYP[d]	SVWN[e]	SVWN[f]
					Charges				
Os	2.32	2.08	1.99	2.27	2.03	1.95	2.30	2.06	1.98
F_1	–0.51	–0.47	–0.46	–0.52	–0.48	–0.47	–0.56	–0.52	–0.50
F_2				–0.49	–0.45	–0.43	–0.44	–0.39	–0.39
F_3							–0.52	–0.48	–0.47
F_4							–0.52	–0.48	–0.48
F_5	–0.48	–0.45	–0.44	–0.51	–0.47	–0.46			
O_1	–0.40	–0.38	–0.37	–0.35	–0.35	–0.34	–0.37	–0.35	–0.34
O_2				–0.38	–0.37	–0.35			
					Valencies				
Os	3.65	4.35	3.64	3.73	0.41	3.67	3.70	4.38	3.68
F_1	0.40	0.51	0.42	0.37	0.48	0.40	0.34	0.45	0.38
F_2				0.40	0.50	0.44	0.46	0.56	0.48
F_3							0.38	0.48	0.42
F_4							0.38	0.49	0.41
F_5	0.39	0.52	0.43	0.40	0.50	0.42			
O_1	0.88	0.94	0.85	0.90	0.98	0.86	0.92	0.98	0.87
O_2				0.90	0.98	0.86			
					Bond Orders				
Os–F_1	0.39	0.50	0.40	0.38	0.48	0.39	0.34	0.45	0.37
Os–F_2				0.41	0.51	0.41	0.45	0.56	0.45
Os–F_3							0.39	0.50	0.40
Os–F_4							0.38	0.49	0.39
Os–F_5	0.40	0.52	0.41	0.42	0.51	0.41			
Os–O_1	0.84	0.92	0.82	0.88	0.96	0.83	0.87	0.94	0.83
Os–O_2				0.86	0.95	0.82			

[a] See Figure 4.4a for the atom labeling scheme. [b] See Figure 4.4b for the atom labeling scheme. [c] See Figure 4.4c for the atom labeling scheme. [d] The Stuttgart basis set was used for Os with the f functional. The aug-cc-pVTZ basis sets were used for fluorine and oxygen. [e] The aug-cc-pVTZ(-PP) basis sets were used for all atoms. [f] The SDDall basis set was used augmented for F and O with two d-type polarization functions.

Table B2. Natural Bond Orbital NPA Charges, Valencies and Bond Orders for *trans*-$OsO_2F_5^-$ and $OsOF_5^-$

	trans-$OsO_2F_5^-$ (D_{5h})[a]			$OsOF_5^-$ (C_{4v})[b]		
	B3LYP[c]	SVWN[d]	SVWN[e]	B3LYP[c]	SVWN[d]	SVWN[e]
			Charges			
Os	2.25	2.02	1.93	2.18	1.93	1.87
F_1	–0.47	–0.43	–0.43	–0.57	–0.52	–0.51
F_2				–0.51	–0.46	–0.45
O_1	–0.44	–0.42	–0.40	–0.38	–0.37	–0.36
			Valencies			
Os	3.72	4.39	3.68	3.00	3.60	2.97
F_1	0.42	0.52	0.45	0.41	0.52	0.44
F_2				0.42	0.53	0.45
O_1	0.82	0.88	0.78	1.01	1.08	0.94
			Bond Orders			
Os–F_1	0.42	0.53	0.43	0.40	0.50	0.41
Os–F_2				0.44	0.56	0.44
Os–O_1	0.81	0.88	0.76	0.96	1.04	0.91

[a] See Figure 4.3a for the atom labeling scheme. [b] See Figure 4.3b for the atom labeling scheme. [c] The Stuttgart basis set was used for Os with the f functional. The aug-cc-pVTZ basis sets were used for fluorine and oxygen. [d] The aug-cc-pVTZ(-PP) basis sets were used for all atoms. [e] The SDDall basis set was used augmented for F and O with two d-type polarization functions.

APPENDIX C

CHAPTER 5: X-RAY CRYSTAL STRUCTURE AND RAMAN SPECTRA OF *cis*-OsO_2F_4 AND THE CH_2CN^- ANION

Table C1. Experimental Geometries for *cis*-OsO_2F_4·[Cs][CH_2CN], *cis*-OsO_2F_4·[$N(CH_3)_4$][CH_2CN], *cis*-OsO_2F_4·[Cs][CH_2CN]·0.3HF, and *cis*-OsO_2F_4 and Calculated Geometries of *cis*-OsO_2F_4 and CH_2CN^-

	exptl.				calc.	
	cis-OsO_2F_4·[Cs][CH_2CN]	*cis*-OsO_2F_4·[$N(CH_3)_4$][CH_2CN]	*cis*-OsO_2F_4·[Cs][CH_2CN]·0.3HF	*cis*-OsO_2F_4	*cis*-OsO_2F_4 (C_{2v})	CH_2CN^- (C_1)
	Bond Lengths (Å)					
Os(1)-O(1)	1.696(3)	1.756(3)	1.724(10)	1.704(10)	1.717	
Os(1)-O(2)		1.670(4)	1.688(12)	1.684(11)	1.717	
Os(1)-F(1)	1.958(2)	1.956(3)	1.948(8)	1.916(8)	1.892	
Os(1)-F(2)		1.937(3)	1.958(8)	1.914(8)	1.892	
Os(1)-F(3)	1.890(3)	1.911(2)	1.909(8)	1.839(10)	1.858	
Os(1)-F(4)	1.886(3)	1.865(3)	1.888(8)	1.837(8)	1.858	
Os(2)-O(3)	1.698(4)					
Os(2)-O(4)	1.713(5)					
Os(2)-F(5)	1.966(4)					
Os(2)-F(6)	1.945(3)					
Os(2)-F(7)	1.889(2)					
Os(2)-F(7A)	1.889(2)					
Os(2)-O/F(8)			1.774(10)			
Os(2)-O(4)			1.685(12)			
Os(2)-F(5)			1.948(11)			
Os(2)-F(6)			1.930(10)			
Os(2)-F(6A)			1.930(10)			
Os(3)-O/F(12)			1.773(9)			
Os(3)-O(6)			1.701(13)			
Os(3)-F(9)			1.927(12)			
Os(3)-F(10)			1.916(10)			
Os(3)-F(10A)			1.916(10)			
C(1)-C(2)	1.449(7)	1.469(6)	1.480(27)			1.396
C(2)-N(1)	1.136(6)	1.144(6)	1.151(27)			1.184
C(1)-H(1A)	0.81(6)		0.835			1.092

C(1)-H(1B)	0.81(6)		1.496		1.092
N(1)---F(13)			1.569(36)		
C(3)-C(4)			1.425(29)		
C(4)-N(2)			1.151(29)		
C(3)-H(3A)			1.086		
C(3)-H(3B)			1.086		
N(2)---F(14)			1.606(60)		
C(5)-C(6)			1.416(29)		
C(6)-N(3)			1.154(30)		
C(5)-H(5A)			0.974		
C(5)-H(5B)			0.974		
N(3)---F(15)			1.280(57)		
N(2)-C(3)		1.480(6)			
N(2)-C(4)		1.489(6)			
N(2)-C(5)		1.496(5)			
N(2)-C(6)		1.505(5)			

Bond Angles (deg)

O(1)-Os(1)-O(2)/(O(1A))	107.3(2)	105.1(2)	109.8(5)	102.8(7)	101.4
O(1)-Os(1)-F(1)	88.2(1)	86.0(2)	86.5(4)	89.4(4)	89.6
O(1)-Os(1)-F(2)	164.5(1)	165.2(2)	164.6(4)	168.9(6)	180.0
O(1)-Os(1)-F(3)	92.6(1)	90.5(1)	91.8(5)	93.6(6)	94.0
O(1)-Os(1)-F(4)	92.4(1)	92.4(2)	92.0(4)	94.3(4)	94.0
O(2)/(O(1A))-Os(1)-F(1)	164.6(1)	168.6(2)	163.7(4)	167.8(6)	180.0
O(2)/(O(1A))-Os(1)-F(2)	88.2(1)	89.6(2)	85.7(4)	88.4(4)	89.6
O(2)/(O(1A))-Os(1)-F(3)	92.6(1)	92.2(2)	93.0(4)	95.1(4)	94.0
O(2)/(O(1A))-Os(1)-F(4)	92.4(1)	95.7(2)	93.2(5)	93.7(5)	94.0
F(1)-Os(1)-F(2)	76.4(2)	79.2(1)	78.1(3)	79.5(5)	79.3
F(1)-Os(1)-F(3)	86.5(1)	84.8(1)	93.2(5)	84.1(5)	85.2
F(1)-Os(1)-F(4)	86.8(1)	86.5(1)	87.1(3)	85.1(4)	85.2
F(2)-Os(1)-F(3)	86.6(1)	87.7(1)	86.2(3)	85.0(3)	85.2
F(2)-Os(1)-F(4)	86.8(1)	87.3(1)	88.0(5)	85.1(5)	85.2
F(3)-Os(1)-F(4)	171.5(2)	170.6(1)	171.1(3)	166.6(6)	170.3

O(3)-Os(2)-O(4)	106.9(2)
O(3)-Os(2)-F(5)	87.2(2)
O(3)-Os(2)-F(6)	163.7(2)
O(3)-Os(2)-F(7)	92.70(8)
O(3)-Os(2)-F(7A)	92.70(8)
O(4)-Os(2)-F(5)	165.9(2)
O(4)-Os(2)-F(6)	89.4(2)
O(4)-Os(2)-F(7)	92.27(8)
O(4)-Os(2)-F(7A)	92.27(8)
F(5)-Os(2)-F(6)	76.5(2)
F(5)-Os(2)-F(7)	86.94(9)
F(5)-Os(2)-F(7A)	86.94(9)
F(6)-Os(2)-F(7)	86.51(8)
F(6)-Os(2)-F(7A)	86.51(8)
F(7)-Os(2)-F(7A)	171.6(2)

O/F(8)-Os(2)-O(4)	99.2(5)
O/F(8)-Os(2)-F(5)	88.8(4)
O/F(8)-Os(2)-F(6)	168.4(5)
O/F(8)-Os(2)-F(6A)	88.8(4)
O/F(8)-Os(2)-F/O(8)	92.8(8)
O(4)-Os(2)-F(5)	168.3(7)
O(4)-Os(2)-F(6)	91.8(5)
O(4)-Os(2)-F(6A)	91.8(5)
O(4)-Os(2)-F/O(8)	99.2(5)
F(5)-Os(2)-F(6)	79.8(4)
F(5)-Os(2)-F(6A)	79.8(4)
F(5)-Os(2)-F(8)/O(3)	89.3(4)
F(6)-Os(2)-F(6A)	87.4(6)
F(6)-Os(2)-F/O(8)	89.1(4)
F(6A)-Os(2)-F/O(8)	168.6(5)

O/F(12)-Os(3)-O(6)	98.8(6)
O/F(12)-Os(3)-F(9)	89.5(4)
O/F(12)-Os(3)-F(10)	168.8(5)
O/F(12)-Os(3)-F(10A)	88.5(4)
O/F(12)-Os(3)-O/F(12)	93.0(7)

O(6)-Os(3)-F(9)			168.0(8)	
O(6)-Os(3)-F(10)			91.9(6)	
O(6)-Os(3)-F(10A)			91.9(6)	
O(6)-Os(3)-F/O(12)			98.8(6)	
F(9)-Os(3)-F(10)			79.5(4)	
F(9)-Os(3)-F(10A)			79.5(4)	
F(9)-Os(3)-O/F(12)			89.5(4)	
F(10)-Os(3)-F(10A)			87.9(6)	
F(10)-Os(3)-O/F(12)			88.5(4)	
F(10A)-Os(3)-O/F(12)			168.8(5)	
C(1)-C(2)-N(1)	179.7(6)	179.1(5)	175(2)	180.4
C(2)-N(1)---F(13)			97(2)	
H(1A)-C(1)-H(1B)	102(6)		135.0	116.2
H(1A)-C(1)-C(2)	116(5)		113.2	118.6
H(1B)-C(1)-C(2)	107(5)		113.2	118.6
C(3)-C(4)-N(2)			175(2)	
C(4)-N(2)---F(14)			121(3)	
H(3A)-C(3)-H(3B)			80.9	
H(3A)-C(3)-C(4)			108.8	
H(3B)-C(3)-C(4)			108.8	
C(5)-C(6)-N(3)			178(2)	
C(6)-N(3)---F(15)			94(3)	
H(5A)-C(5)-H(5B)			78.8	
H(5A)-C(5)-C(6)			117.7	
H(5B)-C(5)-C(6)			117.7	
C(3)-N(2)-C(4)		109.5 (3)		
C(3)-N(2)-C(5)		109.0 (3)		
C(3)-N(2)-C(6)		109.7 (3)		
C(4)-N(2)-C(5)		109.8 (4)		
C(4)-N(2)-C(6)		109.9 (3)		
C(5)-N(2)-C(6)		108.9 (3)		

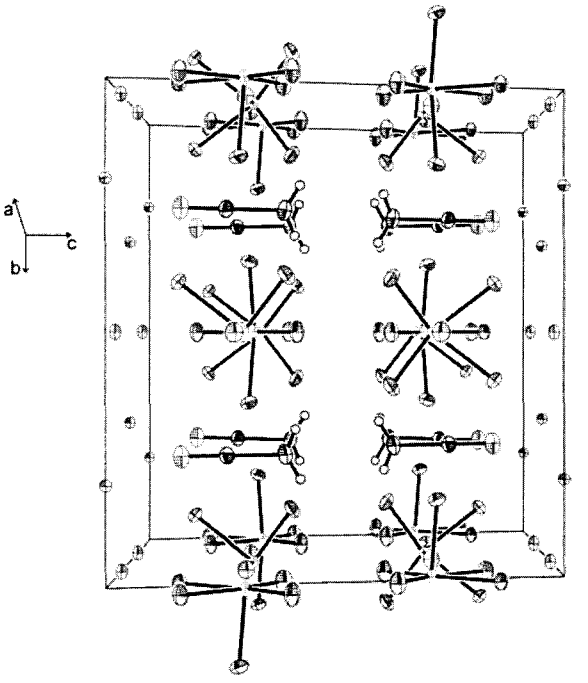

Figure C1. View of the *cis*-OsO_2F_4·[Cs][CH_2CN] crystallographic unit cell along the *a*-axis.

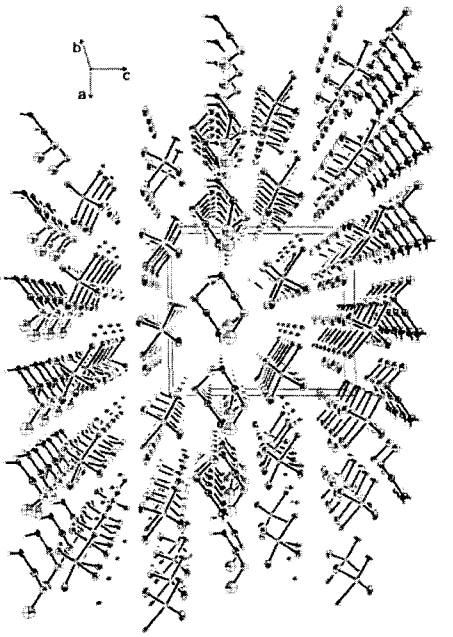

Figure C2. View of the *cis*-OsO_2F_4·[Cs][CH_2CN]·0.3HF crystallographic unit cell along the *b*-axis.

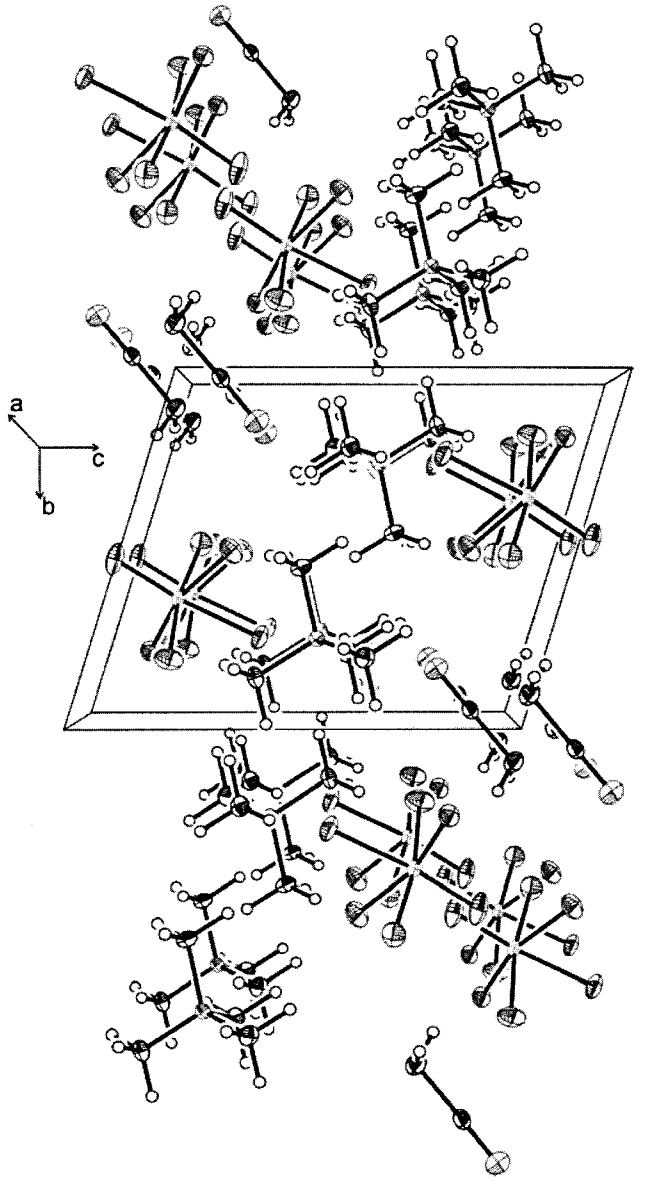

Figure C3. View of the *cis*-$OsO_2F_4 \cdot [N(CH_3)_4][CH_2CN]$ crystallographic unit cell along the *a*-axis

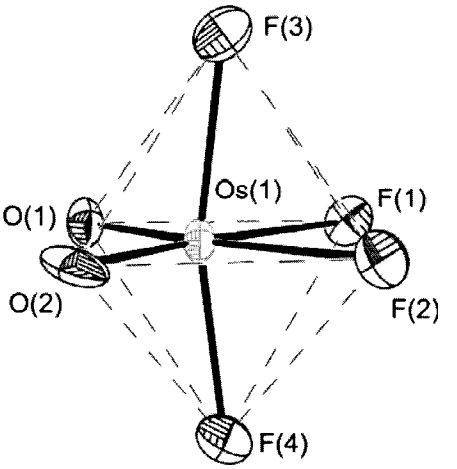

Figure C4. Visualization of the octahedron formed by the light atoms in the X-ray crystal structure of *cis*-OsO_2F_4.

Table C2. Interatomic Distances (Å) Between the Light Atoms Forming the Coordination Spheres of the Os atoms in *cis*-OsO_2F_4, *cis*-OsO_2F_4·[Cs][CH_2CN], *cis*-OsO_2F_4·[$N(CH_3)_4$][CH_2CN], and *cis*-OsO_2F_4·[Cs][CH_2CN]·0.3 HF

	cis-OsO_2F_4· [Cs][CH_2CN]	*cis*-OsO_2F_4· [$N(CH_3)_4$][CH_2CN]	*cis*-OsO_2F_4· [Cs][CH_2CN]· 0.3 HF[a]	*cis*-OsO_2F_4
F(3)···O(1)	2.594(5)	2.614(4)	2.61(1)	2.58(2)
F(3)···O(2)		2.624(5)	2.61(1)	2.60(2)
F(3)···F(1)	2.636(4)	2.618(4)	2.61(1)	2.52(1)
F(3)···F(2)		2.625(4)	2.64(1)	2.54(1)
F(4)···O(1)	2.591(4)	2.606(4)	2.60(1)	2.60(1)
F(4)···O(2)		2.586(5)	2.60(1)	2.57(1)
F(4)···F(1)	2.644(4)	2.609(5)	2.64(1)	2.54(1)
F(4)···F(2)		2.665(4)	2.67(1)	2.54(1)
O(1)···O(2)	2.724(8)	2.721(5)	2.79(1)	2.65(2)
O(1)···F(1)	2.549(4)	2.536(5)	2.52(1)	2.55(1)
O(2)···F(2)		2.549(5)	2.49(1)	2.51(1)
F(1)···F(2)	2.426(7)	2.483(4)	2.46(1)	2.45(1)

[a] Geometrical parameters are taken for the non-disordered OsO_2F_4 molecule in the structural unit.

Table C3. Natural Bond Orbital (NBO) Valencies, Bond Orders and Natural Population Analysis (NPA) Charges for *cis*-OsO_2F_4 (C_{2v})[a]

	SVWN[b]	B3LYP[c]	PBE1PBE[c]
	NPA Charges		
Os	1.96	2.27	2.29
O_1	–0.23	–0.28	–0.28
F_1	–0.38	–0.44	–0.45
F_3	–0.36	–0.41	–0.41
	Valencies		
Os	3.69	3.64	3.69
O_1	0.90	0.92	0.93
F_1	0.48	0.45	0.45
F_3	0.52	0.48	0.49
	Bond Orders		
Os–O_1	0.88	0.89	0.91
Os–F_1	0.47	0.45	0.46
Os–F_3	0.50	0.47	0.48

[a] See Figure 5.6a for the atom labeling scheme. [b] The SDDall basis set augmented for F and O with two d-type polarization functions was used. [c] The Stuttgart basis set was used for Os with the f functional. The aug-cc-pVTZ basis sets were used for all other atoms.

Table C4. Natural Bond Orbital (NBO) Valencies, Bond Orders and Natural Population Analysis (NPA) Charges for CH_2CN^- (C_s)[a]

	B3LYP		PBE1PBE	
	b	*c*	*b*	*c*
	Charges			
C_1	–0.95	–0.97	–0.98	–0.99
C_2	0.20	0.25	0.21	0.25
N	–0.57	–0.63	–0.98	–0.63
H	0.16	0.18	0.17	0.19
	Valencies			
C_1	2.72	2.85	2.73	2.85
C_2	2.97	3.13	2.98	3.14
N	1.77	1.79	1.78	1.79
H	0.77	0.85	0.77	0.85
	Bond Orders			
C–C	1.19	1.24	1.19	1.24
C–N	1.76	1.86	1.77	1.87
C–H	0.76	0.84	0.76	0.84

[a] See Figure 5.6b for the atom labeling scheme. [b] The 6-21G* basis set was used. [c] The aug-cc-pVTZ basis set was used.

APPENDIX D

CHAPTER 6: SYNTHESIS AND X-RAY CRYSTAL STRUCTURE OF $(OsO_3F_2)_2 \cdot 2XeOF_4$ AND THE RAMAN SPECTRUM OF $(OsO_3F_2)_\infty$, $(OsO_3F_2)_2$, AND $(OsO_3F_2)_2 \cdot 2XeOF_4$

Table D1. Raman Spectra Used to Monitor the Formation/Dissociation of $(OsO_3F_2)\cdot 2XeOF_4$ from/to $(OsO_3F_2)_\infty$ and $XeOF_4$, and the Transition of $(OsO_3F_2)_2$ to $(OsO_3F_2)_\infty$ [a]

$(OsO_3F_2)_\infty$	$XeOF_4$	$(OsO_3F_2)_\infty$ $XeOF_4$ $(OsO_3F_2)_2\cdot 2XeOF_4$	$(OsO_3F_2)_2\cdot 2XeOF_4$ $XeOF_4$	$(OsO_3F_2)_2\cdot 2XeOF_4$ $XeOF_4$	$(OsO_3F_2)_2\cdot 2XeOF_4$	$(OsO_3F_2)_2\cdot 2XeOF_4$ $(OsO_3F_2)_2$	$(OsO_3F_2)_2$	$(OsO_3F_2)_2$ $(OsO_3F_2)_\infty$	$(OsO_3F_2)_\infty$
		963(49)	962(32)	963(100)	962(100)	962(90)			
957(100)		958(48)	957(22)	957(69)	957(39)	956(100)	955(100)	956(100)	957(100)
952(29)		952(6)				952(sh)		952(41)	952(29)
949(32)		950(6)			948(1)	948(sh)	948(sh)	949(37)	949(32)
945(30)		945(6)					944(16)	945(34)	945(30)
		940(25)		940(48)	940(47)	940(45)			
			938(16)				937(7)	937(9)	
			928(9)	928(10)					
		921(13)	921(9)	921(29)	921(12)	921(19)			
					911(1)				
	908(12)	908(12)	908(11)						
	902(99)	902(100)	902(100)	901(6)					
					661(1)				
								655(4)	
								650(sh)	
			619(3)	618(5)				612(3)	
					605(1)		604(1), br	605(3)	
596(6)		594(sh)	595(sh)	594(10)	594(6)	594(5)		595(7)	596(6)
	588(100)	588(94)	588(97)	588(7)					
			582(12)	580(7)					
	575(63)	575(62)							
		574(sh)	574(65)	573(57)	572(48)	572(42)		578(2)	
	565(49)	565(44)	565(49)	565(14)					
		560(12)		560(22)	560(12)	560(12)			
			558(17)	556(sh)					
			546(sh)	549(10)				549(3)	
	543(83)	543(80)	543(86)					546(2)	
		540(sh)		540(59)	540(51)	540(45)			
	532(59)	532(59)	532(44)	531(11)					
		525(32)	524(23)	525(68)	525(58)	525(53)			
		519(3)	519(9)	518(sh)					
			514(3)						
			506(2), br	503(15)					
			484(16)	484(10)					
					466(0)				
		451(3)	450(1)	450(6)	450(3)	450(3), br	453(1), br	448(2)	

Table D1. (continued …)

								440(3)	
								414(sh)	
		408(3)	408(1)	409(6)	409(4)	409(4)	409(2)		
						407(3)			
404(5)		405(3)	404(sh)			402(5)		404(7)	404(5)
398(10)		399(3)					399(sh)	398(13)	398(10)
		394(sh)				396(4)	396(9)	394(13)	
	392(3)	392(11)	392(7)	392(19)	392(16)	391(18)		391(29)	
389(28)	386(sh)	388(11)	387(5)	388(14)	388(11)	387(16)	386(13)	385(sh)	389(28)
				382(6)	381(3)	382(7)		381(6)	
	379(20)	378(19)	378(20)		379(19)		376(5)		
		371(18)	371(15)	371(24)		374(4)			
	369(13)	368(13)	368(14)			372(16)			
		364(11)	365(sh)	364(19)	364(14)	364(13)			
					361(sh)				
			356(2)						
			350(1)			349(0)			
							337(1)	341(2)	
323(2)								325(2)	323(2)
								313(2)	
							308(1)		
				301(3)	304(1)				
	294(sh)	293(3)		295(6)	294(1)		293(2)	293(3)	
287(3)	289(75)	289(8)	289(6)		288(4)	288(3)	288(sh)	287(4)	287(3)
			282(1)	281(3)	282(1)		280(sh)		
							276(sh)	277(sh)	
273(6)		274(5)	274(3)	273(10)	274(7)	273(7)	271(4)	272(6)	273(6)
					266(0)				
								260(sh)	
	250(11)		249(9)	250(2)					
		245(sh)			240(sh)			244(2)	
	233(8)	233(8)	233(9)	235(9)	235(5)	234(2)		232(2)	
223(2)					224(0)			223(2)	223(2)
				219(sh)					
215(2)								214(2)	215(2)
		204(2)	203(1)	203(4)	203(2)				
		200(2)	200(1)	200(4)	201(3)	199(0)		199(2)	

Table D1. (continued ...)

				194(2)			192(3)	192(2)	
				188(2)					
				183(2)				184(2)	
176(4)	175(3)	176(2)	175(1)					176(4)	176(4)
		173(2)	172(1)						
		169(sh)	169(sh)	170(3)	170(1)			168(2)	
	166(5)	166(3)	167(3)			164(0)	166(2)		
	161(4)	160(4)	160(3)	160(4)	160(3)	161(0)		163(2)	
		154(1)	157(sh)	156(sh)	154(sh)				
		150(1)	151(1)	152(2)				150(3)	
		143(3)	143(1)	143(5)	143(4)	144(0)			
135(2)		136(2)	137(1)	137(4)	136(3)			135(2)	135(2)
								130(1)	
					121(1)			120(2)	
					118(1)				
		107(1)							
			101(sh)	99(sh)	102(sh)				
	98(3)	98(2)	98(2)	97(2)	98(1)				
		96(sh)						95(sh)	
91(2)				92(sh)				91(sh)	91(2)
	77(5)	79(sh)	77(sh)	78(3)	77(sh)				
			71(3)	72(2)	72(2)			71(2)	
		69(1)						68(sh)	
		64(2)	64(2)	64(3)	64(2)				
					56(0)				
					51(0)				

[a] The Raman spectra were recorded on a microcrystalline sample in a FEP sample tube at −150 °C using 1064-nm excitation. Experimental Raman intensities are given in parentheses and are relative intensities with the most intense band given as 100. The original sample contained $(OsO_3F_2)_\infty$ (column 1) dissolved in $XeOF_4$ (column 2). Dissolution of $(OsO_3F_2)_\infty$ in liquid $XeOF_4$ at 25 °C initially gave a mixture of $(OsO_3F_2)_\infty$, $XeOF_4$, and $(OsO_3F_2)_2{\cdot}2XeOF_4$ (column 3) and upon complete dissolution gave a mixture of $(OsO_3F_2)_2{\cdot}2XeOF_4$, and $XeOF_4$ (column 4). The $XeOF_4$ solvent was slowly removed under vacuum at 0 °C (column 5) and was pumped until it gave rise to only $(OsO_3F_2)_2{\cdot}2XeOF_4$ (column 6). Further pumping of the sample at 0 °C resulted in removal of $XeOF_4$ from the crystal lattice, initially giving a mixture of $(OsO_3F_2)_2{\cdot}2XeOF_4$ and $(OsO_3F_2)_2$ (column 7) and finally the pure $(OsO_3F_2)_2$ dimer (column 8). Heating $(OsO_3F_2)_2$ to room temperature initially gave a mixture of $(OsO_3F_2)_2$ and $(OsO_3F_2)_\infty$ (column 9), and finally the starting material, $(OsO_3F_2)_\infty$ (column 10).

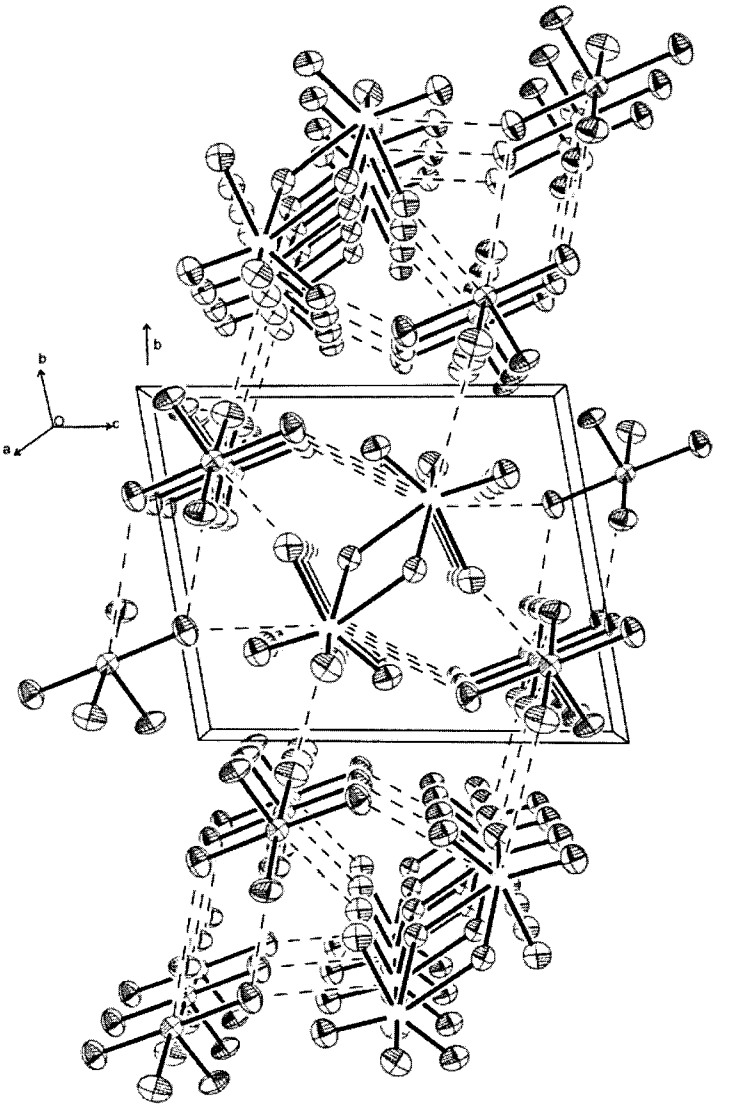

Figure D1. View of the $(OsO_3F_2)_2 \cdot 2XeOF_4$ crystallographic unit cell along the *a*-axis.

Table D2. Experimental Raman Frequencies, Intensities, and Assignments for Gas-Phase $XeOF_4$, and the Calculated Vibrational Frequencies and Intensities for $XeOF_4$

exptl	calcd[b]		assgnts (C_{4v})[e]
gas phase[a]	SVWN[c]	B3LYP[d]	
928	903 (21) [28]	887 (20) [25]	A_1, ν(XeO)
609	611 (<0.1) [259]	593 (<0.1) [282]	E, $\nu_{as}(XeF_{4e})$
577	555 (40) [5]	552 (44) [5]	A_1, $\nu_s(XeF_{4e})$
543	526 (20) [0]	511 (23) [0]	B_2, $\nu_s(XeF_{2e}) - \nu_s(XeF_{2e}')$
362	307 (3) [4]	326 (3) [4]	E, $\delta(OXeF_e) - \delta(OXeF_e)$
287	238 (1) [30]	262 (1) [35]	A_1, $\delta(XeF_{4e})_{umb}$
225	189 (3) [0]	211 (3) [0]	B_1, $\delta(F_eXeF_e') + \delta(F_eXeF_e')$
	158 (<0.1) [0]	160 (<0.1) [0]	B_2, $\rho_w(XeF_{2e}) - \rho_w(XeF_{2e}')$
161	135 (<1) [2]	152 (<1) [1]	E, $\rho_w(XeF_{2e})$

[a] From Ref 101. [b] Values in parentheses denote calculated Raman intensities (amu $Å^{-4}$) and values in square brackets denote calculated infrared intensities (km mol^{-1}). [c] SVWN/SDDall. [d] B3LYP/aug-cc-pVTZ. [e] The atom labeling scheme refers to the figure below. The abbreviations denote stretch (ν), asymmetric (as), symmetric (s), bend (δ), wag (ρ_w), and umbrella (umb). The equatorial fluorine atoms are denoted by F_{4e} or by F_{2e}, and F_{2e}'.

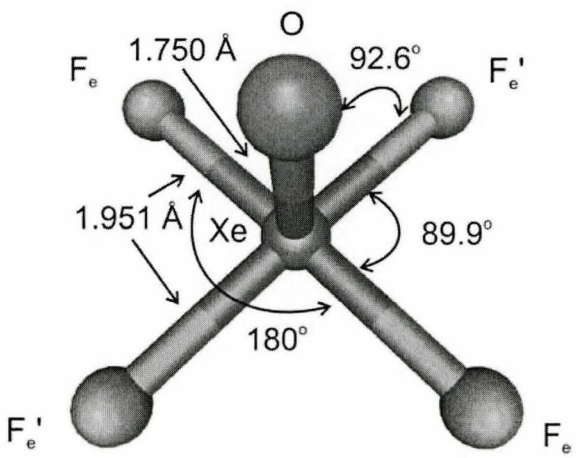

Table D3. Calculated Vibrational Frequencies, Raman and Infrared Intensities and Assignments for $(\mu\text{-}FOsO_3F_2)_2OsO_3F^-$

SVWN[a]	B3LYP[b]	assgnts[c]
971 (158) [44]	1014 (97) [39]	$\nu(Os_bO_t) + \nu(Os_bO_{t1}) + \nu(Os_bO_{t2})$
970 (48) [35]	1008 (56) [54]	$\nu(Os_1O_1) + \nu(Os_1O_2) + \nu(Os_1O_3)$
966 (2) [97]	1007 (72) [67]	$\nu(Os_2O_4) + \nu(Os_2O_5) + \nu(Os_2O_6)$
965 (10) [217]	994 (13) [191]	$\nu(Os_bO_{t1}) - \nu(Os_bO_{t2}) + \nu(Os_bO_t)_{small}$
964 (19) [223]	992 (12) [167]	$\nu(Os_bO_{t1}) + \nu(Os_bO_{t2})_{small} - \nu(Os_bO_t)$
961 (86) [108]	985 (29) [49]	$\nu(Os_1O_2) + \nu(Os_2O_5) - [\nu(Os_1O_3) + \nu(Os_2O_6)] + [\nu(Os_1O_1) + \nu(Os_2O_4)]_{small}$
955 (27) [39]	983 (17) [336]	$\nu(Os_1O_1) + \nu(Os_1O_2) + \nu(Os_2O_3) - [\nu(Os_1O_3) + \nu(Os_2O_5)]$
952 (21) [15]	980 (13) [127]	$\nu(Os_1O_1) + \nu(Os_2O_4) - \nu(Os_1O_2)$
945 (22) [105]	977 (10) [69]	$[\nu(Os_bO_t) + \nu(Os_1O_2) + \nu(Os_2O_4)] - [\nu(Os_bO_{t1}) + \nu(Os_1O_1) + \nu(Os_2O_5)]$
652 (14) [104]	614 (2) [182]	$[\nu(Os_2F_5) + \nu(Os_2F_{t2})] - [\nu(Os_1F_1) + \nu(Os_1F_2)]_{small}$
628 (8) [105]	607 (<1) [145]	$[\nu(Os_1F_1) + \nu(Os_1F_2)] - [\nu(Os_2F_4) + \nu(Os_2F_5)]$
621 (14) [90]	598 (17) [7]	$\nu(Os_bF_t) + [\nu(Os_1F_1) + \nu(Os_1F_2) + \nu(Os_2F_4) + \nu(Os_2F_5)]_{small}$
567 (4) [67]	545 (4) [50]	$\nu(Os_2F_4) - \nu(Os_2F_5)$
560 (7) [47]	542 (3) [38]	$\nu(Os_1F_1) - \nu(Os_1F_2)$
509 (13) [100]	471 (5) [73]	$[\nu(Os_bF_{b1}) + \nu(Os_bF_{b2})] - [\nu(Os_1F_{b1}) + \nu(Os_2F_{b2})]$
477 (4) [97]	443 (<1) [140]	$[\nu(Os_bF_{b1}) - \nu(Os_2F_{b2})] - [\nu(Os_1F_{b1}) + \nu(Os_bF_{b2})]$
391 (13) [3]	416 (3) [3]	$\delta(O_4Os_2O_5) + \delta(F_4Os_2F_5)$
388 (7) [2]	415 (2) [3]	$\delta(O_1Os_1O_2) + \delta(F_1Os_1F_2)$
381 (5) [5]	405 (3) [6]	$\delta(Os_bO_tO_{t1}\ O_{t2})_{oop}$
378 (6) [1]	401 (7) [7]	$\delta(O_{t1}Os_bO_{t2})$
373 (5) [5]	398 (3) [8]	$\delta(O_tOs_bO_{t2}) - \delta(O_tOs_bO_{t1})$
372 (3) [6]	392 (7) [4]	$\delta(O_4Os_2O_6) + \rho_t(O_5Os_2O_6)$
369 (6) [2]	391 (7) [3]	$\rho_t(O_1Os_1O_2) + \delta(O_1Os_1O_3) - \delta(O_6Os_2O_4)_{small}$
365 (5) [7]	389 (2) [27]	$\rho_w(O_4Os_2O_5) - \delta(O_5Os_2O_6)$
362 (6) [14]	383 (2) [36]	$\delta(Os_1O_1O_2O_3)_{oop} + \rho_r(F_{b1}Os_bF_{b2})_{small}$
349 (1) [12]	349 (<1) [18]	$\rho_w(F_{b1}Os_bF_{b2}) + \delta(F_4Os_2F_5)$
339 (<1) [11]	337 (1) [7]	$(\mu\text{-}FOsO_3F_2)_2OsO_3F^-$ deformation mode
314 (<1) [13]	336 (<1) [9]	$\delta(Os_bF_tF_{b1}F_{b2})_{oop} + \delta(O_1Os_1O_2) - \delta(F_1Os_1F_2)$
310 (1) [9]	318 (1) [41]	$\rho_w(F_4Os_2O_4) + \rho_w(F_4Os_2F_{b2})$
303 (1) [18]	306 (2) [14]	} $(\mu\text{-}FOsO_3F_2)_2OsO_3F^-$ deformation modes
284 (5) [15]	293 (1) [18]	
277 (4) [11]	282 (2) [5]	$\delta(F_tOs_bO_t) + \rho_r(O_1Os_1O_3) + \rho_w(F_1Os_1F_2) + \rho_w(F_4Os_2F_5) + \rho_t(O_6Os_2O_4)$
269 (5) [10]	278 (2) [9]	} $(\mu\text{-}FOsO_3F_2)_2OsO_3F^-$ deformation modes
250 (1) [10]	267 (1) [16]	
237 (3) [51]	234 (1) [36]	$\rho_t(F_{b2}Os_bF_t) + \rho_t(F_{b1}Os_bF_t) + \rho_r(O_tOs_bO_{t1})$
235 (<1) [38]	214 (1) [27]	$\delta(F_{b1}Os_bF_{b2}) + \rho_w(F_tOs_bO_t)$
218 (1) [14]	207 (<1) [234]	$\rho_r(F_{b1}Os_bF_{b2}) - \rho_r(O_{t1}Os_bO_{t2}) + \delta(O_4Os_2F_4) + \rho_r(O_5Os_2O_6)$
182 (1) [3]	168 (<1) [2]	} $(\mu\text{-}FOsO_3F_2)_2OsO_3F^-$ deformation modes
169 (1) [1]	166 (<1) [1]	
147 (<1) [3]	155 (<1) [20]	
144 (<1) [1]	146 (<1) [<1]	$\rho_r(O_{t1}Os_bO_{t2}) + \rho_w(O_tOs_bF_t)$
134 (1) [1]	130 (<1) [1]	} $(\mu\text{-}FOsO_3F_2)_2OsO_3F^-$ deformation modes
120 (<1) [1]	128 (<1) [2]	
109 (<1) (<1)	110 (<1) [3]	
95 (<0.1) [4]	66 (<1) [1]	
84 (<0.1) [<1]	44 (<1) [<1]	
81 (<0.1) [1]	37 (<1) [<1]	
65 (<0.1) [<1]	19 (<0.1) [1]	
52 (<1) [<1]	16 (<1) [<1]	
44 (<1) [<1]	14 (<0.1) [1]	
39 (<1) [1]	7 (<0.1) [1]	

Table D3. (continued ...)

[a] SVWN/SDDall. Values in parentheses denote calculated Raman intensities (amu $Å^{-4}$) and values in square brackets denote calculated infrared intensities (km mol^{-1}). [b] B3LYP/Stuttgart for osmium (with F functional) aug-cc-pVTZ for oxygen and fluorine atoms. [c] Assignments for the energy-minimized geometry calculated at the B3LYP level. The atom labeling scheme refers to Figure 6.5. The abbreviations denote stretch (ν), asymmetric (as), symmetric (s), bend (δ), twist (ρ_t) and rock (ρ_r).

Table D4. Natural Bond Orbital (NBO) Charges, Valencies, and Bond Orders for $(\mu\text{-}FOsO_3F_2)_2OsO_3F^-$

	$(\mu\text{-}FOsO_3F_2)_2OsO_3F^-$						
	charges		valencies			bond orders	
atom	SVWN	B3LYP	SVWN	B3LYP	bond	SVWN	B3LYP
Os_1	1.88	2.20	3.61	3.58	$Os_1–O_1$	0.84	0.86
O_1	–0.40	–0.42	0.89	0.90	$Os_1–O_2$	0.84	0.86
O_2	–0.37	–0.42	0.90	0.89	$Os_1–O_3$	0.85	0.86
O_3	–0.39	–0.44	0.90	0.90	$Os_1–F_1$	0.43	0.42
F_1	–0.44	–0.52	0.47	0.44	$Os_1–F_2$	0.42	0.40
F_2	–0.46	–0.53	0.46	0.42	$Os_1–F_{b1}$	0.22	0.17
F_{b1}	–0.53	–0.61	0.55	0.43	$Os_2–O_4$	0.83	0.86
Os_2	1.89	2.20	3.54	3.59	$Os_2–O_5$	0.83	0.86
O_4	–0.35	–0.43	0.86	0.90	$Os_2–O_6$	0.85	0.86
O_5	–0.36	–0.42	0.87	0.89	$Os_2–F_{b2}$	0.42	0.42
O_6	–0.40	–0.45	0.88	0.90	$Os_2–F_4$	0.42	0.42
F_4	–0.47	–0.53	0.44	0.43	$Os_2–F_5$	0.20	0.17
F_5	–0.47	–0.52	0.44	0.43	$Os_b–O_t$	0.84	0.87
F_{b2}	–0.52	–0.61	0.55	0.43	$Os_b–O_{t1}$	0.85	0.87
Os_b	1.88	2.19	3.56	3.55	$Os_b–O_{t2}$	0.84	0.87
O_t	–0.37	–0.39	0.89	0.90	$Os_b–F_{b1}$	0.28	0.26
O_{t1}	–0.37	–0.40	0.89	0.90	$Os_b–F_{b2}$	0.30	0.26
O_{t2}	–0.34	–0.39	0.88	0.90	$Os_b–F_t$	0.46	0.42
F_t	–0.40	–0.50	0.50	0.45	$Os_b–O_{t1}$	0.85	0.87
					$Os_b–O_{t2}$	0.84	0.87

Table D5. Experimental and Calculated Frequencies, Intensities and Assignments for *cis*-OsO_2F_4.

exptl[a]	calcd[b]		assgnts (C_{2v})[e]
	SVWN[c]	B3LYP[d]	
943 (100)	973 (31) [57]	1019 (36) [63]	$\nu_{sym}(OsO_2)$
933 (31)	968 (13) [90]	993 (14) [109]	$\nu_{as}(OsO_2)$
680 (sh)	703 (<1) [166]	684 (21) [78]	$\nu_{as}(OsF_{2a})$
673 (59)	692 (24) [50]	683 (<0.1) [197]	$\nu_{sym}(OsF_{2a}) + \nu_{sym}(OsF_{2e})$
580 (17)	632 (12) [35]	616 (8) [35]	$\nu_{sym}(OsF_{2a}) - \nu_{sym}(OsF_{2e})$
572 (14)	612 (11) [55]	603 (8) [68]	$\nu_{as}(OsF_{2e})$
402 (38)	384 (5) [1]	416 (5) [2]	$\delta(OsO_2)$
350 (31)	330 (4) [3]	348 (4) [0]	$\delta(OsF_{2a}) + \delta(OsF_{2e})$
344 (31)	329 (5) [0]	347 (4) [4]	$\delta(OOsF_e) + \delta(OsF_{2a})$
323 (1)	312 (<1) [11]	329 (<1) [12]	$\rho_r(OsF_{2a})$
314 (1)	298 (1) [19]	316 (1) [24]	$\rho_t(OsO_2)$
266 (2)	253 (<<1) [36]	266 (<0.1) [43]	$\rho_r(OsF_{2e})$
217 (1)	218 (<1) [1]	230 (<1) [2]	$\delta(OsF_{2a}) - \delta(OsF_{2e})$
168 (3)	186 (<1) [<1]	200 (<1) [1]	$\delta(OOsF_e) - \delta(OsF_{2a})$
95 (sh)	100 (<1) [0]	111 (<1) [0]	$\rho_t(OsF_{2e})$

[a] The Raman spectrum was recorded on a microcrystalline sample in a FEP tube at −150 °C using 1064-nm excitation. Experimental Raman intensities are given in parentheses and are relative intensities with the most intense band given as 100. [b] Values in parentheses denote calculated Raman intensities (amu $Å^{-4}$) and values in square brackets denote calculated infrared intensities (km mol^{-1}). [c] SVWN/SDDall. [d] B3LYP/Stuttgart for osmium (with F functional) aug-cc-pVTZ for oxygen and fluorine atoms. [e] The atom labeling scheme refers to the figure below. The abbreviations denote stretch (ν), asymmetric (as), symmetric (s), bend (δ), twist (ρ_t) and rock (ρ_r).

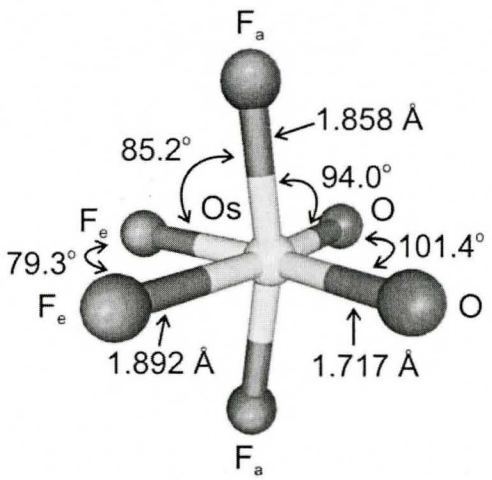

Table D6. Factor-Group Analysis for $(OsO_3F_2)_2{\cdot}2XeOF_4$

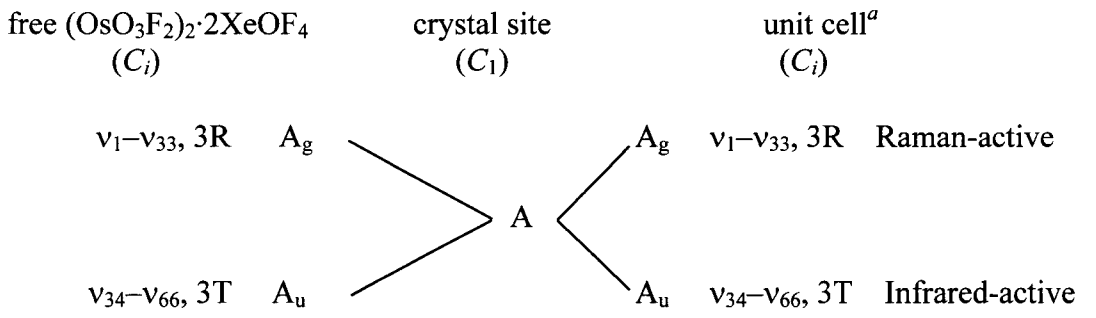

[a] The crystallographic space group is $P\bar{1}$ with $Z = 1$ structural unit per unit cell.

Table D7. Calculated Geometrical Parameters for $(\mu\text{-}FOsO_3F_2)_2OsO_3F^-$

	$(\mu\text{-}FOsO_3F_2)_2OsO_3F^-$							
	SVWN	B3LYP		SVWN	B3LYP		SVWN	B3LYP
				Bond Lenghts (Å)				
Os_1–O_1	1.724	1.698	Os_2–O_4	1.726	1.700	Os_b–O_t	1.718	1.694
Os_1–O_2	1.725	1.699	Os_2–O_5	1.724	1.698	Os_b–O_{t1}	1.717	1.694
Os_1–O_3	1.719	1.695	Os_2–O_6	1.720	1.695	Os_b–O_{t2}	1.716	1.692
Os_1–F_1	1.920	1.922	Os_2–F_4	1.916	1.925	Os_b–F_t	1.902	1.905
Os_1–F_2	1.924	1.926	Os_2–F_5	1.922	1.919	Os_b–F_{b1}	2.067	2.080
Os_1–F_{b1}	2.155	2.227	Os_2–F_{b2}	2.160	2.233	Os_b–F_{b2}	2.064	2.078
				Bond Angles (deg)				
O_1–Os_1–O_2	101.30	101.14	O_4–Os_2–O_5	101.19	101.14	O_t–Os_b–O_{t1}	102.75	102.32
O_1–Os_1–O_3	103.00	102.72	O_4–Os_2–O_6	102.78	102.74	O_t–Os_b–O_{t2}	102.73	102.48
O_1–Os_1–F_1	156.38	157.16	O_4–Os_2–F_4	156.66	156.80	O_t–Os_b–F_t	153.34	155.04
O_1–Os_1–F_2	87.40	87.45	O_4–Os_2–F_5	87.25	87.36	O_t–Os_b–F_{b1}	84.23	84.46
O_1–Os_1–F_{b1}	83.35	82.94	O_4–Os_2–F_{b2}	83.94	83.06	O_t–Os_b–F_{b2}	83.55	83.76
O_2–Os_1–O_3	103.00	102.85	O_5–Os_2–O_6	103.02	102.75	O_{t1}–Os_b–O_{t2}	103.12	102.20
O_2–Os_1–F_1	87.96	87.78	O_5–Os_2–F_4	87.90	87.77	O_{t1}–Os_b–F_t	93.70	93.22
O_2–Os_1–F_2	156.82	156.92	O_5–Os_2–F_5	156.64	157.20	O_{t1}–Os_b–F_{b1}	163.63	165.05
O_2–Os_1–F_{b1}	81.72	81.58	O_5–Os_2–F_{b2}	82.97	82.48	O_{t1}–Os_b–F_{b2}	89.03	88.89
O_3–Os_1–F_1	95.87	95.58	O_6–Os_2–F_4	95.90	95.98	O_{t2}–Os_b–F_t	93.61	93.01
O_3–Os_1–F_2	95.76	95.95	O_6–Os_2–F_5	96.14	95.81	O_{t2}–Os_b–F_{b1}	89.50	89.08
O_3–Os_1–F_{b1}	170.98	171.82	O_6–Os_2–F_{b2}	169.75	171.10	O_{t2}–Os_b–F_{b2}	164.51	165.61
F_1–Os_1–F_2	76.56	77.07	F_4–Os_2–F_5	76.85	77.12	F_t–Os_b–F_{b1}	74.88	76.24
F_1–Os_1–F_{b1}	76.47	77.58	F_4–Os_2–F_{b2}	76.26	76.87	F_t–Os_b–F_{b2}	75.82	77.07
F_2–Os_1–F_{b1}	77.96	78.25	F_5–Os_2–F_{b2}	75.83	77.56	F_{b1}–Os_b–F_{b2}	76.93	78.53
Os_1–F_{b1}–Os_b	129.77	144.67	Os_2–F_{b2}–Os_b	128.80	144.42			

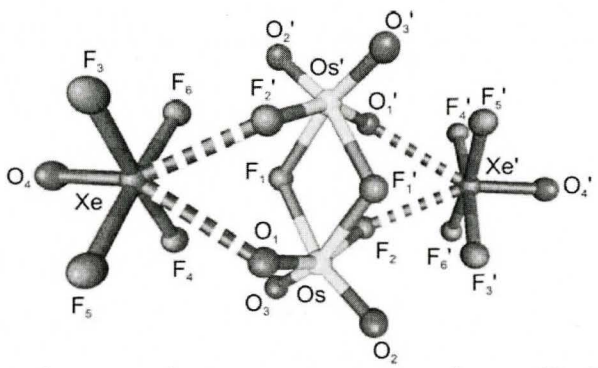

Figure D2. Calculated gas-phase geometry for $(OsO_3F_2)_2{\cdot}2XeOF_4$ (C_1, SVWN/SDDall). The atom labeling scheme is based on the C_i symmetry of the structural unit in the crystallographic unit cell.

Table D8. Natural Bond Orbital (NBO) Charges, Valencies, and Bond Orders for $(OsO_3F_2)_2$ and $(OsO_3F_2)_2{\cdot}2XeOF_4$

	$(OsO_3F_2)_2$				$(OsO_3F_2)_2{\cdot}2XeOF_4$			
	charges		valencies		charges		valencies	
Atom	SVWN	B3LYP	SVWN	B3LYP	SVWN	B3LYP	SVWN	B3LYP
Os	1.88	2.19	3.45	3.48	1.89	2.18	3.47	3.47
O_1	–0.32	–0.37	0.90	0.89	–0.38	–0.36	0.89	0.91
O_2	–0.32	–0.37	0.90	0.91	–0.27	–0.35	0.94	0.92
O_3	–0.32	–0.37	0.90	0.91	–0.27	–0.34	0.93	0.92
F_1	–0.50	–0.59	0.55	0.47	–0.51	–0.58	0.56	0.48
F_2	–0.41	–0.48	0.48	0.44	–0.46	–0.55	0.51	0.45
Xe					2.96	3.13	2.55	2.47
O_4					–0.79	–0.81	0.84	0.81
F_3					–0.53	–0.58	0.36	0.35
F_4					–0.55	–0.58	0.35	0.35
F_5					–0.53	–0.58	0.35	0.35
F_6					–0.55	–0.58	0.36	0.35

	bond orders			
	$(OsO_3F_2)_2$		$(OsO_3F_2)_2{\cdot}2XeOF_4$	
Bond	SVWN	B3LYP	SVWN	B3LYP
Os–O_1	0.84	0.87	0.82	0.87
Os–O_2	0.84	0.87	0.87	0.88
Os–O_3	0.84	0.87	0.87	0.88
Os–F_1	0.25	0.23	0.27	0.23
Os–F_2	0.44	0.43	0.42	0.40
Os–F_1'	0.25	0.23	0.23	0.23
Xe---F_2			0.06	0.04
Xe–O_4			0.92	0.91
Xe–F_3			0.39	0.38
Xe–F_4			0.37	0.38
Xe–F_5			0.39	0.37
Xe–F_6			0.37	0.37
Xe---O_1'			0.03	0.01

APPENDIX E

CHAPTER 7: SYNTHESES AND MULTI-NMR STUDY OF *fac*- AND *mer*-$OsO_3F_2(NCCH_3)$ AND THE X-RAY CRYSTAL STRUCTURE ($n = 2$) AND RAMAN SPECTRUM ($n = 0$) OF *fac*-$OsO_3F_2(NCCH_3)\cdot nCH_3CN$

Table E1. Raman Spectra Acquired During the Removal of CH_3CN from a CH_3CN Solution of *fac*-$OsO_3F_2(NCCH_3)$, and the Raman Spectra of Uncoordinated CH_3CN and of *fac*-$OsO_3F_2(NCCH_3)$ Isolated from SO_2ClF [a]

CH_3CN[b]	*fac*-$OsO_3F_2(NCCH_3)$ ·*n*CH_3CN + free CH_3CN[c,d,e]	*fac*-$OsO_3F_2(NCCH_3)$ ·*n*CH_3CN[c,e,f]	*fac*-$OsO_3F_2(NCCH_3)$[c,g]	*fac*-$OsO_3F_2(NCCH_3)$ ·*n*CH_3CN[c,e,h]	assgnts
2999(54)	2998(32)			3000(21)	
2938(97)	2936(58)			2938(54)	
2248(100)	2248(35)			2248(45)	
1457(11), 1454(7)	1457(8)			1457(7)	
1425(3), 1420(4)	1423(7)				
1376(15), 1371(3)				1376(15)	
1042(1)					
922(20)	920(sh)				CH_3CN (free solvent)
400(3)					
395(12), 392(9)					
386(5)	389(40)[i]				
116(18)				116(14)br	
108(13)					
102(15)					
96(32)					
	3009(16)[j]	3008(15)br[j]			
				2950(sh)	
		2330(28)			
	2250(49)	2251(29)			CH_3CN (crystal lattice)
	1371(11)	1370(10)			
				342(6)	
	289(13), 285(9)				
	3009(16)[j]	3008(15)br[j]	3014(8), 2990(2)	3013(13)br, 2989(7)	
	2941(98)	2941(74), 2930(sh)	2944(43), 2929(24)	2943(45), 2929(24)	
	2337(48)	2336(34)	2332(36)	2331(38)	
			1410(6), 1385(24)	1409(8)	
	1355(12)	1356(14)	1356(14)	1356(16)	
			1041(1), 1029(1)		
		955(9)	956(6), 952(sh)	964(7), 956(8), 950(9)	*fac*-$OsO_3F_2(NCCH_3)$
		944(sh), 940(29)	945(sh), 942(36)	945(sh), 942(42)	
	937(84), 924(37)	936(51), 934(sh), 923(38)	934(33), 924(34)	934(36), 924(36)	
	918(100)	918(100), 909(22)	918(100), 910(30)	918(100), 910(33)	
			598(2)		
	568(12)			574(10)br	
	530(13)	530(11)	529(7)	528(7)	

		415(1)		
		396(sh), 392(19)	393(24)	
389(40)[i]	390(30)	388(50)	388(25)	
378(32), 374(23)	380(37), 378(38), 375(28)	378(40), 374(sh)	380(45), 377(45), 373(sh)	
		326(2)		
		309(4)		
		277(sh)		
		232(1), 228(1)		*fac*-$OsO_3F_2(NCCH_3)$
		216(1)		
		204(2)		
		143(2)		
	120(9)br	121(7)		
		119(sh)		
114(7)br		114(11)		
		106(8)		

[a] The Raman spectra were recorded on samples in a FEP tubes at −150 °C using 1064-nm excitation. Experimental Raman intensities are given in parentheses and are relative intensities with the most intense band given as 100. [b] Solid CH_3CN. [c] The abbreviations denote shoulder (sh) and broad (br). [d] The original sample contained $(OsO_3F_2)_\infty$ dissolved in CH_3CN at 25 °C. Removal of excess CH_3CN solvent at –40 °C gave a mixture that contained a small amount of uncoordinated CH_3CN. [e] The number of solvent molecules, *n*, in the crystal lattice is most likely 2 based on the X-ray crystal structure of *fac*-$OsO_3F_2(NCCH_3)\cdot 2CH_3CN$. [f] Further pumping led to complete removal of uncoordinated CH_3CN solvent and formation of $OsO_3F_2(NCCH_3)\cdot nCH_3CN$. [g] Continued pumping at –40 °C yielded *fac*-$OsO_3F_2(NCCH_3)$. [h] A sample of *fac*-$OsO_3F_2(NCCH_3)$ isolated from SO_2ClF solvent which contained a small amount of uncoordinated CH_3CN in the crystal lattice. [i] Bands at 389 cm^{-1} overlap and arise from CH_3CN (free solvent) and *fac*-$OsO_3F_2(NCCH_3)$. [j] Bands at 3008 and 3009 cm^{-1} overlap and arise from *fac*-$OsO_3F_2(NCCH_3)$ and CH_3CN (crystal lattice).

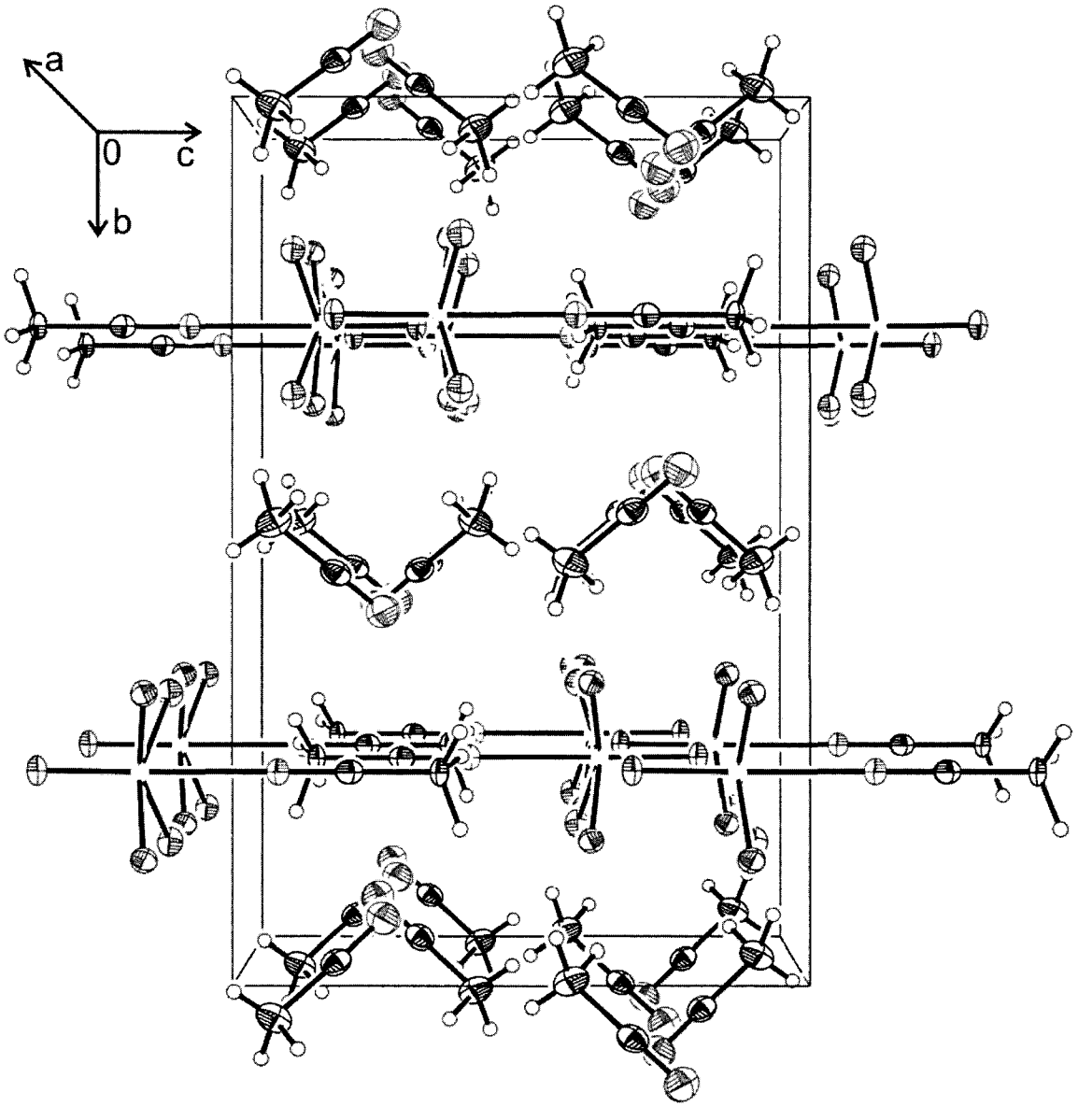

Figure E1. Unit cell of *fac*-$OsO_3F_2(NCCH_3)\cdot 2CH_3CN$ viewed along the *a*-axis.

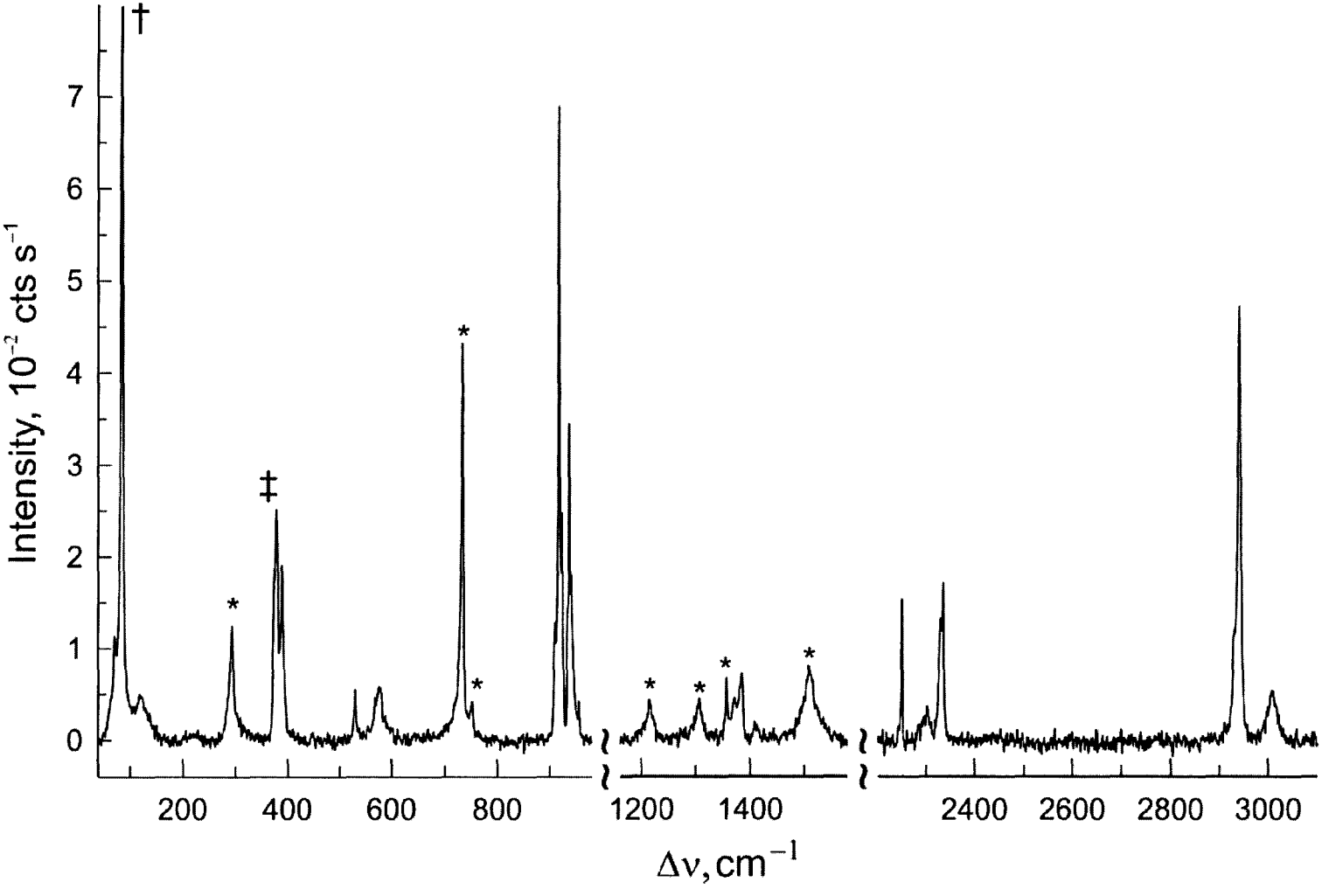

Figure E2. Raman spectrum of $OsO_3F_2(NCCH_3)\cdot n CH_3CN$ recorded at –150 °C using 1064-nm excitation; the symbols denote FEP sample tube lines (*), a band that overlaps with an FEP sample tube line (‡), and an instrumental artifact (†).

Table E2. Factor-group analysis for *fac*-$OsO_3F_2(NCCH_3)\cdot 2CH_3CN$

fac–$OsO_3F_2(NCCH_3)$[a] ($C_{s(xz)}$)	crystal site (C_s)	unit cell[b] (D_{2h})		
$4(\nu_1\text{-}\nu_{15}, R, 2T)$ A′	A′	A_g	$\nu_1\text{-}\nu_{15}$, R, 2T	Raman
		B_{1g}	$\nu_{16}\text{-}\nu_{30}$, 2R, T	
		B_{2g}	$\nu_1\text{-}\nu_{15}$, R, 2T	
		B_{3g}	$\nu_{16}\text{-}\nu_{30}$, 2R, T	
$4(\nu_{16}\text{-}\nu_{30}, 2R, T)$ A″	A″	A_u	$\nu_{16}\text{-}\nu_{30}$, 2R, T	IR
		B_{1u}	$\nu_1\text{-}\nu_{15}$, R, 2T	
		B_{2u}	$\nu_{16}\text{-}\nu_{30}$, 2R, T	
		B_{3u}	$\nu_1\text{-}\nu_{15}$, R, 2T	

[a] The two co-crystallized CH_3CN molecules in the unit cell are not considered for the purpose of the factor-group analysis. [b] The crystallographic space group is *Pnma* with $Z = 4$ structural unit per unit cell.

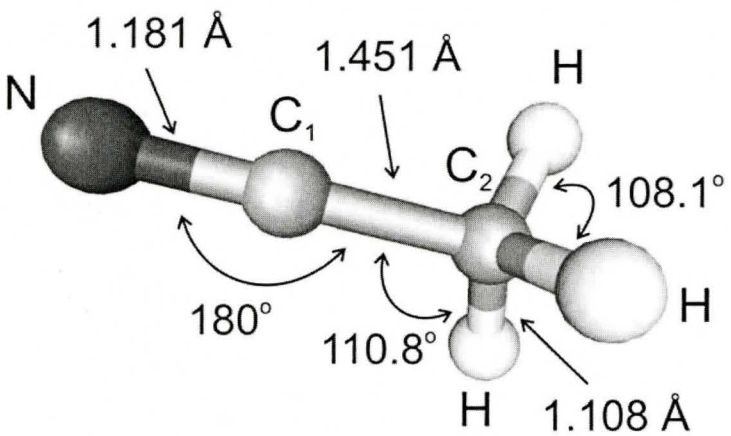

Figure E3. Calculated gas-phase geometry (SVWN) for CH_3CN.

Table E3. Natural Bond Orbital (NBO) Valencies, Bond Orders, and Natural Population Analysis (NPA) Charges for *fac*-$OsO_3F_2(NCCH_3)$, *mer*-$OsO_3F_2(NCCH_3)$, and CH_3CN[a]

	NPA Charges					
	fac-$OsO_3F_2(NCCH_3)$ (C_1)		*mer*-$OsO_3F_2(NCCH_3)$ (C_1)		CH_3CN (C_{3v})	
Atom	SVWN[b]	B3LYP[c]	SVWN[b]	B3LYP[c]	SVWN[b]	B3LYP[d]
Os	1.83	2.16	1.76	2.07		
O_1	–0.38	–0.43	–0.37	–0.41		
O_2	–0.38	–0.43	–0.41	–0.47		
O_3	–0.33	–0.40	–0.41	–0.47		
F_1	–0.46	–0.52	–0.37	–0.43		
F_2	–0.46	–0.52	–0.47	–0.53		
N	–0.41	–0.40	–0.37	–0.36	–0.32	–0.33
C_1	0.49	0.44	0.53	0.50	0.28	0.28
C_2	–0.82	–0.70	–0.83	–0.70	–0.81	–0.69
H	0.30	0.26	0.31	0.27	0.28	0.24
H	0.31	0.26	0.31	0.27	0.28	0.24
H	0.31	0.26	0.31	0.27	0.28	0.24
	Valencies					
Os	3.71	3.58	3.81	3.61		
O_1	0.90	0.89	0.93	0.90		
O_2	0.90	0.89	0.86	0.84		
O_3	0.91	0.89	0.86	0.84		
F_1	0.45	0.43	0.52	0.47		
F_2	0.45	0.43	0.41	0.40		
N	2.10	2.08	2.22	2.22	1.85	1.98
C_1	2.78	2.86	2.77	2.85	2.80	3.00
C_2	3.19	3.24	3.19	3.31	3.18	3.28
H	0.76	0.78	0.76	0.80	0.76	0.79
H	0.76	0.78	0.76	0.80	0.76	0.79
H	0.76	0.78	0.76	0.80	0.76	0.79
	Bond Orders					
Os-O_1	0.84	0.85	0.87	0.85		
Os-O_2	0.84	0.85	0.81	0.79		
Os-O_3	0.87	0.86	0.81	0.79		
Os-F_1	0.42	0.41	0.50	0.46		
Os-F_2	0.42	0.41	0.40	0.37		
Os-N	0.29	0.20	0.40	0.34		
N-C_1	1.76	1.86	1.74	1.83	1.84	1.97
C_1-C_2	0.98	0.96	0.99	0.97	0.94	0.97
C_2-H	0.73	0.75	0.73	0.78	0.74	0.76
C_2-H	0.73	0.76	0.73	0.77	0.74	0.76
C_2-H	0.73	0.76	0.73	0.78	0.74	0.76

[a] For the atom labeling schemes, see Figure 7.6. [b] The SDDall basis set augmented for F and O with two d-type polarization functions by Huzinaga was used.[151] [c] The Stuttgart basis set for Os augmented with one f-type polarization functional was used;[152] aug-cc-pVTZ basis sets were used for all other atoms. [d] The aug-cc-pVTZ basis set was used.

APPENDIX F

CHAPTER 8: SYNTHESES, RAMAN SPECTRA, AND X-RAY CRYSTAL STRUCTURES OF $[XeF_5][\mu\text{-}F(OsO_3F_2)_2]$ AND $[M][OsO_3F_3]$ ($M = XeF_5^+, Xe_2F_{11}^+$)

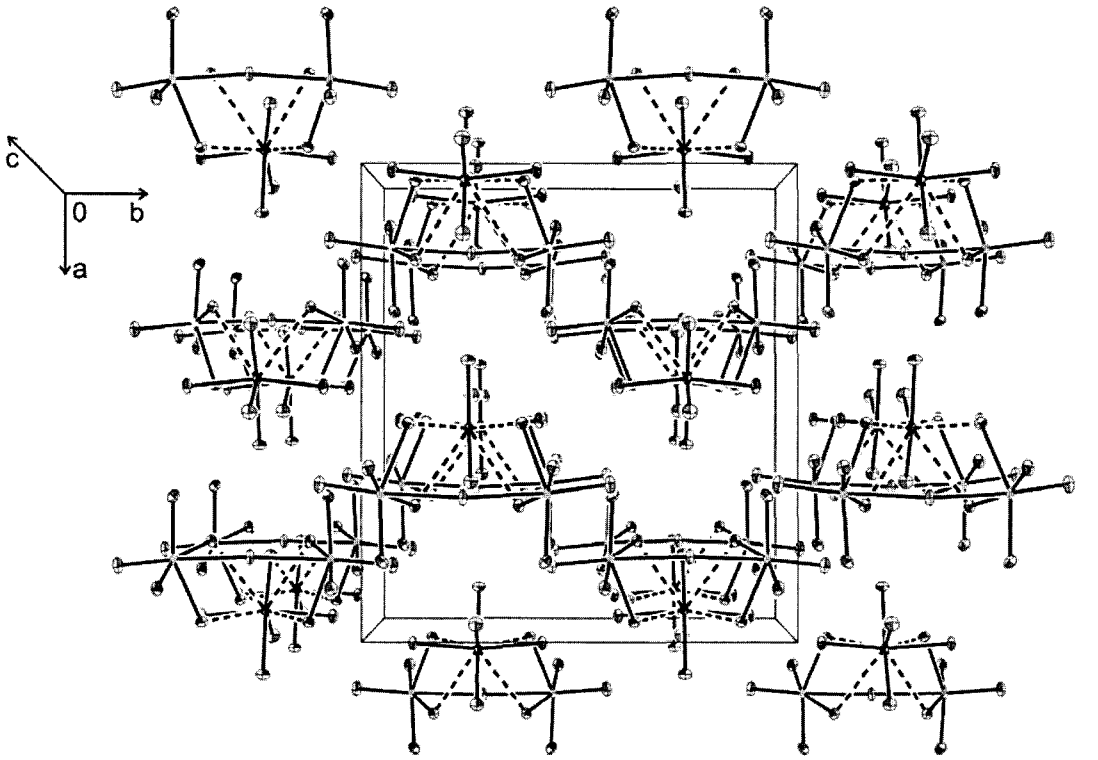

Figure F1. View of the $[XeF_5][\mu\text{-}F(OsO_3F_2)_2]$ crystallographic unit cell along the *c*-axis.

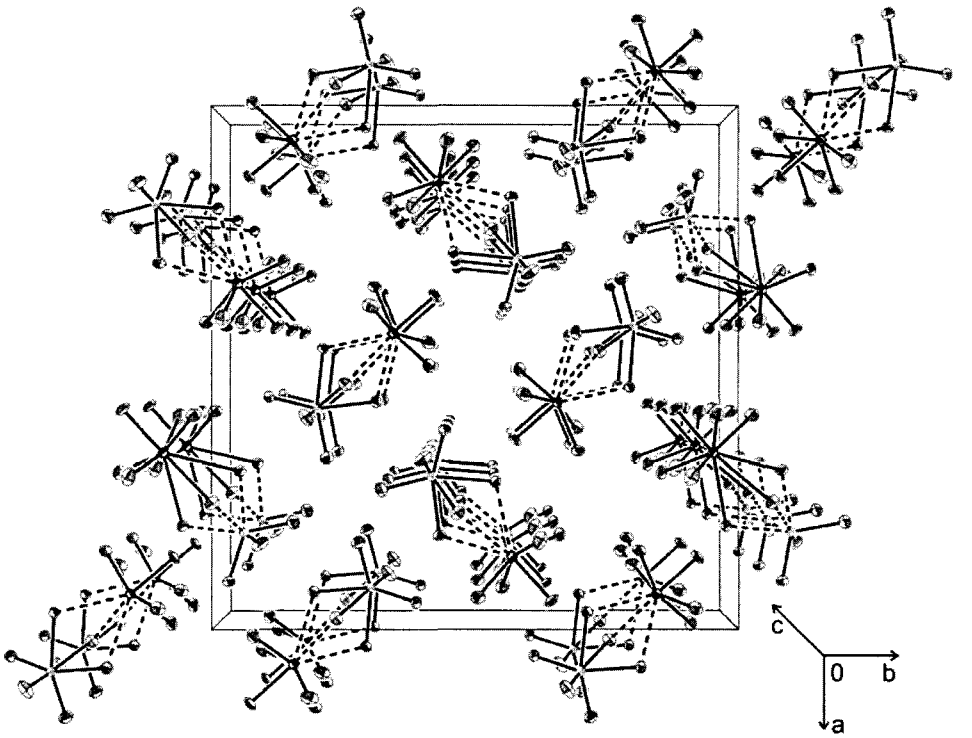

Figure F2. View of the $[XeF_5][OsO_3F_3]$ crystallographic unit cell along the *c*-axis.

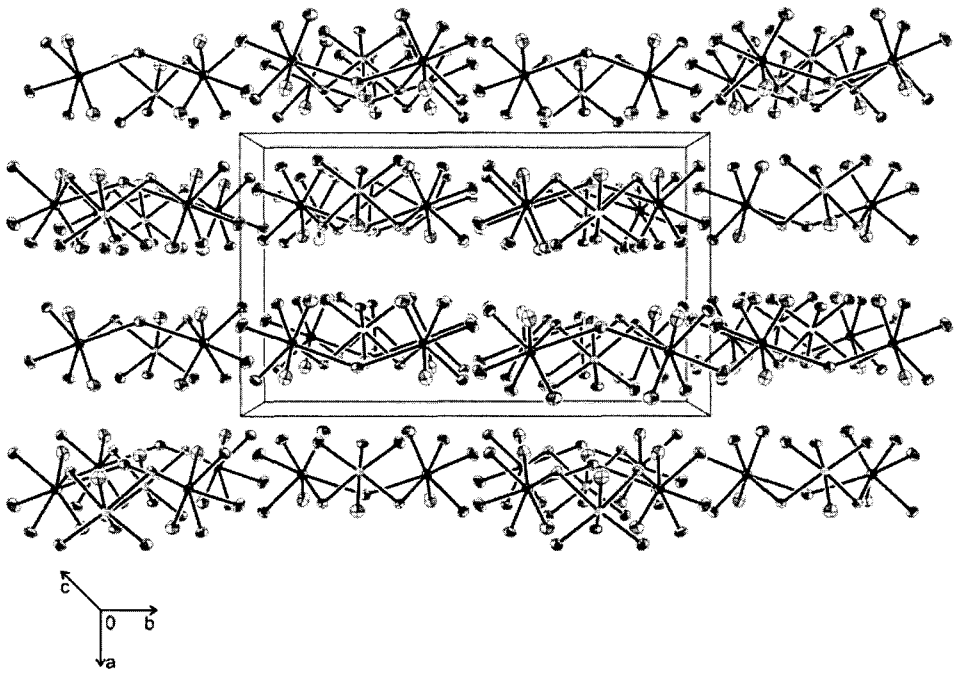

Figure F3. View of the $[Xe_2F_{11}][OsO_3F_3]$ crystallographic unit cell along the *c*-axis.

Table F1. Interatomic Distances (Å) Between the Light Atoms Forming the Coordination Spheres of the Xe and Os atoms in $[XeF_5][\mu\text{-}F(OsO_3F_2)_2]$, $[XeF_5][OsO_3F_3]$, and $[Xe_2F_{11}][OsO_3F_3]$

Contacts[a]	$[XeF_5][\mu\text{-}F(OsO_3F_2)_2]$[b]	$[XeF_5][OsO_3F_3]$[c]	$[Xe_2F_{11}][OsO_3F_3]$[d]
	Cation		
F(1)···F(1A/3/O1B)	2.655(4)	2.449(3)	3.159(3)
F(1)···F(2)	2.418(2)	2.429(3)	2.459(2)
F(1)···F(5/8/6)	2.642(2)	2.700(4)	2.695(2)
F(1)···F(7/5/7)	2.675(2)	2.617(4)	2.637(3)
F(2)···F(2A/3/3)	2.836(4)	2.451(4)	2.643(3)
F(2)···F(5/8/5)	2.618(2)	2.895(4)	2.886(3)
F(2)···F(6/7/6)	2.727(2)	2.656(4)	2.720(2)
F(1A/3/O1B)···F(2A/6/3)	2.418(2)	2.591(3)	2.903(3)
F(1A/O1B)···F(5A/8)	2.642(2)		2.990(3)
F(1A/O1B)···F(7)	2.675(2)		2.916(3)
F(2A/3)···F(5A/5)	2.618(2)		2.666(3)
F(2A/3)···F(6/8)	2.727(2)		2.496(2)
F(4)···F(5)	2.309(2)	2.358(4)	2.357(3)
F(4)···F(5A/8/8)	2.309(2)	2.347(4)	2.336(3)
F(4)···F(6)	2.352(3)	2.354(4)	2.317(3)
F(4)···F(7)	2.345(3)	2.361(4)	2.358(3)
F(5)···F(6)	2.560(2)	2.551(4)	2.598(3)
F(5)···F(7/7/8)	2.570(2)	2.669(4)	2.587(3)
F(5A/6/6)···F(6/7/7)	2.560(2)	2.549(4)	2.640(2)
F(5A/8/8)···F(7)	2.570(2)	2.599(4)	2.526(3)
	Anion		
O(2)···O(1)	2.655(2)	2.663(4)	2.660(4)
O(2)···O(3/3/1A)	2.643(3)	2.666(4)	2.660(4)
O(2)···F(1/1/1A)	2.557(2)	2.630(4)	2.592(3)
O(2)···F(3/3/1)	2.565(2)	2.596(4)	2.592(3)
F(2)···O(1)	2.572(2)	2.603(4)	2.625(3)
F(2)···O(3/3/1A)	2.691(2)	2.642(4)	2.625(3)
F(2)···F(1/1/1A)	2.418(2)	2.429(4)	2.459(2)
F(2)···F(3/3/1)	2.549(2)	2.451(4)	2.459(2)
O(1)···O(3/3/1A)	2.648(3)	2.654(5)	2.636(4)
O(1)···F(3/3/1)	2.599(2)	2.642(4)	2.591(3)
F(1/1/1A)···F(3/3/1)	2.613(2)	2.449(3)	2.548(3)
F(1/1/1A)···O(3/3/1A)	2.634(2)	2.613(4)	2.591(3)

[a] The order of the multiple atom numbering given in parentheses corresponds to the ordering of the contact distance entries. [b] See Figure 8.1b for the atom labeling scheme. [c] See Figure 8.2b for the atom labeling scheme. [d] See Figure 8.3b for the atom labeling scheme.

Table F2. Factor-Group Analysis for $[XeF_5][\mu\text{-}F(OsO_3F_2)_2]$[a]

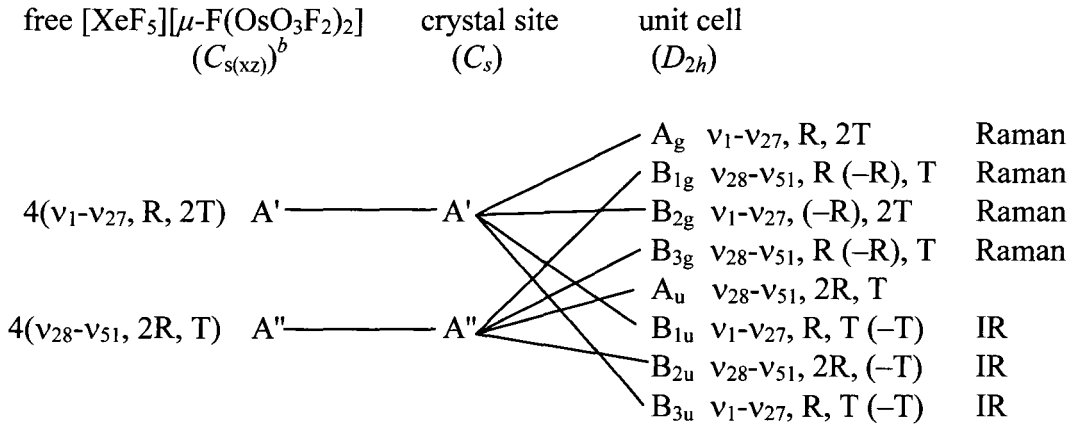

[a] The crystallographic space group is *Pnma* with $Z = 4$ structural units per unit cell. [b] The *xz*-plane is described by the F_4, Xe, and F_3 atoms.

Table F3. Factor-Group Analysis for $[XeF_5][OsO_3F_3]$[a]

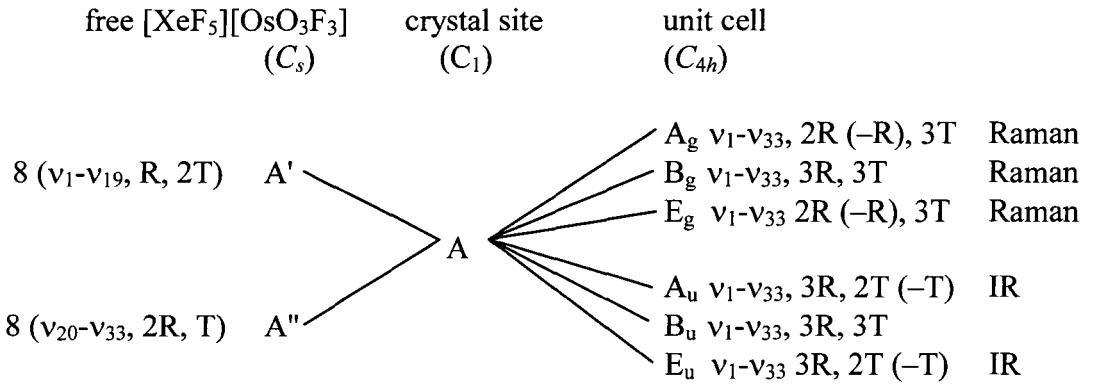

[a] The crystallographic space group is $P4_2/n$ with $Z = 8$ structural units per unit cell.

Table F4. Factor-Group Analysis for $[Xe_2F_{11}][OsO_3F_3]$[a]

free $[Xe_2F_{11}][OsO_3F_3]$ ($C_{s(xz)}$)[b]		crystal site (C_s)	unit cell (D_{2h})	
			A_g ν_1-ν_{29}, R, 2T	Raman
			B_{1g} ν_{30}-ν_{54}, R (–R), T	Raman
$4(\nu_1$-ν_{29}, R, 2T)	A'	A'	B_{2g} ν_1-ν_{29}, (–R), 2T	Raman
			B_{3g} ν_{30}-ν_{54}, R (–R), T	Raman
			A_u ν_{30}-ν_{54}, 2R, T	
			B_{1u} ν_1-ν_{29}, R, T (–T)	IR
$4(\nu_{30}$-ν_{54}, 2R, T)	A"	A"	B_{2u} ν_{30}-ν_{54}, 2R, (–T)	IR
			B_{3u} ν_1-ν_{29}, R, T (–T)	IR

[a] The crystallographic space group is *Pnma* with $Z = 4$ structural units per unit cell. [b] The *xz*-plane is described by the O_2, Os, F_2, and F_3 atoms.

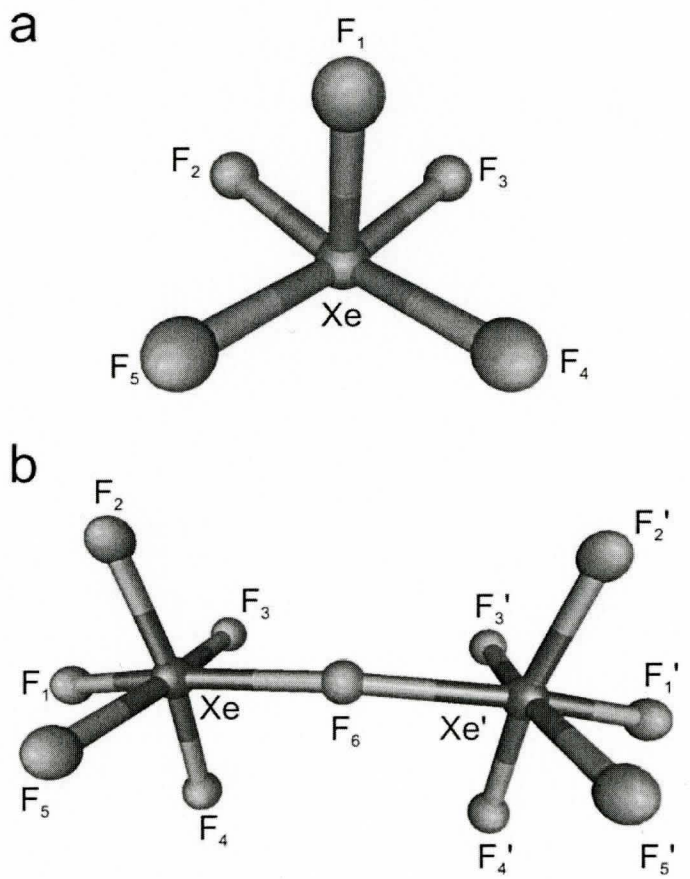

Figure F4. Calculated B3LYP gas-phase geometries and atom numbering scheme used in Tables F6 and F7 for (a) XeF_5^+ and (b) $Xe_2F_{11}^+$.

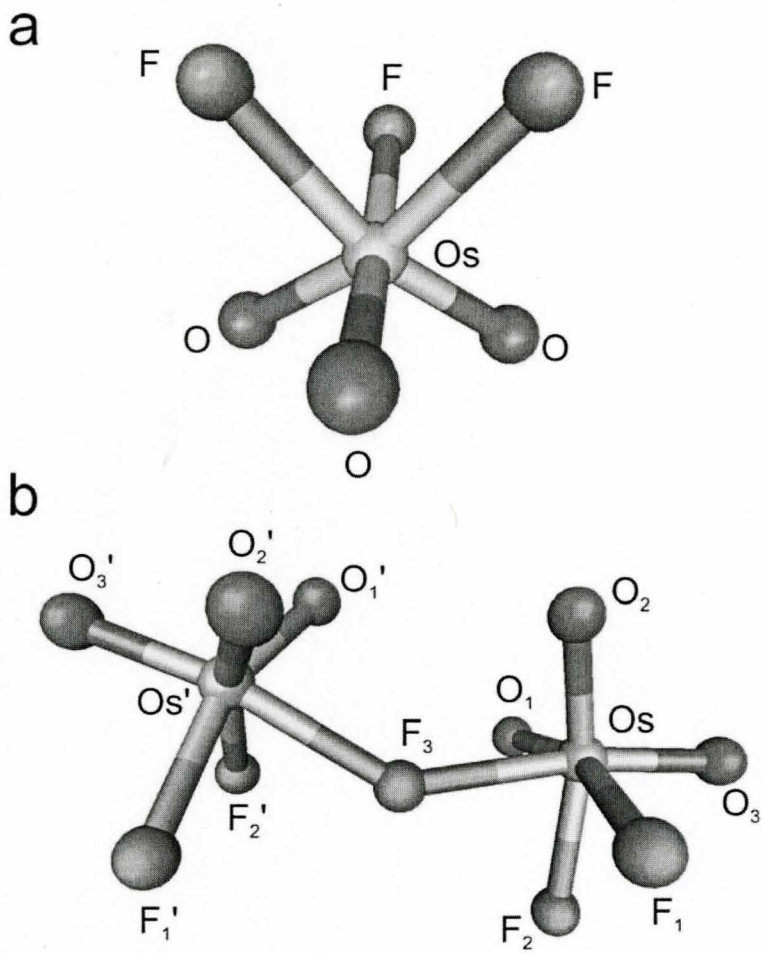

Figure F5. Calculated B3LYP gas-phase geometries and atom numbering scheme used in Tables F5 and F8 for (a) $OsO_3F_3^-$ and (b) μ-$F(OsO_3F_2)_2^-$.

Table F5. Calculated Geometrical Parameters for $OsO_3F_3^-$ (C_{3v})[a]

Bond Lengths(Å)			Bond Angles (deg)		
	SVWN[b]	B3LYP[c]		SVWN[b]	B3LYP[c]
Os–F	1.950	1.961	F–Os–F	78.9	79.4
Os–O	1.737	1.711	F–Os–O	164.1	164.5
			F–Os–O	88.9	88.7
			O–Os–O	101.1	101.0

[a] See Figure F5a for the atom labeling scheme. [b] The SDDall basis set augmented for F and O with two d-type polarization functions was used. [c] The Stuttgart basis set was used for Os with the f functional. The aug-cc-pVTZ basis sets were used for all other atoms.

Table F6. Calculated Geometrical Parameters for $Xe_2F_{11}^+$ (C_s)[a]

	SVWN[b]	B3LYP[c]		SVWN[b]	B3LYP[c]
Bond Lengths (Å)					
Xe–F_1	1.861	1.853	Xe–F_4	1.899	1.895
Xe–F_2	1.912	1.907	Xe–F_5	1.912	1.907
Xe–F_3	1.899	1.895	Xe---F_6	2.264	2.344
Bond Angles (deg)					
F_1–Xe–F_2	82.8	83.5	F_3–Xe–F_4	87.5	88.5
F_1–Xe–F_3	82.4	83.5	F_3–Xe–F_5	165.1	167.0
F_1–Xe–F_4	82.4	83.5	F_3–Xe---F_6	79.2	87.2
F_1–Xe–F_5	82.8	83.6	F_4–Xe–F_5	88.4	89.1
F_1–Xe---F_6	154.4	166.9	F_4–Xe---F_6	79.2	87.2
F_2–Xe–F_3	88.4	89.1	F_5–Xe---F_6	114.1	105.4
F_2–Xe–F_4	165.1	167.0	Xe---F_6---Xe'	141.8	171.2
F_2–Xe–F_5	91.9	90.4			
F_2–Xe---F_6	114.1	105.5			

[a] See Figure F4b for the atom labeling scheme. [b] The SDDall basis set augmented for F and Xe with two d-type polarization functions for each atom. [c] The aug-cc-pVTZ(-PP) basis sets was used.

Table F7. Natural Bond Orbital (NBO) Valencies, Bond Orders, and Natural Population Analysis (NPA) Charges for XeF_5^+ and $Xe_2F_{11}^+$

Atom	XeF_5^+[a]		$Xe_2F_{11}^+$[b]	
	SVWN[c]	B3LYP[d]	SVWN[c]	B3LYP[d]
	charges [valencies]			
Xe	3.08 [2.40]	3.24 [2.44]	3.074 [2.628]	3.289 [2.613]
F_1	–0.38 [0.40]	–0.39 [0.42]	–0.415 [0.440]	–0.437 [0.421]
F_2	–0.42 [0.42]	–0.46 [0.43]	–0.460 [0.449]	–0.502 [0.454]
F_3	–0.42 [0.42]	–0.46 [0.43]	–0.459 [0.432]	–0.491 [0.459]
F_4	–0.42 [0.42]	–0.46 [0.43]	–0.459 [0.432]	–0.491 [0.459]
F_5	–0.42 [0.42]	–0.46 [0.43]	–0.460 [0.449]	–0.502 [0.454]
F_6			–0.640 [0.356]	–0.734 [0.435]
	bond orders			
Xe–F_1	0.50	0.53	0.518	0.514
Xe–F_2	0.48	0.48	0.478	0.482
Xe–F_3	0.48	0.48	0.480	0.491
Xe–F_4	0.48	0.48	0.480	0.491
Xe–F_5	0.48	0.48	0.478	0.482
Xe---F_6			0.185	0.150

[a] See Figure F4a for the atom labeling scheme. [b] See Figure F4b for the atom labeling scheme.[a] The SDDall basis set augmented for F and Xe with two d-type polarization functions. [b] The aug-cc-pVTZ(-PP) basis sets were used for all other atoms.

Table F8. Natural Bond Orbital (NBO) Valencies, Bond Orders and Natural Population Analysis (NPA) Charges for $OsO_3F_3^-$ and μ-$F(OsO_3F_2)_2^-$

Atom	$OsO_3F_3^{-a}$		μ-$F(OsO_3F_2)_2^{-b}$	
	SVWN[c]	B3LYP[d]	SVWN[c]	B3LYP[d]
	charges [valencies]			
Os	1.859 [3.602]	2.174 [3.694]	1.881 [3.538]	2.191 [3.593]
O(1)	–0.440 [0.849]	–0.484 [0.862]	–0.396 [0.869]	–0.431 [0.885]
O(2)	–0.440 [0.849]	–0.484 [0.862]	–0.405 [0.865]	–0.443 [0.886]
O(3)	–0.440 [0.849]	–0.484 [0.862]	–0.409 [0.878]	–0.456 [0.882]
F(1)	–0.513 [0.401]	–0.574 [0.372]	–0.459 [0.441]	–0.527 [0.418]
F(2)	–0.513 [0.401]	–0.574 [0.372]	–0.438 [0.453]	–0.524 [0.419]
F(3)	–0.513 [0.401]	–0.574 [0.372]	–0.550 [0.523]	–0.620 [0.404]
	bond orders			
Os–O(1)	0.813	0.849	0.822	0.858
Os–O(2)	0.813	0.849	0.819	0.857
Os–O(3)	0.813	0.849	0.832	0.854
Os–F(1)	0.388	0.382	0.414	0.410
Os–F(2)	0.388	0.382	0.424	0.412
Os–F(3)	0.388	0.382	0.239	0.206

[a] See Figure F5a for the atom labeling scheme. [b] See Figure F5b for the atom labeling scheme. [c] The SDDall basis set augmented for F and O with two d-type polarization functions. [d] The Stuttgart basis set was used for Os with the f functional. The aug-cc-pVTZ(-PP) basis sets were used for all other atoms.

APPENDIX G

CHAPTER 9: SYNTHESES AND STRUCTURES OF THE MOLECULAR ADDITION COMPOUNDS, $XeOF_4 \cdot NgF_2$ (Ng = Xe or Kr)

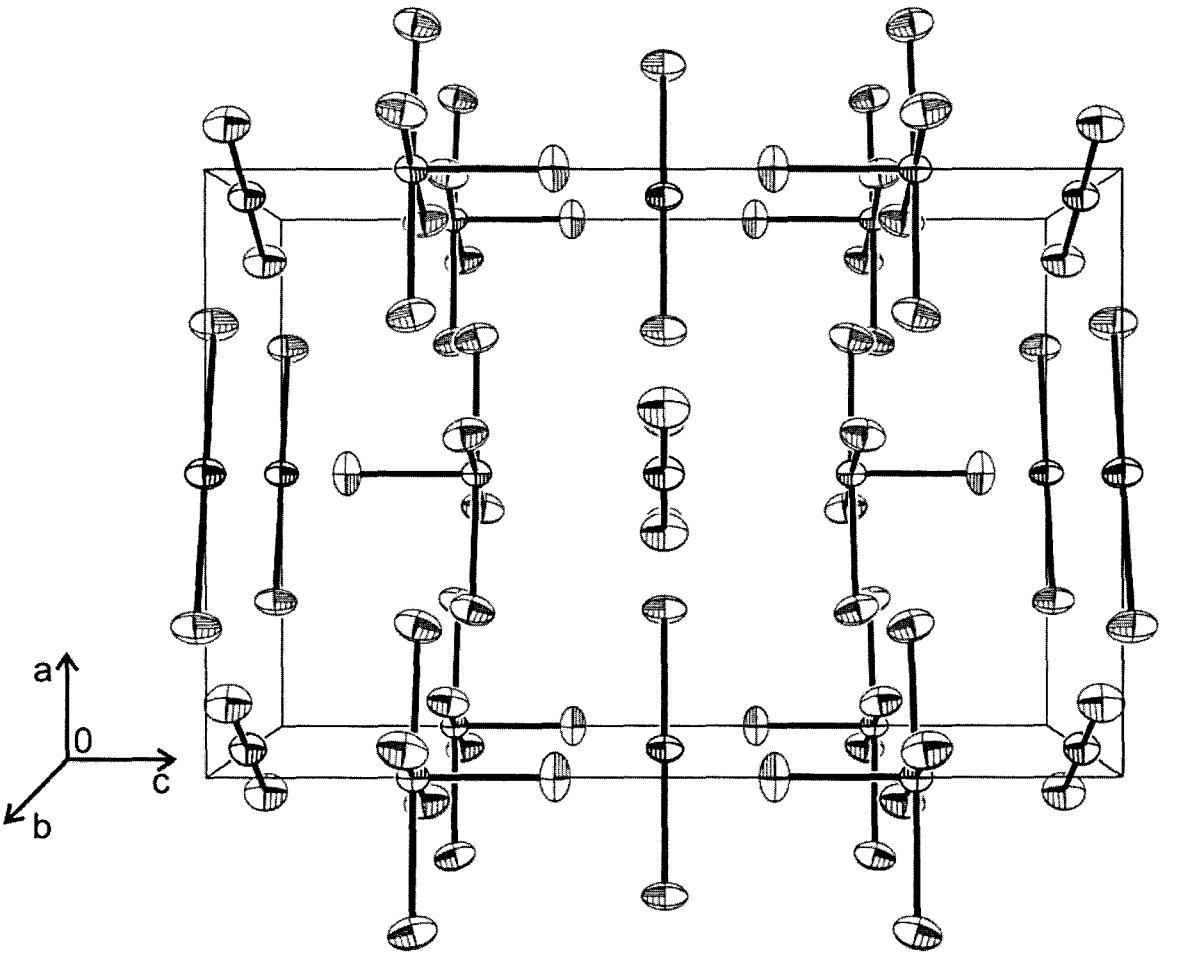

Figure G1. View of $XeOF_4 \cdot XeF_2$ crystallographic unit cell along the *b*-axis.

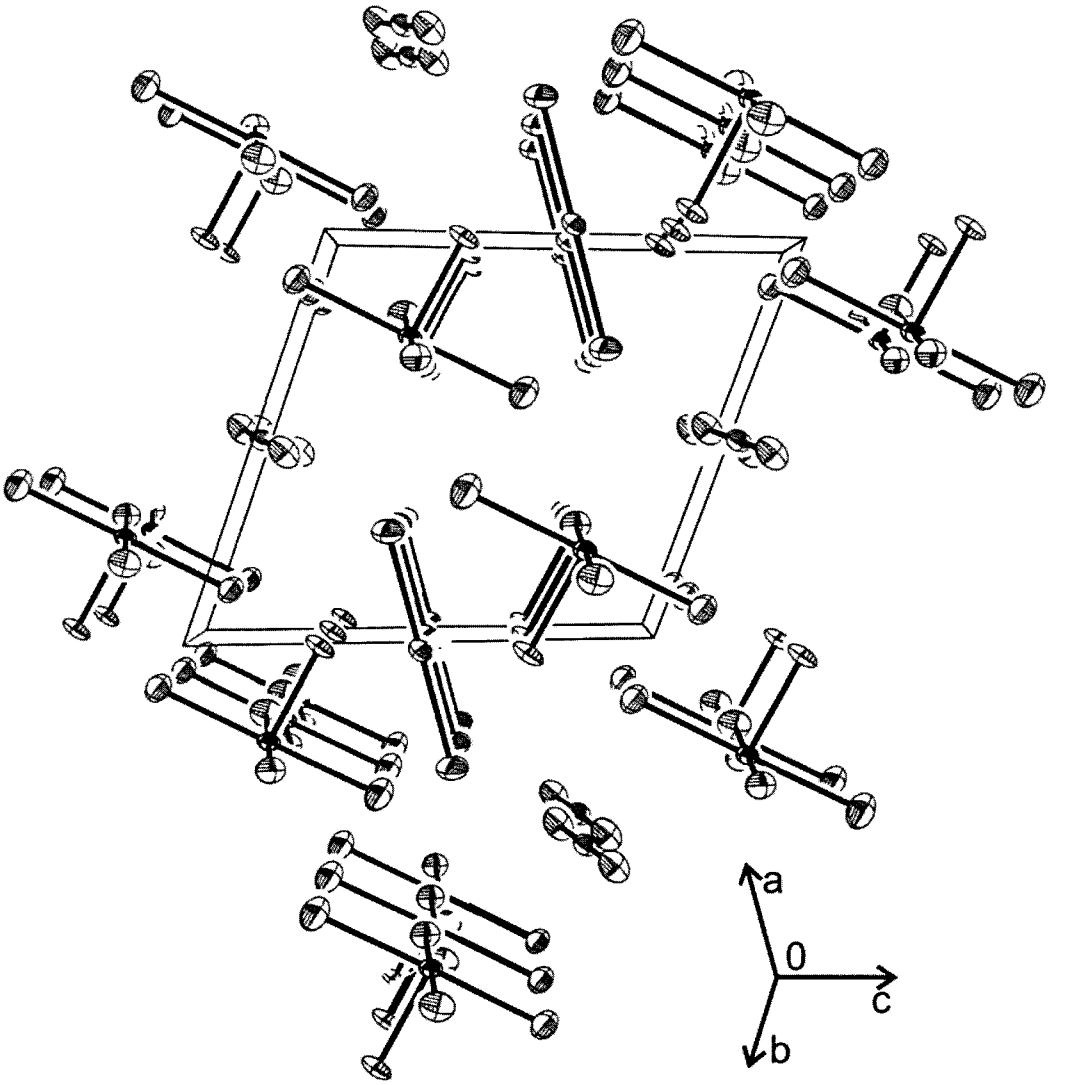

Figure G2. View of $XeOF_4 \cdot KrF_2$ crystallographic unit cell along the *b*-axis.

Table G1. Interatomic Distances (Å) for the Light Atoms that Comprise the Coordination Spheres of the Xe_1 atoms in $XeOF_4 \cdot NgF_2$ (Ng = Xe, Kr)

Contacts[a]	$XeOF_4 \cdot XeF_2$[b]	$XeOF_4 \cdot KrF_2$[c]
O(1)···F(1)	2.550(6)	2.554(3)
O(1)···F(2)		2.547(3)
O(1)···F(3)		2.552(4)
O(1)···F(4)		2.554(4)
F(1)···F(1A/2)	2.76(3)	2.682(3)
F(1)···F(2A)		2.937(3)
F(1)···F(5A/4)	3.10(1)	2.663(3)
F(1)···F(5)	2.783(9)	2.814(4)
F(2)···F(2A)		2.971(4)
F(2)···F(3)		2.724(3)
F(2)···F(6)		3.070(4)
F(3)···F(4)		2.724(3)
F(3)···F(5B)		3.031(4)
F(3)···F(6)		2.801(3)
F(4)···F(5)		3.080(3)
F(4)···F(5B)		2.842(3)
F(5)···F(5A/5B)	2.74(4)	3.192(5)
F(5)···F(2A)		3.115(4)
F(6)···F(5B)		2.969(4)
F(6)···F(2A)		3.777(4)

[a] The order of the multiple atom numbering given in parentheses corresponds to the ordering of the contact distance entries. [b] See Figure 9.3a for the atom labeling scheme. [c] See Figure 9.3b for the atom labeling scheme.

Table G2. Experimental Raman Frequencies, Intensities, and Assignments for Gas-Phase $XeOF_4$, and the Calculated Vibrational Frequencies and Intensities for $XeOF_4$

exptl[a]	calcd (C_{4v})[b]			assgnt[c]
	SVWN	B3LYP	PBE1PBE	
928(s)	920(21)[29]	886(20)[25]	936(20)[28]	A1 ν(XeO)
609(vw)	610(<1)[254]	593(<1)[282]	619(<0.1)[298]	E $\nu_{as}(XeF_2)$
577(vs)	560(38)[5]	552(44)[5]	583(40)[4]	A1 $\nu_s(XeF_4)$
543(m)	533(19)[0]	511(23)[0]	542(21)[0]	B2 $\nu_s(XeF_2) - \nu_s(XeF_2)$
362(w)	312(3)[5]	326(3)[4]	346(2)[6]	E δ(OXeF)
287(m)	242(1)[28]	262(1)[35]	281(1)[37]	A1 $\delta_{umb}(XeF_4)$
225(w)	197(3)[0]	211(0)[3]	219(2)[0]	B1 $\delta(XeF_2) + \delta(XeF_2)$
	161(<0.1)[0]	170(<0.1)[0]	183(<0.1)[0]	B2 $\rho_t(XeF_2) - \rho_t(XeF_2)$
161(w)	143(<1)[1]	152(<1)[1]	155(<1)[1]	E $\rho_w(XeF_2)$

[a] From Ref 101. The abbreviations denote very strong (vs), strong (s), medium (m), weak (w) and very weak (vw). [b] Values in parentheses denote calculated Raman intensities ($Å^4\ u^{-1}$) and values in square brackets denote calculated infrared intensities (km mol^{-1}). The aug-cc-pVTZ(-PP) basis set was used. [c] The atom labeling scheme refers to the figure below. The abbreviations denote stretch (ν), asymmetric (as), symmetric (s), bend (δ), wag (ρ_w), and umbrella (umb). The equatorial fluorine atoms are denoted by F_{4e} or by F_{2e}, and F_{2e}'.

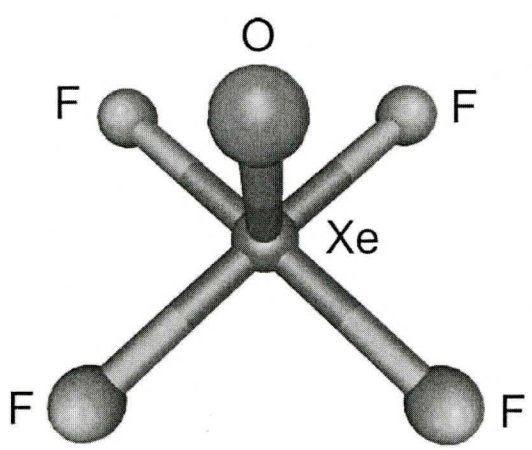

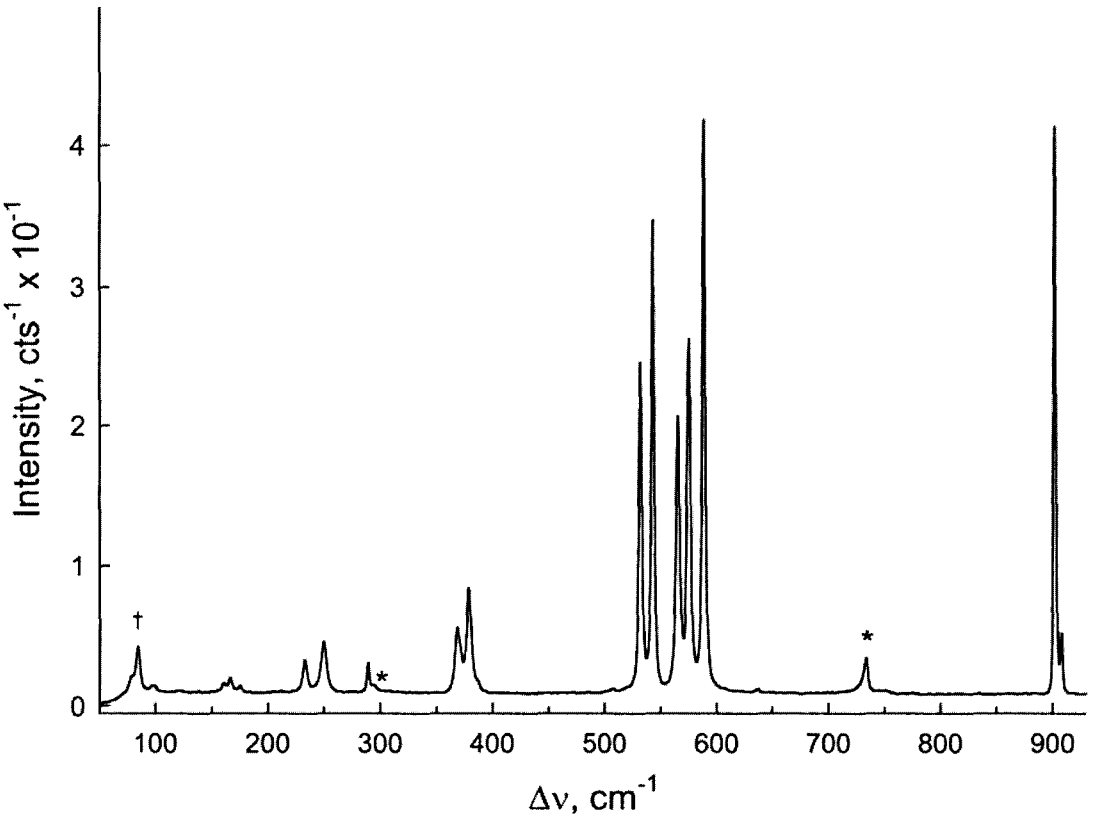

Figure G3. Raman spectrum of solid $XeOF_4$ recorded at –150 °C using 1064-nm excitation; the symbols denote FEP sample tube lines (*) and an instrumental artifact (†).

Table G3. Experimental Raman Frequencies, Intensities, and Assignments for Gas-Phase NgF_2, and the Calculated Vibrational Frequencies and Intensities for NgF_2 (Ng = Xe, Kr)

XeF_2				
exptl [a]	calcd ($D_{\infty h}$)[d]			assgnt[e]
	SVWN	B3LYP	PBE1PBE	
555[b]	570(0)[219]	548(0)[246]	572(0)[261]	Σ_u^- $\nu_{as}(NgF_2)$
497	521(35)[0]	507(47)[0]	534(44)[0]	Σ_g^+ $\nu_s(NgF_2)$
213[b]	203(0)[13]	205(0)[15]	215(0)[15]	Π_u δ(FNgF)
KrF_2				
	613(0)[231]	584(0)[260]	612(0)[287]	Σ_u^- $\nu_{as}(NgF_2)$
462(s)[c]	511(36)[0]	492(52)[0]	525(51)[0]	Σ_g^+ $\nu_s(NgF_2)$
	237(0)[12]	235(0)[13]	249(0)[14]	Π_u δ(FNgF)

[a] from ref 267. [b] determined by IR spectroscopy and reported as intense. [c] from ref 268. [d] Values in parentheses denote calculated Raman intensities ($Å^4$ u^{-1}) and values in square brackets denote calculated infrared intensities (km mol^{-1}). The aug-cc-pVTZ(-PP) basis sets were used. [e] The abbreviations denote stretch (ν), asymmetric (as), symmetric (s), and bend (δ).

Table G4. Calculated Vibrational Frequencies and Assignments of $2XeOF_4 \cdot NgF_2$ (Ng = Xe, Kr)

$2XeOF_4 \cdot XeF_2$[a]			$2XeOF_4 \cdot KrF_2$[a]			assgnts (C_{2h})[b]
SVWN	B3LYP	PBE1PBE	SVWN	B3LYP	PBE1PBE	
921(107)[0]	891(74)[0]	938(62)[0]	921(107)[0]	891(67)[0]	938(57)[0]	A_g ν(XeO) + ν(Xe'O')
920(0)[94]	891(0)[69]	938(0)[74]	921(0)[94]	891(0)[4]	938(0)[70]	B_u ν(XeO) – ν(Xe'O')
594(0)[444]	583(0)[523]	609(0)[545]	594(0)[444]	585(0)[526]	611(0)[550]	A_u (ν(XeF_1) + ν(XeF_4) + ν($Xe'F_2'$) + ν($Xe'F_3'$)) – (ν(XeF_2) + ν(XeF_3) + ν($Xe'F_1'$) + ν(XeF_4'))
596(10)[0]	583(6)[0]	609(7)[0]	596(10)[0]	585(6)[0]	611(7)[0]	A_g (ν(XeF_1) + ν(XeF_2) + ν($Xe'F_1'$) + ν($Xe'F_2'$)) – (ν(XeF_3) + ν(XeF_4) + ν($Xe'F_3'$) + ν($Xe'F_4'$))
592(0)[516]	582(0)[548]	607(0)[567]	592(0)[516]	584(0)[490]	610(0)[455]	B_u (ν(XeF_1) + ν(XeF_2) + ν($Xe'F_3'$) + ν($Xe'F_4'$)) – (ν(XeF_3) + ν(XeF_4) + ν($Xe'F_1'$) + ν($Xe'F_2'$))
591(5)[0]	581(2)[0]	606(2)[0]	591(5)[0]	583(2)[0]	608(2)[0]	B_g (ν(XeF_1) + ν(XeF_4) + ν($Xe'F_1'$) + ν($Xe'F_4'$)) – (ν(XeF_2) + ν(XeF_3) + ν($Xe'F_2'$) + ν($Xe'F_3'$))
514(0)[278]	512(0)[346]	535(0)[375]	550(0)[176]	561(0)[434]	589(0)[500]	B_u ν(NgF_5) – ν(NgF_5')
547(54)[0]	544(64)[0]	575(60)[0]	547(54)[0]	545(71)[0]	575(65)[0]	A_g ν(XeF_1) + ν(XeF_2) + ν(XeF_3) + ν(XeF_4) + ν($Xe'F_1'$) + ν($Xe'F_2'$) + ν($Xe'F_3'$) + ν($Xe'F_4'$)
550(0)[176]	547(0)[109]	576(0)[109]	512(0)[278]	539(0)[63]	568(0)[94]	B_u (ν(XeF_1) + ν(XeF_2) + ν(XeF_3) + ν(XeF_4)) – (ν($Xe'F_1'$) + ν($Xe'F_2'$) + ν($Xe'F_3'$) + ν($Xe'F_4'$)) + ν(NgF_5) – ν(NgF_5')
506(0)[6]	501(0)[3]	532(0)[4]	506(0)[6]	503(0)[2]	533(0)[4]	A_u (ν(XeF_1) + ν(XeF_3) + ν($Xe'F_2'$) + ν($Xe'F_4'$)) – (ν(XeF_2) + ν(XeF_4) + ν($Xe'F_1'$) + ν($Xe'F_3'$))
506(28)[0]	501(41)[0]	531(37)[0]	506(28)[0]	503(41)[0]	533(37)[0]	B_g (ν(XeF_1) + ν(XeF_3) + ν($Xe'F_1'$) + ν($Xe'F_3'$)) – (ν(XeF_2) + ν(XeF_4) + ν($Xe'F_2'$) + ν($Xe'F_4'$))
499(110)[0]	498(134)[0]	523(98)[0]	499(110)[0]	488(128)[0]	520(96)[0]	A_g ν(NgF_5) + ν(NgF_5')
310(0)[7]	326(0)[7]	348(0)[9]	310(0)[7]	327(0)[7]	348(0)[10]	B_u δ($OXeF_3F_4$) + δ($O'Xe'F_1'F_2'$)
310(5)[0]	326(5)[0]	348(5)[0]	310(5)[0]	327(5)[0]	348(5)[0]	A_g δ($OXeF_3F_4$) + δ($O'Xe'F_3'F_4'$)
309(0)[6]	326(0)[7]	347(0)[9]	309(0)[6]	326(0)[7]	347(0)[9]	A_u δ($OXeF_1F_4$) + δ($O'Xe'F_2'F_3'$)
308(4)[0]	326(5)[0]	347(5)[0]	308(4)[0]	326(5)[0]	347(5)[0]	B_g δ($OXeF_1F_4$) + δ($O'Xe'F_1'F_4'$)
250(4)[0]	265(2)[0]	284(2)[0]	250(4)[0]	265(2)[0]	284(2)[0]	A_g δ_{umb}($XeF_1F_2F_3F_4$) + δ_{umb}($Xe'F_1'F_2'F_3'F_4'$)
259(0)[22]	263(0)[92]	282(0)[92]	258(0)[22]	264(0)[52]	283(0)[60]	B_u δ_{umb}($XeF_1F_2F_3F_4$) – δ_{umb}($Xe'F_1'F_2'F_3'F_4'$) – δ(F_5NgF_5')
246(0)[142]	228(0)[53]	238(0)[56]	245(0)[142]	251(0)[84]	265(0)[80]	B_u δ_{ip}(F_5NgF_5')
215(0)[5]	210(0)[7]	220(0)[7]	215(0)[5]	237(0)[6]	251(0)[6]	A_u δ_{oop}(F_5NgF_5')
198(7)[0]	208(5)[0]	217(4)[0]	198(7)[0]	209(5)[0]	217(4)[0]	A_g δ(F_1XeF_4) + δ(F_2XeF_3) + δ($F_1'Xe'F_4'$) + δ($F_2'Xe'F_3'$)
196(0)[5]	207(0)[3]	215(0)[4]	196(0)[5]	209(0)[1]	217(0)[1]	B_u (δ(F_1XeF_4) + δ(F_2XeF_3)) – (δ($F_1'Xe'F_4'$) + δ($F_2'Xe'F_3'$))
177(<0.1)[0]	176(<0.1)[0]	190(<0.1)[0]	177(<0.1)[0]	176(<0.1)[0]	189(<0.1)[0]	B_g ρ_t(F_1XeF_2) + ρ_t(F_3XeF_4) + ρ_t($F_1'Xe'F_2'$) + ρ_t($F_3'Xe'F_4'$)

165(0)[<1]	173(0)[<1]	186(0)[<1]	165(0)[<1]	174(0)[<0.1]	188(0)[<0.1]	A_u ($\rho_t(F_1XeF_2) + \rho_t(F_3XeF_4)$) – ($\rho_t(F_1'Xe'F_2') + \rho_t(F_3'Xe'F_4')$)
180(22)[0]	154(0)[0]	158(1)[0]	149(1)[0]	155(1)[0]	159(1)[0]	A_g ($\delta(F_1XeF_2) + \delta(F_1'Xe'F_2')$) – ($\delta(F_3XeF_4) + \delta(F_3'Xe'F_4')$)
149(0)[6]	153(0)[3]	158(0)[3]	149(0)[6]	155(0)[3]	159(0)[3]	B_u ($\delta(F_1XeF_2) + \delta(F_3'Xe'F_4')$) – ($\delta(F_3XeF_4) + \delta(F_1'Xe'F_2')$)
133(1)[0]	146(1)[0]	149(<1)[0]	133(1)[0]	147(1)[0]	149(<1)[0]	B_g ($\delta(F_1XeF_4) + \delta(F_1'Xe'F_4')$) – ($\delta(F_2XeF_3) + \delta(F_2'Xe'F_3')$)
133(0)[2]	146(0)[1]	149(0)[1]	133(0)[2]	147(0)[1]	149(0)[1]	A_u ($\delta(F_1XeF_4) + \delta(F_2'Xe'F_3')$) – ($\delta(F_2XeF_3) + \delta(F_1'Xe'F_4')$)
149(1)[0]	118(15)[0]	122(12)[0]	180(22)[0]	115(20)[0]	117(15)[0]	A_g $\rho_{rip}(F_5NgF_5')$
89(1)[0]	72(1)[0]	76(1)[0]	90(1)[0]	69(1)[0]	71(1)[0]	B_g $\rho_{roop}(F_5NgF_5')$
90(0)[<1]	58(0)[1]	59(0)[1]	90(0)[<1]	63(0)[1]	64(0)[1]	B_u $NgF_2{\cdot}2XeOF_4$ coupled modes
64(0)[3]	48(0)[2]	52(0)[2]	64(0)[2]	50(0)[2]	53(0)[3]	B_u $NgF_2{\cdot}2XeOF_4$ coupled modes
61(0)[<1]	42(0)[<1]	46(0)[<1]	61(0)[<1]	44(0)[<1]	47(0)[<1]	A_u $NgF_2{\cdot}2XeOF_4$ coupled modes
57(<1)[0]	41(<1)[0]	44(<1)[0]	57(<1)[0]	41(<1)[0]	42(<1)[0]	A_g $\rho_r(XeOF_1F_2F_3F_4) + \rho_r(Xe'O'F_1'F_2'F_3'F_4')$
39(<0.1)[0]	14(<1)[0]	18(<0.1)[0]	39(<0.11)[0]	15(<1)[0]	18(<0.1)[0]	A_g $NgF_2{\cdot}2XeOF_4$ coupled modes
36(<1)[0]	–8(1)[0]	12(1)[0]	25(2)[0]	12(0)[2]	13(0)[2]	B_u $NgF_2{\cdot}2XeOF_4$ coupled modes
25(0)[2]	9(0)[2]	12(0)[2]	24(0)[<0.1]	12(0)[<0.1]	12(0)[<0.1]	A_u ($\rho_t(F_1XeF_2) + \rho_t(F_3XeF_4)$) – ($\rho_t(F_1'Xe'F_2') + \rho_t(F_3'Xe'F_4')$)
8(0)[1]	–7(0)[<0.1]	5(0)[1]	8(0)[<0.1]	6(0)[1]	4(0)[1]	A_u $NgF_2{\cdot}2XeOF_4$ coupled modes
24(0)[<0.1]	4(0)[1]	13(0)[<0.1]	36(<1)[0]	1(1)[0]	10(1)[0]	B_g $NgF_2{\cdot}2XeOF_4$ coupled modes

[a] Values in parentheses denote calculated Raman intensities ($Å^4\ u^{-1}$) and values in square brackets denote calculated infrared intensities (km mol^{-1}). The aug-cc-pVTZ(-PP) basis sets were used. [b] The abbreviations denote stretch (ν), bend (δ), wag (ρ_w), rock (ρ_r), twist (ρ_t), umbrella (δ_{umb}), in-plane (ip), and out-of-plane (oop). See Figure 9.7b and 9.8b for the atom labeling scheme, Ng = Xe and Kr for $2XeOF_4{\cdot}XeF_2$ and $2XeOF_4{\cdot}KrF_2$, respectively.

Table G5. Calculated Vibrational Frequencies of $XeOF_4 \cdot 4XeF_2$

calcd[a]			assgnts[b]
SVWN	B3LYP	PBE1PBE	C_4
909(62)[51]	883(32)[34]	930(30)[39]	A, $\nu(Xe_1O_1)$
576(<1)[250]	579(<0.1)[283]	602(<0.1)[293]	E, $\nu(Xe_1F_2) - \nu(Xe_1F_4)$
570(22)[42]	550(27)[43]	575(39)[41]	A, $[\nu(Xe_2F_5) + \nu(Xe_3F_7) + \nu(Xe_4F_9) + \nu(Xe_5F_{11})]$ $- [\nu(Xe_2F_6) + \nu(Xe_3F_8) + \nu(Xe_4F_{10}) + \nu(Xe_5F_{12})]$
531(10)[4]	540(21)[1]	569(6)[1]	A, $\nu(Xe_1F_1) + \nu(Xe_1F_2) + \nu(Xe_1F_3) + \nu(Xe_1F_4)$
552(1)[500]	538(1)[497]	560(1)[517]	E, $\nu(Xe_2F_6) - \nu(Xe_4F_{10})$
551(23)[0]	535(20)[0]	558(25)[0]	B, $[\nu(Xe_2F_6) + \nu(Xe_4F_{10})] - [\nu(Xe_3F_8) + \nu(Xe_5F_{12})]$
511(63)[0]	503(30)[0]	530(6)[0]	B, $\{[\nu(Xe_1F_1) + \nu(Xe_1F_3)] - [\nu(Xe_1F_2) + \nu(Xe_1F_4)]\}$ $- \{[\nu(Xe_2F_5) + \nu(Xe_4F_9)] - [\nu(Xe_3F_7) + \nu(Xe_5F_{11})]\}$
503(220)[3]	499(156)[4]	524(143)[4]	A, $\nu(Xe_2F_5) + \nu(Xe_3F_7) + \nu(Xe_4F_9) + \nu(Xe_5F_{11})$
506(6)[77]	499(5)[89]	523(4)[118]	E, $\nu(Xe_2F_5) - \nu(Xe_4F_9)$
491(25)[0]	495(73)[0]	522(82)[0]	B, $\{[\nu(Xe_1F_1) + \nu(Xe_1F_3)] - [\nu(Xe_1F_2) + \nu(Xe_1F_4)]\}$ $+ \{[\nu(Xe_2F_5) + \nu(Xe_4F_9)] - [\nu(Xe_3F_7) + \nu(Xe_5F_{11})]\}$
343(4)[4]	341(4)[5]	362(3)[6]	E, $\delta(O_1Xe_1F_1F_2) - \delta(O_1Xe_1F_3F_4)$
288(<1)[30]	278(1)[42]	298(<1)[45]	A, $\delta_{umb}(Xe_1F_1F_2F_3F_4)$
240(2)[0]	218(2)[0]	228(2)[0]	B, $[\delta(F_1Xe_1F_2) + \delta(F_3Xe_1F_4)] + [\rho_w(F_5Xe_2F_6) + \rho_w(F_9Xe_4F_{10})]$ $- [\rho_w(F_7Xe_3F_8) + \rho_w(F_{11}Xe_5F_{12})]$
226(1)[69]	213(<1)[71]	223(<1)[70]	A, $\rho_w(F_5Xe_2F_6) + \rho_w(F_7Xe_3F_8) + \rho_w(F_9Xe_4F_{10}) + \rho_w(F_{11}Xe_5F_{12})$
231(1)[18]	211(<0.1)[16]	221(<1)[19]	E, $\rho_w(F_5Xe_2F_6) - \rho_w(F_9Xe_4F_{10})$ or $\rho_w(F_7Xe_3F_8) - \rho_w(F_{11}Xe_5F_{12})$
214(1)[0]	209(<1)[0]	218(<1)[0]	B, $[\delta(F_1Xe_1F_2) + \delta(F_3Xe_1F_4)] + [\delta(F_5Xe_2F_6) + \delta(F_9Xe_4F_{10})]$ $- [\delta(F_7Xe_3F_8) + \delta(F_{11}Xe_5F_{12})]$
211(<1)[14]	207(<1)[<0.1]	217(<1)[1]	A, $\delta(F_5Xe_2F_6) + \delta(F_9Xe_4F_{10}) + \delta(F_7Xe_3F_8) + \delta(F_{11}Xe_5F_{12})$
211(<0.1)[25]	207(<0.1)[21]	216(<0.1)[20]	E, $[\rho_w(F_5Xe_2F_6) + \rho_w(F_7Xe_3F_8)] - [\rho_w(F_9Xe_4F_{10}) + \rho_w(F_{11}Xe_5F_{12})]$ or $[\rho_w(F_5Xe_2F_6) + \rho_w(F_9Xe_4F_{10})] - [\rho_w(F_7Xe_3F_8) + \rho_w(F_{11}Xe_5F_{12})]$
208(<1)[0]	201(<1)[0]	209(<1)[0]	B, $[\delta(F_1Xe_1F_2) + \delta(F_3Xe_1F_4)] - [\rho_w(F_5Xe_2F_6) + \rho_w(F_9Xe_4F_{10})]$ $+ [\rho_w(F_7Xe_3F_8) + \rho_w(F_{11}Xe_5F_{12})]$
187(1)[0]	193(<1)[0]	207(<1)[0]	B, $\rho_t(F_1Xe_1F_2) - \rho_t(F_3Xe_1F_4)$
160(1)[6]	156(1)[2]	160(<1)[2]	E, $\delta(F_1Xe_1F_3)$
121(1)[<1]	81(2)[1]	88(2)[1]	E, $\rho_t(XeOF_4)$
102(1)[<0.1]	63(1)[<0.1]	68(<1)[<0.1]	A, $XeOF_4 \cdot 4XeF_2$ def
91(<0.1)[0]	55(<0.1)[<0.1]	60(<0.1)[<0.1]	A, $XeOF_4 \cdot 4XeF_2$ def
86(8)[0]	50(3)[0]	54(3)[0]	B, $[\rho_t(F_5Xe_2F_6) + \rho_t(F_9Xe_4F_{10})] - [\rho_t(F_7Xe_3F_8) + \rho_t(F_{11}Xe_4F_{12})]$
88(1)[<1]	49(1)[<1]	53(1)[<1]	E, $4XeF_2$ def
72(<0.1)[<1]	40(<1)[<1]	44(<1)[<1]	A, $\rho_t(Xe_1F_1F_2F_3F_4)$
66(<1)[0]	38(2)[0]	41(2)[0]	B, $4XeF_2$ def
67(<1)[<0.1]	37(<1)[<1]	39(<1)[<1]	A, $XeOF_4 \cdot 4XeF_2$ breathing
57(1)[2]	31(1)[1]	33(1)[1]	E, $XeOF_4 \cdot 4XeF_2$ def
39(<0.1)[0]	24(1)[0]	24(1)[0]	B, $4XeF_2$ def
34(<1)[0]	21(<1)[<0.1]	21(<1)[<0.1]	A, $4XeF_2$ def
52(1)[1]	21(1)[<1]	22(<1)[<1]	E, $XeOF_4 \cdot 4XeF_2$ def
21(2)[0]	11(1)[0]	11(1)[0]	B, $4XeF_2$ def
30(<1)[<0.1]	–7(1)[1]	15(1)[1]	E, $XeOF_4 \cdot 4XeF_2$ def
–12(2)[0]	–16(4)[0]	–14(3)[0]	B, $4XeF_2$ def

[a] Values in parentheses denote calculated Raman intensities ($Å^4\ u^{-1}$) and values in square brackets denote calculated infrared intensities (km mol^{-1}). The aug-cc-pVTZ(-PP) basis sets were used. [b] The abbreviations denote stretch (ν), bend (δ), wag (ρ_w), twist (ρ_t), umbrella (δ_{umb}), deformation mode (def). See Figure 9.7a for the atom labeling scheme.

Table G6. Calculated Bond Lengths and Angles of $XeOF_4$ (C_{4v})[a]

	exptl[b]	calcd (C_{4v})[c]		
		SVWN	B3LYP	PBE1PBE
	Bond Lengths (Å)			
Xe–F_1	1.900(5)	1.939	1.949	1.924
Xe–O	1.70(1)	1.737	1.742	1.726
	Bond Angles (deg)			
F_1–Xe–F_2	90.0	89.9	89.9	89.9
F_1–Xe–F_3	180.0	180.0	180.0	180.0
O–Xe–F	91.8(5)	92.8	92.5	92.0

[a] See Figure 9.7a for the atom labeling scheme. [b] from Ref 103. [c] The aug-cc-pVTZ basis sets were used.

Table G7. Calculated Bond Lengths and Angles of XeF_2[a] and αKrF_2[b].

[c]	exptl	calcd ($D_{\infty h}$)[d]		
		SVWN	B3LYP	PBE1PBE
	Bond Lengths (Å)			
Xe–F_1	1.999(4)	1.993	2.012	1.986
Kr–F_1	1.894(5)	1.870	1.891	1.861
	Bond Angles (deg)			
F_1–Xe–F_2	180	180.0	180.0	180.0
F_1–Ng–F_2	180	180.0	180.0	180.0

[a] from Ref 262 [b] from Ref 126. [c] See Figure 9.7b for the atom labeling scheme. [d] The aug-cc-pVTZ(-PP) basis sets were used.

Table G8. Natural Bond Orbital NPA Charges, Valencies and Bond Orders of $2XeOF_4 \cdot NgF_2$ (Ng = Xe, Kr)[a]

	$2XeOF_4 \cdot XeF_2$ (C_{2h})[b]			$2XeOF_4 \cdot KrF_2$ (C_{2h})[c]		
	SVWN	B3LYP	PBE1PBE	SVWN	B3LYP	PBE1PBE
			Charges			
Xe_1	2.99	3.13	3.17	2.99	3.12	3.16
O_1	–0.78	–0.81	–0.84	–0.78	–0.81	–0.84
F_1	–0.57	–0.59	–0.59	–0.57	–0.59	–0.59
F_2	–0.57	–0.59	–0.59	–0.57	–0.59	–0.59
F_3	–0.55	–0.58	–0.58	–0.55	–0.57	–0.58
F_4	–0.55	–0.58	–0.58	–0.55	–0.57	–0.58
F_5	–0.58	–0.62	–0.63	–0.49	–0.52	–0.53
Ng	1.21	1.25	1.26	1.03	1.05	1.06
			Valencies			
Xe_1	2.76	2.66	2.54	2.76	2.66	2.54
O_1	0.87	0.84	0.81	0.87	0.84	0.81
F_1	0.41	0.39	0.36	0.41	0.39	0.37
F_2	0.41	0.39	0.36	0.41	0.39	0.37
F_3	0.41	0.39	0.37	0.41	0.40	0.37
F_4	0.41	0.39	0.37	0.41	0.40	0.37
F_5	0.42	0.37	0.37	0.42	0.37	0.38
Ng	0.73	0.62	0.64	0.72	0.64	0.68
			Bond Orders			
Xe_1–O_1	0.98	0.96	0.93	0.98	0.95	0.93
Xe_1–F_1	0.42	0.41	0.39	0.42	0.41	0.39
Xe_1–F_2	0.42	0.41	0.39	0.42	0.41	0.39
Xe_1–F_3	0.44	0.42	0.40	0.44	0.42	0.40
Xe_1–F_4	0.44	0.42	0.40	0.44	0.42	0.40
Xe_1---F_5	0.08	0.04	0.03	0.07	0.04	0.03
Ng–F_5	0.32	0.30	0.31	0.33	0.31	0.32

[a] The aug-cc-pVTZ(-PP) basis sets were used. [b] See Figure 9.7b for the atom labeling scheme. [c] See Figure 9.8b for the atom labeling scheme.

Table G9. Natural Bond Orbital NPA Charges, Valencies and Bond Orders of $XeOF_4 \cdot 4XeF_2$ and $XeOF_4 \cdot 2KrF_2$.[a]

$XeOF_4 \cdot 4XeF_2$ (C_4)[b]				$XeOF_4 \cdot 2KrF_2$ (C_1)[c]			
	SVWN	B3LYP	PBE1PBE		SVWN	B3LYP	PBE1PBE
				Charges			
Xe_1	3.01	3.14	3.18	Xe_1	3.00	3.14	3.18
O_1	–0.79	–0.82	–0.84	O_1	–0.79	–0.82	–0.84
F_1	–0.56	–0.58	–0.58	F_1	–0.57	–0.58	–0.59
				F_2	–0.57	–0.58	–0.59
				F_3	–0.57	–0.58	–0.59
				F_4	–0.57	–0.58	–0.59
Xe_2	1.19	1.23	1.24	Kr_1	1.00	1.03	1.05
F_5	–0.61	–0.63	–0.64	F_5	–0.52	–0.54	–0.55
F_6	–0.56	–0.59	–0.60	F_6	–0.46	–0.48	–0.49
				Kr_2	1.00	1.03	1.05
				F_7	–0.52	–0.54	–0.55
				F_8	–0.46	–0.48	–0.49
				Valencies			
Xe_1	2.53	2.44	2.54	Xe_1	2.79	2.44	2.53
O_1	0.80	0.80	0.81	O_1	0.87	0.80	0.81
F_1	0.35	0.35	0.36	F_1	0.41	0.35	0.37
				F_2	0.41	0.35	0.37
				F_3	0.41	0.35	0.37
				F_4	0.41	0.35	0.37
Xe_2	0.68	0.62	0.60	Kr_1	0.70	0.61	0.64
F_5	0.36	0.33	0.32	F_5	0.38	0.33	0.34
F_6	0.37	0.33	0.33	F_6	0.38	0.34	0.36
				Kr_2	0.70	0.61	0.64
				F_7	0.38	0.33	0.34
				F_8	0.38	0.34	0.36
				Bond Orders			
Xe_1–O_1	0.91	0.91	0.93	Xe_1–O_1	0.97	0.91	0.93
Xe_1–F_1	0.37	0.38	0.39	Xe_1–F_1	0.42	0.37	0.39
				Xe_1–F_2	0.42	0.37	0.39
				Xe_1–F_3	0.42	0.37	0.39
				Xe_1–F_4	0.42	0.37	0.39
Xe_1---F_5	0.03	0.01	0.01	Xe_1---F_5	0.07	0.02	0.03
				Xe_1---F_7	0.07	0.02	0.03
Xe_2–F_5	0.30	0.32	0.28	Kr_1–F_5	0.30	0.28	0.29
Xe_2–F_6	0.35	0.28	0.31	Kr_1–F_6	0.37	0.32	0.34
				Kr_2–F_7	0.30	0.28	0.29
				Kr_2–F_8	0.37	0.32	0.34

[a] The aug-cc-pVTZ(-PP) basis sets were used. [b] See Figure 9.7a for the atom labeling scheme. [c] See Figure 9.8a for the atom labeling scheme.

Table G10. Natural Bond Orbital (NBO) Natural Population Analysis Charges, Valencies, and Bond Orders for $XeOF_4$ (C_{4v})[a]

Atom	SVWN	B3LYP	PBE1PBE
		NPA Charges	
Xe	2.97	3.10	3.14
F	–0.55	–0.57	–0.58
O	–0.78	–0.80	–0.83
		Valence	
Xe	2.51	2.46	2.54
F	0.36	0.34	0.36
O	0.81	0.80	0.80
		Bond Order	
Xe–F	0.39	0.38	0.40
Xe–O	0.93	0.92	0.94

[a] The aug-cc-pVTZ(-PP) basis sets were used. See Figure 9.7 for the atom labeling scheme.

Table G11. Natural Bond Orbital (NBO) Natural Population Analysis Charges, Valencies, and Bond Orders for NgF_2 (Ng = Xe, Kr) ($D_{\infty h}$)[a]

	XeF_2			KrF_2		
Atom	SVWN	B3LYP	PBE1PBE	SVWN	B3LYP	PBE1PBE
			NPA Charges			
Ng	1.16	1.21	1.22	0.98	1.01	1.03
F	–0.58	–0.60	–0.61	–0.49	–0.51	–0.52
			Valencies			
Ng	0.63	0.56	0.59	0.70	0.59	0.62
F_1	0.33	0.30	0.31	0.35	0.31	0.33
			Bond Orders			
Ng–F_1	0.32	0.28	0.29	0.35	0.29	0.31

[a] The aug-cc-pVTZ(-PP) basis sets were used. See Figure 9.7 for the atom labeling scheme.